Winter 12-12-2023

Pathogenesis And Pharmacological Mitigation Of Influenza Viruses, Respiratory Syncytial Virus And SARS-CoV-2

Carolin M. Lieber
Georgia State University

Pathogenesis and Pharmacological Mitigation of Influenza Viruses, Respiratory Syncytial Virus and SARS-CoV-2

by

Carolin Maria Lieber

Under the Direction of Richard K. Plemper, Ph.D.

A Dissertation Submitted in Partial Fulfillment of the Requirements for the Degree of

Doctor of Philosophy

in the Institute for Biomedical Sciences

Georgia State University

2023

ABSTRACT

Innumerable future deaths and hospitalizations could be avoided through improved pandemic preparedness and the use of personalized medicine. Here, various animal models have been used to improve an understanding of the pathogenicity and therapeutic treatment potential of three viral pathogens that have a significant impact on public health: severe acute respiratory syndrome coronavirus 2 (SARS-CoV-2), respiratory syncytial virus (RSV), and influenza virus.

Roborovski dwarf hamsters were developed as a novel animal model to study SARS-CoV-2-induced acute lower respiratory tract injury. Dwarf hamsters recapitulate the pathogenicity of SARS-CoV-2 variants of concern (VOC) and demonstrate that the effect size of molnupiravir and paxlovid-like nirmatrelvir/ritonavir is VOC-dependent. Additionally, the ferret model of upper respiratory disease was used to study human-to-human-like transmission of SARS-CoV-2 and define a therapeutic window and human effect-size equivalent dose (HESED) for the approved drugs molnupiravir and paxlovid. Therapeutic administration of molnupiravir successfully prevented contact transmission, whereas paxlovid-like nirmatrelvir/ritonavir only partially reduced upper respiratory viral shedding. Moreover, the oral prodrug of remdesivir parent GS-441524 was shown to be efficacious against SARS-CoV-2 in ferrets.

A broad-spectrum polymerase inhibitor, 4'-Fluorouridine (4'-FlU), was identified and characterized, revealing potent activity against influenza virus, RSV, and SARS-CoV-2. This pre-clinical candidate is orally available and was shown to block replication of RSV in mice and SARS-CoV-2 in ferrets. In the mouse and ferret model, 4'-FlU mitigated lethal infection with pandemic human and highly pathogenic avian influenza. 4'-FlU could overcome moderate

resistance, making this candidate a promising first line defense broad-spectrum antiviral. In parallel, an allosteric orally efficacious AVG-inhibitor series, which targets a dynamic interface in the RSV polymerase, was further developed to proof-of-concept *in vivo* efficacy testing.

To explore a relationship between the gut microbiota and the host response to respiratory viral infections, the impact of the intestinal microbiome on influenza virus infection outcome was investigated. Colonization with segmented filamentous bacteria (SFB) in the gut stably and broadly altered the phenotype of alveolar macrophages (AM) enabling these cells to better protect their hosts from lethal respiratory viral infections. Moreover, gut microbiota-derived metabolites were discovered which conferred protection against SARS-CoV-2.

INDEX WORDS: pandemic preparedness, polymerase inhibitor, intestinal microbiome

Pathogenesis and Pharmacological Mitigation of Influenza Viruses, Respiratory Syncytial Virus and SARS-CoV-2

by

Carolin Maria Lieber

Committee Chair: Richard K. Plemper

Committee: Andrew T. Gewirtz

Timothy L. Denning

Electronic Version Approved:

Office of Academic Assistance – Graduate Programs

Institute for Biomedical Sciences

Georgia State University

October 2023

DEDICATION

I am dedicating this dissertation to my entire family who means the world to me. Especially, I would like to highlight my mum and dad, Marcella and Markus, for the sacrifice they made to support me throughout my life and all the love I have experienced. I also thank my two brothers, Fabian and Benjamin, for always cheering me up and protecting me. Lastly, I would like to express extreme appreciation to my friends, lab mates, and especially my fiancé, Richard, for his patience throughout my PhD.

ACKNOWLEDGEMENTS

First and foremost, I want to express my deepest appreciation to my mentor Dr. Richard K. Plemper. I experienced excellent guidance and support which prepared me for life and made me the person I am now – a scientist! His enthusiasm kept me motivated throughout my PhD. I especially would like to thank him for his endless patience and the option to explore new fields in his laboratory.

I would like to acknowledge the enormous contribution of Dr. Andrew T. Gewirtz and Dr. Timothy L. Denning for their support. I enjoyed all collaborations and Committee meetings throughout my PhD, and I am thankful for the great discussions we had.

A big thank you also to Dr. Oliver Planz who guided me during my master thesis and set an important milestone in my career.

To all current (Josef, Haeji, Jeong, Hongtao, Alex, Michael, Sujay, Yolian, Lauren, Amir, Devin) and former (Venice, Julien, Megha, Mart) members of the Plemper lab; Robert, Dillon, Tahirah and Ryan of the Cox lab; Vu from the Gewirtz lab; the Division of Animal Resources, the High Containment Core and everyone who helped me during the PhD – thank you for the support and conversations of the past years.

But most important of all, I would like to thank my mum and dad, Marcella and Markus, for making great childhood decisions for me and teaching me how to be curious in life. Thank you for making the foundation of my future!

TABLE OF CONTENTS

LIST OF TABLES

LIST OF FIGURES

PREFACE

I was born and raised in Germany where I had the perfect childhood, growing up without any concerns. I had the great honor of attending the University of Tuebingen for my bachelor's and master's degrees, during which I had an opportunity to study abroad at Newcastle University. Throughout the years spent completing my undergraduate and graduate education, I realized that I wanted a future career in research and was therefore very fortunate to have joined the IBMS PhD program at Georgia State University.

Foreshadowing my future career path, I recall that when I was five years of age my parents asked me what I wished for my birthday and I replied: "Mum, can you buy me a microscope – you know, the thing which magnifies all objects!" After receiving my birthday present, I analyzed everything and anything, including but not limited to dust, onion skins, hair, and fly wings. This was my earliest memory of wanting to be a scientist, driven by a curiosity to discover the unknown.

I believe that my dissertation is contributing to the general field of virology, and I hope that future students and scientists will read my work and believe in themselves despite the difficult times experienced throughout a PhD.

1. INTRODUCTION

The overarching goal of this dissertation was to identify, characterize, and efficacy profile broad-spectrum polymerase inhibitors against severe acute respiratory syndrome coronavirus 2 (SARS-CoV-2), respiratory syncytial virus (RSV), and influenza virus to improve disease management and enhance pandemic preparedness. Furthermore, this thesis contributes towards advancing personalized medicine by partially uncovering the well-orchestrated interplay of the gut microbiome and its effect on respiratory viral infections.

RNA-dependent RNA polymerase (RdRP) complexes are, in general, highly conserved across genera and even strain-to-strain, containing multiple domains that confer enzymatic functions essential for viral replication and thus, provide attractive therapeutic targets (Vicenti, Zazzi, & Saladini, 2021). Further, because the RdRP complex functions as both a replicase and transcriptase, selective antiviral targeting can affect the synthesis of progeny genomes and reduce the expression of viral proteins that, for example, antagonize the host antiviral response (Machitani, Yasukawa, Nakashima, Furuichi, & Masutomi, 2020). Mutations to the RdRP complex are often not well tolerated, resulting in a significant viral fitness penalty (Kabinger et al., 2021). Moreover, because viral polymerase inhibitors are not host-directed there is less potential for off-target cytotoxic effects, which can allow them to provide long-term efficacy (Tian et al., 2021).

1.1 Selected Respiratory Viruses

Three human respiratory RNA viruses were studied in this dissertation, SARS-CoV-2, RSV, and influenza virus, each of which causes numerous hospitalizations and deaths annually worldwide (table 1) (Abdelrahman, Li, & Wang, 2020; Griffiths, Drews, & Marchant, 2017;

Juozapaitis & Antoniukas, 2007; Tarsitani et al., 2021; Uyeki, 2017; Yu et al., 2019). RSV is the leading cause of bronchiolitis, viral pneumonia, respiratory failure, mechanical ventilation, and virus-associated death in infants (Smith, Seales, & Budzik, 2017). Invasion of the small airways by influenza virus can quickly lead to the advancement of severe disease and subsequently, viral pneumonia. Further, influenza viremia results in sepsis and can lead to multi-organ failure (Florescu & Kalil, 2014; Kido, Chida, Yao, & Wang, 2010; Lieber et al., 2023; Radovanovic et al., 2022).

Table 1 Estimated Annual Global Public Health Impact of SARS-CoV-2, RSV, and Influenza Virus

Virus	SARS-CoV-2	Respiratory syncytial virus	Influenza virus
Family	*Coronaviridae*	*Paramyxoviridae*	*Orthomyxoviridae*
Cases interpandemic years	No data yet	64,000,000 (NIH, 2022a)	1,000,000,000 (WHO, 2022)
Cases in a pandemic	close to 800 million (WHO, 2023)	Not applicable	1918 Spanish flu: 500 million (Taubenberger & Morens, 2006)
Deaths interpandemic year	No data yet	160,000	650,0000
Deaths in a pandemic	7,000,000	Not applicable	1918 Spanish flu: 20-100 million

Clinical signs of infection are comparable across SARS-CoV-2, RSV, and influenza virus disease, and include common manifestations such as upper respiratory cold-like symptoms, fever, myalgias, and malaise (Meletis et al., 2022). SARS-CoV-2 and influenza virus cause similar additional symptoms such as chills, headache, cough, rhinorrhea, pharyngitis, myalgias, malaise, gastrointestinal (GI) upset, and shortness of breath (Hui & Zumla, 2019; Keilman, 2019; Nypaver, Dehlinger, & Carter, 2021). Because of overlapping, ambiguous disease manifestation, the most accurate way to determine the causative agent is through appropriate testing (Meletis et al., 2022; Mostafa et al., 2021).

1.2 SARS-CoV-2

Severe acute respiratory syndrome coronavirus 2 (SARS-CoV-2), which caused the COVID-19 pandemic, is a single-stranded positive-sense RNA virus with a zoonotic origin (figure 1, made in Biorender) (Sharma, Ahmad Farouk, & Lal, 2021) that transmits via aerosols and respiratory droplets (C. C. Wang et al., 2021). SARS-CoV-2 infection has caused an exorbitant number of cases and deaths around the world since its first introduction into the human population in 2019 (table 1), as well as long-lasting health problems (Crook, Raza, Nowell, Young, & Edison, 2021) and economic burdens (Azzeri et al., 2022; Dubey et al., 2020). After viral spike (S) protein binds to the host cell receptor, angiotensin converting enzyme 2 (ACE2), the virus fuses with the cellular membrane, permitting entry into the cell (Hoffmann et al., 2020). After uncoating, primary translation and polyprotein processing have taken place; viral RNA synthesis and translation occur, followed by progeny particle assembly and exocytotic virion release (V'Kovski, Kratzel, Steiner, Stalder, & Thiel, 2021).

Several different waves of SARS-CoV-2 variants of concern (VOC) have occurred since the end of 2019 (Aleem, Akbar Samad, & Vaqar, 2023; Choi & Smith, 2021). The original isolates (Wuhan isolate and the first isolate in the US – Washington 1 (WA-1)) were rapidly replaced by VOC alpha, followed by VOC beta and VOC gamma as the virus continuously evolved in the human population (Gaebler et al., 2021), improving replicating efficiency and avoiding neutralizing antibody responses. VOC delta, which first occurred in May 2021, showed a high degree of lethality (Adamoski et al., 2022) and caused a peak in severe cases (Hu et al., 2021).

Although not sterilizing, vaccine-induced immunity continued to protect against advance to severe, life-threatening disease (Raman, Patel, & Ranjan, 2021). Due to high transmissibility, VOC omicron replaced VOC delta in November 2021 (Lauring et al., 2022) and a further reduced neutralizing capability of antibodies directed against earlier VOC resulted in large-scale break-through omicron infections in the population (Chenchula, Karunakaran, Sharma, & Chavan, 2022).

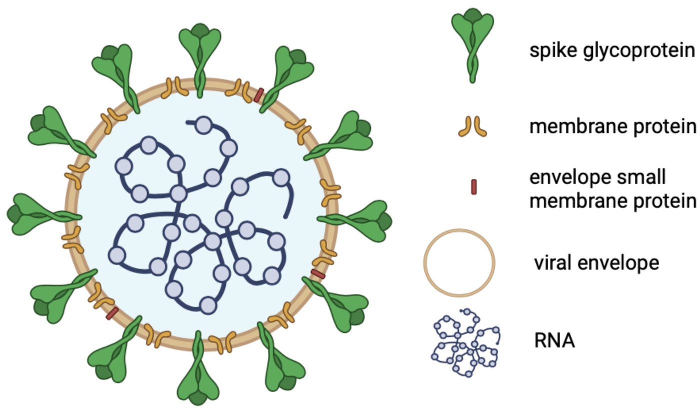

Figure 1 SARS-CoV-2 Schematic

1.3 Animal Models for SARS-CoV-2

During the recent pandemic, animal models, such as hamsters, mice, ferrets, and non-human primates, which were used to study SARS-CoV-2 pathogenesis and transmission dynamics, were instrumental for the rapid development of therapeutic agents and vaccines (H. Chu, Chan, & Yuen, 2022). Table 2 summarizes the most common models and provides insight into disease severity, whether a model can be used for transmission studies, and the scope of respiratory tract invasion ((H. Chu et al., 2022) – Chu et al., 2022 table 1, modified).

Table 2 Characteristics of Different Animal Models for In Vivo SARS-CoV-2 Studies

Animal model	Respiratory infection	Clinical disease	Transmission	Details or examples	Reference
Nonhuman primates	Robust virus replication in the upper and lower respiratory tracts	Mild to moderate	Efficient	Rhesus Macaques, Cynomolgus Macaques, Common Marmosets, Baboons	(H. Chu et al., 2022; Lu et al., 2020)
Ferrets	Robust virus replication in the upper respiratory tract	Mild	Efficient		(Cox, Wolf, Lieber, et al., 2021; Cox, Wolf, & Plemper, 2021; Lieber et al., 2022)
Wild-type mice	Robust virus replication in the lower and upper respiratory tracts, rapid viral clearance	Mild	No transmission	C57BL/6, BALB/c	(Brown et al., 2022; Uraki et al., 2022)
Transgenic mice	Robust virus replication in the upper and lower respiratory tracts, brain and other organs	Mild to lethal	Not efficient	Heterozygous K18-hACE2 C57BL/6J mice	(Oladunni et al., 2020; Ulbegi Polat et al., 2023; Uraki et al., 2022; Zheng et al., 2021)
Syrian Golden hamsters	Robust virus replication in the upper and lower respiratory tracts	Mild to moderate	Efficient		(Blaurock et al., 2022; Sia et al., 2020; Uraki et al., 2022)
Transgenic Syrian Golden hamsters	Robust virus replication in the upper and lower respiratory tracts	Mild to lethal	Not tested – most likely efficient transmission	K18-hACE2 transgenic hamster lines (line M51 and line M41)	(Golden et al., 2022; Uraki et al., 2022)

Roborovski dwarf hamsters	Robust virus replication in the upper and lower respiratory tracts	Mild to lethal	No transmission		(Cox et al., 2023; Lieber et al., 2022; Trimpert, Vladimirova, Dietert, Abdelgawad, Kunec, Dökel, et al., 2020)

1.4 Influenza Viruses

Influenza viruses belong to the Orthomyxoviridae family and are negative-sense single-stranded RNA viruses with a segmented genome (figure 2, made in Biorender) (Pleschka, 2013; Taubenberger & Kash, 2010).

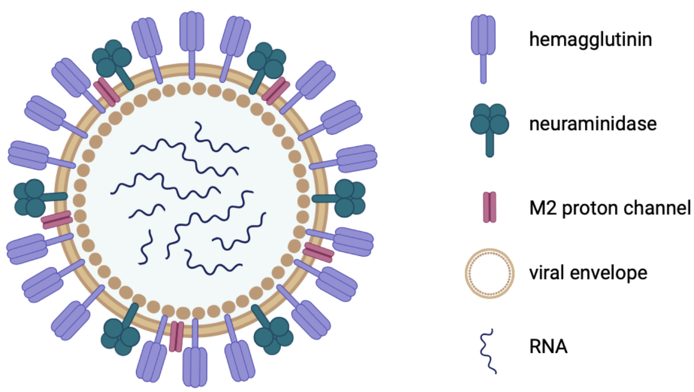

Figure 2 Influenza Virus Schematic

Influenza virus infects many avian and mammalian species (Zhang, Hale, Xu, & Sun, 2013) and is subtyped by antigenic surface glycoproteins (Hemagglutinin – HA and Neuraminidase – NA). All eight genes and their respective functions are listed in table 3 (Chauhan & Gordon, 2022), each of which are vital to the viral life cycle and, thus, need to be carefully combined when building and rescuing influenza viruses with various reporter functions through reverse genetics (Nogales, Baker, & Martínez-Sobrido, 2015).

Table 3 Overview Segments Influenza Virus

Gene	Function
Polymerase Basic Protein 1 (PB1)	Component of the RNA dependent RNA Polymerase (RdRP), endonuclease activity, elongation
Polymerase Basic Protein 2 (PB2)	Component of the RdRP, cap recognition
Polymerase Acidic protein (PA)	Component of the RdRP, protease
Hemagglutinin (HA)	Surface glycoprotein, receptor binding, fusion activity, major antigen
Neuraminidase (NA)	Surface glycoprotein, neuraminidase activity
Nucleocapsid Protein (NP)	RNA binding, RNA synthesis, RNA nuclear import
Matrix protein (M)	M1: matrix protein, interaction with viral ribonucleoprotein (vRNPs) and surface glycoproteins, nuclear export, budding; M2: membrane protein, ion channel activity, assembly
Non-Structural protein (NS)	NS1: multifunctional protein, viral IFN antagonist; NEP (nuclear export protein)/NS2: nuclear export of vRNPs

Influenza viruses affect 10% of the population every year and cause substantial morbidity, mortality and economic burden (table 1) (Uyeki, 2017). The efficacy of currently approved influenza antivirals is limited by the rapid emergence of viral resistance (Gaitonde, Moore, & Morgan, 2019) and even the approved vaccine, which is always based on the current dominant virus strains on the other hemisphere and therefore just a prediction (Steinbrück, Klingen, & McHardy, 2014), shows only moderate efficacy due to frequent antigenic drifts (process by which mutations in the HA head domain become fixed in the virus population and non-drifted variants are out-competed) (Krammer et al., 2018) and antigenic shifts (happens when influenza viruses swap gene segments – reassortment) (Webster & Govorkova, 2014).

Since the vaccine production timeline is approximately 6 months, highly specific vaccines can result in failures if the vaccine strain does not match the currently circulating strain (Bartley, Cadar, & Martin, 2021).

Influenza viruses have been the cause of several pandemics during the 20th and the 21st centuries (Elderfield & Barclay, 2011; Hsieh et al., 2006). The 1918 H1N1 pandemic (Spanish flu) was the worst outbreak of human infectious disease in history and caused up to 100 million deaths worldwide (also due to secondary infections, the catastrophic nutritional conditions in the aftermath of World War 1, and close quarters during troop movements) (Taubenberger & Morens, 2006). It was not until 1933 that the causative agent of influenza virus was discovered. An H2N2 pandemic affected the world in 1957 and then, in 1968, an H3N2 pandemic occurred (Akin & Gözel, 2020). H1N1 caused an additional pandemic in 1977 and more recently in 2009 (Akin & Gözel, 2020). During the swine-origin pandemic the severity of the disease was similar to seasonal influenza in uncomplicated cases showing low rates of infections, hospitalizations, and death in the elderly since neutralizing antibodies were still present from earlier exposures to the virus (Fineberg, 2014; Shanks & Brundage, 2012). Adding to the history of influenza, the recent "Bird Flu" (H5N1) distributed globally amongst birds (Sutton, 2018) and required in the 2021-2022 season poultry cullings of more than 49 million animals in the US alone (CDC, 2023c). Direct transmission of influenza from bird-to-human is fatal in 60% of cases; however, so far there have been less than 1,000 cases because the avian H5N1 strains are not yet capable of efficient human-to-human transmission (Wang, Zhu, Yang, & Shu, 2021).

1.5 Animal Models for Influenza Viruses

The three most frequently used animal models to study influenza viruses are mice, ferrets and guinea pigs. However, cotton rats, Syrian hamsters, cats, dogs, domestic pigs and non-human primates have also been used (Thangavel & Bouvier, 2014). An advantage of the ferret model is that the symptoms of an influenza virus infection mimic that of humans, displaying fever, nasal discharge, lethargy, weakness, anorexia, sneezing, and even multi-organ system dysfunction in severe cases (Lieber et al., 2023; Marriott et al., 2021). Furthermore, the ferret model can be used to study direct transmission events (Lieber et al., 2023). Mice (Bartley, Zhou, Kuchel, Weinstock, & Haynes, 2017; Eisfeld, Gasper, Suresh, & Kawaoka, 2018; Rodriguez, Nogales, & Martínez-Sobrido, 2017) and guinea pigs (Pica, Chou, Bouvier, & Palese, 2012) develop milder symptoms but the ease of handling, lower costs, and availability of reagents make these models, especially mice, a frequently used species for initial pre-clinical testing (Vandamme, 2014).

1.6 Respiratory Syncytial Virus

RSV (figure 3, made in Biorender), a member of the *Pneumoviridae* family, is the leading cause of viral deaths in infants worldwide (table 1) (Young & Smitherman, 2021). Reinfections can occur throughout life and can be life-threatening to elderly and/or immunocompromised patients (Falsey, Hennessey, Formica, Cox, & Walsh, 2005). Until May of 2023, the only approved immune prophylaxis was a humanized monoclonal antibody, palivizumab, that was administered to high-risk patients. However, high costs prohibited its broader application (Xu et al., 2021). On May 3rd 2023, the FDA approved the first vaccine for RSV in adults over 60 years of age (FDA, 2023a) and later that month a further vaccine was approved for the prevention of

RSV in adults of the same age range (Pfizer, 2023). The vaccines both contain the stabilized prefusion conformation of the RSV fusion protein (RSVpreF Abrysvo, Pfizer and RSVPreF3 Arexy, GSK) (CDC, 2023a; Leroux-Roels et al., 2023). Furthermore, the CDC now recommends a new preventive RSV shot in the form of a stabilized antibody (nirsevimab-alip) for all babies and toddlers (CNN, 2023; FDA, 2023b).

RSV transmits by means of respiratory droplets and direct contact with the virus (Williams, Sinha, Barr, & Zambon, 2021). Infected individuals are often contagious between 3-8 days and begin to shed virus as early as two days prior to symptom onset (CDC, 2023b).

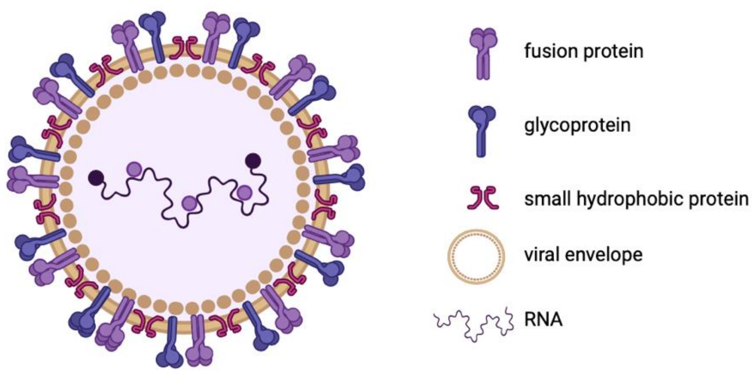

Figure 3 Respiratory Syncytial Virus Schematic

1.7 Animal Models for RSV

The main animal models for RSV are non-human primates, cotton rats, mice, and newborn lambs (Taylor, 2017). Most of these models (all except chimpanzees) are semi-permissive for RSV replication and experimental infection with the requirement of large inoculums. Clinical signs of disease are little or entirely absent.

RSV was first isolated from chimpanzees, when 14 out of 20 animals living in a captive colony showed respiratory illness characterized by coughing, sneezing and nasal discharge (Blount, Morris, & Savage, 1956) – the 6 animals which did not develop clinical signs had pre-existing RSV-specific serum antibodies. Chimpanzees shed large quantities of virus, which resembles efficient virus shedding from human hosts (Belshe et al., 1977; Crowe, Collins, London, Chanock, & Murphy, 1993), and remain the only animal model with animal-to-animal transmission (Taylor, 2017). Furthermore, chimpanzees have been used to evaluate the virulence and protective efficacy of vaccine candidates (Crowe, Bui, Davis, Chanock, & Murphy, 1994).

Rodents are more commonly used to study RSV infections and explore biomarkers for the host immune response and viral pathogenesis (Boukhvalova & Blanco, 2013; Openshaw, 2013). Cotton rats are semi-permissive for RSV replication, but approximately 100-fold more permissive than BALB/c mice (per inoculum dose of virus) (Byrd & Prince, 1997) with high virus titers in the lungs. Mice, especially BALB/c mice, show intermediate susceptibility (Prince, Horswood, Berndt, Suffin, & Chanock, 1979) and minimal clinical signs of disease. Humanized mice lacking $CD8^+$ T cells experience weight loss and pulmonary pathology characterized by peribronchiolar inflammation (Sharma et al., 2016; Taylor, 2017). Ferrets display RSV titers in the nasal lavages (Prince & Porter, 1976) and lung, and further species like guinea pigs and Syrian hamsters show low-level virus replication in the upper and lower respiratory tract (Hegele, Robinson, Gonzalez, & Hogg, 1993; Wright, Woodend, & Chanock, 1970). In addition, neonatal lambs can be infected and exhibit slight fever, cough and macroscopic lung lesions

(Olivier, Gallup, de Macedo, Varga, & Ackermann, 2009; Taylor, 2017). In this dissertation, mice were used as an experimental model of RSV disease.

1.8 Requirements for Broad Spectrum, First-line of Defense Antivirals

Poor pandemic preparedness has contributed to many deaths and severe cases in the COVID-19 pandemic and, more general, in the annual seasonal peaks of RSV and influenza virus infections (Godshall & Banach, 2021; Lieber & Plemper, 2022). Breakthrough infections are common even though vaccines were developed in a record time for SARS-CoV-2. Therefore, first-line of defense therapeutics are urgently needed, but successful candidates must respond to several requirements (Lieber & Plemper, 2022): first-line of defense antivirals must be orally bioavailable to efficiently reach outpatients, pre-approved for human use before the onset of a novel pandemic, carry a wide safety margin to allow administration to a wide patient population, and have a broad indication spectrum to target a range of viral pathogens of different families. Secondary development criteria include suitability for stockpiling at ambient temperature and established path to cost-effective production at scale in existing facilities.

1.9 Antivirals and Developmental Candidates Studied in this Dissertation

This dissertation evaluated six antiviral drugs and drug candidates. Table 4 provides general information, route of administration, and current approval status for human use for each of these.

Table 4 Overview Antiviral Drugs and Candidates Used in this Dissertation

Antiviral	General	Route	Viral Targets	Approval	References
Paxlovid (nirmatrelvir/ ritonavir)	Combination of two drugs: 3-chymotrypsin-like cysteine protease ($3CL^{pro}$) inhibitor nirmatrelvir and the antiretroviral drug ritonavir	Oral	SARS-CoV-2; ritonavir: discovered and used for HIV	Yes	(Cao et al., 2023; J. Liu et al., 2023; Owen et al., 2021)
Molnupiravir	Ester prodrug of N^4-hydroxycitidine (NHC), NHC-TP (TP: triphosphate) is incorporated by the viral polymerase into progeny viral antigenomes and genomes and induces viral error catastrophe	Oral	Broad-spectrum: influenza viruses, paramyxoviruses and pneumoviruses, alphaviruses and beta-coronaviruses	Yes (conditionally for SARS-CoV-2)	(Cox et al., 2022; Cox, Wolf, & Plemper, 2021; Lieber et al., 2022; Toots et al., 2020; Yoon et al., 2018)
Remdesivir (GS-441524)	Mono-phosphoramidate prodrug of a ribonucleoside analog	Intra-venously	Developed against RSV, first approved small molecule drug for treatment of COVID-19	Yes	(Gottlieb et al., 2022; Kokic et al., 2021; Pruijssers et al., 2020)
GS-621763	Oral prodrug of remdesivir parent	Oral	SARS-CoV-2	No	(Cox, Wolf, Lieber, et al., 2021)
4'-Fluorouridine (4'-FlU)	4'-FlU induces delayed/immediate chain termination after incorporation into the nascent RNA strand of RSV and SARS-CoV-2/ influenza viruses, respectively	Oral	Paramyxovirus and rhabdovirus families, beta-coronavirus SARS-CoV-2 and orthomyxo-viruses	No	(Lieber et al., 2023; Sourimant, Lieber, Aggarwal, et al., 2022)

AVG inhibitor series	Allosteric inhibitors of RSV RNA synthesis	Oral	RSV	No	(Cox et al., 2018; Sourimant, Lieber, Yoon, et al., 2022)

1.10 Microbiome Plays an Important Role in a Variety of Diseases

The effect of the microbiome on a variety of diseases (figure 4) (Oncodesign-services, 2023) shows the complexity of the interactions between the gut and other organs (El-Sayed, Aleya, & Kamel, 2021; Heintz-Buschart & Wilmes, 2018). The microbiome is a highly dynamic symbiotic bacterial population of an organism with frequent updates and publications (Gopalakrishnan, Helmink, Spencer, Reuben, & Wargo, 2018). An effort is being made to uncover links between the microbiome and organs. The gut-organ axis is a multi-directional and multi-channel communication system that allows the gut and extraintestinal organs to communicate with one another and is essential to understand how the gut microbiome affects human health (Fredell, 2023). A possible interplay of specific components of the microbiome and the host response to respiratory viral infections could have implications for viral disease outcome and uncover currently underappreciated risk correlates for advance of a patient to severe respiratory viral disease (El-Sayed et al., 2021).

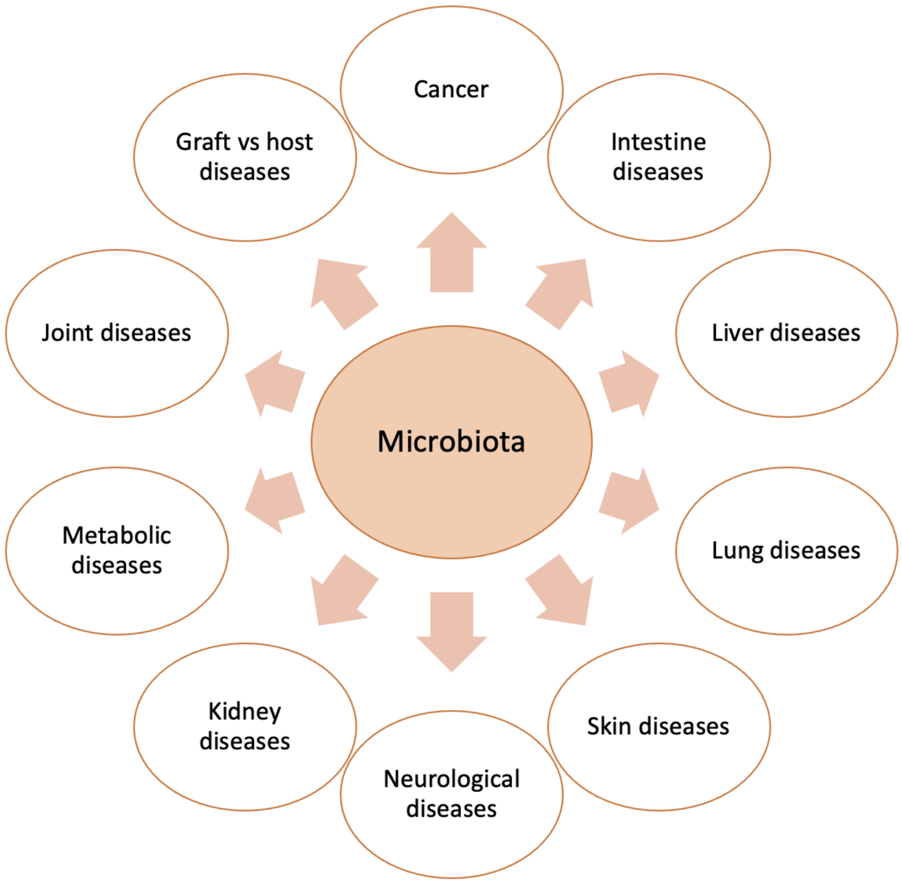

Figure 4 The Microbiome Plays an Important Role in a Variety of Diseases

The focus of the microbiome chapter of this dissertation is on two specific components of the microbiota. The first is segmented filamentous bacteria (SFB), a gram-positive, spore forming bacteria, which is a major contributor to spontaneous host resistance to rotavirus (RV) infection (Ngo, Shi, Jiang, & Gewirtz, 2023). The second is gut microbiota-derived metabolites like short-chain fatty acids (SCFA) which promote adaptive antiviral immunity (Brown et al., 2022).

2. RESULTS AND DISCUSSIONS

This dissertation is divided into four result sections based on thematic areas:

i) antiviral drug development and characterization with the goal to lower transmission of COVID-19 and improve future pandemic preparedness. In this section, a Roborovski dwarf hamster model of severe COVID-19-like lower respiratory tract disease was established and the impact of paxlovid and molnupiravir on controlling virus transmission determined.

ii) development of the first-in-class broad-spectrum viral polymerase inhibitor 4'-Fluorouridine (4'-FlU), which was shown to be orally efficacious against RSV, SARS-CoV-2 and influenza viruses. Current work focusses on the development of a full resistance profile of 4'-FlU against influenza viruses.

iii) discovery and characterization of a non-nucleoside, orally efficacious small-molecule inhibitor of the RSV RNA-dependent RNA polymerase. These studies identified a dynamic interface in the respiratory syncytial virus polymerase as novel druggable target.

iv) evaluation of a possible link between the microbiome composition and host susceptibility to severe respiratory viral disease. This sub-project identified microbiome-dependent reprogramming of alveolar macrophages as a determinant for severity of influenza virus disease in mice and revealed a protective role of short chain fatty acid-rich diet against SARS-CoV-2 infection.

Each of the following sections is organized around the relevant publications that summarize the results of my studies, providing for each title, author list, reference information, and the main article with figures formatted to the respective journal style. When applicable, links to publicly available supplementary information files are provided, which entail additional experimental results, in depth description of experimental methods, statistical analyses, all quantitative raw data, and large genomics and proteomics datasets.

2.1 Research Topic: SARS-CoV-2

2.1.1 SARS-CoV-2 VOC Type and Biological Sex Affect Molnupiravir Efficacy in Severe COVID-19 Dwarf Hamster Model

nature communications

Article

https://doi.org/10.1038/s41467-022-32045-1

SARS-CoV-2 VOC type and biological sex affect molnupiravir efficacy in severe COVID-19 dwarf hamster model

Received: 1 March 2022

Accepted: 14 July 2022

Published online: 29 July 2022

Check for updates

Carolin M. Lieber[1,5], Robert M. Cox[1,5], Julien Sourimant[1], Josef D. Wolf[1], Kate Juergens[2], Quynh Phung[2], Manohar T. Saindane[3], Meghan K. Smith[3], Zachary M. Sticher[3], Alexander A. Kalykhalov[3], Michael G. Natchus[3], George R. Painter[3], Kaori Sakamoto[4], Alexander L. Greninger[2] & Richard K. Plemper[1]

SARS-CoV-2 variants of concern (VOC) have triggered infection waves. Oral antivirals such as molnupiravir promise to improve disease management, but efficacy against VOC delta was questioned and potency against omicron is unknown. This study evaluates molnupiravir against VOC in human airway epithelium organoids, ferrets, and a lethal Roborovski dwarf hamster model of severe COVID-19-like lung injury. VOC were equally inhibited by molnupiravir in cells and organoids. Treatment reduced shedding in ferrets and prevented transmission. Pathogenicity in dwarf hamsters was VOC-dependent and highest for delta, gamma, and omicron. All molnupiravir-treated dwarf hamsters survived, showing reduction in lung virus load from one (delta) to four (gamma) orders of magnitude. Treatment effect size varied in individual dwarf hamsters infected with omicron and was significant in males, but not females. The dwarf hamster model recapitulates mixed efficacy of molnupiravir in human trials and alerts that benefit must be reassessed in vivo as VOC evolve.

By May 2022, SARS-CoV-2 has resulted in over 522 million cases and >6.2 million deaths worldwide[1]. Vaccines are widely available[2,3], but recuring global infection waves have been fueled by limited longevity of vaccine-induced immunity, the hesitancy of population subgroups to vaccinate[4,5], and increasingly contagious and/or vaccine-insensitive variants of concern (VOC) alpha (B.1.1.7 lineage), beta (B.1.351 lineage), gamma (P.1 lineage), delta (B.1.617.2 lineage), and omicron (B1.1.529 lineage)[6,7]. VOC delta was the prevalent circulating variant during Summer and Fall 2021 due to replication to high titers, prolonged shedding from infected individuals, and propensity to induce break-through infections in vaccinees[8–10]. Since its first appearance in November 2021, VOC omicron has rapidly replaced delta as the dominant circulating strain in most geographical regions[11], propelled by sharply reduced sensitivity to neutralizing antibodies directed against earlier lineages and greatly increased infectivity[12]. Although clinical signs associated with VOC omicron are typically milder than those of its predecessors, record-high daily infection rates have driven high absolute hospitalization numbers, creating an urgent need for therapeutics to improve disease management.

Molnupiravir was the first orally available SARS-CoV-2 inhibitor approved for outpatient use against COVID-19[13]. Intermediate results of the early months of a large efficacy trial revealed an encouraging 50% reduction in hospitalizations in the treatment group, but later analysis of the full dataset showed only a 30% lower hospitalization rate overall[14]. Based on the geographical location of trial participants and VOC prevalence in the earlier versus later phase of the trial, an

[1]Center for Translational Antiviral Research, Institute for Biomedical Sciences, Georgia State University, Atlanta, GA 30303, USA. [2]Virology Division, Department of Laboratory Medicine, University of Washington, Seattle, WA 98185, USA. [3]Emory Institute for Drug Development, Emory University, Atlanta, GA 30329, USA. [4]Department of Pathology, College of Veterinary Medicine, University of Georgia, Athens, GA 30602, USA. [5]These authors contributed equally: Carolin M. Lieber, Robert M. Cox. e-mail: rplemper@gsu.edu

advisory board to the FDA considered the lower efficacy of molnupiravir against VOC delta as a possible explanation for the mixed results[15]. However, VOC delta was efficiently inhibited by the molnupiravir parent metabolite N^4-hydroxycytidine (NHC) in ex vivo studies[16], suggesting unchanged sensitivity to the drug.

Human airway epithelium organoids, ferrets, mice, and Syrian golden hamsters have emerged as preclinical models to assess the efficacy of anti-SARS-CoV-2 drug candidates. Ferrets recapitulate the predominant clinical presentation of SARS-CoV-2 in younger patients, characterized by a high viral load in the upper respiratory tract, strong viral shedding, and efficient airborne transmission[17–19]. By contrast, Syrian golden hamsters infected with SARS-CoV-2 develop transient pneumonia but do not recapitulate hallmark features of life-threatening severe COVID-19. Disease typically remains mild-to-asymptomatic in golden hamsters and animals fully recover within two weeks[20]. Lethal disease with severe histopathology affecting lung, liver, and kidney can be induced in transgenic K18-hACE2 mice expressing human ACE2, but organ distribution of the receptor is non-physiological, resulting in rapid neuro-invasion of the virus and the development of acute, lethal viral encephalitis[21], which is not seen in human patients. Lacking is an efficacy model that recapitulates the acute lung injury of life-threatening COVID-19, thereby offering a relevant experimental platform to test the effect of molnupiravir on mitigating lung damage caused by different VOC and explore the impact of treatment on disease outcomes.

In this work, we test molnupiravir against a panel of VOC in cultured cells, human airway epithelium organoids, ferrets, and Roborovski dwarf hamsters, since these dwarf hamsters developed acute diffuse alveolar pneumonia and succumbed to infection[22,23] when infected with original SARS-CoV-2 isolates from 2020. We show that pathogenicity in dwarf hamsters is VOC-dependent with the highest lethality in the case of delta, gamma, and omicron. Independent of VOC tested, all molnupiravir-treated dwarf hamster survived infection, meeting a primary efficacy marker. However, the treatment effect size is VOC-specific and in animals infected with VOC omicron, virus load reduction was significant in males, but not females.

Results

For quantitative comparison of molnupiravir activity against VOC alpha, beta, gamma, delta, and omicron in cultured cells, we determined half-maximal antiviral concentrations (EC_{50}s) on VeroE6 cells stably expressing TMPRSS2 (Vero-TMPRSS2) (Fig. 1a). The molnupiravir parent compound NHC was used in all ex vivo experiments. Under these experimental conditions, inhibitory values were similar for the original SARS-CoV-2 WA1 isolate and all VOC tested, ranging from 0.19 (gamma) to 0.62 (beta) μM.

Consistent activity of molnupiravir against VOC in human airway organoids

To validate activity in disease-relevant primary human tissues, we added at the time of infection NHC at 10 μM, equivalent to NHC plasma concentrations reached in human patients[24], to the basolateral chamber of well-differentiated primary human airway epithelium (HAE) cultures grown at the air-liquid interface. After apical infection with the panel of five VOC, we titered apically shed progeny virions after 1, 2, and 3 days. The treatment instantly suppressed virus replication in the case of VOC alpha, beta, and delta, and within 2 days reduced the progeny load of all VOC to the level of detection (Fig. 1b). Parallel assessment of transepithelial electrical resistance (TEER) as an indicator of an intact tight junction network demonstrated that the drug preserved the integrity of the infected organoids (Supplementary Fig. 1). vehicle-treated controls showed significant reductions in TEER after infection, reflecting the breakdown of epithelium organization. Confocal microscopy confirmed that 10 μM basolateral NHC suppressed viral replication, whereas abundant viral antigen (SARS-CoV-2 nucleocapsid and spike protein) was detected in vehicle-treated epithelia (Fig. 1c, Supplementary Figs. 2, 3).

Efficacy of molnupiravir against VOC upper respiratory disease and transmission in ferrets

To assess in vivo efficacy of molnupiravir against VOC, we infected ferrets intranasally with 1×10^5 pfu of VOC alpha, beta, gamma, delta, and omicron and monitored virus replication in the upper respiratory tract. All treated animals were dosed orally at 5 mg/kg b.i.d., starting 12 hours after infection (Fig. 2a) when shed SARS-CoV-2 becomes first detectable in ferret nasal lavages[18,19]. Lavage titers were determined in 12-hour intervals for the first 48 hours after infection, and once daily thereafter. Titers of shed VOC alpha, gamma, delta, and omicron peaked 1–2 days after infection at approximately 10^3 to 10^4 pfu per ml in vehicle-treated animals (Fig. 2b). Treatment with molnupiravir reduced shed progeny titers of all VOC to detection level within 12 hours. Consistent with previous experience with the ferret model[18,19], infected animals developed no clinical signs. VOC beta did not establish a productive infection and was eliminated from further ferret experiments (Supplementary Fig. 3).

To explore the impact of treatment on transmission, we co-housed infected and treated source animals with uninfected and untreated sentinels for 48 hours, starting 42 hours after initiation of treatment (Fig. 2c). VOC delta was excluded from transmission studies, since we had not detected any infectious particles in nasal lavages of molnupiravir-treated animals at any time and nasal turbinates of treated animals extracted four days after infection did not contain any infectious particles (Supplementary Fig. 5). We tested VOC alpha in an independent transmission study, but included transmission arms in the efficacy studies with VOC gamma and omicron (Fig. 2b) to reduce overall animal numbers. After separation of source and contact animals on day 4 after infection, untreated sentinels were monitored for an additional four days for shed virions and viral RNA in nasal lavages, and then terminal titers in nasal turbinates were determined.

VOC alpha and gamma spread efficiently from vehicle-treated source animals to the sentinels (Fig. 2d, e), whereas VOC omicron did not transmit (Fig. 2f). RNA of VOC alpha and gamma became first detectable in nasal lavages of the contacts within 12 hours after initiation of co-housing, shed infectious particles emerged after 12 (VOC alpha) to 36 (VOC gamma) hours (Fig. 2e, f), and infectious alpha and gamma, but not omicron, particles were detectable in nasal turbinates extracted from sentinels of vehicle-treated source animals at study end (Supplementary Fig. 6). Treatment with molnupiravir fully suppressed transmission. No infectious particles or viral RNA were detectable in lavages of untreated sentinels, and nasal turbinates of these animals were virus and viral RNA-free at terminal assessment (Fig. 2e, f; Supplementary Fig. 6). These data demonstrate that oral molnupiravir is highly effective in controlling replication of all VOC in the ferret upper respiratory tract, significantly reducing shed virus titers and rapidly suppressing the spread of transmission-competent VOC to untreated naïve contacts.

Different degrees of acute lung pathogenesis of VOC in Roborovski dwarf hamsters

To explore VOC pathogenicity in a candidate model of lethal COVID-19, we infected Roborovski dwarf hamsters intranasally with 1×10^5 pfu each of the original SARS-CoV-2 WA1 isolate or VOC alpha, beta, gamma, and omicron, or 3×10^4 pfu of VOC delta (Fig. 3a) and monitored clinical signs and survival. Dwarf hamsters showed a rapid decline characterized by ruffled fur, lethargy, and dyspnea within two days of infection, which was accompanied by hypothermia and moderate to substantial loss of body weight (Fig. 3b, c). Severity and time to onset of clinical signs varied among—in order of increasing pathogenicity—VOC alpha, beta, omicron, gamma, and delta. Pathogenesis of VOC gamma was comparable to that of the original WA1 isolate. The

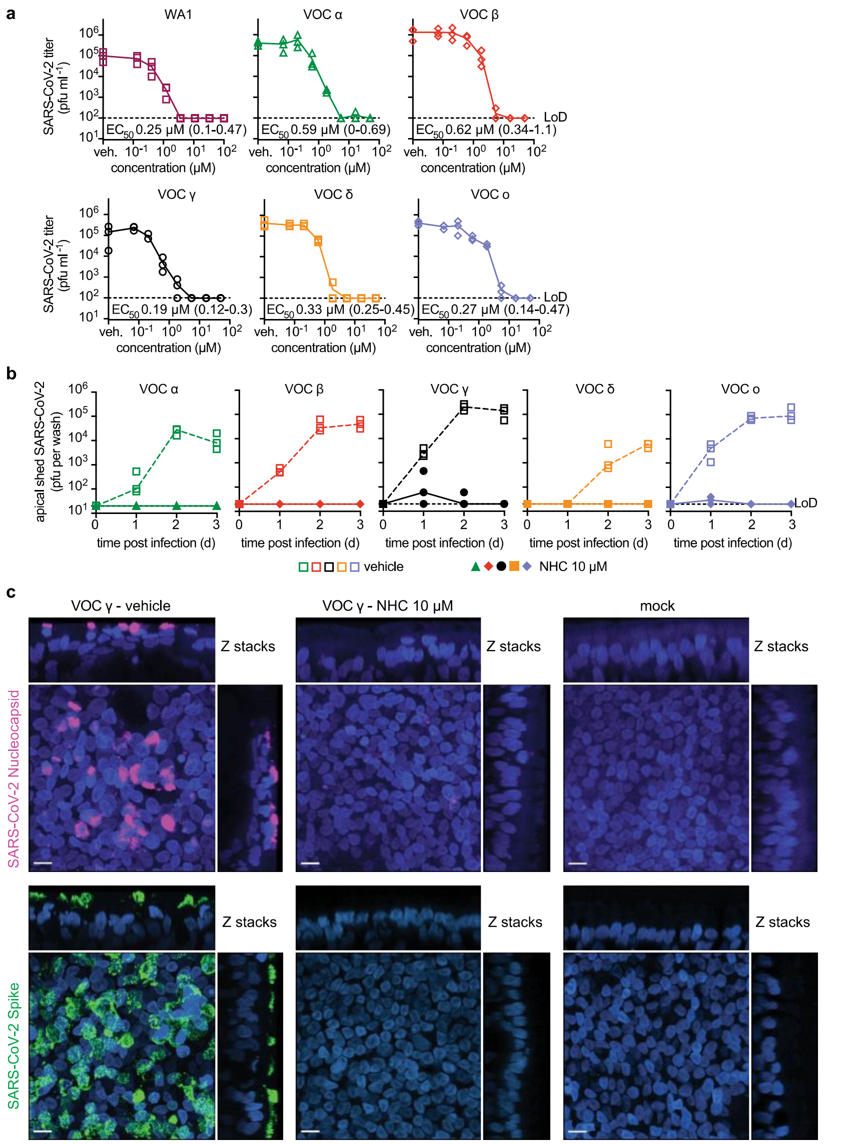

Fig. 1 | Efficacy of NHC against VOC in cultured cells and primary HAEs. **a** NHC dose-response assays against SARS-CoV-2 WA1 and VOC alpha, beta, gamma, delta, and omicron on VeroE6-TMPRSS2 cells. EC_{50} values from non-linear regression modeling are shown with 95% confidence intervals in parenthesis. **b** Activity of 10 μM basolateral NHC administered against VOC as in **a** on well-differentiated primary HAE organoids. Apically shed virus was harvested every 24 hours during a 3-day period after infection. **a**, **b** represent independent biological repeats, lines intersect group means. LoD limit of detection. **c** Confocal microscopy of primary HAE organoids infected with SARS-CoV-2 VOC gamma. Basolateral NHC suppresses virus replication at 10 μM. SARS-CoV-2 nucleocapsid (pink; α-SARS-CoV-2 nucleocapsid), SARS-CoV-2 spike (green; α-SARS-CoV-2 S) and nuclei (DAPI) were detected. Z stacks are shown, scale bars 10 μm. Per condition and viral target, two independent transwells were processed, one stained for SARS-CoV-2 spike and one for SARS-CoV-2 nucleocapsid; representative fields of view are shown. Source data are provided as a Source Data file.

median survival of infected animals was shortened to 5.75 (WA1), 6 (omicron), 3.5 (beta, gamma), and 3 (delta) days after infection (Fig. 3d; Table 1). Approximately 80% of animals inoculated with VOC alpha survived the infection, making alpha the least lethal of the VOC tested.

We intended to determine viral tissue tropism and gross lung pathology three days after infection of subsets of dwarf hamsters with WA1 or the VOC associated with the overall highest mortality rate, gamma, delta, and omicron. However, animals infected with delta succumbed to infection before the predefined endpoint, preventing analysis. Animals infected with WA1, gamma, or omicron consistently showed the highest viral RNA load in the lung, followed by the small and large intestine and spleen (Fig. 3e). Macroscopic analysis of extracted lungs showed substantial gross tissue damage involving large surface areas (Fig. 3f, Supplementary Fig. 7) and titration of lung homogenates confirmed fulminant viral pneumonia with median virus load of 1×10^5 pfu/g lung tissue or greater (Fig. 3g).

Article https://doi.org/10.1038/s41467-022-32045-1

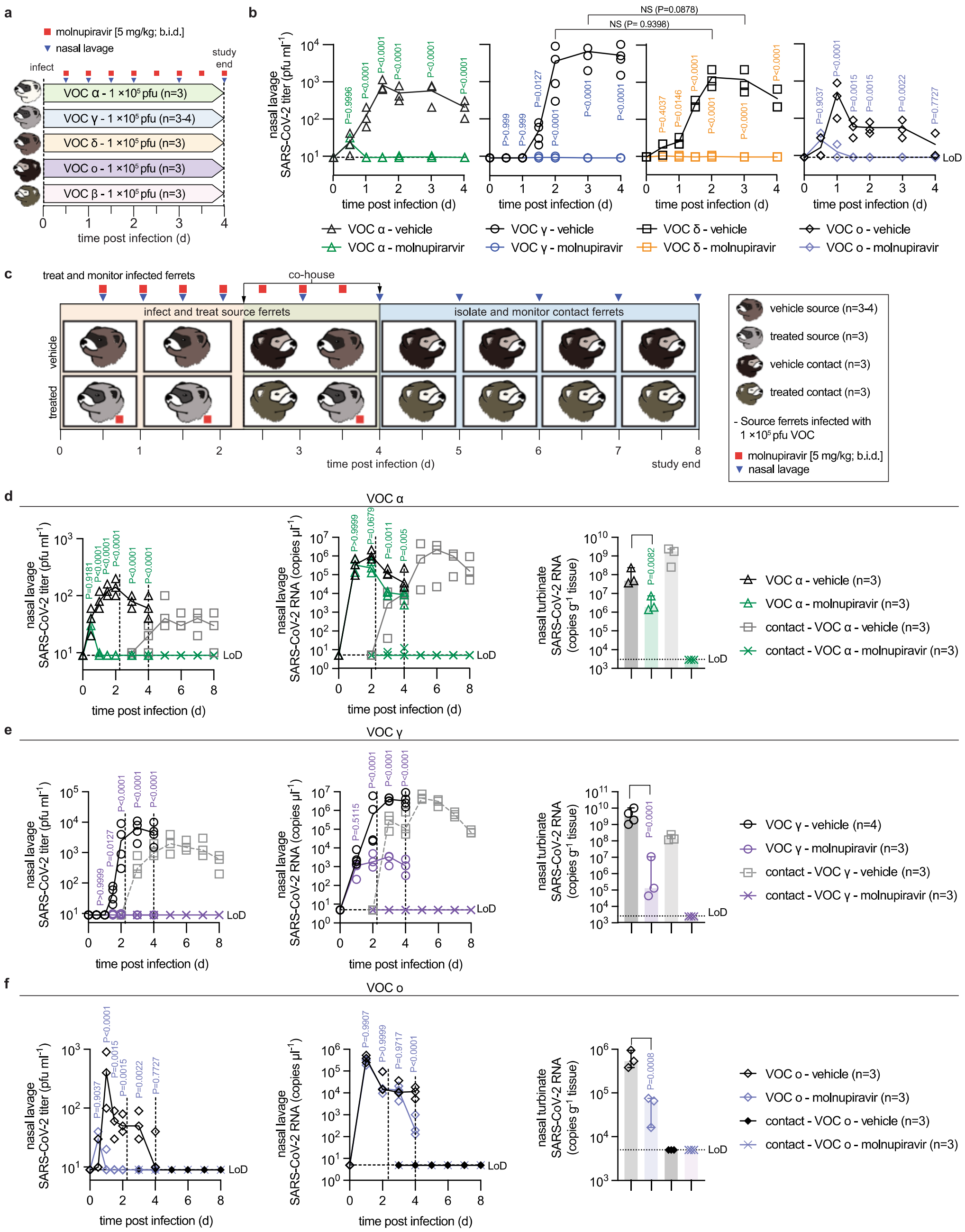

A follow-up study with VOC delta at reduced inoculum amount (1×10^4 pfu intranasally) and shortened time to analysis (Fig. 3h) demonstrated the onset of lung tissue damage (Fig. 3i, Supplementary Fig. 8) and presence of high lung virus loads (Fig. 3j) only 12 hours after infection. Comparison analysis of VOC gamma 24 hours after infection confirmed that rapid viral invasion of the dwarf hamsters was not limited to VOC delta.

Effect of VOC type and biological sex on prevention of lethal viral pneumonia

VOC gamma, delta, and omicron were selected for an efficacy study assessing mitigation of viral pneumonia and acute lung injury with molnupiravir. Animals were inoculated with 1×10^4 pfu intranasally to prevent premature death, followed by initiation of treatment (250 mg/kg orally b.i.d.) 12 hours after infection (Fig. 4a), when lung

Fig. 2 | Therapeutic molnupiravir is efficacious against a panel of VOC in ferrets. **a** Treatment and monitoring schematic. Ferrets ($n = 6$ total per VOC tested) were infected intranasally with 1×10^5 pfu of VOC and treated orally with vehicle or molnupiravir (5 mg/kg b.i.d.), starting 12 hours after infection. **b** Infectious SARS-CoV-2 titers in nasal lavages of vehicle or molnupiravir-treated animals. **c** Schematic of transmission studies with VOC alpha, gamma, and omicron. For VOC alpha, fresh source ferrets ($n = 6$) were used, for VOC gamma and omicron, transmission arms were added to **b**. Source animals were co-housed at a 1:1-ratio with uninfected and untreated contacts starting 42 hours after the beginning of treatment. Nasal lavages were obtained twice daily in the first 48 hours after infection, thereafter once daily. Nasal turbinates were extracted from source animals 4 days after infection and untreated sentinels continued for an additional 4 days. **d**–**f** Transmission study with VOC alpha (**d**), gamma (**e**), and omicron (**f**). Shown are infectious titers in nasal lavages (left), viral RNA copies in the lavages (center), and nasal turbinate titers (right). Symbols in **b**, **d**–**f** represent independent biological repeats (virus load of individual animals), lines (**b**, **d**–**f**) intersect group medians, and columns (**c**, **e**–**g**) show group medians ±95% confidence intervals. Statistical analysis with one-way (**d**–**f** turbinate titers) or two-way (**b**, **d**–**f** lavage titers) ANOVA with Tukey's (**d**–**f** turbinate titers) or Sidak's (**b**, **d**–**f** lavage titers) posthoc multiple comparison tests; *P* values are shown, NS not significant, LoD limit of detection. Source data are provided as a Source Data file.

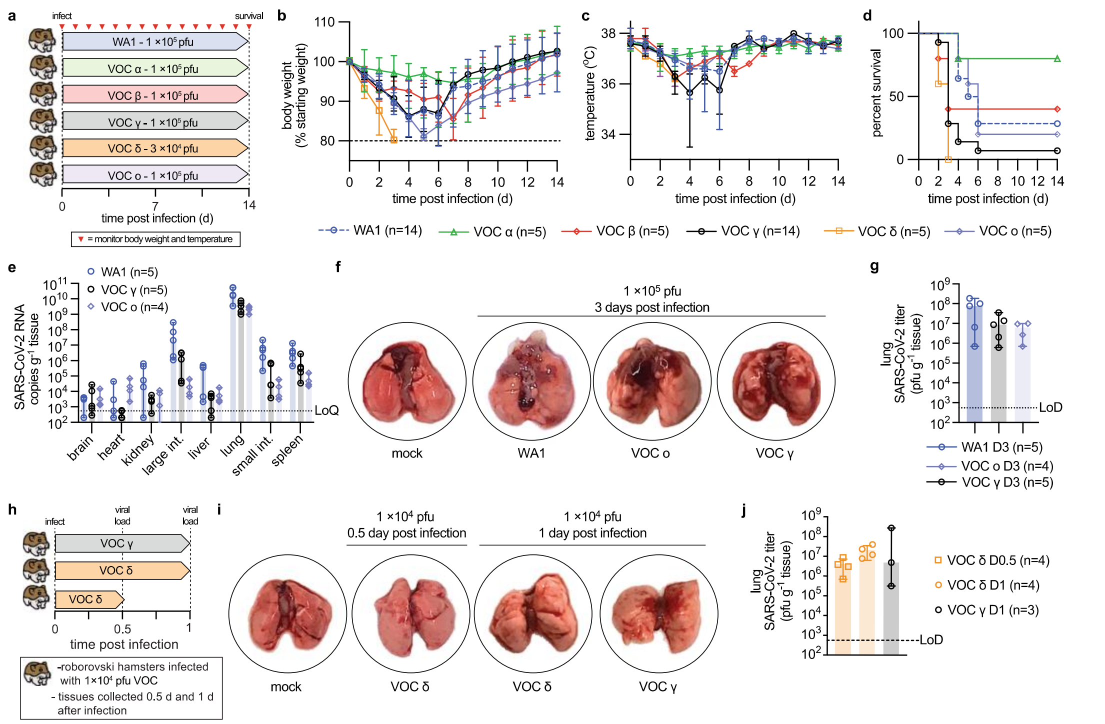

Fig. 3 | VOC pathogenesis in Roborovski dwarf hamsters. **a** Schematic of the dwarf hamster pathogenesis study. Animals were monitored for up to 14 days after intranasal infection with 1×10^5 pfu each (VOC delta 3×10^4 pfu per animal). Clinical signs were assessed once daily (red triangles). **b**, **c** Body weight (b) and temperature (c) of infected dwarf hamsters. **d** Survival curves of infected dwarf hamsters from **a**. **e** Viral RNA copies in select organs extracted from infected dwarf hamsters 3 days after infection. **f** Images of lungs from dwarf hamsters mock infected or inoculated with 1×10^5 pfu of WA1, VOC omicron, or VOC gamma 3 days after infection. **g** Infectious titers from the lungs of dwarf hamsters shown in **f**. **h** Schematic of the dwarf hamster pathogenesis study utilizing 1×10^4 pfu of VOC delta and gamma. **i** Images of lungs extracted from dwarf hamsters mock infected or inoculated with 1×10^4 pfu of VOC omicron or VOC gamma 0.5 (delta) and 1 day (delta and gamma) after infection. **j** Infectious titers from the lungs of dwarf hamsters shown in **i**. Symbols represent independent biological repeats (**e**, **g**, **j**), lines intersect group medians (**b**, **c**), columns show group medians (**e**, **g**, **j**), and error bars represent 95% confidence intervals. LoD limit of detection, LoQ limit of quantitation. Source data are provided as a Source Data file.

virus load was high and first lung lesions became detectable (Fig. 3i, j). The higher molnupiravir dose compared to that administered to ferrets was used to compensate for the high metabolic activity of the dwarf hamsters[25] and is consistent with the dose level administered to other rodent species[26,27]. Oral molnupiravir alleviated clinical signs (Supplementary Fig. 9) and ensured complete survival of all treated animals independent of VOC type, whereas approximately 50% (gamma) and 90% (delta, omicron) of animals in the vehicle groups succumbed to the infection within 2 to 7 days (Fig. 4b). Lung virus load assessed three days after infection was consistently high (approximately 10^7–10^8 pfu/g lung tissue) in all vehicle-treated groups (Fig. 4c). Treatment significantly lowered lung titers independent of VOC type, but effect size varied greatly from approximately 1 (delta) to over 4 (gamma) orders of magnitude. Although likewise statistically significant compared to vehicle-treated animals, the impact of molnupiravir on omicron lung load showed major variation between individual animals, creating low, high, and super responder groups characterized by lung titer reductions of ~1, 4, and >5 orders of magnitude, respectively (Fig. 4c). Infectious titers in the lung were closely mirrored by viral RNA copies present in lung and tracheas (Supplementary Fig. 10).

Having powered this study with approximately equal numbers of male and female animals in each group, we queried the dataset for a possible impact of biological sex on outcome (Fig. 4d). No significant

Table 1 | Analysis of dwarf hamster survival after infection with different VOC

ID	Median survival (d)	Survival (%)	Animal number (*n*)	Comparison	*P* value
WA1	5.75	28.571	14	–	n.a.
				VOC α	0.0873
				VOC β	0.6119
				VOC γ	0.0031
				VOC δ	<0.0001
				VOC ο	0.9988
VOC α	n.d.	80	5	–	n.a.
				VOC β	0.1591
				VOC γ	0.0032
				VOC δ	0.0031
				VOC ο	0.1177
VOC β	3	40	5	–	n.a.
				VOC γ	0.3278
				VOC δ	0.1729
				VOC ο	0.8741
VOC γ	3	7.143	14	–	n.a.
				VOC δ	0.0505
				VOC ο	0.0555
VOC δ	3	0	5	–	n.a.
				VOC ο	0.0031
VOC ο	6	20	5	–	n.a.

Significance of differences in survival curves was determined with a two-sided Log-rank (Mantel–Cox) test. Source data are provided as a Source Data file.

differences in lung virus load between males and females were detected in any of the three vehicle groups, which was consistent with the absence of a correlation between biological sex and probability of survival of the vehicle-treated animals in our survival study (Supplementary Fig. 11). Comparison of lung virus burden of males and females in the molnupiravir-treated groups revealed no statistically significant differences in effect size in animals infected with VOC gamma or delta, but biological sex had a statistically significant influence on molnupiravir benefit of animals infected with omicron (Fig. 4d, Table 2). Whereas lung titer reductions in treated males were highly significant compared to vehicle-treated males, females, or all vehicle-treated animals combined, no significant change in lung virus load against any of these vehicle groups was detected in females treated with molnupiravir.

Pharmacokinetic (PK) properties of molnupiravir in dwarf hamsters

To explore whether in the dwarf hamster model PK properties of molnupiravir are unexpectedly affected by biological sex of the animals, we determined plasma profiles and tissue distribution after a single oral molnupiravir dose of 250 mg/kg body weight, administered to groups of males and females. As observed in other species[28], the ester prodrug was rapidly hydrolyzed at intestinal absorption, leaving essentially only the molnupiravir parent NHC detectable in plasma samples (Fig. 5a). No major differences in PK parameters were observed between male and female dwarf hamsters (Fig. 5b, Supplementary Table 2). Tissue exposure of the corresponding bioactive anabolite NHC triphosphate (NHC-TP) was highest in spleen and lung, sustained in respiratory tissues at levels exceeding 10 nmol NHC-TP/g tissue over a ≥8-hour period after dosing, and consistent between male and female animals (Fig. 5c).

VOC-specific adaptation of SARS-CoV-2 in dwarf hamsters

In earlier studies with SARS-CoV-2 in the ferret model[18], we noted the rapid appearance of characteristic host adaptation mutations such as an L260F substitution in nsp6 and a Y453F mutation in spike[29] in virus populations extracted from ferret nasal turbinates. To probe for possible virus adaptations to the dwarf hamsters, we sequenced whole genomes of virus populations recovered from the different vehicle or molnupiravir treatment groups. No dwarf hamster-typical mutations were detected that were dominant across all VOC populations, but we detected several VOC type-specific substitutions with >20% allele frequency compared to the respective virus inoculum. Irrespective of treatment status, a spike D142G substitution was present in nearly all VOC delta populations, but no dominating mutations emerged in spike proteins of the different VOC gamma and omicron dwarf hamster reisolates (Supplementary Table 1). All recovered VOC gamma populations harbored an nsp6 V181F substitution and all VOC omicron populations contained the nsp6 L260F mutation that was originally considered to be characteristic for adaptation to weasels[18]. However, none of the recovered VOC delta populations contained substitutions in nsp6. We found isolated additional substitutions in some virus populations recovered from individual animals in the respective infection and treatment groups (Supplementary Table 1), but detected no correlation to relative viral fitness in vehicle-treated dwarf hamsters or link to molnupiravir treatment success.

Molnupiravir-mediated mitigation of lung histopathology

Macroscopic assessment of the lungs extracted three days after infection revealed severe tissue damage with large lesions covering ~30% (omicron) to 50% (gamma, delta) of the lung surface area of vehicle-treated animals (Fig. 6a, Supplementary Fig. 12). Molnupiravir treatment significantly reduced macroscopic tissue damage independent of VOC type (Fig. 6a, Supplementary Fig. 13). Histological examination of lungs extracted from animals infected with VOC gamma and delta revealed markers of severe viral infection in vehicle-treated animals, including perivascular cuffing, alveolitis, hyalinization of blood vessels, interstitial pneumonia, and leucocyte infiltration (Fig. 6b, Supplementary Fig. 14). One of the VOC gamma-infected animals developed pronounced peribronchiolar metaplasia. Due to the high lethality of VOC delta, only one animal of the vehicle group reached the predefined endpoint for tissue harvest in this study, whereas the others died prematurely and could not be examined. Molnupiravir alleviated histopathology associated with either VOC, decreasing immune cell infiltration and reducing signs of inflammation. Greater residual damage was detected in treated animals infected with VOC delta compared to gamma, which was consistent with the significantly greater molnupiravir-mediated reduction in gamma lung load detected in the efficacy study (Fig. 4c).

Immunohistochemistry analysis of the lung sections identified abundant viral antigen in animals of the vehicle-treated groups (Fig. 6c). Lung sections of molnupiravir-treated animals returned variable results depending on VOC, ranging from strong staining after infection with delta to complete absence of viral antigen after VOC gamma. This differential staining intensity recapitulated the differences observed in lung virus load and viral RNA copies after treatment of animals infected with VOC delta versus gamma (Fig. 4c, Supplementary Fig. 9). When we examined lung sections of molnupiravir-treated animals and surviving members of the vehicle groups two weeks after infection, no viral antigen was detectable and only minor signs of infection were visible (Supplementary Fig. 15), indicating that histopathological damage was transient in survivors.

These results demonstrate that acute lung injury occurs rapidly in the dwarf hamster model. Molnupiravir consistently improves clinical signs and overall disease outcomes independent of infecting VOC. However, the degree of lung virus load reduction is greatly affected by

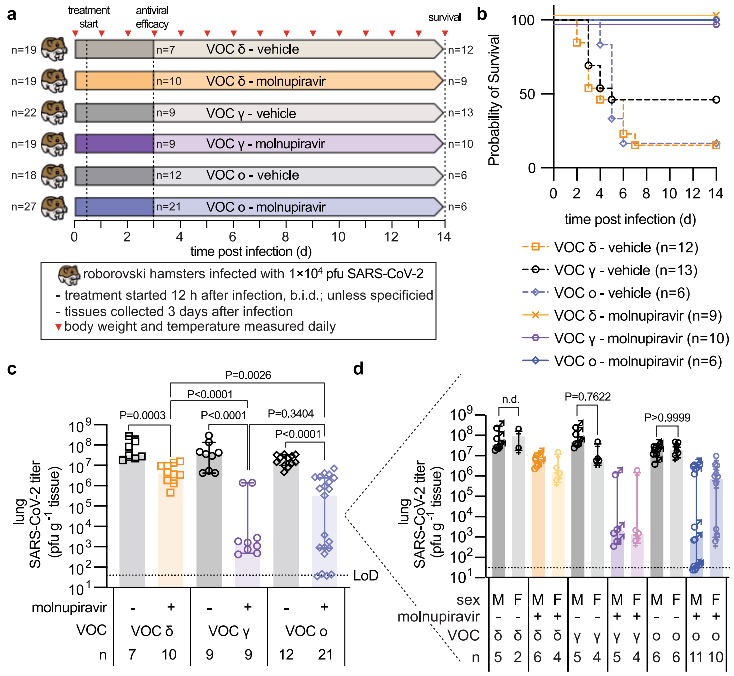

Fig. 4 | Effects of therapeutic molnupiravir on SARS-CoV-2 lung virus load. **a** Schematic of the dwarf hamster efficacy study. Animals were monitored for up to 14 days after intranasal infection with 1×10^4 pfu each. Clinical signs were assessed once daily (red triangles). Groups of dwarf hamsters were euthanized 3 days after infection to assess viral load and perform histological examinations. **b** Survival curves of infected dwarf hamsters from **a**. **c** Infectious titers from the lungs of dwarf hamsters 3 days after infection as shown in **a**. **d** Role of biological sex on antiviral efficacy shown in **c**. Symbols represent independent biological repeats, columns show group medians (**c**, **d**), and error bars represent 95% confidence intervals. Significance was determined using unpaired two-tailed *t* tests (**c**) or two-way ANOVA with Sidak's posthoc multiple comparison tests without further adjustments (**d**); *P* values are shown. Source data are provided as a Source Data file.

VOC type and, in the case of infection with VOC omicron, influenced by the biological sex of the treated animal.

Discussion

This study demonstrates efficacy of molnupiravir against relevant SARS-CoV-2 VOC alpha, gamma, delta, and omicron in human airway organoids, the ferret transmission model, and the Roborovski dwarf hamster model of life-threatening viral pneumonia. We show that the dwarf hamsters provide a robust experimental system to explore degrees of pathogenicity of different VOC[30–33]. The implications of these efficacy models for the anticipated pharmacological impact of molnupiravir are four-fold:

i. Direct antiviral potency of the molnupiravir parent NHC against all VOC including delta and omicron was virtually identical in cultured cells and human organoids, and closely resembled that reported for the original WA1 isolate[18]. We consider this outcome unsurprising since extensive past attempts to induce resistance to molnupiravir through adaptation of different viral targets had remained unsuccessful[28,34,35]. Based on a high genetic barrier preventing viral escape and the broad antiviral indication spectrum of molnupiravir[18,34,36], there is no molecular rationale why genetically closely related SARS-CoV-2 VOC that has no history of prior molnupiravir exposure should be inherently less sensitive to the drug.

ii. Treatment with molnupiravir significantly reduced VOC shedding from the upper respiratory tract of ferrets, shortening the time in which a host is infectious. Accordingly, molnupiravir suppressed transmission to untreated sentinels. No VOC-specific differences in drug efficacy were apparent. However, all VOC, but gamma, also grew to lower titers in the ferret upper respiratory tract than WA1[18] and omicron did not transmit at all. By contrast, original SARS-CoV-2 isolates spread readily between ferrets through contact and airborne transmission[37] and direct and reverse zoonotic transmission in the field have been reported for closely related minks[38]. Presumably reflecting increasing SARS-CoV-2 adaptation to the human host, this reduced ferret permissiveness for SARS-CoV-2 VOC interfered with a meaningful comparison analysis of treatment efficacy.

iii. It was speculated that the variable clinical performance of molnupiravir in the interim versus complete trial analysis could be attributable to lower effectiveness of the drug against VOC delta[15]. Delta indeed surged only when the trial was underway and a large subgroup of trial participants was enrolled from the South American region[14], in which gamma happened to be dominant until Fall 2021. By revealing a strong correlation between effect size of molnupiravir efficacy and VOC type under controlled experimental conditions, the dwarf hamster model suggests VOC-dependent therapeutic benefit as a tangible explanation for the clinical conundrum. At present we cannot conclusively address, however, whether the difference in virus load reduction between VOC gamma and delta in dwarf hamsters recapitulates the variable clinical success of molnupiravir because of a common mechanism or due to a phenocopy effect. Although VOC delta and gamma replicated to similar lung titers in vehicle-treated animals, delta was associated with the shortest time-to-death. Individual VOC could indirectly modulate molnupiravir PK properties differentially by spreading to organs other than lung with distinct kinetics. However, our analysis of viral organ distribution in the

https://doi.org/10.1038/s41467-022-32045-1

Table 2 | Analysis of biological sex as a variable in molnupiravir efficacy in dwarf hamsters

VOC delta		molnupiravir all	molnupiravir male	molnupiravir female
molnupiravir	all	n.a.	0.9992	0.987
molnupiravir	male	0.9992	n.a.	0.7337
molnupiravir	female	0.987	0.7337	n.a.
vehicle	all	0.0003	0.0126	0.0003
vehicle	male	0.0011	0.0272	0.0007
vehicle	female	n.d.	n.d.	n.d.

VOC gamma		molnupiravir all	molnupiravir male	molnupiravir female
molnupiravir	all	n.a.	0.9999	0.9999
molnupiravir	male	0.9999	n.a.	0.9999
molnupiravir	female	0.9999	0.9999	n.a.
vehicle	all	0.0001	0.0001	0.0001
vehicle	male	0.0001	0.0001	0.0001
vehicle	female	0.0006	0.0021	0.0056

VOC omicron		molnupiravir all	molnupiravir male	molnupiravir female
molnupiravir	all	n.a.	0.9889	0.9857
molnupiravir	male	0.9889	n.a.	0.5376
molnupiravir	female	0.9857	0.5376	n.a.
vehicle	all	0.0002	0.0001	0.0611
vehicle	male	0.0067	0.0012	0.2249
vehicle	female	0.0063	0.0012	0.2155

Significance was determined using two-way ANOVA with Sidak's multiple comparisons post-hoc test without further adjustments. Numbers specify *P* values; dark grey shading, *P* values >0.05; light grey shading, *P* values <0.05. Source data are provided as a Source Data file.

dwarf hamsters revealed very low viral RNA burden in liver, the primary site of drug metabolism[39], and sustained antiviral NHC-TP exposure levels were reached in all tissues but brain. Alternatively, the rapid-onset lung histopathology seen with VOC delta may directly contribute to lower effect size of therapy.

iv. Unexpectedly, molnupiravir efficacy against VOC omicron was variable between individual dwarf hamsters. Biological sex of the animals emerged as a correlate for therapeutic benefit of molnupiravir use against omicron, with treated males faring better overall than females. By contrast, biological sex had no effect on treatment benefit when dwarf hamsters were infected with VOC gamma or delta, which matched human trial data reported for these VOC[14]. Dwarf hamsters are outbred and animals used in this study were not raised under controlled conditions, introducing individual differences in body weight, age, microbiome, drug metabolism, and/or prior disease history as additional variables, which certainly are all equally present also in human patients. However, dwarf hamsters were randomly assigned to the different study groups and these factors, if indeed of importance, should have resulted in equal individual variation in viral load in the vehicle group or in animals infected with VOC gamma or delta. Whole genome sequence analysis of VOC omicron populations recovered from the dwarf hamsters at the end of infection revealed furthermore no correlation between potential differential VOC omicron adaptation to the dwarf hamster host and effect size of molnupiravir therapy, pointing overall to high variability of omicron disease dynamics in treated dwarf hamsters.

In the absence of controlled clinical data assessing molnupiravir efficacy against omicron, it is currently unclear to what degree the dwarf hamster-derived results extend to human therapy. Our study demonstrates, however, that pharmacological mitigation of severe COVID-19 is complex and that attempts to predict drug efficacy based on unchanged ex vivo inhibitory concentrations alone[16] may be premature. The dwarf hamster-based results illuminates that VOC-specific differences in treatment effect size may be present in vivo, alerting to the need to continuously reassess therapeutic benefit of approved antivirals for individual patient subgroups as SARS-CoV-2 evolves and potential future VOC may emerge.

Methods

Ethics statement

All experiments involving infectious SARS-CoV-2 were approved by the Georgia State Institutional Biosafety Committee under protocol B20016 and performed in BSL-3/ABSL-3 facilities at the Georgia State University.

All animal studies were performed in compliance with the Guide for the Care and Use of Laboratory Animals of the National Institutes of Health and the Animal Welfare Act Code of Federal Regulations. Experiments with SARS-CoV-2 involving ferrets and dwarf hamsters were approved by the Georgia State Institutional Animal Care and Use Committee under protocols A20031 and A21019, respectively.

Study design

This study used female ferrets (*Mustela putorius furo*) family mustelids, genus mustela, 6–10 months of age, and male and female Roborovski dwarf hamsters (*Phodopus roborovskii*), family cricetidae, genus phodopus, 3-10 months of age as in vivo models to assess the therapeutic efficacy of orally administered molnupiravir against infections with different SARS-CoV-2 VOC. Ferrets were used to examine the effect of molnupiravir on upper respiratory infection and transmission. Roborovski dwarf hamsters were used to study the effects of molnupiravir treatment on severe disease associated with lower respiratory tract infection and acute lung injury. VOC were administered to animals through intranasal inoculation. For ferrets, upper respiratory tract viral titers were assessed routinely through nasal lavages and upper respiratory tract tissues. For dwarf hamsters, animals were monitored twice daily for clinical signs, and viral loads were determined in respiratory tract tissues at endpoint. Virus loads were determined by plaque assays and RT-qPCR quantitation.

Cells

African green monkey kidney cells VeroE6 (ATCC CRL-1586™), Calu-3 (ATCC HB-55™), and VeroE6-TMPRSS2 (BPS Bioscience #78081) were cultivated at 37 °C with 5% CO_2 in Dulbecco's Modified Eagle's Medium (DMEM) supplemented with 7.5% heat-inactivated fetal bovine serum (FBS). Normal human bronchial/tracheal epithelial cells (NHBE) (Lonza

Article https://doi.org/10.1038/s41467-022-32045-1

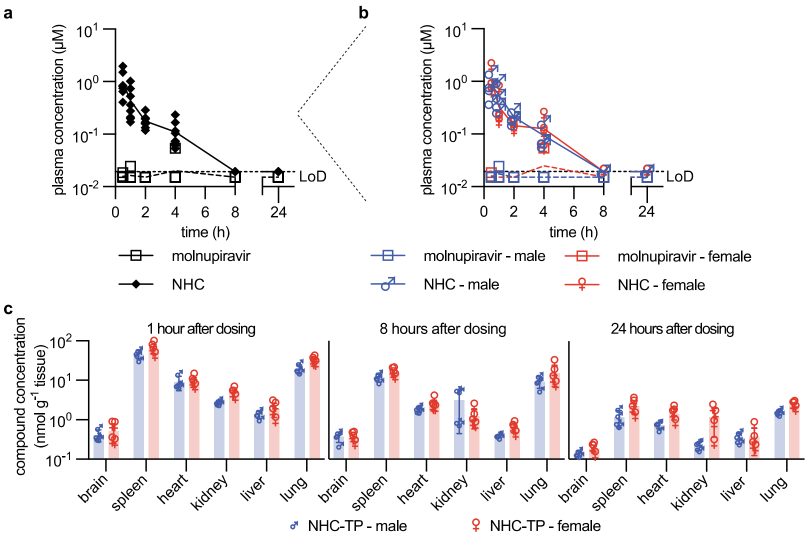

Fig. 5 | Single oral dose PK properties of molnupiravir in Roborovski dwarf hamsters. Male and female dwarf hamsters were gavaged with molnupiravir at (250 mg/kg body weight). **a** Plasma concentrations of molnupiravir and NHC, determined over a 24-hour period after dosing. **b** Plasma concentrations from **a**, showing male and female subgroups; LoD level of detection (0.0193 µM for NHC (shown); 0.0152 µM for molnupiravir). **c** Tissue distribution of NHC-TP 1-, 8-, and 24-hours after dosing in male and female dwarf hamsters. Symbols show results for individual animals (**a**–**c**), columns represent group means (**c**); $n = 4$ each per biological sex and time point (**a**–**c**). Source data are provided as a Source Data file.

Bioscience, cat# CC-2540S, lot# 0000646466, passage 3, donor M4) from a 38-year-old male were expanded in PneumaCult-Ex Plus (Stemcell Technologies cat# 05040) and differentiated in PneumaCult-ALI (Stemcell Technologies cat# 05001) for 8 weeks following the manufacturer's instructions. To protect the privacy of donors and tissue suppliers, Lonza Bioscience does not provide copies of donor records or tissue source agreements to customers. Lonza holds donor consent and legal authorizations that give permission for all research use. These consent and authorization documents do not identify specific types of research testing. If used for research purposes only, the donor consent applies. All cells were authenticated and checked for mycoplasma prior to use.

Antibodies

SARS-CoV-2 N and goblet cells were co-stained using rabbit anti-SARS-CoV-2 Nucleocapsid monoclonal antibody (HL453) (Invitrogen, cat# MA5-36272; validation datasheet at https://www.thermofisher.com/antibody/product/SARS-CoV-2-Nucleocapsid-Antibody-clone-HL453-Monoclonal/MA5-36272) (1:100 dilution) and mouse anti-MUC5AC (45M1) (ThermoFisher, cat# MA5-12175; validation datasheet at https://www.thermofisher.com/antibody/product/MUC5AC-Antibody-clone-45M1-Monoclonal/MA5-12175) (1:200 dilution) as primary antibodies, respectively. Donkey anti-goat (Alexa Fluor® 568 (ThermoFisher Scientific, cat# A-11057; validation datasheet at https://www.thermofisher.com/antibody/product/Donkey-anti-Goat-IgG-H-L-Cross-Adsorbed-Secondary-Antibody-Polyclonal/A-11057) and rabbit anti-mouse IgG (H + L) cross-adsorbed secondary antibody (Alexa Fluor® 488) (ThermoFisher Scientific, cat# A-11059; validation datasheet at https://www.thermofisher.com/antibody/product/Rabbit-anti-Mouse-IgG-H-L-Cross-Adsorbed-Secondary-Antibody-Polyclonal/A-11059) (1:500 dilution) were used as secondary antibodies. For staining of SARS-CoV-2 S, mouse anti-SARS-CoV-1 and 2 Spike protein monoclonal antibody (1A9) (Abcam, cat# ab273433; validation datasheet at https://www.abcam.com/sars-spike-glycoprotein-antibody-1a9-ab273433.html) (1:200 dilution) and goat anti-mouse IgG (H + L) highly cross-adsorbed secondary antibody (Alexa Fluor® 488) (Invitrogen, cat# A-11029; validation datasheet at https://www.thermofisher.com/antibody/product/Goat-anti-Mouse-IgG-H-L-Highly-Cross-Adsorbed-Secondary-Antibody-Polyclonal/A-11029) (1:500 dilution), were used as primary and secondary antibodies, respectively. For staining of ciliated cells, rabbit anti-beta IV tubulin recombinant antibody conjugated with Alexa Fluor® 647 (EPR16775) (Abcam, cat# ab204034; validation datasheet at https://www.abcam.com/alexa-fluor-647-beta-iv-tubulin-antibody-epr16775-ab204034.html) (1:100 dilution) was used.

Viruses

The following SARS-CoV-2 isolates were obtained from BEI resources, amplified on Calu-3 cells. SARS-CoV-2 (WA1; lineage A, isolate USA-WA1/2020, BEI cat# NR-52281), VOC alpha (lineage B.1.1.7, isolate USA/CA_CDC_5574/2020, BEI cat# NR-54011), VOC beta (lineage B.1.351, isolate hCoV-19/South Africa/KRISP-K005325/2020, BEI cat# NR-54009), and VOC gamma (lineage P.1., isolate hCoV-19/Japan/TY7-503/2021 (Brazil P.1), BEI cat# NR-54982). VOC delta (lineage B.1.617.2, clinical isolate #2333067) and VOC omicron (lineage B.1.1.529, WA-UW-21120120771) were obtained from the Northwestern Reference laboratory and amplified on Calu-3 cells. All viruses were authenticated by whole genome next-generation sequencing prior to use.

Virus yield reduction

12-well plates were seeded with 2×10^5 cells per well the day before infection. Each isolate was diluted in DMEM to achieve a multiplicity of infection of 0.1 pfu/cell, adsorbed on cells for 1 hour at 37 °C followings which the inoculum was removed and replaced with DMEM with 2% heat-inactivated FBS. The media contained additionally 0.1% DMSO (vehicle) and the indicated concentration of NHC (EIDD-1931). After 48 hours at 37 °C, the cell supernatant was harvested aliquoted, and frozen at −80 °C before titration by standard plaque assay. Log viral titers were normalized using the average top plateau of viral titers to define 100% and were analyzed through 4-parameter variable slope non-linear regression modeling slope to determine EC_{50} and 95% confidence intervals (Prism; GraphPad).

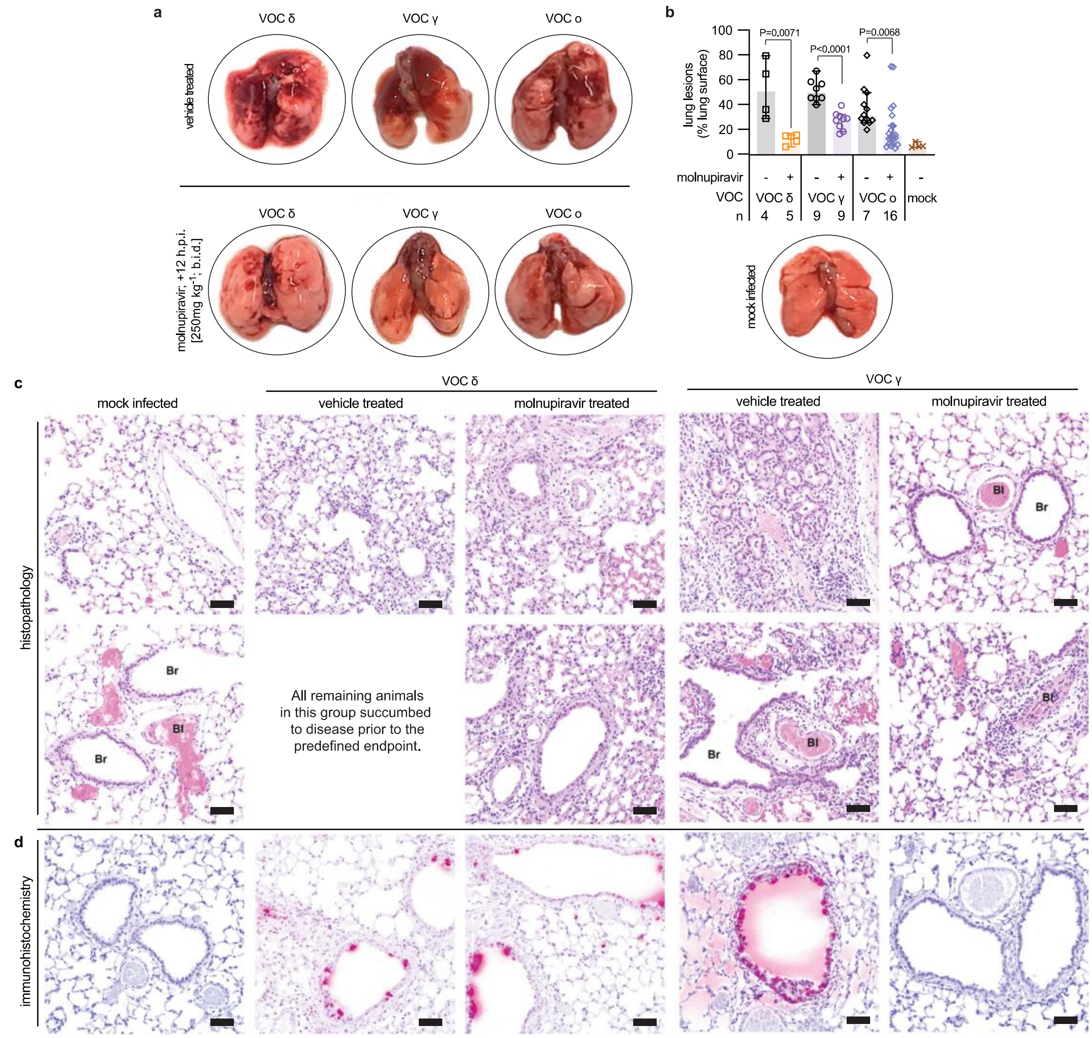

Fig. 6 | Molnupiravir mitigates lung histopathology in VOC-infected dwarf hamsters. a Images of lungs from dwarf hamsters mock infected or inoculated with 1×10^4 pfu of VOC delta, gamma, or omicron, treated with vehicle or molnupiravir, and harvested 3 days after infection. **b** Quantitation of macroscopic lesions as a percent of total visible lung surface area for infected dwarf hamsters treated with vehicle or molnupiravir; *n* values are shown. Mock infected lungs ($n = 4$) were included as a reference. Symbols represent independent biological repeats, columns show group medians. Significance was determined using unpaired two-tailed *t* tests; *P* values are shown. **c**, **d** Histopathology (**c**) and immunohistochemistry (**d**) of dwarf hamster lung slices from groups harvested 3 days after infection. Staining with hematoxylin and eosin (**c**) or α-SARS-CoV-2 S (**d**). Br bronchioles, Bl blood vessel, scale bar 50 µm. Each image represents tissue from an individual animal, all individual animals analyzed are shown in Supplementary Fig. 14. Source data are provided as a Source Data file.

Confocal microscopy

Eight-week differentiated HAE cells were infected (or mock-infected) with 3×10^4 pfu of SARS-CoV-2 VOC and fixed on day 3 after infection. For co-staining of SARS-CoV-2 N and goblet cells, cells were permeabilized for 30 minutes with a 200 µl apical overlay of PBS with 0.1% Triton X-100 and 3% bovine serum albumin (BSA), then the overlay was removed and cells were apically incubated with 100 µl of primary antibodies in wash buffer (PBS with 0.05% Tween20 and 0.3% BSA) for 1 hour at RT. After three 5-minute 200 µl-washes with wash buffer, cells were incubated with secondary antibodies in wash buffer for 1 hour at RT. Cells were subsequently incubated with Hoechst 34580 (1:1000 dilution in wash buffer) for 5 minutes and washed three times. Membranes were then excised and mounted using Prolong Diamond antifade mountant overnight at RT (ThermoFisher Scientific). For co-staining of SARS-CoV-2 S and ciliated cells, the same method was used with a saturation step with PBS with 0.05% Tween20 and 3% BSA in lieu of a permeabilization step. Image captures were performed with a Zeiss Axio Observer Z.1 and an LSM 800 confocal microscope with AiryScan, controlled with the Zeiss Zen 3.1 Blue software package (Windows 10). Representative pictures were taken with a ×63 Plan-Apochromat (NA: 1.40, oil) objective. Digital pictures are pseudocolored for optimal presentation. For clarity of presentation, the intensity of staining was digitally balanced in between different virus isolates with Zeiss Zen 3.1 Blue, while keeping the same processing for the conditions that are directly compared (vehicle vs treatment).

Plaque assay

Samples were serially diluted (tenfold dilutions starting at a 1:10 initial dilution) in DMEM medium supplemented with 2% FBS containing Antibiotic-Antimycotic (Gibco). The serial dilutions were added to Vero E6 cells seeded in 12-well plates at 3×10^5 cells per well 24 hours before. The virus was allowed to adsorb for 1 hour at 37 °C. Subsequently, the inoculum was removed, and the cells were overlaid with 1.2% Avicel (FMC BioPolymer) in DMEM and incubated for 3 days at 37 °C with 5% CO_2. After three days, the Avicel was removed, cells were washed once with PBS, fixed with 10% neutral buffered formalin, and plaques were visualized using 1% crystal violet. For dwarf hamsters infected with VOC gamma, delta, and omicron, plaque assays were performed with VeroE6-TMPRSS2 cells.

In vivo efficacy of molnupiravir in ferrets against VOC

Ferrets were purchased fromTriple F Farms, PA. Groups of ferrets were inoculated with 1×10^5 pfu of VOC alpha or delta (1 ml; 0.5 ml per nare). Twelve hours after infection, groups of ferrets were treated twice daily (b.i.d.) with vehicle (1% methylcellulose) or molnupiravir at a dose of 5 mg/kg in 1% methylcellulose. Treatments were administered by oral gavage and continued every 12 hours until 4 days after infection. All ferrets were euthanized 4 days after infection and tissues were harvested to determine SARS-CoV-2 titers and the presence of viral RNA.

Efficacy and contact transmission of VOC in ferrets

Two groups of six source ferrets were inoculated intranasally with 1×10^5 pfu of VOC alpha, gamma, or omicron. After 12 hours, groups of source ferrets were further divided into two groups, receiving vehicle ($n = 3$ for VOC alpha; $n = 4$ for VOC gamma) or molnupiravir treatment (5 mg/kg b.i.d.) administered by oral gavage. At 54 hours after infection, each source ferret was co-housed with uninfected and untreated contacts. Ferrets were co-housed until 96 hours after infection, when source ferrets were euthanized and contact ferrets were housed individually. All contact ferrets were monitored for 4 days after separation from source ferrets and then euthanized. Nasal lavages were performed on source ferrets twice daily until cohousing started. After cohousing started, nasal lavages were performed on all ferrets every 24 hours. Nasal turbinates were harvested for all ferrets after euthanization to determine infectious titers and the presence of viral RNA.

In vivo pathogenicity of VOC in dwarf hamsters

Female and male dwarf hamsters (2–4 months of age) were purchased from Dierengroothandel Ron Van Der Vliet, Netherlands. The dwarf hamsters were permanently quarantine-housed under ABSL-2 conditions until study start. After a minimum resting period of 2 weeks after arrival, animals were randomly assigned to groups for individual studies, transferred into an ABSL-3 facility immediately prior to study start, and housed singly in ventilated negative-pressure cages during the studies. To establish a pathogenicity profile, dwarf hamsters were inoculated intranasally with 1×10^5 pfu in 50 µl (25 µl per nare), unless otherwise stated (VOC delta 3×10^4). The dwarf hamsters were anaesthetized with dexmedetomidine/ketamine before inoculation. Groups of dwarf hamsters were euthanized 14 days after infection and their organs were harvested to determine the presence of viral RNA in different tissues (WA1 and VOC gamma only).

In vivo efficacy of molnupiravir in dwarf hamsters

Groups of dwarf hamsters were inoculated with 1×10^4 pfu in 50 µl (25 µl per nare). At 12 hours after infection, the dwarf hamsters were treated b.i.d. with vehicle (1% methylcellulose) or molnupiravir at a dosage of 250 mg/kg body weight, respectively. The compound was administered via oral gavage in 1% methylcellulose. After the start of treatment, b.i.d. dosing was continued until 12 days after infection. Subgroups of dwarf hamsters were euthanized 3 days after infection. All studies were terminated 14 days after infection. Organs were harvested to determine virus titers and the presence of viral RNA in different tissues. For PK studies, dwarf hamsters received a single oral dose of 250 mg/kg body weight molnupiravir. Blood was sampled at 0.5, 1, 2, 4, 8, and 24 hours after dosing from four animals per biological sex and plasma extracts prepared. Individual dwarf hamsters were sampled not more than twice. Organ samples were extracted 1, 8, and 24 hours after dosing. Molnupiravir, and NHC and its anabolites were analyzed using a qualified LC/MS/MS method[28], calculations with WinNonlin 8.3.3.33.

Titration of SARS-CoV-2 in tissue extracts

For virus titration, the organs were weighed and homogenized in PBS. The homogenates were centrifuged at $2000 \times g$ for 5 minutes at 4 °C. The clarified supernatants were harvested, frozen, and used in subsequent plaque assays. For detection of viral RNA, the harvested organs were stored in RNAlater at −80 °C. The tissues were homogenized, and the total RNA was extracted using a RNeasy mini kit (Qiagen).

Quantitation of SARS-CoV-2 RNA copy numbers

SARS-CoV-2 RNA was detected using the nCoV_IP2 primer-probe set (National Reference Center for Respiratory Viruses, Institute Pasteur) which targets the SARS-CoV-2 RdRP gene. RT-qPCR reactions were performed using an Applied Biosystems 7500 real-time PCR system using the StepOnePlus 2.1 real-time PCR package. The nCoV_IP2 primer-probe set (nCoV_IP2-12669Fw ATGAGCTTAGTCCTGTTG; nCoV_IP2-12759Rv CTCCCTTTGTTGTGTTGT; nCoV_IP2-12696bProbe(+) 5'FAM-AGATGTCTTGTGCTGCCGGTA-3'BHQ-1) was used in combination with TaqMan fast virus 1-step master mix (ThermoFisher Scientific) to detect viral RNA. A standard curve was created using a PCR fragment (nt 12669-14146 of the SARS-CoV-2 genome) generated from viral complementary DNA using the nCoV_IP2 forward primer and the nCoV_IP4 reverse primer to quantitate the RNA copy numbers. RNA copy numbers were normalized to the weight of tissues used.

SARS-CoV-2 genome sequencing

SARS-CoV-2 positive specimens were sequenced using metagenomic next-generation sequencing[40], Swift Biosciences SNAP panel[41], and/or Illumina COVIDSeq following the manufacturer's protocol. Sequencing reads were analyzed and visualized using cutadapt 1.9, bwa version 0.7.17, Picard 2.18.15, VarScan 2.3, Annovar 2018Apr16 version for the Longitudinal Analysis of Viral Alleles (LAVA; available at https://github.com/michellejlin/lava) pipeline with references MZ433225.1 for VOC gamma, NC_045512.2 for VOC delta, and OL965129.1 for VOC omicron[42]. Sequencing reads are available in NCBI BioProject PRJNA803552 (https://www.ncbi.nlm.nih.gov/bioproject/?term=PRJNA803552).

Statistics and reproducibility

The Microsoft Excel (versions 16.52) and Numbers (version 10.1) software packages were used for most data collection. The GraphPad Prism (version 9.1.0) software package was used for data analysis. Reverse transcription RT-qPCR data were collected and analyzed using the StepOnePlus (version 2.1; Applied Biosystems) software package. Figures were assembled using Adobe Illustrator (version CS6). Power analyses were carried out using GPower 3.1. T-tests were used to evaluate statistical significance between experiments with two sets of data. One- and two-way ANOVAs with Dunnett's, Tukey's, or Sidak's comparisons post-hoc tests without further modifications were used to evaluate statistical significance when more than two groups were compared or datasets contained two independent variables, respectively. Specific statistical tests are specified in the figure legends for individual studies. The Supplementary Dataset 1 summarize all statistical analyses (effect sized, P values, and degrees of freedom), respectively. Effect sizes between groups were calculated as $\eta^2 = \frac{SS_{effect}}{SS_{total}}$

for one-way ANOVA and $\omega^2 = \frac{SS_{effect} - (df_{effect}) \times (MS_{error})}{MS_{error} + SS_{total}}$ for two-way ANOVA; df_{effect}, degrees of freedom for the effect; SS_{total}, sum of squares for total; SS_{effect}, sum of squares for the effect; MS_{error}, mean square error. Effective concentrations for antiviral potency were calculated from dose-response datasets through four-parameter variable slope regression modelling. A biological repeat refers to measurements taken from distinct samples, and the results obtained for each individual biological repeat are shown in the figures along with the exact size (n, number) of biologically independent samples, animals, or independent experiments. The measure of the center (connecting lines and columns) is the mean throughout unless otherwise specified. The statistical significance level (α) was set to <0.05 for all experiments. Exact P values are shown in Supplementary Dataset 1 and in individual graphs when possible.

Reporting summary

Further information on research design is available in the Nature Research Reporting Summary linked to this article.

Data availability

The metagenomic sequencing reads generated in this study have been deposited in the NCBI BioProject database under accession code PRJNA803552. All other data generated in this study are provided in this published article and the Supplementary Information/Source Data file. Source data are provided in this paper.

Code availability

Metagenomic sequencing reads were analyzed and visualized using the LAVA pipeline[42] (available at https://github.com/michellejlin/lava). All commercial computer codes and algorithms used are specified in the Methods section.

References

1. WHO. *WHO Coronavirus (COVID-19) Dashboard*, <https://covid19.who.int> (2021).
2. Polack, F. P. et al. Safety and efficacy of the BNT162b2 mRNA Covid-19 vaccine. *N. Engl. J. Med.* **383**, 2603–2615 (2020).
3. Jackson, L. A. et al. An mRNA vaccine against SARS-CoV-2 - preliminary report. *N. Engl. J. Med.* **383**, 1920–1931 (2020).
4. Dror, A. A. et al. Vaccine hesitancy: the next challenge in the fight against COVID-19. *Eur. J. Epidemiol.* **35**, 775–779 (2020).
5. Fisher, K. A. et al. Attitudes toward a potential SARS-CoV-2 vaccine: a survey of U.S. adults. *Ann. Intern. Med.* **173**, 964–973 (2020).
6. Garcia-Beltran, W. F. et al. Multiple SARS-CoV-2 variants escape neutralization by vaccine-induced humoral immunity. *Cell* **184**, 2372–2383.e2379 (2021).
7. Zhou, D. et al. Evidence of escape of SARS-CoV-2 variant B.1.351 from natural and vaccine-induced sera. *Cell* **184**, 2348–2361 e2346 (2021).
8. Mlcochova, P. et al. SARS-CoV-2 B.1.617.2 Delta variant replication and immune evasion. *Nature* **599**, 114–119 (2021).
9. Reardon, S. How the Delta variant achieves its ultrafast spread. *Nature*, https://doi.org/10.1038/d41586-021-01986-w (2021).
10. Planas, D. et al. Reduced sensitivity of SARS-CoV-2 variant Delta to antibody neutralization. *Nature* **596**, 276–280 (2021).
11. Kupferschmidt, K. & Vogel, G. Omicron threat remains fuzzy as cases explode. *Science* **375**, 9–10 (2022).
12. Perez-Then, E. et al. Neutralizing antibodies against the SARS-CoV-2 Delta and Omicron variants following heterologous CoronaVac plus BNT162b2 booster vaccination. *Nat. Med.*, https://doi.org/10.1038/s41591-022-01705-6 (2022).
13. GOV.UK First oral antiviral for COVID-19, Lagevrio (molnupiravir), approved by MHRA https://www.gov.uk/government/news/first-oral-antiviral-for-covid-19-lagevrio-molnupiravir-approved-by-mhra. (2021).
14. Molnupiravir - US Food and Drug Administration (https://www.fda.gov/media/154472/download). (2021).
15. Kozlov, M. Merck's COVID pill loses its lustre: what that means for the pandemic. *Nature* (2021).
16. Prince, T. et al. Antiviral activity of molnupiravir precursor NHC against SARS-CoV-2 Variants of Concern (VOCs) and its therapeutic window in a human lung cell model. *bioRxiv* https://doi.org/10.1101/2021.11.23.469695 (2021).
17. Sourimant, J. et al. 4′-Fluorouridine is an oral antiviral that blocks respiratory syncytial virus and SARS-CoV-2 replication. *Science*, eabj5508 (2021).
18. Cox, R. M., Wolf, J. D. & Plemper, R. K. Therapeutically administered ribonucleoside analogue MK-4482/EIDD-2801 blocks SARS-CoV-2 transmission in ferrets. *Nat. Microbiol.* **6**, 11–18 (2021).
19. Cox, R. M. et al. Oral prodrug of remdesivir parent GS-441524 is efficacious against SARS-CoV-2 in ferrets. *Nat. Commun.* **12**, 6415 (2021).
20. Gruber, A. D., Firsching, T. C., Trimpert, J. & Dietert, K. Hamster models of COVID-19 pneumonia reviewed: how human can they be? *Vet. Pathol.*, 3009858211057197, https://doi.org/10.1177/03009858211057197 (2021).
21. Lee, C. Y. & Lowen, A. C. Animal models for SARS-CoV-2. *Curr. Opin. Virol.* **48**, 73–81 (2021).
22. Trimpert, J. et al. The Roborovski Dwarf hamster is a highly susceptible model for a rapid and fatal course of SARS-CoV-2 Infection. *Cell Rep.* **33**, 108488 (2020).
23. Zhai, C. et al. Roborovski hamster (Phodopus roborovskii) strain SH101 as a systemic infection model of SARS-CoV-2. *Virulence* **12**, 2430–2442 (2021).
24. Painter, W. P. et al. Human safety, tolerability, and pharmacokinetics of molnupiravir, a novel broad-spectrum oral antiviral agent with activity against SARS-CoV-2. *Antimicrob. Agents Chemother.* https://doi.org/10.1128/AAC.02428-20 (2021).
25. Bauer, B. A. & Besch-Williford, C. in *The Laboratory Rabbit, Guinea Pig, Hamster, and Other Rodents* (eds. M. A. Suckow, K. A. Stevens, & R. P. Wilson) Ch. 37, 935–946 (Academic Press, 2012).
26. Rosenke, K. et al. Orally delivered MK-4482 inhibits SARS-CoV-2 replication in the Syrian hamster model. *Nat. Commun.* **12**, 2295 (2021).
27. Wahl, A. et al. SARS-CoV-2 infection is effectively treated and prevented by EIDD-2801. *Nature* **591**, 451–457 (2021).
28. Toots, M. et al. Characterization of orally efficacious influenza drug with high resistance barrier in ferrets and human airway epithelia. *Sci. Transl. Med.* **11**, https://doi.org/10.1126/scitranslmed.aax5866 (2019).
29. Oude Munnink, B. B. et al. Transmission of SARS-CoV-2 on mink farms between humans and mink and back to humans. *Science* **371**, 172–177 (2021).
30. Fisman, D. N. & Tuite, A. R. Evaluation of the relative virulence of novel SARS-CoV-2 variants: a retrospective cohort study in Ontario, Canada. *CMAJ* **193**, E1619–E1625 (2021).
31. Ong, S. W. X. et al. Clinical and virological features of SARS-CoV-2 variants of concern: a retrospective cohort study comparing B.1.1.7 (Alpha), B.1.315 (Beta), and B.1.617.2 (Delta). *Clin. Infect. Dis.*, https://doi.org/10.1093/cid/ciab721 (2021).
32. Sheikh, A. et al. SARS-CoV-2 Delta VOC in Scotland: demographics, risk of hospital admission, and vaccine effectiveness. *Lancet* **397**, 2461–2462 (2021).
33. Nealon, J. & Cowling, B. J. Omicron severity: milder but not mild. *Lancet*, https://doi.org/10.1016/S0140-6736(22)00056-3 (2022).
34. Urakova, N. et al. beta-d-N (4)-hydroxycytidine is a potent anti-alphavirus compound that induces a high level of mutations in the viral genome. *J. Virol.* **92**, https://doi.org/10.1128/JVI.01965-17 (2018).

35. Agostini, M. L. et al. Small-molecule antiviral beta-d-N (4)-hydroxycytidine inhibits a proofreading-intact coronavirus with a high genetic barrier to resistance. *J. Virol.* **93**, https://doi.org/10.1128/JVI.01348-19 (2019).
36. Yoon, J. J. et al. Orally efficacious broad-spectrum ribonucleoside analog inhibitor of influenza and respiratory syncytial viruses. *Antimicrob. Agents Chemother.* **62**, https://doi.org/10.1128/AAC.00766-18 (2018).
37. Richard, M. et al. SARS-CoV-2 is transmitted via contact and via the air between ferrets. *Nat. Commun.* **11**, 3496 (2020).
38. Enserink, M. Coronavirus rips through Dutch mink farms, triggering culls. *Science* **368**, 1169 (2020).
39. Remmer, H. The role of the liver in drug metabolism. *Am. J. Med.* **49**, 617–629 (1970).
40. Greninger, A. L. et al. Rapid metagenomic next-generation sequencing during an investigation of hospital-acquired human parainfluenza virus 3 infections. *J. Clin. Microbiol.* **55**, 177–182 (2017).
41. Addetia, A. et al. Sensitive recovery of complete SARS-CoV-2 genomes from clinical samples by use of swift biosciences' SARS-CoV-2 multiplex amplicon sequencing panel. *J. Clin. Microbiol.* **59**, https://doi.org/10.1128/JCM.02226-20 (2020).
42. Lin, M. J., Shean, R. C., Makhsous, N. & Greninger, A. L. LAVA: a streamlined visualization tool for longitudinal analysis of viral alleles. *bioRxiv*, https://doi.org/10.1101/2019.12.17.879320 (2019).

Acknowledgements

We thank members of the GSU High Containment Core and the Department for Animal Resources for support, and A.L. Hammond for critical reading of the manuscript. This work was supported, in part, by Public Health Service grants AI071002 (to R.K.P.) and AI141222 (to R.K.P.), from the NIH/NIAID. The funders had no role in study design, data collection, interpretation, or the decision to submit the work for publication.

Author contributions

C.M.L., R.M.C., and R.K.P. conceived and designed the experiments. C.M.L., R.M.C., J.S., J.D.W., and R.K.P. conducted most of the experiments. K.J, Q.P., and A.L.G. performed next-generation sequencing. M.T.S. performed chemical synthesis. M.S., Z.S., and A.A.K. performed mass spectrometry analysis. M.G.N. and G.R.P. provided critical materials. K.S. performed histopathology of organ samples. C.M.L., R.M.C., J.S., A.L.G., and R.K.P. analyzed the data. R.M.C. and R.K.P. wrote the manuscript.

Competing interests

M.G.N. and G.R.P. are coinventors on patent 20190022116, N^4-Hydroxycytidine and derivatives and anti-viral uses related thereto, covering composition of matter and method of use of EIDD-2801 for antiviral therapy. This study could affect their personal financial status. All other authors declare no competing interests.

Additional information

Supplementary information The online version contains supplementary material available at https://doi.org/10.1038/s41467-022-32045-1.

Correspondence and requests for materials should be addressed to Richard K. Plemper.

Peer review information *Nature Communications* thanks Megan Shaw and the other anonymous reviewer(s) for their contribution to the peer review of this work. Peer review reports are available.

2.1.2 *Comparing Molnupiravir and Nirmatrelvir/Ritonavir Efficacy and the Effects on SARS-CoV-2 Transmission in Animal Models*

nature communications

Article https://doi.org/10.1038/s41467-023-40556-8

Comparing molnupiravir and nirmatrelvir/ritonavir efficacy and the effects on SARS-CoV-2 transmission in animal models

Received: 28 November 2022

Accepted: 1 August 2023

Published online: 07 August 2023

Check for updates

Robert M. Cox[1,5], Carolin M. Lieber[1,5], Josef D. Wolf[1], Amirhossein Karimi[1], Nicole A. P. Lieberman[2], Zachary M. Sticher[3], Pavitra Roychoudhury[2], Meghan K. Andrews[3], Rebecca E. Krueger[3], Michael G. Natchus[3], George R. Painter[3,4], Alexander A. Kolykhalov[3], Alexander L. Greninger[2] & Richard K. Plemper[1]

Therapeutic options against SARS-CoV-2 are underutilized. Two oral drugs, molnupiravir and paxlovid (nirmatrelvir/ritonavir), have received emergency use authorization. Initial trials suggested greater efficacy of paxlovid, but recent studies indicated comparable potency in older adults. Here, we compare both drugs in two animal models; the Roborovski dwarf hamster model for severe COVID-19-like lung infection and the ferret SARS-CoV-2 transmission model. Dwarf hamsters treated with either drug survive VOC omicron infection with equivalent lung titer reduction. Viral RNA copies in the upper respiratory tract of female ferrets receiving 1.25 mg/kg molnupiravir twice-daily are not significantly reduced, but infectious titers are lowered by >2 log orders and direct-contact transmission is stopped. Female ferrets dosed with 20 or 100 mg/kg nirmatrelvir/ritonavir twice-daily show 1–2 log order reduction of viral RNA copies and infectious titers, which correlates with low nirmatrelvir exposure in nasal turbinates. Virus replication resurges towards nirmatrelvir/ritonavir treatment end and virus transmits efficiently (20 mg/kg group) or partially (100 mg/kg group). Prophylactic treatment with 20 mg/kg nirmatrelvir/ritonavir does not prevent spread from infected ferrets, but prophylactic 5 mg/kg molnupiravir or 100 mg/kg nirmatrelvir/ritonavir block productive transmission. These data confirm reports of similar efficacy in older adults and inform on possible epidemiologic benefit of antiviral treatment.

Vaccines and antivirals have helped to limit disease severity in the coronavirus disease 2019 (COVID-19) pandemic. However, extensive viral spread continues, affecting even those with vaccine or naturally-acquired immunity[1–3]. The rise of new SARS-CoV-2 variants of concern (VOC) capable of escaping preexisting immunity has undermined the hope of rapidly ending the pandemic through large-scale vaccination campaigns[1,4,5], and indirect immune imprinting may never allow vaccine boosters to be successful against future viral evolution. In 2021,

[1]Center for Translational Antiviral Research, Georgia State University Institute for Biomedical Sciences, Atlanta, GA 30303, USA. [2]Virology Division, Department of Laboratory Medicine and Pathology, University of Washington, Seattle, WA 98185, USA. [3]Emory Institute for Drug Development, Emory University, Atlanta, GA, USA. [4]Department of Pharmacology, Emory University, Atlanta, GA 30322, USA. [5]These authors contributed equally: Robert M. Cox, Carolin M. Lieber. e-mail: rplemper@gsu.edu

Article https://doi.org/10.1038/s41467-023-40556-8

the FDA granted emergency use authorizations for two orally available antivirals, molnupiravir and paxlovid[6,7]. Molnupiravir, a prodrug of the broad-spectrum nucleoside analog N[4]-hydroxycytidine[8], targets the viral RNA polymerase, triggering lethal viral mutagenesis[9,10]. Paxlovid consists of two components, the peptidomimetic viral main protease (M^{pro}) inhibitor nirmatrelvir and the cytochrome P450 enzyme inhibitor ritonavir[11], which is required to improve pharmacokinetic properties of nirmatrelvir. Having formed covalent dead-end complexes with nirmatrelvir, M^{pro} is unable to process the viral polyprotein, interrupting the viral replication cycle. Initial phase II/III clinical trials suggested superior efficacy of paxlovid compared to molnupiravir, reporting 89% versus 30% reduction in patient hospitalization and death[12,13].

These initial data and extensive public discussion of possible carcinogenic potential of molnupiravir triggered elevation of paxlovid to standard-of-care (SOC)-like status for treatment of vulnerable patient populations in the United States[14]. However, a carcinogenicity study in the Tg.rasH2 mouse model to assess carcinogenic potential of molnupiravir demonstrated that continuous dosing for 6 months was not carcinogenic[15], addressing speculations about drug safety. Recent large-scale clinical trials and retrospective assessments of therapeutic benefit have revealed that efficacy of paxlovid is substantially lower than initially seen against VOC delta[12,16,17], whereas therapeutic benefit of molnupiravir in older adults was underestimated[15,17] and molnupiravir treatment reduced the time to first recovery of high-risk vaccinated adults by ~4 days[18]. In these studies, neither drug provided significant therapeutic benefit to younger adults below 65 years of age[12,19].

Assessing the effect of post-exposure prophylactic treatment of household contacts of a confirmed SARS-CoV-2 case with paxlovid, the Evaluation of Protease Inhibition for COVID-19 in Post-Exposure Prophylaxis (EPIC-PEP) trial showed a slight reduction of preventing transmission, but benefit was not statistically significant[20,21]. Preliminary results of the comparable prevention of household transmission MOVe-AHEAD trial with molnupiravir revealed a similarly reduced likelihood of contacts to turn SARS-CoV-2 PCR test positive post-baseline, which was also not statistically significant[22]. Both prophylactic trials monitored viral RNA copy numbers as a primary endpoint. Clinical reports demonstrated rebounding virus replication in patients who have received paxlovid[2,23,24] or molnupiravir[25] and anecdotal cases of SARS-CoV-2 transmission at rebound have further questioned whether treatment may provide epidemiologic benefit through reducing the risk of SARS-CoV-2 spread. Mustelids such as mink and ferret are highly permissive for SARS-CoV-2, experiencing high virus loads predominantly in the upper respiratory tract and supporting efficient virus spread[26–28]. Using the ferret SARS-CoV-2 transmission model, we have established in previous work that oral molnupiravir blocks productive, direct-contact transmission of infectious particles to untreated sentinel ferrets within 18 h of treatment start[27,29], but paxlovid has not been tested in the transmission model.

In this work, we compare efficacy of molnupiravir and nirmatrelvir/ritonavir in the Roborovski dwarf hamster model of severe COVID-19-like viral pneumonia and the ferret transmission model. Results demonstrate that both drugs provide significant therapeutic benefit against SARS-CoV-2 pneumonia when administered early after infection. Both the rodent and non-rodent animal model reveal a non-linear correlation of viral RNA copy number and infectious viral titer reduction after treatment with molnupiravir, whereas reductions by nirmatrelvir/ritonavir are directly proportional. Infectious virus load in the upper respiratory tract emerges as a correlate for SARS-CoV-2 transmission success in ferrets, and molnupiravir treatment completely suppresses transmission at all dose levels tested, including those not associated with a significant reduction of viral RNA copy numbers in the upper respiratory tract.

Results

To validate sourced nirmatrelvir stocks (Fig. 1a), we determined antiviral potency on cultured VeroE6-TMPRSS2 cells against SARS-CoV-2 isolates representing lineage A (USA-WA1/2020), lineage B.1.1.7 (VOC alpha; hCoV-19/USA/CA/UCSD_5574/2020), lineage B.1.351 (VOC beta; hCoV-19/South Africa/KRISP-K005325/2020), lineage P.1 (VOC gamma; hCoV-19/Japan/TY7-503/2021), lineage B.1.617.2 (VOC delta; clinical isolate #233067), lineage B.1.1.529 (VOC omicron; hCoV-19/USA/WA-UW-21120120771/2021) lineage BA.2 (clinical isolate 22012361822A), lineage BA.2.12.1 (hCoV-19/USA/WA-CDC-UW22050170242/2022), and linage BA.4 (hCoV-19/USA/WA-CDC-UW22051283052/2022) (Fig. 1b).

In vitro efficacy of nirmatrelvir against current VOC

Infected cells were incubated with serial dilutions of nirmatrelvir in media containing 2 μM CP-100356, a P-glycoprotein inhibitor added to limit rapid compound efflux[30]. Nirmatrelvir exhibited nanomolar potency against all VOCs tested, returning half-maximal (EC_{50}) and 90% maximal (EC_{90}) concentrations ranging from 21.1 to 327.6 nM and 32.8 to 421.4 nM, respectively, which recapitulated results of previous in vitro dose-response studies[31,32].

Prevention of severe SARS-CoV-2 disease in Roborovski dwarf hamsters

We determined single-oral dose pharmacokinetics (PK) properties of nirmatrelvir delivered alone or in combination with ritonavir. Hamsters were administered 250 mg/kg nirmatrelvir with or without 83.3 mg/kg ritonavir. In the absence of ritonavir, 250 mg/kg nirmatrelvir delivered a plasma exposure level of 22,400 h × ng/ml (Fig. 2a, Table 1). When combined with ritonavir, nirmatrelvir plasma exposure

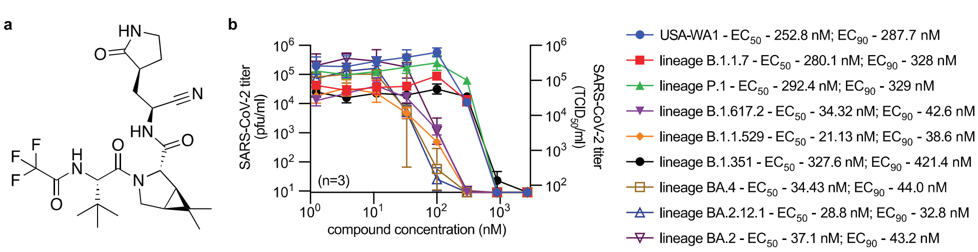

Fig. 1 | In vitro antiviral activity of nirmatrelvir. **a** Structure of nirmatrelvir. **b** Nirmatrelvir dose-response assays against SARS-CoV-2 WA1, and lineages B.1.1.7 (VOC α), B.1.351 (VOC β), P.1 (VOC γ), B.1.617.2 (VOC δ), B.1.1.529, BA.2, B1.2.12.1, and BA.4 on VeroE6-TMPRSS2 cells. The number of independent repeats (*n*) used in each experiment is shown (*n* = numbers of biologically independent samples). Symbols represent, and lines intersect, group geometric means ± SD; numbers denote 50 and 90% inhibitory concentrations (EC_{50} and EC_{90}, respectively), determined through non-linear 4-parameter variable slope regression modeling. Source data are provided as a Source data file.

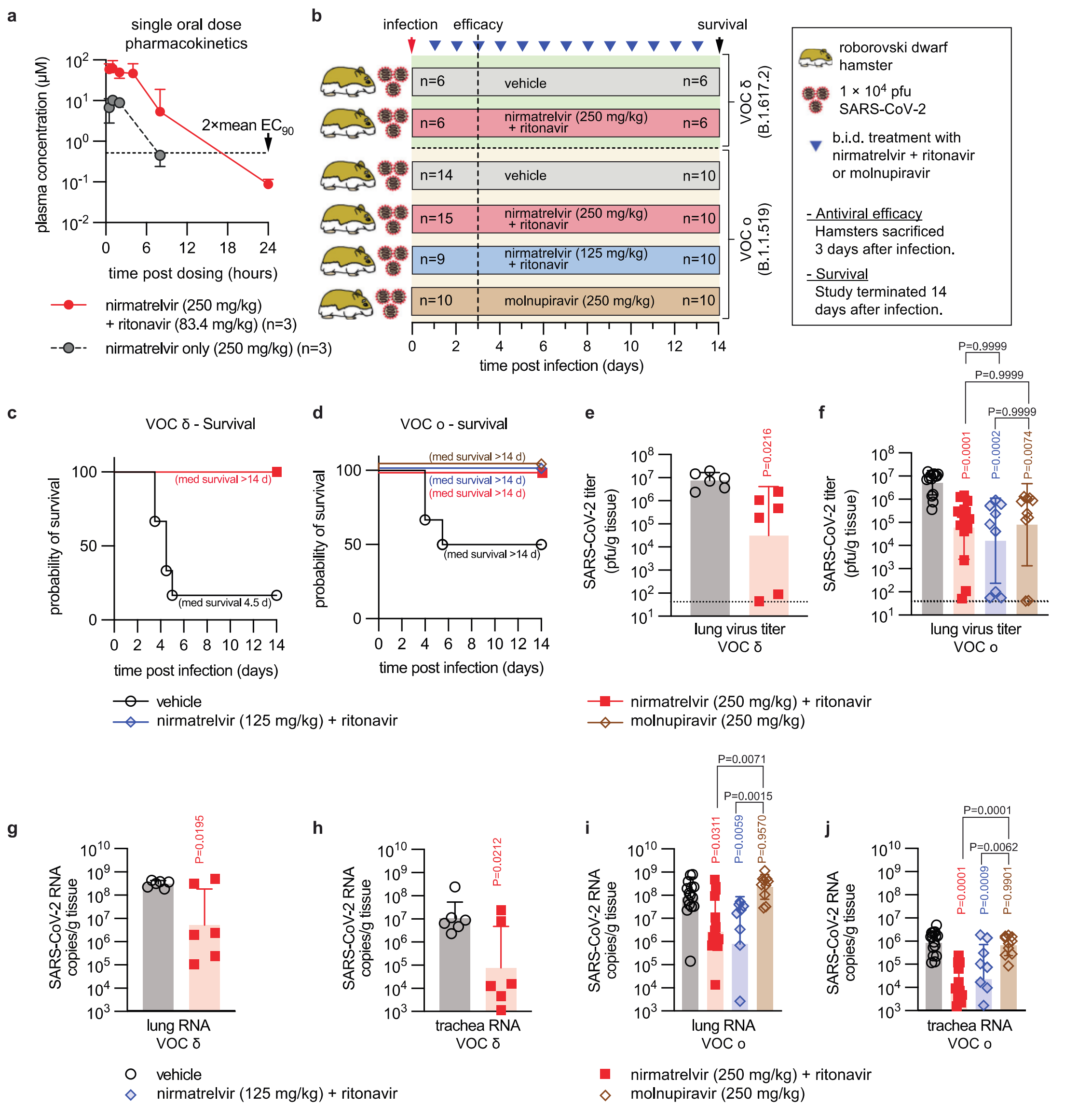

Fig. 2 | Efficacy of paxlovid and molnupiravir in Roborovski dwarf hamsters. **a** Plasma concentration of nirmatrelvir over 24-h after dosing. Single oral dose of nirmatrelvir (250 mg/kg), with (red circles) or without (black circles) ritonavir (83.4 mg/kg). Symbols show group geometric means ± SD and lines intersect means. Dotted line indicates 2 × mean EC_{90} against different VOC, determined in cell culture in Fig. 1b. **b** Antiviral efficacy study schematic. Animals were infected intranasally with 1×10^4 pfu of VOC delta or omicron and monitored for 14 days after infection. Clinical signs were assessed once daily (blue triangles). Viral load was determined in a duplicate set of animals 3 days after infection. The numbers of animals (*n* = number of independent animals) used in the efficacy (left) and survival (right) studies are shown. **c**, **d** Survival curves of VOC delta (**c**) or omicron (**d**) infected dwarf hamsters from (**b**) Log-rank (Mantel-Cox) test, median survival (med survival) is shown. **e**, **f** Lung virus titers 3 days after infection with VOC delta (**e**) or omicron (**f**) as shown in (**b**); dotted lines denote limit of detection. **g**–**j** Lung (**g**, **i**) and trachea (**h**, **j**) viral RNA copies after infection with VOC delta (**e**) or omicron (**f**) as shown in (**b**). Symbols represent independent biological repeats; columns show group geometric means ± SD. Significance was determined using unpaired 2-sided t tests (**e**, **g**, **h**) or one-way ANOVA Tukey's post hoc test (**i**, **j**) or Kruskal–Wallis test and Dunn's post hoc test (**f**); *P* values are shown. Source data are provided as a Source data file.

was 215,000 h × ng/ml, confirming that ritonavir, equivalent to its effect in human patients, efficiently slows nirmatrelvir metabolism in the dwarf hamsters. Previously, we have demonstrated that 250 mg/kg molnupiravir yields plasma exposure of N^4-hydroxycytidine, the systemic metabolite of molnupiravir[33], of 376 h × ng/ml in dwarf hamsters[29]. Human patients taking paxlovid or molnupiravir show nirmatrelvir exposure of 28,220 h × ng/ml[34,35] and N^4-hydroxycytidine exposure of 8200 h × ng/ml[36], respectively.

Matching the design of our previous molnupiravir dwarf hamster efficacy studies[29], we initiated oral treatment with paxlovid 12 h after intranasal infection of the dwarf hamsters with 1×10^4 pfu of VOC delta or omicron (lineage B.1.1.529), and continued treatment in a twice-daily

Table 1 | Single dose pharmacokinetics of nirmatrelvir or nirmatrelvir/ritonavir in Roborovski dwarf hamster and human plasma

Drug	Species	Dose (mg/kg)	T_{max} (h)	C_{max} (ng/ml)	AUC_{inf} (hours × ng/ml)	$t_{1/2}$ (h)	Reference
Nirmatrelvir/ ritonavir	Roborovski dwarf hamster	250/83	1	34,200	215,000	2.21	This study
Nirmatrelvir	Roborovski dwarf hamster	250	1	5320	22,400	1.36	This study
Nirmatrelvir/ ritonavir	Human	250/100[a]	2.75	2882	28,220	6.94	34
Molnupiravir	Human	800[a]	1.75	2770	8200	1.18	36
Molnupiravir	Roborovski dwarf hamster	250	0.5	251	376	1.62	29

[a]Human doses are expressed as absolute amount, not mg/kg.

(b.i.d.) regimen (Fig. 2b). In the VOC omicron infection group, we included molnupiravir, dosed at 250 mg/kg b.i.d., and low-dose paxlovid (125 mg/kg nirmatrelvir and 83.3 mg/kg ritonavir) arms for comparison of effect size and/or dose-dependency of potency. The 12-h time-to-treatment-onset was chosen due to rapid disease progression in the dwarf hamster model[29], which mimics human patients at transition stage to complicated COVID-19. As we have reported for molnupiravir treatment after VOC delta infection[29], all treated dwarf hamsters met the primary efficacy endpoint and survived infection independent of VOC used, meeting the primary efficacy endpoint (Fig. 2c, d). By contrast, 83% and 50% of vehicle-treated animals had succumbed to the disease 6 days after infection with VOC delta and omicron, respectively. Drug-treated animals displayed minimal, if any, clinical signs, whereas dwarf hamsters in vehicle groups experienced hypothermia and body weight loss (Supplementary Fig. 1).

Virus burden in lungs of duplicate sets of equally infected and treated dwarf hamsters was determined 3 days after infection to determine effect size of treatment. Both VOC delta and omicron replicated efficiently in the dwarf hamsters, each reaching peak lung virus loads of ~10^7 pfu/g lung tissue (Fig. 2e, f). Treatment of VOC delta-infected dwarf hamsters with paxlovid significantly lowered virus burden, resembling the reduction in VOC delta lung titer that we had previously observed after treatment with molnupiravir[29]. However, effect size of treatment varied by several orders of magnitude between individual animals. We had noticed variation in effect size in molnupiravir-treated dwarf hamsters infected with VOC omicron before, but not VOC delta[29]. Head-to-head comparison of paxlovid and molnupiravir under identical experimental conditions in dwarf hamsters infected with VOC omicron demonstrated statistically significant reduction in lung virus load by either drug compared to vehicle-treated hamsters, but no statistically significant differences in effect size between both drugs or between the paxlovid dose groups (Fig. 2f).

Assessment of viral RNA copies in the lung and, in addition, trachea samples after infection with VOC delta (Fig. 2g, h) and omicron (Fig. 2i–k) revealed proportional reduction of viral RNA and infectious particles in lung samples of paxlovid-treated animals. However, no statistically significant reduction in lung viral RNA copies was detected in animals of the molnupiravir group, despite the highly significant reduction in infectious virus titer in these samples. Viral RNA copies in trachea samples of the respective paxlovid and molnupiravir groups mirrored the lung data. These results reveal similar efficacy of paxlovid and molnupiravir in reducing infectious virus titers in lung and preventing lethal disease in the dwarf hamster model. The non-linear correlation between reduction of infectious viral titers and viral RNA copy numbers in molnupiravir recipients suggested that a large proportion of viral RNA synthesized in molnupiravir-experienced animals may be bio-inactive.

To assess possible virus rebound after treatment, we discontinued treatment with either paxlovid (250 mg/kg nirmatrelvir/ritonavir, b.i.d.) or molnupiravir (250 mg/kg b.i.d.) five days after infection with VOC omicron and determined lung virus load on days 5 and 9 (Fig. 3a). All treated animals survived without developing clinical signs, whereas vehicle-treated animals experienced severe weight loss and hypothermia, and ~50% succumbed to infection by day 5 (Fig. 3b, c). Infectious VOC omicron titers in lungs were reduced equally by paxlovid and molnupiravir compared to peak titers (day 3) in vehicle-treated animals (Fig. 3d). On day 5, no statistically significant differences between either treatment group and vehicle-treated animals were detectable. Lung virus load in all groups approached the limit of detection by day 9 without signs of virus rebound in the treatment groups.

Paxlovid treatment of SARS-CoV-2 infection in ferrets

To assess the impact of nirmatrelvir treatment on upper respiratory disease, we employed the SARS-CoV-2 ferret infection model[27,28,37,38]. To ensure cross-species consistency of nirmatrelvir PK, we again administered the compound first in a single oral dose at two levels, 20 mg/kg and 100 mg/kg, each in combination with 6 mg/kg ritonavir. Overall nirmatrelvir plasma exposure in ferrets was 32,700 h × ng/ml and 49,500 h × ng/ml for the 20 and 100 mg/kg groups, respectively (Fig. 4a; Table 2), indicating a dose-dependent, but not dose-proportional, PK profile of paxlovid.

Both dose levels were advanced to efficacy testing after intranasal infection of ferrets with 1×10^5 pfu of SARS-CoV-2 isolate USA-WA1/2020 (lineage A), which most efficiently replicates and spreads in ferrets[27,29,37,39,40] and other members of the Mustela genus[41,42]. Treatment was initiated 12 h after infection and continued b.i.d., and nasal lavages collected twice daily to determine shed virus load (Fig. 4b). Characteristic for this model[27,28,37,38], SARS-CoV-2-infected ferrets displayed no overt clinical signs (Supplementary Fig. 2). Virus replicated efficiently in vehicle-treated animals, reaching plateau titers of ~10^5 pfu/ml shed virus and 10^5 RNA copies/µl nasal lavage 48 h after infection, which were maintained until study day 4 (Fig. 4c, d). By study end, both infectious viral titers and viral RNA copies in lavages of the 20 mg/kg nirmatrelvir/ritonavir group were reduced by ~1.4 log orders.

Ferrets receiving 100 mg/kg nirmatrelvir/ritonavir experienced a significant titer reduction in nasal lavages, but did not fully clear the infection. Rather, we noted a slight increase of virus replication in both nirmatrelvir/ritonavir dose groups 3.5 days after treatment start. Whole genome sequencing of virus populations in nasal lavage and turbinate samples taken from these animals revealed that most had acquired an N501T or Y453F substitution in the spike protein, which are characteristic for SARS-CoV-2 adaptation to replication in mustelids[27] (Supplementary Fig. 3), but no signature resistance mutation to nirmatrelvir in nsp5[43–45] emerged as allele-dominant (uploaded as NCBI BioProject PRJNA894555). At study end, infectious titers and viral RNA copies in nasal turbinate tissues were statistically significantly reduced in nirmatrelvir/ritonavir-treated animals compared to the vehicle group (Fig. 4e, f).

Effect of paxlovid treatment on transmission from SARS-CoV-2-infected ferrets

To examine the effect of nirmatrelvir/ritonavir treatment on SARS-CoV-2 spread, we subjected treated ferrets to a direct-contact transmission study, first co-housing infected and treated source ferrets with untreated contact animals 42 h after treatment initiation (Fig. 5a). Source animals were infected intranasally with SARS-CoV-2 WA1 as before, followed by nirmatrelvir/ritonavir treatment in a b.i.d. regimen

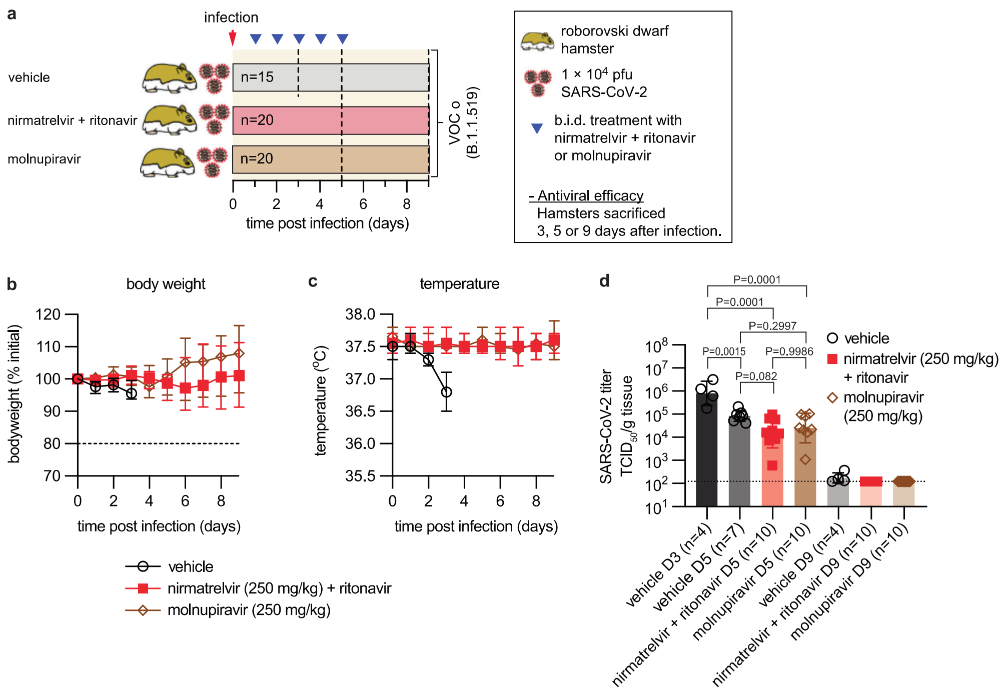

Fig. 3 | VOC omicron lung virus load following antiviral treatment. a Schematic of the study design. Treatment with nirmatrelvir/ritonavir or molnupiravir was initiated 12 h after infection, continued b.i.d., and terminated 5 days after infection. **b**, **c** Roborovski dwarf hamster body weight (**b**) and temperature (**c**) in animals infected with VOC omicron and treated with drug or vehicle. Symbols show, and lines intersect, group means ± SD. Dotted line in (**b**) denotes predefined endpoint. **d** Infectious virus titers in lung tissue extracted on days 3 (D3; vehicle only), 5 (D5), and 9 (D9) after infection. The number of animals (n = independent animals) used in each experiment is specified. Symbols represent independent biological repeats (individual animals); columns denote geometric means ± SD. Two-way ANOVA with main effects only, Tukey's multiple comparison post hoc test; P values are shown. Dotted line denotes limit of detection. Source data are provided as a Source data file.

at 20 or 100 mg/kg. For comparison with the only drug in clinical use that reportedly suppresses viral transmission in this model[27,29], we added molnupiravir treatment groups, dosed orally b.i.d. at 1.25 mg/kg, 2.5 mg/kg, or 5 mg/kg. All treatments were initiated 12 h after infection. Equivalent amounts of shed infectious viral particles were detected in all source animal groups at the time of treatment start, confirming productive infection of all animals (Fig. 5b, c, Supplementary Fig. 4). None of the animals developed clinical signs (Supplementary Fig. 5). Shed virus and RNA copy numbers of vehicle and nirmatrelvir/ritonavir-treated sources resembled that of the initial efficacy study (Supplementary Fig. 6), whereas shed infectious titers in two of the three molnupiravir arms rapidly declined, reaching detection level ~3 days after treatment start (Fig. 5b–d). Recapitulating the dwarf hamster results, viral RNA copy numbers and infectious viral titers in lavages of molnupiravir-treated ferrets followed a non-linear correlation, amounting only to an ~0.5 log order difference to vehicle-treated animals in the 1.25 mg/kg molnupiravir group by study end (Fig. 5e), but a statistically highly significant reduction in infectious titers of approximately two orders of magnitude (Fig. 5c).

SARS-CoV-2 spread rapidly to sentinels of vehicle-treated source animals. As noted before[27,29], molnupiravir treatment of source animals rapidly reduced infectious viral titers, suppressing all transmission to untreated naïve contacts in all molnupiravir dose groups including the 1.25 mg/kg group (Fig. 5c, e). By contrast, viral spread to sentinels of ferrets receiving 20 mg/kg b.i.d. nirmatrelvir/ritonavir was delayed, but ultimately all contacts were infected and viral titers in nasal lavages were virtually identical to those of sentinels of vehicle-treated animals, indicating uninterrupted transmission. Treating source ferrets with 100 mg/kg nirmatrelvir/ritonavir reduced transmission rates, but productive viral transfer still occurred in one of the three contact pairs examined (Fig. 5b, d). Again, virus populations in lavage and turbinate samples of these animals had acquired mustelid-characteristic species adaptation mutations in the spike protein in most cases (Supplementary Fig. 7), but whole genome sequencing did not reveal any allele-dominant resistance mutation to nirmatrelvir in nsp5 (uploaded as NCBI BioProject PRJNA894555).

Viral titers and RNA copies in nasal turbinates determined 4 days after infection in source animals and 4 days after the end of co-housing in contact animals (study day 8) revealed turbinate titers and viral RNA copies in sentinels of sources that had received 20 mg/kg nirmatrelvir/ritonavir indistinguishable from those of animals that had been co-housed with vehicle-treated sources (Fig. 5d, e). One of three contacts of the 100 mg/kg nirmatrelvir/ritonavir recipients showed vehicle-equivalent viral burden in upper respiratory tissues at study end. No infectious particles or viral RNA was detectable in nasal turbinates extracted from contacts of all molnupiravir treatment groups (Fig. 5h, i), confirmed a sterilizing effect of molnupiravir on transmission in all dose groups. Comparison of infectious titers (Fig. 5h) versus viral RNA copies (Fig. 5i) in turbinates of the different molnupiravir dose level source animals underscored the notion that a large proportion of viral RNA synthesized in the presence of molnupiravir was bio-inactive.

We hypothesized that the discrepancy between comparable performance of nirmatrelvir/ritonavir and molnupiravir in dwarf hamster lung tissue and differential effect on viral spread may be due to poor

Article https://doi.org/10.1038/s41467-023-40556-8

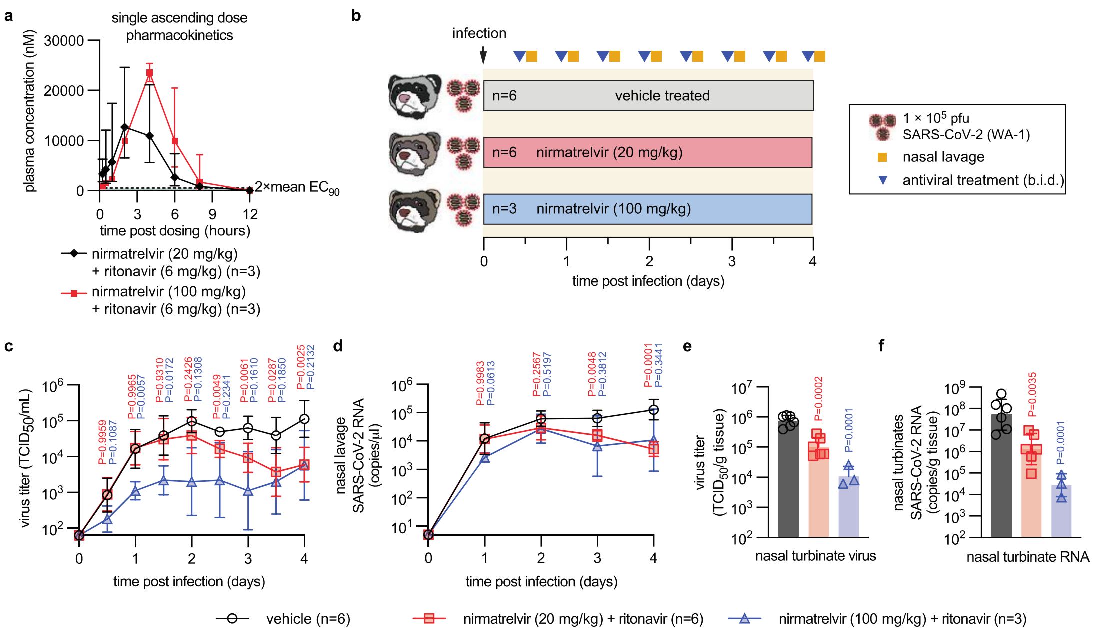

Fig. 4 | Efficacy of paxlovid in ferrets. a Plasma concentration of nirmatrelvir determined over a 12-h period after a single oral dose. Nirmatrelvir was dosed at 20 mg/kg (black diamonds) or 100 mg/kg (red squares), each in combination with 6 mg/kg ritonavir. Symbols represent group means ± SD and lines intersect means. Dotted line indicates 2 × mean EC_{90} against different VOC, determined in cell culture in Fig. 1b. **b** Antiviral efficacy study schematic. Ferrets (*n* = 15 total) were infected intranasally with 1×10^5 pfu of SARS-CoV-2 USA/WA-1. After 12 h, groups of ferrets were treated orally with vehicle or 20 mg/kg or 100 mg/kg nirmatrelvir/ritonavir. The number of animals (*n* = independent animals) used in each experiment is specified. **c**, **d** Infectious SARS-CoV-2 titers (**c**) and SARS-CoV-2 RNA copies (**d**) in nasal lavages of animals shown in (**b**). **e**, **f** Infectious titers (**e**) and SARS-CoV-2 RNA copies (**f**) in nasal turbinates extracted four days after infection. Symbols in (**c**–**f**) represent independent biological repeats (virus load of individual animals); lines (**c**, **d**) intersect, and columns (**e**, **f**) show, group geometric means ± SD. Statistical analysis with one-way (**e**, **f**) or two-way (**c**, **d**) ANOVA with Dunnett's (**c**–**f**) post hoc tests; *P* values are shown. Source data are provided as a Source data file.

Table 2 | Single dose pharmacokinetics of nirmatrelvir/ritonavir in ferret and human plasma

Drug	Species	Dose (mg/kg)	T_{max} (h)	C_{max} (ng/ml)	AUC_{inf} (hours × ng/ml)	$t_{1/2}$ (h)	Reference
Nirmatrelvir/ritonavir	Ferret	20/6	2.33	8990	32,700	1.05	This study
Nirmatrelvir/ritonavir	Ferret	100/6	4	11,800	49,500	0.74	This study
Nirmatrelvir/ritonavir	Human	250/100[a]	2.75	2882	28,220	6.94	34
Molnupiravir	Human	800[a]	1.75	2770	8200	1.18	36
Molnupiravir	Ferret	4	1.7	907	3421	8.2	33
Molnupiravir	Ferret	7	1.5	2851	7569	9.2	33
Molnupiravir	Ferret	20	1.8	3992	18,793	4.7	33
Molnupiravir	Macaque	130	1.62	2644	25,299	1.77	33

[a]Human doses are expressed as absolute amount, not mg/kg.

nirmatrelvir exposure in upper respiratory tract tissues. Assessing drug levels at anticipated peak (3 h after dosing, ~30 min after plasma C_{max}) and trough (12 h after dosing) revealed statistically significantly lower nirmatrelvir levels in nasal turbinates compared to all other soft tissues but brain (Fig. 5j).

Prophylactic treatment of uninfected direct contact ferrets

In the EPIC-PEP and MOVe-AHEAD trials, prophylactic administration of paxlovid or molnupiravir, respectively, to adults exposed to household members did not significantly reduce the risk of infection[20–22]. We prophylactically treated uninfected ferrets with 20 mg/kg or 100 mg/kg nirmatrelvir/ritonavir or 5 mg/kg molnupiravir, all in b.i.d. regimen, followed by co-housing with infected, but untreated, source animals 12 h later (Fig. 6a). Treatment of the sentinels was continued b.i.d. for 5.5 days, shed virus in nasal lavages of source and sentinels monitored daily, and virus load in the upper respiratory tract determined 6 days after infection.

We detected shed virus in lavages of all contacts receiving vehicle within 24 h of co-housing, indicating productive transmission (Fig. 6b). Again, none of the animals developed clinical signs (Supplementary Fig. 8). Prophylactic 20 mg/kg nirmatrelvir/ritonavir delayed transmission by ~48 h, but ultimately all sentinels were productively infected and shed virus titers reached by study end were indistinguishable from those of the vehicle group. In contrast, no infectious SARS-CoV-2 particles emerged in lavages of sentinels prophylactically treated with 100 mg/kg nirmatrelvir/ritonavir or 5 mg/kg molnupiravir. Quantitation of viral RNA in lavage samples groups largely mirrored the virus titer profiles (Fig. 6c). However, low amounts (<10^3 RNA copies/µl) of

Article https://doi.org/10.1038/s41467-023-40556-8

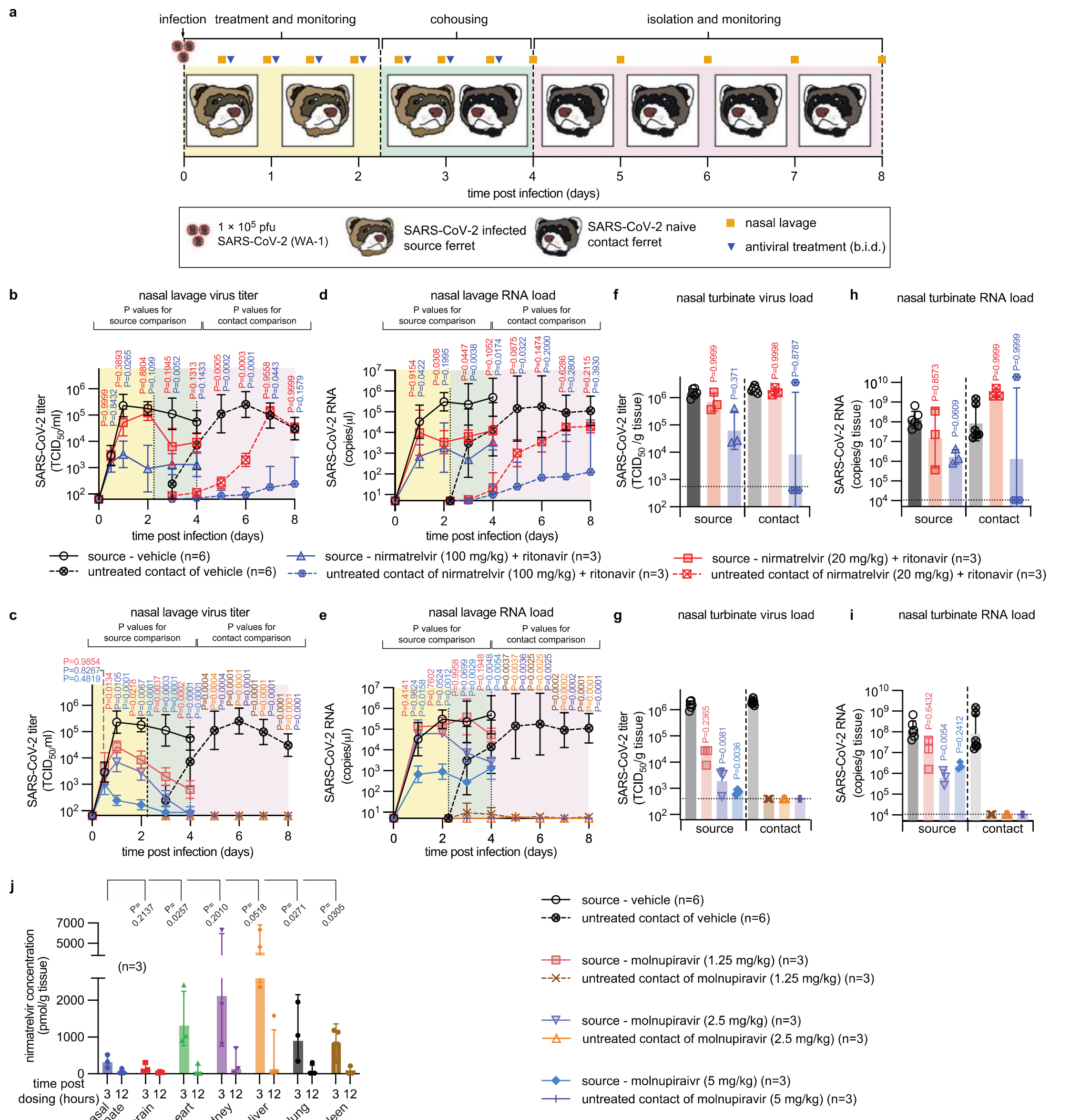

Fig. 5 | Effect of treatment with paxlovid or molnupiravir on SARS-CoV-2 transmission. a Transmission study schematic. **b**–**i** Direct-contact transmission study. Results are disaggregated into nirmatrelvir/ritonavir (**b**–**e**) and molnupiravir (**f**–**i**) treatment groups; vehicle-treated animals are shown in both sets. Infectious titers (**b**, **c**) and RNA copies (**d**, **e**) of SARS-CoV-2 present in nasal lavages of source and contact ferrets. Nasal turbinate titers (**f**, **g**) and RNA copies (**h**, **i**) in nasal turbinates extracted from source and contact animals on study days 4 and 8, respectively. Symbols (**b**–**e**) represent, and lines intersect, geometric means ± SD; x-axes denote level of detection. Symbols (**f**–i) represent independent biological repeats (results from individual animals); columns denote geometric means ± SD; dotted lines specify level of detection. **j** nirmatrelvir exposure in selected ferret organs at anticipated peak and trough after single-dose administration of nirmatrelvir + ritonavir. The number of animals (*n* = independent animals) used in each experiment is specified. Symbols represent independent biological repeats (results from individual animals); columns denote means ± SD. Statistical analysis with one-way (**f**–**i**) or two-way (**b**–**e**) ANOVA with Dunnett's post hoc tests (**b**–**e**), Kruskal–Wallis test with Dunn's post hoc tests (**f**–**i**), or ratio paired two-sided t test (**j**); *P* values are shown. Source data are provided as a Source data file.

SARS-CoV-2 RNA were present also in lavages of the 5 mg/kg molnupiravir and 100 mg/kg nirmatrelvir/ritonavir groups, demonstrating that co-housing with untreated source animals efficiently exposed sentinels of all four study arms to SARS-CoV-2. Infectious virus load in nasal turbinates of animals treated with 20 mg/kg nirmatrelvir/ritonavir was statistically indistinguishable from that found in the vehicle group (Fig. 6d). Turbinates of one of the contacts treated with 100 mg/kg nirmatrelvir/ritonavir harbored some infectious particles, whereas turbinates of all sentinels receiving 5 mg/kg molnupiravir did not contain infectious SARS-CoV-2 at study end. We detected high RNA

Article https://doi.org/10.1038/s41467-023-40556-8

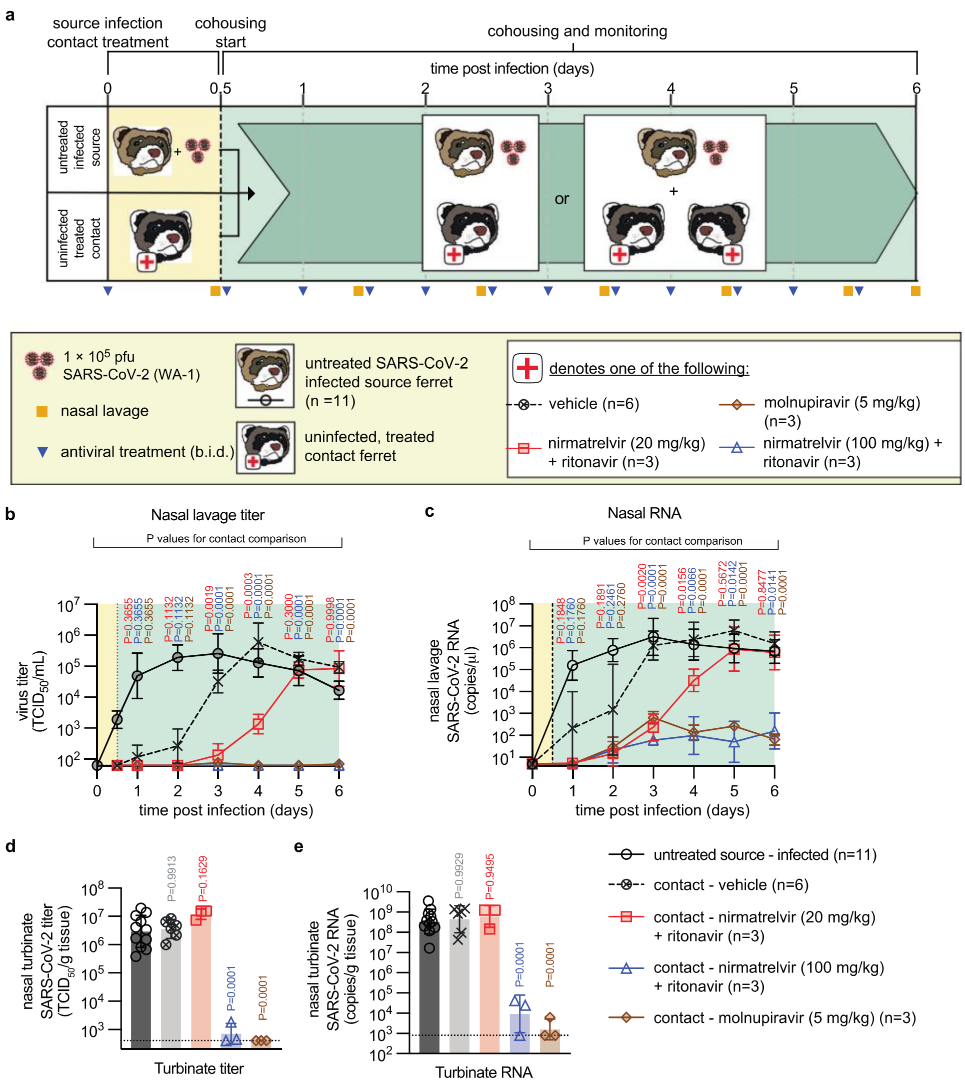

Fig. 6 | Prophylactic treatment of close contacts with paxlovid or molnupiravir. a Prophylaxis study schematic. **b**, **c** Infectious titers (**b**) and RNA copies (**c**) of SARS-CoV-2 present in nasal lavages of source and contact ferrets. The number of animals (*n* = independent animals) used in each experiment is specified. **d**, **e** Nasal turbinate titers (**d**) and RNA copies (**e**) in nasal turbinates extracted from source and contact animals on study day 6. Symbols (**b**, **c**) represent, and lines intersect, geometric means ± SD; x-axes denote level of detection. Symbols (**d**, **e**) represent independent biological repeats (results from individual animals); columns denote geometric means ± SD; dotted lines specify level of detection. Statistical analysis with one-way (**d**, **e**) or two-way (**b**, **c**) ANOVA with Dunnett's (**b**–**e**) post hoc tests; *P* values are shown. Source data are provided as a Source data file.

copy numbers in all 20 mg/kg nirmatrelvir/ritonavir recipients, which were statistically equivalent to those derived from vehicle-treated animals (Fig. 6e). Low levels of viral RNA were furthermore observed in the turbinates of two animals of the 100 mg/kg nirmatrelvir/ritonavir group and one animal in the 5 mg/kg molnupiravir group. One 100 mg/kg nirmatrelvir/ritonavir animal and the other two 5 mg/kg molnupiravir recipients remained viral RNA free.

Discussion

The retrospective analyses of members of Clalit Health Services[16,19] and a retrospective cohort study from the Hong Kong VOC omicron wave[17] demonstrated that both paxlovid[16] and molnupiravir[19] significantly lowered the risk of progression to severe disease and deaths in older adults. However, a direct comparison of drug efficacy was not possible due to imbalances in baseline characteristics of the study groups such as patient comorbidities, age, and vaccine status[46]. To assess efficacy of both drugs against COVID-19 of different severity under equivalent experimental conditions, we employed the Roborovski dwarf hamster and ferret models of SARS-CoV-2 infection.

Establishing a correlation between animal and human dose levels is complex. Interspecies allometric scaling to convert dose-based systemic exposure from animals to humans can confound predictive power of animal models[47]. Although no scaling was required for our study since plasma exposure levels of both nirmatrelvir[34] and N^4-hydroxycytidine[36], the systemic metabolite of molnupiravir[33] were known (included in Tables 1, 2), comparison dose selections can still be undermined by, for instance, host species-specific differences in drug plasma binding, tissue penetration, viral replication kinetics, and drug half-life.

To place ferret dose levels in context to clinical data, we therefore evaluated for each drug individually treatment effect size in the animal model and human patients. Since accurate and reproducible quantitation of infectious viral titers in human nasopharyngeal swabs is difficult[48], viral RNA copies have become the clinical standard and RNA copy number reduction in the upper respiratory tract represents the sole quantitative biomarker that is available across multiple species including humans. Clinical trials reported an ~0.5 log order reduction of viral RNA copies by molnupiravir[49], and 0.89–0.93 log orders by paxlovid[12,21]. An equivalent effect size was achieved in the ferret upper respiratory tract by 1.25 mg/kg molnupiravir (~0.5 log order reduction) and 20 mg/kg nirmatrelvir/ritonavir (1.4 log order reduction), each administered in b.i.d. regimen.

In the case of paxlovid, the correlation between viral RNA copy and infectious titer reductions was approximately linear in the models. A viral mutagen such as molnupiravir, however, once incorporated into viral RNA, can destroy bioactivity of this RNA without proportionally reducing the number of physical RNA copies, which may result in underappreciation of its antiviral effect based on RNA copy numbers alone. Both the dwarf hamster and ferret model illustrate that this difference between reduction of infectious virus titer and viral RNA molecules becomes most pronounced at low molnupiravir exposure, veering in some cases from statistically insignificant (RNA copies) to several orders of magnitude (infectious titer) in the same sample.

It is undocumented at present whether a similar discrepancy between viral RNA copy number and infectious viral titer reduction applies to clinical samples. Since the effect is consistent across rodent and non-rodent host models and appears to be directly linked to the mechanism of action of molnupiravir, quantitating viral RNA copies without assessing RNA bioactivity may be at risk of being misleading in the case of viral mutagens such as molnupiravir and may, therefore, not represent an informative primary endpoint for clinical trials. Support for this notion comes from qualitative infectious viral load data determined in the phase 2a clinical trial of molnupiravir[49]. After a 5-day treatment course, infectious virus particles could be isolated from patients in the placebo group, but not from patients receiving molnupiravir, although these patients experienced only an ~0.5 log order decrease in viral RNA copies in the upper respiratory tract.

An antiviral effect size-based approach could not be applied to the dwarf hamster model of acute SARS-CoV-2 pneumonia, since viral RNA copy number reductions in the human lower respiratory tract are unknown. Based on our PK information, N^4-hydroxycytidine[29] plasma exposure in dwarf hamsters was over 20-fold lower than that in humans, whereas nirmatrelvir exposure exceeded that achieved in humans by over 7.5-fold, suggesting that the dwarf hamster model may overestimate efficacy of nirmatrelvir/ritonavir against acute lung disease.

Acknowledging this caveat, the dwarf hamster model supported three major conclusions: (i) both drugs met the primary efficacy endpoint, ensuring complete survival of treated animals; (ii) both drugs statistically significantly reduced lung virus burden compared to vehicle-treated animals; and (iii) treatment benefit provided by either drug showed variations between individual animals when dwarf hamsters were infected with VOC omicron. We have recently reported that in the case of molnupiravir, biological sex of the treated dwarf hamsters contributes to effect[29]. Although not powered for a full statistical analysis, nirmatrelvir/ritonavir performance in dwarf hamsters did not suggest an equivalent role of biological sex on effect size against VOC omicron. We hypothesize that differences in the kinetics of viral host invasion between individual dwarf hamsters may contribute to this variation of effect size. In toto, the dwarf hamster model recapitulated the main conclusions of retrospective clinical studies in older adults[17]; both drugs mitigated advance to severe disease, preventing acute lung injury and death.

Prolonged self-isolation periods after a positive SARS-CoV-2 test impose considerable social hardship on the individual patient and economic burden on societies[50–52], which has resulted in eroding public compliance with self-quarantine during the course of the pandemic[53]. In addition to direct therapeutic benefit, pharmacologically shortening the duration of the infectious period will improve patient quality of life and may provide epidemiologic benefit through interruption of viral transmission chains[54,55]. We have established efficient suppression of SARS-CoV-2 transmission in the ferret model by molnupiravir dosed at 5 mg/kg b.i.d.[27,29] and experimental nucleoside analog antivirals[37] in previous work, and demonstrated in this study that therapeutic administration of 1.25 mg/kg molnupiravir or 100 mg/kg nirmatrelvir/ritonavir to ferrets fully or partially, respectively, suppressed transmission to untreated direct contacts. At these dose levels, either drug reduced shed infectious viral titers to ~10^3 $TCID_{50}$ units/ml nasal lavage fluid, which appears to represent a threshold for productive direct-contact SARS-CoV-2 transmission in the ferret model. SARS-CoV-2 transmitted in all pairs of the 20 mg/kg nirmatrelvir/ritonavir group, which reduced viral titers to ~10^4 $TCID_{50}$ units/ml nasal lavage fluid, indicating that infectious viral titer in the ferret upper respiratory tract is a correlate for transmission success.

Whole genome sequencing of virus populations isolated from paxlovid-experienced ferrets provided no evidence that replication resurgence and transmission both from and to paxlovid-treated animals in our study were supported by emerging resistance to nirmatrelvir[43–45]. Rather, poor control of SARS-CoV-2 spread in ferrets coincided with significantly lower nirmatrelvir levels in the upper respiratory tract than lung and other soft tissues but brain, identifying nasal turbinates as a privileged organ of low nirmatrelvir exposure. This effect could be ferret-specific, since tissue drug exposure levels cannot be readily determined in humans. However, rebounding virus replication in paxlovid recipients[2,23,24] and the lack of efficacy in patients <65 years of age, in which SARS-CoV-2 infection resides primarily in the upper respiratory tract, are consistent with low nirmatrelvir exposure also in human upper respiratory tissues.

Prophylactic dosing of contact ferrets with 20 mg/kg paxlovid did not prevent transmission from infected animals, recapitulating the outcome of the failed EPIC-PEP trial[20,21] trial. Interestingly, 20 mg/kg nirmatrelvir/ritonavir was also the ferret dose that mediated a similar viral RNA copy number reduction to that seen in humans receiving paxlovid. Since also prophylactic molnupiravir did not prevent infection in the MOVe-AHEAD trial[22], an equally negative outcome of prophylactic 1.25 mg/kg molnupiravir was likely, prompting us not to commit additional animals for an experimental confirmation. However, 5 mg/kg prophylactic molnupiravir fully, and 100 mg/kg prophylactic nirmatrelvir/ritonavir partially, suppressed infection, indicating that higher dose levels, as long as compatible with safety margins, provide prophylactic efficacy in ferrets.

Trials with appropriately selected endpoints will be required to determine whether molnupiravir over-proportionally reduces infectious SARS-CoV-2 titers, compared to viral RNA copy numbers, also in the human upper respiratory tract. Due to differences in the dynamics of viral host invasion and replication in humans versus animals, extrapolation of therapeutic time windows from animal models to human patients is challenging. Despite the potential of host species-specific effects, this study affirms retrospective clinical analyses that early treatment of older adult patients at elevated risk of progression to severe COVID-19 with either paxlovid or molnupiravir will provide significant therapeutic benefit. We demonstrate in two animal model species, one rodent and one non-rodent, that infectious particle titers, but not viral RNA copy numbers, should be assessed to determine efficacy of a viral mutagen such as molnupiravir. Infectious viral load in the upper respiratory tract emerged as a correlate for SARS-CoV-2 transmission success in ferrets. Therapeutic molnupiravir, administered at a dose not associated with a significant reduction of viral RNA copy numbers, completely suppressed transmission in ferrets.

Methods

Ethics and inclusion statement

All in vivo studies were performed in compliance with the Guide for the Care and Use of Laboratory Animals, National Institutes of Health guidelines, and the Animal Welfare Act Code of Federal Regulations. Experiments with SARS-CoV-2 involving ferrets were approved by the Georgia State Institutional Animal Care and Use Committee under protocol A20031. Experiments with SARS-CoV-2 involving Roborovski dwarf hamsters were approved by the Georgia State Institutional Animal Care and Use Committee under protocol A21019. All experiments using infectious SARS-CoV-2 strains were approved by the Georgia State Institutional Biosafety Committee under protocol B20016 and performed in BSL-3/ABSL-3 facilities at the Georgia State University.

Study design

Male and female Roborovski dwarf hamsters (*Phodopus roborovskii*, 3–4 months old) and female ferrets (*Mustela putorius furo*, 6–10 months old) were used as in vivo models to assess the therapeutic efficacy of orally administered nirmatrelvir against infection with SARS-CoV-2. Prior to studies, hamsters and ferrets were rested for at least five days. Roborovski dwarf hamsters were used to study the effects of nirmatrelvir treatment on severe disease associated with lower respiratory tract infection, acute lung injury, and death. Ferrets were used to examine the effect of nirmatrelvir on upper respiratory infection and transmission. SARS-CoV-2 infections were established in animals through intranasal inoculation. For hamsters, animals were monitored regularly for clinical signs and viral loads were determined in respiratory tract tissues at endpoint. For ferrets, upper respiratory tract viral titers were assessed at least once daily through nasal lavages. In addition, upper respiratory tract tissues were harvested at endpoint to assess upper respiratory tract viral loads. Virus loads were determined by plaque assays or $TCID_{50}$ and RT-qPCR quantitation.

Cells

VeroE6-TMPRSS2 (BPS Bioscience #78081) and Calu-3 (ATCC HB-55™) cells were cultivated at 37 °C with 5% CO_2 in Dulbecco's modified Eagle's medium (DMEM) supplemented with 7.5% heat-inactivated fetal bovine serum (FBS). All cells were authenticated phenotypically and tested routinely in 3-months intervals for absence of mycoplasma contamination prior to use.

Viruses

SARS-CoV-2 USA-WA1 (lineage A, isolate USA-WA1/2020, BEI cat# NR-52281) was obtained from BEI resources and amplified on Calu-3 cells. SARS-CoV-2 isolates for lineage B.1.1.7 (VOC α; hCoV-19/USA/CA/UCSD_5574/2020), lineage B.1.351 (VOC β; hCoV-19/South Africa/KRISP-K005325/2020), lineage P.1 (VOC γ; hCoV-19/Japan/TY7-503/2021), lineage B.1.617.2 (VOC δ; clinical isolate #233067), lineage B.1.1.529 (VOC o; hCoV-19/USA/WA-UW-21120120771/2021) lineage BA.2 (clinical isolate 22012361822A), lineage BA.2.12.1 (hCoV-19/USA/WA-CDC-UW22050170242/2022), and lineage BA.4 (hCoV-19/USA/WA-CDC-UW22051283052/2022) were obtained from UW Virology and amplified on Calu-3 cells. All viruses were titered on VeroE6-TMPRSS2 cells and virus stocks were authenticated by whole genome next-generation sequencing prior to use.

Virus yield reduction

Nirmatrelvir was dissolved in water-free DMSO at 10 mM stock concentration and stored in single-use aliquots at −80 °C. Cells were seeded 14 h prior to experimentation in 24-well plates at 2×10^5 cells per well in 400 μl per well DMEM + 7.5% FBS supplemented with 2 μM CP-100356. Serial dilutions were generated in culture media containing 2 μM CP-100356 spanning a final concentration range from 2700 to 1.4 nM (3-fold serial dilution; 8 steps; dilution series were prepared 2-fold overconcentrated (54000 to 2.8 nM)). Every concentration of each test article was assessed in 3 biological (independent) repeats. Vehicle-treated control cultures DMSO volume equivalents corresponding to the highest test compound concentration. Serial dilutions were transferred to target wells (500 μl per well), immediately followed by infection with SARS-CoV-2 (multiplicity of infection 0.1 pfu per cell) in 100 μl per well (viral dilution media contained 2 μM CP-100356). Infected plates were incubated in a humidified incubator at 37 °C and 5% CO_2 for 48 h. Progeny virus titers in culture supernatants were determined through plaque-forming or $TCID_{50}$ assay on Vero-E6-TMPRSS2 cells. Inhibitory concentrations were calculated based on 4-parameter variable slope regression models.

SARS-CoV-2 titration by plaque assay

All samples were serially diluted in DMEM media supplemented with 2% FBS and antibiotic-antimycotic solution (Gibco). Dilutions were added to VeroE6-TMPRSS2 cells seeded 24 h earlier in 12-well plates at 3×10^5 cells per well. Dilutions were allowed to adsorb for 2 h at 37 °C. Following adsorption, inoculum was removed, and cells were overlaid with 1.2% Avicel (FMC BioPolymer) in DMEM supplemented with antibiotic-antimycotic solution and incubated at 37 °C with 5% CO_2. After incubating for 3 days, Avicel was removed, cells were washed with PBS and fixed with 10% neutral buffered formalin. Plaques were visualized using 1% crystal violet.

Single-dose pharmacokinetics in hamsters

Groups of hamsters were administered a single oral dose of nirmatrelvir (250 mg/kg; 0.5% MC with 2% Tween80) with or without ritonavir (83.4 mg/kg; 20% ethanol). Blood was harvested retro-orbitally using plain micro-hematocrit capillary tubes (Duran Wheaton Kimble) and collected in K_2EDTA capillary tubes (Sarstedt Microvette CB300) 0.5, 1, 2, 4, 8, and 24 h after dosing. Plasma was clarified by centrifugation (4 °C, 450 × *g*, 5 min). To determine tissue concentrations of nirmatrelvir, groups of hamsters were sacrificed 1, 8, and 24 h after dosing and selected tissues were harvested, flash-frozen in liquid nitrogen, and stored at −80 °C. Nirmatrelvir concentrations were analyzed using a qualified LC/MS/MS method, and PK parameters were calculated using non-compartmental analysis with WinNonlin 8.3.3.33. MS analysis defined the analyte area response, internal area response, and transitions (Q1 to Q3). Raw MS data are shown in Supplementary Data 2.

Hamster efficacy studies

Groups of male and female Roborovski dwarf hamsters were anesthetized using ketamine/dexmedetomidine and infected with 10^4 pfu per animal (50 μl total volume, 25 μl per nare). Anesthesia was reversed with atipamezole. Hamsters were monitored daily (body weight, temperature, and clinical score). Treatment started 12 h after infection with nirmatrelvir (200 μl, 0.5% MC with 2% Tween80; 250 mg/kg or 125 mg/kg b.i.d.) and ritonavir (50 μl, 20% EtOH; 83.3 mg/kg, b.i.d.). Treatment continued twice daily for 5 and 7 days after infection for VOC δ and VOC o, respectively. Treatment was discontinued for VOC δ after 5 days due to treated hamsters developing pronounced diarrhea. Groups of hamsters were euthanized three days after infection to assess lower respiratory tract viral load. Lungs were harvested, washed with sterile phosphate buffered saline, and homogenized in PBS supplemented with antibiotic-antimycotic using a bead blaster (3 bursts of 30 s at 4 °C each, 30 s pause between bursts; Bead Blaster 24R, Benchmark). Lung homogenates were clarified by centrifugation (20,000 × *g*, 10 min, 4 °C), aliquoted, and stored at −80 °C until processed. For RNA quantification, lungs and tracheas were harvested and homogenized in RNeasy RNA lysis buffer (Qiagen) in accordance with the manufacturers protocol.

Assessing viral rebound in hamsters

Male and female dwarf hamsters (6 months old) were randomly assigned in different groups. Upon arrival, all animals were rested for 72 h prior to being transferred into single-ventilated cages to an ABSL-3 facility. For infections, animals were anesthetized using ketamine/dexdomitor and infected intranasally with 10^4 pfu (50 µl) SARS-CoV-2 VOC o (B.1.1.519). Treatment was initiated 12 h post infection using nirmatrelvir (200 µl, 0.5% MC with 2% Tween80; 250 mg/kg) and ritonavir (50 µl, 20% EtOH; 83.3 mg/kg, b.i.d.), molnupiravir (200 µl, 1% MC; 250 mg/kg; b.i.d.) or vehicle (200 µl, 0.5% MC with 2% Tween80). Twice-daily treatment continued until five days post infection. Vehicle animals were euthanized on days 3, 5, and 9, nirmatrelvir and molnupiravir-treated hamsters were euthanized on days 5 and 9. Lungs were harvested, washed with sterile phosphate buffered saline, and homogenized in PBS supplemented with antibiotic-antimycotic using a bead blaster (3 bursts of 30 s at 4 °C each, 30 s pause between bursts; Bead Blaster 24R, Benchmark). Lung homogenates were clarified by centrifugation (20,000 × *g*, 10 min, 4 °C), aliquoted and stored at −80 °C until processed. Virus titers were determined by $TCID_{50}$ assays.

Single ascending dose pharmacokinetics in ferrets

Groups of ferrets were administered a single oral dose of nirmatrelvir at a dosage of 20 mg/kg ($n = 3$) or 100 mg/kg ($n = 3$); (2 ml; 0.5% MC with 2% Tween80) with ritonavir (1 ml; 6 mg/kg; 20% EtOH). A dosage of 6 mg/kg ritonavir was selected based on previous studies in ferrets (*53*). Drug was administered by oral gavage using a 12 french catheter (Cure Medical). After each gavage, the catheter line was flushed using high calorie liquid diet (3.5 ml; DYNE, PetAg). Blood was harvested in K_2EDTA capillary tubes (Sarstedt Microvette CB300) at 0.25, 0.5, 1, 2, 4, 6, 8, and 12 h after dosing. Plasma was clarified by centrifugation (4 °C, 450 × *g*, 5 min), aliquoted and stored at −80 °C. To determine tissue concentrations of nirmatrelvir, groups of ferrets were sacrificed 3 and 12 h after dosing and selected tissues were harvested, flash-frozen in liquid nitrogen, and stored at −80 °C. Nirmatrelvir concentrations were analyzed using a qualified LC/MS/MS method, and PK parameters were calculated using non-compartmental analysis with WinNonlin 8.3.3.33. Raw MS data are shown in Supplementary Data 2.

In vivo efficacy testing in ferrets against VOCs

Groups of ferrets were anesthetized with ketamine/dexmedetomidine and inoculated with 1×10^5 pfu of SARS-CoV-2 USA-WA1 (lineage A, isolate USA-WA1/2020, BEI cat# NR-52281; 1 ml, 0.5 ml per nare). Following infection, anesthesia was reversed using atipamezole. Treatment was initiated 12 h after infection and continued twice daily until study end (4 days after infection). Ferrets were treated with vehicle ($n = 6$; 0.5% MC with 2% Tween80), nirmatrelvir/ritonavir (20 ($n = 6$) or 100 ($n = 3$) mg/kg nirmatrelvir; 6 mg/kg ritonavir). Treatments were administered by oral gavage using a 12 french catheter (Cure Medical), starting 12 h after infection in consecutive 2 ml (20 or 100 mg/kg nirmatrelvir; 2 ml 0.5% MC with 2% Tween80) and 1 ml (6 mg/kg ritonavir; 1 ml 20% ethanol) dose volumes. Molnupiravir was formulated in 1% methylcelluose and administered in 3 ml dose volume. After each gavage, the catheter line was flushed using high calorie liquid diet (3.5 ml; DYNE, PetAg). Nasal lavages were collected every 12 h after study start in sterile PBS containing antibiotics and antimycotics (Anti-Anti; Gibco). All ferrets were euthanized 4 days after infection and tissues were harvested to determine SARS-CoV-2 titers and the presence of viral RNA.

Effect of treatment on SARS-CoV-2 contact transmission in ferrets

A group of source ferrets were inoculated intranasally with 1×10^5 pfu of SARS-CoV-2 USA-WA1 (lineage A, isolate USA-WA1/2020, BEI cat# NR-52281; 1 ml, 0.5 ml per nare). Twelve hours after infections, source ferrets were further divided into groups ($n = 3$), receiving vehicle, molnupiravir (1.25 mg/kg, b.i.d.; 2.5 mg/kg, b.i.d.; or 5 mg/kg, b.i.d.;), or nirmatrelvir (20 or 100 mg/kg, b.i.d. in 2 mL 0.5% MC with 2% Tween80 + ritonavir (6 mg/kg in 1 ml 20% ethanol)), in all cased administered via oral gavage. At 54 h after infection, each source ferret was co-housed with one uninfected and untreated contact ferret. Co-housing continued until 96 h after infection, when sourced ferrets were euthanized and contact ferrets were separated and housed individually. All contact ferrets were monitored for 4 days after separation from source ferrets and then euthanized. Nasal lavages were performed on source ferrets twice daily until co-housing ended. After co-housing started, nasal lavages were performed on all contact ferrets every 24 h. Upon euthanizing ferrets, nasal turbinates were harvested to determine infectious titers and the presence of viral RNA.

Effect of prophylactic treatment on direct contact transmission

At study onset, one group of source ferrets were inoculated intranasally with 1×10^5 pfu of SARS-CoV-2 USA-WA1 (lineage A, isolate USA-WA1/2020, BEI cat# NR-52281; 1 ml, 0.5 ml per nare) and isolated from uninfected ferrets. At the same time, twice-daily treatment regimens were initiated on groups of uninfected ferrets using nirmatrelvir (20 mg/kg) + ritonavir ($n = 3$) or nirmatrelvir (100 mg/kg) + ritonavir ($n = 3$), molnupiravir (5 mg/kg; $n = 3$), or vehicle. Nirmatrelvir was administered in 2 ml (20 or 100 mg/kg in 0.5% MC with 2% Tween80) followed by administration of ritonavir in 1 ml (6 mg/kg in 1 ml 20% ethanol). Molnupiravir was administered in 3 ml (1% methylcellulose). The catheter line was then flushed using high calorie liquid diet (3.5 ml; DYNE, PetAg). Treatment was continued for 6 days until study end. Twelve hours after infection, untreated and infected source ferrets were co-housed with treated contact ferrets. Per approved IACUC protocols, maximal density in the ventilated large animal caging system is 3 ferrets/cage. Therefore, an asymmetrical co-housing matrix had to be applied, consisting of a randomly assigned source to contact animal ratio of either 1:1 or 1:2. After co-housing commenced, nasal lavages were collected every 24 h, and ferrets were monitored until study end. Six days after infecting source ferrets, all animals were euthanized, and nasal turbinates were harvested to determine infectious titers and the presence of viral RNA.

Titration of SARS-CoV-2 in tissue extracts

For virus titration, the organs were weighed and homogenized in PBS supplemented with antibiotic-antimycotic solution (Gibco). Tissues were homogenized using a bead blaster (3 bursts of 30 s at 4 °C each, 30 s pause between bursts; Bead Blaster 24 R, Benchmark). Tissue homogenates were clarified by centrifugation (20,000 × *g* for 5 min at 4 °C). The clarified supernatants were harvested, frozen and used in subsequent $TCID_{50}$ or plaque assays. For detection of viral RNA, the harvested organs were homogenized in lysis buffer (Qiagen), and the total RNA was extracted using a RNeasy mini kit (Qiagen). For nasal lavages, RNA was extracted using a Quick-RNA Viral Kit (Zymo) in accordance with the manufacturer's protocols.

Quantitation of SARS-CoV-2 RNA

SARS-CoV-2 RNA was detected using the nCoV_IP2 primer-probe set (nCoV_IP2-12669Fw ATGAGCTTAGTCCTGTTG; nCoV_IP2-12759Rv CTCCCTTTGTTGTGTTGT; nCoV_IP2-12696bProbe(+) 5'FAM-AGATGTC TTGTGCTGCCGGTA-3'BHQ-1) (National Reference Center for Respiratory Viruses, Institut Pasteur). RT-qPCR reactions were performed using an QuantStudio 3 real-time PCR system using the QuantStudio Design and Analysis package. The nCoV_IP2 primer-probe set was used with Taqman Fast Virus 1-step master mix (Thermo Fisher Scientific) to detect viral RNA. A PCR fragment (nt 12669-14146 of the SARS-CoV-2 genome) generated from viral complementary DNA using the nCoV_IP2 forward primer and the nCoV_IP4 reverse primer (nCoV_IP4-14146Rv CTGGTCAAGGTTAATATAGG) was used to create a standard curve to quantitate the RNA copy numbers. RNA copy numbers were normalized to the weight of tissues used.

SARS-CoV-2 genome sequencing

SARS-CoV-2 positive specimens were sequenced using IDT xGen SARS-CoV-2 Amplicon Panel (previously Swift Biosciences SNAP panel), following the manufacturer's protocol. Sequencing reads were processed and analyzed using TAYLOR default settings available at https://github.com/greninger-lab/covid_swift_pipeline (https://doi.org/10.5281/zenodo.6142073). Sequencing reads are available in NCBI BioProject under access code PRJNA894555.

Statistics and reproducibility

The Microsoft Excel (versions 16.52) and Numbers (version 10.1) software packages were used for data collection. The GraphPad Prism (version 9.4.1) software package was used for data analysis. Reverse transcription RT-qPCR data were collected and analyzed using the QuantStudio Design and Analysis (version 1.5.2; Applied Biosystems) software package. Figures were assembled and generated with Adobe Illustrator (version 27.5). T-tests were used to evaluate statistical significance between experiments with two sets of data. To evaluate statistical significance when more than two groups were compared or datasets contained two independent variables, one- and two-way ANOVAs, respectively, were used with Tukey's, Dunnett's, or Sidak's multiple comparisons post hoc tests as specified in figure legends. Specific statistical tests are specified in the figure legends for individual studies. Supplementary Data 1 summarizes statistical analyses (effect sized, *P* values, and degrees of freedom) of the respective datasets. Effect sizes between groups were calculated as $\eta^2 = (SS_{effect})/(SS_{total})$ for one-way ANOVA and $\omega^2 = (SS_{effect} - (df_{effect})(MS_{error}))/MS_{error} + SS_{total}$ for two-way ANOVA; SS_{effect}, sum of squares for the effect; SS_{total}, sum of squares for total; df_{effect}, degrees of freedom for the effect; MS_{error}, mean square error. Effective concentrations for antiviral potency were calculated from dose-response virus yield reduction assay datasets through four-parameter variable slope regression modeling. A biological repeat refers to measurements taken from distinct samples, and the results obtained for each individual biological repeat are either shown in the figures along with the exact size (n, number) of biologically independent samples, animals, and independent experiments or results are presented as geometric means ± SD along with the exact size (n, number) of biologically independent samples represented. The measure of the center (connecting lines and columns) is specified in the figure legends. The statistical significance level (α) was set to <0.05 for all experiments. Exact *P* values are shown in Supplementary Data 1 and in individual graphs when possible. Quantitative source data for each biologically independent sample are provided in the Source data file.

Reporting summary

Further information on research design is available in the Nature Portfolio Reporting Summary linked to this article.

Data availability

The amplicon tiling sequencing reads generated in this study have been deposited in the NCBI BioProject database under accession code PRJNA894555. All other data generated in this study are provided in this article, the supplementary information, supplementary data files, and the Source data file. Source data are provided with this paper.

Code availability

Sequencing reads were analyzed using the TAYLOR pipeline (available at https://github.com/greninger-lab/covid_swift_pipeline). All commercial computer codes and algorithms used are specified in "Methods".

References

1. Garcia-Beltran, W. F. et al. Multiple SARS-CoV-2 variants escape neutralization by vaccine-induced humoral immunity. *Cell* **184**, 2372–2383.e2379 (2021).
2. Wang, Z. et al. mRNA vaccine-elicited antibodies to SARS-CoV-2 and circulating variants. *Nature* **592**, 616–622 (2021).
3. Zhou, D. et al. Evidence of escape of SARS-CoV-2 variant B.1.351 from natural and vaccine-induced sera. *Cell* **184**, 2348–2361.e2346 (2021).
4. Cao, Y. et al. Humoral immune response to circulating SARS-CoV-2 variants elicited by inactivated and RBD-subunit vaccines. *Cell Res.* **31**, 732–741 (2021).
5. Tuekprakhon, A. et al. Antibody escape of SARS-CoV-2 Omicron BA.4 and BA.5 from vaccine and BA.1 serum. *Cell* **185**, 2422–2433.e2413 (2022).
6. Cavazzoni, P. *Emergency Use Authorization* 108 (2022).
7. Cavazzoni, P. *Emergency Use Authorization* 105 (2022).
8. Yoon, J. J. et al. Orally efficacious broad-spectrum ribonucleoside analog inhibitor of influenza and respiratory syncytial viruses. *Antimicrob. Agents Chemother*. **62**, 10–1128 (2018).
9. Crotty, S., Cameron, C. E. & Andino, R. RNA virus error catastrophe: direct molecular test by using ribavirin. *Proc. Natl Acad. Sci. USA* **98**, 6895–6900 (2001).
10. Urakova, N. et al. beta-d-N (4)-hydroxycytidine is a potent anti-alphavirus compound that induces a high level of mutations in the viral genome. *J. Virol.* **92**, 10-1128 (2018).
11. Zeldin, R. K. & Petruschke, R. A. Pharmacological and therapeutic properties of ritonavir-boosted protease inhibitor therapy in HIV-infected patients. *J. Antimicrob. Chemother.* **53**, 4–9 (2004).
12. Hammond, J. et al. Oral nirmatrelvir for high-risk, nonhospitalized adults with Covid-19. *N. Engl. J. Med.* **386**, 1397–1408 (2022).
13. Jayk Bernal, A. et al. Molnupiravir for oral treatment of Covid-19 in nonhospitalized patients. *N. Engl. J. Med.* **386**, 509–520 (2022).
14. Zhou, S. et al. beta-d-N4-hydroxycytidine inhibits SARS-CoV-2 through lethal mutagenesis but is also mutagenic to mammalian cells. *J. Infect. Dis.* **224**, 415–419 (2021).
15. *Merck and Ridgeback Biotherapeutics Provide Update on New Clinical and Non-Clinical Studies of LAGEVRIO™ (molnupiravir)*. https://www.merck.com/news/merck-and-ridgeback-biotherapeutics-provide-update-on-new-clinical-and-non-clinical-studies-of-lagevrio-molnupiravir/ (2022).
16. Arbel, R. et al. Nirmatrelvir use and severe Covid-19 outcomes during the Omicron surge. *N. Engl. J. Med.* **387**, 790–798 (2022).
17. Wong, C. K. H. et al. Real-world effectiveness of early molnupiravir or nirmatrelvir-ritonavir in hospitalised patients with COVID-19 without supplemental oxygen requirement on admission during Hong Kong's omicron BA.2 wave: a retrospective cohort study. *Lancet Infect. Dis*. **22,** 1681–1693 (2022).
18. Butler, C. C. et al. Molnupiravir plus usual care versus usual care alone as early treatment for adults with COVID-19 at increased risk of adverse outcomes (PANORAMIC): an open-label, platform-adaptive randomised controlled trial. *Lancet* **401**, 281–293 (2023).
19. Arbel, A. et al. Molnupiravir use and severe Covid-19 outcomes during the Omicron surge. *Res. Sq.* Preprint (Version 1) available at Research Square https://doi.org/10.21203/rs.3.rs-2115769/v1 (2022).
20. NCT05047601. *A Study of a Potential Oral Treatment to Prevent COVID-19 in Adults Who Are Exposed to Household Member(s) With a Confirmed Symptomatic COVID-19 Infection*. https://clinicaltrials.gov/ct2/show/NCT05047601?term=NCT05047601&draw=2&rank=1 (2022).
21. Pfizer. *Pfizer Shares Top-Line Results from Phase 2/3 EPIC-PEP Study of PAXLOVID™ for Post-Exposure Prophylactic Use*. https://www.pfizer.com/news/press-release/press-release-detail/pfizer-shares-top-line-results-phase-23-epic-pep-study (2022).

22. *Merck Provides Update on Phase 3 MOVe-AHEAD Trial Evaluating LAGEVRIO™ (molnupiravir) for Post-exposure Prophylaxis for Prevention of COVID-19*. https://www.merck.com/news/merck-provides-update-on-phase-3-move-ahead-trial-evaluating-lagevrio-molnupiravir-for-post-exposure-prophylaxis-for-prevention-of-covid-19/ (2023).
23. Anderson, A. S., Caubel, P. & Rusnak, J. M. Nirmatrelvir–ritonavir and viral load rebound in Covid-19. *N. Engl. J. Med.* **387**, 1047–1049 (2022).
24. Charness, M. E. et al. Rebound of SARS-CoV-2 infection after nirmatrelvir-ritonavir treatment. *N. Engl. J. Med.* **387**, 1045–1047 (2022).
25. Wang, L. et al. COVID-19 rebound after Paxlovid and Molnupiravir during January–June 2022. Preprint at *medRxiv* https://doi.org/10.1101/2022.06.21.22276724 (2022).
26. Oude Munnink, B. B. et al. Transmission of SARS-CoV-2 on mink farms between humans and mink and back to humans. *Science* **371**, 172–177 (2021).
27. Cox, R. M., Wolf, J. D. & Plemper, R. K. Therapeutically administered ribonucleoside analogue MK-4482/EIDD-2801 blocks SARS-CoV-2 transmission in ferrets. *Nat. Microbiol.* **6**, 11–18 (2021).
28. Kim, Y. I. et al. Infection and rapid transmission of SARS-CoV-2 in ferrets. *Cell Host Microbe* **27**, 704–709.e702 (2020).
29. Lieber, C. M. et al. SARS-CoV-2 VOC type and biological sex affect molnupiravir efficacy in severe COVID-19 dwarf hamster model. *Nat. Commun.* **13**, 4416 (2022).
30. Hoffman, R. L. et al. Discovery of ketone-based covalent inhibitors of coronavirus 3CL proteases for the potential therapeutic treatment of COVID-19. *J. Med Chem.* **63**, 12725–12747 (2020).
31. Owen, D. R. et al. An oral SARS-CoV-2 M(pro) inhibitor clinical candidate for the treatment of COVID-19. *Science* **374**, 1586–1593 (2021).
32. Vangeel, L. et al. Remdesivir, Molnupiravir and Nirmatrelvir remain active against SARS-CoV-2 Omicron and other variants of concern. *Antivir. Res.* **198**, 105252 (2022).
33. Toots, M. et al. Characterization of orally efficacious influenza drug with high resistance barrier in ferrets and human airway epithelia. *Sci. Transl. Med.* **11**, eaax5866 (2019).
34. Singh, R. S. P. et al. Innovative randomized phase I study and dosing regimen selection to accelerate and inform pivotal COVID-19 trial of nirmatrelvir. *Clin. Pharm. Ther.* **112**, 101–111 (2022).
35. Toussi, S. S. et al. Pharmacokinetics of oral nirmatrelvir/ritonavir, a protease inhibitor for treatment of COVID-19, in subjects with renal impairment. *Clin. Pharm. Ther.* **112**, 892–900 (2022).
36. Painter, W. P. et al. Human safety, tolerability, and pharmacokinetics of molnupiravir, a novel broad-spectrum oral antiviral agent with activity against SARS-CoV-2. *Antimicrob. Agents Chemother.* **65**, e02428-20 (2021).
37. Cox, R. M. et al. Oral prodrug of remdesivir parent GS-441524 is efficacious against SARS-CoV-2 in ferrets. *Nat. Commun.* **12**, 6415 (2021).
38. Shi, J. et al. Susceptibility of ferrets, cats, dogs, and other domesticated animals to SARS-coronavirus 2. *Science* **368**, 1016–1020 (2020).
39. Patel, D. R. et al. Transmission and protection against reinfection in the ferret model with the SARS-CoV-2 USA-WA1/2020 reference isolate. *J. Virol.* **95**, e0223220 (2021).
40. Sourimant, J. et al. 4′-Fluorouridine is an oral antiviral that blocks respiratory syncytial virus and SARS-CoV-2 replication. *Science* **375**, 161–167 (2022).
41. Sikkema, R. S. et al. Risks of SARS-CoV-2 transmission between free-ranging animals and captive mink in the Netherlands. *Transbound Emerg. Dis.* **69**, 3339–32349 (2022).
42. Virtanen, J. et al. Experimental infection of mink with SARS-COV-2 Omicron variant and subsequent clinical disease. *Emerg. Infect. Dis.* **28**, 1286–1288 (2022).
43. Heilmann, E. et al. SARS-CoV-2 3CL(pro) mutations selected in a VSV-based system confer resistance to nirmatrelvir, ensitrelvir, and GC376. *Sci. Transl. Med.* **15**, eabq7360 (2022).
44. Hu, Y. et al. Naturally occurring mutations of SARS-CoV-2 main protease confer drug resistance to nirmatrelvir. *ACS Cent. Sci.* https://doi.org/10.1021/acscentsci.3c00538 (2023).
45. Iketani, S. et al. Multiple pathways for SARS-CoV-2 resistance to nirmatrelvir. *Nature* **613**, 558–564 (2023).
46. Zarebska-Michaluk, D. & Flisiak, R. Early oral antiviral use in patients hospitalised with COVID-19. *Lancet Infect. Dis.* **22**, 1650–1651 (2022).
47. Nair, A. B. & Jacob, S. A simple practice guide for dose conversion between animals and human. *J. Basic Clin. Pharm.* **7**, 27–31 (2016).
48. Wolfel, R. et al. Virological assessment of hospitalized patients with COVID-2019. *Nature* **581**, 465–469 (2020).
49. Fischer, W. A. 2nd et al. A phase 2a clinical trial of molnupiravir in patients with COVID-19 shows accelerated SARS-CoV-2 RNA clearance and elimination of infectious virus. *Sci. Transl. Med.* **14**, eabl7430 (2022).
50. De Giacomo, A. et al. Psychological impact of the SARS-CoV-2 pandemic in children with neurodevelopmental disorders and their families: evaluation before and during covid-19 outbreak among an Italian sample. *Riv. Psichiatr.* **56**, 205–210 (2021).
51. Tang, S., Xiang, M., Cheung, T. & Xiang, Y. T. Mental health and its correlates among children and adolescents during COVID-19 school closure: The importance of parent-child discussion. *J. Affect Disord.* **279**, 353–360 (2021).
52. Wu, C. et al. Analysis of psychological status and effect of psychological intervention in quarantined population during the epidemic of SARS-CoV-2. *Medicine* **100**, e25951 (2021).
53. Panda, P. K. et al. Psychological and behavioral impact of lockdown and quarantine measures for COVID-19 pandemic on children, adolescents and caregivers: a systematic review and meta-analysis. *J. Trop. Pediatr.* **67**, fmaa122 (2021).
54. Chung, P. C. & Chan, T. C. Impact of physical distancing policy on reducing transmission of SARS-CoV-2 globally: perspective from government's response and residents' compliance. *PLoS ONE* **16**, e0255873 (2021).
55. Wilder-Smith, A. What is the vaccine effect on reducing transmission in the context of the SARS-CoV-2 delta variant? *Lancet Infect. Dis.* **22**, 152–153 (2022).

Acknowledgements

We thank the Georgia State University Department of Animal Resources and High Containment Core for Assistance and J-J Yoon for technical support. This study was supported, in part, by public health service grants AI141222 (to R.K.P.) and AI171403 project 1 (to R.K.P.) and Scientific Core D (to A.L.G.) from the NIH/NIAID.

Author contributions

R.M.C., C.M.L., and R.K.P. conceived and designed the experiments. R.M.C., C.M.L., J.D.W., A.K., and R.K.P. conducted most of the experiments. R.M.C. created all figure schematics. A.L.G., N.A.P.L., and P.R. performed next-generation sequencing. M.K.A., R.E.K., Z.M.S., and A.A.K. performed mass spectrometry analysis. M.G.N. and G.R.P. provided critical materials. R.M.C., C.M.L., N.A.P.L., A.L.G., and R.K.P. analyzed the data. R.M.C. and R.K.P. wrote the manuscript.

Competing interests

G.R.P., MGN., and A.A.K. receive licensing fees and royalties based on Emory's sublicense of the molnupiravir technology to Ridgeback Biotherapeutics, and a family member of GRP serves as the Chief Medical

Officer of Ridgeback. This technology is the subject of the research described in this paper. The terms of this arrangement have been reviewed and approved by Emory University in accordance with its conflict-of-interest policies. R.K.P. reports contract testing from Enanta Pharmaceuticals and Atea Pharmaceuticals, and research support from Gilead Sciences, outside of the described work. R.M.C. reports consulting for Merck & Co, outside of the described work. A.L.G. reports contract testing from Abbott, Cepheid, Novavax, Pfizer, Janssen, and Hologic and research support from Gilead Sciences and Merck, outside of the described work. All other authors declare that they have no competing interests to report.

Additional information

Supplementary information The online version contains supplementary material available at https://doi.org/10.1038/s41467-023-40556-8.

Correspondence and requests for materials should be addressed to Richard K. Plemper.

Peer review information *Nature Communications* thanks the anonymous reviewer(s) for their contribution to the peer review of this work. A peer review file is available.

2.1.3 Oral Prodrug of Remdesivir Parent GS-441524 is Efficacious Against SARS-CoV-2 in Ferrets

nature COMMUNICATIONS

ARTICLE

Check for updates

https://doi.org/10.1038/s41467-021-26760-4 OPEN

Oral prodrug of remdesivir parent GS-441524 is efficacious against SARS-CoV-2 in ferrets

Robert M. Cox[1], Josef D. Wolf[1], Carolin M. Lieber[1], Julien Sourimant[1], Michelle J. Lin[2], Darius Babusis[3], Venice DuPont[3], Julie Chan[3], Kim T. Barrett[3], Diane Lye[3], Rao Kalla[3], Kwon Chun[3], Richard L. Mackman[3], Chengjin Ye[4], Tomas Cihlar[3], Luis Martinez-Sobrido[4], Alexander L. Greninger[2], John P. Bilello[3] & Richard K. Plemper[1✉]

Remdesivir is an antiviral approved for COVID-19 treatment, but its wider use is limited by intravenous delivery. An orally bioavailable remdesivir analog may boost therapeutic benefit by facilitating early administration to non-hospitalized patients. This study characterizes the anti-SARS-CoV-2 efficacy of GS-621763, an oral prodrug of remdesivir parent nucleoside GS-441524. Both GS-621763 and GS-441524 inhibit SARS-CoV-2, including variants of concern (VOC) in cell culture and human airway epithelium organoids. Oral GS-621763 is efficiently converted to plasma metabolite GS-441524, and in lungs to the triphosphate metabolite identical to that generated by remdesivir, demonstrating a consistent mechanism of activity. Twice-daily oral administration of 10 mg/kg GS-621763 reduces SARS-CoV-2 burden to near-undetectable levels in ferrets. When dosed therapeutically against VOC P.1 gamma γ, oral GS-621763 blocks virus replication and prevents transmission to untreated contact animals. These results demonstrate therapeutic efficacy of a much-needed orally bioavailable analog of remdesivir in a relevant animal model of SARS-CoV-2 infection.

[1] Center for Translational Antiviral Research, Institute for Biomedical Sciences, Georgia State University, Atlanta, GA, USA. [2] Virology Division, Department of Laboratory Medicine and Pathology, University of Washington, Seattle, WA, USA. [3] Gilead Sciences Inc, Foster City, CA, USA. [4] Texas Biomedical Research Institute, San Antonio, TX, USA. ✉email: rplemper@gsu.edu

The global COVID-19 pandemic has resulted in far more than 150 million cases and an estimated 3.5 million deaths. The socioeconomic and geopolitical impact of the pandemic is unprecedented and will most likely become fully evident only in postpandemic years. To date, remdesivir is the only small molecule antiviral therapeutic approved by the FDA for the treatment of COVID-19[1]. Originally discovered for respiratory syncytial virus[2], remdesivir is a mono-phosphoramidate prodrug of a ribonucleoside analog that must be administered intravenously[3]. The obligatory parenteral delivery limits access of COVID-19 outpatients to remdesivir treatment, thereby narrowing the therapeutic window in which a direct-acting antiviral targeting an acute viral infection is expected to have its greatest effect[4].

Orally active COVID-19 therapeutics have the potential to maximize patient benefit and ideally prevent progression to severe disease. Several oral therapeutic candidates such as EIDD-2801/molnupiravir[5–7] and AT-527[8] are in advanced stages of clinical trials, but currently, only remdesivir has shown confirmed efficacy for COVID-19 treatment in humans[9]. Following intravenous administration and despite its short plasma half-life, remdesivir is sufficiently stable in non-rodent species to distribute to tissues, such as the lung, where it is rapidly converted to its monophosphate metabolite and then efficiently anabolized to the bioactive triphosphate GS-443902 (Fig. 1a)[2,10,11]. An alternative strategy to generate GS-443902 could be to directly administer the remdesivir parent nucleoside GS-441524, but due to less efficient metabolism of GS-441524 to its monophosphate, higher daily systemic exposures of GS-441524 than those obtained from intravenous remdesivir are required to generate equivalent concentrations of GS-443902 in lung tissue. In addition, GS-441524 has displayed poor oral bioavailability in several species[2,12,13]. In order to obtain high exposures after oral delivery, a prodrug strategy to improve oral absorption was employed leading to the identification of GS-621763, which demonstrated high oral bioavailability in two relevant animal species including non-human primates[2].

SARS-CoV-2 efficiently infects mustelids such as ferrets and mink, and both the direct and reverse zoonotic transmission between mink and humans have been reported[14,15]. Infected ferrets show only mild clinical signs, but the virus readily replicates in the upper respiratory tract and shed virus load in nasal lavages is high, supporting efficient animal-to-animal transmission[6]. Consequently, ferrets recapitulate the presentation of SARS-CoV-2 in the majority of human cases, especially in children and younger adults[16,17].

In this study, we used the ferret model to test the oral anti-SARS-CoV-2 efficacy of GS-621763. The GS-621763 prodrug is presystemically hydrolyzed to afford high systemic exposures of GS-441524 (Fig. 1a). Having determined the plasma pharmacokinetic (PK) profile following oral administration of GS-621763 in ferrets, we examined the effect of oral GS-621763 administered therapeutically against the original SARS-CoV-2 USA-WA1/2020 (WA1/2020) strain and the recently emerged, highly prevalent VOC P.1 (γ) lineage[18,19].

Results

Prior to in vivo testing, we assessed antiviral potency of both GS-621763 and its metabolite GS-441524 against lineage A isolate WA1/2020 and three recently emerged VOC, hCoV-19/USA/CA_UCSD_5574/2020 ((α), lineage B.1.1.7; CA/2020), hCoV-19-South Africa/KRISP-K005325/2020 ((β), lineage B.1.351; SA/2020), and hCoV-19/Japan/TY7-503/2021 ((γ), lineage P.1; BZ/2021) in cultured cells.

Antiviral activity against VoCs. Half-maximal effective concentrations (EC_{50}) in SARS-CoV-2-infected Vero E6 cells were highly consistent, ranging from 0.11 to 0.73 µM for GS-621763 (Fig. 1b, Supplementary Table 1) and from 0.11 to 0.68 µM for GS-441524 (Fig. 1c, Supplementary Table 1). Analogous potency ranges were obtained when luciferase-expressing WA1/2020 reporter viruses were examined in dose-response assays in A549 cells stably expressing human ACE2 (A549-hACE2) (Supplementary Table 1)[20]. Toxicity-testing of GS-621763, remdesivir, and GS-441524 in different cell lines and primary human cells derived from different donors revealed half-maximal cytotoxic concentrations (CC_{50}) of 40 to >100 µM (Fig. 1d, Supplementary Table 1), 36 to >100 µM (Supplementary Fig. 1, Supplementary Table 1) and >100 µM (Fig. 1e, Supplementary Table 1), respectively, corresponding to selectivity indices ($SI = CC_{50}/EC_{50}$) of GS-621763 > 137 in VeroE6 and >51 in A549-ACE2 cells. The efficacy of GS-441524 and GS-621763 was in parallel assessed on well-differentiated primary human airway epithelium cultures grown at the air-liquid interface and apically infected with VOC γ (Fig. 1f–g). Basolaterally added GS-441524 or GS-621763 displayed similar potency in this disease-relevant human tissue model, returning EC_{50} values of 2.83 and 3.01 µM, respectively. Parallel measurement of transepithelial electrical resistance demonstrated that epithelium integrity was fully preserved at basolateral drug concentrations ≥3 µM.

Pharmacokinetics following oral administration. Assessment of GS-621763 plasma PK parameters in the ferret revealed excellent oral bioavailability (Fig. 2a), extensive cleavage presystemically to generate high exposures of GS-441524 in the blood (Supplementary Table 2), efficient distribution to soft tissues of the respiratory system (lung), and confirmed anabolism to bioactive GS-443902 (Supplementary Table 3). Following a single 30 mg/kg oral dose of GS-621763 in ferrets, the daily systemic exposure ($AUC_{0\text{-}24h}$) of GS-441524 was 81 µM.h, 4.5 fold higher than the exposure following IV remdesivir at 10 mg/kg and approximately 10-fold greater than that observed following an 200/100 mg IV remdesivir dose in human[21]. Lower levels of bioactive GS-443902 were formed from oral 30 mg/kg GS-621763 dosing compared to 10 mg/kg IV remdesivir (Supplementary Table 3), illustrating the difference in intracellular activation efficiency of the phosphoramidate prodrug remdesivir compared to systemic parent nucleoside GS-441524.

Prophylactic efficacy in ferrets. To test antiviral efficacy, we infected ferrets intranasally with 1×10^5 plaque-forming units (pfu) of WA1/2020, followed by twice daily (b.i.d.) oral treatment with GS-621763 at 20 mg/kg body weight for four days (Fig. 2b). Treatment was initiated at the time of infection, nasal lavages collected in 12-h intervals, and respiratory tissues harvested 4 days after infection. Shed SARS-CoV-2 load in nasal lavages of vehicle-treated animals reached plateau 1.5 days after infection at approximately 1×10^4 pfu/mL, whereas virus was transiently detectable in lavages of only one ferret of the GS-621763-treatment group at 12 h after infection (Fig. 2c). Clinical signs overall are minor in the ferret model[6]. However, only animals of the vehicle group showed elevated body temperature (Fig. 2d) and reduced weight gain (Fig. 2e). The virus was undetectable in the nasal turbinates extracted from treated animals 4 days after infection, compared to a robust load of approximately 5×10^4 pfu/g nasal turbinate of animals of the vehicle group (Fig. 2f). Viral RNA copy numbers found in lavages (Fig. 2g) and turbinates (Fig. 2h) mirrored the infectious titer results, revealing a consistent, statistically significant difference between the vehicle and treatment groups of two and three orders of magnitude, respectively. Consistent with prior studies[6], no infectious virions or viral RNA were detectable in the lower respiratory tract (Fig. 2i, j).

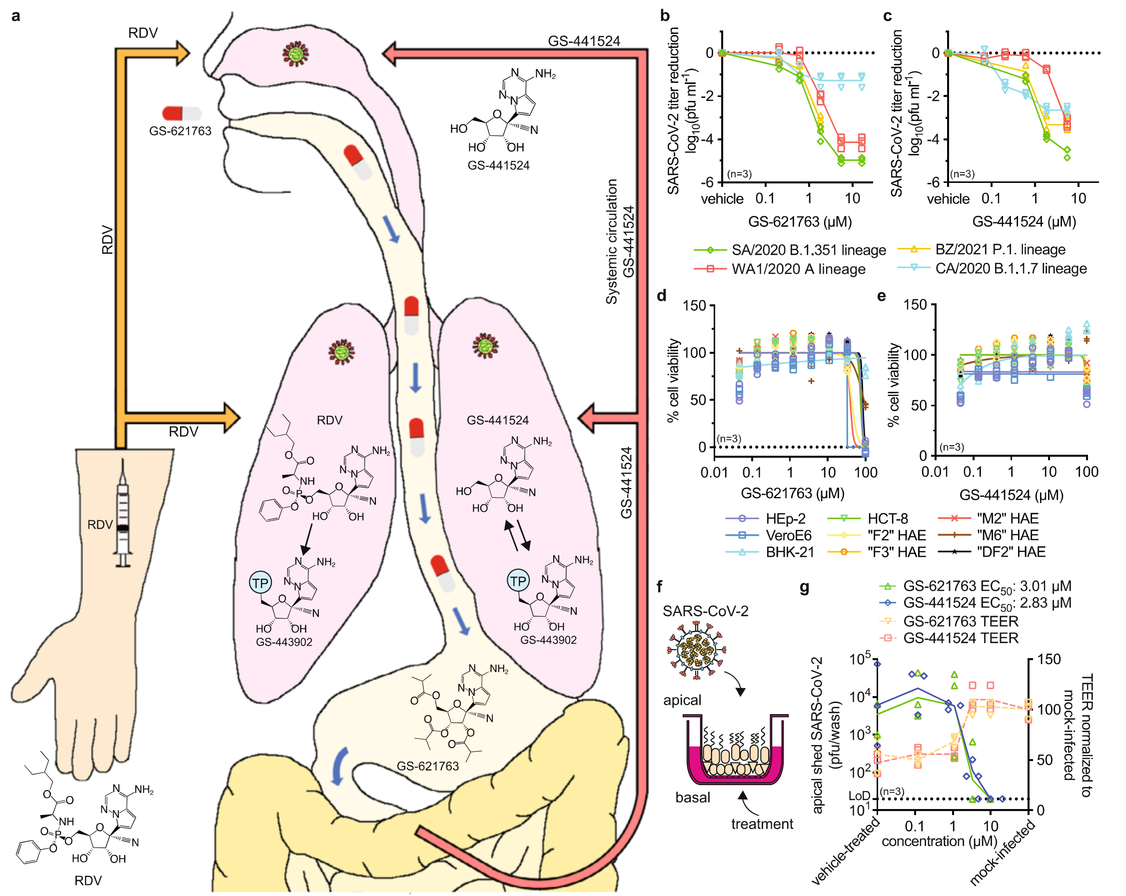

Fig. 1 Antiviral potency of remdesivir analog GS-621763. a Schematic depicting metabolism of remdesivir (RDV; orange arrows) and GS-621763 (red/white pills; red arrows) after injection or oral uptake, respectively. Remdesivir distributes into tissues (e.g., lung) and is efficiently metabolized intracellularly to GS-443902 (TP = triphosphate). Conversely, GS-441524 is the dominant plasma metabolite after intestinal absorption of orally administered GS-627163 and is subsequently anabolized to GS-443902 in the tissues. **b–c** Virus yield reduction of SARS-CoV-2 clinical isolates WA1/2020 (red squares), CA/2020 (blue triangles), SA/2020 (green diamonds), and BZ/2021 (yellow triangles) representing the A, B.1.1.7 (α), B.1.351 (β) and P.1 (γ) lineages, respectively, by GS-621763 (b) and GS-441524 (c) on VeroE6 cells. EC_{50} concentrations are specified in Supplementary Table 1. **d–e** In vitro cytotoxicity profiles of GS-621763 (d) and GS-441524 (e) on VeroE6 (blue squares), HEp-2 (purple circles), BHK-21 (light blue triangles), HCT-8 (green triangles) and a panel of primary HAE cells from independent donors ("F2" (yellow diamonds), "F3" (orange circles), "M2" (red "×" symbols), "M6" (brown "+" symbols), "DF2" (black stars)). **f** schematic of well-differentiated air-liquid interface HAE cultures. **g** HAEs were infected from the apical side with SARS-CoV-2 VOC γ and treated from the basolateral side with GS-621763 or GS-441524. Apically shed virus titers (green triangles and blue diamonds for GS-621763 or GS-441524, respectively) on day after infection and the impact of treatment on preserving tissue integrity (transepithelial electrical resistance (TEER) (orange triangles and red squares for GS-621763 or GS-441524, respectively) are shown. LoD, the limit of detection. In (**b–e, g**), symbols represent individual biological repeats ($n = 3$), lines (**b–c, g**) intersect the mean, lines in (**d–e**) depict nonlinear regression models.

Therapeutic efficacy and lowest efficacious dose. To determine the lowest efficacious dose in a clinically more relevant therapeutic setting, we initiated oral treatment 12 h after infection, when the shed virus is first detectable in nasal lavages, at the 10 mg/kg and 3 mg/kg body weight levels, administered b.i.d. (Fig. 3a). EIDD-2801/molnupiravir at 5 mg/kg b.i.d. was given as reference following an identical therapeutic b.i.d. regimen[6]. EIDD-2801 was included as a reference compound, since at the time of study EIDD-2801 was the only nucleoside analog with demonstrated oral efficacy against SARS-CoV-2 in the ferret model. Shed virus load was significantly lower in all treated animals than in the vehicle group within 12 h of treatment onset (Fig. 3b). Virus load in nasal lavages of ferrets receiving GS-621763 at 3 mg/kg plateaued approximately one order of magnitude lower than in those from vehicle animals, while treatment with GS-621763 at 10 mg/kg or EIDD-2801/molnupiravir reduced shedding to near-detection level by day 3 after infection. Consistent with this inhibitory effect, treatment with 3 mg/kg GS-621763 reduced burden in the turbinates by one order of magnitude (Fig. 3c), while virus burden approached the limit of detection in animals of the 10 mg/kg GS-621763 and EIDD-2801/molnupiravir treatment groups. No significant differences in clinical signs were noted between vehicle animals and any of the treatment groups (Fig. 3d, e).

Viral RNA was detectable in nasal lavages and turbinates of all animals, underscoring efficient infection. However, RNA copies

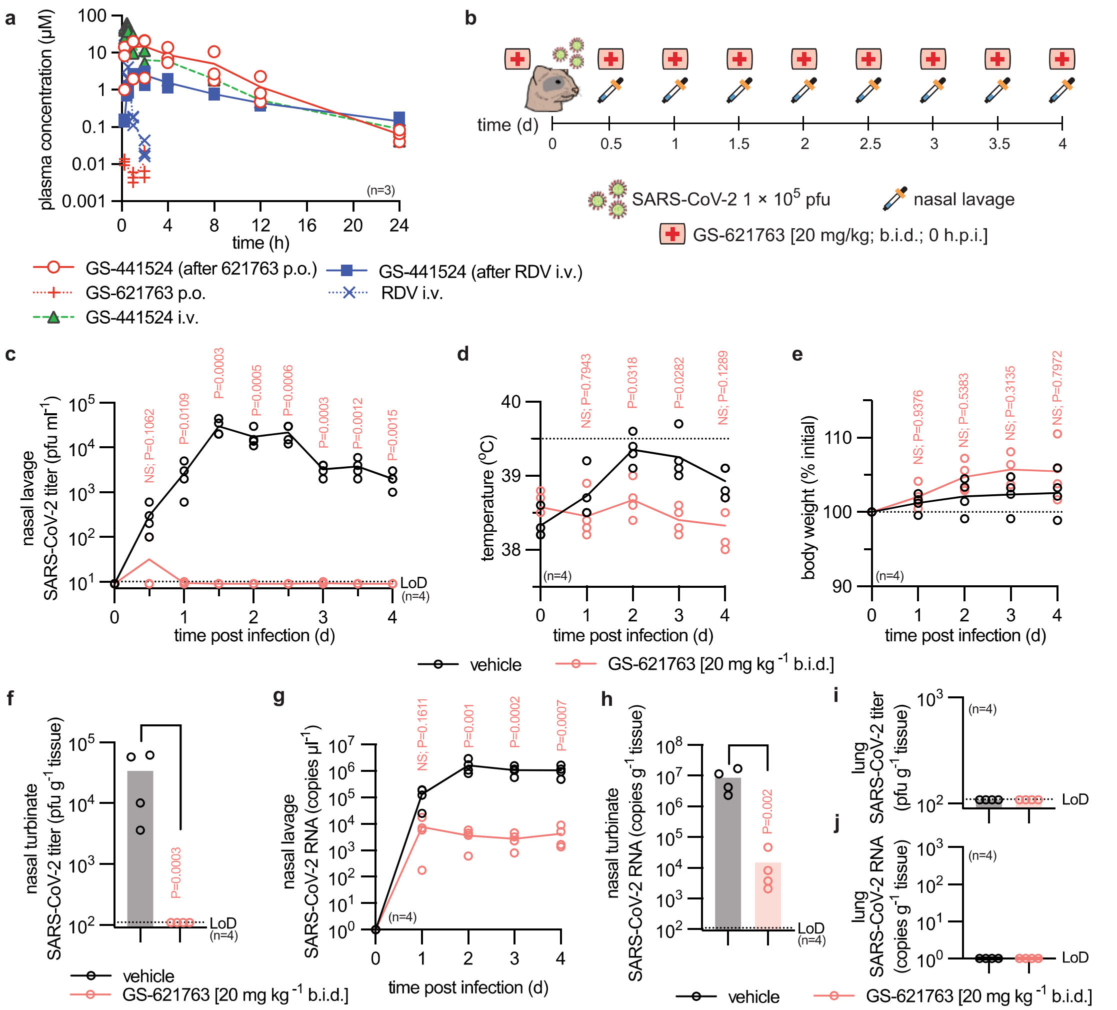

Fig. 2 Prophylactic efficacy of GS-621763. a Single-dose PK study in ferrets showing plasma concentrations of GS-441524, GS-621763, and remdesivir (RDV) as specified after dosing with GS-621763 (30 mg/kg; p.o.; red "+" symbols), remdesivir (10 mg/kg; i.v.; blue "×" symbols), and GS-441524 (20 mg/kg; i.v.; green triangles). Symbols represent individual biological repeats ($n = 3$), lines depict sample means. **b**, Schematic of the prophylactic efficacy study design. Ferrets were infected intranasally with 1×10^5 pfu WA1/2020 (virus symbol). Groups ($n = 4$) were gavaged b.i.d. (first aid symbol) with vehicle or GS-621763 (20 mg/kg) starting at the time of infection. Nasal lavages (pipet symbol) were harvested twice daily. All animals were terminated 4 days after infection. **c** Virus titers from nasal lavages; LoD, limit of detection. **d** Temperature measurements collected once daily. **e** Body weight measured once daily. **f** Infectious titers of SARS-CoV-2 in nasal turbinates harvested four days after infection. **g** SARS-CoV-2 RNA copies present in nasal lavages. **h**, SARS-CoV-2 RNA copies detected in nasal turbinates. **i–j** SARS-CoV-2 infectious particles (**i**) and SARS-CoV-2 RNA copies (**j**) in lungs four days after infection. Symbols for vehicle-treated and GS-621763 treated ferrets are shown as black and red circles, respectively (**c–j**). The number of independent biological repeats (individual animals) is shown in each subpanel, symbols represent independent biological repeats, lines (**c–e**, **g**) and bar graphs (**f**, **h–j**) connect or show samples mean, respectively, and *P* values are stated. 2-way ANOVA with Sidak's post hoc multiple comparison tests (**c–e**, **g**) or two-tailed *t* test (**f**, **h**).

showed a statistically significant mean reduction in the 10 mg/kg GS-621763 and EIDD-2801/molnupiravir groups compared to vehicle (Fig. 3f, g). These results confirm the oral efficacy of therapeutic GS-621763 against WA1/2020 in a relevant animal model of upper respiratory infection.

Inhibition of replication and transmission of VOC γ. To probe the anti-SARS-CoV-2 indication spectrum of GS-621763, we applied the efficacious regimen, 10 mg/kg GS-621763 b.i.d. started 12 h after infection, to recently emerged VOC γ[22] in a combined efficacy and transmission study (Fig. 4a). After an initial replication delay, the shed virus became detectable in vehicle-treated animals 1.5 days after infection, then rapidly reached a robust plateau of nearly 10^4 pfu/mL nasal lavage on day 2 after infection (Fig. 4b). Quantitation of viral RNA copies mimicked the profile of the infectious titers, although a low viral RNA load was present in lavages already on the first day after infection (Fig. 4c). Viral titers and RNA copies in nasal turbinates determined 4 days after infection were likewise high, ranging from 10^4 to 10^5 pfu/g tissue (Fig. 4d) and 10^8 to 10^{10} RNA copies/g tissue (Fig. 4e), respectively. However, no infectious VOC γ virions or viral RNA were

NATURE COMMUNICATIONS | https://doi.org/10.1038/s41467-021-26760-4 ARTICLE

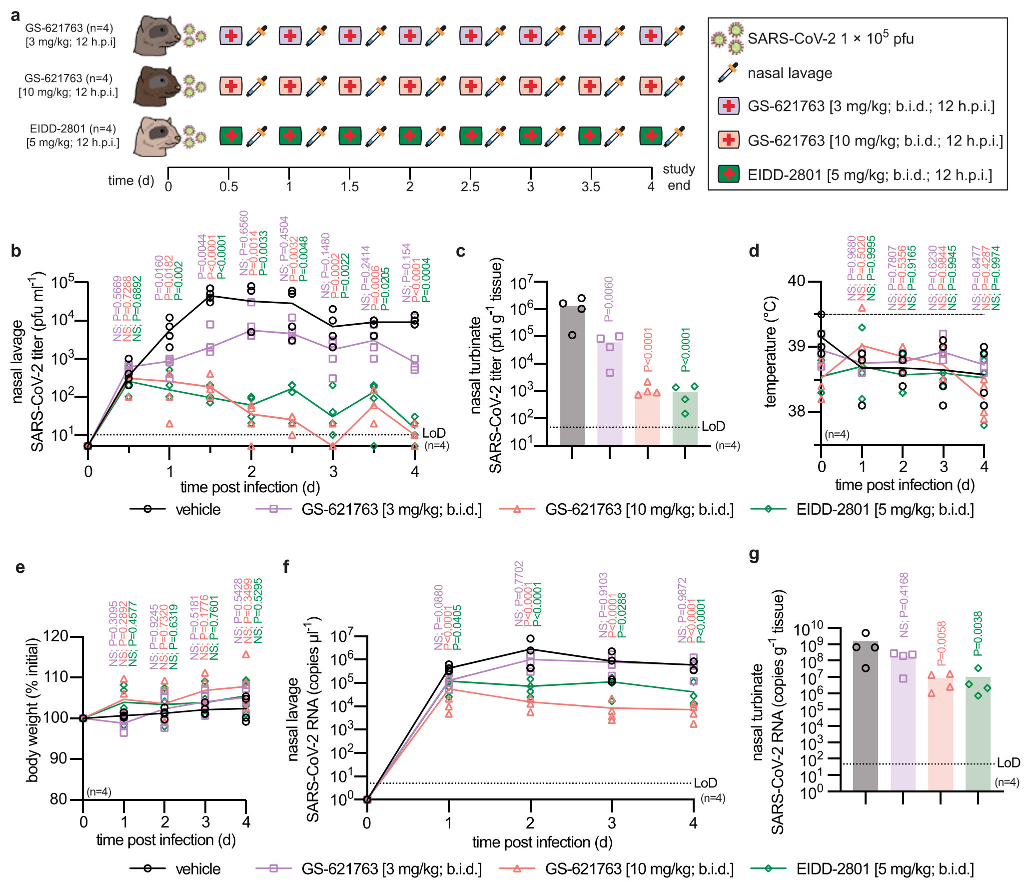

Fig. 3 Therapeutic efficacy of GS-621763. **a** Schematic of the therapeutic efficacy study design. Ferrets were infected intranasally with 1×10^5 pfu WA1/2020. Symbols as described for Fig. 2a. Starting 12 h after infection, groups of ferrets ($n = 4$) were gavaged b.i.d. with vehicle (black circles in b–g), GS-621763 (3 mg/kg (purple first aid symbol; purple circles in **b–g**) or 10 mg/kg (pink first aid symbol; red circles in **b–g**)), or treated with EIDD-2801 (5 mg/kg (green first aid symbol; green diamonds in b-g)). Nasal lavages were harvested twice daily. Animals were terminated 4 days after infection. **b** Virus titers from nasal lavages. **c**, Infectious titers of SARS-CoV-2 in nasal turbinates harvested four days after infection. **d** Temperature measurements collected once daily. **e** Body weight measured once daily. **f** SARS-CoV-2 RNA copies present in nasal lavages. **g** SARS-CoV-2 RNA copies detected in nasal turbinates. The number of independent biological repeats (individual animals) is shown in each subpanel. Symbols represent independent biological repeats, lines (**b, d, e, f**) and bar graphs (**c, g**) connect or show samples mean, respectively, and *P* values are stated. 1-way (**c, g**) or 2-way (**b, d, e, f**) ANOVA with Dunnett's post hoc multiple comparison tests. LoD limit of detection.

detected in the lungs of any of these animals (Fig. 4f, g), and no clinical signs such as changes in body weight or fever emerged (Supplementary Fig. 2a, b). This presentation mimicked our previous experience with WA1/2020[6], indicating that VOC γ does not invade the ferret host more aggressively than WA1/2020. Treatment of VOC γ infection with oral GS-621763 was highly efficacious, reducing both shed virus burden and tissue titers to undetectable levels (Fig. 4b, d) and lowering viral RNA copies in nasal lavages and turbinates by over three orders of magnitude (Fig. 4c, e).

Whole genome sequencing of the virus inoculum and virus populations extracted from nasal turbinates confirmed the presence of mutations characteristic for the P.1 VOC[23] (Fig. 4h, Supplementary Dataset 1). In addition, we noted an L260F substitution in nsp6 associated with SARS-CoV-2 adaptation to weasels[14] that had a 60%-allele frequency in the VOC γ inoculum. Four days after infection of ferrets, this mutation had become fully dominant and a second characteristic weasel mutation, Y453F in the spike protein that was first noted in several clusters of SARS-CoV-2 outbreaks in mink farms[14], had emerged in addition (Fig. 4h, Supplementary Dataset 1). We furthermore noted the presence of an F184V exchange in nsp6 of the VOC γ inoculum, which arose during amplification in VeroE6 cells[23] and was rapidly counterselected against in the ferret host. In contrast, the WA1/2020 inoculum used for our ferret studies did not contain any unreported additional changes (Fig. 4h, Supplementary Dataset 2). WA1/2020 also acquired a weasel-characteristic mutation when passaged through ferrets, N501T in the receptor binding domain of the spike protein[14], but no changes in nsp6 were detected and only one animal harbored a virus population with Y453F substitution in low (8%) allele frequency. Neither the GS-621763-experienced VOC γ nor WA1/2020 populations contained remdesivir resistance mutations previously selected in SARS-CoV-2 (i.e., E802D in nsp12[24]) or the related mouse hepatitis virus[25] (i.e., F476L and V553L in nsp12) nor did any new variants arise in nsp12 at >5% allele

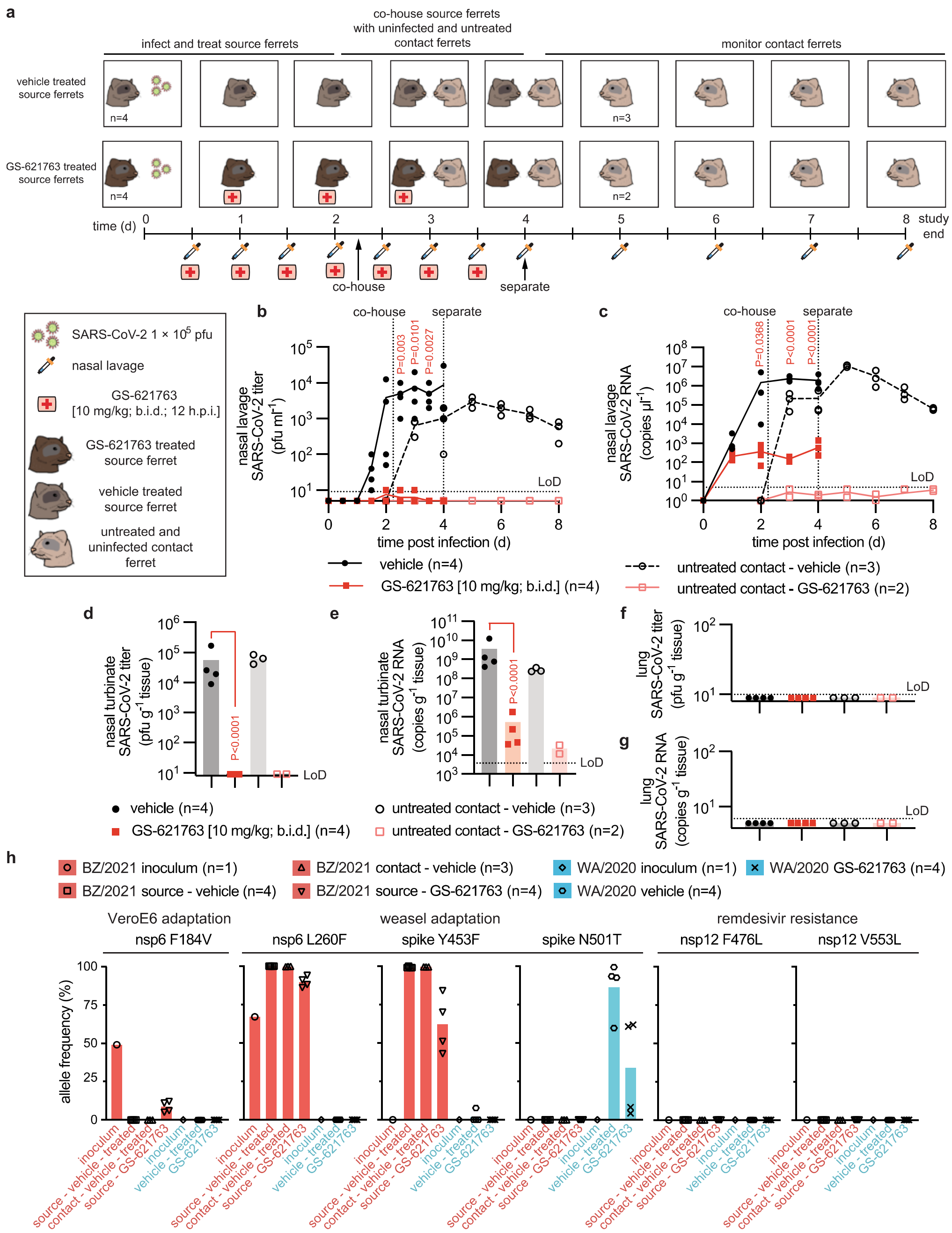

frequency, when viruses were extracted from treated animals at the time of termination (Fig. 4h, Supplementary Datasets 1, 2).

All vehicle-treated animals efficiently transmitted VOC γ to untreated direct-contact ferrets (Fig. 4b–e). Co-housing was started 54 h after infection and continued until termination of the source animals. Shed VOC γ replicated in the contacts without delay, becoming first detectable in nasal lavages within 12 h after initiation of co-housing. This altered replication profile corroborated VOC γ adaptation to the ferret host in the source animals, and virus populations recovered from contacts of vehicle-treated source animals indeed contained both the L260F exchange in nsp6 and the Y453F mutation in spike (Fig. 4h, Supplementary Dataset 1). Consistent with efficient inhibition of VOC γ replication in the treated source animals by oral GS-621763, treatment completely blocked virus transmission to untreated direct-contact animals. None of the contacts of treated source ferrets shed infectious particles or viral RNA at any time (Fig. 4b, c), infectious viral particles were absent from nasal turbinates 5.5 days after initiation

Fig. 4 GS-621763 blocks replication and transmission of SARS-CoV-2 VOC γ a, Schematic of the efficacy and contact transmission study design. All ferrets were infected intranasally with 1×10^5 pfu BZ/2021 (virus symbol). Symbols as described for Fig. 2a. Groups of ferrets ($n = 4$) were gavaged b.i.d. with vehicle (black circles in **b–g**) or GS-621763 (10 mg/kg; red squares in **b–g**) starting at 12 h after infection. Nasal lavages were harvested twice daily. On the second day after infection, vehicle and GS-621763 ferrets were cohoused with untreated contact ferrets (black open circles and red open squares for vehicle and GS-621763 contact ferrets, respectively). Source ferrets were terminated 4 days after infection and all contact animals were terminated on study day 8. **b** Virus titers from nasal lavages. **c**, SARS-CoV-2 RNA copies present in nasal lavages. **d** Infectious titers of SARS-CoV-2 in nasal turbinates harvested four days after infection. **e** SARS-CoV-2 RNA copies detected in nasal turbinates. **f** Infectious titers of SARS-CoV-2 in lung tissue. **g** SARS-CoV-2 RNA copies present in lung tissue. In (**b–g**), the number of independent biological repeats (individual animals) is shown in each subpanel. Symbols represent independent biological repeats, lines (**b, c**) and bar graphs (**d–g**) connect or show sample means, respectively, and P values are stated. 1-way (**d, e**) or 2-way (**b, c**) ANOVA with Tukey's (**d, e**) or Sidak's (**b, c**) post hoc multiple comparison tests. **h**, Metagenome sequence analysis of inoculum WA1/2020 (blue bar; black diamonds; $n = 1$) and BZ/2021 (red bar; black circles; $n = 1$) viruses, BZ/2021 RNA extracted from ferret nasal turbinates four days after infection (red bars; black squares and downward pointing triangles for vehicle ($n = 4$) and GS-621763 treated ($n = 4$) ferrets, respectively), WA1/202 RNA extracted from ferret nasal turbinates four days after infection (blue bars; black hexagons and "×" symbols for vehicle ($n = 4$) and GS-621763 treated ($n = 4$) ferrets, respectively) and BZ/2021 populations extracted from nasal lavages of contacts of vehicle-treated source animals (red bars; black upward pointing triangles; $n = 3$). Relative allele frequencies of signature residues are shown. Symbols represent independent biological repeats (virus population of individual animals), columns show group means. LoD limit of detection.

of co-housing (Fig. 4d), and only a low level of viral RNA ($<10^5$ copies/g nasal turbinate) was detected in nasal turbinates of the contact animals (Fig. 4e).

Discussion

This study demonstrates oral efficacy of the remdesivir analog GS-621763 against the early clinical SARS-CoV-2 isolate WA1/2020 and one of the recently emerged VOC in the ferret model. After oral administration of GS-621763, only low systemic levels of intact prodrug were transiently observed. The parent nucleoside GS-441524 was the major metabolite detected in blood, more than three orders of magnitude higher than intact prodrug, indicating efficient conversion upon intestinal absorption. GS-441524 metabolism inside cells to the same intracellular bioactive triphosphate GS-443902 in tissues links GS-621763 to the well-understood mechanism of action of remdesivir, which blocks SARS-CoV-2 replication by triggering delayed chain termination of the nascent viral RNA chain[26] and/or template-dependent inhibition after incorporation into viral antigenomic RNA[27]. Systemic GS-441524 is less efficient at forming the bioactive GS-443902 in the lungs of ferrets compared to systemic remdesivir, but the exposure of GS-441524 achieved following oral dosing of GS-621763 is sufficient to overcome this difference and generate substantial levels of bioactive GS-443902. The more persistent but lower plasma levels of GS-441524 following intravenous remdesivir are a result of efficient formation of triphosphate in tissues from remdesivir, followed by slow dephosphorylation to GS-441524, which then appears in plasma, as evidenced by its similar half-life with that of the triphosphate GS-443902 in PBMC[21].

Although GS-443902 levels in ferret respiratory tissues after a single 30 mg/kg oral dose of GS-621763 trailed those of intravenous 10 mg/kg remdesivir by approximately fourfold at 24 h, a minimal daily oral dose of 20 mg/kg GS-621763 (10 mg/kg b.i.d.) provided full therapeutic benefit, rapidly reducing shed virus titers to near-undetectable. However, as the GS-443902 active metabolite is quantitated from gross tissue samples, we cannot compare GS-443902 levels resulting from either GS-621763 or remdesivir dosing in distinct respiratory cell types. If human oral bioavailability of GS-621763 is consistent with that observed in ferrets, and the model is predictive of antiviral potential, the dose levels identified in the ferret study as fully efficacious in upper respiratory tract correspond to a feasible human daily dose of approximately 250 mg oral GS-621763.

An observed difference of approximately two to three orders of magnitude between the infectious titers and viral RNA copy numbers in the ferrets closely resembled that described in earlier reports[6,28,29], demonstrating high reproducibility of the model. At present, the correlation between upper respiratory tract SARS-CoV-2 load at early stages after human infection and the likelihood of progression to viral pneumonia and severe COVID-19 has not been fully understood. However, clinical studies have linked higher upper respiratory virus burden to a heightened patient risk of developing severe COVID-19, requiring intubation or intensive care, and having an unfavorable outcome[30]. Based on these clinical data and the rapid reduction of upper respiratory virus burden seen in the ferret model, we expect that early initiation of oral treatment, ideally immediately following a positive diagnostic test and before the onset of clinical signs[31,32], holds high promise to block viral invasion of the lower respiratory tract and viral pneumonia that necessitates hospitalization.

Recently emerged SARS-CoV-2 variants such as VOC γ are a major concern because of their high prevalence and increased frequency of transmission[18,33]. Ferrets infected with VOC γ did not develop more severe clinical signs than after infection with WA1/2020 and the virus did not advance to the lower respiratory tract, indicating that pathogenicity of this VOC is not fundamentally different from that of WA1/2020 in this model. Peak viral burden and shed virus loads of VOC γ-infected ferrets were equivalent to those of WA1/2020. Reflecting that analysis of circulating SARS-CoV-2 VOC worldwide has yielded no evidence of widespread transmission of remdesivir-resistant strains[24,25,34], GS-621763 and its metabolite GS-441524 were comparably potent against VOC α, β, and γ as against WA1/2020 in cell culture. Importantly, oral GS-621763 was highly efficacious against VOC γ in vivo, reducing infectious titers to near-undetectable levels rapidly after treatment initiation. Whole genome sequencing of GS-621763-experienced viruses recovered from treated ferrets likewise revealed no allele variations in candidate remdesivir resistance sites, indicating that SARS-CoV-2 does not rapidly escape from inhibition by GS-621763 in vivo.

Based on the high transmissibility of VOC γ in the field and very efficient direct-contact transmission of SARS-CoV-2 between ferrets[35], we assessed the impact of oral GS-621763 on VOC γ spread among ferrets. To recapitulate what we consider a realistic scenario for exploring pharmacological interference in community transmission, we therapeutically treated the infected source animals but left their contacts untreated. In this relevant experimental setting, treatment with the same GS-621763 dose of 10 mg/kg b.i.d. completely blocked transmission of VOC γ, resembling the performance of oral EIDD-2801/molnupiravir in the model[6].

These results build confidence that a new generation of orally available broad-spectrum antivirals is emerging that should allow initiation of treatment early after infection and promise to efficiently interrupt community transmission chains. In addition to immediately contributing to ending the COVID-19 pandemic and containing the continued evolution of increasingly contagious SARS-CoV-2 VOC[36–38], an oral analog of the broad-spectrum antiviral drug remdesivir with confirmed in vivo efficacy may become a cornerstone in the first-line defense against future pandemic threats.

Methods

Study design. Ferrets (*Mustela putorius furo*) were used as an in vivo model to determine efficacy of the orally available remdesivir analog GS-621763 against SARS-CoV-2 infection and transmission to untreated and uninfected contact animals. Oral bioavailability and pharmacokinetic properties of GS-621763 in ferrets were assessed prior to infecting any animals with SARS-CoV-2. For efficacy and transmission studies, anesthetized ferrets were inoculated intranasally with SARS-CoV-2. Nasal lavages were performed periodically at predefined time points to measure virus load. Temperature and body weight were measured once daily for all animals. At four days after infection (study day 8 for contact ferrets), animals were euthanized and nasal turbinates extracted to measure virus load in the upper respiratory tract. SARS-CoV-2 titers were determined by plaque assay and viral RNA copies quantified by RT-qPCR.

Cells and viruses. African green monkey kidney VeroE6 (ATCC®, cat# CRL-1586™), human lung adenocarcinoma epithelial Calu-3 (ATCC® HTB-55™), human epithelial/HeLa contaminant HEp-2 (ATCC®, cat# CCL-23™), and baby hamster kidney BHK-21 (ATCC®, cat# CCL-10™) cells were cultivated in a humidified chamber at 37 °C and 5% CO_2 in Dulbecco's Modified Eagle's medium (DMEM) (Corning, cat# 10-013-CV, lot# 05721000) supplemented with 7.5% (10% for Calu-3) heat-inactivated fetal bovine serum (FBS) (Corning, cat# 35-010-CV, lot# 14020001). Human epithelial colon adenocarcinoma HCT-8 cells (ATCC® cat# CCL-244™ lot# 70036111) were cultivated at 37 °C and 5% CO_2 in Roswell Park Memorial Institute (RPMI-1640) medium (Quality biological, cat# 112-024-101, lot# 723411) supplemented with 2 mM L-glutamine (Gibco, cat# 23030-081) and 10% heat-inactivated FBS.

A549-hACE2 cells that stably express human angiotensin-converting enzyme 2 (hACE2) were grown in the culture medium supplemented with 10 μg/mL Blasticidin S. Primary human airway epithelial (HAE) cells from multiple donors were cultivated at 37 °C and 5% CO_2 in Bronchial Epithelial Cell Growth Medium (BEGM) BulletKit following the provider's instructions (Lonza, cat# CC-3171 lot# 0000889952 with supplement cat# CC-4175 lot# 0000848033). Human Bronchial Tracheal Epithelial cells (HBTEC) were derived from the following donors: "F2" from a 29-year old Caucasian female (Lifeline, cat# FC-0035, lot# 5101); "F3" from a 42-year old Caucasian female (Lonza, cat# CC-2540S, lot# 0000519670); "M2" from a 40-year old Caucasian male (Lonza, cat# CC-2540S, lot# 0000667744); and "M6" from a 48-year old Caucasian male (Lonza, cat# CC-2540S, lot# 0000544414). Diseased (Asthma) Human Bronchial Epithelial (DHBE) cells "DF2" were from a 55-year old Caucasian female (Lonza, cat# 00194911 S, lot# 0000534647). Primary HAE was used for cytotoxicity assays at passage ≤3. Cell lines were routinely checked for mycoplasma and bacterial contamination.

SARS-CoV-2 strains were obtained from BEI and propagated using Calu-3 cells supplemented with 2% FBS in accordance with approved biosafety level 3 protocols. Virus stocks were stored at −80 °C. Stock virus titers were determined by plaque assay and stocks authenticated through metagenomic sequencing.

Plaque assays. Vero E6 cells were seeded in 12-well plates at 3×10^5 cells per well. The following day, samples were serially diluted in DMEM containing Antibiotic-Antimycotic (Gibco) supplemented with 2% FBS. Dilutions were then added to cells and incubated for 1 h at 37 °C. Cells were subsequently overlayed with 1.2% Avicel 581-NF (FMC BioPolymer) in DMEM containing Antibiotic-Antimycotic (Gibco) and allowed to incubate for 3 days at 37 °C with 5% CO_2. After 3 days, the overlay was removed, cells were washed once with phosphate buffered saline (PBS) and fixed with neutral buffered formalin (10%) for 15 min. Plaques were then visualized using 1% crystal violet followed by washing with water.

Compound sources and chemical synthesis. Remdesivir was either purchased from MedChemExpress (cat# HY-104077, batch# 46182) or synthesized at Gilead Sciences, Inc. GS-441524 was either purchased from MedChemExpress (cat# HY-103586, batch# 62110) or synthesized at Gilead Sciences Inc. GS-621763 was synthesized at Gilead Sciences Inc:[2] ^{1}H NMR (300 MHz, $CHCl_3$-d_3) δ 11.15 (bs, 1H), 8.27 (bs, 1H), 7.95 (s, 1H), 7.32 (m, 1H), 7.07 (m, 1H), 6.05 (d, $J = 6.0$ Hz, 1H), 5.44 (t, $J = 5.1$ Hz, 1H), 4.66 (t, $J = 3.6$ Hz, 1H), 4.32 (m, 2H), 2.73–2.52 (m, 3H), 1.27–1.14 (m, 18H). LC-MS (B) $m/z = 502.2$ [M + H], 500.1 [M – H]. All EIDD-2801/molnupiravir used in this study was provided by Gilead Sciences Inc., sourced from MedChemExpress.

Cytotoxicity assays. In each well of 96-well plates, 7500 cells were seeded (Corning, cat# 3598). Cells were incubated with threefold serial dilutions of compound from a 100 μM maximum concentration. Each plate included 4 wells of positive (100 μM cycloheximide (Millipore Sigma, cat# C7698-5G)) and negative (vehicle (0.2% dimethyl sulfoxide (DMSO)) controls for normalization. Plates were incubated in a humidified chamber at 37 °C and 5% CO_2 for 72 h. PrestoBlue™ Cell Viability Reagent (ThermoFisher Scientific, cat# A13262) was added in each well (10 μl/well) and fluorescence recorded on a Synergy H1 multimode microplate reader (BioTek) after 1-h incubation (excitation 560 nm, emission 590 nm). Raw data was normalized with the formula: % cell viability = 100 × (signal sample—signal positive control)/(signal negative control—signal positive control). Fifty percentage cytotoxic concentrations (CC_{50}) and 95% confidence intervals after nonlinear regression were determined using the inhibitor vs normalized response equation in Prism 9.1.0 for MacOS (GraphPad). For cytotoxicity assays in A549-hACE2 cells, compounds (200 nl) were spotted onto 384-well plates prior to seeding 5000 A549-hACE2 cells/well in a volume of 40 μl culture medium. The plates were incubated at 37 °C for 48 h with 5% CO_2. On day 2, 40 μl of CellTiter-Glo (Promega) was added and mixed 5 times. Plates were read for luminescence on an Envision (PerkinElmer) and CC_{50} values calculated using a nonlinear four parameter regression model.

Virus yield reduction. In 12-well plates 16 h before infection, 2×10^5 VeroE6 cells were seeded per well. Confluent monolayers were then infected with the indicated virus at a multiplicity of infection (MOI) of 0.1 pfu/cell for 1 h at 37 °C with frequent rocking. Inoculum was removed and replaced with 1 mL of DMEM with 2% FBS and the indicated concentration of compound. Cells were incubated at 37 °C and 5% CO_2 for 48 h. Supernatant were harvested, aliquoted and stored at −80 °C before being analyzed by plaque assay.

Reporter virus assays. A549-hACE2 cells (12,000 cells per well in medium containing 2% FBS) were plated into a white clear-bottomed 96-well plate (Corning) at a volume of 50 μl. On the next day, compounds were added directly to cultures as 3-fold serial dilutions with a Tecan D300e digital liquid dispenser, with DMSO volumes normalized to that of the highest compound concentration (final DMSO concentration < 0.1%). The diluted compound solutions were mixed with 50 μl of SARS-CoV-2-Nluc (MOI 0.025 pfu/cell), expressing a nano luciferase reporter protein (kind gift of Xuping Xie and Pei-Yong Shi (University of Texas Medical Branch; Galveston, TX)). At 48 h postinfection, 75 μl Nano luciferase substrate solution (Promega) was added to each well. Luciferase signals were measured using an Envision microplate reader (Perkin Elmer). The relative luciferase signals were calculated by normalizing the luciferase signals of the compound-treated groups to that of the DMSO-treated groups (set as 100%). EC_{50} values were calculated using a nonlinear four parameter variable slope regression model.

Air-liquid interface (ALI) human airway epithelial cells (HAE) shed viral titer reduction. Approximately 150,000 viable "F3" cells per cm^2 at passage three were seeded on Transwell 6.5 mm polyester membrane insert with 0.4 μm pore size (Corning, cat# 3470). Upon reaching confluence (day 4 postseeding), basal media was removed and replaced with PneumaCult-Ex Plus (Stemcell Technologies cat# 05040), while apical media was removed to create an air-liquid interface. Beating ciliae, mucus production and transepithelial electrical resistance (TEER) > 300 Ohm*cm^2 were noticeable ~3 weeks post ALI, confirming successful differentiation. Cells were maintained in a differentiated state with weekly apical washes of mucus with PBS for 5 months before infection. One hour prior to infection, TEER was measured with 150 μl PBS and basal media was replaced with fresh media containing indicated serial dilutions (threefold down from 10 μM) of GS-621763 or GS-441524 or vehicle (dimethylsulfoxide 0.1%). The apical side was infected with ~25,000 PFU of SARS-CoV-2 gamma isolate grown on Calu-3 cells (lineage P.1., isolate hCoV-19/Japan/TY7-503/2021 (BZ/2021; Brazil P.1), BEI cat# NR-54982) in 100 μl DMEM for 1 h at 37 °C, then the inoculum was removed and washed with PBS twice. Cells were incubated for 3 days at 37 °C before final TEER measure and fixation with 10 % neutral buffered formalin for 1 h. Shed apical viruses were harvested with 200 μl PBS for 30 min at 37 °C 48 and 72 h postinfection and viral titers were estimated by plaque assay. To determine EC50s, log viral titers were normalized using the average top plateau of viral titers to define 100% and were analyzed with a nonlinear regression with the variable slope with Prism 9.0.1 for MacOS (GraphPad). TEER were measured with the EVOM or EVOM3 system (World Precision Instruments).

Pharmacokinetics. Female ferrets were either intravenously administered 10 mg/kg remdesivir as a 30-min infusion or orally administered 30 mg/kg GS-621763, after which plasma was isolated at 7–9 timepoints postadministration. Plasma samples underwent methanol protein precipitation followed by centrifugation. The resulting supernatants were isolated, evaporated to dryness under nitrogen and reconstituted with 5% acetonitrile for injection onto an LC-MS/MS system (Sciex API-4500). Concentrations of remdesivir, GS-621763, and GS-441524 were determined using 9-point calibration curves spanning at least 3 orders of magnitude, with quality control samples to ensure accuracy and precision, prepared in normal ferret plasma. Analytes were separated by a 50 × 3.0 mm, 2.55 μm Synergi Polar-RP 30 A column (Phenomenex, Inc.) using a mobile phase A consisting of 10 mM ammonium formate with 0.1% formic acid and a mobile phase B consisting of 0.1% formic acid in acetonitrile. A multi-stage linear gradient from 5% to 95% mobile phase B at a flow rate of 1 mL/min was employed for analyte separation (Shimadzu). Pharmacokinetic parameters were calculated using Phoenix WinNonlin (version 8.2, Certara) and concentration-time profiles generated using Prism (version 8, GraphPad). Ferret lungs were collected at 24 h following initiation of drug administration. Whole tissues were quickly isolated and immediately placed into liquid nitrogen and stored at -80 °C until processing and LC-MS/MS analysis[2]. Reported values for lung total nucleosides are the sum of (GS-441524 and mono-, di-, and triphosphate (GS-443902) metabolites).

Ferret efficacy studies. Female ferrets (6–10 months old, *Mustela putorius furo*) were purchased from Triple F Farms. Ferrets were rested for 7 days after arrival. Ferrets were then housed individually or in groups of 2 in ventilated negative-pressure cages in an ABSL-3 facility. Based on the previous experiments[6], ferrets were randomly assigned to groups ($n = 4$) and used as an in vivo model to examine the efficacy of orally administered compounds against SARS-CoV-2 infection. No blinding of investigators was performed. Ferrets were anesthetized using dexmedetomidine/ketamine and infected intranasally with 1×10^5 pfu 2019-nCoV/USA-WA1/2020 in 1 mL (0.5 mL per nare). Body weight and rectal temperature were measured once daily. Nasal lavages were performed twice daily using 1 mL sterile PBS (containing Antibiotic-Antimycotic (Gibco)). Nasal lavage samples were stored at -80 °C until virus titration could be performed by plaque assay. Treatment (once daily (q.d.) or twice daily (b.i.d.)) was initiated at either 0 or 12 h after infection and continued until 4 days postinfection with either vehicle (2.5% dimethyl sulfoxide; 10% Kolliphor HS-15; 10% Labrasol; 2.5% propylene glycol; 75% water) or compound. Four days after infection, ferrets were euthanized, and tissues and organs were harvested and stored at -80 °C until processed.

Contact transmission in ferrets. Eight ferrets were anesthetized and inoculated intranasally with 1×10^5 pfu of hCoV-19/Japan/TY7-503/2021. Twelve hours after infection, ferrets were split into two groups ($n = 4$; 2 ferrets per cage) and treated with vehicle or GS-621763 (10 mg kg^{-1}) twice daily (b.i.d.) via oral gavage. At 54 h after infection, uninfected and untreated contact ferrets (two contacts for GS-621763; three contacts for vehicle) were co-housed with source ferrets. Co-housing was continued until 96 h after infection and source ferrets were euthanized. Contact ferrets were housed individually and monitored for an additional 4 days after separation from source ferrets and subsequently euthanized. Nasal lavages were performed on all source ferrets every 12 h and all contact ferrets every 24 h. For all ferrets, nasal turbinates and lung tissues were harvested to determine viral titers and the detection of viral RNA.

SARS-CoV-2 titration in tissue extracts. Selected tissues were weighed and mechanically homogenized in sterile PBS. Homogenates were clarified by centrifugation (2000× *g*) for 5 min at 4 °C. Clarified homogenates were then serially diluted and used in plaque assays to determine virus titer as described above.

Quantitation of SARS-CoV-2 RNA copy numbers. To probe viral RNA in selected tissues, samples were harvested and stored in RNAlater at −80 °C. Total RNA from tissues was isolated using a RNeasy mini kit (Qiagen), in accordance with the manufacturer's protocol. For nasal lavage samples, total RNA was extracted using a ZR viral RNA kit (Zymo Research) in accordance with the manufacturer's protocol. SARS-CoV-2 RNA was detected using the nCoV_IP2 primer-probe set (National Reference Center for Respiratory Viruses, Pasteur Institute) (Supplementary Table 4). An Applied Biosystems 7500 using the StepOnePlus real-time PCR system was used to perform RT-qPCR reactions. The nCoV_IP2 primer-probe set was using in combination with TaqMan fast virus 1-step master mix (Thermo Fisher Scientific) to detect viral RNA. SARS-CoV-2 RNA copy numbers were calculated using a standard curve created from serial dilutions of a PCR fragment (12669-14146 nt of the SARS-CoV-2 genome). For RNA copies in tissue samples, RNA copies were normalized to the weights of the tissues used.

Next-generation sequencing. To authenticate virus stocks, metagenomic sequencing was performed as described[39,40], while to sequence lower viral load in vivo samples the COVID-Seq (Illumina) amplicon tiling protocol was used. For metagenomic sequencing, viral RNA was treated with Turbo DNase I (Thermo Fisher), converted to cDNA using random hexamers and SuperScript IV reverse transcriptase, and double-stranded cDNA created using Sequenase v2.0. Sequencing libraries for both sets of libraries were generated using Nextera Flex (Illumina) and cleaned using 0.8 × Ampure XP beads and pooled equimolarly before sequencing on an Illumina 1 × 100 bp NextSeq2000 run. Raw fastq reads were adapter- and quality-trimmed with Trimmomatic v0.39[41]. To interrogate potential resistance alleles, reference-based mapping to NC_045512.2 was carried out using our modified Longitudinal Analysis of Viral Alleles (LAVA—https://github.com/michellejlin/lava)[42] pipeline. LAVA constructs a candidate reference genome from early passage virus using bwa[43], removes PCR duplicates with Picard, calls variants with VarScan[44,45], and converts these changes into amino acid changes with Annovar[46]. Consensus sequences were called with TAYLOR[39] and deposited in NCBI GenBank. Accession numbers (Supplementary Table 5) are as follows: input strain WA1/2020, MZ433205; WA1/2020 recovered from ferrets, MZ433206 - MZ433213; input strain BZ/2021, MZ433225; BZ/2021 recovered from source ferrets, MZ433214 - MZ433221; BZ/2021 recovered from contacts of vehicle-treated source ferrets, MZ433222–MZ433224. Raw reads for these sequences are publicly available on SRA (BioProject PRJNA740065).

Ethics statement. All in vivo efficacy studies were conducted at Georgia State University in compliance with the Animal Welfare Act Code of Federal Regulations and the Guide for the Care and Use of Laboratory Animals of the National Institutes of Health. All studies involving SARS-CoV-2-infected ferrets were approved by the Georgia State Institutional Animal Care and Use Committee under protocol A20031. Experiments at Georgia State University using infectious SARS-CoV-2 were performed in BSL-3/ABSL-3 facilities at Georgia State University and approved by the Georgia State Institutional Biosafety Committee under protocol B20016. Experiments at Gilead Sciences, Inc. using infectious SARS-CoV-2 were performed in a BSL-3 facility and approved by an institutional biosafety committee.

Statistics and reproducibility. The Microsoft Excel (versions 16.42, 16.43, and 16.48), GraphPad Prism (versions, 8.0, 9.0.1, and 9.1.0), and Numbers (version 10.1) software packages were used for data collection and analysis. One-way or two-way ANOVA with Dunnett's or Tukey's multiple comparisons post hoc test were used to evaluate statistical significance when comparing more than two groups or two independent variables. When comparing two variables, a two-tailed unpaired t-test was performed to determine statistical significance. The specific statistical test used to individual studies is specified in the figure legends. RT-qPCR data were collected and analyzed using the StepOnePlus (version 2.1; Applied Biosystems) software package. Final figures were assembled in Adobe Illustrator (version CS6). All numerical raw data and summaries of individual statistical analyses are provided in supplementary datasets 3 and 4. Effect sizes between groups in the ANOVAs were calculated as $\eta^2 = (SS_{effect})/(SS_{total})$ for one-way ANOVA and $\omega^2 = (SS_{effect} - (df_{effect})(MS_{error}))/MS_{error} + SS_{total}$ for two-way ANOVA (SS_{effect}, sum of squares for the effect; SS_{total}, the sum of squares for total; df_{effect}, degrees of freedom for the effect; MS_{error}, mean squared error). The statistical significance level α was set to <0.05 for all experiments. Exact P values are shown in the individual graphs. Appropriate sample sizes were determined using power analyses (GPower 3.1; University of Duesseldorf).

Reporting Summary. Further information on research design is available in the Nature Research Reporting Summary linked to this article.

Data availability

All next-generation sequencing data is publicly available on SRA (BioProject PRJNA740065). All accession codes for sequence data are available in Supplementary Table 5. Sequencing data is summarized in Supplementary Data 1–2. All data generated and analyzed during this study are included in this published article (and its supplementary information files). Source data and statistical analyses for Figs. 1–4, Supplementary Tables 13 and Supplementary Figs. 1–2 are provided with the paper in Supplementary Data 3–4.

Code availability

This study does not use proprietary codes. All computer codes and algorithms used are specified in the Methods section.

Received: 30 July 2021; Accepted: 22 October 2021;
Published online: 05 November 2021

References

1. U.S. Food & Drug *Administration. FDA Approves First Treatment for COVID-19.* https://www.fda.gov/news-events/press-announcements/fda-approves-first-treatment-covid-19 (last accessed 06/06/2021), 2020).
2. Mackman, R. L. et al. Prodrugs of a 1′-CN-4-Aza-7,9-dideazaadenosine C-Nucleoside Leading to the Discovery of Remdesivir (GS-5734) as a Potent Inhibitor of Respiratory Syncytial Virus with Efficacy in the African Green Monkey Model of RSV. *J. Med. Chem.* **64**, 5001–5017 (2021).
3. Siegel, D. Discovery and Synthesis of a Phosphoramidate Prodrugof a Pyrrolo[2,1-f][triazin-4-amino] Adenine C-Nucleoside (GS-5734) for theTreatment of Ebola and Emerging Viruses. *J. Med. Chem* **60**, 1648–1661 (2017).
4. Meganck, R. M. & Baric, R. S. Developing therapeutic approaches for twenty-first-century emerging infectious viral diseases. *Nat. Med.* **27**, 401–410 (2021).
5. Toots, M. et al. Characterization of orally efficacious influenza drug with high resistance barrier in ferrets and human airway epithelia. *Sci. Transl. Med.* **11**, eaax5866 (2019).

6. Cox, R. M., Wolf, J. D. & Plemper, R. K. Therapeutically administered ribonucleoside analogue MK-4482/EIDD-2801 blocks SARS-CoV-2 transmission in ferrets. *Nat. Microbiol* **6**, 11–18 (2021).
7. Painter W. P. et al. Human Safety, Tolerability, and Pharmacokinetics of a Novel Broad-Spectrum Oral Antiviral Compound, Molnupiravir, with Activity Against SARS-CoV-2. *medrxiv*, https://doi.org/10.1101/2020.12.10.20235747 (2020).
8. Good, S. S. et al. AT-527, a Double Prodrug of a Guanosine Nucleotide Analog, Is a Potent Inhibitor of SARS-CoV-2 In Vitro and a Promising Oral Antiviral for Treatment of COVID-19. *Antimicrob. Agents Chemother.* **65**, e02479–20 (2021).
9. Beigel, J. H. et al. Remdesivir for the Treatment of Covid-19 - Final Report. *N. Engl. J. Med* **383**, 1813–1826 (2020).
10. Pruijssers, A. J. et al. Remdesivir Inhibits SARS-CoV-2 in Human Lung Cells and Chimeric SARS-CoV Expressing the SARS-CoV-2 RNA Polymerase in Mice. *Cell Rep.* **32**, 107940 (2020).
11. Humeniuk, R. et al. Safety, Tolerability, and Pharmacokinetics of Remdesivir, An Antiviral for Treatment of COVID-19, in Healthy Subjects. *Clin. Transl. Sci.* **13**, 896–906 (2020).
12. Wei, D. et al. Potency and pharmacokinetics of GS-441524 derivatives against SARS-CoV-2. *Bioorg. Med. Chem.* **46**, 116364 (2021).
13. Li, Y. et al. Remdesivir Metabolite GS-441524 Effectively Inhibits SARS-CoV-2 Infection in Mouse Models. *J. Med. Chem.*, https://doi.org/10.1021/acs.jmedchem.0c01929 (2021).
14. Oude Munnink, B. B. et al. Transmission of SARS-CoV-2 on mink farms between humans and mink and back to humans. *Science* **371**, 172–177 (2021).
15. Richard, M. et al. SARS-CoV-2 is transmitted via contact and via the air between ferrets. *Nat. Commun.* **11**, 3496 (2020).
16. Felsenstein, S. & Hedrich, C. M. SARS-CoV-2 infections in children and young people. *Clin. Immunol.* **220**, 108588 (2020).
17. Zhu, N. et al. A Novel Coronavirus from Patients with Pneumonia in China, 2019. *N. Engl. J. Med* **382**, 727–733 (2020).
18. *Tracking SARS-CoV-2 variants"*. www.who.int. *Retrieved 1 June 2021*., 2021).
19. Faria, N. R. et al. Genomics and epidemiology of the P.1 SARS-CoV-2 lineage in Manaus, Brazil. *Science* **372**, 815–821 (2021).
20. Mossel, E. C. et al. Exogenous ACE2 expression allows refractory cell lines to support severe acute respiratory syndrome coronavirus replication. *J. Virol.* **79**, 3846–3850 (2005).
21. Humeniuk, R. et al. Pharmacokinetic, Pharmacodynamic, and Drug-Interaction Profile of Remdesivir, a SARS-CoV-2 Replication Inhibitor. *Clin. Pharmacokinet.* **60**, 569–583 (2021).
22. Fiege, J. K. et al. Single cell resolution of SARS-CoV-2 tropism, antiviral responses, and susceptibility to therapies in primary human airway epithelium. *PLoS Pathog.* **17**, e1009292 (2021).
23. bei RESOURCES https://www.beiresources.org/Catalog/animalviruses/NR-54982.aspx retrieved on 06/09/2021. (2021).
24. Szemiel, A. M. et al. In vitro evolution of Remdesivir resistance reveals genome plasticity of SARS-CoV-2. *bioRxiv*, 2021.2002.2001.429199, https://doi.org/10.1101/2021.02.01.429199 (2021).
25. Agostini, M. L. et al. Coronavirus Susceptibility to the Antiviral Remdesivir (GS-5734) Is Mediated by the Viral Polymerase and the Proofreading Exoribonuclease. *mBio* **9**, e00221–18 (2018).
26. Gordon, C. J. et al. Remdesivir is a direct-acting antiviral that inhibits RNA-dependent RNA polymerase from severe acute respiratory syndrome coronavirus 2 with high potency. *J. Biol. Chem.* **295**, 6785–6797 (2020).
27. Tchesnokov, E. P. et al. Template-dependent inhibition of coronavirus RNA-dependent RNA polymerase by remdesivir reveals a second mechanism of action. *J. Biol. Chem.* **295**, 16156–16165 (2020).
28. Park, S. J. et al. Antiviral Efficacies of FDA-Approved Drugs against SARS-CoV-2 Infection in Ferrets. *mBio* **11**, https://doi.org/10.1128/mBio.01114-20 (2020).
29. Shi, J. et al. Susceptibility of ferrets, cats, dogs, and other domesticated animals to SARS-coronavirus 2. *Science* **368**, 1016–1020 (2020).
30. Maltezou, H. C. et al. Association Between Upper Respiratory Tract Viral Load, Comorbidities, Disease Severity, and Outcome of Patients With SARS-CoV-2 Infection. *J. Infect. Dis.* **223**, 1132–1138 (2021).
31. de Wit, E. et al. Prophylactic and therapeutic remdesivir (GS-5734) treatment in the rhesus macaque model of MERS-CoV infection. *Proc. Natl Acad. Sci. U. S. A* **117**, 6771–6776 (2020).
32. Williamson, B. N. et al. Clinical benefit of remdesivir in rhesus macaques infected with SARS-CoV-2. *Nature* **585**, 273–276 (2020).
33. Faria, N. R. et al. Genomics and epidemiology of a novel SARS-CoV-2 lineage in Manaus, Brazil. *medRxiv*, https://doi.org/10.1101/2021.02.26.21252554 (2021).
34. Lo, M. K. et al. Remdesivir targets a structurally analogous region of the Ebola virus and SARS-CoV-2 polymerases. *Proc. Natl Acad. Sci.* **117**, 26946–26954 (2020).
35. Kutter, J. S. et al. SARS-CoV and SARS-CoV-2 are transmitted through the air between ferrets over more than one meter distance. *Nat. Commun.* **12**, 1653 (2021).
36. Abdool Karim, S. S. & de Oliveira, T. New SARS-CoV-2 Variants - Clinical, Public Health, and Vaccine Implications. *N. Engl. J. Med* **384**, 1866–1868 (2021).
37. Pearson, C. A. B. et al. Estimates of severity and transmissibility of novel SARS-CoV-2 variant 501Y.V2 in South Africa. https://cmmid.github.io/topics/covid19/sa-novel-variant.htm (London: CMMID Repository, 2021).
38. Davies, N. G. et al. Estimated transmissibility and impact of SARS-CoV-2 lineage B.1.1.7 in England. *Science* **372**, eabg3055 (2021).
39. Addetia, A. et al. Sensitive Recovery of Complete SARS-CoV-2 Genomes from Clinical Samples by Use of Swift Biosciences' SARS-CoV-2 Multiplex Amplicon Sequencing Panel. *J. Clin. Microbiol.* **59**, e02226–20 (2020).
40. Greninger, A. L. et al. Rapid Metagenomic Next-Generation Sequencing during an Investigation of Hospital-Acquired Human Parainfluenza Virus 3 Infections. *J. Clin. Microbiol.* **55**, 177–182 (2017).
41. Bolger, A. M., Lohse, M. & Usadel, B. Trimmomatic: a flexible trimmer for Illumina sequence data. *Bioinformatics* **30**, 2114–2120 (2014).
42. Lin, M. J., Shean, R. C., Makhsous, N. & Greninger, A. L. LAVA: a streamlined visualization tool for longitudinal analysis of viral alleles. *bioRxiv*, 2019.2012.2017.879320, https://doi.org/10.1101/2019.12.17.879320 (2019).
43. Li, H. & Durbin, R. Fast and accurate short read alignment with Burrows-Wheeler transform. *Bioinformatics* **25**, 1754–1760 (2009).
44. Koboldt, D. C. et al. VarScan: variant detection in massively parallel sequencing of individual and pooled samples. *Bioinformatics* **25**, 2283–2285 (2009).
45. Koboldt, D. C., Larson, D. E., Chen, K., Ding, L. & Wilson, R. K. Massively parallel sequencing approaches for characterization of structural variation. *Methods Mol. Biol.* **838**, 369–384 (2012).
46. Wang, K., Li, M. & Hakonarson, H. ANNOVAR: functional annotation of genetic variants from high-throughput sequencing data. *Nucleic Acids Res* **38**, e164 (2010).

Acknowledgements

We thank BEI Resources for SARS-CoV-2 isolates, X. Xie and P.-Y. Shi for providing SARS-CoV-2-Nluc, A. Shornikov of the Gilead Sample Bank group for compound distribution, the High Containment Core and the Department for Animal Research of Georgia State University for support, and A. L. Hammond and D. Porter for critical reading of the manuscript.

Author contributions

J.P.B. and R.K.P. coordinated the study. R.M.C. and J.S. performed virus-stock preparations and virus titrations. R.M.C., J.D.W., C.M.L. and R.K.P. performed animal inoculations, nasal lavage sampling, animal necropsies, and/or titration of virus from ferrets R.M.C. extracted RNA from all animal samples and performed all RT-qPCR experiments and analyses. J.S. performed virus reduction assays and cytotoxicity assessments. D.B. coordinated pharmacokinetics studies in ferrets. K.T.B. and D.L. prepared compound formulations. V.D.P., J.P.B. and J.C. performed reporter virus and cytotoxicity assays in ACE2-A549 cells. R.K, K.C. and R.L.M. synthesized and sourced compounds. M.J.L. and A.L.G. performed all next-generation sequencing and analyses. R.M.C. created all figure schematics. R.M.C., J.S., J.P.B. and R.K.P. were responsible for experimental design, data analysis, and data presentation. R.M.C., J.D.W., C.M.L., J.S., D.B., L.S.M., A.L.G., R.L.M., C.Y., J.P.B. and T.C. edited the manuscript. J.P.B. and R.K.P. conceived and designed the study. R.K.P. wrote the manuscript. This work was supported by Gilead Sciences Inc. and, in part, by Public Health Service grants AI153400 (to RKP) and AI141222 (to RKP) from the NIH/NIAID. NIH/NIAID had no role in study design, data collection, and interpretation, or the decision to submit the work for publication.

Competing interests

All authors affiliated with Gilead Sciences may hold stock or stock options in Gilead Sciences Inc. R.K.P. was the principal investigator of a Gilead-sponsored research agreement with Georgia State University. He has received funding from Gilead Sciences Inc. to support parts of this work. All other authors declare no competing interests.

Additional information

Supplementary information The online version contains supplementary material available at https://doi.org/10.1038/s41467-021-26760-4.

Correspondence and requests for materials should be addressed to Richard K. Plemper.

Peer review information *Nature Communications* thanks Ralph Tripp and the other, anonymous, reviewer(s) for their contribution to the peer review of this work. Peer reviewer reports are available.

2.2 Research Topic: 4’-Fluorouridine

2.2.1 4’-Fluorouridine is an Oral Antiviral that Blocks Respiratory Syncytial Virus and SARS-CoV-2 Replication

RESEARCH

RESEARCH ARTICLE

CORONAVIRUS

4′-Fluorouridine is an oral antiviral that blocks respiratory syncytial virus and SARS-CoV-2 replication

Julien Sourimant[1], Carolin M. Lieber[1], Megha Aggarwal[1], Robert M. Cox[1], Josef D. Wolf[1], Jeong-Joong Yoon[1], Mart Toots[1], Chengin Ye[2], Zachary Sticher[3], Alexander A. Kolykhalov[3,4], Luis Martinez-Sobrido[2], Gregory R. Bluemling[3,4], Michael G. Natchus[3], George R. Painter[3,4,5], Richard K. Plemper[1,6*]

The COVID-19 pandemic has underscored the critical need for broad-spectrum therapeutics against respiratory viruses. Respiratory syncytial virus (RSV) is a major threat to pediatric patients and older adults. We describe 4′-fluorouridine (4′-FlU, EIDD-2749), a ribonucleoside analog that inhibits RSV, related RNA viruses, and severe acute respiratory syndrome coronavirus 2 (SARS-CoV-2), with high selectivity index in cells and human airway epithelia organoids. Polymerase inhibition within in vitro RNA-dependent RNA polymerase assays established for RSV and SARS-CoV-2 revealed transcriptional stalling after incorporation. Once-daily oral treatment was highly efficacious at 5 milligrams per kilogram (mg/kg) in RSV-infected mice or 20 mg/kg in ferrets infected with different SARS-CoV-2 variants of concern, initiated 24 or 12 hours after infection, respectively. These properties define 4′-FlU as a broad-spectrum candidate for the treatment of RSV, SARS-CoV-2, and related RNA virus infections.

The COVID-19 experience has highlighted the need for orally bioavailable broad-spectrum antivirals that may be quickly deployed against newly emerging viral pathogens. Remdesivir—a direct-acting broad-spectrum antiviral—is still the only small-molecule therapeutic approved for use against severe acute respiratory syndrome coronavirus 2 (SARS-CoV-2) infection in the United States, but it requires intravenous administration. The ensuing restriction to hospitalized patients compromises its clinical effect as treatment is initiated too late in the infection cycle (1). We have demonstrated the efficacy of orally available EIDD-2801 (molnupiravir) against influenza viruses in human organoid models and ferrets (2), and subsequent animal and human data showed that the antiviral efficacy of molnupiravir extends to SARS-CoV-2 in vivo (3, 4). Molnupiravir acts by inducing lethal viral mutagenesis after incorporation into viral genomic RNA of influenza viruses (2) and betacoronaviruses (5). The drug was recently approved in the United Kingdom and is currently considered for emergency use authorization against COVID-19 in the United States. However, even with this accelerated development timeline, molnupiravir only became available to patients nearly 2 years into the pandemic. To have a substantial effect on a mounting pandemic, an antiviral must be approved for human use before a new pathogen emerges, making the case for the development of broad-spectrum antivirals.

We have identified respiratory syncytial virus (RSV) disease as a viable primary indication for a candidate broad-spectrum antiviral, on the basis of the unaddressed major health threat imposed by RSV and well-established protocols for clinical trials of anti-RSV therapeutics. RSV infections are responsible for over 58,000 hospitalizations of children <5 years of age in the United States annually, and ~177,000 hospitalizations of adults > the age of 65 (6–9). Despite this major health and economic burden, no therapeutics have been licensed specifically

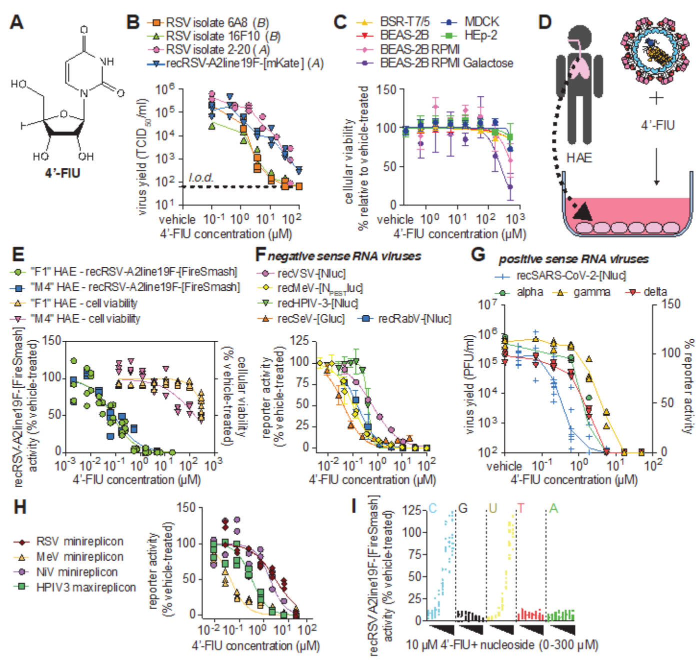

Fig. 1. 4′-FlU is a potent broad-spectrum antiviral. (A) Chemical structure of 4′-FlU. (B) Virus yield reduction of RSV clinical isolates 6A8, 16F10, 2-20, and recombinant recRSV-A2line19F-[mKate] [(A) or (B) antigenic subgroup]. (C) HEp-2, MDCK, BHK-T7, and BEAS-2B cell lines were assayed for reduction in cell metabolism by 4′-FlU. (D and E) recRSV-A2line19F-[FireSMASh] dose response inhibition and cytotoxicity assay with human airway epithelial (HAE) cells (D) from two donors in the presence of indicated 4′-FlU concentrations (E). (F) Dose-response inhibition of a panel of recombinant mononegaviruses by 4′-FlU. (G) Dose-response inhibition of recSARS-CoV-2-[Nluc] and virus yield reduction of alpha, gamma, and delta VoC isolates by 4′-FlU. (H) Dose-response inhibition of transiently expressed polymerase complexes from mononegaviruses MeV, RSV, NiV, or HPIV-3 by 4′-FlU (I) recRSV-A2line19F-[FireSMASh]-infected cells were treated with 10 mM of 4′-FlU and serial dilutions of exogenous nucleotides in extracellular media. Viral activity was determined by reporter activity. Symbols represent independent repeats [(B), (E), (G), (H), and (I)] or mean with standard deviation [(C) and (F)], and lines represent means. n ≥ 3, EC_{50}s, and CC_{50}s are reported in tables S1 and S2, and all source data are provided in data S2.

for treatment of RSV disease (10). Anti-RSV drug discovery efforts have increasingly focused on inhibiting the viral RNA-dependent RNA polymerase (RdRP) complex (11). The core polymerase machinery comprises the large (L) polymerase protein, its obligatory cofactor [the phosphoprotein (P)], and the encapsidated negative-sense RNA genome (11). Allosteric inhibitors of RSV L have potent activity as seen, for instance, with the experimental drug candidates AVG-233 (12) and inhaled PC786 (13).

In search of a drug that is active against RSV and SARS-CoV-2, is orally available, and acts through a distinct mechanism of activity (MOA) from molnupiravir, we explored 4′-fluorine substitutions in a series of analogs of the molnupiravir parent molecule N^4-hydroxycytidine (NHC) (14). The focus on 4′-fluorine ribose substitutions was motivated by the small atomic radius and strong stereoelectronic effect of fluorine that can influence backbone conformation flexibility, which may lead to improved selectivity indices (SIs), increased lipophilicity, and greater metabolic stability (15). A synthetic intermediate in the approach to 4′-fluoro-N^4-hydroxycytidine (compound 5 in fig. S1) was deprotected to provide 4′-FlU (Fig. 1A), which emerged as a broadly active antiviral when biotested.

4′-FlU is a broad-spectrum mononegavirus inhibitor with high SI

Following the approach of using RSV disease as a primary indication to advance a new candidate broad-spectrum antiviral, we first assessed activity of 4′-FlU against a recombinant RSV A2-line19F (recRSV A2-L19F) (16) and clinical RSV isolates on immortalized HEp-2 cells. The compound showed potent dose-dependent activity against all RSV strains tested, returning half-maximal effective concentrations (EC_{50} values) ranging from 0.61 to 1.2 μM (Fig. 1B and table S1). This cell culture potency was on par with the previously reported anti-RSV activity of NHC (fig. S2). Global metabolic activity of established human and animal cell lines (HEp-2, MDCK, BHK-T7, and BEAS-2B) remained unaltered after they were exposed to 4′-FlU (up to 500 μM), indicating that the antiviral effect is a result of cytotoxicity (Fig. 1C and table S2). When glucose was replaced with galactose as a carbohydrate source to link cell metabolic activity strictly to mitochondrial oxidation (17), we determined a half-maximal

[1]Center for Translational Antiviral Research, Georgia State University, Atlanta, GA 30303, USA [2]Texas Biomedical Research Institute, San Antonio, TX 78227, USA [3]Emory Institute for Drug Development, Emory University, Atlanta, GA 30322, USA [4]Drug Innovation Ventures at Emory (DRIVE), Atlanta, GA 30322, USA [5]Department of Pharmacology, Emory University School of Medicine, Atlanta, GA 30322, USA [6]Department of Pediatrics, Emory University School of Medicine, Atlanta, GA 30322, USA
*Corresponding author. Email: rplemper@gsu.edu

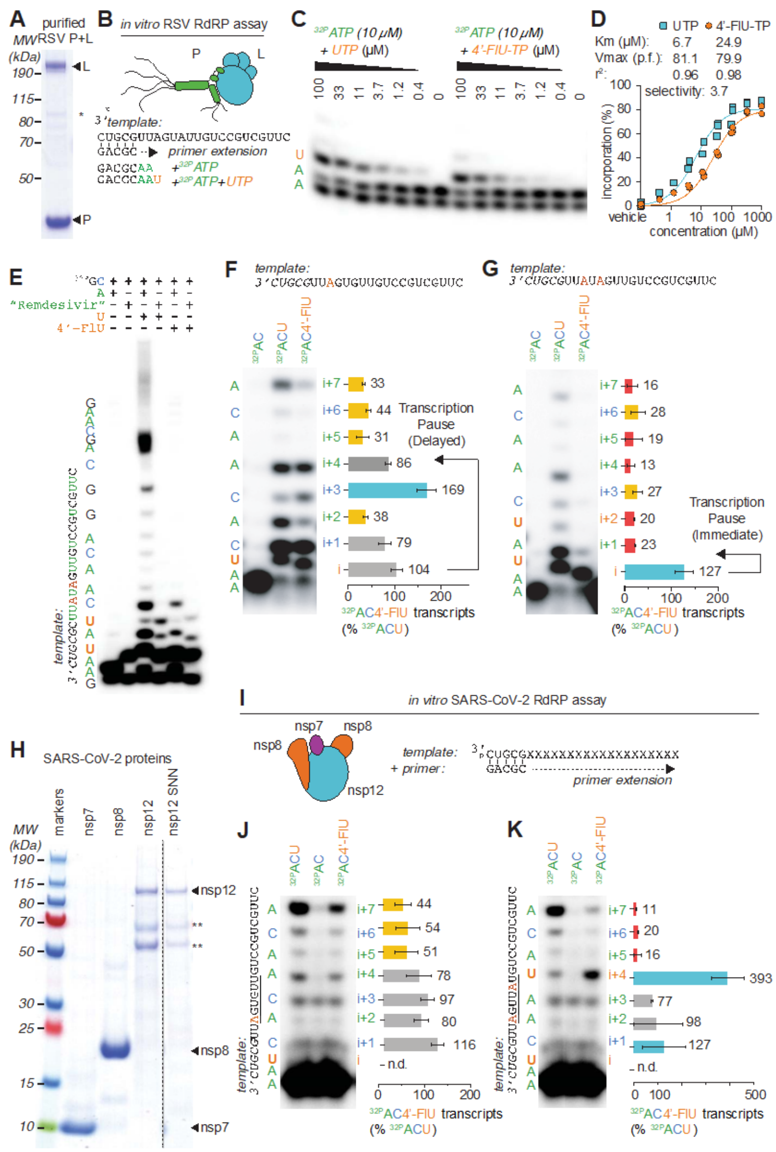

Fig. 2. 4′-FlU induces a delayed stalling of RSV and SARS-CoV-2 RdRP. (A) SDS-PAGE with Coomassie blue staining of recombinant RSV RdRP complexes (L and P proteins). (B) Schematics of the primer extension assay. (C) Urea-polyacrylamide gel electrophoresis (PAGE) fractionation of RNA transcripts produced through primer extension by the RSV RdRP in the presence of the indicated nucleotides (n = 3). (D) Kinetic analysis of autoradiographs from (C). Nonlinear regression with the Michaelis-Menten model. K_m and V_{max} with 95% confidence intervals (CIs) and goodness of fit (r^2) are indicated. (E to G) Urea-PAGE fractionation of RNA transcripts produced by RSV RdRP in the presence of the indicated templates and nucleotides. "Remdesivir" denotes the addition of the remdesivir active metabolite GS-443902, a well-characterized "delayed chain terminator". 4′-FlU-TP bands in (F) to (G) were normalized to the corresponding band after UTP incorporation. Bars represent mean and error bars represent standard deviation (n = 3). (H) Purified recombinant SARS-CoV-2 RdRP complexes (nsp7, 8, and 12 proteins) "nsp12 SNN" denotes a catalytically inactive mutant. (I to K) Urea-PAGE fractionation of RNA transcripts produced by SARS-CoV-2 RdRP in the presence of the indicated templates and nucleotides. Stars denote cellular contaminants. Uncropped autoradiograph replicates are provided in data S1.

cytotoxic concentration (CC_{50}) of 4′-FlU of 250 μM (Fig. 1C and table S2).

When tested on disease-relevant primary human airway epithelial cells (HAEs) derived from two different donors (Fig. 1D), 4′-FlU showed a ≥17-fold increase in anti-RSV potency relative to that on HEp-2 cells; however, the low cytotoxicity levels remained unchanged (CC_{50} 169 μM) (Fig. 1E), resulting in a high SI ($SI = EC_{50}/CC_{50}$) of ≥1877. Consistent with these findings, quantitative immunocytochemistry on HAE cells confirmed that 4′-FlU reduced steady-state levels of nuclear- (SDH-A; IC_{50} 272.8 μM) and mitochondrial- (COX-I; IC_{50} 146.8 μM) encoded proteins only at high concentrations (fig. S3).

We next explored the 4′-FlU indication spectrum. We assessed a panel of negative-sense RNA viruses of the paramyxovirus and rhabdovirus families, including measles virus (MeV), human parainfluenza virus type 3 (HPIV3), Sendai virus (SeV), vesicular stomatitis virus (VSV), and rabies virus (RabV). Like RSV, these viruses belong to the mononegavirus order, and we found that 4′-FlU demonstrated submicromolar active concentrations (Fig. 1F and table S1). Testing a representative of phylogenetically distant positive-sense RNA viruses, the betacoronavirus SARS-CoV-2 was also sensitive to 4′-FlU, with EC_{50} values ranging from 0.2 to 0.6 μM against isolates of different lineages (Fig. 1G and table S1).

At initial mechanistic characterization, 4′-FlU inhibited RSV and paramyxovirus RdRP complex activity in cell–based minireplicon systems (Fig. 1H and table S1). The RdRP activity of Nipah virus (NiV)—a highly pathogenic zoonotic paramyxovirus with pandemic potential (18)—was also efficiently inhibited by 4′-FlU in a NiV minireplicon reporter assay. The antiviral effect of 4′-FlU was dose-dependently reversed by addition of an excess of exogenous pyrimidines (cytidine and uridine)—but not purines—to the cultured cells, which is consistent with competitive inhibition of RdRP activity (2, 19) (Fig. 1I).

Incorporation of 4′-FlU by RSV and SARS-CoV-2 RdRP causes sequence-modulated transcriptional stalling

To characterize the molecular MOA of 4′-FlU, we purified recombinant RSV L and P proteins expressed in insect cells (Fig. 2A) and determined performance of the bioactive 5′-triphosphate form of 4′-FlU (4′-FlU-TP) within in vitro primer extension assays (20) (Fig. 2B). In the presence of radio-labeled adenosine triphosphate (ATP) and an increasing amount of uridine triphosphate (UTP), RSV RdRP complexes elongated the primer until reaching a G in third position on the template strand, and continued further upon addition of CTP (Fig. 2C) (fig. S4 and data S1). Replacing UTP with 4′-FlU-TP resulted in efficient primer extension up to the third nucleotide, confirming that RSV RdRP recognizes and incorporates 4′-FlU in place of UTP (Fig. 2C). Incorporation kinetics (21) showed only a moderate reduction in substrate affinity for 4′-FlU-TP compared with UTP (Fig. 2D). Further addition of CTP to the reaction mix resulted in limited elongation rather than the expected full-length product, which suggested delayed polymerase stalling by incorporated 4′-FlU (fig. S4 and data S1). Direct side-by-side comparison with GS-443902—the active metabolite of remdesivir

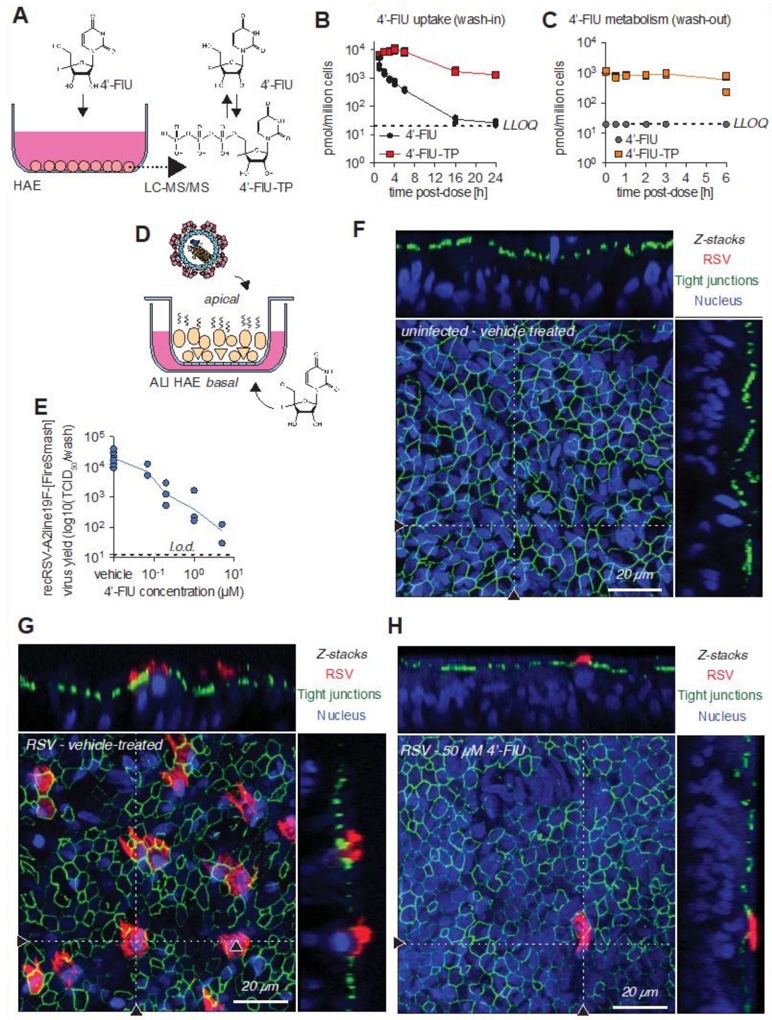

Fig. 3. 4′-FlU is efficiently anabolized in HAE cells and is efficacious in human airway epithelium organoids. (A to C) 4′-FlU cellular uptake and metabolism in "F1" HAE cells quantified by mass spectrometry (A). Intracellular concentration of 4′-FlU(-TP) after exposure to 20 μM 4′-FlU for 0, 1, 2, 3, 4, 6, 16, and 24 hours (B), or 24-hour incubation followed by removal of the compound for 0, 0.5, 1, 2, 3, and 6 hours before quantification (C) (n = 3). The low limit of quantitation (LLOQ) for 4′-FlU (19.83 pmol/ 10^6 cells) is indicated by the dashed line. (D) HAE cells were matured at the air-liquid interface (ALI). (E) Virus yield reduction of recRSV-A2line19F-[FireSMASh] was shed from the apical side in ALI HAE after incubation with serial dilutions of 4′-FlU on the basal side (n = 3). (F to H) Confocal microscopy of ALI HAE cells infected with recRSV-A2line19F-[FireSMASh], at 5 days after infection. RSV-infected cells, tight junctions, and nuclei were stained with anti-RSV, anti-ZO-1, and Hoechst 34580. z-stacks of 30 1-mm slices with 63 × oil objective. Dotted lines, x-z and y-z stacks; scale bar, 20 mm. In all panels, symbols represent independent biological repeats and lines represent means.

and a "delayed polymerase stalling" inhibitor well characterized for SARS-CoV-2—along with RSV and other RNA viruses (21, 22), corroborated this antiviral effect of 4′-FlU-TP (Fig. 2E and data S1).

When a modified template coded for incorporation of only a single UTP (Fig. 2F and data S1), primers elongated preferentially to position i + 3 after 4′-FlU-TP, whereas the efficiency of full elongation was strongly reduced compared with extension in the presence of UTP. However, repositioning the incorporation site further downstream in the template triggered immediate polymerase stalling at position i (fig. S5), indicating template sequence dependence of the inhibitory effect. Transcription stalling at i or i + 3 was also observed after multiple 4′-FlU incorporations: An AxAxxx template (Fig. 2G) and direct tandem incorporations through an AAxxAx template (fig. S5) caused stalling at position i, whereas increasing spacer length between the incorporated uridines shifted preferential stalling to i+3 (fig. S5). This variable delayed polymerase-stalling event within one to four nucleotides of the incorporation site was equally prominent when we examined de novo initiation of RNA synthesis at the promoter with a synthetic native RSV promoter sequence rather than extension of primer-template pairs (fig. S6).

Purification of a core SARS-CoV-2 polymerase complex [nonstructural proteins (nsp) 7, 8, and 12] from bacterial cell lysates (23, 24) (Fig. 2H) and assessment of RdRP bioactivity in equivalent primer-extension in vitro polymerase assays (Fig. 2I) again demonstrated incorporation of 4′-FlU-TP in place of UTP by the coronavirus RdRP (Fig. 2J), but there was no sign of immediate polymerase stalling. However, SARS-CoV-2 polymerase stalling was triggered by multiple incorporations of 4′-FlU-TP, and was particularly prominent when a second incorporation of 4′-FlU-TP occurred at the i+4 position (Fig. 2K and fig. S7). Primer extension was blocked when the nsp12 subunit was omitted or an nsp12 variant carrying mutations in the catalytic site was used, confirming specificity of the reaction (fig. S7 and data S1).

4′-FlU is rapidly anabolized, metabolically stable, and potently antiviral in disease-relevant well-differentiated HAE cultures

Quantitation of 4′-FlU and its anabolites in primary HAE cells (Fig. 3A) demonstrated rapid intracellular accumulation of 4′-FlU, reaching a level of 3.42 nmol/million cells in the first hour of exposure (Fig. 3B). Anabolism to bioactive 4′-FlU-TP was efficient, resulting in concentrations of 10.38 nmol per million cells at peak (4 hours after start of exposure) and 1.31 nmol per million cells at plateau (24 hours). The anabolite was metabolically stable, remaining present in sustained concentrations of

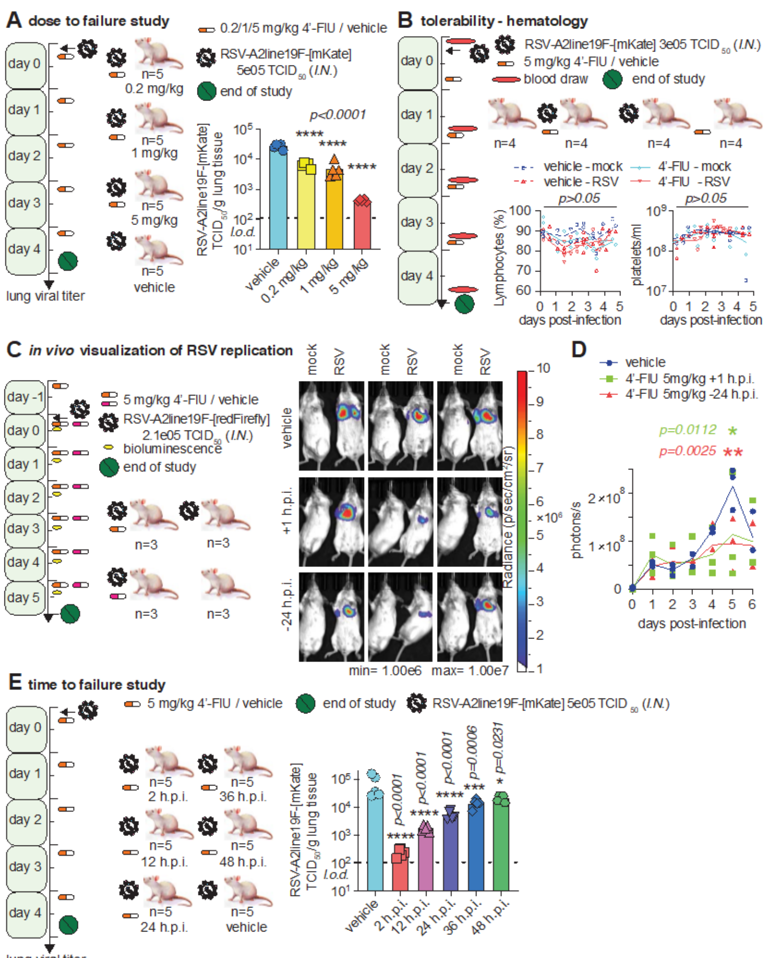

Fig. 4. Therapeutic oral efficacy of 4′-FlU in the RSV mouse model. (A) Balb/cJ mice were inoculated with recRSV-A2line19F-[mKate] and treated as indicated. At 4.5 days after infection, viral lung titers were determined with $TCID_{50}$ titration (n = 5). (B) Balb/cJ mice were inoculated with recRSV-A2line19F-[mKate] or mock-infected, and treated as indicated. Blood samples were collected before infection and at 1.5, 2.5, 3.5, and 4.5 days after infection; lymphocyte proportions with platelets/ml are represented over time (n = 4). (C) Balb/cJ mice were inoculated with recRSV-A2line19F-[redFirefly] and treated as indicated. In vivo luciferase activity was measured daily. (D) Total photon flux from mice lungs from (C) over time (n = 3). (E) Balb/cJ mice were inoculated with recRSV-A2line19F-[mKate] and treated as indicated. At 4.5 days after infection, viral lung titers were determined with $TCID_{50}$ titration (n = 5). In all panels, symbols represent individual values, and bars or lines represent means. One-way ordinary analysis of variance (ANOVA) with Tukey's post hoc multiple comparisons (B) and (I) or two-way ANOVA with Dunnett's post hoc multiple comparison (C) and (G). h.p.i., hours post-infection.

~1 nmol/million cells over a 6-hour monitoring period, corresponding to an extrapolated half-life of 9.7 hours (Fig. 3C).

To explore efficacy in a disease-relevant human tissue model, we cultured the HAEs at the air-liquid interface, inducing the formation of a well-differentiated three-dimensional (3D) airway epithelium that included ciliated and mucus-producing cells (25) (Fig. 3D). Adding 4′-FlU to the basolateral chamber of the transwells after apical infection of the epithelium with RSV potently reduced apical virus shedding with an EC_{50} of 55 nM (Fig. 3E). Overall titer reduction spanned nearly four orders of magnitude, ranging from 3.86×10^4 median tissue culture infectious dose ($TCID_{50}$) in control cells to 78.18 $TCID_{50}$ at 5 nM basolateral 4′-FlU, approaching the level of detection.

Confocal microscopy validated formation of a pseudostratified organization of the epithelium with tight junctions in the airway epithelium tissue model (Fig. 3F), visualized efficient RSV replication in vehicle-treated tissue models (Fig. 3G), and confirmed near-sterilizing antiviral efficacy in the presence of 50 nM basolateral 4′-FlU (Fig. 3H and figs. S8 and S9). Under the latter conditions, positive staining for RSV antigens was rarely detected.

4′-FlU is orally efficacious in a therapeutic dosing regimen in a small-animal model of RSV infection

To test 4′-FlU efficacy in vivo, we used the mouse model of RSV infection (supplementary text), challenging animals with recRSV-A2-L19F, which efficiently replicates in mice (16). In a dose-to-failure study, we infected BALB/cJ mice intranasally and initiated once-daily oral treatment 2 hours after infection at 0.2, 1, or 5 mg 4′-FlU per kilogram of body weight. Treatment at all dose levels resulted in a statistically significant reduction in lung virus load compared with vehicle-treated animals (Fig. 4A). The antiviral effect was dose dependent and approached nearly two orders of magnitude at the 5 mg/kg dose. Consistent with high metabolic stability in HAEs, a twice-daily dosing regimen did not significantly enhance efficacy (fig. S10). Because animal appearance, body weight, temperature (fig. S11), and relative lymphocyte and platelet counts (Fig. 4B and fig. S12) were unchanged in the 5 mg/kg group compared with vehicle-treated animals, we selected this dose for further studies.

For a longitudinal assessment of therapeutic benefit, we used an in vivo imaging system (IVIS) with a red-shifted luciferase (26) expressing an RSV reporter virus generated for this study. This assay allows for a noninvasive spatial appreciation of intrahost viral dissemination. Daily imaging (Fig. 4C and fig. S13) revealed considerable reduction of bioluminescence intensity in lungs of 4′-FlU-treated animals at 5 days after infection, corresponding to peak viral replication, independent of whether treatment was initiated 24 hours before or 1 hour after infection (Fig. 4D). This IVIS profile is consistent with reduced viral replication and ameliorated viral pneumonia in treated animals.

To probe the therapeutic window of 4′-FlU, we initiated treatment at 2, 12, 24, 36, and 48 hours after infection. All treatment groups showed a statistically significant reduction of lung virus burden compared with vehicle-treated animals, but effect size was dependent on the time of treatment initiation (Fig. 4E and fig. S14). On the basis of our experience with

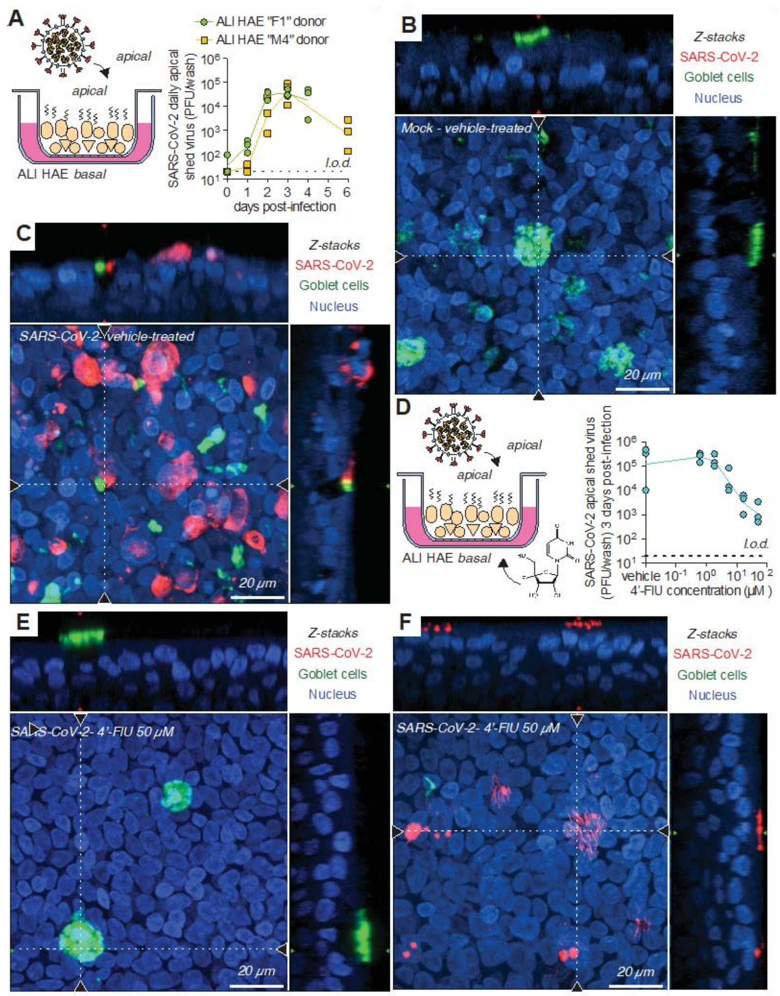

Fig. 5. Efficacy of 4′-FlU against SARS-CoV-2 replication in HAE organoids. (A) Multicycle growth curve of SARS-CoV-2 WA1 isolate on ALI HAE from two donors. Shed virus was harvested daily and titered by plaque assay (n = 3). (B and C) Confocal microscopy of ALI HAE cells from "F1" donor mock-infected (B) or infected (C) with SARS-CoV-2 WA1 isolate, 3 days after infection. SARS-CoV-2 infected cells, goblet cells, and nuclei were stained with anti-SARS-CoV-2 N immunostaining, anti-MUC5AC immunostaining, and Hoechst 34580, pseudocolored in red, green, and blue, respectively. z-stacks of 35-mm slices (1 mm thick) with 63× objective with oil immersion. Dotted lines represent the location of x-z and y-z stacks; scale bar, 20 mm. In all panels, symbols represent independent biological repeats and lines represent means. (D) Virus yield reduction of SARS-CoV-2 WA1 clinical isolate shed from the apical side in ALI HAE after incubation with serial dilutions of 4′-FlU on the basal side (n = 3). (E and F) Confocal microscopy of ALI HAE cells infected with SARS-CoV-2 WA1 isolate and treated with 50 mM 4′-FlU 3 days after infection. Rare ciliated cells positive for N are represented in (F).

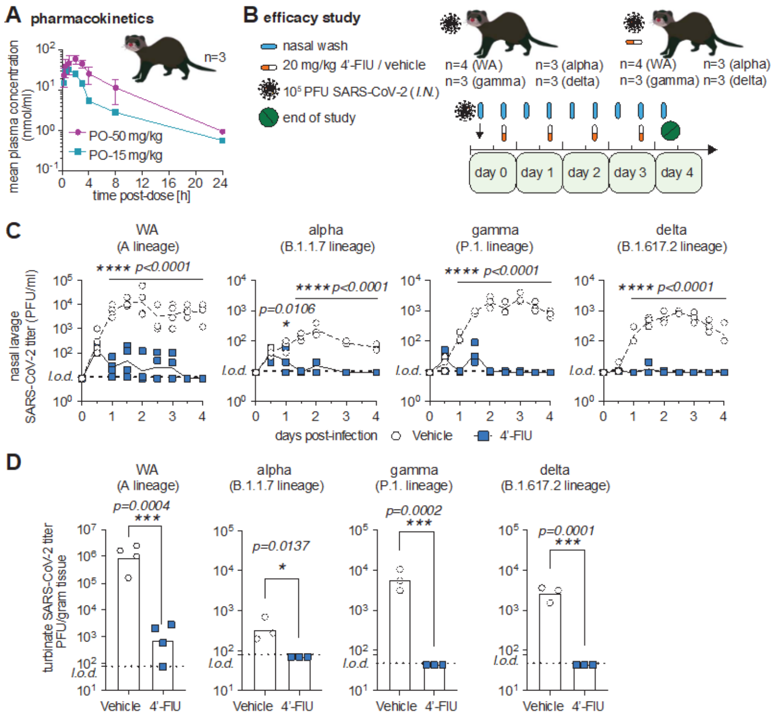

Fig. 6. Therapeutic oral efficacy of 4'-FlU against different SARS-CoV-2 isolates in ferrets. (A) Single oral dose (15 or 50 mg/kg bodyweight) pharmacokinetic properties of 4'-FlU in ferret plasma (n = 3). (B) Ferrets were inoculated with SARS-CoV-2 WA1 or VoC alpha, gamma, or delta, and treated as indicated. (C) Nasal lavages were performed twice daily and viral titers were determined by plaque assay [n = 4 (WA1) or n = 3 (alpha, gamma, delta)]. (D) Viral titers in nasal turbinates 4 days after infection. In all panels, symbols represent individual independent biological repeats and lines show mean values. Two-way ANOVA with Sidak's post hoc multiple comparison (C) and unpaired t test (D).

therapeutic intervention in related respiratory RNA viruses that cause lethal disease (25), we required a reduction in lung virus load of at least one order of magnitude. With this constraint, the therapeutic window of 4'-FlU was extended to 24 hours after infection in mice.

4'-FlU is effective against SARS-CoV-2 in HAE and the ferret model

To test activity against SARS-CoV-2 in the human airway organoids, we first confirmed that the WA1 isolate replicated efficiently in the HAEs of all donors tested (Fig. 5, A to C, and fig. S15). Treatment of infected organoids with basolateral 4'-FlU dose-dependently reduced apical virus shedding, albeit with a limited maximal effect size of ~ two orders of magnitude at 50 nM (Fig. 5D). Confocal microscopy revealed that the epithelium was largely devoid of SARS-CoV-2 nucleocapsid proteins under these conditions (Fig. 5E), with only sporadic staining detectable in a small subset of ciliated cells (Fig. 5F and fig. S15).

To probe for a corresponding antiviral effect in vivo, we determined the efficacy of oral 4'-FlU against an early pandemic isolate (WA1) and VoC alpha, gamma, and delta in the ferret model (27), which recapitulates hallmarks of uncomplicated human infection (3). For dose level selection in ferrets, we determined single oral dose ferret pharmacokinetic (PK) profiles of 4'-FlU. When administered at 15 or 50 mg/kg, peak plasma concentrations (C_{max}) of 4'-FlU reached 34.8 and 63.3 nM, respectively, and overall exposure was 154 ± 27.6 and 413.1 ± 78.1 hours×nmol/ml, respectively, revealing good oral dose-proportionality (Fig. 6A and table S3). On the basis of this PK performance, we selected once-daily dosing at 20 mg/kg body weight for efficacy tests (Fig. 6B).

Intranasal infection of ferrets with 1×10^5 PFU of each isolate resulted in rapid viral shedding into the upper respiratory tract, which plateaued in vehicle-treated animals 48 to 60 hours after infection (Fig. 6C). Therapeutic treatment with 4'-FlU initiated 12 hours after infection reduced virus burden in nasal lavages by approximately three orders of magnitude (WA1) to <50 PFU/ml within 12 hours of treatment onset. All three VoC were highly sensitive to 4'-FlU, remaining below the level of detection 36 to 48 hours after onset of oral treatment. Viral titers in nasal turbinate tissue extracted 4 days after infection (Fig. 6D) and associated viral RNA copy numbers (fig. S16) correlated with this reduction in shed virus load. Shedding of infectious particles ceased completely in all animals after 2.5 days of treatment (3 days post-infection).

Conclusions

This study identifies and characterizes the ribonucleoside analog 4'-FlU, which potently inhibits pathogens of different clinically relevant negative and positive-sense RNA virus families. The compound causes delayed stalling of RSV and SARS-CoV-2 polymerases within in vitro RdRP assays, reminiscent of the antiviral effect of remdesivir (28, 29). However, 4'-FlU can also trigger immediate RdRP stalling depending on sequence context, suggesting steric hindrance of polymerase advance or of accommodating the next incoming nucleotide as the underlying MOA. We cannot exclude that additional effects further enhance the antiviral effect in cellula as proposed for other nucleoside analogs (30). Slightly lower sensitivity of SARS-CoV-2 to 4'-FlU compared with RSV could be a result of the exonuclease activity of the coronavirus polymerase, which can eliminate ribonucleoside analogs (31, 32). Alternatively, coronavirus RdRP may have a greater capacity to tolerate the compound, because SARS-CoV-2 RdRP showed a higher tendency than RSV polymerase to advance after 4'-FlU-TP incorporation in the RdRP assays, which do not contain exonuclease functionality.

Once-daily oral administration to mice and ferrets significantly reduced the burden of RSV and SARS-CoV-2, respectively, when treatment was initiated up to 24 (RSV) or 12 (SARS-CoV-2) hours after infection. Because RSV (33) and SARS-CoV-2 (34) host invasion is slower in humans, these data outline a viable therapeutic window for human treatment. Equally potent activity against SARS-CoV-2 VoC alpha, gamma, and delta demonstrated broad anticoronavirus efficacy of 4'-FlU, building confidence that the compound will remain active against future VoC that may be increasingly less responsive to spike-targeting vaccines or antibody therapeutics. Formal tolerability studies are pending, but 4'-FlU was well tolerated by the human organoid models and efficacious in murids and mustelids. Blood analysis of treated mice uncovered no antiproliferative effect of 4'-FlU on the hematopoietic system. These results establish 4'-FlU as a broad-spectrum orally efficacious inhibitor of major RNA viruses, making it a promising therapeutic option for RSV disease and COVID-19, and a much-needed contributor to improvement of pandemic preparedness.

REFERENCES AND NOTES

1. J. H. Beigel et al., N. Engl. J. Med. 383, 1813–1826 (2020).
2. M. Toots et al., Sci. Transl. Med. 11, eaax5866 (2019).
3. R. M. Cox, J. D. Wolf, R. K. Plemper, Nat. Microbiol. 6, 11–18 (2021).
4. G. R. Painter et al., Antiviral Res. 171, 104597 (2019).
5. T. P. Sheahan et al., Sci. Transl. Med. 12, eabb5883 (2020).
6. A. R. Falsey, P. A. Hennessey, M. A. Formica, C. Cox, E. E. Walsh, N. Engl. J. Med. 352, 1749–1759 (2005).
7. B. Rha et al., Pediatrics 146, e20193611 (2020).
8. T. Shi et al., J. Infect. Dis. 222 (suppl. 7), S577–S583 (2020).
9. T. Shi et al., Lancet 390, 946–958 (2017).
10. G. S. Cockerill, J. A. D. Good, N. Mathews, J. Med. Chem. 62, 3206–3227 (2019).
11. R. Fearns, R. K. Plemper, Virus Res. 234, 87–102 (2017).
12. R. M. Cox et al., J. Biol. Chem. 293, 16761–16777 (2018).
13. J. DeVincenzo et al., J. Infect. Dis. jiaa716 (2020).
14. J. J. Yoon et al., Antimicrob. Agents Chemother. 62, e00766-18 (2018).
15. P. Richardson, Expert Opin. Drug Discov. 16, 1261–1286 (2021).
16. M. L. Moore et al., J. Virol. 83, 4185–4194 (2009).
17. L. D. Marroquin, J. Hynes, J. A. Dykens, J. D. Jamieson, Y. Will, Toxicol. Sci. 97, 539–547 (2007).
18. S. P. Luby, Antiviral Res. 100, 38–43 (2013).
19. Based on the current knowledge of the pyrimidine salvage pathway, it must be assumed that the large excess of extracellular cytidine leads to conversion of CTP to UTP via cytidine deaminase (CDA), competing with 4'-FlU.
20. B. Ludeke, R. Fearns, Virology 540, 66–74 (2020).
21. E. P. Tchesnokov, J. Y. Feng, D. P. Porter, M. Götte, Viruses 11, 326 (2019).
22. C. J. Gordon et al., J. Biol. Chem. 295, 6785–6797 (2020).
23. T. L. Dangerfield, N. Z. Huang, K. A. Johnson, Expression and purification of tag-free SARS-CoV-2 RNA-dependent RNA polymerase in Escherichia coli. STAR Protoc 2, 100357 (2021).
24. Our nsp12 preparations contain a mixture of 'GroEL' and 'tf', and nsp12 as described before, the latter representing 19% and 18% of the protein content of the preparations containing catalytically active and inactive nsp12, respectively.
25. M. Toots et al., Transl. Res. 218, 16–28 (2020).
26. S. M. Coleman, A. McGregor, Future Virol. 10, 169–183 (2015).
27. Male ferrets were not included in this study for practical reasons as they are territorial and available ABSL3 space cannot accommodate the number of cages that this study would require to achieve meaningful statistical power.
28. G. Kokic et al., Nat. Commun. 12, 279 (2021).
29. E. P. Tchesnokov et al., J. Biol. Chem. 295, 16156–16165 (2020).
30. J. J. Feld, J. H. Hoofnagle, Nature 436, 967–972 (2005).
31. E. C. Smith, H. Blanc, M. C. Surdel, M. Vignuzzi, M. R. Denison, PLOS Pathog. 9, e1003565 (2013).
32. E. Minskaia et al., Proc. Natl. Acad. Sci. U.S.A. 103, 5108–5113 (2006).
33. C. M. El Saleeby, A. J. Bush, L. M. Harrison, J. A. Aitken, J. P. Devincenzo, J. Infect. Dis. 204, 996–1002 (2011).
34. B. Oberfeld et al., Cell 181, 954–954.e1 (2020).

ACKNOWLEDGMENTS

We thank C. F. Basler for providing the Calu-3 cells, D. Waugh for plasmid pRK792-encoding TEV protease (Addgene plasmid #8830), the Georgia State University High Containment Core and the Department for Animal Research for support, and A. L. Hammond for critical reading of the manuscript. Funding: This work was supported in part by Public Health Service grants AI153400, AI071002, and AI141222 (to R.K.P.) from the NIH/NIAID. The funders had no role in the study design, data collection and interpretation, or the decision to submit the work for publication. Author contributions: Conceptualization: M.G.N., G.R.P., and R.K.P. Investigation: J.S., R.M.C., M.T., J.Y., C.M.L., M.A., J.D.W., Z.S., and R.K.P. Resources: G.R.B., A.A.K., L.M.S., and R.K.P. Visualization: G.R.B. and J.S. Validation: J.S. and R.K.P. Funding acquisition: R.K.P. Project administration: M.G.N. and R.K.P. Supervision: G.R.P. and R.K.P. Writing – original draft: J.S. and R.K.P. Writing – review and editing: J.S. and R.K.P. Competing interests: G.R.B. and G.R.P. are coinventors on patent WO 2019/1736002 covering composition of matter and use of EIDD-2749 and its analogs as an antiviral treatment. This study could affect their personal financial status. All other authors declare that they have no competing interests. Data and materials availability: All data are available in the main text or the supplementary materials. Materials and methods are available as supplementary materials at the Science website. Transfer of EIDD-2749 material to other institutions for research purposes is covered by MTAs from Emory University.

SUPPLEMENTARY MATERIALS

science.org/doi/10.1126/science.abj5508
Materials and Methods
Supplementary Text
Figs. S1 to S18
Tables S1 to S3
References (35, 36)
MDAR Reproducibility Checklist
Data S1 and S2

View/request a protocol for this paper from Bio-protocol.

19 May 2021; resubmitted 4 October 2021
Accepted 29 November 2021
Published online 2 December 2021
10.1126/science.abj5508

Science
AAAS

Supplementary Materials for

4'-Fluorouridine is a broad-spectrum orally efficacious antiviral blocking respiratory syncytial virus and SARS-CoV-2 replication

Julien Sourimant[1], Carolin M Lieber[1], Megha Aggarwal[1], Robert M Cox[1], Josef D Wolf[1], Jeong-Joong Yoon[1], Mart Toots[1], Chengin Ye[2], Zachary Sticher[3], Alexander A Kolykhalov[3,4], Luis Martinez-Sobrido[2], Gregory R Bluemling[3,4], Michael G Natchus[3], George R Painter[3,4,5], Richard K Plemper[1,6]*

Correspondence to: plemper@gsu.edu

This PDF file includes:

Materials and Methods
Supplementary Text

Materials and Methods

Study design

The objectives of this study were to explore the mechanism of action and preclinical efficacy of the ribonucleoside analog 4'-FlU against RSV and SARS-CoV-2, using disease-relevant human airway epithelium models and appropriate animal models to assess bioavailability and antiviral efficacy, the mouse model for RSV and the ferret model for SARS-CoV-2. Treatment was considered efficacious when statistically significant reduction in virus titers in nasal lavages (ferrets) and respiratory tissues (mice and ferrets) was observed. Efficacy and cytotoxicity of the drug candidate in multiple cell lines including human airway epithelium were assessed by four-parameter variable-slope regression modeling of 50% inhibitory and cytotoxic concentrations. Timeline endpoints were predefined before initiation of experiments. The number of animal per group (3 to 5, as specified in each figure legend) in *in vivo* efficacy experiments has been selected to provide sufficient statistical power to detect a significant biological effect such as a reduction in viral titers of at least one order of magnitude, based on our previous experience with these models. Before initiation of each individual study, animals were randomly assigned to treatment and control groups. No blinding was used. Primary numerical data are shown in Data S2.

Experimental design of mice experiments

6-8–week old female Balb/cJ mice (Jackson laboratory, cat# 000651) were housed in an ABSL-2 facility and rested for 4-5 days. For efficacy studies, mice were randomly divided into groups (n=5) and infected intranasally with 5×10^5 $TCID_{50}$ (25 µl per nare) of recRSV-A2line19F-[mKate] in PBS while under anesthesia with ketamine/xylazine. Treatment (4'-FlU or vehicle) was administrated at the indicated time post-infection via oral gavage in a 200 µl suspension of 0.5% Tween80 in 10 mM sodium citrate in water. Temperature and food consumption were monitored daily, body weight was determined twice daily. All animals were euthanized at 4.5 days after infection and lungs were harvested. To determine lung viral titers, lungs were weighted and homogenized with a bead beater in 300 µl PBS in 3 bursts of 20 seconds by 5-minute rest on ice after each cycle. Samples were clarified for 5 minutes at 4°C and 20,000×g, supernatant aliquoted and stored at -80°C before being titrated by median tissue culture infectious dose ($TCID_{50}$) normalized per gram of lung tissue and per ml of lysate. For *in vivo* live imaging, mice were infected with recRSV-A2line19F-[redFirefly] in PBS and treatment was initiated at the indicated time. Bioluminescence was monitored once daily at the indicated time after isoflurane anesthesia and retro-orbital injection with 100 µl of 100 mg/ml D-luciferin (Goldbio). Acquisition was initiated 30s after substrate injection in an IVIS Spectrum (Caliper LifeSciences). Acquisition parameters were a sequence of 9×30-second exposures with medium binning (binning=8), small aperture (f=1) and large field of view (D - 22) using Living Image 4.5.4 Software for Windows 10. For tolerability study, mice were infected with 300,000 $TCID_{50}$ recRSV-A2line19F-[mKate] or mock and treated with 5mg/kg mice body weight 4'-FlU at 12 hours post-infection once daily for 4 days. Blood samples were collected prior to infection and at 1.5, 2.5, 3.5, and 4.5 days post-infection. Complete blood counts were performed with a VETSCAN HM5 (Abaxis) following the manufacturer's protocol.

Experimental design of ferret experiments

6-10–month old female ferrets (*Mustela putorius furo*; Triple F Farms) were used as an *in vivo* model to examine the therapeutic efficacy of orally administered 4’-FlU against SARS-CoV-2 infection. Group sizes of 3-4 ferrets were used for efficacy studies. Animals were randomly assigned to the different study groups. No blinding was performed. Viruses were administered to animals through intranasal inoculation. Ferrets were inoculated with SARS-CoV-2 (1×10^5 pfu of 2019-nCoV/USA-WA1/2020 or hCoV-19/USA/CA_CDC_5574/2020) in 1 ml (0.5 ml per nare). At 12 hours after infection, a group of ferrets was treated once daily (*q.d.*) with vehicle (10 mM sodium citrate with 0.5% (v/v) Tween 80) or 4’-FlU at a dosage of 20 mg kg^{-1}, respectively. Nasal lavages were collected every 12 hours for all ferrets. Once daily dosing was continued for 4 days post infection. All animals were euthanized 4 days after the infection was started. Organs and tissues were harvested and stored at -80°C until processed.
For virus titration, samples were weighed and homogenized in sterile PBS. Tissue homogenates were clarified by centrifugation (2,000×g for 5 minutes at 4°C). The clarified supernatants were then harvested and used in plaque assays. For detection of viral RNA, total RNA was extracted from organs using a RNeasy mini kit (Qiagen), in accordance with the manufacturer’s protocol. Total RNA was extracted from nasal lavages using a ZR viral RNA kit (Zymo Research) in accordance with the manufacturer’s protocols. Virus titers were determined by plaque assays and viral RNA copy numbers were determined by RT–qPCR quantitation.

SARS-CoV-2 RNA copy numbers

Detection of SARS-CoV-2 RNA was performed using the nCoV_IP2 primer–probe set (National Reference Center for Respiratory Viruses, Pasteur Institute). RT–qPCR reactions were performed on an Applied Biosystems 7500 real-time PCR system using the StepOnePlus real-time PCR system. Viral RNA was detected using the nCoV_IP2 primer–probe set in combination with TaqMan fast virus 1-step master mix (Thermo Fisher Scientific). Viral RNA copy numbers were determined based on a standard curve created using a PCR fragment (nucleotides 12669–14146 of the SARS-CoV-2 genome) as previously described. The RNA values were normalized to the weights of the tissues used.

Institutional Animal Care and Use Committee (IACUC) approval statement.

All animal work was performed at Georgia State University in compliance with the Guide for the Care and Use of Laboratory Animals of the National Institutes of Health. Mouse work was approved by the GSU Institutional Animal Use and Care Committee (IACUC) under protocols A17019 and A20012, ferret work was approved under protocol A20031.

Cells

African green monkey kidney cells VeroE6 (ATCC® CRL-1586™), Vero/hSLAM (expressing human signaling lymphocytic activation molecule), Madin-Darby canine kidney cells (MDCK, ATCC® CCL-34™), human lung adenocarcinoma epithelial cells Calu-3 (ATCC® HTB-55™), human epithelial/HeLa contaminant HEp-2 cells (ATCC® CCL-23™), human bronchial epithelial BEAS-2B (ATCC® CRL-9609™) and baby hamster kidney cells (BHK-21; ATCC® CCL-10™) stably expressing either T7 polymerase (BSR-T7/5) or G protein of rabies virus strain SAD-B19 (BSR-RVG) were cultivated at 37°C and 5% CO_2 in Dulbecco’s Modified Eagle’s medium (DMEM) supplemented with 7.5% fetal bovine serum (FBS). Insect cells from Spodoptera Frugiperda (SF9, ATCC® CRL-1711™) were propagated in suspension using Sf-900 II serum-free media (SFM) (Thermo Scientific) at 28°C. All cell lines used in this study are routinely checked for mycoplasma and microbial contamination. Mammalian cell transfections were performed using GeneJuice transfection reagent (Invitrogen) while insect cell transfections were performed using Cellfectin II transfection reagent (Gibco). All cell lines were routinely checked for mycoplasma contamination. Normal primary human bronchial/tracheal epithelial cells (HBTEC) from a 30-year old female (LifeLine Cell Technology, cat# LM-0050, lot# 3123, passage 2, “donor F1”) were grown in BronchiaLife cell culture medium (LifeLine Cell Technology). Normal human bronchial/tracheal epithelial cells (NHBE) (Lonza Bioscience, cat# CC-2540S, lot# 0000646466, passage 2, donor “M4”) from a 38 year-old male were cultured in PneumaCult-Ex Plus (Stemcell Technologies cat# 05040) following the manufacturer’s instructions.

Plasmids

Plasmids to rescue recombinant RSV A2 with line19 F harboring a mKate reporter (labelled here as recRSV-A2line19F-[mKate]) or RSV A2 with line19 F with hyperfusogenic F_D489E substitution and FireSMASh reporter (labelled here as recRSV-A2line19F-[FireSmash]) were previously described. To rescue a recombinant RSV harboring a red-shifted firefly luciferase (labelled as recRSV-A2line19F-[redFirefly]), we swapped the mKate reporter of the pSynkRSV-line19F vector with the redFirefly sequence in a succession of steps: 1) We fused immediately downstream of the redFirefly sequence from pCMV-Red Firefly (ThermoFisher Scientific cat. 16156) a sequence containing the RSV L noncoding region, L gene end, NS1/NS2 intergenic junction with a BlpI restriction site, mimicking the sequence downstream of mKate on the pSynkRSV-line19F vector. The assembly was used with NEBuilder (New England Biolabs) and the primer sets 5’- GCGGCCGCAAAATCAGCC and 5’-TCATCACATCTTGGCCACGG for pCMV-Red Firefly and with 5’-ccgtggccaagatgtgatgaGTATTCAATTATAGTTATTAAAAACTTAACAG) and 5’-gaggctgattttgcggccgcGCTAAGCAAGGGAGTTAAATTTAAG for the downstream sequence with BlpI. 2) The sequence of redFirely and its downstream sequence up to the BlpI site were amplified by PCR to insert a second BlpI site immediately upstream of the redFirefly sequence using primers 5’-catcatGCTTAGCatggaaaatatggaaaacg and 5’-gaggctgattttgcggccgcGCTAAGCAAGGGAGTTAAATTTAAG, mimicking the sequence upstream of mKate on the pSynkRSV-line19F vector. The amplified product was digested with BlpI (New England Biolabs) and purified. 3) Since BlpI is not a unique site on the pSynkRSV-line19F vector, we generated an intermediate shuttle vector by inserting a fragment from pSynkRSV-line19F vector encompassing the leader promoter sequence to the nucleoprotein gene and containing mKate, by digesting it with AvrII (New England Biolabs) and PmeI (New England Biolabs). In parallel we digested and purified the backbone of a pCDNA 3.1 (ThermoFisher Scientific cat. V79020) with AvrII (New England Biolabs) and PmeI (New England Biolabs), and the two fragments were ligated with the t4 ligase ((New England Biolabs). 4) The shuttle vector was opened with BlpI to release the mKate segment and the backbone purified, and ligated to the purified amplicon of step (2) containing redFirefly. 5) The shuttle vector with redFirefly was opened with AvrI and PmeI and the insert ligated back to the backbone of the pSynkRSV-line19F vector. The final construct was confirmed with Sanger sequencing. For expression of SARS-CoV-2 nsp12, nsp8 and nsp7, SARS-CoV-2 RNA was isolated from stocks of isolate USA-WA1/2020 (BEI# NR-52281) and reverse transcribed using superscript III (Invitrogen). The resulting cDNA was used as a template for the amplification of nsp7, nsp8 and nsp12 encoding genes the primer 5’-

CTGGACATATGGGCAGCAGCCATCATCATCATCATCACAGCAGCGGCGAAAACCTG TATTTTCAGGGCTCTAAAATGTCAGATGTAAAG and 5'-CTAGAGCGGCCGCCTATTGTAAGGTTGCCCTGTTG (nsp7), 5'-CTGGATCTAGAAATAATTTTGTTTAACTTTAAGAAGGAGATATAATGGGCAGCAGCC ATCATCATCATCAT and 5'-CTAGAGCGGCCGCCTACTGTAATTTGACAGCAGAATTG (nsp8), and 5'-CTGGACATATGTCAGCTGATGCACAATCG and 5'-CTAGACTCGAGGCCCTGAAAATACAGGTTTTCGCCGCTGCTCTGTAAGACTGTATGC GGTG (nsp12). PCR amplified products were individually cloned into pET30a(+) expression vector (Novagen) with tobacco etch virus protease-cleavable 6×His tag at the N-terminus of nsp7 and nsp8, and at the C-terminus of nsp12 using appropriate restriction sites and cloning strategies, bringing the cloned genes under T7 promoter control. A catalytically inactive variant of nsp12 was generated by site-directed mutagenesis, modifying residues 762-SDD in the conserved catalytic motif C to 762-SNN with appropriately designed primers.

Viruses

Recombinant RSVs were rescued as described previously, briefly BSR-T7/5 cells were co-transfected with the cDNA genome along with helper plasmids encoding the RSV L, N, P and M2-1 protein, further amplified on HEp-2 cells after a freeze-thaw cycle and supernatant clarification (1800×g, 5 minutes, 4°C). Stocks were prepared as described previously by infecting 50% confluent HEp-2 cells in 15cm dishes at a multiplicity of infection (MOI) of 0.01 $TCID_{50}$/cell, incubated at 37°C overnight then transferred to 32°C for five days. Infected cells were scraped, virions released with a freeze/thaw cycle and supernatant clarified (1800×g, 5 minutes, 4°C). Screening-grade stocks of recRSV-A2line19F-[FireSmash]) were grown in the presence of 3 µM asunaprevir to reduce accumulation of Firefly luciferase and further purified at the interface of a 20%/60% sucrose gradient in TNE buffer (50 mM Tris/Cl pH 7.2, 10 mM EDTA) with centrifugation at 30,000rpm on a SW41 rotor (Beckman Coulter) for 2 hours at 4°C. Clinical RSV B isolates 16F10 (GenBank: KY674983.1) and 6A8 (GenBank: MF001044.1) were a kind gift from A. Greninger. Samples were collected from patient nasal wash specimens in 2017, cultured on primary rhesus monkey kidney (RhMK) cells, and amplified once on HEp-2 cells prior to use in this study. RSV viral titers were determined using standard 50% tissue infective dose ($TCID_{50}$) assay in HEp-2 cells and 96 well plates, with a Spearman and Karber based method using either fluorescence or immunostaining for detection. Recombinant measles virus strain Edmonston with nano luciferase reporter including a destabilizing PEST sequence (labelled here as recMeV-[N_{PEST}luc]) was rescued and amplified on Vero/hSLAM cells. Recombinant respiroviruses human parainfluenza 3 virus with Nano luciferase reporter (HPIV3-JS NanoLuc, labelled here recHPIV-3-[Nluc]), Sendai virus with Gaussia luciferase reporter labelled here recSeV-[Gluc] were rescued and amplified on VeroE6 cells. Recombinant rhabdoviruses, vesicular stomatitis virus (Indiana strain) with Nano luciferase reporter (labelled here as recVSV-[Nluc]) and rabies virus strain SAD-B19 with G deletion and Nano luciferase reporter (labelled here as recRabV-[Nluc]) were rescued and authenticated through RT-PCR and Sanger-sequencing. SARS-CoV-2 early isolate USA-WA1/2020 (BEI# NR-52281) A lineage, and variants of concerns (VoC) alpha (isolate USA/CA_CDC_5574/2020 (BEI# NR-54011) B.1.1.7 lineage), gamma (isolate hCoV-19/Japan/TY7-503/2021 (BEI#: NR-54982) P.1. lineage) and delta (isolates hCoV-19/USA/PHC658/2021 (BEI#: NR-55611) (VeroE6 virus yield reduction) and GISAID 2333067 (efficacy in ferrets) lineage B.1.617.2), were sequence-validated and amplified on Calu-3 cells, in DMEM supplemented with 2% FBS following approved procedures in biosafety level 3 containment. Recombinant SARS-CoV-2 with USA-WA1/2020 genetic background expressing Nanoluciferase reporter, denoted recSARS-CoV-2-[Nluc] in this manuscript, has been previously described (*35*).

Minireplicon assays
For RSV-derived minireplicon assays, a plasmid expressing the RSV minigenome containing the firefly luciferase reporter, under control of RNA pol I promoter, and a set of helper plasmids expressing codon-optimized RSV P, L, N and M2-1 proteins, under the control of CMV promoter, were co-transfected with GeneJuice reagent (Millipore Sigma) following manufacturer's instructions in 50% confluent HEK-293T cells. For dose-response experiments, cells were transfected in 96-well plate format. 3-fold serial dilutions of compounds 4'-FlU or NHC were prepared in triplicate using a Nimbus liquid handler (Hamilton) and transferred on transfected cells 4 hours post-transfection. At 48 hours post-transfection, luciferase activities were determined using ONE-Glo luciferase substrate (Promega) and a H1 synergy plate reader (BioTek). Each plate contained 4 wells of each positive and negative controls (minireplicon with media containing dimethyl sulfoxide (DMSO) or minireplicon with L-expressing plasmid replaced by pCDNA3.1). Normalized luciferase activities were analyzed with the formula: % inhibition = $(\text{Signal}_{\text{Sample}} - \text{Signal}_{\text{Min}})/(\text{Signal}_{\text{Max}} - \text{Signal}_{\text{Min}}) \times 100$, and dose response curves were further analyzed by normalized non-linear regression with variable slope to determine 50% effective concentration (EC_{50}) and 95% CIs Prism 9.0.1 for MacOS (GraphPad). Similarly, luciferase activities from MeV strain Edmonston-based minireplicon (firefly luciferase), NiV minireplicon (Nano luciferase) and the recHPIV3-JS-NanoLuc (Nano luciferase, labelled in this context as HPIV3 maxireplicon), were transfected in BSR-T7/5 as previously described.

Dose response antiviral assays
For reporter-based dose-response assays, 3-fold serial dilutions of 4'-FlU or NHC were prepared in triplicate using a Nimbus liquid handler (Hamilton) and transferred to 96-well plates seeded the day before at 50% confluence in 96-well plate format. Immediately after addition of compound, cells were infected with either recRSV-A2line19F-[FireSmash], recMeV-[NPESTluc] recHPIV-3-[Nluc], recSeV-[Gluc], recVSV-[Nluc], or recRabV-[Nluc] at MOI 0.2 $TCID_{50}$/cell. At 48 hours post-transfection, luciferase activities of reporter-expressing viruses were determined using either ONE-Glo luciferase substrate, Nano-Glo Dual-Luciferase substrate (Promega) and a H1 synergy plate reader (Biotek). Each plate contained 4 wells each of positive and negative control (infected cells with media containing DMSO or 100 μM cycloheximide, respectively). Normalized luciferase activities were analyzed with the formula: % inhibition = $(\text{Signal}_{\text{Sample}} - \text{Signal}_{\text{Min}})/(\text{Signal}_{\text{Max}} - \text{Signal}_{\text{Min}}) \times 100$, and dose response curves were further analyzed by normalized non-linear regression with variable slope to determine 50% effective concentration (EC_{50}) and 95% CIs with Prism 9.0.1 for MacOS (GraphPad). For RSV virus yield reduction, HEp-2 cells were infected with recRSV-A2line19F-[mKate] or clinical isolates in 12-well plate format at MOI 0.1 $TCID_{50}$/cell for 2 hours at 37°C. Inoculum was removed and replaced with DMEM with 2% FBS and indicated concentrations of compound and cells were incubated for 3 days. Viral titers were determined by standard $TCID_{50}$ with fluorescence or immunostaining for detection. For SARS-CoV-2 virus yield reduction on VeroE6 cells, cells were seeded in 12-well plates (300,000 cells per well) the day before infection, infected at a MOI of 0.1 PFU/cell with a 1 hour absorption step and inoculum was removed and replaced with fresh

DMEM with 2% FBS and indicated concentrations of 4'-FlU (vehicle: 0.1% DMSO). Infected cells were incubated with compound for 48 hours at 37 °C, followed by virus titration by standard plaque assay. Log viral titers were normalized using the average top plateau of viral titers to define 100% and were analyzed with a non-linear regression with variable slope to determine EC_{50} and 95% CIs with Prism 9.0.1 for MacOS (Graphpad).

Cytotoxicity assays

To determine the effect of compound on cell metabolism, HEp-2, MDCK, Beas-2B, or BHK-T7 cells were seeded at 50% confluence in 96-well plates and were incubated with 3-fold serial dilution of 4'-FlU from 500 μM as described for dose-response assays, including positive and negative controls for normalization. After 48-hour incubation at 37°C, cells were incubated with PrestoBlue (ThermoFisher Scientific) for 1 hour at 37°C and fluorescence measured with a H1 synergy plate reader (Biotek). 50% cytotoxic concentrations (CC_{50}) and 95% CIs after normalized non-linear regression and variable slope were determined using Prism 9.0.1 for MacOS (GraphPad). To uncover potential mitochondrial toxicity masked by the Crabtree effect, BEAS-2B cells were also incubated in the presence of glucose-free RPMI media supplemented with galactose as carbohydrate source. To further assess the potential inhibitory effect on mitochondrial and nuclear polymerases, HBTEC cells were seeded at 50% confluence in 96 well plates and incubated with 3-fold dilutions of compound, and intracellular concentration of two mitochondrial proteins, the mitochondrial DNA-encoded COX-I and the nuclear DNA-encoded SDH-A was determined with the in-cell ELISA Mitobiogenesis kit following the manufacturer's instructions (Abcam cat# ab110217).

Ribonucleotide competition of RSV inhibition

HEp-2 cells were infected with RSV-A2line19F-[FireSMASh] at a MOI of 0.1 $TCID_{50}$/cell, maintenance media was supplemented with 4'-FlU at 10 μM alone or in combination with 0.1 to 300 μM exogenous ribonucleosides (Sigma-Aldrich). Firefly luciferase reporter activity was quantified at 48 hours post-infection. Values are expressed relative to the values for the vehicle-treated samples.

Recombinant RSV L and P protein production and purification

For purification of RSV L and P proteins (A2 strain), a pFastBac Dual plasmid (Invitrogen) containing the codon-optimized open reading frames of L and P proteins under the control of polyhedrin and p10 promoters, respectively, was used to recover recombinant baculoviruses using the Bac-to-Bac Baculovirus Expression System and SF9 cells. The P protein sequence contains a C-terminal 6-histidines tag separated by a tobacco etch virus (TEV) cleavage site, allowing co-purification of L-P complexes by immobilized metal affinity chromatography (IMAC). SF9 cells were infected in suspension with MOI 1 PFU/cell for 72-80 hours, pelleted and gently lysed on ice for 45 minutes with a buffer containing 50 mM NaH_2PO_4 [pH 8.0], 150 mM NaCl, 20 mM imidazole, 0.5% NP-40 with Pierce Protease Inhibitor and Pierce universal nuclease (ThermoFisher Scientific). Clarified lysates (30 minutes, 15,000×g, 4°C) were incubated for 2 hours with shaking with pre-equilibrated HisPur Ni-NTA Resin (ThermoFisher Scientific). After 5 washes with 10 bed volumes of lysis buffer with 60 mM imidazole, proteins were eluted with 3 bed volumes of lysis buffer with 250 mM imidazole. Eluates were dialyzed overnight in storage buffer: 20 mM Tris-HCl [pH 7.4], 150 mM NaCl, 10% glycerol, 1 mM dithiothreitol, aliquoted and stored at -80°C. Uncropped SDS-PAGE scans are available in Data S1.

Recombinant SARS-CoV-2 nsp7, nsp8, and nsp12 protein production and purification
The sequence confirmed constructs of nsp7 and nsp8 were transformed into BL21(DE3)pLysS cells. For the expression of nsp12 in *E. coli*, first chaperon plasmid pG-Tf2 (Takara Biosciences) was transformed into BL21 cells to enhance correct folding and solubility of recombinant proteins, followed by transformation with pET30a-nsp12 plasmid. The transformed cells were grown in Luria-Bertani (LB) broth for nsp7 and nsp8 at 37°C until the OD_{600} reached 0.6. nsp7 and nsp8 cultures were induced with 0.5 mM isopropyl β-d-1-thiogalactopyranoside (IPTG) (Teknova) and the temperature was reduced to 18°C. The expression culture was grown for ~16 hours. nsp12 expression was performed by growing the cells in Terrific broth (TB) at 37°C until the OD_{600} reached 0.6. Tetracycline was added to a final concentration of 10 ng/ml and the temperature was reduced to 18°C. After half an hour incubation, 0.5 mM IPTG was added to the culture and incubated at 18°C for ~16 hours. Cells were harvested by centrifugation and the cell pellet was stored at -20°C until further use. The cell pellet was resuspended in lysis buffer (Tris 50 mM pH 8.0, NaCl 200 mM, glycerol 10%, 20 mM imidazole, protease inhibitor cocktail (Pierce), Pierce universal nuclease (ThermoFisher Scientific)) with 0.3mg/ml lysozyme and incubated on ice for ~20 minutes. The samples were sonicated for ~6-8 minutes. Cell debris were separated by centrifugation at 14,000×g for 30 minutes, clarified supernatant collected, and loaded on to HisPur Ni-NTA resin (ThermoFisher Scientific) pre-equilibrated with lysis buffer and incubated for ~45 minutes at 4°C. Beads were washed extensively with wash buffer (Tris 50 mM pH 8.0, NaCl 200 mM, 10% glycerol containing 20-100 mM imidazole), and proteins eluted with Tris 50 mM pH 8.0, NaCl 200 mM, glycerol 10% containing 250 mM imidazole. The purified fractions were pooled, and the histidine tag was cleaved by adding TEV protease to the purified protein which was also simultaneously dialyzed overnight against the 1 L dialysis buffer (Tris 30 mM pH 7.4, NaCl 150 mM, glycerol 10%). Dialyzed 6×His tag cleaved proteins were re-incubated with HisPur Ni-NTA resin pre-equilibrated with Tris 50 mM pH 7.4, NaCl 200 mM, glycerol 10%, 20mM imidazole for 15 minutes. Flow through containing the tag cleaved proteins was collected and the resin was further washed with buffer containing imidazole. The desired His tag cleaved fractions were pooled and dialyzed against storage buffer (Tris 25 mM pH 7.4, NaCl 150 mM, glycerol 10%, DTT 1 mM) at 4°C overnight. The proteins were concentrated to final concentrations of 60, 30 and 6 ∝M for nsp7, nsp8 and nsp12 respectively, flash frozen and stored at -80°C for further use. Two additional polypeptides that co-purified with nsp12 likely represent host Gro-EL (60 kDa) and trigger factor (Tf) (56 kDa) proteins. Uncropped SDS-PAGE scans are available in Data S1.

***In vitro* RNA synthesis assays**
3’ primer-extension assays were performed based on an established assay with modifications. Briefly, purified polymerase complexes (100-200 ng of L protein) were incubated in 5 µl final volume with a transcription buffer containing 20 mM Tris-HCl pH 7.4 [RT], 30 mM NaCl, 10% glycerol, 1 mM dithiothreitol, 8 mM $MgCl_2$, 4 µM RNA template, 20 µM RNA primer, indicated concentrations of nucleotides and 1 µCi of (alpha)32P-labelled ATP (Perkin-Elmer). HPLC-purified 5’ phosphorylated RNA templates and non-phosphorylated RNA primers (SIGMA-ALDRICH) were used to reduce non-specific extension of the template. Reactions were performed for 1 hour at 30°C and the reaction was stopped with 1 volume of deionized

formamide with 25 mM ethylenediaminetetraacetic acid (EDTA). Following 5 minutes denaturation at 95 °C, samples were separated by 7M urea Tris-Borate-EDTA 20% polyacrylamide gel electrophoresis and visualized by autoradiography with X-ray films (CL-XPosure, ThermoFisher Scientific) or with a storage phosphor screen BAS IP MS 2040 E (GE Healthcare Life Sciences) and imaged with Typhoon FLA 7000 (GE Healthcare Life Sciences). Densitometry analysis was performed using FIJI 2.1.0. For quantifications of nucleotide incorporation kinetics, the intensity of each band corresponding to a primer-extension product was individually measured for each lane, and either the band corresponding to the UTP incorporation or the pooled primer-extension products following initial UTP incorporation were normalized to the pooled intensities of all the primer-extension products in that lane. As an optional assistance to data visualization, we implemented the following color-coding: 0-25% red, 25-75% orange, 75-125% grey, >125%: blue. Enzyme kinetics (V_{max} and Km) were determined using the Michaelis-Menten equation with Prism 9.0.0 for macOS (GraphPad). Nucleoside selectivity was determined using the nucleotide analog/nucleotide ratio of each Vmax/Km ratios. For side-by-side comparison of elongation products, reactions were performed as previously noted with saturating concentration of 300 µM of UTP or 4'-FlU-TP. Each band corresponding to a primer-extended product containing 4'-FlU-TP was directly normalized to the equivalent UTP-containing band. For *de novo* RNA synthesis, an RNA template corresponding to the 25 nt of the RSV trailer complement sequence was incubated at 2 µM with RSV RdRP (100-200 ng of L), 8 mM $MgCl_2$, 1 mM dithiothreitol, indicated concentrations of each nucleotides and 10 µCi of (alpha)32P-labelled GTP (Perkin-Elmer), 20 mM Tris-HCl [pH 7.4], 15 mM NaCl, 10 % glycerol. Reactions were equilibrated 5 minutes at 30°C before addition of RSV RdRP, then incubated at 30°C for 3 hours. RNAs were precipitated overnight at -20°C with 2.5 volumes of ethanol, 0.1 volume of 3M sodium acetate plus 625 ng of glycogen (ThermoFisher Scientific). Pellets were washed with 75% ethanol, dried and resuspended in 10 µl of 50% deionized formamide. After 5 minutes denaturation at 95°C, RNAs were separated as described previously and visualized by autoradiography using CL-XPosure™ Film (ThermoFisher Scientific). SARS-CoV-2 polymerase *in vitro* assays were set up analogous to the protocol described above. All three separately purified proteins nsp7 (6 ∝M), nsp8 (3 ∝M) and nsp12 (300 nM) were incubated in 20 mM Tris-HCl pH 7.4, 10% glycerol, 1 mM dithiothreitol, 5 mM $MgCl_2$, 1 µM RNA template, 20 µM RNA primer, 20 nM ATP, 20 nM CTP and 1 µCi of (alpha)32P-labelled ATP (Perkin-Elmer). Primer-template sets were used as described above. For the comparison of primer extension reaction 200 nM of UTP or 4'-FlU-TP was used. Uncropped autoradiograms including biological repeats are available in Data S1. GS-443902 (remdesivir triphosphate) was provided by MedChemExpress cat# HY-126303C.

Cellular uptake and anabolism

10^5 HBTECs were seeded per well in 24-well plates. The next day the media was supplemented with 20 µM 4'-FlU or vehicle (DMSO). For wash-in studies, cell culture media was removed at the indicated time-point and cells were washed twice with Dulbecco's modified phosphate buffered saline without calcium and magnesium (DPBS) and harvested using 500 µl of ice-cold 70% methanol. Cellular extracts were clarified by centrifugation at 16,000×g for 10 minutes at 4°C and stored at -20°C until further analysis. For wash-out studies, cells were incubated in the presence of 20 µM 4'-FlU or vehicle (DMSO) for 24 hours, then washed twice with DPBS and incubated with maintenance media for the indicated time point before harvesting. 4'-FlU and 4'-FlU-TP anabolite were quantitated by qualified internal standard-based LC-MS/MS method using an Agilent 1200 system (Agilent Technologies) equipped with a SeQuant ZIC-pHILIC column (The Nest Group). MS analysis was performed on a QTrap 5500 mass spectrometer (AB Sciex) using negative-mode electrospray ionization (ESI) in the multiple-reaction-monitoring (MRM) mode. Data analysis was done with Analyst software (AB Sciex). The lower limit of quantitation (LLOQ) for 4'-FlU was 1.04 ng/ml of the cell extraction solution, which corresponded to 19.83 pmol/10^6 cells in these experiments.

Air-liquid interfaces of primary human airway epithelial (HAE) cells
30,000 HBTEC or NHBE cells at passage 2 were seeded on 6 mm 0.4 μm pore size polyester inserts (Corning Costar Transwell) and differentiated at an air-liquid interface using Air-Liquid Interface Differentiation Medium (Lifeline cell technology, cat# LL-0023) for the former or Pneumacult-ALI (Stemcell Technologies cat# 05001) according to the manufacturer's instruction. Transepithelial electrical resistance was monitored using the EVOM instrument and STX2 electrode (World Precision Instrument).

Apical shed viral titer determination
Differentiated primary cells were washed on the apical side with phosphate-buffered saline (PBS) without calcium and magnesium. Cells were infected apically either with recRSV-A2line19F-[mKate] (500,000 $TCID_{50}$) or SARS-CoV-2 for (40,000 PFU) for 2 hours at 37°C. Compound was added in the basal media at the indicated concentrations and 0.1% final DMSO. To harvest shed virus, ALI-HAE cells were incubated apically with 200 μl Dulbecco's phosphate-buffered saline without calcium and magnesium at 37°C for 30 minutes, aliquoted and stored at -80°C before titration. For RSV, shed viruses were harvested at peak at day 3 post-infection, and tittered by standard $TCID_{50}$. For SARS-CoV-2, samples were harvested at 24, 48, 72 and 96 hours post-infection ("donor F1") or 24, 48, 72 and 144 hours post-infection ("donor M4"), For SARS-CoV-2 titration, VeroE6 cells were seeded in 12-well plates at 200,000 cells per well. The next day, samples were thawed and serially diluted three times with 10-fold dilutions in DMEM. VeroE6 cell-culture media was removed and cells were incubated with 100 μl of diluted inoculum with rocking every 10 minutes for 1 hour at 37°C. The overlay medium (DMEM+2% FBS+1.2% microcrystalline cellulose Avicel 581-NF (FMC)) was added on the cells and the plates were incubated for three days at 37°C. The plaques were revealed after two washes with PBS, 1-hour fixation with 10% neutral buffered formalin, and 15 minutes coloration with a 1% crystal violet solution in 20% ethanol.

Antibodies
For immunostaining of infected cells in virus titer determination, fixed and permeabilized cells were successively stained with goat anti-RSV 1:1000 (Millipore Sigma, cat. AB1128) followed by donkey anti-goat HRP-coupled 1:1000 (Jackson Immunoresearch cat. 705-035-147) and infected cells were visualized with Trueblue peroxidase substrate according to the manufacturer's instructions (KPL). For RSV confocal microscopy experiments, fixed and permeabilized cells were stained with mouse anti-(human) ZO-1 1:50 (BD Biosciences, cat. 610966), goat anti-RSV 1:1000 (Millipore Sigma, cat. AB1128), rabbit anti-beta IV Tubulin recombinant antibody Alexa Fluor® 647-conjugated [EPR16775] 1:100 (Abcam, cat. ab204034) followed by donkey anti-goat Alexa Fluor 568 1:500 (ThermoFisher Scientific, cat. A-11057) and rabbit anti-mouse IgG (H+L) cross-adsorbed secondary antibody, Alexa Fluor 488 1:500 (ThermoFisher Scientific, cat. A1059). For SARS-CoV-2 confocal microscopy, cells were

stained with rabbit anti-SARS-CoV-2 Nucleocapsid monoclonal antibody (HL453) (Invitrogen, MA5-36272) 1:100 and mouse anti-MUC5AC 1:200 (ThermoFisher MA5-12175), followed by donkey anti-goat Alexa Fluor 568 1:500 (ThermoFisher Scientific, cat. A-11057) and rabbit anti-mouse IgG (H+L) Cross-Adsorbed Secondary Antibody, Alexa Fluor 488 1:500 (ThermoFisher Scientific, cat. A-11059).

Confocal microscopy

Differentiated human airway epithelial cells were either infected (or mock-infected) with recRSV-A2line19F-[FireSmash] (500,000 $TCID_{50}$), washed with PBS daily and fixed at 5 days post-infection with 200 µl of 4% paraformaldehyde in PBS for 1 hour at RT, or were infected (or mock-infected) with 40,000 plaque-forming units of SARS-CoV-2 isolate USA-WA1/2020 (BEI# NR-52281) and fixed at day 3 post-infection. Cells were permeabilized for 20 minutes with PBS with 0.1% Triton X-100 and 3% bovine serum albumin (BSA). After three 5-minute washes with wash buffer (PBS with 0.3% BSA), cells were incubated with 100 µl of primary antibody in wash buffer for 1 hour at RT. After 3×5 minutes 200 µl washes with wash buffer, cells were incubated with secondary antibody in wash buffer for 1hour at RT. Cells were washed and incubated with Hoechst 34580 at 1/1000 in wash buffer for 5 minutes. After three 5-minute washes with wash buffer, membranes were cut and mounted between glass slides and coverslips using Prolong Diamond antifade mountant (ThermoFisher Scientific) and edges were sealed with nail polish. Image capture were performed with a Zeiss LSM 800 confocal microscope coupled with an Airyscan module and the Zeiss Zen Blue software.

Statistical analysis

Source data for all numerical assays conducted in this study are provided in Data S2. Excel and GraphPad Prism software packages were used for data analysis. One-way and two-way ANOVA or mixed-effects model analysis as appropriate with Tukey's, Sidak's or Dunnett's multiple comparisons post-hoc tests without further adjustments - as specified in figure legends - were used to evaluate statistical significance when more than two groups or two parameters were compared. The specific statistical test applied to individual studies is specified in figure legends. When calculating antiviral potency and cytotoxicity, effective concentrations were calculated from dose-response data sets through 4-parameter variable slope regression modeling, and values are expressed with 95% CIs when they could be determined. Biological repeat refers to measurements taken from distinct samples, and results obtained for each biological repeat are shown in the figures along with the exact sample size (n). For all experiments, the statistical significance level alpha was set to <0.05, exact P values are shown in individual graphs.

Synthetic chemistry

5'-Deoxy-5'-iodouridine (Fig. S16). A 1 L three-necked round-bottomed flask flushed with argon and fitted with a thermometer and addition funnel was charged with uridine (35 g, 143 mmol), triphenylphosphine (56.4 g, 215 mmol), imidazole (14.64 g, 215 mmol), and anhydrous THF (400 ml). The suspension was stirred vigorously for 30 minutes while cooling to 0°C and then treated with a THF (100 ml) solution of iodine (40 g, 157.7 mmol) dropwise over a 2-hour period. The mixture was warmed to room temperature. After 16 hours, tlc (10% methanol in methylene chloride) indicated complete consumption of starting uridine. The mixture was concentrated under vacuum followed by a solvent exchange with isopropanol (400 ml). Upon cooling with an ice-bath the product precipitated out of solution as a white solid which was

collected by vacuum filtration and washed with ice-cold isopropanol (150 ml) followed by hexanes (100 ml) to give 5’-deoxy-5’-uridine (35 g, 69% yield).
^{1}H NMR (400 MHz, DMSO-d_6) δ 11.40 (s, 1H), 7.68 (d, *J* = 8.1 Hz, 1H), 5.80 (d, *J* = 5.9 Hz, 1H), 5.68 (dd, *J* = 8.0, 2.2 Hz, 1H), 5.50 (d, *J* = 5.8 Hz, 1H), 5.38 (d, *J* = 5.0 Hz, 1H), 4.19 (q, *J* = 5.7 Hz, 1H), 3.86 (dq, *J* = 14.0, 4.5 Hz, 2H), 3.55 (dd, *J* = 10.5, 5.4 Hz, 1H), 3.40 (dd, *J* = 10.5, 6.5 Hz, 1H).
4’,5’-Didehydro-5’-deoxyuridine (Fig. S16). In a 1 L round-bottomed flask, a suspension of 5’-deoxy-5’-iodouridine (34.55 g, 226 mmol) in methanol (350 ml) was treated with sodium methoxide (67.3 ml, 293 mmol). Upon heating to 60°C the mixture became homogeneous. After 3.5 hours, the mixture was cooled to room temperature and acidified to pH 7 by treating with dry ice. The mixture was filtered, concentrated under vacuum and then purified by column chromatography over silica gel using a mobile phase of 10% methanol in methylene chloride to give 4’,5’-Didehydro-5’-deoxyuridine (11.2 g, 51% yield) as a white solid.
^{1}H NMR (400 MHz, DMSO-d_6) δ 11.44 (s, 1H), 7.59 (d, *J* = 8.1 Hz, 1H), 5.96 (d, *J* = 5.4 Hz, 1H), 5.64 (d, *J* = 8.1 Hz, 1H), 5.60 (d, *J* = 5.8 Hz, 1H), 5.46 (d, *J* = 5.7 Hz, 1H), 4.38 (t, *J* = 5.5 Hz, 1H), 4.33 (s, 1H), 4.24 (q, *J* = 5.5 Hz, 1H), 4.17 (d, *J* = 1.8 Hz, 1H).
5’-Deoxy-4’-fluoro-5’-iodouridine (Fig. S16). An oven-dried 500 ml round-bottomed flask was charged with 4’,5’-didehydro-5’-deoxyuridine (6.55 g, 29 mmol) and anhydrous acetonitrile (60 ml). The suspension was stirred vigorously for 30 minutes, cooled to 0°C under argon and then treated with triethylamine-trihydrofluoride (2.36 ml, 14.5 mmol) followed by the addition of *N*-iodosuccinimide (8.47 g, 37.7 mmol). After 1 hour at 0°C, the mixture was warmed to room temperature for 16 hours and then filtered. The collected solid was washed with methylene chloride (75 ml) followed by ether (75 ml) and then dried under high vacuum to give 5’-deoxy-4’-fluoro-5’-iodouridine (4.2 g, 40%) as an off-white solid.
^{1}H NMR (400 MHz, Methanol-d_4) δ 7.77 (d, *J* = 8.1 Hz, 1H), 6.05 (s, 1H), 5.69 (d, *J* = 8.1 Hz, 1H), 4.43 (dd, *J* = 18.2, 6.5 Hz, 1H), 4.25 (d, *J* = 6.6 Hz, 1H), 3.85 – 3.63 (m, 2H).
^{19}F NMR (376 MHz, Methanol-d_4) δ -112.49 (ddd, *J* = 20.9, 18.1, 6.1 Hz).
2’,3’-Di-*O*-acetyl-5’-deoxy-4’-fluoro-5’-iodouridine (Fig. S16). A 500 ml round-bottomed flask was charged with 5’-deoxy-5’-iodo-4’-fluorouridine (15 g, 40.3 mmol), 4-dimethylaminopyridine (250 mg, 2.02 mmol),triethylamine (16.8 ml, 120.9 mmol) and methylene chloride (200 ml). The mixture was treated dropwise with acetic anhydride (11.4 ml, 120.9 mmol) while maintaining a reaction temperature below 30°C. After 3 hours at room temperature, the reaction mixture was quenched with saturated sodium bicarbonate solution. The organic layer was separated, washed with water followed by 1N HCl, dried and concentrated under vacuum to give 2’,3’-di-*O*-acetyl-5’-deoxy-4’-fluoro-5’-iodouridine (16 g, 87%) as an off-white solid.
^{1}H NMR (400 MHz, DMSO-d_6) δ 11.60 (d, *J* = 2.1 Hz, 1H), 7.77 (d, *J* = 8.0 Hz, 1H), 6.03 (d, *J* = 2.4 Hz, 1H), 5.83 – 5.67 (m, 2H), 5.57 (dd, *J* = 7.4, 2.4 Hz, 1H), 3.63 (dd, *J* = 11.8, 8.2 Hz, 1H), 3.51 (dd, *J* = 22.9, 11.8 Hz, 1H), 2.09 (s, 6H).
^{19}F NMR (376 MHz, DMSO-d_6) δ -105.54 (m).
5’-(3-Chlorobenzoyloxy)-2’,3’-di-*O*-acetyl-4’-fluorouridine (Fig. S16). A 100 ml round-bottomed flask was charged with tetrabutylammonium hydrogen sulfate (3.64 g, 10.7 mmol)1-[(4R,6R)-4’-FlUoro-4-(iodomethyl)-2,2-dimethyl-6,6a-dihydro-3aH-furo[3,4-d][1,3]dioxol-6-yl]pyrimidine-2,4-dione (11.7g, 28.39mmol), 3-chlorobenzoic acid (1.76 g, 11.2 mmol), potassium phosphate dibasic (1.68 g, 9.65 mmol) and water (11 ml). After stirring for 20 minutes, the mixture was treated with a methylene chloride (30 ml) solution of 2’,3’-di-*O*-acetyl-

5’-deoxy-4’-fluoro-5’-iodouridine (2.00 g, 4.38 mmol) followed by the addition of 3-chloroperoxybenzoic acid (4.93 g, 22.0 mmol) in 4 portions over a 30-minute period. The mixture continued to stir at RT for 16 hours. The mixture was periodically treated with additional potassium phosphate dibasic to maintain pH 3.5. The reaction mixture was quenched by addition of sodium sulfite (5 g) in small portions while maintaining a reaction temperature below 30°C. After stirring for an additional 15 minutes, the mixture was filtered through a pad of Celite. The aqueous layer of the filtrate was extracted with methylene chloride (2 × 15 ml), and then combined organic layers were concentrated under vacuum. The resulting residue was redissolved in ethyl acetate (100 ml) and washed with 1N HCl (2 × 50 ml) followed by saturated sodium carbonate solution (2 × 50 ml). The organic layer was concentrated and the resulting solid purified by column chromatography over silica gel (21 mm x 160 mm) using an ethyl acetate/hexane gradient to give 5’-(3-chlorobenzoyloxy)-2’,3’-di-*O*-acetyl-4’-fluorouridine (1.1 g, 52% yield) as a white solid.

^{1}H NMR (400 MHz, DMSO-d_6) δ 11.59 (s, 1H), 7.94 (d, *J* = 7.7 Hz, 1H), 7.89 (s, 1H), 7.78 (d, *J* = 8.1 Hz, 2H), 7.60 (t, *J* = 7.9 Hz, 1H), 6.10 (s, 1H), 5.94 (dd, *J* = 20.2, 7.4 Hz, 1H), 5.64 (dd, *J* = 30.4, 7.6 Hz, 2H), 4.73 – 4.48 (m, 2H), 2.09 (s, 3H), 2.01 (s, 3H).

^{19}F NMR (376 MHz, DMSO-d_6) δ -115.94 (dt, *J* = 20.7, 10.6 Hz).

4’-Fluorouridine (6) (Fig. S16). A thick wall round-bottomed pressure vessel was charged with 5’-(3-chlorobenzoyloxy)-2’,3’-di-*O*-acetyl-4’-fluorouridine (1.55 g, 3.2 mmol) and 4N ammonia in methanol (4.15 ml, 191.8 mmol). The mixture was stirred at RT for 1.5 hours after which time tlc (10% methanol in methylene chloride) indicated complete consumption of starting material. The mixture was concentrated under vacuum at 19°C, and the resulting residue triturated with methyl *ter*t-butyl ether. The solid was co-evaporated with methanol and then recrystallized from ethanol (15 ml) to give 4’-fluorouridine (300 mg, 36% yield) as a white solid.

^{1}H NMR (400 MHz, DMSO-d_6) δ 11.41 (s, 1H), 7.67 (d, *J* = 8.1 Hz, 1H), 5.97 (d, *J* = 2.8 Hz, 1H), 5.66 (d, *J* = 5.4 Hz, 1H), 5.64 (d, *J* = 8.1 Hz, 1H), 5.47 (t, *J* = 5.9 Hz, 1H), 5.16 (d, *J* = 8.8 Hz, 1H), 4.24 (ddd, *J* = 17.7, 8.8, 6.5 Hz, 1H), 4.12 (td, *J* = 6.0, 2.8 Hz, 1H), 3.54 (t, *J* = 5.6 Hz, 2H).

^{19}F NMR (376 MHz, DMSO-d_6) δ -120.94 (dt, *J* = 17.7, 5.4 Hz).

LCMS Calculated for $C_9H_{12}FN_2O_6$ [M+H$^+$]: 263.0; found: 263.0

2’,3’-Di-*O*-benzyloxycarbonyl-5’-deoxy-4’-fluoro-5’-iodouridine (Fig. S17). A 150 ml round-bottomed flask was charged with 5’-deoxy-5’-iodo-4’-fluorouridine (2.6 g, 6.99 mmol) and methylene chloride (35 ml). After stirring for 20 minutes at RT, the suspension was cooled to 0°C and treated with benzyl chloroformate (4.49 ml, 31.44 mmol) followed by dropwise addition of 1-methylimidazole (3.34 ml, 41.93 mmol) over a 10-minute period. The mixture was stirred an additional 10 minutes at 0°C and then allowed to slowly warm to room temperature. After 18 hours, the turbid mixture was diluted with methylene chloride (120 ml) and washed with 0.5 M HCl solution (75 ml), water (50 ml), and brine (50 ml). The organic layer was separated, dried over sodium sulfate and concentrated under vacuum. The resulting residue was purified by column chromatography over silica gel (80 g) eluting with a methylene chloride/methanol gradient. Pure product containing fractions were combined and concentrated under vacuum to give 2’,3’-di-*O*-benzyloxycarbonyl-5’-deoxy-4’-fluoro-5’-iodouridine (4.2 g, 94% yield) as a white solid.

^{1}H NMR (400 MHz, $CDCl_3$) δ 9.02 (s, 1H), 7.44 – 7.28 (m, 10H), 7.14 (d, *J* = 8.0 Hz, 1H), 5.86 – 5.72 (m, 2H), 5.69 – 5.57 (m, 2H), 5.19 (d, *J* = 4.3 Hz, 2H), 5.09 (d, *J* = 3.1 Hz, 2H), 3.71 – 3.35 (m, 2H).

^{19}F NMR (376 MHz, $CDCl_3$) δ -107.06 (td, *J* = 18.6, 7.3 Hz).
2',3'-Di-*O*-benzyloxycarbonyl-4'-fluorouridine (Fig. S17). In a 100 ml round-bottomed flask a 55% tetrabutylammonium hydroxide solution in water (8.04 ml, 9.37mmol) was adjusted to pH 3.5 by dropwise addition of trifluoroacetic acid (0.72 ml, 9.37 mmol) while maintaining a temperature below 25°C. The mixture was then treated with a methylene chloride (15 ml) solution of 2',3'-di-*O*-benzyloxycarbonyl-5'-deoxy-4'-fluoro-5'-iodouridine (2 g, 3.12mmol) followed by addition of 3-chloroperbenzoic acid (3.6 g, 15.62 mmol) in portions over a 30 minutes period. After 1 hour the pH drifted to pH 1.4. The mixture was adjusted back to pH 3.5 with 1N sodium hydroxide and allowed to stir for 16 hours after which time tlc (10% methanol in methylene chloride) and LCMS indicated complete conversion. The reaction mixture was quenched by addition of sodium thiosulfate (3.21 g, 20.31 mmol) slowly in portions while maintaining a temperature below 25°C. After stirring for 30 minutes, the methylene chloride layer was separated, and the aqueous layer extracted with additional methylene chloride (2 × 30 ml). Combined organic layers were dried over sodium sulfate, concentrated, and purified by column chromatography over silica gel (80 g) eluting with 60% ethyl acetate in hexanes followed by a second column of silica gel (80 g) eluting with a methylene chloride/methanol gradient to give 2',3'-di-*O*-benzyloxycarbonyl-4'-fluorouridine (1.05 g , 63% yield) as a white solid.
^{1}H NMR (400 MHz, $CDCl_3$) δ 9.30 (s, 1H), 7.39 – 7.29 (m, 10H), 7.21 (d, *J* = 8.1 Hz, 1H), 5.83 (dd, *J* = 17.8, 7.0 Hz, 1H), 5.77 – 5.71 (m, 2H), 5.61 (dd, *J* = 7.0, 2.4 Hz, 1H), 5.17 (d, *J* = 4.8 Hz, 2H), 5.09 (s, 2H), 3.86 (q, *J* = 5.8, 4.9 Hz, 2H), 3.06 (s, 1H).
^{19}F NMR (376 MHz, $CDCl_3$) δ -121.03 (dt, *J* = 17.7, 4.6 Hz).

4'-Fluorouridine 5'-*O*-triphosphate (Fig. S17). A 10 ml round-bottomed flask charged with 2',3'-di-*O*-benzyloxycarbonyl-4'-fluorouridine (348 mg, 0.66 mmol) and anhydrous trimethyl phosphate (3.5 ml). After stirring for 20 minutes at room temperature, the solution was cooled to 0°C and treated with 1-methyl-imidazole (115 ∝L, 1.44 mmol) followed by dropwise addition of phosphorus oxychloride (122 ∝L, 1.31 mmol) over a 40-minute period. The mixture continued to stir at 0°C for 3.5 hours after which time tlc (10% methanol in DCM and then 7:2:1 *i*PrOH:NH_4OH:water) indicated complete phosphorylation. The mixture was treated with tributylamine (0.94 ml, 3.94 mmol), tris(tetrabutylammonium)pyrophosphate (887 mg, 0.98 mmol), and anhydrous DMF (1.5 ml). After 1 hour at RT, the reaction mixture was quenched with 100 mM TEAB (20 ml), stirred for 1 hour, degassed by pump-fill with argon (3x) and treated with 10% palladium on carbon (100 mg). After cooling with an ice-bath, the mixture was pump-filled with hydrogen (2×) followed by vigorous stirring under atm pressure of hydrogen for 30 minutes. After vacuum evacuation of the reaction vessel, the mixture was filtered through a pad of Celite and the collected palladium washed with water (2 × 20 ml). Combined filtrates were washed with ether (4 × 60 ml) and then concentrated under vacuum at 25°C. After co-evaporation with water (2 × 25 ml), the crude triphosphate was purified by column chromatography over DEAE-Sephadex GE A-25 (10 mm × 130 mm) eluting with a buffer gradient from 100 mM (450 ml) to 500 mM TEAB (450 ml). Pure product containing fractions as determined by tlc (8:1:1 NH_4OH:iPrOH:water) were combined and concentrated under vacuum with the bath temperature set at 25°C. The solid was dissolved in methanol (1 ml) and treated with saturated solution of sodium perchlorate in acetone (10 ml). The resulting white precipitate was collected by centrifuge, washed with acetone (5 × 5 ml), dissolved in water (1

ml), and concentrated by lyophilization to yield 4’-fluoro-uridine 5’-*O*-triphosphate (3.14 mg, 0.81% yield) as the tetrasodium salt.
^{1}H NMR (400 MHz, D_2O) δ 7.77 (d, *J* = 8.0 Hz, 1H), 6.15 (d, *J* = 1.9 Hz, 1H), 5.91 (d, *J* = 8.1 Hz, 1H), 4.72 – 4.57 (m, 1H), 4.41 (d, *J* = 6.3 Hz, 1H), 4.30 (ddd, *J* = 10.2, 6.3, 3.0 Hz, 1H), 4.17 (dt, *J* = 10.8, 5.0 Hz, 1H). ^{31}P NMR (162 MHz, D_2O) δ -7.81(d), -11.84 (d, *J* = 19.2 Hz), -22.23 (t). ^{19}F NMR (376 MHz, D_2O) δ -121.09 (unresolved dt, *J* = 19.2 Hz). LCMS Calculated for $C_9H_{13}FN_2O_{15}P_3$ [M-H$^+$]: 500.9; found: 500.8

Supplementary text

Limitations of the mouse model for RSV. The mouse model for RSV infection does not fully recapitulate human infection. Specifically, mice do not exhibit major clinical signs and the first site of virus replication is the lower respiratory tract, resulting in viral pneumonia, whereas in the human host RSV initially replicates in upper respiratory tissues and progression to the small airways marks transition to severe disease. The most robust and widely accepted measure for antiviral efficacy is therefore the measure of viral lung titers at the peak of replication (day 4-5 after infection). In addition to determining lung virus load, we followed viral replication longitudinally, using a recombinant virus that expresses a luciferase reporter and live bioluminescence imaging of whole animals (Figure 4C). This model provides a spatial localization of replication and allows for the visualization of RSV replication over time with a reduced number of animals. It comes with additional limitations, however, since it measures expression of a luciferase reporter encoded by the viral genome rather than actual titers of infectious progeny virions in the lung. As previously reported (36), a high baseline luciferase signal is derived from the incoming virus inoculum and thus independent of productive virus replication. Due to high stability of the luciferase protein, subsequent replication can only result in a comparably moderate increase in signal strength over time, inherently limiting the dynamic range of the RSV IVIS assay.

2.2.2 4'-Fluorouridine is a Broad Spectrum Orally Available First-line Antiviral that May Improve Pandemic Preparedness

DNA AND CELL BIOLOGY
Volume 41, Number 8, 2022

Pp. 699–704
DOI: 10.1089/dna.2022.0312

DNACB BITS

4′-Fluorouridine Is a Broad-Spectrum Orally Available First-Line Antiviral That May Improve Pandemic Preparedness

Carolin M. Lieber and Richard K. Plemper

The COVID-19 pandemic has highlighted the urgent need for the development of broad-spectrum antivirals to enhance preparedness against future spillover of zoonotic viruses with pandemic potential into the human population. Currently, the direct-acting orally available SARS-CoV-2 inhibitors molnupiravir and paxlovid are approved for human use under emergency use authorization. A promising next-generation therapeutic candidate is the orally available ribonucleoside analog 4′-fluorouridine (4′-FlU) that had potent antiviral efficacy against different viral targets, including SARS-CoV-2 in human organoids and animal models. Although a nucleoside analog inhibitor such as molnupiravir that targets the viral RNA-dependent RNA polymerase (RdRP) complex, 4′-FlU showed a distinct mechanism of activity, delayed chain termination, compared with molnupiravir's induction of viral error catastrophe. This review will focus on some currently approved and emerging medicines developed against SARS-CoV-2, examining their potential to form a pharmacological first-line defense against zoonotic viruses with pandemic potential.

Keywords: SARS-CoV-2, ribonucleoside analog, 4′-fluorouridine, antiviral, pandemic preparedness, COVID-19

Introduction

SARS-CoV-2 HIT A world poorly prepared for a major pandemic caused by a newly emerged respiratory virus. Initially, no approved vaccines or therapeutics against betacoronaviruses existed, personal protective equipment was in short supply, and capacity of critical medical devices such as ventilators did not meet patient needs. As of May 2022, far over 500 million confirmed SARS-CoV-2 infections have been reported and over 6 million case fatalities have occurred worldwide (WHO, 2022). Beyond the direct threat to human health, the socioeconomic impact worldwide has been devastating (Bartsch *et al.*, 2020).

Product Profile of First-Line Therapeutics

Although novel vaccines were developed in record time, the broad-spectrum nucleoside analog antiviral remdesivir was approved for treatment of SARS-CoV-2 infection, and antibody therapeutics were rapidly generated and approved for clinical use, these measures came too late to influence the course of the critical first months of the COVID-19 pandemic. To reach the overarching goal of improving preparedness against future viral threats with pandemic potential, effective first-line antivirals are urgently needed. The SARS-CoV-2 experience has highlighted several product profile criteria that must be met for this intended use:

- *Oral bioavailability*. Pharmacological intervention in acute RNA virus infections has been challenging due to typically narrow therapeutic windows (Meganck and Baric, 2021; Plemper, 2021; Sourimant *et al.*, 2021). Because clinical signs are largely consequences of the host antiviral immune responses, viral titers are typically in rapid decline when patients advance to complicated disease and are hospitalized (van Kampen *et al.*, 2021), marking a transition point at which antiviral therapeutics designed to interfere with the viral

Center for Translational Antiviral Research, Georgia State University, Atlanta, Georgia, USA.

life cycle and reduce viral load cease to be efficacious and treatment goals shift to immunomodulatory therapy or supportive care. Remdesivir must be delivered intravenously and is, therefore, unavailable to most patients before hospitalization (Beigel *et al.*, 2020). Mixed remdesivir performance likely reflects the problem that the therapeutic window for a direct acting antiviral has essentially closed when the patient presents with severe disease. We propose that efficiently reaching an outpatient population before advance to severe disease is best achieved with an orally bioavailable drug that does not require trained health care professionals and sterile equipment for delivery.

- *Preapproved for human use*. Spillover of animal viruses into the human population stands at the beginning of most viral pandemics. COVID-19 has re-emphasized that an antiviral must be approved for human use before a new pathogenic emerges to potentially stamp out a nascent pandemic. Despite unprecedented short timelines from first appearance of SARS-CoV-2 to vaccine launch and emergency approval of paxlovid and molnupiravir, the window of opportunity to regionally contain the virus and avoid a global pandemic was likely very short-lived once efficient human-to-human transmission had begun. This short timeline is incompatible with even the most accelerated approval process. Accordingly, developmental antiviral candidates must have a well-defined primary indication that provides a path to clinical testing and regulatory approval for human use in interpandemic years, or before a novel pandemic viral threat first emerges.
- *Broad indication spectrum*. A wide antiviral target range spanning ideally viral pathogens of different families will often coincide with the request for a viable primary indication for clinical testing. Beyond ensuring a path to approval, broad-spectrum activity of first-line antivirals will be imperative for improving pandemic preparedness, since the nature of the next pandemic viral threat is unknown. Several pathogens in at least eight different viral families have been recognized for their high pandemic potential (Fernandez-Montero *et al.*, 2020), undermining feasibility of preemptively developing and clinically advancing a very large panel of individually targeted antivirals.
- *High tolerability*. The drug safety profile must be compatible with administration to outpatients at the earliest disease stages. This intended application will require high tolerability with a wide safety margin. Especially use at the onset of a potential pandemic, before the scope of the health threat has been fully appreciated by the public, sets narrow limits for acceptable side effects. Tolerability profiles and pharmacokinetic properties must furthermore answer to the high replication dynamics of RNA viruses causing acute diseases, which requires rapid buildup of high drug levels and sustained exposure in disease-relevant tissues.
- *Suitable for stockpiling*. To be able to rapidly respond to a newly emerged threat, a sufficiently large number of doses must be readily deployable. This requirement is best met if the drug product is amenable to cost-effective large-scale production and is shelf-stable at ambient temperature for stockpiling.

Oral SARS-CoV-2 Therapeutics with Emergency Use Authorization

None of the currently available direct-acting antivirals used for the treatment of SARS-CoV infection meets all these requests. Of the orally bioavailable candidates, emergency use authorization has been granted by the FDA in 2021 to the nucleoside analog inhibitor molnupiravir and the viral protease inhibitor paxlovid.

Molnupiravir

Molnupiravir is the oral ester prodrug of N^4-hydroxycitidine (NHC) (Fig. 1A), which has demonstrated broad-spectrum antiviral activity against influenza viruses (Toots *et al.*, 2019; Toots and Plemper, 2020), paramyxoviruses and pneumoviruses (Yoon *et al.*, 2018), alphaviruses (Urakova *et al.*, 2018), and the beta-coronaviruses (Agostini *et al.*, 2019). Only free NHC efficiently reaches the circulation after oral administration of molnupiravir due to rapid hydrolysis of the ester during intestinal absorption (Kabinger *et al.*, 2021). Upon cellular uptake, NHC is anabolized to the bioactive triphosphate form, NHC-TP, which is incorporated by the viral polymerase into progeny viral antigenomes and genomes in place of endogenous cytidine triphosphate (CTP).

Accordingly, molnupiravir does not act as a chain-terminator but, rather, once incorporated it spontaneously switches between two tautomeric forms, the oxime and hydroxylamine, which base-pair as uridine triphosphate (UTP) and CTP, respectively (Kabinger *et al.*, 2021). Owing to this spontaneous change in base-pairing, progeny genomes or antigenomes generated from a template containing incorporated NHC will harbor randomly distributed transition mutations in low allele frequency (Toots *et al.*, 2019), which rapidly compromise integrity of the genomes and ultimately result in collapse of the viral population. This mechanism of antiviral activity follows the random lethal viral mutagenesis or error catastrophe model that was first described for ribavirin by example of picornavirus inhibition (Crotty *et al.*, 2001).

Presumably due to the close chemical similarity of NHC to endogenous cytidine, molnupiravir is not recognized by the proofreading activity of the beta-coronavirus polymerase (Bouvet *et al.*, 2012; Robson *et al.*, 2020), escaping excision postincorporation. Furthermore, the genetic barrier of molnupiravir against emergence of viral resistance is unusually high, very likely reflecting that the viral RNA-dependent RNA polymerase (RdRP) complex cannot solve the sterical challenge to differentiate between NHC-TP and endogenous CTP. Despite extensive attempts to resistance profile the drug against different viral targets, no valid escape mutations have been reported so far (Urakova *et al.*, 2018; Toots *et al.*, 2019) and no viral resistance has been noted in the clinic (Holman *et al.*, 2021; Painter *et al.*, 2021).

Whereas there is demonstrated evidence that NHC-TP is also recognized by host RNA polymerases and incorporated into host RNAs when present at very drug high concentration (Toots *et al.*, 2019), host RNAs are typically short-lived and never serve as template for further amplification. Clinical trials have demonstrated that a 5-day molnupiravir regimen of 800 mg orally twice daily is very well tolerated

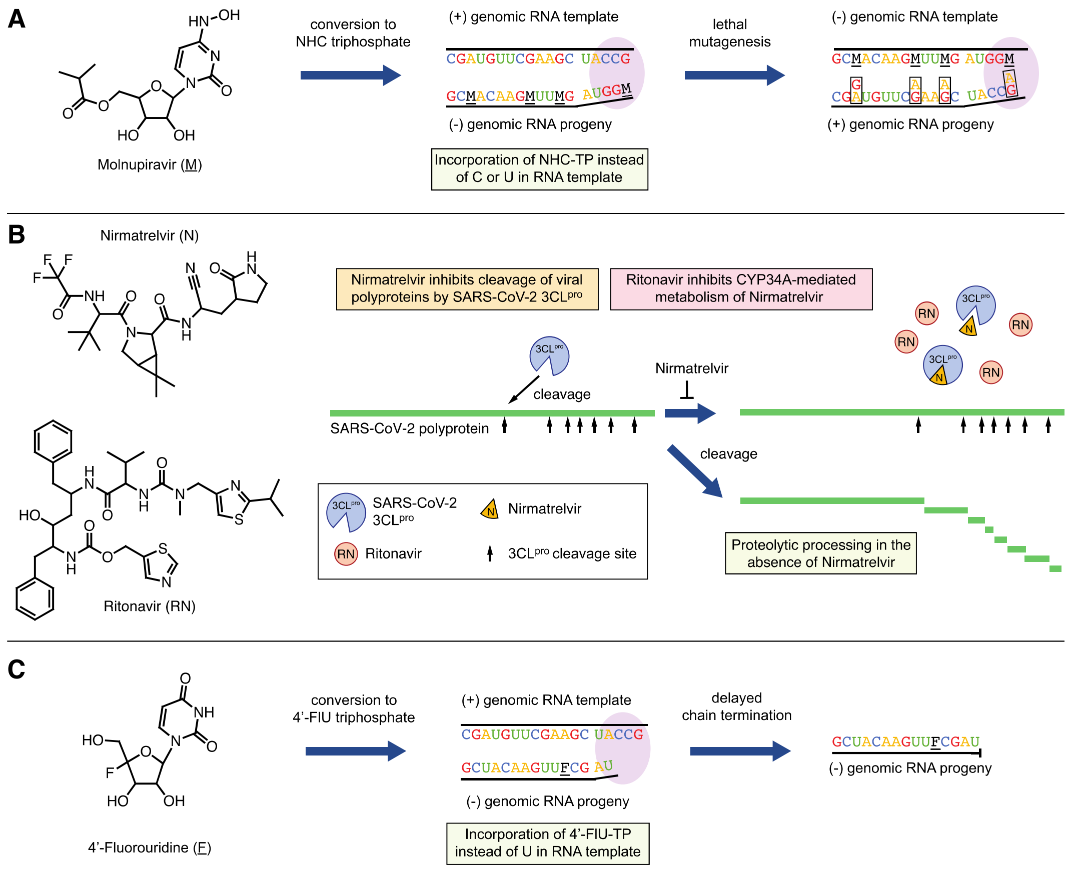

FIG. 1. Structures and mechanism of action of different SARS-CoV-2 inhibitors. **(A–C)** Overview of ribonucleoside analog inhibitors molnupiravir and 4′-FlU, and protease inhibitor paxlovid (Fig. 1B). Molnupiravir induces viral error catastrophe **(A)**. After incorporation, the drug spontaneously undergoes tautomeric conversions, resulting in base-pairing as C or U, respectively. Amplification of an RNA template containing NHC results randomly distributed low allele-frequency transition mutations. Nirmatrelvir is a peptidomimetic blocking the activity of the SARS-CoV-2-3CL protease through formation of a covalent dead-end complex **(B)**. Ritonavir addresses poor PK, performance of nirmatrelvir by manipulating activity of the cytochrome P450 system. 4′-FlU induces delayed chain termination after incorporation into the nascent RNA strand **(C)**. RdRP stalling typically takes place three to four nucleotides after incorporation of 4′-FlU-TP, presumably due to altered secondary structure of the nascent RNA strand that cannot be accommodated by the polymerase complex. 4′-FlU, 4′-fluorouridine; NHC, N^4-hydroxycitidine; PK, pharmacokinetic; RdRP, RNA-dependent RNA polymerase; TP, triphosphate.

with no evidence of hematologic toxicities or other side effects (Fischer *et al.*, 2021; Painter *et al.*, 2021; Jayk Bernal *et al.*, 2022a). Of greater concern are long-term consequences due to potential incorporation of NHC into host DNA.

However, metabolism of NHC leads to uridine and no evidence of transribosylation has been noted (Hernandez-Santiago *et al.*, 2004). Animal studies revealed low teratogenic potential of molnupiravir (Merck, 2022) and no mutagenic activity at antiviral concentrations (Zhou *et al.*, 2021). Although these animal toxicology data are highly encouraging, long-term follow-up clinical data are still lacking, underscoring that any therapeutic intervention decision must be based on careful evaluation of the individual risk/benefit ratio for the patient.

Molnupiravir was equally efficacious against the original SARS-CoV-2 strain and subsequently emerged variants of concern (VOC) in cultured cells and primary human airway epithelium organoids, including VOC delta and omicron (Lieber *et al.*, 2022). Interesting, clinical data indicated that patients infected with VOC gamma experienced greater benefit from molnupiravir than those suffering from VOC delta (Jayk Bernal *et al.*, 2022b).

Although not recapitulated by *ex vivo* models, a Roborovsky dwarf hamster model of acute SARS-CoV-2 induced lung injury revealed a significantly greater effect size of molnupiravir-mediated virus load reduction when animals were infected with VOC gamma compared with delta (Lieber *et al.*, 2022). Only VOC omicron-infected dwarf hamster showed a significant biological sex-dependent difference in response to treatment. The relevance of this observation for human treatment is unknown at present, but the dwarf hamster data re-emphasize that treatment efficacy may vary dependent on VOC and must, therefore, be reevaluated continuously as SARS-CoV-2 further evolves.

Paxlovid

Paxlovid is a combination drug of the SARS-CoV-2 3-chymotrypsin-like cysteine protease ($3CL^{pro}$) inhibitor nirmatrelvir (Fig. 1B) and the antiretroviral drug ritonavir (Reina and Iglesias, 2022). $3CL^{pro}$ is instrumental for betacoronavirus replication (Chen *et al.*, 2005), proteolytically processing the viral polyproteins to liberate individual viral polypeptides such as the RdRP subunits and viral helicase that are essential for replication and transcription (Mody *et al.*, 2021).

Nirmatrelvir is a peptidomimetic that directly targets the active site of $3CL^{pro}$, forming a permanent covalent bond with the catalytic cysteine (Pavan *et al.*, 2021). Similar to many peptidomimetic protease inhibitors, however, nirmatrelvir shows poor metabolic stability *in vivo*, rapidly becoming a target of liver oxidation through the cytochrome P450 system (Eng *et al.*, 2022). In initial animal model proof-of-concept studies against SARS-CoV-2, nirmatrelvir monotherapy had to be administered at an unrealistic 1000 mg/kg body weight dose to compensate for its poor pharmacokinetic profile (Owen *et al.*, 2021).

Originally developed as an inhibitor of HIV protease, ritonavir acts off-target as a strong inhibitor of cytochrome P450 key enzymes P450-3A4 (CYP3A4) and P450-2D6 (CYP2D6) (Kumar *et al.*, 1996), reducing the rate of P450-mediated drug detoxification. This ability of ritonavir to improve drug pharmacokinetic profiles through slowing liver oxidation has resulted in its use as combination drug with, for instance, other HIV protease inhibitors and most recently nirmatrelvir (Eng *et al.*, 2022). However, the downside of this fix of the pharmacokinetic shortcomings of nirmatrelvir is the very high potential of ritonavir for severe and sometimes fatal drug–drug interactions with dozens of approved medications, since drug levels are broadly affected when activity of the P450 system is manipulated.

Contraindications include drugs for the treatment of heart conditions, blood pressure regulators, immunosuppressants, some chemotherapeutics, and asthma and allergy medications (Talha and Dhamoon, 2022). Accordingly, paxlovid is poorly compatible with treatments for many conditions that represent major risk factors for the advance of a COVID-19 patient to severe life-threatening disease (Hammond *et al.*, 2022).

Taken twice daily in a 5-day regimen similar to that of molnupiravir (Jayk Bernal *et al.*, 2022b), paxlovid has shown strong efficacy in a clinical trial, reducing COVID-19-related deaths or hospitalizations by a claimed 89% in unvaccinated patients compared with the placebo control group (Mahase, 2021). In contrast to a large body of literature characterizing molnupiravir efficacy in multiple SARS-CoV-2 animal models (Cox *et al.*, 2021b), experimental animal model data for nirmatrelvir are limited (Owen *et al.*, 2021; Eng *et al.*, 2022), and none have yet been released for paxlovid. Although sparse, the available evidence does not provide an obvious reason for the seemingly greater therapeutic benefit of paxlovid in clinical trials since antiviral effect size of both drugs appears to be similar in animals.

Possible explanations for the conundrum may be differences in trial design (Fischer *et al.*, 2022) and patient groups eligible for enrollment—paxlovid could not be tested in patients taking other medications with metabolism highly dependent on cytochrome P450 CYP3A4 or known as strong inducers of CYP3A4. As more clinical data with recently emerged VOC become available, it will be important to evaluate whether the claimed efficacy difference between molnupiravir and paxlovid is real. Urgently needed are furthermore head-to-head comparisons of both drugs under experimentally controlled conditions in relevant animal models.

Next-Generation First-Line Antiviral Developmental Candidate 4′-Fluorouridine

4′-Fluorouridine (4′-FlU) (Sourimant *et al.*, 2022) is a recently identified novel competitive ribonucleoside analog inhibitor (Fig. 1C) that is structurally distinct from known nucleoside analogs with activity against SARS-CoV-2 such as molnupiravir and remdesivir (Kokic *et al.*, 2021). Carrying a ribose modification, the compound showed broad-spectrum activity against a wide range of negative and positive-sense RNA viruses, including pathogens of the paramyxovirus, pneumovirus, and beta-coronavirus families (Sourimant *et al.*, 2022).

Biochemical RdRP assays with purified recombinant SARS-CoV-2 and respiratory syncytial virus (RSV) polymerase complexes identified sequence context-dependent delayed chain termination, preferentially three to four nucleotides after incorporation of bioactive 4′-FlU triphosphate (4′-FlU-TP), as the mechanism of activity. This antiviral effect resembles that described for the bioactive parent compound of remdesivir (Kokic *et al.*, 2021) and is most likely due to altered RNA secondary structure after single or tandem incorporation of the analog that ultimately cannot be accommodated by the viral polymerase (Sourimant *et al.*, 2022). In contrast to molnupiravir, 4′-FlU has not shown any mutagenic effect in biochemical and cell-based assays.

Unlike remdesivir, however, 4′-FlU was efficiently delivered orally, resulting in sustained tissue exposure of bioactive 4′-FlU-TP in different animal species. Dosed orally once daily, the compound potently inhibited original SARS-CoV-2, recently emerged SARS-CoV-2 VOC, and RSV replication in different animal models (Sourimant *et al.*, 2022). Efficacy against SARS-CoV-2 and RSV was furthermore confirmed in disease-relevant primary human airway epithelium organoids, although RSV and other mononegaviruses showed greater sensitivity to 4′-FlU than SARS-CoV-2.

This difference in potency likely reflects that some incorporated 4′-FlU moieties may be recognized by the coronavirus proofreading machinery and excised, and/or that the coronavirus polymerase may have greater tolerance to accommodate altered RNA secondary structures than mononegavirus polymerases. Based on high oral bioavailability, strong metabolic stability *in vivo* confirmed broad-spectrum antiviral efficacy, and suitability for stock-piling; however, 4′-FlU meets the key criteria of a first-line antiviral. A unique strength compared with existing COVID-19 medicines are pharmacokinetic properties compatible with once-daily dosing, which represents a major advance in ensuring patient compliance.

Going forward, the best first-line defense against future pandemic viral threats will in our opinion realistically not come in the form of a single ''magic bullet'' drug, but of a panel of broad-spectrum orally available antivirals with overlapping, but not identical, indication range. These drugs must be urgently approved for human use and will likely have distinct strengths and liabilities, providing alternative options to address specific needs of individual patient subgroups.

Currently existing drugs that we consider to be part of this panel are molnupiravir, favipiravir (Ghasemnejad-Berenji and Pashapour, 2021), and—with the restriction of a limited indication spectrum covering only the beta-coronaviruses—paxlovid. Promising future contenders that should be fast-tracked are experimental antivirals such as 4′-FlU and, for instance, an orally available chemical analog of remdesivir (Cox *et al.*, 2021a). If ultimately grown to a size of 5–10 qualified drugs, this panel could be game-changing in establishing control at an early stage of future pandemic viral threats.

Acknowledgments

We thank members of the Plemper Lab for discussion and A.L. Hammond for critical reading of the article.

Disclosure Statement

No competing financial interests exist.

Funding Information

This study was supported, in part, by Public Health Service grants AI071002 (to R.K.P.) and AI141222 (to R.K.P.), from the NIH/NIAID. The funders had no role in study design, data collection, and interpretation, or the decision to submit the study for publication.

References

Agostini, M.L., Pruijssers, A.J., Chappell, J.D., Gribble, J., Lu, X., Andres, E.L., *et al.* (2019). Small-molecule antiviral beta-d-N (4)-hydroxycytidine inhibits a proofreading-intact coronavirus with a high genetic barrier to resistance. J Virol **93,** e01348-19.

Bartsch, S.M., Ferguson, M.C., McKinnell, J.A., O'Shea, K.J., Wedlock, P.T., Siegmund, S.S., *et al.* (2020). The potential health care costs and resource use associated with COVID-19 in the United States. Health Aff (Millwood) **39,** 927–935.

Beigel, J.H., Tomashek, K.M., Dodd, L.E., Mehta, A.K., Zingman, B.S., Kalil, A.C., *et al.* (2020). Remdesivir for the treatment of Covid-19—Final report. N Engl J Med **383,** 1813–1826.

Bouvet, M., Imbert, I., Subissi, L., Gluais, L., Canard, B., and Decroly, E. (2012). RNA 3′-end mismatch excision by the severe acute respiratory syndrome coronavirus nonstructural protein nsp10/nsp14 exoribonuclease complex. Proc Natl Acad Sci U S A **109,** 9372–9377.

Chen, S., Chen, L., Tan, J., Chen, J., Du, L., Sun, T., *et al.* (2005). Severe acute respiratory syndrome coronavirus 3C-like proteinase N terminus is indispensable for proteolytic activity but not for enzyme dimerization. Biochemical and thermodynamic investigation in conjunction with molecular dynamics simulations. J Biol Chem **280,** 164–173.

Cox, R.M., Wolf, J.D., Lieber, C.M., Sourimant, J., Lin, M.J., Babusis, D., *et al.* (2021a). Oral prodrug of remdesivir parent GS-441524 is efficacious against SARS-CoV-2 in ferrets. Nat Commun **12,** 6415.

Cox, R.M., Wolf, J.D., and Plemper, R.K. (2021b). Therapeutically administered ribonucleoside analogue MK-4482/EIDD-2801 blocks SARS-CoV-2 transmission in ferrets. Nat Microbiol **6,** 11–18.

Crotty, S., Cameron, C.E., and Andino, R. (2001). RNA virus error catastrophe: direct molecular test by using ribavirin. Proc Natl Acad Sci U S A **98,** 6895–6900.

Eng, H., Dantonio, A.L., Kadar, E.P., Obach, R.S., Di, L., Lin, J., *et al.* (2022). Disposition of nirmatrelvir, an orally bioavailable inhibitor of SARS-CoV-2 3C-like protease, across animals and humans. Drug Metab Dispos **50,** 576–590.

Fernandez-Montero, J.V., Soriano, V., Barreiro, P., de Mendoza, C., and Artacho, M.A. (2020). Coronavirus and other airborne agents with pandemic potential. Curr Opin Environ Sci Health **17,** 41–48.

Fischer, W., Eron, J.J., Holman, W., Cohen, M.S., Fang, L., Szewczyk, L.J., *et al.* (2021). Molnupiravir, an oral antiviral treatment for COVID-19. medRxiv. [Epub ahead of print]; DOI: 10.1101/2021.06.17.21258639.

Fischer, W.A., 2nd, Eron, J.J., Jr., Holman, W., Cohen, M.S., Fang, L., Szewczyk, L.J., *et al.* (2022). A phase 2a clinical trial of molnupiravir in patients with COVID-19 shows accelerated SARS-CoV-2 RNA clearance and elimination of infectious virus. Sci Transl Med **14,** eabl7430.

Ghasemnejad-Berenji, M., and Pashapour, S. (2021). Favipiravir and COVID-19: a simplified summary. Drug Res (Stuttg) **71,** 166–170.

Hammond, J., Leister-Tebbe, H., Gardner, A., Abreu, P., Bao, W., Wisemandle, W., *et al.* (2022). Oral nirmatrelvir for high-risk, nonhospitalized adults with Covid-19. N Engl J Med **386,** 1397–1408.

Hernandez-Santiago, B.I., Beltran, T., Stuyver, L., Chu, C.K., and Schinazi, R.F. (2004). Metabolism of the anti-hepatitis C virus nucleoside beta-D-N4-hydroxycytidine in different liver cells. Antimicrob Agents Chemother **48,** 4636–4642.

Holman, W., Holman, W., McIntosh, S., Painter, W., Painter, G., Bush, J., *et al.* (2021). Accelerated first-in-human clinical trial of EIDD-2801/MK-4482 (molnupiravir), a ribonucleoside analog with potent antiviral activity against SARS-CoV-2. Trials **22,** 561.

Jayk Bernal, A., Gomes da Silva, M.M., Musungaie, D.B., Kovalchuk, E., Gonzalez, A., Delos Reyes, V., *et al.* (2022a). Molnupiravir for oral treatment of Covid-19 in nonhospitalized patients. N Engl J Med **386,** 509–520.

Jayk Bernal, A., Gomes da Silva, M.M., Musungaie, D.B., Kovalchuk, E., Gonzalez, A., Delos Reyes, V., *et al.* (2022b). Molnupiravir for oral treatment of Covid-19 in nonhospitalized patients. N Engl J Med **386,** 509–520.

Kabinger, F., Stiller, C., Schmitzová, J., Dienemann, C., Kokic, G., Hillen, H.S., *et al.* (2021). Mechanism of molnupiravir-induced SARS-CoV-2 mutagenesis. Nat Struct Mol Biol **28,** 740–746.

Kokic, G., Hillen, H.S., Tegunov, D., Dienemann, C., Seitz, F., Schmitzova, J., *et al.* (2021). Mechanism of SARS-CoV-2 polymerase stalling by remdesivir. Nat Commun **12,** 279.

Kumar, G.N., Rodrigues, A.D., Buko, A.M., and Denissen, J.F. (1996). Cytochrome P450-mediated metabolism of the HIV-1 protease inhibitor ritonavir (ABT-538) in human liver microsomes. J Pharmacol Exp Ther **277,** 423–431.
Lieber, C.M., Cox, R.M., Sourimant, J., Wolf, J.D., Juergens, K., Phung, Q., *et al.* (2022). SARS-CoV-2 variant of concern type and biological sex affect efficacy of molnupiravir in dwarf hamster model of severe COVID-19. bioRxiv:2022 .2002.2004.479171. [Epub ahead of print]; DOI: 10.1101/ 2022.02.04.479171.
Mahase, E. (2021). Covid-19: pfizer's paxlovid is 89% effective in patients at risk of serious illness, company reports. BMJ **375,** n2713.
Meganck, R.M., and Baric, R.S. (2021). Developing therapeutic approaches for twenty-first-century emerging infectious viral diseases. Nat Med **27,** 401–410.
Merck. (2022). Fact Sheet for Healthcare Providers: emergency use authorization for Lagevrio™(molnupiravir) Capsules. https://www.merck.com/wp-content/uploads/sites/5/2021/11/ molnupiravir-hcp-fact-sheet.pdf (last accessed June 29, 2022).
Mody, V., Ho, J., Wills, S., Mawri, A., Lawson, L., Ebert, M., *et al.* (2021). Identification of 3-chymotrypsin like protease (3CLPro) inhibitors as potential anti-SARS-CoV-2 agents. Commun Biol **4,** 93.
Owen, D.R., Allerton, C.M.N., Anderson, A.S., Aschenbrenner, L., Avery, M., Berritt, S., *et al.* (2021). An oral SARS-CoV-2 M(pro) inhibitor clinical candidate for the treatment of COVID-19. Science **374,** 1586–1593.
Painter, W.P., Holman, W., Bush, J.A., Almazedi, F., Malik, H., Eraut, N., *et al.* (2021). Human safety, tolerability, and pharmacokinetics of molnupiravir, a novel broad-spectrum oral antiviral agent with activity against SARS-CoV-2. Antimicrob Agents Chemother **65,** e02428-20.
Pavan, M., Bolcato, G., Bassani, D., Sturlese, M., and Moro, S. (2021). Supervised molecular dynamics (SuMD) insights into the mechanism of action of SARS-CoV-2 main protease inhibitor PF-07321332. J Enzyme Inhib Med Chem **36,** 1646–1650.
Plemper R.K. (2021). Editorial overview: special issue on antiviral strategies in Current Opinion in Virology. Curr Opin Virol **50,** 95–96.
Reina, J., and Iglesias, C. (2022). [Nirmatrelvir plus ritonavir (Paxlovid) a potent SARS-CoV-2 3CLpro protease inhibitor combination]. Rev Esp Quimioter **35,** 236–240.
Robson, F., Khan, K.S., Le, T.K., Paris, C., Demirbag, S., Barfuss, P., *et al.* (2020). Coronavirus RNA proofreading: molecular basis and therapeutic targeting. Mol Cell **79,** 710–727.
Sourimant, J., Aggarwal, M., and Plemper, R.K. (2021). Progress and pitfalls of a year of drug repurposing screens against COVID-19. Curr Opin Virol **49,** 183–193.
Sourimant, J., Lieber, C.M., Aggarwal, M., Cox, R.M., Wolf, J.D., Yoon, J.J., *et al.* (2022). 4'-Fluorouridine is an oral antiviral that blocks respiratory syncytial virus and SARS-CoV-2 replication. Science **375,** 161–167.
Talha, B., and Dhamoon, A.S. (2022). Ritonavir. In *StatPearls* [Internet]. Treasure Island (FL): StatPearls Publishing.
Toots, M., and Plemper R.K. (2020). Next-generation direct-acting influenza therapeutics. Transl Res **220,** 33–42.
Toots, M., Yoon, J.J., Cox, R.M., Hart, M., Sticher, Z.M., Makhsous, N., *et al.* (2019). Characterization of orally efficacious influenza drug with high resistance barrier in ferrets and human airway epithelia. Sci Transl Med 11. [Epub ahead of print]; DOI: 10.1126/scitranslmed.aax5866.
Urakova, N., Kuznetsova, V., Crossman, D.K., Sokratian, A., Guthrie, D.B., Kolykhalov, A.A., *et al.* (2018). Beta-d-N (4)-hydroxycytidine is a potent anti-alphavirus compound that induces a high level of mutations in the viral genome. J Virol 92. DOI: 10.1128/JVI.01965-17.
van Kampen J.J.A., van de Vijver, D., Fraaij P.L.A., Haagmans, B.L., Lamers, M.M., Okba, N., *et al.* (2021). Duration and key determinants of infectious virus shedding in hospitalized patients with coronavirus disease-2019 (COVID-19). Nat Commun **12,** 267.
WHO. WHO Coronavirus (COVID-19) Dashboard. Available at https://covid19.who.int Last accessed March 2, 2022.
Yoon, J.J., Toots, M., Lee, S., Lee, M.E., Ludeke, B., Luczo, J.M., *et al.* (2018). Orally efficacious broad-spectrum ribonucleoside analog inhibitor of influenza and respiratory syncytial viruses. Antimicrob Agents Chemother **62,** e00766-18.
Zhou, S., Hill, C.S., Sarkar, S., Tse, L.V., Woodburn, B.M.D., Schinazi, R.F., *et al.* (2021). Beta-d-N4-hydroxycytidine inhibits SARS-CoV-2 through lethal mutagenesis but is also mutagenic to mammalian cells. J Infect Dis **224,** 415–419.

Address correspondence to:
Richard K. Plemper, PhD
Center for Translational Antiviral Research
Georgia State University
Atlanta, GA 30303
USA

E-mail: rplemper@gsu.edu

Received for publication May 26, 2022; accepted May 26, 2022.

2.2.3 4'-Fluorouridine Mitigates Lethal Infection with Pandemic Human and Highly Pathogenic Avian Influenza Viruses

PLOS PATHOGENS

RESEARCH ARTICLE

4′-Fluorouridine mitigates lethal infection with pandemic human and highly pathogenic avian influenza viruses

Carolin M. Lieber[1], Megha Aggarwal[1], Jeong-Joong Yoon[1], Robert M. Cox[1], Hae-Ji Kang[1], Julien Sourimant[1], Mart Toots[1], Scott K. Johnson[2], Cheryl A. Jones[2], Zachary M. Sticher[3], Alexander A. Kolykhalov[3], Manohar T. Saindane[3], Stephen M. Tompkins[2], Oliver Planz[4], George R. Painter[3], Michael G. Natchus[3], Kaori Sakamoto[5], Richard K. Plemper[1]**

1 Center for Translational Antiviral Research, Georgia State University Institute for Biomedical Sciences, Atlanta, Georgia, United States of America, **2** Center for Vaccines and Immunology, University of Georgia, Athens, Georgia, United States of America, **3** Emory Institute for Drug Development, Emory University, Atlanta, Georgia, United States of America, **4** Department of Immunology, Interfaculty Institute for Cell Biology, Eberhard Karls University Tübingen, Tübingen, Germany, **5** Department of Pathology, College of Veterinary Medicine, University of Georgia, Athens, Georgia, United States of America

* rplemper@gsu.edu

Citation: Lieber CM, Aggarwal M, Yoon J-J, Cox RM, Kang H-J, Sourimant J, et al. (2023) 4'-Fluorouridine mitigates lethal infection with pandemic human and highly pathogenic avian influenza viruses. PLoS Pathog 19(4): e1011342. https://doi.org/10.1371/journal.ppat.1011342

Editor: Matthias Johannes Schnell, Thomas Jefferson University - Center City Campus: Thomas Jefferson University, UNITED STATES

Received: December 1, 2022

Accepted: April 3, 2023

Published: April 17, 2023

Peer Review History: PLOS recognizes the benefits of transparency in the peer review process; therefore, we enable the publication of all of the content of peer review and author responses alongside final, published articles. The editorial history of this article is available here: https://doi.org/10.1371/journal.ppat.1011342

Data Availability Statement: All relevant data are within the manuscript and its Supporting Information files.

Abstract

Influenza outbreaks are associated with substantial morbidity, mortality and economic burden. Next generation antivirals are needed to treat seasonal infections and prepare against zoonotic spillover of avian influenza viruses with pandemic potential. Having previously identified oral efficacy of the nucleoside analog 4'-Fluorouridine (4'-FlU, EIDD-2749) against SARS-CoV-2 and respiratory syncytial virus (RSV), we explored activity of the compound against seasonal and highly pathogenic influenza (HPAI) viruses in cell culture, human airway epithelium (HAE) models, and/or two animal models, ferrets and mice, that assess IAV transmission and lethal viral pneumonia, respectively. 4'-FlU inhibited a panel of relevant influenza A and B viruses with nanomolar to sub-micromolar potency in HAE cells. *In vitro* polymerase assays revealed immediate chain termination of IAV polymerase after 4'-FlU incorporation, in contrast to delayed chain termination of SARS-CoV-2 and RSV polymerase. Once-daily oral treatment of ferrets with 2 mg/kg 4'-FlU initiated 12 hours after infection rapidly stopped virus shedding and prevented transmission to untreated sentinels. Treatment of mice infected with a lethal inoculum of pandemic A/CA/07/2009 (H1N1)pdm09 (pdmCa09) with 4'-FlU alleviated pneumonia. Three doses mediated complete survival when treatment was initiated up to 60 hours after infection, indicating a broad time window for effective intervention. Therapeutic oral 4'-FlU ensured survival of animals infected with HPAI A/VN/12/2003 (H5N1) and of immunocompromised mice infected with pdmCa09. Recoverees were protected against homologous reinfection. This study defines the mechanistic foundation for high sensitivity of influenza viruses to 4'-FlU and supports 4'-FlU as developmental candidate for the treatment of seasonal and pandemic influenza.

Funding: This study was supported, in part, by public health service grant AI141222 (to R.K.P.) from the NIH/NIAID. The funders had no role in study design, data collection and analysis, decision to publish, or preparation of the manuscript.

Competing interests: I have read the journal's policy and the authors of this manuscript have the following competing interests: MGN and GRP are co-inventors on patent WO 2019/1736002 covering composition of matter and use of 4'-FlU (EIDD-2749) and its analogs as an antiviral treatment. This study could affect their personal financial status. RKP reports contract testing from Enanta Pharmaceuticals and Atea Pharmaceuticals, and research support from Gilead Sciences, outside of the described work. All other authors declare that they have no competing interests.

Author summary

Next-generation antiviral therapeutics are needed to better mitigate seasonal influenza and prepare against zoonotic virus spillover from animal reservoirs. At greatest risk are the immunocompromised and patients infected with highly pathogenic influenza viruses. In this study, we have demonstrated efficacy of a broad-spectrum nucleoside analog, 4'-fluorouridine, against a representative panel of influenza viruses in cell culture, human airway epithelium (HAE) cells, and two animal models, ferrets and mice. Acting as an immediate chain terminator of the influenza virus polymerase, once-daily oral treatment protected against lethal infection with seasonal and highly pathogenic avian influenza viruses, prevented viral transmission to untreated sentinels, and mitigated lethal infection of immunocompromised hosts. These results support the developmental potential of 4'-fluorouridine for treatment of vulnerable patient groups and mitigation of pandemic influenza, providing a path towards a much-needed additional therapeutic option for improved disease management.

Introduction

Influenza A viruses (IAV) are zoonotic negative sense, segmented RNA viruses with high pandemic potential [1]. Wild aquatic birds are a major natural reservoir for avian influenza viruses, creating high opportunity for spread into the poultry industry and spillover of HPAI viruses into the human population with potentially catastrophic consequences [2,3]. The 2021–2022 H5N1 HPAID epidemic specifically is the largest on record, having reached an unprecedented geographical expansion and requiring the culling of 48 million birds so far [4]. Approximately 14 IAV pandemics have occurred in the past 500 years [5], six of which were concentrated in the last 120 years alone. Most deadly of these outbreaks was the 1918 "Spanish Flu" pandemic, which was caused by an H1N1 subtype IAV of unusual virulence that accounted for approximately 500 million infected people, equating to nearly a third of the world population at the time, and 50 million death [6]. Case fatality rates were particularly high in young children, 20–40 year old adults, and the elderly above 65 years of age [6]. Subsequent pandemics in the 20th century included the Asian influenza of 1957 and the Hong Kong influenza of 1968, which were caused by IAV of H2N2 and H3N2 subtypes, respectively [7], and the swine origin H1N1 outbreak of 2009 [8]. Although considered less pathogenic than several of the earlier pandemic strains, pdm09 IAV is still estimated to have caused 151,000 to 575,400 deaths worldwide and major economic damage [9].

Influenza viruses cause rapid-onset disease with high fever, cough, body aches, rhinorrhea, and nasal congestion [10]. Advance to severe disease is marked by virus invasion of the small airways and viral pneumonia, which can lead to sepsis due to a hyperinflammatory systemic response [11]. Other serious complications include myocarditis, encephalitis, myositis, and multi-organ failure [12,13]. At greatest risk of life-threatening influenza are children less than 2 years of age, older adults, pregnant women, and patients with pre-existing conditions such as asthma, diabetes, or chronic heart disease [14]. Vaccine prophylaxis is available, but the efficacy of the seasonal tetravalent influenza vaccine is moderate, ranging from 40 to 60% even under optimal conditions in interpandemic years [15]. Effectiveness of the vaccine can be substantially lower in older adults, who are at greatest risk of progressing to severe disease, or when vaccine components and circulating strains are poorly matched [15]. Multiple avenues are being pursued to develop a broad-spectrum influenza vaccine, but none have yet achieved regulatory approval [16].

To improve disease management especially in vulnerable patient groups, rapidly respond to endemic outbreaks of seasonal influenza when the vaccine is not optimally matched, and to prepare for the pandemic threat originating from zoonotic transmission of HPAI viruses, effective therapeutics are urgently needed. Three classes of antiviral drugs have received approval by the FDA for treatment of influenza thus far. The M2 channel blocking adamantanes (amantadine and rimantadine), the neuraminidase inhibitors (oral oseltamivir, inhaled zanamivir, intravenous peramivir), and, most recently, the PA endonuclease inhibitor baloxavir marboxil [17]. Of these, use of the adamantanes has been discontinued due to widespread pre-existing resistance in human influenza viruses and natural IAV reservoirs [18]. Pre-existing signature resistance mutations against the neuraminidase inhibitors were furthermore detected in 2009 pandemic viruses [19], giving rise to the concern that future effectiveness of this inhibitor class may be questionable [20]. Although baloxavir marboxil is the newest influenza drug, resistance has developed rapidly and was even observed in human patients during the early clinical trials, resulting in rebound of virus replication [21–23]. Novel therapeutic options are therefore needed to broaden the available anti-influenza virus drug arsenal.

In search of suitable broad-spectrum developmental candidates, we explored in this study antiviral potency, *in vivo* efficacy, and mechanism of action of 4'-FlU against the influenza virus indication. Recently, we reported that 4'-FlU is a highly potent inhibitor of SARS-CoV-2 and pathogens of the mononegavirus order [24,25], establishing oral efficacy in animal models of SARS-CoV-2 and RSV infection. Having demonstrated that this nucleoside analog functions as an immediate chain terminator of influenza virus polymerase, we assessed oral efficacy in two different animal models, mice and ferrets, against pandemic human and HPAI viruses. Influenza treatment paradigms developed in these models outline an unusually broad time window for successful therapeutic interference with a lethal viral challenge. These results support the development of 4'-FlU as a therapeutic candidate for the treatment of influenza with the potential to improve preparedness against zoonotic spillover of avian IAVs with pandemic potential into the human population.

Results

To explore whether the indication spectrum of 4'-FlU (Fig 1A) extends to the orthomyxoviruses, we examined activity of the compound against seasonal and pandemic IAVs representing H1N1 and H3N2 subtypes and influenza B virus (IBV) isolates representing the Yamagata and Victoria lineages in cell culture (Fig 1B). In parallel, we determined activity of 4'-FlU against a recombinant pandemic A/California/07/2009 (H1N1) (pdmCa09), A/swine/Spain/53207/2004 (H1N1), B/Memphis/20/1996, and B/Malaysia/2506/2004 on non-differentiated primary human airway epithelium (HAE) cells (Fig 1C), explored 4'-FlU potency against a recombinant A/WSN/33 (H1N1)-based reporter virus [26] on a panel of non-differentiated primary HAEs representing 10 distinct donors (S1A Fig), and generated an airway epithelium model through differentiation of HAEs at air-liquid interface to test inhibition of pdmCa09 through basolateral 4'-FlU in a disease-relevant *ex vivo* tissue model (S1B Fig). Most viral isolates tested were efficiently inhibited by the compound, consistently returning 50% and 90% inhibitory concentrations (EC_{50} and EC_{90}, respectively) in the nanomolar range with steep Hill slopes independent of host cell type. The least sensitive were A/swine/Spain/53207/2004 (H1N1), B/Memphis/20/1996, and B/Malaysia/2506/2004, but 4'-FlU inhibitory concentrations remained in the low-micromolar range. Recapitulating our previous experience with 4'-FlU performance on respiratory epithelium cultures [24], potency of 4'-FlU against pdmCa09 was greater in the differentiated HAE model (EC_{90} 0.07 μM) than on cell lines (EC_{90} 0.7 μM) or undifferentiated primary cells (EC_{90} 3.33 μM). Combined with a 50% cytotoxic

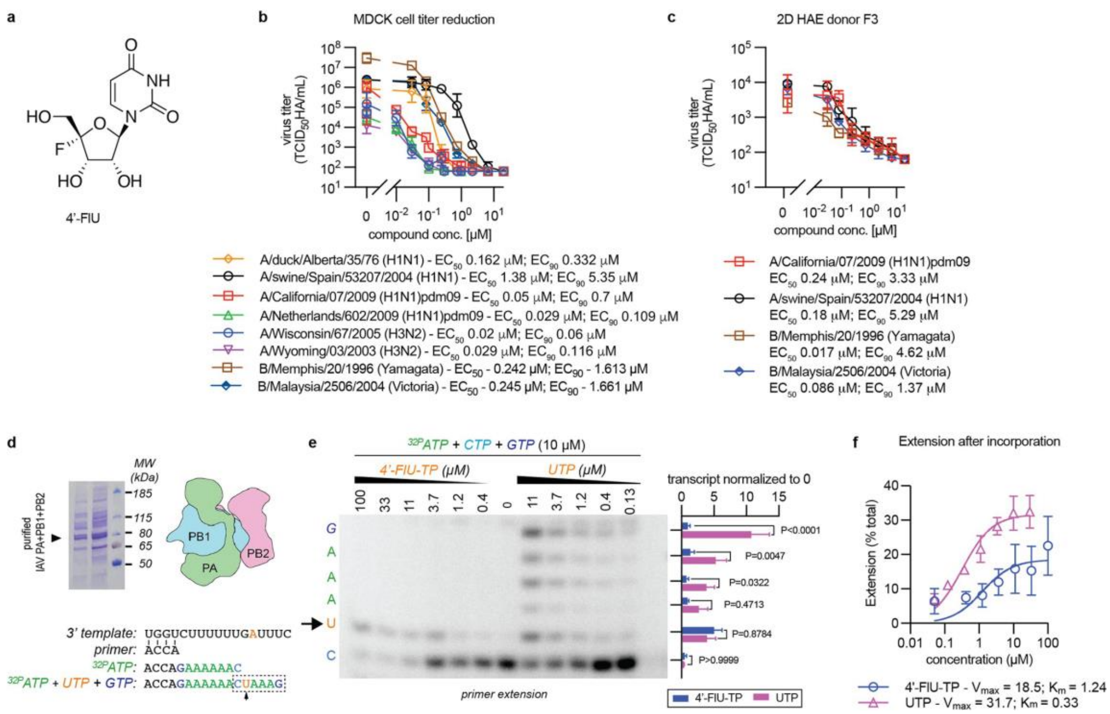

Fig 1. *In vitro* potency and MOA of 4'-FlU against influenza viruses. a) Structure of 4'-FlU. **b)** Dose-response assay of 4'-FlU on MDCK cells. Cells were infected with different subtype IAVs or different IBV isolates. **c)** 4'-FlU antiviral activity in 2D HAE cultures. Dose-response assays of 4'-FlU against A/California/07/2009 (H1N1), A/swine/Spain/53207/2004 (H1N1), A/Wisconsin/67/2005 (H3N2), B/Memphis/20/1996 (Yamagata lineage), and B/Malaysia/2506/2004 (Victoria lineage) on undifferentiated HAEs derived from a healthy female donor. Lines in (b-c) intersect, and symbols show, geometric means ± SD (n = 3); EC_{50} and EC_{90} values based on 4-parameter variable slope regression modeling are given. **d)** Coomassie blue staining of purified recombinant IAV RdRP proteins after gel electrophoresis and RNA template sequences used in primer extension assays. **e)** *In vitro* RdRP assay in the presence of ^{32}P-ATP, CTP, GTP, and UTP or 4'-FlU-TP as indicated. Representative autoradiogram showing the sequence section highlighted by dashed box in (d); the first incorporation of UTP or 4'-FlU-TP is after position $i = 8$ of the amplicon (arrow). The sequence of the amplicon and results of phosphoimager-quantitation of relative signal intensities observed in the presence of 11 μM UTP or 4'-FlU-TP are specified to the left and right of the autoradiogram, respectively. Quantitation graph shows mean values of independent experiments (n = 3) ± SD; analysis with 1-way ANOVA with Dunnett's *post hoc* test; P values are shown in the graph. Uncropped autoradiogram and replicates are provided in (S2 Fig). **F)** Kinetic analysis of 4'-FlU-TP and UTP incorporation into the amplicon shown in (e) and (S2 Fig). Lines represent non-linear regression kinetics with Michaelis-Menten model, K_m and V_{max} are shown, error bars represent 95% CI.

https://doi.org/10.1371/journal.ppat.1011342.g001

concentration (CC_{50}) of 4'-FlU of 468 μM [24] in primary HAEs from the same donor as used in the differentiated HAE model, we calculated a selectivity index (SI = CC_{50}/EC_{50}) of 4'-FlU against pdmCa09 of 15,600 in this disease-relevant human tissue model. Transepithelial electrical resistance (TEER) between basolateral and apical chamber of the air-liquid interface cultures was unchanged throughout the study (S1C Fig), confirming our previous observation that 4'-FlU does not disrupt epithelium integrity [24] and, in the case of vehicle-treated wells, that the epithelium maintains barrier function despite productive IAV replication [27].

4'-FlU is an immediate chain terminator of influenza virus polymerase

Through biochemical RdRP assays using purified recombinant RSV and SARS-CoV-2 polymerase complexes and synthetic template RNA, we have demonstrated that incorporation of 4'-FlU triphosphate (4'-FlU-TP) into nascent chain RNA triggers delayed termination of the

RNA-dependent RNA polymerases from a negative sense (RSV) and a positive sense (SARS--CoV-2) RNA virus. Whereas variations in stalling efficiencies were observed between sequences and polymerase, position *i*+3 marked the predominant stalling site [24]. Following expression of IAV RdRP PA, PB1, and PB2 subunits in insect cells, we subjected affinity chromatography purified, reconstituted IAV polymerase to the equivalent biochemical RdRP assay in the presence of increasing concentrations of 4'-FlU-TP or UTP (Figs 1D, 1E and S2A to S2E). 4'-FlU-TP was incorporated instead of UTP when the polymerase reached the first adenosine in the template RNA as we had noted before in RSV and SARS-CoV-2 RdRP assays [24], but then triggered immediate chain termination of IAV RdRP. Densitometric quantitation of relative amplicon intensities to compare incorporation rates of the analog relative to UTP revealed an approximately 4-fold higher affinity of IAV polymerase for endogenous UTP than for 4'-FlU-TP (Fig 1F).

These results demonstrate high sensitivity of influenza virus polymerases to 4'-FlU and identify sequence-independent immediate chain termination at position *i* as a predominant mechanism of influenza virus RdRP inhibition by the compound.

Pharmacokinetic (PK) properties of 4'-FlU in mouse plasma and tissues

We have previously demonstrated oral bioavailability of 4'-FlU in ferrets and efficient intracellular anabolism to 4'-FlU-TP with prolonged tissue exposure levels [24]. To assess cross-species conservation of PK profiles between IAV efficacy models used in this study, ferrets and mice, we subjected the compound to a single-dose oral PK study in mice, measuring 4'-FlU plasma concentrations and corresponding 5'-triphosphate levels in selected soft tissues after oral dosing at 1.5 mg/kg body weight (Fig 2A and 2B). Free 4'-FlU reached a maximal plasma exposure of approximately 1 μM 90 minutes after oral administration, far exceeding the cell culture EC_{90} concentration against the influenza virus test panel. Plasma levels were sustained high over a 12-hour period after dosing. Corresponding 4'-FlU-TP tissue exposure levels 12 hours after dosing were approximately 1 nmol/g tissue in all organs but brain and kidney, underscoring suitability of 4'-FlU for *in vivo* efficacy testing against IAV.

Late-onset treatment with 4'-FlU mediates complete survival of IAV-infected animals

For mouse efficacy studies, animals were infected intranasally with a lethal inoculum amount of pdmCa09, which replicates efficiently in mice without a requirement for species adaptation [28]. Infection results in severe viral pneumonia with major clinical signs such as weight loss and hypothermia. To establish the lowest efficacious dose, we examined 3 4'-FlU dose levels in a survival study, each administered by oral gavage on three consecutive days in a once daily (q.d.) regimen starting at the time of infection (Fig 2C). All animals treated at the 2 mg/kg dose level survived, whereas all mice of the vehicle-treated and lowest dose (0.08 mg/kg) groups succumbed to infection within 5 days of inoculation (Fig 2D) and experienced clinical signs (S3A and S3B Fig). Animals receiving the intermediate 4'-FlU dose (0.4 mg/kg) had prolonged survival, but ultimately all died.

Having established 2 mg/kg 4'-FlU administered q.d. as a low efficacious dose, we next determined the latest time for initiation of effective treatment at this dose level (Fig 2E). All vehicle-treated animals again succumbed to infection within 5 days of inoculation (Fig 2F). In contrast, treatment start at 2.5 days after infection, which corresponds to 0.5 days after the onset of major clinical signs (S3C and S3D Fig) ensured complete survival, and 80% of animals of a group receiving the first dose 3 days after infection survived, outlining a broad therapeutic time window for treatment of influenza with 4'-FlU. Therapeutic benefit of late-onset

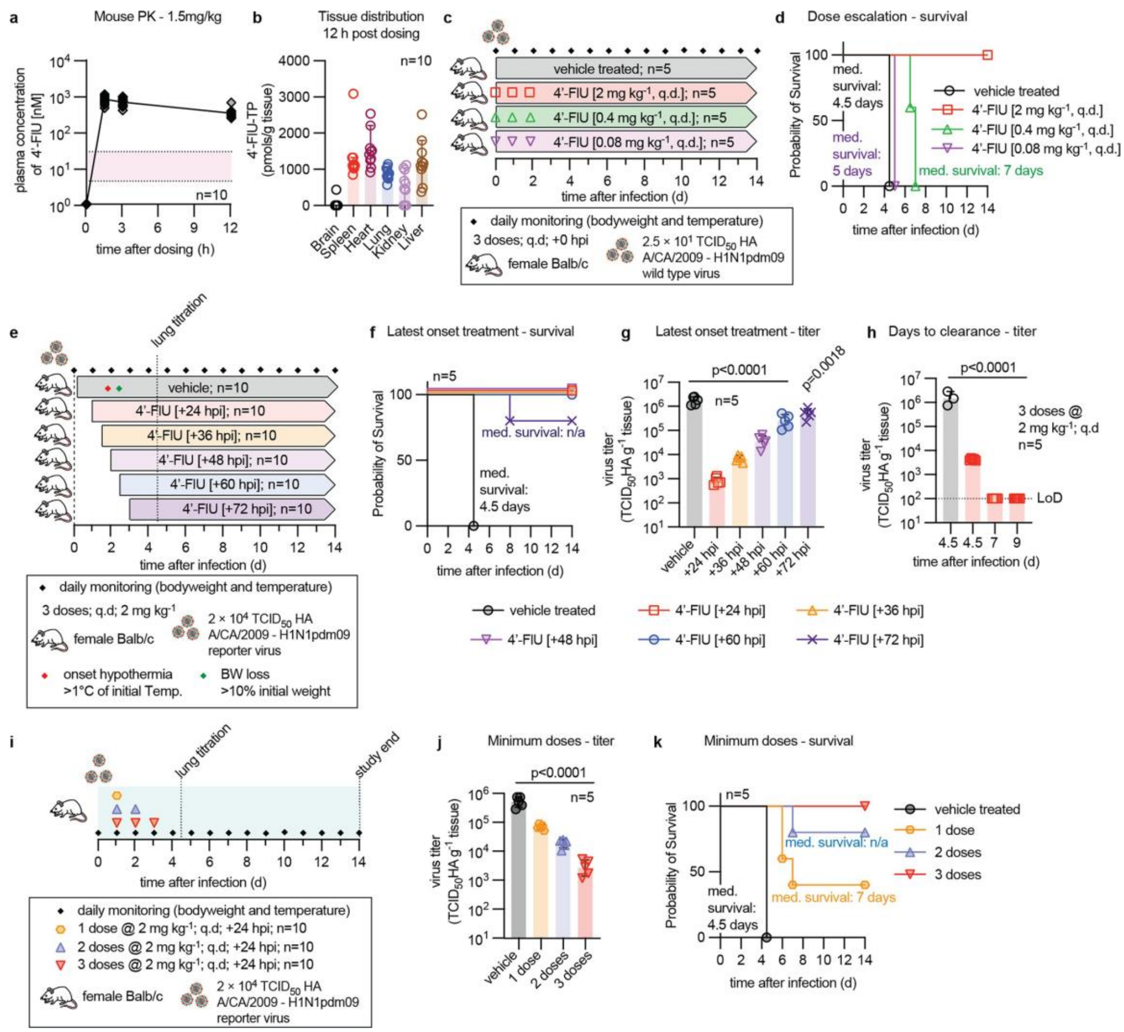

Fig 2. Treatment paradigms of 4'-FlU in mice. a) Mouse plasma exposure after a single oral dose of 1.5 mg/kg bodyweight. The red area denotes cell culture $EC_{90} \pm 1 \times SD$ against WSN, all donors as shown in (S1A Fig). **b)** Tissue distribution of bioactive anabolite 4'-FlU-TP in animals shown in (a) 12 hours after dosing. **c)** Schematic of dose-to-failure study against standard recA/CA/2009 (H1N1). **d)** Survival of animals treated as specified in (c). Median survival (med. survival) time in days is specified; Kaplan-Meier simple survival analysis. **e)** Study schematic to determine the therapeutic time window of oral 4'-FlU in mice, using recA/CA/2009-maxGFP-HA (H1N1) as viral target. **f)** Survival of animals treated as specified in (e). Median survival time in days is specified; Kaplan-Meier simple survival analysis. **g)** Lung viral load of a set of animals treated as in (e) was determined 4.5 days after infection. **h)** Time-to-viral-clearance study. Mice were infected and treated with 4'-FlU at 2 mg/kg starting 24 hours after infection and continued q.d. Lung virus load was determined in vehicle-treated animals 4.5 days after infection, and in 4'-FlU-treated animals 4.5, 7, and 9 days after infection. **i)** Schematic of minimal-number-of-doses finding study. **j)** Lung viral load of animals treated as in (i), determined 4.5 days after infection. **k)** Survival of a set of animals treated as in (i). Median survival time in days is specified; Kaplan-Meier simple survival analysis. Columns in (b) represent data medians with 95% CI, columns in (g-h,j) represent geometric means ± SD; symbols specify individual animals; statistical analysis in (g-h,j) with 1-way ANOVA with Dunnett's *post hoc* test.

https://doi.org/10.1371/journal.ppat.1011342.g002

treatment was corroborated by a significant reduction in lung virus load compared to vehicle-treated controls at 4.5 days after infection, determined in a parallel set of equally treated animals (Fig 2G). Within 7 days, virus became undetectable in lungs of animals that were treated starting 24 hours after infection with oral 4'-FlU (2 mg/kg q.d.; 3 doses total), indicating that viral replication had ceased (Fig 2H). No rebound of virus replication was observed within a 9-day period after infection (S3E and S3F Fig). These results define a broad therapeutic time window for effective treatment of IAV infection with 4'-FlU.

To determine the minimal number of oral 4'-FlU doses (2 mg/kg q.d.) for complete survival, we again initiated treatment 24 hours after infection, in this study comparing the effect of a single vs double or triple doses (Fig 2I). Lung virus load was assessed 4.5 days after infection and survival monitored in a parallel set of equally treated animals. The number of doses administered correlated with antiviral effect size, but even a single dose of 4'-FlU resulted in a statistically significant reduction in lung virus load of approximately one order of magnitude (Fig 2J). Reduced viral burden translated to survival of some animals in the single and double dose groups. However, three doses were required for full therapeutic benefit (Fig 2K) and only mild clinical signs (S3G and S3H Fig).

4'-FlU effect on IAV transmission in the ferret model

Since mice, in contrast to ferrets, do not shed IAVs, we next explored anti-IAV efficacy of 4'-FlU in the ferret model. Guided by the dosing regimen established in mice, we treated animals infected intranasally with pdmCa09 with either 2 mg/kg (standard dose) or 0.5 mg/kg (low dose), administered orally starting 24 hours after infection (Fig 3A). Animals received one (2 mg/kg level) or two doses (either 2 or 0.5 mg/kg level) total. Fever is the predominant clinical sign associated with pdmCa09 IAV infection in ferrets. Monitoring body temperature continuously telemetrically, we observed significant reduction in all treated animals within 24 hours of the first dose, whereas vehicle-treated animals showed a prolonged fever plateau (S4A Fig). Viral titers in nasal lavages were statistically significantly reduced compared to those of vehicle animals, but effect size was lower in animals of the low dose than the standard dose group, and virus rebounded 2.5 days after infection in the single standard dose group (Fig 3B). In contrast, two standard doses 4'-FlU given q.d. were sterilizing within 2 days of treatment initiation. Virus load in nasal turbinates assessed 4 days after infection corroborated the lavage titers, revealing a dose-dependent significant antiviral effect of two doses, whereas a single dose had no significant effect on virus titer in turbinates at the time of tissue harvest (Fig 3C). Examination of lower respiratory tract tissues, trachea, and bronchoalveolar lavage fluid (BALF) revealed, however, that a single standard dose of 4'-FlU administered at the time of onset of clinical signs completely suppressed the development of viral pneumonia (Fig 3D).

To determine the effect of 4'-FlU on virus spread, we treated in a direct-contact transmission study source ferrets infected with pdmCa09 with the compound as before, starting 12 or 24 hours after infection (Fig 3E). Co-housing of source ferrets with untreated sentinels in a 1:1 ratio was initiated 2.5 days after study start. pdmCa09 rapidly spread from vehicle-treated source ferrets to their direct contacts, which first became virus-positive in nasal lavages only 12 hours after the beginning of co-housing (Fig 3F) and had progressed to viral pneumonia with high turbinate, lung and trachea virus load by study end (Fig 3G and 3H) and clinical signs (S4B to S4E Fig). Treatment of source animals with 4'-FlU initiated 12 or 24 hours after infection in each case resulted in exponential decline in shed virus load, but virus was undetectable in lavages of the 12-hour treatment group by the time of co-housing whereas approximately 10^4 $TCID_{50}$ units/ml lavage remained detectable in lavages of the 24-hour treatment group at that time. We did not detect any virus transmission to untreated sentinels of the

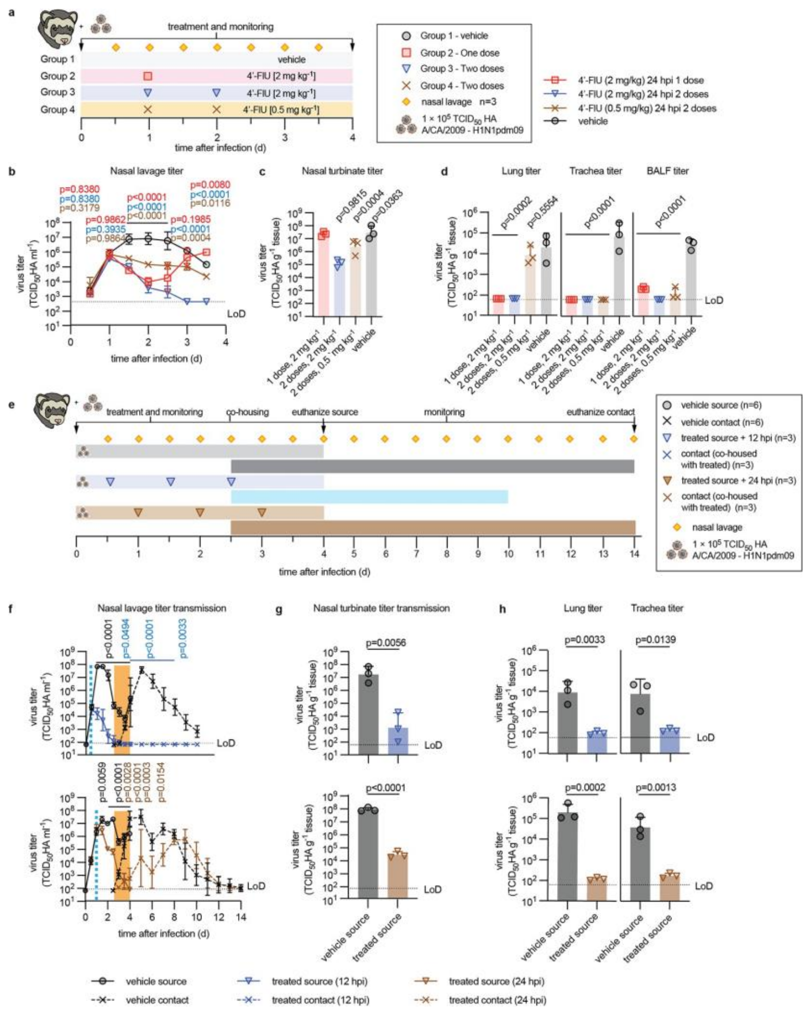

Fig 3. *In vivo* efficacy of 4'-FlU in the ferret transmission model. a) Ferret efficacy study schematic. **b)** Ferret shed viral titers in nasal lavages (n = 3). **c-d)** Tissue and BALF viral titers determined 4 days after infection. **e)** Transmission study schematic. Treatment of source ferrets was started 12 or 24 hours after infection, animals were co-housed with untreated contact ferrets 2.5 days after infection. **f)** Ferret shed viral titers in nasal lavages of source animals and their sentinels. Light blue dashed line marks time of treatment onset; orange box highlights co-housing period. **g-h)** Virus load in nasal turbinates (g) and lung and trachea tissues (h) in source animals, collected 4 days after infection, respectively. Lines in (b,f) intersect, and symbols show, geometric means ± SD; 2-way ANOVA with Tukey's *post hoc* test, P values are specified (in (f), P values in black compare source animals, P values in blue and brown compare contact ferrets). Columns in (c-d,g-h) represent geometric means ± SD; symbols show individual animals; 1-way ANOVA with Dunnett's *post hoc* test (c-d) or unpaired t-test (g-h); P values are specified.

https://doi.org/10.1371/journal.ppat.1011342.g003

12-hour group. However, low-grade transmission to direct contacts of the 24-hour treatment group occurred, characterized by delayed onset of virus shedding compared to sentinels of vehicle-treated source animals and a reduced peak shed virus load (Fig 3H). Shedding from all sentinels that became virus-positive ceased approximately 12 days after the beginning of co-housing. These results confirm cross-species anti-IAV efficacy of 4'-FlU, reveal that a single oral dose is sufficient to prevent advance to severe influenza, and demonstrate a shortened window in which a treated case remains fully infectious.

Mitigation of IAV pathogenesis and lung histopathology by 4'-FlU

To better understand the impact of 4'-FlU on mitigating immunopathogenesis, the major driver of clinical signs associated with influenza virus infection, we determined inflammatory cytokine profiles for a 10-day period after infection of mice with pdmCa09 using a 6-plex Th17 cytokine assay (Fig 4A). Treated animals received the 3-dose standard 4'-FlU regimen as before, started 24 hours after infection. Lung tissue for histopathology was extracted from parallel sets of equally treated animals 5 or 21 days after infection. Lung titers in vehicle-treated animals demonstrated fast-onset viral pneumonia, approaching a burden of 10^6 infectious units/g lung tissue 4 days after infection, when all animals of the vehicle group had succumbed to infection with major clinical signs (Figs 4B, S5A and S5B). Pro-inflammatory cytokines rapidly increased in the BALF of these animals, revealing a very strong antiviral response until death of the vehicle animals as expected after infection with pdmCa09 (Figs 4C, 4D and S6). Treatment with 4'-FlU again efficiently suppressed virus replication within 24 hours of the first dose (Fig 4B). Coinciding with the reduction in virus burden of treated animals by approximately two orders of magnitude by day 3 after infection, the proinflammatory response was greatly alleviated (Figs 4C, 4D and S6) and all treated animals survived (S5A Fig).

Consistent with a better clinical outcome (S7A and S7B Fig), lowered viral load, and mitigated innate antiviral response in 4'-FlU treated vehicle animals, analysis of lung histopathology 5 days after infection revealed reduced lung lesions and alleviated cellular infiltrates in lung tissue of treated animals (Figs 4E and S8). Overall combined histopathology scores of individual animals representing the degree of cellular infiltrates into alveoli and bronchioles, the extent of perivascular cuffing, and the severity of interstitial pneumonia, pleuritis, and vasculitis were statistically significantly lower in the treatment than vehicle group (Figs 4F and S9).

4'-FlU control of influenza in immunocompromised hosts and of HPAI infection

In the clinic, the risk of progression to severe disease and poor overall outcome is greatly increased when immunocompetence of the patient is impaired or after zoonotic spillover of HPAIs into the human population [29,30]. To first assess the potential of 4'-FlU to pharmacologically manage influenza in high-risk hosts, we infected interferon α/β receptor knockout (IFNAR1 KO) and V(D)J recombination activation gene RAG-1 KO mice with pdmCa09. Whereas the former cannot mount an effective type I IFN innate response [31,32], the latter are compromised in their cell-mediated adaptive immunity due to a lack of mature T and B cells [33]. Oral treatment with 4'-FlU was initiated 24 hours after infection at standard and a high-dose (10 mg/kg) level, then continued q.d. for a total of 7 doses of each group (Fig 5A). Independent of 4'-FlU dose level, all treated animals of the RAG-1 KO and IFNAR1 KO groups survived, whereas all animals in the vehicle-treated groups developed severe clinical signs (S10A to S10D Fig) and succumbed to infection within 4 days (Fig 5B). Reduction in lung virus load of treated vs vehicle animals after three q.d. 4'-FlU doses (day 4 after infection) was dose level-dependent, but even at the standard dose, this reduction exceeded two orders of magnitude in either knockout mouse strain (Fig 5C).

Next, we explored 4'-FlU efficacy against HPAIs, initially testing potency against polymerases derived from A/CA/07/2009 (H1N1), A/VN/12/2003 (H5N1), and A/Anhui/1/2013 (H7N9) in minireplicon dose-response assays (Fig 5D). The compound dose-dependently

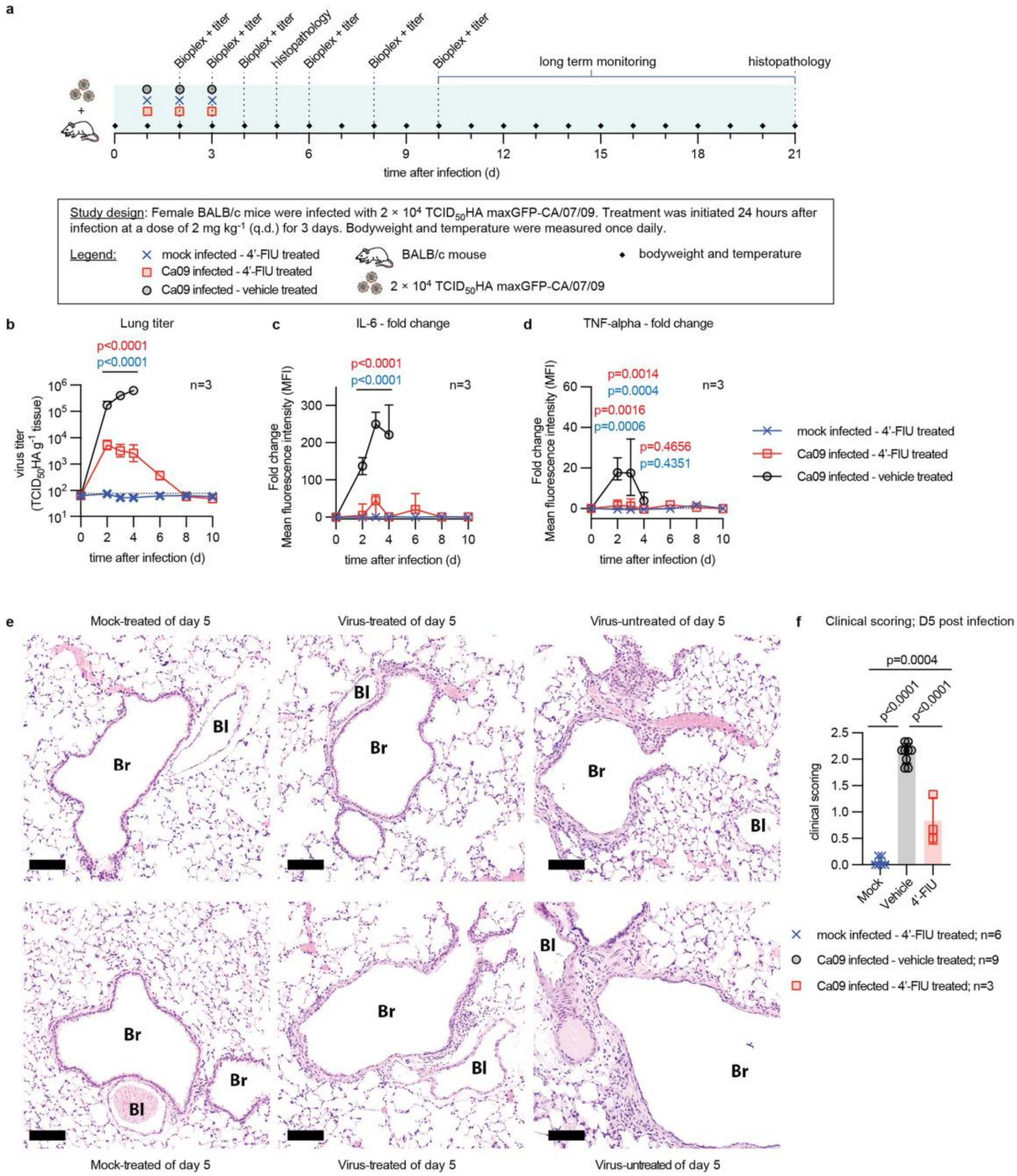

Fig 4. Effect of 4'-FlU on the antiviral immune response and lung histopathology. a) *In vivo* Bioplex and histopathology study schematic. **b)** Lung viral titers in animals treated as in (a). **c-d)** Changes in IL-6 (c) and TNF-α (d) levels present in BALF of animals treated as in (a), relative to levels at time of infection. Lines in (b) intersect, and symbols show, geometric means ± SD, lines in (c-d) intersect, and symbols show, data medians with 95% CI; 2-way ANOVA with Tukey's *post hoc* test; P values are given. **e)** Representative photomicrographs of lung tissue extracted 5 days after infection of animals treated as in (a). Tissues

of two individual animals per study arm are shown at 10× magnification; scale bar denotes 100 μm; Br, Bronchiole; Bl, Blood vessel. **f)** Histopathology scores of animals treated as in (a). Lungs were extracted 5 days after infection. Scores for each animal represents a mean of individual alveolitis, bronchiolitis, vasculitis, pleuritis, perivascular cuffing (PVC), and interstitial pneumonia (IP) scores. Columns represent data medians with 95% CI; symbols show mean scores for each individual animal; 1-way ANOVA with Dunnett's *post hoc* test, P values and n values for each study arm are specified.

https://doi.org/10.1371/journal.ppat.1011342.g004

inhibited activity of either HPAI-derived polymerase complex, reaching active concentrations resembling that observed against pdmCa09 RdRP. Selecting A/VN/12/2003 (H5N1), which causes lethal encephalitis in mice [34], for a proof-of-concept efficacy study of 4'-FlU against zoonotic HPAIs, we started treatment at the 5 mg/kg dose level 12 or 24 hours after infection and continued q.d. thereafter (Fig 5E). This elevated dose was chosen to compensate for lower brain tissue exposure of 4'-FlU (Fig 2A) when treating infection by a CNS-invasive IAV. None of the animals of either 4'-FlU treatment group developed clinical signs even when treatment was initiated 24 hours after infection (Fig 5F), and all treated animals survived (Fig 5G). In contrast, 19 out of 20 vehicle-treated animals succumbed to A/VN/12/2003 (H5N1) with a median survival time of 9 days after infection, developing clinical signs on day 7 after infection followed by rapid further deterioration (Fig 5F). Vehicle-treated animals experienced high lung virus loads three days after infection (Fig 5H). Treatment reduced HPAI burden by several orders of magnitude to limit of detection. These results confirm uncompromised efficacy of 4'-FlU in high-risk immunocompromised hosts and against highly pathogenic zoonotic viruses with high pandemic concern.

Anti-IAV immune status of 4'-FlU-treated recoveries

Highly efficacious antivirals may suppress host immune activation, especially when treatment is started early in the course of infection, which may leave the host susceptible to subsequent re-infection and may potentially even result in exacerbated disease [35–37]. To explore the effect of 4'-FlU on subsequent homotypic IAV rechallenge of recoveries, we infected animals with pdmCa09 and started standard 3-dose 4'-FlU treatment at three time points, therapeutically at 24 and 48 hours after infection and prophylactically at 12 hours before infection (Fig 6A). For this study, mice were inoculated with aerosolized virus in a temperature and airflow-controlled aerosol chamber using an Aeroneb nebulizer (S11A and S11B Fig) to better mimic natural infection. Prior to study start, we performed pilot experiments to determine suitable exposure time (S12A to S12C Fig), infectious dose (S13A and S13B Fig) and proof-of-concept for 4'-FlU efficacy (S14A to S14D Fig) after infection with aerosolized virus. Mirroring the outcome of our previous efficacy studies, animals of all treatment groups survived the original infection, whereas all animals of the vehicle group reached predefined clinical endpoints 9 days after infection and had to be terminated (Fig 6B) with major clinical signs (S15A and S15B Fig). To assess the status of humoral anti-Ca09 immunity, we collected blood samples from the treated recoverees 4, 8, and 12 weeks after the original infection and determined neutralizing antibody (nAb) titers. Mice in both therapeutic treatment groups mounted a robust humoral anti-IAV response, whereas no nAbs were detectable in the prophylactically treated animals 8 weeks after the original infection (Fig 6C). Upon homotypic rechallenge with aerosolized pdmCa09 10 weeks after the original infection, however, all 4'-FlU-experienced recoverees had a significant benefit over a new set of IAV-naïve mice (Fig 6D). All animals of the therapeutic groups survived with significant boost in nAb titers relative to week 8 levels. Remarkably, four of the five animals treated prophylactically with 4'-FlU at the time of the original infection also survived the homotypic rechallenge and mounted a robust humoral anti-Ca09 response by week 12. In contrast, all newly added IAV-inexperienced animals succumbed to infection within 9 days, confirming efficient virus delivery through aerosolization

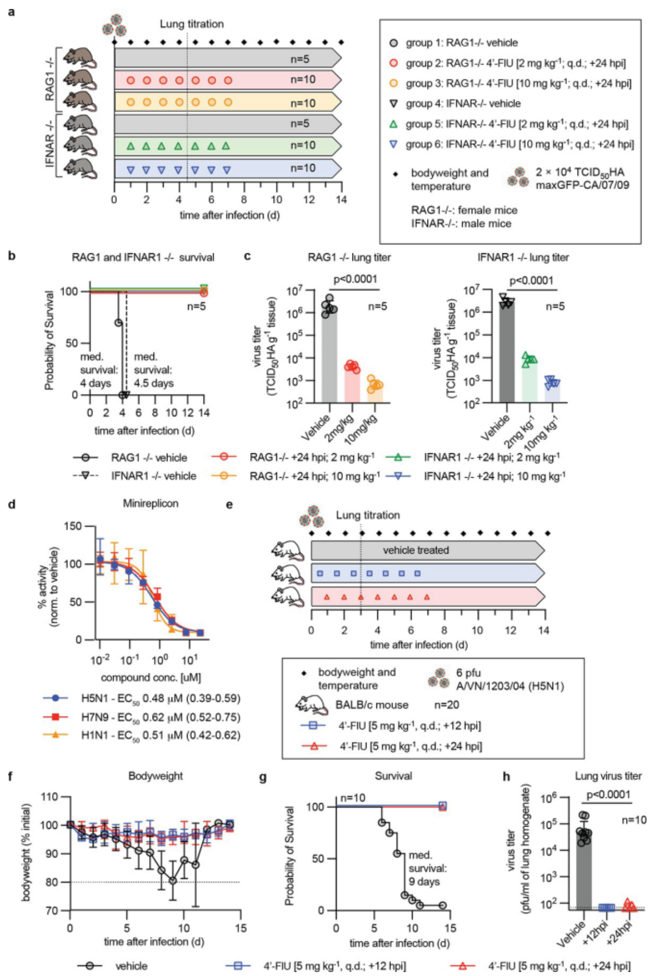

Fig 5. Efficacy of 4'-FlU in an immunocompromised host and against HPAI. a) Efficacy study schematic in immunocompromised mice, lacking B and T cells (RAG1 KO) or IFN1 receptor function (IFNar1 KO). **b)** Survival study of animals treated as shown in (a). Median survival time in days is specified; Kaplan-Meier simple survival analysis. **c)** Lung viral load in animals from (a), determined 4.5 days after infection. **d)** Dose-response minigenome assay with RdRP complexes derived from IAV subtypes H1N1, H5N1, and H7N9. Lines represent 4-parameter variable slope regression models; symbols show data medians with 95% CI; n = 3. EC_{50} concentrations and 95% CI are specified. **e)** Efficacy study schematic of 4'-FlU against HPAI H5N1. **f)** Body weight measurements of animals shown in (e). Lines intersect, and symbols show, data means ± SD, normalized to animal body weight at study start. Dashed line shows predefined endpoint. **g)** Survival study of animals infected with HPAI and treated as shown in (e). Median survival time in days is specified; Kaplan-Meier simple survival analysis. **h)** Lung virus load on day 3 after infection. Columns in (c,h) represent geometric means ± SD; symbols show individual animals; 1-way ANOVA with Dunnett's *post hoc* test; P values and n values are specified.

https://doi.org/10.1371/journal.ppat.1011342.g005

at rechallenge. Animals of the treatment group remained disease-free during rechallenge, and clinical signs were alleviated in mice of the prophylactic group (S15C and S15D Fig). Independent of the original 4'-FlU regimen applied, we did not detect any signs of exacerbated disease upon rechallenge of treatment-experienced recoverees.

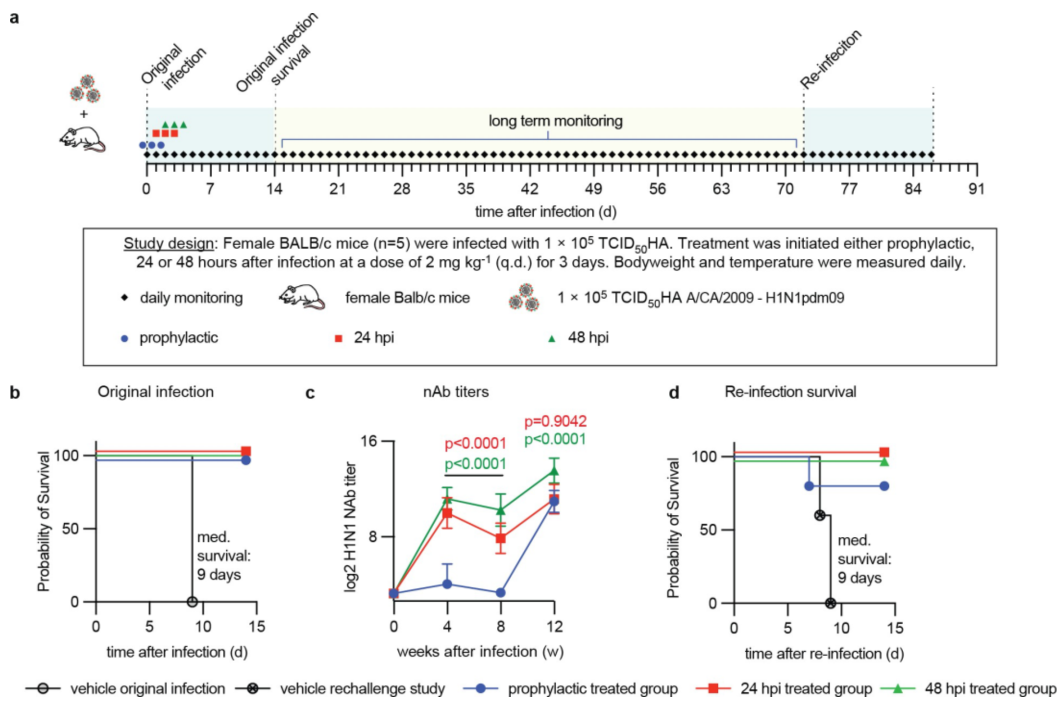

Fig 6. Reinfection of 4'-FlU-experienced animals with homotypic H1N1. a) Schematic of the treatment and reinfection study. For infection and reinfection, mice received aerosolized pdmCa09. **b)** Survival study of animals infected, treated, and reinfected as shown in (a). Median survival time in days is specified; Kaplan-Meier simple survival analysis. **c)** Anti-H1N1 neutralizing antibody (nAb) titers developing in animals from (a). Lines intersect, and symbols show, geometric means ± SD; 2-way ANOVA with Tukey's *post hoc* test; P values are specified. **d)** Survival of animals after re-infection. Median survival time in days is specified; Kaplan-Meier simple survival analysis. N numbers for animals in (a-d) are specified in (a).

https://doi.org/10.1371/journal.ppat.1011342.g006

Discussion

Treatment of influenza has remained challenging, despite the current availability of two different FDA-approved drug classes, the neuraminidase and endonuclease inhibitors [38]. The main obstacles to more successful antiviral therapies are narrow therapeutic time windows [39], poor patient compliance [40], and impaired immunocompetence of older adults at greatest risk of advance to severe disease [17], defining key developmental objectives for the next generation of influenza therapeutics.

Demonstrating antiviral potency in cell culture, human airway epithelium cells, and/or efficacy in two relevant *in vivo* infection models, ferrets and mice, this study establishes oral efficacy of once-daily administered 4'-FlU, a broad-spectrum antiviral ribonucleoside analog [24,25], against seasonal, pandemic, and HPAI IAV strains. Designed to expand the first-line pharmacological arsenal against RNA viruses of pandemic concern, we have previously shown activity of 4'-FlU against SARS-CoV-2, pneumoviruses such as RSV, paramyxoviruses, and other members of the mononegaviruses [24]. Mechanistic characterization consistently demonstrated that incorporation of 4'-FlU-TP into the nascent RNA strand induces polymerase chain termination [24]. Unique to 4'-FlU of all chain-terminating ribonucleoside analogs analyzed [25], however, the modus of 4'-FlU-induced termination varies dependent on RdRP target. IAV RdRP stalled immediately upon incorporation, RSV polymerase termination was delayed at position *i*+3 after incorporation, and SARS-CoV-2 polymerase termination was delayed and dependent on sequence context, requiring incorporation of at least two 4'-FlU moieties in close repetition [24]. Delayed chain termination typically reflects that incorporation of the nucleoside analog alters secondary structure of the nascent strand, which interferes with polymerase processivity [25,41,42]. Accordingly, we hypothesize that distinct mechanisms of action (MOAs) against betacoronaviruses, pneumoviruses, and orthomyxoviruses are due to different capabilities of the respective polymerase complexes to accommodate 4'-FlU-specific secondary structure changes.

In clinical trials of baloxavir marboxil, viral resistance emerged rapidly, resulting in rebound of virus replication in 82.1% of treated patients [23]. Whole genome sequencing of 4'-FlU-experienced virus populations isolated from infected and treated animals showed no allele-dominant divergence from the inoculum population [24]. However, future full resistance profiling of 4'-FlU against influenza viruses will be required to better appreciate the height of the genetic barrier against viral escape from inhibition and explore the molecular basis for the slight virus strain-dependent differences in sensitivity to 4'-FlU that we observed in cell culture dose-response assays. Greater potency of 4'-FlU on differentiated HAE models compared undifferentiated HAEs and immortal cell lines especially likely reflects more efficient intracellular anabolism of the compound to the bioactive triphosphate form 4'-FlU-TP and altered viral replication kinetics in differentiated versus undifferentiated HAEs.

Very likely representing a direct consequence of the distinct MOAs, we found influenza viruses to be highly sensitive to inhibition by 4'-FlU, followed by RSV and SARS-CoV-2. Dose-finding in the mouse model identified effective levels in the low mg/kg range and three doses administered q.d. to be sufficient for achieving full therapeutic benefit, which resembled efficacy performance of baloxavir marboxil [43] and far outpaced that of the neuraminidase inhibitors [44]. Whereas therapeutic oseltamivir lacked efficacy in mice infected with pdm09 IAV isolates [45] and baloxavir marboxil ensured only partial survival when treatment was started later than 24 hours after infection [43], treatment with 4'-FlU mediated unprecedented complete survival of all treated animals when the inhibitor was first administered as late as 60 hours after infection, at the time when lung virus burden approached peak titer [46] and major clinical signs had manifested. If predictive of the treatment of human disease, this substantially widened therapeutic time window may be game-changing for influenza therapy.

Since clinical signs of influenza are largely a result of immunopathogenesis [47], we asked whether 4'-FlU may impact the quality of the antiviral immune response and potentially trigger exacerbated disease upon homotypic re-infection. Cytokine profiling showed an alleviated pro-inflammatory response in animals dosed therapeutically with 4'-FlU, but assessment of neutralizing antibody titers revealed that each of the treated animals had mounted a robust humoral response. Consistent with our previous observation of low cytotoxic and cytostatic potential of 4'-FlU [24], these results indicate that mitigated immunopathogenesis in treated animals is a consequence of reduced virus load rather than a direct immunomodulatory effect of the compound. Although essentially sterilizing, even prophylactic treatment resulted in partial protection of animals at re-infection despite the absence of neutralizing antibodies, indicating that treated animals also mounted a viable cell-mediated adaptive response [48,49].

Beyond individual patient benefit through mitigation of lethal infection and alleviation of viral pneumonia and lung immunopathogenesis, 4'-FlU statistically significant reduced upper respiratory tract virus load and viral shedding when treating 12 hours after infection, resulting in fully suppressed spread to untreated direct-contact sentinels in the highly sensitive ferret transmission model [50]. Later treatment initiation still reduced transmission efficiency, manifesting in delayed onset of virus replication and reduced upper respiratory tract peak virus load, which serves as a biomarker for risk of progression to severe viral pneumonia [51]. If equally applicable to the human host, pharmacological block or mitigation of transmission provides a promising path towards outbreak control through efficient interruption of community transmission chains, mitigating the health threat and economic burden [52] of endemic and pandemic influenza.

At greatest risk of life-threatening disease are the immunocompromised [53,54] and patients infected with zoonotic HPAI viruses [55,56]. When assessed in an immunocompromised mouse model, baloxavir marboxil returned a significantly prolonged time to death, but ultimately all animals succumbed to the infection [57]. In contrast, treatment with 4'-FlU mediated complete survival of all animals in two distinct immunocompromised mouse models, underscoring powerful antiviral activity that does not strictly depend on a fully immunocompetent host to clear the infection [58]. Adding efficient control of highly pathogenic zoonotic IAVs, we propose that 4'-FlU meets key efficacy requirements of a next-generation antiviral clinical candidate that strengthens pandemic preparedness and provides a much-needed alternative option for management of seasonal and pandemic influenza viruses.

Material and methods

Ethics statement

All animal work was performed in compliance with the *Guide for the Care and Use of Laboratory Animals* of the National Institutes of Health and the Animal Welfare Act Code of Federal Regulations. Experiments involving mice and ferrets were approved by the Georgia State University Institutional Animal Care and Use Committee (IACUC) under protocols A20012 and A21020, respectively. *In vivo* experimentation with HPAI viruses was approved by the University of Georgia at Athens IACUC under protocol A2020 03–033. All experiments using infectious material were approved by the Georgia State University and the University of Georgia at Athens Institutional Biosafety Committees (IBCs) and performed in BSL-2/ABSL-2 or BSL-3/ABSL-3 containment facilities, respectively. Experiments involving highly pathogenic avian influenza (HPAI) viruses were reviewed and approved by the IBC of the University of Georgia at Athens and were conducted in enhanced biosafety level 3 (BSL3+) containment according to guidelines for the use of select agents approved by the Centers for Disease Control and Prevention (CDC).

Study design

Cells, ferrets and mice were used as *in vitro*, *ex vivo* and *in vivo* models, respectively, to examine efficacy of 4'-FlU against influenza infections. Biochemical RdRP assays were added for mechanistic characterization against the influenza virus target. Viruses were administered through intranasal or aerosolized (mice only) inoculation and virus load monitored periodically in nasal lavages (ferrets only), and in respiratory tissues of ferrets and mice extracted 4 days and 3–14 days, respectively, after infection. Virus titers were determined through $TCID_{50}$-titration.

Cells, viruses, and compound synthesis

MDCK (ATCC CCL-34) and 293T (ATCC CRL-3216) cells were cultured in Dulbecco's modified Eagle's medium (DMEM) supplemented with 7.5% heat-inactivated fetal bovine serum (FBS) at 37˚C and 5% CO_2. Human primary cells were grown in epithelial differentiation medium [24]. A/swine/Spain/53207/2004 (H1N1), A/Wisconsin/67/2005 (H3N2), A/California/07/2009 (H1N1)pdm09, A/Netherlands/602/2009 (H1N1)pdm09, A/WSN/33 (H1N1), A/Wyoming/03/2003 (H3N2), B/Memphis/20/1996 (Yamagata), and B/Malaysia/2506/2004

(Victoria) were propagated on MDCK cells using serum-free DMEM supplemented with 0.5% Trypsin. All influenza A viruses were grown at 37˚C, influenza B viruses at 32˚C. A/Viet Nam/1203/2004 (H5N1) and A/duck/Alberta/35/76 (H1N1) were propagated in the allantoic cavity of embryonated hen eggs at 37˚C for 24 or 48 hours, respectively, clarified, aliquoted, and stored at −80˚C. Virus stock titers were determined through $TCID_{50}$-titration or plaque assay (A/Viet Nam/1203/2004 (H5N1)), stocks were stored in aliquots at -80˚C. Recombinant influenza viruses were recovered using an 8-plasmid system generated for A/CA/07/2009 (H1N1) that was based on original reports for laboratory-adapted IAV [59]. Reporter viruses were generated through insertion of a nanoLuc or maxGFP-encoding ORF in frame at the 5'-end of the viral HA ORF, separated by a 2A cleavage site as described for other recombinant IAVs [60]. Genetic stability of the resulting nanoLuc-HA and maxGFP-HA segments was validated through sequence confirmation after 10 consecutive viral passages on MDCK cells. 4'-FlU was synthesized from 5'-(3-chlorobenzoyloxy)-2',3'-di-O-acetyl-4'-fluorouridine and 4N ammonia in methanol as previously described [24], authenticated through elemental analysis, and stored as dry powder. Working aliquots were dissolved in DMSO or 10 mM sodium citrate with 0.5% Tween 80 for *in vitro* and *in vivo* studies, respectively.

Virus titration

Virus samples were serially diluted (10-fold starting at 1:10 initial dilution) in serum-free DMEM supplemented with 0.5% Trypsin (Gibco). Serial dilutions were added to MDCK cells seeded in 96-well plate at 1×10^4 cells per well 24 hours before infection. Infected plates were incubated for 72 hours at 37˚C with 5% CO_2, followed by transfer of culture supernatants to suspension of chicken red blood cells and scoring of wells based on hemagglutination activity. A/Viet Nam/1203/2004 (H5N1) virus and samples were titered by plaque assay; serially diluted 10-fold in DMEM with 2% FBS, added to MDCK cells in 12-well plates and overlaid with DMEM+2% FBS with 1.2% Avicel microcrystalline cellulose. Plates were incubated for 48 hours at 37˚C with 5% CO_2, then washed, fixed with methanol:acetone (80:20), and counter-stained with crystal violet to visualize plaques.

Dose-response assays

Active concentrations (EC_{50} and EC_{90}) of 4'-FlU were calculated through 4-parameter variable slope regression modeling of dose-response assay data, derived from progeny virus yield ($TCID_{50}$) assays, luciferase reporter virus assays, or minigenome assays as specified. To test compound potency, 4-FlU was in all dose-response assays assessed in 3-fold serial dilutions, each tested in 3 independent repeats (biological repeats), with starting concentrations of 20 μM 4'-FlU. Control wells received vehicle (DMSO) volume equivalents. Dose-response assays on MDCK cells and 2D HAE cultures were carried out in 96-well plate format (1.5×10^4 cells/well) or 24-well plate format (1.5×10^5 cells/well), respectively. MDCK cells were infected in serum-free DMEM supplemented with 0.5% TPCK-treated trypsin (Gibco) with an MOI of 0.02 $TCID_{50}$ units/cell, HAE cultures were infected in BronchiaLife media (LifeLine) supplemented with 0.75 μg/ml TPCK-treated trypsin with an MOI of 1.0 $TCID_{50}$ units/cell. Culture supernatants were removed 24 (HAE cultures) or 36–48 hours (MDCK cells) after infection and viral titers determined through $TCID_{50}$ titration. For luciferase reporter viruses, relative luciferase activity was read *in situ* using a BioTek Synergy H1 multi-mode reader and signals normalized according to the formula % relative activity = $(RLU_i - RLU_{min})/(RLU_{max} - RLU_{min}) \times 100$, with RLU_i specifying sample luciferase value, RLU_{min} specifying values from equally transfected, vehicle-treated cells that did not receive the PB2 subunit encoding plasmid, and RLU_{max} specifying values from fully transfected, vehicle-treated cells.

Primary human airway epithelium cultures grown at air-liquid interface

Primary HAEs (3×10^5/well) at passage <3 were seeded on 6.5 mm 0.4 μm pore size polyester transwell inserts (Corning Costar Transwell) and differentiated for at least 21 days at air-liquid interface using Air-Liquid Interface Differentiation Medium (LifeLine Cell Technology). Developing HAEs were washed apically at least once per week to remove mucus. Transepithelial/transendothelial resistance (TEER) was measured every 24 hours for 3 days after infection using an EVOM volt/ohm meter coupled with STX2 electrode (World Precision Instruments). For infection, virus (5,000 $TCID_{50}$ units/transwell) was added apically. Compound was administered to the basolateral chamber, starting with a highest concentration of 0.5 μM 4'-FlU in dose-response assays, and exchanged once daily. Each concentration was tested in three independent replicates (biological repeats). Apically shed virus titers were determined through $TCID_{50}$ titration on MDCK cells as described above.

Minigenome assay

293T cells were seeded and transfected with 1.0 μg of luciferase-encoding reporter plasmid [26] and 0.5 μg each of PB1, PB2, NP and PA expression plasmids derived from A/California/07/2009 (H1N1), A/Viet Nam/1203/2004 (H5N1), and A/Anhui/1/2013 (H7N9), respectively. Three hours post transfection, 4'-FlU or vehicle (DMSO) volume equivalents were added in 3-fold serial dilution series starting at 20 μM 4'-FlU concentration, followed by incubation for 30 hours at 37˚C and determination of luciferase activity using a BioTek Synergy H1 multimode plate reader. Relative activities were calculated according to the formula % relative activity = $(RLU_i - RLU_{min})/(RLU_{max} - RLU_{min}) \times 100$, with RLU_i specifying sample luciferase value, RLU_{min} specifying values from equally transfected, vehicle-treated cells that did not receive the PB2 subunit encoding plasmid, and RLU_{max} specifying values from fully transfected, vehicle-treated cells.

Recombinant IAV RdRP expression and purification

A/CA/07/2009 (H1N1)-derived PA, PB1, and PB2 expression plasmids were subcloned into the pFastbac Dual plasmid expression vector (Invitrogen) with polyhedrin promoter control. An TEV protease-cleavable N-terminal hexahistidine-tag was added to the PA subunit to facilitate purification of the complex through affinity chromatography. The individual plasmids were transformed in DH10bac cells and the resulting bacmid transfected into SF9 cells. After virus recovery, SF9 cells were infected with the three individual viruses in the ratio of 1:1:2. Cells were harvested after 72 hours and lysed in lysis buffer (Tris 50 mM pH 7.4, NaCl 300 mM, NP 40 0.5%, protease inhibitor cocktail, glycerol 10%, TCEP 0.5 mM) on ice for two hours, followed by sonication. Clarified supernatant was incubated at 4˚C for 1 hour with Ni-NTA beads which were pre-equilibrated with Tris 50 mM pH 7.4, NaCl 300 mM, NP 40 0.2%, glycerol 10%, TCEP 0.5 mM containing 20 mM imidazole. After extensive washing with Tris 50 mM pH 7.4, NaCl 300 mM, NP 40 0.2%, glycerol 10%, TCEP 0.5 mM containing 20–50 mM imidazole, protein complexes were eluted in buffer Tris 50 mM pH 7.4, NaCl 300 mM, NP 40 0.2%, glycerol 10%, TCEP 0.5 mM containing 250 mM imidazole. Eluted protein fractions were pooled and loaded on heparin HP columns, which were flushed with buffer A (Tris 50 mM pH 7.4, NaCl 250 mM, glycerol 10%), then 0–100% of buffer B (Tris 50 mM pH 7.4, NaCl 1M, glycerol 10%) diluted in buffer A. The polymerase complex peak was observed in ~80% buffer B, which corresponds to approximately 900 mM NaCl in the buffer. Peak fractions were collected separately and dialyzed against buffer C (Tris/Cl 50 mM pH 7.4, NaCl 150 mM, glycerol 10%) in dialyzing cassettes at 4˚C overnight. Purified protein complexes were harvested, aliquoted and stored at -80˚C until use.

In vitro RdRP primer extension assay

In vitro primer extension assays were carried out essentially as described [24,61]. Briefly, RdRP assay reactions were set up in 20 mM Tris-HCl pH 7.4, 10% glycerol, 1 mM TCEP, 3 mM MnCl2, 2 μM RNA template, 100 μM RNA primer, and nucleotides and 1 μCi of α^{32}P-labelled ATP (Perkin-Elmer) as specified in the figure legends, followed by incubation at 30˚C for 10 minutes. Polymerase complexes were added to the reaction and incubation continued for 1 hour at 30˚C. Reactions were stopped with 1 volume of deionized formamide containing 25 mM ethylenediaminetetraacetic acid (EDTA), followed by a denaturation step at 95˚C. Amplicons were fractionated on 20% polyacrylamide gels with 7M urea, using a Tris-Borate-EDTA electrophoresis buffer. Amplicons were visualized by autoradiography, using a storage phosphor screen BAS IP MS 2040 E (GE Healthcare Life Sciences) and Typhoon FLA 7000 (GE Healthcare Life Sciences) imager. Densitometry analysis was performed using FIJI 2.1.0. To determine enzyme kinetics (V_{max} and K_m), Michaelis-Menten equation was applied in Prism 9.4.1 (GraphPad).

Pharmacokinetic property and tissue distribution profiling in mice

Male and female C57BL/6J mice were rested for 3 days prior to study start. Then, animals were gavaged with 1.5 mg/kg bodyweight 4'-FlU in 10 mM sodium citrate with 0.5% Tween 80, final gavage volume 200 μl. Blood samples (150 μl) were taken at 90 minutes, 3 hours and 12 hours after dosing, cleared (2,000 rpm, 5 minutes, 4˚C), and extracted plasma stored at -80˚C. Organ samples (lung, brain, spleen, heart, kidney and liver) were harvested 12 hours after dosing and snap-frozen in liquid nitrogen. Animal tissues were homogenized with 70% acetonitrile in water that included internal standards. Animal plasma and tissue concentrations of 4'FlU and 4'-FlU-TP were measured by a qualified LC/MS/MS method in MRM mode on a QTRAP 5500 (Sciex, Santa Clara, CA, USA) instrument.

Intranasal infection of mice

Female or male mice (5–8 weeks of age, Balb/c, RAG1 KO or IFNar KO) were purchased from Jackson Laboratories. Upon arrival, mice were rested for at least 3 days, then randomly assigned to study groups and housed under ABSL-2 or ABSL-3 conditions for infections with A/CA/07/2009 (H1N1) recombinants or A/VN12/2003 (H5N1), respectively. Bodyweight was determined twice daily, body temperature determined once daily rectally. For infections, animals were anesthetized with isoflurane or isoflurane/ketamine (H5N1 challenge only), followed by intranasal inoculation with 2.5×10^1 $TCID_{50}$ units/animal of A/CA/07/2009 (H1N1), 1×10^3–1×10^5 $TCID_{50}$ units/animal of GFP or nanoLuc expressing reporter virus versions of A/CA/07/2009 (H1N1), or 6×10^1 of A/VN12/2003 (H5N1). In all cases, virus inoculum was diluted in 50 μl and administered in amounts of 25 μl per nare. Animals were euthanized and organs harvested at predefined time points or when animals reached humane study endpoints.

4'-FlU anti-IAV efficacy studies in mice

Mice were inoculated intranasally with IAV stocks as described, followed by treatment with 4'-FlU at specified dose levels and starting time points through oral gavage. Unless specified otherwise, treatment was continued q.d. Each individual study contained animals receiving equal volumes of vehicle through oral gavage. At study end point, lung tissue was harvested for virus titration or histopathology assessment. For tissue fixation, lungs were perfused using 10% neutral-buffered formalin [10% formalin, NaH_2PO_4 (4 g/liter), and Na_2HPO_4 (6.5 g/liter)], dissected, and fixed for 24 hours. Formalin-fixed lungs were transferred to 70% EtOH after 72 hours, embedded in paraffin, sectioned (5-μm thickness), and stained with hematoxylin and eosin. Slides were evaluated by a licensed pathologist. A pathology score range of 0 to 3 was used to evaluate tissue damage. For analysis of proinflammatory cytokine levels through Bio-plex, lungs of euthanized mice were lavaged with 1 ml sterile PBS to extract BALFs, and cleared BALF analyzed against the Standard Th17-panel (Bio-Rad) according to the manufacturer's instructions.

Efficacy studies in ferrets

Female ferrets (6–10 months of age) were purchased from Triple F Farms. Upon arrival, ferrets were rested for 1 week, then randomly assigned to study groups and housed in groups of three animals under ABSL-2 conditions. In some studies, animals received a temperature sensor for continued telemetric measurement of body temperature. Otherwise, body temperature was determined rectally once daily. Dexmedetomidine/ketamine anesthetized animals were inoculated intranasally with 1×10^5 $TCID_{50}$ units of A/CA/07/2009 (H1N1) in a volume of 500 μl per nare. Nasal lavages were performed twice daily using 1 ml of PBS containing 2× antibiotics-antimycotics (Gibco). Treatment with 4'-FlU through oral gavage followed a q.d. regimen. Ferrets were terminated four days post infection and BALF and organ (lungs, turbinates and tracheas) samples extracted for virus titrations.

Ferret transmission studies

Female ferrets (3–8 months of age) were anesthetized with dexmedetomidine/ketamine and infected intranasally with 1×10^5 $TCID_{50}$ units of A/CA/07/2009 (H1N1) as before. Nasal lavages were performed every 12 hours, bodyweight and temperature determined once daily. Treatment of source animals was initiated 12 or 24 hours after infection at a dose of 2mg/kg bodyweight, and continued q.d. for three doses total. Starting day 2.5 after infection, uninfected and untreated contact animals were added to the infected and treated source ferrets to allow direct-contact transmission, and co-housing continued until termination of the source ferrets on study day 4. Sentinels were subjected to once daily nasal lavages and monitored until study day 10 or, when infectious particles were detected in lavages of contacts of 4'-FlU-treated source animals, study day 14.

Virus titration from tissue samples

Organs were weighed and homogenized in 300 μl PBS using a beat blaster, set to 3 cycles of 30 seconds each at 4˚C, separated by 1-minute rest periods. Homogenates were cleared (10 minutes at 20,000 × g and 4˚C), and cleared supernatants stored at -80˚C until virus titration. Viral titers were expressed as $TCID_{50}$ units per gram input tissue. For A/VN12/2003 (H5N1), lungs were homogenized using a TissueLyzer (Qiagen), clarified by centrifugation, supernatants aliquoted, and then stored at -80˚C. A/VN12/2003 (H5N1) virus titer was determined by plaque assay and expressed as PFU per ml of lung homogenate.

Infection of mice with aerosolized A/CA/07/2009 (H1N1)

An Aeroneb (Kent Scientific) system was used to infect mice (female Balb/c, 6–8 weeks of age) with aerosolized IAV. Conscious animals were transferred to an aerosol chamber placed on a heat pad adjusted to 37˚C to prevent condensation, connected to the nebulizer unit (Aeroneb with palladium mesh) and air pump with airflow restrictor. For condition-finding experiments, the nebulizer chamber was loaded with virus inoculum diluted to 1×10^3–1×10^5 $TCID_{50}$ A/CA/07/2009 (H1N1) per ml in sterile PBS, airflow adjusted to 1 l/minute, and animals continuously exposed for 3, 10, or 30 minutes. For treatment studies, conditions were adjusted to 1×10^5 $TCID_{50}$/ml in sterile PBS, 10 minutes exposure time, and 1 l/minute airflow.

Re-infection of 4'-FlU-experienced mice with A/CA/07/2009 (H1N1)

Mice infected with aerosolized A/CA/07/2009 (H1N1) as above were treated q.d. with 4'-FlU or vehicle as specified, and monitored for 10 weeks or until humane endpoints were reached. Blood was collected 4 and 8 weeks after infection and A/CA/07/2009 (H1N1)-neutralizing antibody titers determined. Treated recoverees were reinfected with homotypic, aerosolized A/CA/07/2009 (H1N1) 10 weeks after the original infection along with a fresh set of naïve animals, followed by monitoring for an additional 14 days and final blood collection at study end. No treatment was administered after reinfection.

Neutralizing antibody titers in mice

Plasma was prepared from blood samples (2,000 rpm, 10 minutes, 4˚C) and stored at -80˚C until analysis. Heat-inactivated plasma was incubated with 100 $TCID_{50}$ units of A/CA/07/2009 (H1N1) for 90 minutes, followed by serial dilution and transfer to MDCK cells, and plates incubated for 3 days at 37˚C. Remaining infectivity was visualized through hemagglutination activity on chicken red blood cells.

Statistical analysis

For statistical analysis of studies consisting of only two groups, unpaired two-tailed t-tests were applied. When comparing more than two study groups, 1-way analysis of variance (ANOVA) or 2-way ANOVA with multiple comparison *post hoc* tests as specified were used to assess statistical difference between samples. Statistical analyses were carried out in Prism version 9.4.1 (GraphPad). The number of individual biological replicates (n values) and exact P values are shown in the figures when possible. The threshold of statistical significance (α) was set to 0.05. All quantitative source data and statistical analyses are shown in S1 and S2 data files, respectively.

Supporting information

S1 Fig. 4'-FlU activity in undifferentiated and differentiated HAE cultures. a) 4'-FlU antiviral activity in 2D HAE cultures. Dose-response assays of 4'-FlU against a A/WSN/33 (H1N1) nano-luciferase reporter virus (WSN-nanoLuc) on undifferentiated HAEs derived from 10 different healthy donors, five male and five female. Lines represent 4-parameter variable slope regression models; symbols show data means ± SD; n = 6. EC_{50} and EC_{90} concentrations are specified. **b)** Dose-response assay of 4'-FlU against pdmCa09 on a well-differentiated HAE culture grown at air-liquid interface. Cultures were infected apically, compound was added to the basolateral chamber; line intersects, and symbols show, geometric means ± SD of apically shed virus (n = 3). EC_{50} and EC_{90} values based on 4-parameter variable slope regression modeling are shown. **c)** TEER measurements of HAE cultures from (b). Symbols show individual measurements (individual transwells); lines intersect, and symbols show, data means ± SD.
(TIF)

S2 Fig. Urea-PAGE fractionation (uncropped) of RNA transcripts. a) Template and primer used in the reaction. **b-e)** Independent repeats of primer extension assay by IAV polymerase. Dashed rectangle shows insert presented in Fig 1E. Replicates were included in quantitations presented in Fig 1E and 1F.
(TIF)

S3 Fig. Clinical signs in 4'-FlU-treated mice used to establish treatment paradigms. a-h) Body weight measurements taken twice daily (a, c, e, g) and rectal body temperature determined once daily (b, d, f, h). Dashed horizontal line specifies humane endpoint of 20% body weight loss; lines intersect, and symbols show, data means ± SD; n values are specified in main Fig 2. Results are shown for lowest efficacious dose (a-b), latest onset of efficacious treatment (c-d), virus clearance (e-f) and minimal number of doses required (g-h) studies.
(TIF)

S4 Fig. Clinical signs in 4'-FlU treated ferrets. a) Continuous telemetric assessment of body temperature of ferrets in the 4'-FlU efficacy study. **b-e)** Once-daily body weight (b, d) and rectal body temperature (c, e) of ferrets involved in the pdmCa09 transmission studies. Lines intersect, and symbols show, data means ± SD. Dashed lines in (a,c,e) represent onset of fever; dashed lines in (b,d) specify predefined endpoint.
(TIF)

S5 Fig. Clinical signs in 4'-FlU-treated mice used in immune response-mitigation study. a-b) Body weight measurements taken twice daily (a), and rectal body temperature determined once daily (b). Lines intersect, and symbols show, data means ± SD; n values are specified in Fig 4. Dashed line in (a) specifies predefined endpoint.
(TIF)

S6 Fig. Changes in select BALF cytokine levels in infected and 4'-FlU-treated mice. IFNy, IL-1b, IL-10, and IL-17a levels present in BALF of animals treated as in Fig 4A are shown, calculated relative to levels at time of infection. Lines intersect, and symbols show, data medians with 95% CI; 2-way ANOVA with Tukey's *post hoc* test; P values are specified.
(TIF)

S7 Fig. Clinical signs of mice involved in mitigation of histopathology study. a-b) Body weight measurements taken twice daily (a), and rectal body temperature determined once daily (b). Lines intersect, and symbols show, data means ± SD. Dashed line in (a) specifies predefined endpoint.
(TIF)

S8 Fig. Photomicrographs of lung tissues. Lungs were extracted on study days 5 or 21 (infected and treated animals only) of all animals examined in this study; tissue section were H&E stained; dashed rectangle shows sections presented in Fig 4E.; magnification 10×; scale bar 100 μm; Br, bronchiole; Bl or arrowhead, blood vessel.
(TIF)

S9 Fig. Detailed histopathological scores of all animals examined in this study. Individual clinical scores for alveolitis, bronchiolitis, perivascular cuffing (PVC), vasculitis, interstitial pneumonia (IP), and pleuritis. Columns show data medians, symbols represent individual animals; 1-way ANOVA with Tukey's *post hoc* test; p values are specified; n values are specified in Fig 4F.
(TIF)

S10 Fig. Clinical signs in pdmCa09-infected immunocompromised mice treated with 4'-FlU. a-c) Shown are body weight measurements taken twice daily (a, c), and rectal body temperature (b, d) determined once daily. Lines intersect, and symbols show, data means ± SD; n values are specified in Fig 5. Results are shown for RAG1 KO (a-b) and IFNAR1 KO (c-d) animals. Dashed lines in (a,c) specify predefined endpoint.
(TIF)

S11 Fig. Set-up of the Aeroneb nebulizer infection system. a-b) Schematic representation of the system (a) and photograph of the assembly (b).
(TIF)

S12 Fig. Variation of duration of animal exposure in the aerosolization chamber. a-b) Body weight measurements taken twice daily (a), and rectal body temperature (b) determined once daily. Lines intersect, and symbols show, data means ± SD. **c)** Lung viral titers determined 4 days after infection. Columns represent geometric means ± SD; symbols show individual animals (n = 4). Dashed line in (a) specifies predefined endpoint.
(TIF)

S13 Fig. Variation of pdmCa09 inoculum amount for infection in the aerosolization chamber. a) Body weight measurements taken twice daily. Lines intersect, and symbols show, data means. **b)** Lung viral titers determined 4 days after infection. Columns represent data mean with range; symbols show individual animals (n = 2). Dashed line in (a) specifies predefined endpoint.
(TIF)

S14 Fig. 4'-FlU efficacy confirmation after infection with aerosolized inoculum virus. a) Efficacy study schematic; n values are specified. **b-c)** Body weight measurements of animals from (a) taken twice daily (a), and rectal body temperature (b) determined once daily. Lines in (b-c) intersect, and symbols show, data means ± SD. **d)** Lung viral titers determined 4 days after infection. Columns represent geometric means ± SD, symbols show individual animals; 1-way ANOVA with Dunnett's *post hoc* test; P values are specified. Dashed line in (d) specifies limit of detection.
(TIF)

S15 Fig. Clinical signs of mice infected and reinfected with pdmCa09. a-d) Body weight measurements taken twice daily (a, c), and rectal body temperature determined once daily (b, d). Lines intersect, and symbols show, data means ± SD. Results are shown for animals after the original infection (a-b) and after homotypic reinfection (c-d). Dashed lines in (a,c) specify predefined endpoint.
(TIF)

S1 Data. All quantitative source data generated in this study.
(XLSX)

S2 Data. All statistical analyses performed for this study.
(XLSX)

Acknowledgments

We thank AC Lowen and SM Kang for IAV and IBV virus isolates and the Georgia State University Department of Animal Resources for Assistance.

Author Contributions

Conceptualization: Richard K. Plemper.

Data curation: Carolin M. Lieber, Megha Aggarwal, Robert M. Cox.

Formal analysis: Carolin M. Lieber, Megha Aggarwal, Julien Sourimant, Alexander A. Kolykhalov, Stephen M. Tompkins, Oliver Planz, Kaori Sakamoto, Richard K. Plemper.

Funding acquisition: Richard K. Plemper.

Investigation: Carolin M. Lieber, Megha Aggarwal, Jeong-Joong Yoon, Robert M. Cox, Hae-Ji Kang, Julien Sourimant, Mart Toots, Scott K. Johnson, Cheryl A. Jones, Zachary M. Sticher, Manohar T. Saindane, Kaori Sakamoto, Richard K. Plemper.

Methodology: Manohar T. Saindane.

Project administration: Michael G. Natchus, Richard K. Plemper.

Supervision: Alexander A. Kolykhalov, Stephen M. Tompkins, George R. Painter, Michael G. Natchus, Richard K. Plemper.

Validation: Richard K. Plemper.

Writing – original draft: Carolin M. Lieber, Richard K. Plemper.

Writing – review & editing: Robert M. Cox, Julien Sourimant, Stephen M. Tompkins, George R. Painter, Michael G. Natchus, Kaori Sakamoto.

References

1. Greenwood M. THE EPIDEMIOLOGY OF INFLUENZA. Br Med J. 1918; 2(3021):563–6. Epub 1918/11/23. https://doi.org/10.1136/bmj.2.3021.563 PMID: 20769264; PubMed Central PMCID: PMC2342100.
2. Sendor AB, Weerasuriya D, Sapra A. Avian Influenza. StatPearls. Treasure Island (FL): StatPearls Publishing, StatPearls Publishing LLC.; 2022.
3. Christie Wilcox TS. Unprecedented Avian Flu Epidemic Could Presage Year-Round Outbreaks 2022. Available from: https://www.the-scientist.com/news-opinion/unprecedented-avian-flu-epidemic-could-presage-year-round-outbreaks-70584?utm_campaign=TS_DAILY_NEWSLETTER_2022&utm_medium=email&_hsmi=228465931&_hsenc=p2ANqtz-8TgW7-yAeXmDwdZXM5FZG2PFR9rD1ZgiLLf7s9vbRNouK_QcXXckHpbv606nJ0vnXWU8KCDXHcq6xrTI8qoiSj6M0XPA&utm_content=228465931&utm_source=hs_email.
4. ECDC. 2021–2022 data show largest avian flu epidemic in Europe ever, last excessed 10/21/2022: European Centre for Disease Prevention and Control; 2022. Available from: https://www.ecdc.europa.eu/en/news-events/2021-2022-data-show-largest-avian-flu-epidemic-europe-ever.
5. Morens DM, Taubenberger JK. Pandemic influenza: certain uncertainties. Rev Med Virol. 2011; 21(5):262–84. Epub 20110627. https://doi.org/10.1002/rmv.689 PMID: 21706672; PubMed Central PMCID: PMC3246071.
6. CDC. History of 1918 Flu Pandemic, last excessed 10/07/2022: Centers for Disease Control and Prevention; 2018. Available from: https://www.cdc.gov/flu/pandemic-resources/1918-commemoration/1918-pandemic-history.htm.
7. Taubenberger JK, Kash JC, Morens DM. The 1918 influenza pandemic: 100 years of questions answered and unanswered. Sci Transl Med. 2019; 11(502). Epub 2019/07/26. https://doi.org/10.1126/scitranslmed.aau5485 PMID: 31341062.
8. Cheung JTL, Lau EH, Jin Z, Zhu H, Guan Y, Peiris M. Influenza A virus transmission in swine farms and during transport in the swine supply chain. Transbound Emerg Dis. 2022; 69(5):e3101–e10. Epub 2022/07/27. https://doi.org/10.1111/tbed.14667 PMID: 35881331.
9. CDC. 2009 H1N1 Pandemic (H1N1pdm09 virus), last excessed 10/07/2022: Centers for Disease Control and Prevention; 2019. Available from: https://www.cdc.gov/flu/pandemic-resources/2009-h1n1-pandemic.html.
10. Yang JH, Huang PY, Shie SS, Yang S, Tsao KC, Wu TL, et al. Predictive Symptoms and Signs of Laboratory-confirmed Influenza: A Prospective Surveillance Study of Two Metropolitan Areas in Taiwan.

Medicine (Baltimore). 2015; 94(44):e1952. Epub 2015/11/12. https://doi.org/10.1097/MD.0000000000001952 PMID: 26554802; PubMed Central PMCID: PMC4915903.

11. Florescu DF, Kalil AC. The complex link between influenza and severe sepsis. Virulence. 2014; 5 (1):137–42. Epub 2013/11/21. https://doi.org/10.4161/viru.27103 PMID: 24253109; PubMed Central PMCID: PMC3916367.

12. Kido H, Chida J, Yao M, Wang S. [Mechanisms of multi-organ failure in severe influenza]. Nihon Rinsho. 2010; 68(8):1565–73. Epub 2010/08/19. PMID: 20715496.

13. Radovanovic M, Petrovic M, Barsoum MK, Nordstrom CW, Calvin AD, Dumic I, et al. Influenza Myopericarditis and Pericarditis: A Literature Review. J Clin Med. 2022; 11(14). Epub 2022/07/28. https://doi.org/10.3390/jcm11144123 PMID: 35887887; PubMed Central PMCID: PMC9316162.

14. Vousden N, Knight M. Lessons learned from the A (H1N1) influenza pandemic. Best Pract Res Clin Obstet Gynaecol. 2021; 76:41–52. Epub 2020/11/05. https://doi.org/10.1016/j.bpobgyn.2020.08.006 PMID: 33144076; PubMed Central PMCID: PMC7550184.

15. CDC. Vaccine Effectiveness: How Well Do Flu Vaccines Work?, last excessed 10/05/2022: Centers for Disease Control and Prevention; 2022. Available from: https://www.cdc.gov/flu/vaccines-work/vaccineeffect.htm.

16. Pleguezuelos O, James E, Fernandez A, Lopes V, Rosas LA, Cervantes-Medina A, et al. Efficacy of FLU-v, a broad-spectrum influenza vaccine, in a randomized phase IIb human influenza challenge study. NPJ Vaccines. 2020; 5(1):22. Epub 2020/03/21. https://doi.org/10.1038/s41541-020-0174-9 PMID: 32194999; PubMed Central PMCID: PMC7069936.

17. CDC. Influenza Antiviral Medications: Summary for Clinicians, last excessed 10/05/2022: Centers for Disease Control and Prevention; 2022. Available from: https://www.cdc.gov/flu/professionals/antivirals/summary-clinicians.htm.

18. Nelson MI, Simonsen L, Viboud C, Miller MA, Holmes EC. The origin and global emergence of adamantane resistant A/H3N2 influenza viruses. Virology. 2009; 388(2):270–8. Epub 2009/04/28. https://doi.org/10.1016/j.virol.2009.03.026 PMID: 19394063; PubMed Central PMCID: PMC2705899.

19. Hussain M, Galvin HD, Haw TY, Nutsford AN, Husain M. Drug resistance in influenza A virus: the epidemiology and management. Infect Drug Resist. 2017; 10:121–34. Epub 2017/05/02. https://doi.org/10.2147/IDR.S105473 PMID: 28458567; PubMed Central PMCID: PMC5404498.

20. CDC. Antiviral Drug Resistance among Influenza Viruses, last excessed 10/07/2022: Centers for Disease Control and Prevention; 2016. Available from: https://www.cdc.gov/flu/professionals/antivirals/antiviral-drug-resistance.htm.

21. Patel MC, Mishin VP, De La Cruz JA, Chesnokov A, Nguyen HT, Wilson MM, et al. Detection of baloxavir resistant influenza A viruses using next generation sequencing and pyrosequencing methods. Antiviral Res. 2020; 182:104906. Epub 2020/08/18. https://doi.org/10.1016/j.antiviral.2020.104906 PMID: 32798601; PubMed Central PMCID: PMC7426223.

22. CDC. Influenza Antiviral Drug Baloxavir Marboxil, last excessed 10/03/2022: Centers for Disease Control and Prevention; 2022. Available from: https://www.cdc.gov/flu/treatment/baloxavir-marboxil.htm.

23. Ince WL, Smith FB, O'Rear JJ, Thomson M. Treatment-Emergent Influenza Virus Polymerase Acidic Substitutions Independent of Those at I38 Associated With Reduced Baloxavir Susceptibility and Virus Rebound in Trials of Baloxavir Marboxil. J Infect Dis. 2020; 222(6):957–61. Epub 2020/04/08. https://doi.org/10.1093/infdis/jiaa164 PMID: 32253432.

24. Sourimant J, Lieber CM, Aggarwal M, Cox RM, Wolf JD, Yoon JJ, et al. 4'-Fluorouridine is an oral antiviral that blocks respiratory syncytial virus and SARS-CoV-2 replication. Science. 2022; 375(6577):161–7. Epub 2021/12/03. https://doi.org/10.1126/science.abj5508 PMID: 34855509.

25. Lieber CM, Plemper RK. 4'-Fluorouridine Is a Broad-Spectrum Orally Available First-Line Antiviral That May Improve Pandemic Preparedness. DNA Cell Biol. 2022; 41(8):699–704. Epub 20220705. https://doi.org/10.1089/dna.2022.0312 PMID: 35788144; PubMed Central PMCID: PMC9416544.

26. Yan D, Weisshaar M, Lamb K, Chung HK, Lin MZ, Plemper RK. Replication-Competent Influenza Virus and Respiratory Syncytial Virus Luciferase Reporter Strains Engineered for Co-Infections Identify Antiviral Compounds in Combination Screens. Biochemistry. 2015; 54(36):5589–604. Epub 2015/08/27. https://doi.org/10.1021/acs.biochem.5b00623 PMID: 26307636; PubMed Central PMCID: PMC4719150.

27. Wu NH, Yang W, Beineke A, Dijkman R, Matrosovich M, Baumgartner W, et al. The differentiated airway epithelium infected by influenza viruses maintains the barrier function despite a dramatic loss of ciliated cells. Sci Rep. 2016; 6:39668. Epub 20161222. https://doi.org/10.1038/srep39668 PMID: 28004801; PubMed Central PMCID: PMC5177954.

28. Kiseleva I, Rekstin A, Al Farroukh M, Bazhenova E, Katelnikova A, Puchkova L, et al. Non-Mouse-Adapted H1N1pdm09 Virus as a Model for Influenza Research. Viruses. 2020; 12(6). Epub 2020/06/04. https://doi.org/10.3390/v12060590 PMID: 32485821; PubMed Central PMCID: PMC7354452.

29. Hayden FG. Prevention and treatment of influenza in immunocompromised patients. Am J Med. 1997; 102(3A):55–60; discussion 75–6. Epub 1997/03/17. https://doi.org/10.1016/s0002-9343(97)80013-7 PMID: 10868144.

30. Kunisaki KM, Janoff EN. Influenza in immunosuppressed populations: a review of infection frequency, morbidity, mortality, and vaccine responses. Lancet Infect Dis. 2009; 9(8):493–504. Epub 2009/07/25. https://doi.org/10.1016/S1473-3099(09)70175-6 PMID: 19628174; PubMed Central PMCID: PMC2775097.

31. Arimori Y, Nakamura R, Yamada H, Shibata K, Maeda N, Kase T, et al. Type I interferon limits influenza virus-induced acute lung injury by regulation of excessive inflammation in mice. Antiviral Res. 2013; 99 (3):230–7. Epub 2013/06/01. https://doi.org/10.1016/j.antiviral.2013.05.007 PMID: 23721943.

32. Jackson. B6(Cg)-Ifnar1tm1.2Ees/J, last excessed 10/08/2022: The Jackson Laboratory; 2022. Available from: https://www.jax.org/strain/028288.

33. Jackson. B6.129S7-Rag1tm1Mom/J, last excessed 10/08/2022: The Jackson Laboratory; 2022. Available from: https://www.jax.org/strain/002216.

34. Bissel SJ, Giles BM, Wang G, Olevian DC, Ross TM, Wiley CA. Acute murine H5N1 influenza A encephalitis. Brain Pathol. 2012; 22(2):150–8. Epub 2011/07/01. https://doi.org/10.1111/j.1750-3639.2011.00514.x PMID: 21714828; PubMed Central PMCID: PMC3204170.

35. Sonoguchi T, Sakoh M, Kunita N, Satsuta K, Noriki H, Fukumi H. Reinfection with influenza A (H2N2, H3N2, and H1N1) viruses in soldiers and students in Japan. J Infect Dis. 1986; 153(1):33–40. Epub 1986/01/01. https://doi.org/10.1093/infdis/153.1.33 PMID: 3941288.

36. Memoli MJ, Han A, Walters KA, Czajkowski L, Reed S, Athota R, et al. Influenza A Reinfection in Sequential Human Challenge: Implications for Protective Immunity and "Universal" Vaccine Development. Clin Infect Dis. 2020; 70(5):748–53. Epub 2019/04/07. https://doi.org/10.1093/cid/ciz281 PMID: 30953061; PubMed Central PMCID: PMC7319262.

37. CDC. Background and Guidance on the Use of Influenza Antiviral Agents, last excessed 10/07/2022: Centers for Disease Control and Prevention; 2016. Available from: https://www.cdc.gov/flu/professionals/antivirals/antiviral-use-influenza.htm.

38. FDA. Influenza (Flu) Antiviral Drugs and Related Information, last excessed 10/03/2022: U.S. Food and Drug Administration; 2020. Available from: https://www.fda.gov/drugs/information-drug-class/influenza-flu-antiviral-drugs-and-related-information.

39. Xiao X, Wang C, Chang D, Wang Y, Dong X, Jiao T, et al. Identification of Potent and Safe Antiviral Therapeutic Candidates Against SARS-CoV-2. Front Immunol. 2020; 11:586572. Epub 2020/12/17. https://doi.org/10.3389/fimmu.2020.586572 PMID: 33324406; PubMed Central PMCID: PMC7723961.

40. Smith LE D'Antoni D, Jain V, Pearce JM, Weinman J, Rubin GJ. A systematic review of factors affecting intended and actual adherence with antiviral medication as treatment or prophylaxis in seasonal and pandemic flu. Influenza Other Respir Viruses. 2016; 10(6):462–78. Epub 2016/07/12. https://doi.org/10.1111/irv.12406 PMID: 27397480; PubMed Central PMCID: PMC5059947.

41. Tchesnokov EP, Obikhod A, Schinazi RF, Götte M. Delayed chain termination protects the anti-hepatitis B virus drug entecavir from excision by HIV-1 reverse transcriptase. J Biol Chem. 2008; 283 (49):34218–28. Epub 2008/10/23. https://doi.org/10.1074/jbc.M806797200 PMID: 18940786; PubMed Central PMCID: PMC2590697.

42. Kokic G, Hillen HS, Tegunov D, Dienemann C, Seitz F, Schmitzova J, et al. Mechanism of SARS-CoV-2 polymerase stalling by remdesivir. Nat Commun. 2021; 12(1):279. Epub 2021/01/14. https://doi.org/10.1038/s41467-020-20542-0 PMID: 33436624; PubMed Central PMCID: PMC7804290.

43. Fukao K, Ando Y, Noshi T, Kitano M, Noda T, Kawai M, et al. Baloxavir marboxil, a novel cap-dependent endonuclease inhibitor potently suppresses influenza virus replication and represents therapeutic effects in both immunocompetent and immunocompromised mouse models. PLoS One. 2019; 14(5): e0217307. Epub 2019/05/21. https://doi.org/10.1371/journal.pone.0217307 PMID: 31107922; PubMed Central PMCID: PMC6527232 Research, Co., Ltd, an affiliation of Shionogi. This does not alter our adherence to PLOS ONE policies on sharing data and materials.

44. Wong ZX, Jones JE, Anderson GP, Gualano RC. Oseltamivir treatment of mice before or after mild influenza infection reduced cellular and cytokine inflammation in the lung. Influenza Other Respir Viruses. 2011; 5(5):343–50. Epub 2011/06/15. https://doi.org/10.1111/j.1750-2659.2011.00235.x PMID: 21668689; PubMed Central PMCID: PMC4942046.

45. Pizzorno A, Abed Y, Rhéaume C, Boivin G. Oseltamivir-zanamivir combination therapy is not superior to zanamivir monotherapy in mice infected with influenza A(H3N2) and A(H1N1)pdm09 viruses. Antiviral Res. 2014; 105:54–8. Epub 2014/03/04. https://doi.org/10.1016/j.antiviral.2014.02.017 PMID: 24583158.

46. Garigliany MM, Habyarimana A, Lambrecht B, Van de Paar E, Cornet A, van den Berg T, et al. Influenza A strain-dependent pathogenesis in fatal H1N1 and H5N1 subtype infections of mice. Emerg Infect Dis.

2010; 16(4):595–603. Epub 2010/03/31. https://doi.org/10.3201/eid1604.091061 PMID: 20350372; PubMed Central PMCID: PMC3321946.

47. Gounder AP, Boon ACM. Influenza Pathogenesis: The Effect of Host Factors on Severity of Disease. J Immunol. 2019; 202(2):341–50. Epub 2019/01/09. https://doi.org/10.4049/jimmunol.1801010 PMID: 30617115; PubMed Central PMCID: PMC6327976.

48. Iwasaki A, Medzhitov R. Control of adaptive immunity by the innate immune system. Nat Immunol. 2015; 16(4):343–53. Epub 2015/03/20. https://doi.org/10.1038/ni.3123 PMID: 25789684; PubMed Central PMCID: PMC4507498.

49. Chern YJ, Tai IT. Adaptive response of resistant cancer cells to chemotherapy. Cancer Biol Med. 2020; 17(4):842–63. Epub 2020/12/11. https://doi.org/10.20892/j.issn.2095-3941.2020.0005 PMID: 33299639; PubMed Central PMCID: PMC7721100.

50. Stannard HL, Mifsud EJ, Wildum S, Brown SK, Koszalka P, Shishido T, et al. Assessing the fitness of a dual-antiviral drug resistant human influenza virus in the ferret model. Commun Biol. 2022; 5(1):1026. Epub 2022/09/29. https://doi.org/10.1038/s42003-022-04005-4 PMID: 36171475; PubMed Central PMCID: PMC9517990 employees of F. Hoffmann-La Roche. All other authors declare no competing interests.

51. Lee N, Chan PK, Hui DS, Rainer TH, Wong E, Choi KW, et al. Viral loads and duration of viral shedding in adult patients hospitalized with influenza. J Infect Dis. 2009; 200(4):492–500. Epub 2009/07/14. https://doi.org/10.1086/600383 PMID: 19591575; PubMed Central PMCID: PMC7110250.

52. de Courville C, Cadarette SM, Wissinger E, Alvarez FP. The economic burden of influenza among adults aged 18 to 64: A systematic literature review. Influenza Other Respir Viruses. 2022; 16(3):376–85. Epub 2022/02/06. https://doi.org/10.1111/irv.12963 PMID: 35122389; PubMed Central PMCID: PMC8983919.

53. Health WSDo. Are you at high risk for flu?, last excessed 10/08/2022. 2022.

54. CDC. Flu Symptoms & Complications, last excessed 10/06/2022. 2022.

55. CDC. HPAI A H5 Virus Background and Clinical Illness, last excessed 10/07/2022. 2015.

56. ECDC. Facts about avian influenza in humans, last excessed 10/10/2022: European Centre for Disease Prevention and Control; 2022. Available from: https://www.ecdc.europa.eu/en/avian-influenza-humans/facts.

57. Kiso M, Yamayoshi S, Murakami J, Kawaoka Y. Baloxavir Marboxil Treatment of Nude Mice Infected With Influenza A Virus. J Infect Dis. 2020; 221(10):1699–702. Epub 2019/12/15. https://doi.org/10.1093/infdis/jiz665 PMID: 31837268; PubMed Central PMCID: PMC7184910.

58. Kimura K, Adlakha A, Simon PM. Fatal case of swine influenza virus in an immunocompetent host. Mayo Clin Proc. 1998; 73(3):243–5. Epub 1998/03/25. https://doi.org/10.4065/73.3.243 PMID: 9511782.

59. Neumann G, Watanabe T, Ito H, Watanabe S, Goto H, Gao P, et al. Generation of influenza A viruses entirely from cloned cDNAs. Proc Natl Acad Sci U S A. 1999; 96(16):9345–50. Epub 1999/08/04. https://doi.org/10.1073/pnas.96.16.9345 PMID: 10430945; PubMed Central PMCID: PMC17785.

60. Nogales A, Ávila-Pérez G, Rangel-Moreno J, Chiem K, DeDiego ML, Martínez-Sobrido L. A Novel Fluorescent and Bioluminescent Bireporter Influenza A Virus To Evaluate Viral Infections. J Virol. 2019; 93 (10). Epub 2019/03/15. https://doi.org/10.1128/JVI.00032-19 PMID: 30867298; PubMed Central PMCID: PMC6498038.

61. Carey MF, Peterson CL, Smale ST. The primer extension assay. Cold Spring Harb Protoc. 2013; 2013 (2):164–73. Epub 2013/02/05. https://doi.org/10.1101/pdb.prot071902 PMID: 23378648.

2.2.4 Influenza A Virus Resistance to 4'-Fluorouridine Coincides with Viral Attenuation In Vitro and In Vivo

bioRxiv preprint doi: https://doi.org/10.1101/2023.10.20.563370; this version posted October 21, 2023.

Influenza A virus resistance to 4'-fluorouridine coincides with viral attenuation *in vitro* and *in vivo*

Carolin M Lieber[1], Hae-Ji Kang[1], Megha Aggarwal[1], Nicole A Lieberman[2], Elizabeth B Sobolik[2], Jeong-Joong Yoon[1], Michael G Natchus[3], Robert M Cox[1], Alexander L Greninger[2], Richard K Plemper[1#]

[1]Center for Translational Antiviral Research, Georgia State University Institute for Biomedical Sciences, Atlanta, GA 30303, USA

[2]Virology Division, Department of Laboratory Medicine and Pathology, University of Washington Medical Center, Seattle, WA 98195, USA

[3]Emory Institute for Drug Development, Emory University School of Medicine, Atlanta, GA 30322, USA

#corresponding author: rplemper@gsu.edu

Abstract

Pre-existing or rapidly emerging resistance of influenza viruses to approved antivirals makes the development of novel therapeutics to mitigate seasonal influenza and improve preparedness against future influenza pandemics an urgent priority. We have recently identified the chain-terminating broad-spectrum nucleoside analog clinical candidate 4'-fluorouridine (4'-FlU) and demonstrated oral efficacy against seasonal, pandemic, and highly pathogenic avian influenza viruses in the mouse and ferret model. Here, we have resistance-profiled 4'-FlU against a pandemic A/CA/07/2009 (H1N1) (CA09). *In vitro* viral adaptation yielded six independently generated escape lineages with distinct mutations that mediated moderate resistance to 4'-FlU in the genetically controlled background of recombinant CA09 (recCA09). Mutations adhered to three distinct structural clusters that are all predicted to affect the geometry of the active site of the viral RNA-dependent RNA polymerase (RdRP) complex for phosphodiester bond formation. Escape could be achieved through an individual causal mutation, a combination of mutations acting additively, or mutations functioning synergistically. Fitness of all resistant variants was impaired in cell culture, and all were attenuated in the mouse model. Oral 4'-FlU administered at lowest-efficacious (2 mg/kg) or elevated (10 mg/kg) dose overcame moderate resistance when mice were inoculated with 10 LD_{50} units of parental or resistant recCA09, demonstrated by significantly reduced virus load and complete survival. In the ferret model, invasion of the lower respiratory tract by variants representing four adaptation lineages was impaired. Resistant variants were either transmission-incompetent, or spread to untreated sentinels was fully blocked by therapeutic treatment of source animals with 4'-FlU.

Author Summary

Reduced sensitivity to FDA-approved influenza drugs is a major obstacle to effective antiviral therapy. We have previously demonstrated oral efficacy of a novel clinical candidate drug, 4'-FlU, against seasonal, pandemic, and highly pathogenic avian influenza viruses. In this

study, we have determined possible routes of influenza virus escape from 4'-FlU and addressed whether resistance imposes a viral fitness penalty, affecting pathogenicity or ability to transmit. We identified three distinct clusters of mutations that lead to moderately reduced viral sensitivity to the drug. Testing of resistant variants against two chemically unrelated nucleoside analog inhibitors of influenza virus, conditionally approved favipiravir and the broad-spectrum SARS-CoV-2 drug molnupiravir, revealed cross-resistance of one cluster with favipiravir, whereas no viral escape from molnupiravir was noted. We found that the resistant variants are severely attenuated in mice, impaired in their ability to invade the lower respiratory tract and cause viral pneumonia in ferrets, and transmission-defective or compromised. We could fully mitigate lethal infection of mice with the resistant variants with standard or 5-fold elevated oral dose of 4'-FlU. These results demonstrate that partial viral escape from 4'-FlU is feasible in principle, but escape mutation clusters are unlikely to reach clinical significance or persist in circulating influenza virus strains.

Introduction

Seasonal influenza viruses cause a significant public health and socioeconomic burden [1, 2]. Approximately one billion people are infected annually worldwide [3], and millions require hospitalization and advanced care. Case fatalities exceed 600,000 in interpandemic years, and can be substantially higher when zoonotic influenza viruses spill over into the human population, causing large-scale pandemics [4]. A multivalent annual influenza vaccine provides moderate protection, but vaccine efficacy is moderate under the best of circumstances, and compromised in particular in the most vulnerable patient populations such as older adults and the immunocompromised [5-7]. Benefit rapidly declines when vaccines are poorly matched with circulating virus strains or when novel, pandemic virus strains emerge [8, 9].

Three different classes of antivirals are currently FDA approved for use against influenza: the adamantes (i.e. amantadine), which block the viral M2 channel [10]; the inhibitors of viral neuraminidase (NA) activity (i.e. oseltamivir phosphate) [11, 12]; and the PA endonuclease blocker baloxavir marboxil [13, 14]. Although originally effective when administered early after infection, each of these classes has a low genetic barrier against viral resistance. Excessive veterinary use of the adamantes has led to widespread preexisting presence of the signature M2 S31N resistance mutation in circulating human and animal influenza A virus (IAV) strains [15, 16], and their use for influenza therapy is no longer recommended by the Centers for Disease Control and Prevention since 2006 [17, 18].

Whereas neuraminidase inhibitors are still in clinical use, resistance mutations emerge rapidly in the viral NA protein in treatment-experienced virus populations and have been found in circulating strains. For instance, over 99% of seasonal H1N1 isolates was oseltamivir-resistant in April 2009, immediately before the emergence of the 2009 swine origin IAV pandemic [19, 20]. Although pandemic 2009 (pdm09) H1N1 strains were initially sensitive to oseltamivir, pre-existing resistance emerged in later stages of the pandemic and high transmission of oseltamivir-resistant pdm09 viruses was detected in some communities [20, 21].

The most recent addition to the antiviral arsenal against influenza, baloxavir marboxil, demonstrated strong efficacy after administration of a single dose [22]. However, treatment-emergent resistance, a signature PA I38T/M/F substitution, appeared almost instantaneously, resulting in rebound of virus replication in 10% of treated patients in a phase 3 clinical trial [14, 23].

The nucleoside analog inhibitor favipiravir, which was conditionally approved in Japan for treatment of pandemic influenza virus infections when other influenza drugs are ineffective [24, 25], has a substantially higher barrier against viral escape. Favipiravir-resistant variants did not emerge in clinical trials [24], but an *in vitro* adaptation identified a K229R mutation in the PB1 subunit of the RdRP complex that reduced viral susceptibility to the drug when combined with a compensatory PA P653L mutation that partially restored viral fitness [26]. It is uncertain, however, whether escape from favipiravir may amount to a clinical problem.

We have recently identified 4'-FlU, an orally efficacious nucleoside analog with broad spectrum activity against multiple positive and negative strand RNA viruses including beta-coronaviruses [27, 28], RSV and paramyxoviruses [27], and both seasonal and highly pathogenic avian influenza viruses [29]. Inducing immediate chain termination of the IAV polymerase, 4'-FlU displayed an unusually wide therapeutic time window in the lethal pdm09 H1N1 mouse model, mediating complete survival of animals when treatment was initiated up to 60 hours after infection [29].

To explore the developmental potential of 4'-FlU for influenza therapy, we resistance profiled the compound in this study and assessed fitness and pathogenesis of resistant recombinants *in vitro* and *in vivo*, employing both the lethal mouse and ferret transmission model. We have identified three distinct clusters that induce moderate resistance to 4'-FlU. All three are predicted to affect the geometry of the central polymerase cavity that harbors the active site for phosphodiester bond formation. Resistance in all cases coincided with viral attenuation *in vitro* and *in vivo*. 4'-FlU treatment at the lowest efficacious (2 mg/kg) and/or moderately elevated (10 mg/kg) dose mediated complete survival after inoculation of animals with 10 LD_{50} of the different resistant strains and suppressed viral transmission. These results define a high genetic barrier of 4'-FlU against influenza virus escape from inhibition.

Results

Dose-response assessment of 4'-FlU against recCA09 returned 50 and 90% inhibitory concentrations (EC_{50} and EC_{90}, respectively) of 0.14 and 0.24 µM (S1 Fig), which was consistent with our previous observations [29].

IAV adaption identifies distinct mutations mediating partial escape from 4'-FlU

Starting with an EC_{90}-equivalent compound concentration, we gradually adapted recCA09 to growth in the presence of 4'-FlU through dose-escalation serial passaging in six independent lineages (Fig 1a). At every passage, progeny virus titers were determined, viral RNA extracted, and fresh cells infected at a controlled multiplicity of infection (MOI) of 0.01 $TCID_{50}$ units/cell. Four additional adaptation lineages were carried out in the presence of vehicle (DMSO) volume equivalents. After 9-10 passages gradually exceeding 2.5 ∝M 4'-FlU, which was the sterilizing concentration of recCA09 at study start (S1 Fig), adaptation candidates replicated productively in the presence of 6 to 20 µM 4'-FlU (Fig 1b), whereas DMSO-experienced virus populations remained fully sensitive to 4'-FlU (Fig 1c). Whole genome sequencing of 4'-FlU-experienced virus populations at study end and selected intermediate passages identified in each lineage at least one, and up to three, point mutations in RdRP subunits that had become allele-dominant, but were absent in the vehicle-treated virus populations (Fig 1d; S1 Table; S1 Data). Two adaptation lineage pairs, #1/#5 and #4/#6, shared one common substitution, PB1 V285I and PB2 488C, respectively (Fig 1e). Although not identical, lineages #2 and #3 harbored allele-dominant mutations in immediate vicinity of each other in PB2 (E191K and K189R, respectively). Other mutations were unique to the individual lineages. Individual mutations in three lineages (#4, #5, and #6) emerged with distinct dynamics, possibly indicating fitness compensatory effects of the substitutions appearing in later passages.

We rebuilt all mutations in polymerase subunits in a recCA09-maxGFP background, which expresses a maxGFP from the HA segment [29, 30]. Infection of MDCK cells with the resulting recombinants in the presence or absence of 4'-FlU revealed different degrees of reduced susceptibility to the inhibitor compared to that of the genetic parent virus (Fig 1f; S2 Fig).

Three pathways to achieve viral resistance to 4'-FlU

To quantify robustness of viral resistance in an otherwise unchanged viral background, we rebuilt in parallel a set of non-reporter recCA09 variants. Dose-response assays against 4'-FlU demonstrated a 2 to 25-fold increase in EC_{99} concentrations of 4'-FlU against the different virus lineages, confirming moderate resistance to 4'-FlU (Fig 2a; S2 Table). A favipiravir-resistant recCA09 carrying the PB1 K229R and PA P653L point mutations previously described [26] showed unchanged sensitivity to 4'-FlU. The inverse experiment, testing the recCA09 panel against nucleosides analogs currently in clinical use for respiratory virus indications, favipiravir and molnupiravir [31, 32], revealed slightly decreased (favipiravir) or increased (molnupiravir) viral susceptibility, but only lineage #4 showed cross-resistance with favipiravir that reached an EC_{99} change >10-fold (Fig 2b and c; S3 and S4 Tables).

Whereas maximal growth rates of resistant viruses were unchanged to that of their genetic parent in multi-step growth curves on MDCK cells, maximal progeny titers reached were reduced by up to 1.5 orders of magnitude (Fig 2d; S5 Table). To directly compare relative fitness of mutants and their genetic parent, we co-infected cells with a 10:1-mixture of mutant to parent, followed by five serial passages with whole genome sequencing of the viral populations after each passage (Fig 2e). Relative allele frequencies of mutations in lineages #1, #2, and #3 plummeted rapidly, indicating a fitness penalty compared to the parent virus (Fig 2f; S2 Data). Lineage #4 co-replicated with the genetic parent without substantial change in relative allele frequencies, and one substitution each of lineages #5 and #6, V285I in PB1 and Y488C in PB2, respectively, disappeared rapidly, whereas others co-existed with the parent allele.

To better differentiate the contribution of discrete mutations to the resistance phenotype, we rebuilt all substitutions individually in recCA09 reporter virus expressing a nano luciferase from the HA segment (recCA09-nanoLuc), followed by luciferase-based dose-response assays (Fig 2g; Table 1; S3 Fig). Three different pathways to viral escape emerged: i) individual mutations caused resistance (i.e. PB1 V285I in lin #1 and #5), sometimes in combination with an enhancer (lin #5); ii) resistance was based on additive effects (i.e. lin #3); or iii) resistance arose from synergy (i.e. lin #2, #4, and #6). In one case (lin #4), the individual role of one mutation (PB2 T491M) could not be assessed, since this substitution was viable only in the context of the PB2 Y488C exchange (Table 1).

None of the combinations of mutations required for moderate resistance to 4'-FlU existed in complete IAV genome sequences available in the NCBI Virus database (S4 Fig). Although some mutations were present individually, all remained below 1% relative frequency except PB1

M339I and PB2 E191K in complete and partial sequences (S6 Table), confirming our previous observation that circulating human and avian IAVs are efficiently inhibited by the compound [29].

Spatial localization implicates resistance mutations with altered RdRP geometry

We localized all resistance mutations in structural models of the influenza virus polymerase complex, built on the coordinates released for influenza virus C (ICV) [33], the 1918 H1N1 IAV [34], and a bat IAV [35] (Fig 3a; S5a to c Fig). The spatial positions of the mutations were virtually identical in the ICV (Fig 3a) and 1918 H1N1 structures (S5a Fig), which are both considered to represent a pre-initiation conformation of the polymerase. However, mechanistic assessment was based on the ICV structure, which represents the intact RdRP complex, whereas the 1918 H1N1 IAV model lacks parts of the PA and PB2 subunits and the bat IAV represents an alternate cap-binding conformation. Most mutations were posited in the central RdRP cavity, either in immediate proximity to the catalytic site for phosphodiester bond formation (lin. #1 and 5; Fig 3b and lin. #4 and 6; Fig 3c) or at positions in short-range proximity to the GDN active site (lin. #2 and 3; Fig 3d). Noticeable exceptions were the PB2 E180K/E191K and PB2 K189R charge-reversal substitutions in lin. #2 and lin. #3, respectively, which may affect structural mobility of PB2 and may alter cap RNA loading into the central cavity.

Overall, altered geometry of the polymerase active site, achieved through combinations of mutations in distinct sets, emerged as the common theme across all resistance lineages (S7 Table). These changes may either increase selectivity of the polymerase complex for substrate triphosphates or, more likely based on *in vitro* RdRP assay results of immediate chain termination [29], increase spatial flexibility at the active site to better accommodate secondary structure changes introduced by incorporation of the 4'-FlU analog into the nascent RNA strand [27, 29]. Structural limits for flexibility appear to be tight, however, since different artificially engineered combinations of independently emerged signature resistance mutations did not result in bioactive polymerase complexes that could support productive virus replication (S8 Table).

These findings pinpoint residues defining the geometry of the central RdRP cavity as instrumental for moderately reduced polymerase susceptibility to inhibition by 4'-FlU, and suggest that the genetic barrier preventing emergence of more robust resistance may be major.

All 4'-FlU-experienced resistant variants are attenuated *in vivo*

In the Balb/cJ mouse model, infection of animals with equal infectious particle amounts of the resistant variants or parent recCA09 followed by daily monitoring of clinical signs provided no indication of enhanced disease (S6 Fig). To compare pathogenicity with parent recCA09, we determined LD_{50} inoculum amounts (Fig 4a). Relative to recCA09, all resistant strains were attenuated, ranging from 25-fold (lin. #4) to 1,000-fold (lin. #5) higher LD_{50} values (Fig 4b to d). Despite the fitness disadvantage *in vitro* and attenuation *in vivo*, genetic stability of the resistant strains was high in mice in the absence of compound (Fig 4e). Relative allele frequency of all mutations but PB1 M290V was near 100% in virus populations isolated from lung tissue 5 to 10 days after infection (S3 Data), when individual animals reached endpoints.

To explore the effect of resistance on *in vivo* drug efficacy, animals were infected with $10\times LD_{50}$ equivalents of each variant, followed 24 hours after infection by five doses of 4'-FlU at 2 (lowest efficacious standard dose) or 10 (elevated dose) mg/kg bodyweight, administered orally q.d. (Fig 4f). Animals in survival groups were monitored for 14 days, lung virus loads were determined in subgroups 4.5 days after infection. Standard dose resulted in complete survival of animals infected with parent recCA09 or all resistant variants except lin. #5, which showed 50% survival (Fig 4g and h; S7 Fig). All vehicle-treated animals succumbed by day 4 after infection. Elevated dose of 4'-FlU resulted in complete survival also of animals infected with lin. #5. Lung virus loads mirrored survival data, showing significant reductions in all cases after both standard and elevated dose of 4'-FlU (Fig 4h). However, effect size was greatest in the case of parent recCA09 and lin. #2 (undetectable after elevated dose) and least pronounced in animals infected with lin. #5.

These data demonstrate that resistant variants are attenuated, albeit still pathogenic in the mouse model. However, moderate resistance to 4’-FlU can be overcome pharmacologically *in vivo*.

4’-FlU prevents transmission of resistant variants in the ferret model

Two resistant variants, lin. #4 and lin. #5, were selected for direct-contact transmission studies in the ferret model based on highest pathogenicity and greatest resistance to 4’-FlU, respectively. Treatment of source ferrets with three oral doses of 4’-FlU at 2 mg/kg bodyweight each was initiated 12 hours after infection and 36-hour\co-housing started 2.5 dpi, after administration of the last compound dose (Fig 5a). Source animals were euthanized at the end of the co-housing period and contacts monitored until study day 8.

Treatment of source animals with 4’-FlU alleviated clinical signs in all study arms (S8 Fig). recCA09 was first detectable in nasal lavages of all sentinels of vehicle-treated ferrets at the end of the contact period (Fig 5b), confirming efficient IAV transmission in the ferret model [29]. Consistent with our previous observations [29], 4’-FlU was highly efficacious of reducing shed virus load in the treated source animals, resulting in a complete block of transmission. Peak shed virus load of recCA09 lin. #4 was reduced in vehicle-treated animals by approximately one order of magnitude compared to parental recCA09 (Fig 5c), whereas recCA09 lin. #5 reached similar peak titers (Fig 5d). However, recCA09 lin. #4 efficiently spread from vehicle-treated source to contact animals, while recCA09 lin. #5 was transmission-incompetent. Oral treatment of recCA09 lin. #4-infected animals with standard dose 4’-FlU completely blocked transmission, suggesting that moderate resistance does not compromise pharmacological control of IAV.

Nasal turbinate (Fig 5e), trachea (Fig 5f), and lung (Fig 5g) titers determined at study end reflected the efficient block of parent and mutant recCA09 transmission by 4’-FlU. Independent of inoculum variant, virus was undetectable in all tissues harvested from sentinels of 4’-FlU-treated source animals. Treatment furthermore suppressed viral invasion of the lower respiratory tract in animals infected with recCA09 (Fig 5f and g). In contrast, trachea load of vehicle-treated animals infected with recCA09 lin. #4 or #5 was reduced by approximately 2.5 orders of magnitude compared to parental recCA09 and viral pneumonia was alleviated in the absence of treatment, confirming attenuation of these variants.

Whole genome sequencing of the different virus populations extracted from animal lungs at study endpoints revealed genetic stability of recCA09 lin. #4 through the course of the study in both source and, after successful transmission from vehicle-treated animals, contact ferrets (Fig 5h; S4 Data). However, both mutations present in the recCA09 lin. #5 inoculum, PA N222S and PB1 V285I, were rapidly counter-selected against in ferrets, resulting in relative allele frequencies of approximately 25 and 5%, respectively, in the vehicle-treated source animals at 4 dpi. Virus load in all other recCA09 lin. #5 groups was too low to support a reliable whole genome analysis.

These data demonstrate that moderate resistance to 4'-FlU is achievable, but in all cases coincided with viral attenuation represented by alleviated clinical signs, reduced tissue virus burden, and impaired invasion of the lower respiratory tract. Even transmission of variants with the most robust resistance phenotype or greatest residual pathogenicity is compromised an/or readily controlled by standard dose 4'-FlU.

Discussion

Pre-existing or rapidly emerging widespread resistance to antiviral countermeasures, both small-molecule drugs and biologics, has undermined antiretroviral monotherapy [36], invalidated the use of first-generation therapeutic antibodies against SARS-CoV-2 [37], negatively impacted COVID-19 vaccine efficacy [38], destroyed efficacy of one of three FDA-approved influenza drug classes [17, 18], and compromises the benefit of a second influenza drug class [39]. Early profiling of the viral escape landscape is therefore essential in drug development. Although there is little precedent for antivirals inducing resistant variants with increased pathogenicity, the prospect of triggering enhanced disease could be catastrophic in the clinic and must be examined prior to formal preclinical development.

The broad-spectrum nucleoside analog inhibitor 4'-FlU is a clinical candidate for different RNA virus indications [27, 29]. If ultimately FDA approved for influenza therapy, the compound will represent a first-in-class, expanding the anti-influenza virus arsenal to four distinct drug types. Compared to allosteric small-molecule drugs, nucleoside analogs typically show a higher genetic barrier against viral escape [40]. Influenza virus escape from the viral mutagen favipiravir can be achieved *ex vivo* through a combination of a causal mutation mediating escape and a compensatory mutation that partially restores viral fitness [26]. These favipiravir-resistant viruses were transmission-competent in the ferret model [41], but their susceptibility to favipiravir treatment was not tested *in vivo* and no resistance to favipiravir emerged in clinical trials [42, 43]. Our IAV adaptation study to 4'-FlU supports five major conclusions:

i) Viral escape from 4'-FlU inhibition is possible, but the genetic barrier to escape is high and robust resistance, defined as an increase in inhibitory concentration by >100-fold, could not be achieved. This result underscores that it is challenging to increase selectivity of the viral polymerase complex for endogenous nucleotides over analog inhibitors without compromising overall RdRP bioactivity. In our previous *in vivo* efficacy studies with 4'-FlU, we did not observe any compound-induced changes in viral polymerase components when 4'-FlU-experienced virus populations reisolated from infected and treated animals were subjected to whole genome sequencing [27, 29]. Although one cannot definitively address the question of whether our *ex vivo* adaptation study was exhaustive, the redundancies of signature resistance mutations across independent adaptation lineages and the paucity of additional mutations arising from viral escape *in vivo* strongly support that major hot-spots of IAV resistance to 4'-FlU have been appreciated in our study.

ii) Remarkably, three distinct avenues to partial resistance to 4'-FlU were available to CA09: a single causal substitution, optionally combined with an enhancer; additive action of mutations of minor phenotypic effect in isolation; and synergy between substitutions, that in isolation do not alter sensitivity to 4'-FlU. The viral fitness landscape especially for some synergistic mutations was extremely narrow, since rebuilding them in isolation (i.e. PB2 T491M) or in subsets (i.e. PB2 Y488C with PA S395N or PB2 T491M with PA S395N) did not result in viable polymerase complexes. The dynamics of gradual acquisition of these mutations in viral adaptation and their disappearance during *ex vivo* co-culture with standard recCA09 are consistent with strong interdependence of specific combinations for RdRP bioactivity. Precedent for synergistic effects of individual mutations leading to reduced viral drug susceptibility was established by drug resistant HIV [44], SARS-CoV-2 escape from protease inhibitors [45], and reduced IAV resistance to neuraminidase [46, 47] and experimental entry [48] inhibitors. Exploitation of three distinct mechanistic pathways to reduce viral susceptibility to inhibition is unique to 4'-FlU, however, and suggests that a dominant hot spot of viral escape that results in robust resistance does not exist. Multiple avenues for viral escape furthermore distinguish 4'-FlU from favipiravir, for which only a single combination carrying resistance was previously identified [26]. Our work expanded the favipiravir resistance panel by a novel combination of substitutions that provided moderate escape from favipiravir. However, introducing the previously identified favipiravir escape mutation [26] into the recCA09 background did not result in resistance to 4'-FlU. Resistance to 4'-FlU did furthermore not coincide with reduced sensitivity to broad-spectrum molnupiravir, establishing a promising foundation for combination therapies with nucleoside analog inhibitors.

iii) Although mechanistically distinct, escape mutations of all lineages located predominantly to the central cavity of the RdRP complex, either in direct proximity to residues contacting the RNA template and nascent strands (i.e. lineages #1, 4, 5, 6) or at domains predicted to affect the spatial orientation of these residues through long-range structural effects. In all cases, these substitutions are predicted to alter the symmetry of the central polymerase cavity, most likely increasing tolerance of the RdRP complex to accommodate secondary structure changes introduced by addition of 4'-FlU to the nascent RNA strand. We have demonstrated previously that 4'-FlU inhibits IAV RdRP by immediate chain termination, but acts as a delayed or sequence context-dependent delayed chain terminator on RSV and SARS-CoV-2 polymerases, respectively [27, 29]. These changes were reflected by corresponding potency differences of 4'-FlU against these viral targets in cell culture. Coincidentally, attempts to resistance profile RSV against 4'-FlU have been unsuccessful to date. We hypothesize that IAV RdRP may have access to a fitness landscape of moderately increased structural flexibility in the central RdRP cavity while maintaining bioactivity, whereas tolerance of RSV and SARS-CoV-2 to accommodate secondary structure changes cannot be further expanded without loss of polymerase function. This notion implies that a hard ceiling of reducing susceptibility to 4'-FlU exists also for IAV RdRP that cannot be broken without eliminating all bioactivity.

iv) Resistant variants are attenuated *in vivo*, albeit not apathogenic, and remaining clinical signs can be mitigated with 4'-FlU therapy. A primary objective of resistance profiling a novel developmental candidate is to establish whether viral escape may coincide with increased pathogenicity. Although rare in response to small-molecule drugs, any risk of triggering enhanced disease would halt further preclinical and clinical development of a compound. Our study returned a clean escape profile for 4'-FlU without any evidence of exacerbated disease by resistant variants in a rodent and non-rodent model. To our surprise, only the least pathogenic resistant variant, based on LD_{50}, could not be fully controlled *in vivo* by standard dose 4'-FlU. The data provide strong evidence, however, that viral escape will not undermine sustained therapeutic benefit of 4'-FlU, since a moderate increase in dose levels fully suppressed clinical signs caused by this variant and resulted in complete survival of infected animals. This feature distinguishes 4'-FlU from non-competitive IAV inhibitors such as baloxavir marboxil and oseltamivir, that do not show a strong direct correlation between resistance and virus fitness penalty.

v) 4'-FlU resistant variants are transmission-impaired, and spread of those with residual transmission competence can be suppressed with 4'-FlU treatment. Two constellations pose a particular risk to trigger the development of wide-spread pre-existing resistance to an antiviral in circulating viruses: an escape mutation that provides a transmission advantage; or a combination of saturating selective pressure on circulating viruses with unaltered transmissibility of resistant variants. The former drove, for instance, the evolution of SARS-CoV-2 variants of concern with increasingly greater transmissibility [38] and the latter is best exemplified by large scale use of the adamantes in the poultry industry, which destroyed clinical benefit of the M2 channel blockers [15, 16]. Neither of these constellations appears to be met in the case of 4'-FlU, since signature resistance mutations of adaptation lineage pair #1/5 interrupted transmission competence and spread of moderately resistant variants of the lineage #4/6 pair could be readily suppressed with 4'-FlU treatment. These results suggest that clinical use of 4'-FlU would be unlikely to promote evolution of circulating IAV strains, thus setting the stage for long-term therapeutic benefit.

Although results in cell culture and rodent and non-rodent *in vivo* models of IAV infection support that the 4'-FlU resistance profile determined in this study is not limited to a specific experimental system, it is currently unknown whether *ex vivo* and animal model-based results of viral attenuation equally apply to the human host. Other limitations of the study include that individual resistance mutations could be IAV strain and/or subtype specific, that the specific structural state of the RdRP complex targeted by the inhibitor is unknown, and that human dose levels, and therefore by extension drug tissue exposure in the clinic, are currently undetermined. These precautions notwithstanding, this study defines mechanisms reducing susceptibility of the IAV polymerase complex to a chain-terminating nucleoside analog inhibitor and demonstrate in rodent and non-rodent animals models that influenza virus escape from the developmental drug 4'-FlU is mandatorily linked to viral attenuation and reduced transmission competence.

Material and Methods

Study design

Cells, mice, and ferrets were used as *in vitro* and *in vivo* models to examine the resistance profile of 4'-FlU against influenza viruses. *In silico* modelling was added for mechanistic characterization. Viruses were administered through intranasal inoculation and virus load monitored periodically in nasal lavages (ferrets only), and in respiratory tissues of ferrets and mice extracted 4 days (mice and ferrets) and 8 days (ferret contacts) after infection. Virus titers were determined through 50% tissue culture infectious dose ($TCID_{50}$) titration.

Cells and Viruses

HEK293T human kidney cells (293T; ATCC® CRL-3216) and Madin-Darby canine kidney cells (MDCK; ATCC® CCL-34™) were maintained at 37°C and 5% CO_2 in Dulbecco's Modified Eagle's medium (DMEM) supplemented with 7.5% fetal bovine serum (FBS). Mammalian cell transfections were performed using GeneJuice transfection reagent (Invitrogen).

$TCID_{50}$ titration

For virus titrations, MDCK cells were seeded in 96-well plates (1.5×10^4 cells/well) in 8 replicates/dilution tested. Virus samples were serially diluted 10-fold, and diluents transferred to each well. After incubation at 37°C for 72 hours, viral presence in culture supernatants was determined by hemagglutination assay using 0.5% chicken erythrocytes or direct assessment through fluorescence microscopy in the case of GFP-expressing recCA09 reporter viruses. Raw data were analyzed by the Reed and Muench method.

Virus adaptation

MDCK cells were infected with IAV recCA09-GFP at an MOI of 0.01 $TCID_{50}$ units/ml and incubated with 0.25 µM of 4'-FlU or DMSO. Green fluorescence was monitored as a marker for virus replication and virus populations were harvested based on fluorescence saturation. Virus populations were titered after each passage. Fresh MDCK cells were infected with the harvested virus populations at an MOI of 0.01 $TCID_{50}$ units/cell in the presence of 4'-FlU at specified concentrations or vehicle (DMSO) volume equivalents. Each passage was MOI controlled and the drug concentration kept fixed or doubled for the subsequent passage depending on visual assessment of fluorescence intensity. Viral RNA was isolated from different passages of all lineages for whole genome sequence analysis.

Sequencing

For the determination of viral RNA from stocks and supernatants/organ homogenates, Quick-RNA Viral Kit (Zymo Research) was used and cDNA copies were generated using random hexamer primers and SuperScript III reverse transcriptase (Invitrogen). To identify mutated genomic regions, RNA extracts of virus populations were subjected to Sanger and/or whole genome sequencing as specified.

qPCR for CA09 matrix and hemagglutinin

RT-qPCR was used to measure IAV RNA abundance. Primers and probes were designed to hybridize to the matrix or hemagglutinin sequences. AgPath-ID™ One-Step RT-PCR reagents (Thermo AM1005) kit was used according to manufacturer's instructions. Amplifications were carried out on a QuantStudio5 (Thermo # A34322) instrument.

Sequencing protocol selection

All viral samples derived from *in vitro* experiments were sequenced by shotgun metagenomics. All samples derived from *in vivo* studies were sequenced using hybridization capture (only exception sample "ferret WT-C1-1: wildtype untreated contact replicate 1", which was sequenced by amplification of the genomic RNA segments with primers specific for the homologous termini of each genomic segment).

Metagenomic cDNA synthesis

Metagenomic sequencing libraries were prepared by DNAse-treatment of RNA extracts, followed by double-stranded cDNA synthesis, bead-linked tagmentation and adapter-ligation of double-stranded cDNA, cycle-limited amplification of tagmented cDNA with primer pairs that contain unique 10nt indexes. The indexed libraries were normalized and pooled for 1 × 101 or 2 × 151 cycle sequencing. Before cDNA synthesis, RNA extracts were treated with Turbo DNAse

(Thermo #AM1907). After DNA digest, first-strand cDNA synthesis was performed using SuperScript IV (Thermo #18090010) and random hexamers (Thermo #N8080127).

Subsequent second-strand synthesis was performed using the Sequenase 2.0 kit (Thermo #70775Z1000UN) and amplicons cleaned with 1.8 × AMPure XP magnetic beads (Beckman Coulter #A63882). Purified cDNA samples were stored at -20°C until library preparation.

Metagenomic DNA library preparation

Metagenomic libraries were prepared from the double-stranded cDNA using the Illumina DNA Prep with Enrichment Kit (Illumina #20025524) and IDT® for Illumina® DNA/RNA UD Indexes Set D (Illumina #20042667). Concentrations of 1.8 × AMPure XP magnetic bead purified libraries were measured using Qubit™ 1× dsDNA High Sensitivity Assay Kit (Thermo #Q33231) and a Qubit™ Flex Fluorometer (Thermo #Q33327). Library concentrations were normalized and libraries were pooled. The average library size for the pool was determined using an Agilent DNA D1000 Tape Station kit (Agilent #5067).

Illumina respiratory virus hybridization capture

Hybridization capture was performed with an Illumina RNA Prep with Enrichment (L) Tagmentation kit (Illumina #20040537), IDT for Illumina DNA/RNA UD Indexes (Illumina #20027213), and Respiratory Virus Oligo Panel v2 (Illumina #20044311). Tagmented cDNAs were amplified to add indexes and adapters, and the resulting libraries normalized using Qubit for 1- or 3-plex enrichment by hybridization to sequence-specific biotinylated probes. The captured sequences were washed, eluted, and amplified to generate copies of the enriched libraries, which were further amplified and cleaned with AMPure XP Beads, normalized, and pooled for 1 × 101 or 2 × 151 cycle sequencing on an Illumina NovaSeq or NextSeq2000 instrument.

IAV whole genome sequencing by amplification

Three primers that hybridize to the 12 nucleotides at the 3’ end and 13 nucleotides at the 5’ end of each IAV genomic RNA segment were used to amplify the viral genome: Uni12/Inf-1 (5′-

GGGGGGAGCAAAAGCAGG-3′), Uni12/Inf-3 (5′-GGGGGGAGCGAAAGCAGG-3’), and Uni13/Inf-1 (5′-CGGGTTATTAGTAGAAACAAGG-3′) [49]. One-step RT-PCR was performed using the Superscript III One-Step RT-PCR System with HiFi Platinum Taq DNA polymerase (Thermo #12574035). After amplification, samples were cleaned with 0.8 × AMPure XP Beads (Beckman Coulter #A63882) and products fractionated on a 1.2 % Lonza FlashGel to visualize sizes. Of the cleaned PCR product, 25-100 ng were used to prepare sequencing libraries.

Sequencing data processing

Sequencing reads from raw FASTQ files were trimmed and filtered using fastp. The reads were trimmed to remove adapter sequences and long homopolymer sequences (>10 base pairs). Reads with more than 50 % unqualified bases (phred <15) and reads shorter than 50 base pairs for 101 bp cycles or shorter than 75 bp for 151 bp cycles were filtered from downstream analysis. After trimming and filtering, reads from Influenza A/California/07/2009 (H1N1) cultured in MDCK cells were assembled into a consensus sequence using REVICA (https://github.com/greninger-lab/revica) with the A/California/07/2009 (H1N1) isolate sequence (RefSeq GCF_001343785.1 [50]) as the initial reference. This wildtype inoculum consensus sequence was used as the reference for variant analysis in the subsequent experiments. Variant analysis was performed using RAVA (https://github.com/greninger-lab/lava/tree/Rava_Slippage-Patch). Samples with average depth <20 were excluded from the *in vitro* sequencing experiments. Samples with depth <20 at any of the lineage-associated mutation loci were excluded from the *in vivo* sequencing experiments. *In vivo* samples with low coverage by hybridization capture were re-sequenced. The reads from each replicate were analyzed separately, then combined if both replicates had similar allele frequencies at each lineage-associated locus. Raw reads are available in NCBI BioProject PRJNA1028360 (S1 to S4 Data).

Recovery of recCA09 variants

HEK 293T cells (2.5 × 10^5/ml) were seeded in 6-well plates with DMEM (7.5 % FBS). After overnight incubation, wells were transfected with 0.5 µg DNA total concentration of eight (NA, M1, NP, NS, PA, PB1, PB2, HA/HA-nLuc/HA-maxGFP) viral plasmids, followed by 14-hour incubation and media replacement with DMEM containing 1 µg/ml tosylsulfonyl phenylalanyl chloromethyl keton (TPCK)-trypsin. Two days after media replacement, 2 ml of cell culture supernatant was collected and transferred to fresh MDCK cells, followed by incubation for 2 days collection of culture supernatants, amplification of recovered virus populations, and $TCID_{50}$ titration. Total RNA was extracted from the infected MDCK cell supernatants and viral genomes authenticated by Sanger sequencing and/or whole genome sequencing.

Dose-response inhibition assays

To measure inhibition of recCA09-nanoLuc reporter viruses, 3-fold serial dilutions of 4'-FlU were prepared in 96-well plate format. MDCK cells were seeded in white-clear bottom 96 well plates (1.5 × 10^4 cells/well) and 4'-FlU serial dilutions added. After incubation for 30 hours, luciferase activities in each well were determined, and raw data normalized for equally infected wells that had received vehicle (DMSO) volume equivalents. For virus yield-based dose-response assays with non-reporter viruses, MDCK cells were plated in 24 well plates (1 × 10^5/well), infected with the different virus lineages as specified (MOI 0.01 $TCID_{50}$ units/cell), and compound added in 3-fold serial dilutions. After 3 days of incubation, progeny virus titers were measured by $TCID_{50}$ titration.

Fluorescence microscopy

MDCK cells were plated in 96 well plates (1.5 × 10^4/well) and incubated overnight. Following infection with an MOI of 0.01 $TCID_{50}$ units/cell and addition of 4'-FlU after removal of the virus inoculum, plates were incubated for 60 hours at 37°C. Microphotographs were taken at 10× magnification at a ZEISS Observer.D1 fluorescence microscope, using the X-Cite Series 120Q; AxioCam MRc software package (AxioVision Rel. 4.8). All fluorescence conditions were examined and documented in two independent repeats.

Viral fitness tests

MDCK cells (2.5 × 10^5/well) in 6-well plate format were infected with a mixture of mutant and genetic parent recCA09 at an MOI ratio of 0.1 (mutant) to 0.01 (WT) $TCID_{50}$ units/cell. Culture supernatants were harvested after 72-hour incubation, subjected to $TCID_{50}$ titration and total RNA extraction, and infection of fresh MDCK cells at an MOI of 0.01 $TCID_{50}$ units/cell. The procedure was repeated for a total of 5 passages and all RNA extracts subjected to whole genome sequencing.

Viral growth curves

95%-confluent MDCK cells were infected with mutated influenza viruses at an MOI of 0.01 $TCID_{50}$ units/cell, followed by incubation in TPCK-trypsin media at 37°C and 5% CO_2. Cell supernatants were harvested in 12-hour intervals for a total experiment window of 84 hours and progeny virus titers determined through $TCID_{50}$ titration. Growth curves for each variant were generated in three independent experimental repeats.

Homology modeling and structural mapping of 4'-FlU resistance mutations

Homology models of H1N1 CA09 polymerase were generated based on the coordinates reported for influenza C (PDBID 5d9a) [33] or bat influenza A (PDB 4wsb) [35] polymerase. Homology models were generated using the SWISS-MODEL homology modeling server. Spatial organization of 4'-FlU mutations was determined by mapping each mutation in Pymol. The structure of authentic 1918 H1N1 influenza polymerase (PDBID 7ni0) [34] was used to verify the accuracy of homology models. Although each structure analyzed were in pre-initiation states, the locations of all identified mutations, except Y488C and T491M, were conserved across all models. The positions of the Y488C and T491M differed between the homology model based on the bat influenza virus (PDBID 4wsb) and the other structures, reflecting a different orientation of the PB2 cap binding domain.

Sequence alignments

Mutated residues were aligned to all complete and partial influenza A virus sequences available in the NIH NCBI Virus sequence database. FASTA files were downloaded and opened in MAFFT version 7. Sequences were aligned and alignments downloaded, opened in Jalview (2.11.2.7), and the relative frequencies of allele polymorphisms at 4'-FlU resistance sites determined.

Intranasal infection of mice

Female mice (6-8 weeks of age, Balb/c) were purchased from Jackson Laboratories. Upon arrival, mice were rested for at least 5 days, then randomly assigned to study groups and housed under ABSL-2 conditions for infections with recCA09. Bodyweight was determined twice daily, body temperature determined once daily rectally. For infections, animals were anesthetized with isoflurane, followed by intranasal inoculation with $1\times10^{0} – 5\times10^{3}$ $TCID_{50}$ units/animal of recCA09 variants. In all cases, virus inoculum was administered in amounts of 50 µl/animal (25 µl/nare). Animals were euthanized and organs harvested at predefined time points or when animals reached predefined humane endpoints.

Pathogenicity and efficacy studies in mice

Mice were inoculated intranasally with IAV stocks as above, followed in efficacy studies by q.d. oral treatment with 4'-FlU at 2 or 10 mg/kg BW, starting 24 hours after infection, for 5 doses total. Each study contained animals receiving equal volumes of vehicle through oral gavage. At study end, lung tissues were harvested and subjected to virus titration or RNA extraction and whole genome sequencing.

Ferret transmission studies

Female ferrets (5-8 months of age) were purchased from Triple F Farms. Upon arrival, ferrets were rested for 1 week, then randomly assigned to study groups and housed under ABSL-2+ conditions. Bodyweight and body temperature (rectally) were determined once daily. Dexmedetomidine/ketamine anesthetized animals were inoculated intranasally with 1×10^{5}

$TCID_{50}$ units of recCA09 in a volume of 500 µl per nare (1,000 µl per animal). Nasal lavages were performed twice daily using 1 ml of PBS containing 2× antibiotics-antimycotics (Gibco). Oral treatment with 2 mg/kg bodyweight 4'-FlU or vehicle control (source animals only) was initiated 12 hours after infection, and continued q.d. for 3 doses total. Beginning 2.5 dpi, uninfected and untreated contact animals were added to the infected and treated source ferrets in a 1:1-ratio to allow direct-contact transmission. Co-housing continued until termination of the source ferrets 4 days after the original infection. Respiratory tissue samples (lungs, tracheas, and nasal turbinates) were extracted for virus titrations and whole genome sequencing (lungs only). Sentinels were subjected to once daily nasal lavages and monitored until study day 8, when respiratory tissues were harvested and analyzed.

Virus titration and whole genome sequencing from *in vivo* tissue samples

Organs were weighed and homogenized in 300 µl PBS (for titrations) or 300 µl RLT (for RNA extraction) using a beat blaster, set to 3 cycles of 30 seconds each at 4°C, interspersed with 30-second rest periods. Homogenates were cleared (10 minutes at 10,000 × g and 4°C), and cleared supernatants stored at -80°C until virus titration/ spin through a QIA shredder column (Qiagen). Viral titers were expressed as $TCID_{50}$ units per gram source tissue.

Statistical analyses and software

For statistical analysis of studies consisting of two groups, unpaired two-tailed t-tests were applied. When comparing more than two study groups, 1-way or 2-way analysis of variance (ANOVA) with multiple comparison *post hoc* tests as specified were used to assess statistical difference between samples. The number of individual biological replicates (n values) and exact P values are shown in the figures or schematics. The threshold of statistical significance (α) was set to 0.05. Source data and statistical analysis are shown in the S5 Data and S6 Data files, respectively. Statistical analyses were carried out in Prism version 10.0.3 (GraphPad), graphs were assembled in R, Prism 10.0.3, Adobe illustrator 2022, or PyMOL. Sequence alignments were performed with MAFFT version 7 and Jalview 2.11.2.7. Cartoons and study design overviews were created in Biorender and assembled in Adobe Illustrator 2022.

Ethical compliance

All animal work was performed in compliance with the *Guide for the Care and Use of Laboratory Animals* of the National Institutes of Health and the Animal Welfare Act Code of Federal Regulations. Experiments involving mice and ferrets were approved by the Georgia State University Institutional Animal Care and Use Committee (IACUC) under protocols A20012 and A21020, respectively. All experiments using infectious material were approved by the Georgia State University Institutional Biosafety Committee (IBC) and performed in BSL-2/ABSL-2+ containment facilities.

Acknowledgements

We thank the Georgia State University Department of Animal Resources for assistance, M. T. Saindane for chemical synthesis, and A. I. Leach and M. R. Sirrine for help with sequence data analysis. This works was supported, in part, by Public Health Service Grant AI141222 from the NIH/NIAID.

Competing Interests

MGN is a coinventor on patent WO 2019/1736002 covering composition of matter and use of 4'-FlU (EIDD-2749) and its analogs as an antiviral treatment. This study could affect his personal financial status. RKP reports contract testing from Enanta Pharmaceuticals and Atea Pharmaceuticals, and research support from Gilead Sciences, outside of the described work. ALG reports contract testing from Abbott, Cepheid, Novavax, Pfizer, Janssen and Hologic, research support from Gilead, outside of the described work. All other authors declare that they have no competing interests.

References

1. Putri W, Muscatello DJ, Stockwell MS, Newall AT. Economic burden of seasonal influenza in the United States. Vaccine. 2018;36(27):3960-6. Epub 2018/05/29. doi: 10.1016/j.vaccine.2018.05.057. PubMed PMID: 29801998.

2. Dhanasekaran V, Sullivan S, Edwards KM, Xie R, Khvorov A, Valkenburg SA, et al. Human seasonal influenza under COVID-19 and the potential consequences of influenza lineage elimination. Nat Commun. 2022;13(1):1721. Epub 2022/04/02. doi: 10.1038/s41467-022-29402-5. PubMed PMID: 35361789; PubMed Central PMCID: PMCPMC8971476.

3. Flu FF. Insights on Influenza 2022 [updated February 9, 2022; cited 2023 September 20]. Available from: https://www.familiesfightingflu.org/number-of-flu-cases-worldwide/#:~:text=An%20estimated%201%20billion%20people,due%20to%20flu%20each%20year.

4. Kilbourne ED. Influenza pandemics of the 20th century. Emerg Infect Dis. 2006;12(1):9-14. Epub 2006/02/24. doi: 10.3201/eid1201.051254. PubMed PMID: 16494710; PubMed Central PMCID: PMCPMC3291411.

5. Smetana J, Chlibek R, Shaw J, Splino M, Prymula R. Influenza vaccination in the elderly. Hum Vaccin Immunother. 2018;14(3):540-9. Epub 2017/07/15. doi: 10.1080/21645515.2017.1343226. PubMed PMID: 28708957; PubMed Central PMCID: PMCPMC5861798.

6. Bosaeed M, Kumar D. Seasonal influenza vaccine in immunocompromised persons. Hum Vaccin Immunother. 2018;14(6):1311-22. Epub 2018/02/28. doi: 10.1080/21645515.2018.1445446. PubMed PMID: 29485353; PubMed Central PMCID: PMCPMC6037456.

7. Hughes K, Middleton DB, Nowalk MP, Balasubramani GK, Martin ET, Gaglani M, et al. Effectiveness of Influenza Vaccine for Preventing Laboratory-Confirmed Influenza Hospitalizations in Immunocompromised Adults. Clin Infect Dis. 2021;73(11):e4353-e60. Epub 2021/01/04. doi: 10.1093/cid/ciaa1927. PubMed PMID: 33388741; PubMed Central PMCID: PMCPMC8664442.

8. Tricco AC, Chit A, Soobiah C, Hallett D, Meier G, Chen MH, et al. Comparing influenza vaccine efficacy against mismatched and matched strains: a systematic review and meta-analysis. BMC Med. 2013;11:153. Epub 2013/06/27. doi: 10.1186/1741-7015-11-153. PubMed PMID: 23800265; PubMed Central PMCID: PMCPMC3706345.

9. Costa JCD, Siqueira MM, Brown D, Lopes JO, Costa BCD, Gama EL, et al. Vaccine Mismatches, Viral Circulation, and Clinical Severity Patterns of Influenza B Victoria and Yamagata Infections in Brazil over the Decade 2010-2020: A Statistical and Phylogeny-Trait Analyses. Viruses. 2022;14(7). Epub 2022/07/28. doi: 10.3390/v14071477. PubMed PMID: 35891457; PubMed Central PMCID: PMCPMC9321334.

10. Nisar T, Sutherland-Foggio H, Husar W. Antiviral amantadine. Lancet Neurol. 2019;18(12):1080. Epub 2020/01/25. doi: 10.1016/s1474-4422(19)30361-8. PubMed PMID: 31973807.

11. Parra-Rojas C, Nguyen VK, Hernandez-Mejia G, Hernandez-Vargas EA. Neuraminidase Inhibitors in Influenza Treatment and Prevention-Is It Time to Call It a Day? Viruses. 2018;10(9). Epub 2018/08/29. doi: 10.3390/v10090454. PubMed PMID: 30149615; PubMed Central PMCID: PMCPMC6163920.

12. Jefferson T, Jones MA, Doshi P, Del Mar CB, Hama R, Thompson MJ, et al. Neuraminidase inhibitors for preventing and treating influenza in adults and children. Cochrane Database Syst Rev. 2014;2014(4):Cd008965. Epub 2014/04/11. doi: 10.1002/14651858.CD008965.pub4.

13. Dufrasne F. Baloxavir Marboxil: An Original New Drug against Influenza. Pharmaceuticals (Basel). 2021;15(1). Epub 2022/01/22. doi: 10.3390/ph15010028. PubMed PMID: 35056085; PubMed Central PMCID: PMCPMC8779813.

14. Hayden FG, Sugaya N, Hirotsu N, Lee N, de Jong MD, Hurt AC, et al. Baloxavir Marboxil for Uncomplicated Influenza in Adults and Adolescents. N Engl J Med. 2018;379(10):913-23. Epub 2018/09/06. doi: 10.1056/NEJMoa1716197. PubMed PMID: 30184455.

15. Wang J, Wu Y, Ma C, Fiorin G, Wang J, Pinto LH, et al. Structure and inhibition of the drug-resistant S31N mutant of the M2 ion channel of influenza A virus. Proc Natl Acad Sci U S A. 2013;110(4):1315-20. Epub 2013/01/11. doi: 10.1073/pnas.1216526110. PubMed PMID: 23302696; PubMed Central PMCID: PMCPMC3557100 W.F.D., R.A.L., M.L.K., and L.H.P. are members of the scientific advisory board of Influmedix, Inc.

16. Thomaston JL, DeGrado WF. Crystal structure of the drug-resistant S31N influenza M2 proton channel. Protein Sci. 2016;25(8):1551-4. Epub 2016/04/16. doi: 10.1002/pro.2937. PubMed PMID: 27082171; PubMed Central PMCID: PMCPMC4972211.

17. Hersh AL, Maselli JH, Cabana MD. Changes in prescribing of antiviral medications for influenza associated with new treatment guidelines. Am J Public Health. 2009;99 Suppl 2(Suppl 2):S362-4. Epub 2009/10/08. doi: 10.2105/ajph.2009.171462. PubMed PMID: 19797750; PubMed Central PMCID: PMCPMC4504359.

18. Hayden FG. Antiviral resistance in influenza viruses--implications for management and pandemic response. N Engl J Med. 2006;354(8):785-8. Epub 2006/02/24. doi: 10.1056/NEJMp068030. PubMed PMID: 16495389.

19. Storms AD, Gubareva LV, Su S, Wheeling JT, Okomo-Adhiambo M, Pan CY, et al. Oseltamivir-resistant pandemic (H1N1) 2009 virus infections, United States, 2010-11. Emerg Infect Dis. 2012;18(2):308-11. Epub 2012/02/07. doi: 10.3201/eid1802.111466. PubMed PMID: 22305467; PubMed Central PMCID: PMCPMC3310472.

20. Calatayud L, Lackenby A, Reynolds A, McMenamin J, Phin NF, Zambon M, et al. Oseltamivir-resistant pandemic (H1N1) 2009 virus infection in England and Scotland, 2009-2010. Emerg Infect Dis. 2011;17(10):1807-15. Epub 2011/10/18. doi: 10.3201/eid1710.110117. PubMed PMID: 22000349; PubMed Central PMCID: PMCPMC3310668.

21. Le QM, Wertheim HF, Tran ND, van Doorn HR, Nguyen TH, Horby P. A community cluster of oseltamivir-resistant cases of 2009 H1N1 influenza. N Engl J Med. 2010;362(1):86-7. Epub 2009/12/17. doi: 10.1056/NEJMc0910448. PubMed PMID: 20007549.

22. Baker J, Block SL, Matharu B, Burleigh Macutkiewicz L, Wildum S, Dimonaco S, et al. Baloxavir Marboxil Single-dose Treatment in Influenza-infected Children: A Randomized, Double-blind, Active Controlled Phase 3 Safety and Efficacy Trial (miniSTONE-2). Pediatr Infect Dis J. 2020;39(8):700-5. Epub 2020/06/10. doi: 10.1097/inf.0000000000002747. PubMed PMID: 32516282; PubMed Central PMCID: PMCPMC7360097.

23. Jones JC, Pascua PNQ, Harrington WN, Webby RJ, Govorkova EA. Multiple polymerase acidic (PA) I38X substitutions in influenza A(H1N1)pdm09 virus permit polymerase activity and cause reduced baloxavir inhibition. J Antimicrob Chemother. 2021;76(4):957-60. Epub 2020/12/23. doi: 10.1093/jac/dkaa527. PubMed PMID: 33351916; PubMed Central PMCID: PMCPMC7953318.

24. Shiraki K, Daikoku T. Favipiravir, an anti-influenza drug against life-threatening RNA virus infections. Pharmacol Ther. 2020;209:107512. Epub 2020/02/26. doi: 10.1016/j.pharmthera.2020.107512. PubMed PMID: 32097670; PubMed Central PMCID: PMCPMC7102570.

25. Doi Y, Hibino M, Hase R, Yamamoto M, Kasamatsu Y, Hirose M, et al. A Prospective, Randomized, Open-Label Trial of Early versus Late Favipiravir Therapy in Hospitalized Patients with COVID-19. Antimicrob Agents Chemother. 2020;64(12). Epub 2020/09/23. doi: 10.1128/aac.01897-20. PubMed PMID: 32958718; PubMed Central PMCID: PMCPMC7674035.

26. Goldhill DH, Te Velthuis AJW, Fletcher RA, Langat P, Zambon M, Lackenby A, et al. The mechanism of resistance to favipiravir in influenza. Proc Natl Acad Sci U S A. 2018;115(45):11613-8. Epub 2018/10/26. doi: 10.1073/pnas.1811345115. PubMed PMID: 30352857; PubMed Central PMCID: PMCPMC6233120.

27. Sourimant J, Lieber CM, Aggarwal M, Cox RM, Wolf JD, Yoon JJ, et al. 4'-Fluorouridine is an oral antiviral that blocks respiratory syncytial virus and SARS-CoV-2 replication. Science. 2022;375(6577):161-7. Epub 2021/12/03. doi: 10.1126/science.abj5508. PubMed PMID: 34855509.

28. Lieber CM, Plemper RK. 4'-Fluorouridine Is a Broad-Spectrum Orally Available First-Line Antiviral That May Improve Pandemic Preparedness. DNA Cell Biol. 2022;41(8):699-704. Epub 2022/07/06. doi: 10.1089/dna.2022.0312. PubMed PMID: 35788144; PubMed Central PMCID: PMCPMC9416544.

29. Lieber CM, Aggarwal M, Yoon JJ, Cox RM, Kang HJ, Sourimant J, et al. 4'-Fluorouridine mitigates lethal infection with pandemic human and highly pathogenic avian influenza viruses. PLoS Pathog. 2023;19(4):e1011342. Epub 20230417. doi: 10.1371/journal.ppat.1011342. PubMed PMID: 37068076; PubMed Central PMCID: PMCPMC10138230.

30. Nogales A, Ávila-Pérez G, Rangel-Moreno J, Chiem K, DeDiego ML, Martínez-Sobrido L. A Novel Fluorescent and Bioluminescent Bireporter Influenza A Virus To Evaluate Viral Infections. J Virol. 2019;93(10). Epub 2019/03/15. doi: 10.1128/jvi.00032-19. PubMed PMID: 30867298; PubMed Central PMCID: PMCPMC6498038.

31. Toots M, Yoon JJ, Hart M, Natchus MG, Painter GR, Plemper RK. Quantitative efficacy paradigms of the influenza clinical drug candidate EIDD-2801 in the ferret model. Transl Res. 2020;218:16-28. Epub 2020/01/17. doi: 10.1016/j.trsl.2019.12.002. PubMed PMID: 31945316; PubMed Central PMCID: PMCPMC7568909.

32. Toots M, Yoon JJ, Cox RM, Hart M, Sticher ZM, Makhsous N, et al. Characterization of orally efficacious influenza drug with high resistance barrier in ferrets and human airway epithelia. Sci Transl Med. 2019;11(515). Epub 2019/10/28. doi: 10.1126/scitranslmed.aax5866. PubMed PMID: 31645453; PubMed Central PMCID: PMCPMC6848974.

33. Hengrung N, El Omari K, Serna Martin I, Vreede FT, Cusack S, Rambo RP, et al. Crystal structure of the RNA-dependent RNA polymerase from influenza C virus. Nature. 2015;527(7576):114-7. Epub 2015/10/28. doi: 10.1038/nature15525. PubMed PMID: 26503046; PubMed Central PMCID: PMCPMC4783868.

34. Keown JR, Zhu Z, Carrique L, Fan H, Walker AP, Serna Martin I, et al. Mapping inhibitory sites on the RNA polymerase of the 1918 pandemic influenza virus using nanobodies. Nat Commun. 2022;13(1):251. Epub 2022/01/13. doi: 10.1038/s41467-021-27950-w. PubMed PMID: 35017564; PubMed Central PMCID: PMCPMC8752864.

35. Reich S, Guilligay D, Pflug A, Malet H, Berger I, Crépin T, et al. Structural insight into cap-snatching and RNA synthesis by influenza polymerase. Nature. 2014;516(7531):361-6. Epub 2014/11/20. doi: 10.1038/nature14009. PubMed PMID: 25409151.

36. Kirschner DE, Webb GF. Understanding drug resistance for monotherapy treatment of HIV infection. Bull Math Biol. 1997;59(4):763-85. doi: 10.1007/BF02458429. PubMed PMID: 9214852.

37. Jaki L, Weigang S, Kern L, Kramme S, Wrobel AG, Grawitz AB, et al. Total escape of SARS-CoV-2 from dual monoclonal antibody therapy in an immunocompromised patient. Nat Commun. 2023;14(1):1999. Epub 20230410. doi: 10.1038/s41467-023-37591-w. PubMed PMID: 37037847; PubMed Central PMCID: PMCPMC10085998.

38. Grana C, Ghosn L, Evrenoglou T, Jarde A, Minozzi S, Bergman H, et al. Efficacy and safety of COVID-19 vaccines. Cochrane Database Syst Rev. 2022;12(12):CD015477. Epub 20221207. doi: 10.1002/14651858.CD015477. PubMed PMID: 36473651; PubMed Central PMCID: PMCPMC9726273.

39. Uehara T, Hayden FG, Kawaguchi K, Omoto S, Hurt AC, De Jong MD, et al. Treatment-Emergent Influenza Variant Viruses With Reduced Baloxavir Susceptibility: Impact on Clinical and Virologic Outcomes in Uncomplicated Influenza. J Infect Dis. 2020;221(3):346-55. doi: 10.1093/infdis/jiz244. PubMed PMID: 31309975.

40. Delang L, Vliegen I, Froeyen M, Neyts J. Comparative study of the genetic barriers and pathways towards resistance of selective inhibitors of hepatitis C virus replication. Antimicrob Agents Chemother. 2011;55(9):4103-13. Epub 20110627. doi: 10.1128/AAC.00294-11. PubMed PMID: 21709100; PubMed Central PMCID: PMCPMC3165355.

41. Goldhill DH, Yan A, Frise R, Zhou J, Shelley J, Gallego Cortes A, et al. Favipiravir-resistant influenza A virus shows potential for transmission. PLoS Pathog. 2021;17(6):e1008937. Epub 20210601. doi: 10.1371/journal.ppat.1008937. PubMed PMID: 34061908; PubMed Central PMCID: PMCPMC8195362.

42. Takashita E, Ejima M, Ogawa R, Fujisaki S, Neumann G, Furuta Y, et al. Antiviral susceptibility of influenza viruses isolated from patients pre- and post-administration of favipiravir. Antiviral Res. 2016;132:170-7. Epub 20160616. doi: 10.1016/j.antiviral.2016.06.007. PubMed PMID: 27321665.

43. Marathe BM, Wong SS, Vogel P, Garcia-Alcalde F, Webster RG, Webby RJ, et al. Combinations of Oseltamivir and T-705 Extend the Treatment Window for Highly Pathogenic Influenza A(H5N1) Virus Infection in Mice. Sci Rep. 2016;6:26742. Epub 20160525. doi: 10.1038/srep26742. PubMed PMID: 27221530; PubMed Central PMCID: PMCPMC4879667.

44. Tonini M, De Petris G, Onori L, Manzo L, Rizzi CA, Crema A. The role of GABAA receptor function in peristaltic activity of the guinea-pig ileum: a comparative study with bicuculline, SR 95531 and picrotoxinin. Br J Pharmacol. 1989;97(2):556-62. doi: 10.1111/j.1476-5381.1989.tb11985.x. PubMed PMID: 2547476; PubMed Central PMCID: PMCPMC1854512.

45. Moghadasi SA, Heilmann E, Khalil AM, Nnabuife C, Kearns FL, Ye C, et al. Transmissible SARS-CoV-2 variants with resistance to clinical protease inhibitors. Sci Adv. 2023;9(13):eade8778. Epub 20230329. doi: 10.1126/sciadv.ade8778. PubMed PMID: 36989354; PubMed Central PMCID: PMCPMC10058310.

46. Hurt AC, Holien JK, Parker MW, Barr IG. Oseltamivir resistance and the H274Y neuraminidase mutation in seasonal, pandemic and highly pathogenic influenza viruses. Drugs. 2009;69(18):2523-31. doi: 10.2165/11531450-000000000-00000. PubMed PMID: 19943705.

47. Baz M, Abed Y, McDonald J, Boivin G. Characterization of multidrug-resistant influenza A/H3N2 viruses shed during 1 year by an immunocompromised child. Clin Infect Dis. 2006;43(12):1555-61. Epub 20061108. doi: 10.1086/508777. PubMed PMID: 17109288.

48. Blick TJ, Sahasrabudhe A, McDonald M, Owens IJ, Morley PJ, Fenton RJ, et al. The interaction of neuraminidase and hemagglutinin mutations in influenza virus in resistance to 4-guanidino-Neu5Ac2en. Virology. 1998;246(1):95-103. doi: 10.1006/viro.1998.9194. PubMed PMID: 9656997.

49. Zhou B, Wentworth DE. Influenza A virus molecular virology techniques. Methods Mol Biol. 2012;865:175-92. doi: 10.1007/978-1-61779-621-0_11. PubMed PMID: 22528160.

50. Garten RJ, Davis CT, Russell CA, Shu B, Lindstrom S, Balish A, et al. Antigenic and genetic characteristics of swine-origin 2009 A(H1N1) influenza viruses circulating in humans. Science. 2009;325(5937):197-201. Epub 2009/05/26. doi: 10.1126/science.1176225. PubMed PMID: 19465683; PubMed Central PMCID: PMCPMC3250984.

51. Chu C, Fan S, Li C, Macken C, Kim JH, Hatta M, et al. Functional analysis of conserved motifs in influenza virus PB1 protein. PLoS One. 2012;7(5):e36113. Epub 20120515. doi: 10.1371/journal.pone.0036113. PubMed PMID: 22615752; PubMed Central PMCID: PMCPMC3352917.

Table 1. Polymerase mutations that emerged in adaptation to 4'-FlU, rebuilt as emerged (lineages #1-6) and individually or sub-combinations (sub-lineages #II-VI) in recCA09.

adaptation lineage	PA	PB1	PB2	EC$_{90}$ [µM]	predicted effect
#1		V285I		16.8 µM	causal
#5	N222S	V285I		49.4 µM	
V-1	N222S			3.9 µM	enhancer
#2		T46A	E191K + E180K	6.5 µM	
II-1		T46A		0.4 µM	synergistic
II-2			E191K + E180K	1.3 µM	synergistic
#3		M290V	K189R	13.2 µM	
III-1		M290V		3.5 µM	additive
III-2			K189R	5.2 µM	additive
#4	S395N		Y488C + T491M	7.2 µM	
IV-1	S395N			0.9 µM	synergistic
IV-2			Y488C + T491M	3.4 µM	synergistic
IV-3[A]	S395N		Y488C	revertant to WT	
IV-4[A]			T491M	revertant to WT	
IV-5[A]	S395N		T491M	no recovery	
#6	M579I	M339I	Y488C	5.8 µM	
VI-1			Y488C	0.7 µM	synergistic
VI-2	M579I	M339I		3.7 µM	synergistic
VI-3	M579I			1.0 µM	synergistic
VI-4		M339I		1.3 µM	synergistic
VI-5	M579I		Y488C	1.1 µM	synergistic

[A]not recoverable

Figure captions

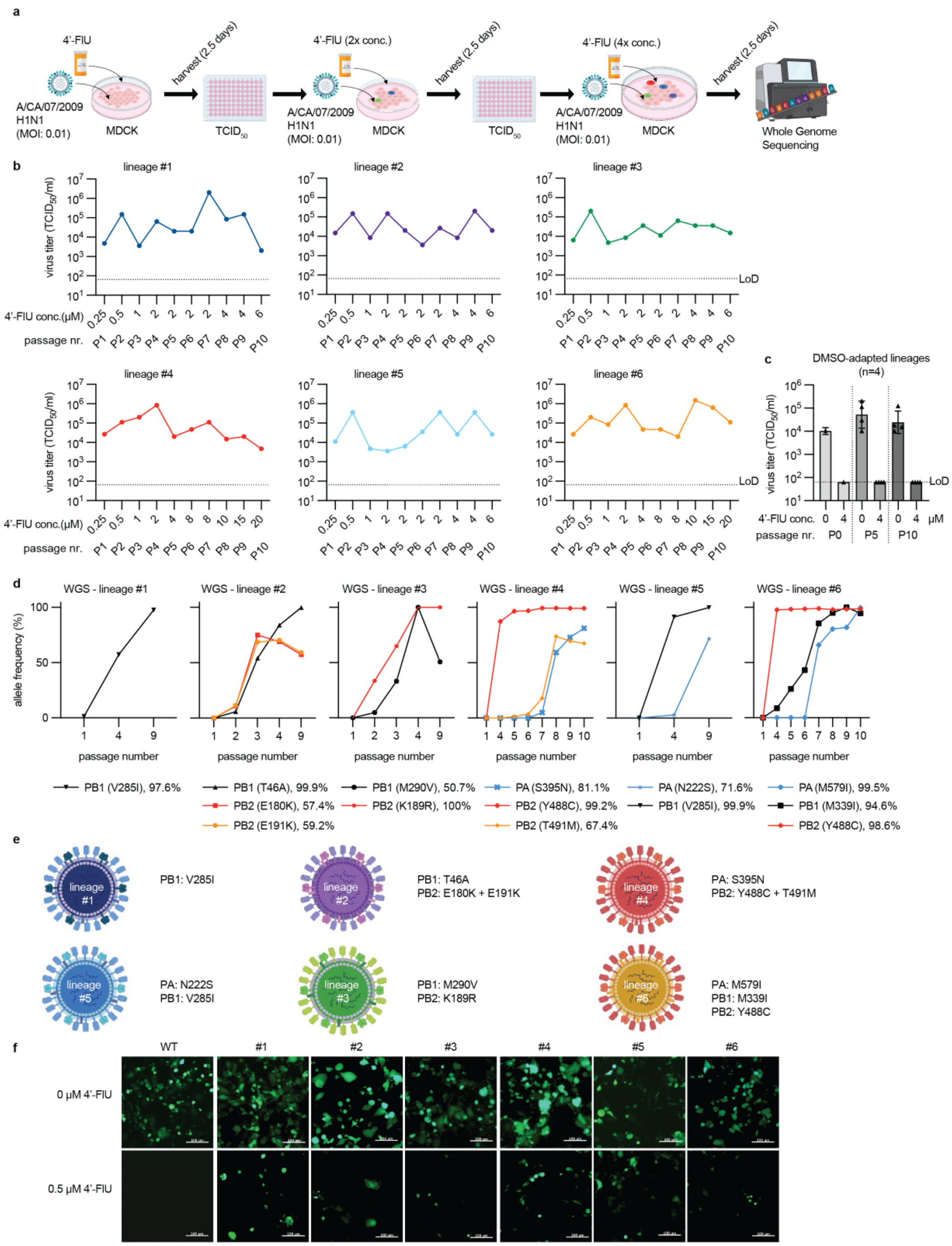

Figure 1: Adaptation of CA09 to 4'-FlU. **a)** Schematic of the adaptation strategy. Six independent lineages were generated in 10 consecutive passages. **b)** Virus titers after each passage (P1-P10). Corresponding 4'-FlU concentrations are shown for each passage and lineage. LoD, limit of detection. **c)** Virus titers of four vehicle (DMSO) volume equivalent adaptation lineages generated in parallel. Shown are titers after passages 0 (P0), 5 (P5), and 10 (P10). **d)** Whole genome sequencing (WGS) of adaptation lineages from (b). Shown are relative allele frequencies of mutations in RdRP subunits that reached >50% prevalence and were absent in DMSO-experienced reference lineages. **e)** Color-coding schematic and substitutions in RdRP subunits in the six adaptation lineages after P10. Relative allele frequencies at adaptation end are shown in parenthesis. **f)** Fluorescence microphotographs of genetic parent recCA09-GFP (WT) and variants harboring the mutations shown in (e) after growth in the presence or absence of 4'-FlU. Scale bar, 100 μm.

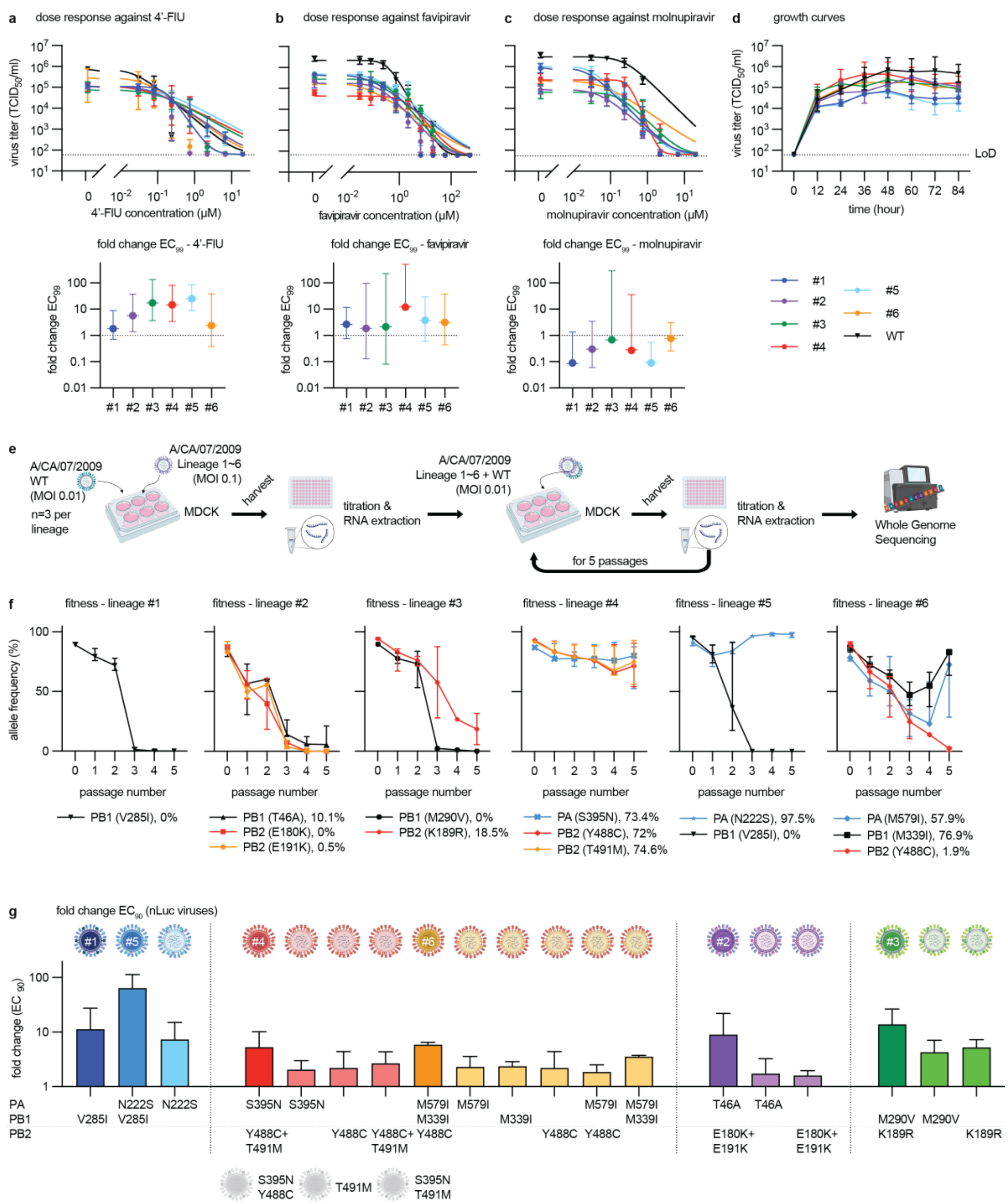

Figure 2: Validation of moderate resistance to 4'-FlU through engineered recCA09. **a-c)** Virus titer reduction-based dose response assays of six recCA09 harboring candidate mutations from (Fig 1e) against 4'-FlU (a), favipiravir (T-705) (b), and the active metabolite of molnupiravir

(EIDD-1931) (c). Upper panels: dose response assay results. Symbols represent geometric means ± geometric SD, lines show 4-parameter variable slope regression models. Bottom panel: fold change EC_{99} relative to parental recCA09. Symbols show means, whiskers denote 95% confidence intervals (CI); n = 3. **d)** Growth curves of the rebuilt recCA09 adaptation lineages and parental recCA09. Symbols show geometric means ± geometric SD, lines connect means. **e)** Schematic of *ex vivo* assessment of relative viral fitness through coinfection with parental recCA09 in a 10:1 ratio. **f)** Whole genome sequencing of co-infection populations from (e). Relative allele frequencies of resistance mutations in RdRP subunits are shown after each of five consecutive passages. Symbols represent medians ± 95% confidence intervals (CI), lines connect medians; n=3. Next generation sequencing over time. Lineages 1 to 6 with co-infected WT are displayed. **h)** Re-validation of resistance mutations singly and in combination in recCA09-nanoLuc reporter virus background. Fold-change of EC_{90} values relative to parental recCA09-nanoLuc are shown. Regression models were developed based on luciferase dose-response assays. Columns show mean EC_{90} values + SD; n=3; greyed virion schematics denote mutation combinations that were non-recoverable.

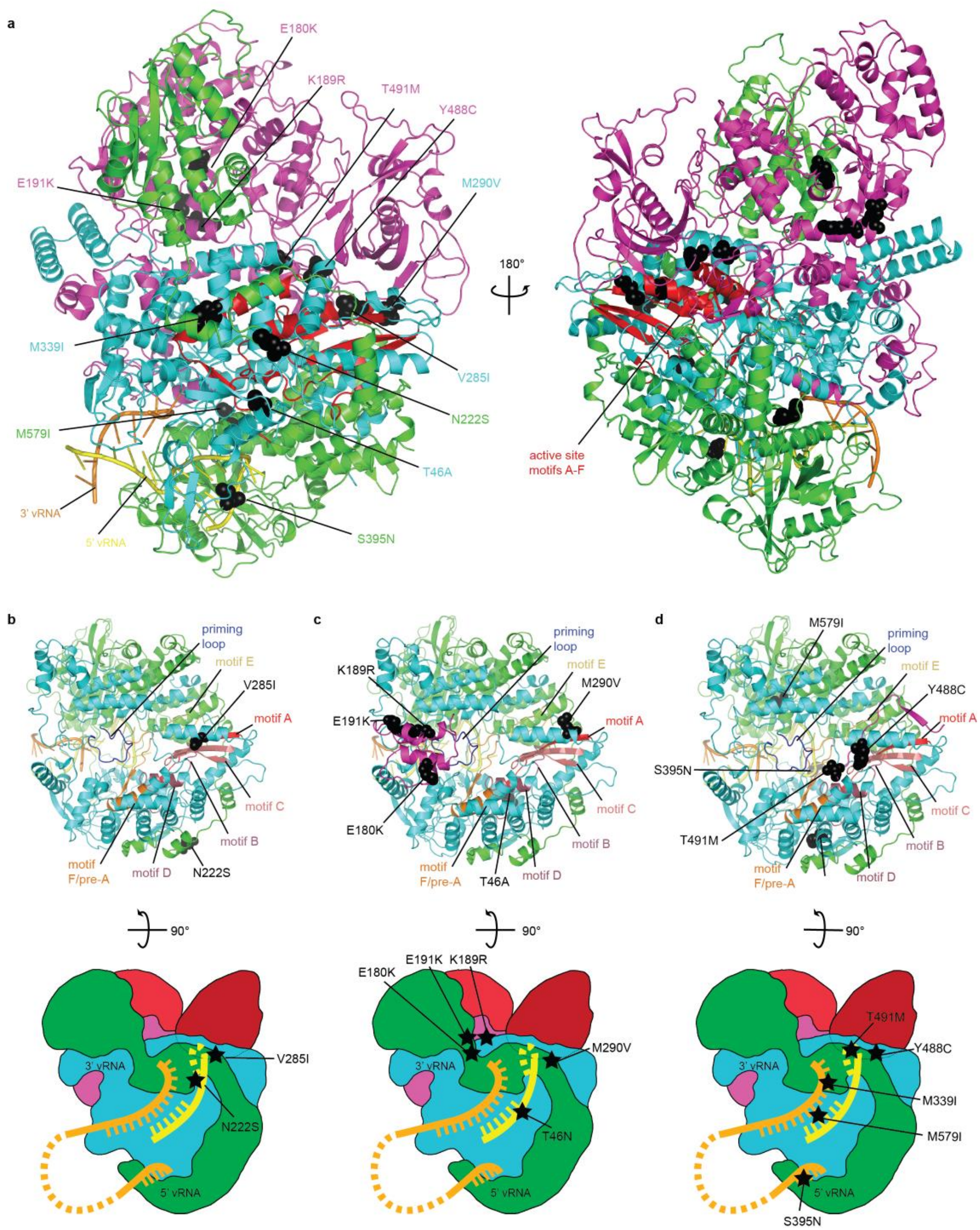

828

829 **Figure 3:** Structural mechanism of CA09 resistance to 4'-FlU. **a)** Overview of the locations of

resistance mutations identified in viral adaptation to growth in the presence of 4'-FlU. Mutation denotations are color-coded by polymerase subunit (PA=green, PB1=cyan, PB2=magenta). The active site of the RdRP complex for phosphodiester bond formation is shown in red. **b-d)** Ribbon representations (top) and polymerase schematics (bottom) highlighting the mutations associated with the distinct paths to resistance identified for lineages #1/5 (b), #2/3 (c), and #4/6 (d). Motif A-F [51] of the IAV RdRP are shown; orange, template RNA strand; yellow, nascent RNA strand. Homology models of the CA09 polymerase were created using SWISS-MODEL based on PDB ID 5d9a; images were created using Pymol.

Lieber et al

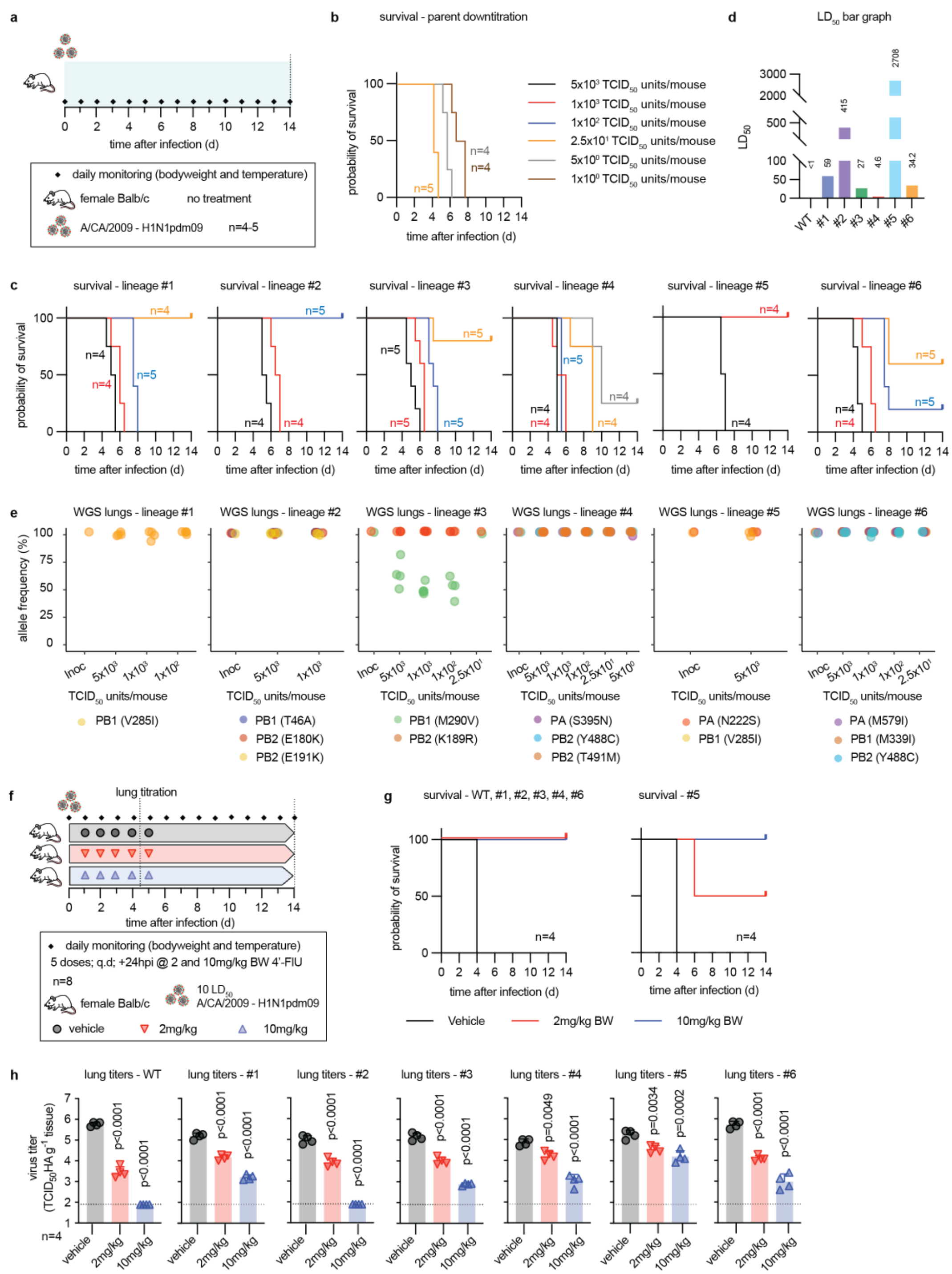
a
time after infection (d)
daily monitoring (bodyweight and temperature)
female Balb/c
no treatment
A/CA/2009 - H1N1pdm09
n=4-5
b
survival - parent downtitration
probability of survival
5x10³ TCID50 units/mouse
1x10³ TCID50 units/mouse
1x10² TCID50 units/mouse
2.5x10¹ TCID50 units/mouse
5x10⁰ TCID50 units/mouse
1x10⁰ TCID50 units/mouse
d
LD50 bar graph
LD50
WT
#1
#2
#3
#4
#5
#6
c
survival - lineage #1
survival - lineage #2
survival - lineage #3
survival - lineage #4
survival - lineage #5
survival - lineage #6
time after infection (d)
e
WGS lungs - lineage #1
WGS lungs - lineage #2
WGS lungs - lineage #3
WGS lungs - lineage #4
WGS lungs - lineage #5
WGS lungs - lineage #6
allele frequency (%)
TCID50 units/mouse
PB1 (V285I)
PB1 (T46A)
PB2 (E180K)
PB2 (E191K)
PB1 (M290V)
PB2 (K189R)
PA (S395N)
PB2 (Y488C)
PB2 (T491M)
PA (N222S)
PB1 (V285I)
PA (M579I)
PB1 (M339I)
PB2 (Y488C)
f
lung titration
time after infection (d)
daily monitoring (bodyweight and temperature)
5 doses; q.d; +24hpi @ 2 and 10mg/kg BW 4'-FlU
n=8
female Balb/c
10 LD50
A/CA/2009 - H1N1pdm09
vehicle
2mg/kg
10mg/kg
g
survival - WT, #1, #2, #3, #4, #6
survival - #5
probability of survival
Vehicle
2mg/kg BW
10mg/kg BW
h
lung titers - WT
lung titers - #1
lung titers - #2
lung titers - #3
lung titers - #4
lung titers - #5
lung titers - #6
virus titer (TCID50HA g⁻¹ tissue)
n=4
p<0.0001
p=0.0049
p=0.0034
p=0.0002
vehicle
2mg/kg
10mg/kg

Figure 4: 4'-FlU-resistant recCA09 are attenuated in mice. **a)** Schematic of the pathogenicity study. Mice were monitored for 14 days or until predefined endpoints were reached. **b-d)** Assessment of LD_{50} nasal inoculum. Survival curves after infection with varying inoculum amounts of parent recCA09 (WT) (b) and resistant recCA09 (c) were used to calculate LD_{50} values (d) through Mantel-Cox analysis; n numbers as specified. **e)** Whole genome sequencing of virus populations recovered from mouse lungs at endpoint. Relative allele frequencies of resistance mutations at the time of infection (Inoc) and endpoint for each of the different inoculum groups are shown. Symbols represent virus populations recovered from individual animals. **f)** Schematic of *in vivo* efficacy study. Mice were infected with 10 LD_{50} units of parent or resistant recCA09; treatment with 4'-FlU at standard (2 mg/kg) and elevated (10 mg/kg) oral dose was initiated 24 hours after infection. **g)** Survival curves. Shown are results for parental recCA09 (WT) and lineages #1/2/3/4/6 (left) and parental recCA09 and lineage #5 (right); n=4. **h)** Lung virus load 4.5 dpi of animals from (f). Symbols represent individual animals, columns show geometric means + geometric SD. Statistical analysis with 1-way ANOVA and Dunnett's multiple comparison post-hoc test; p values are stated; n=4.

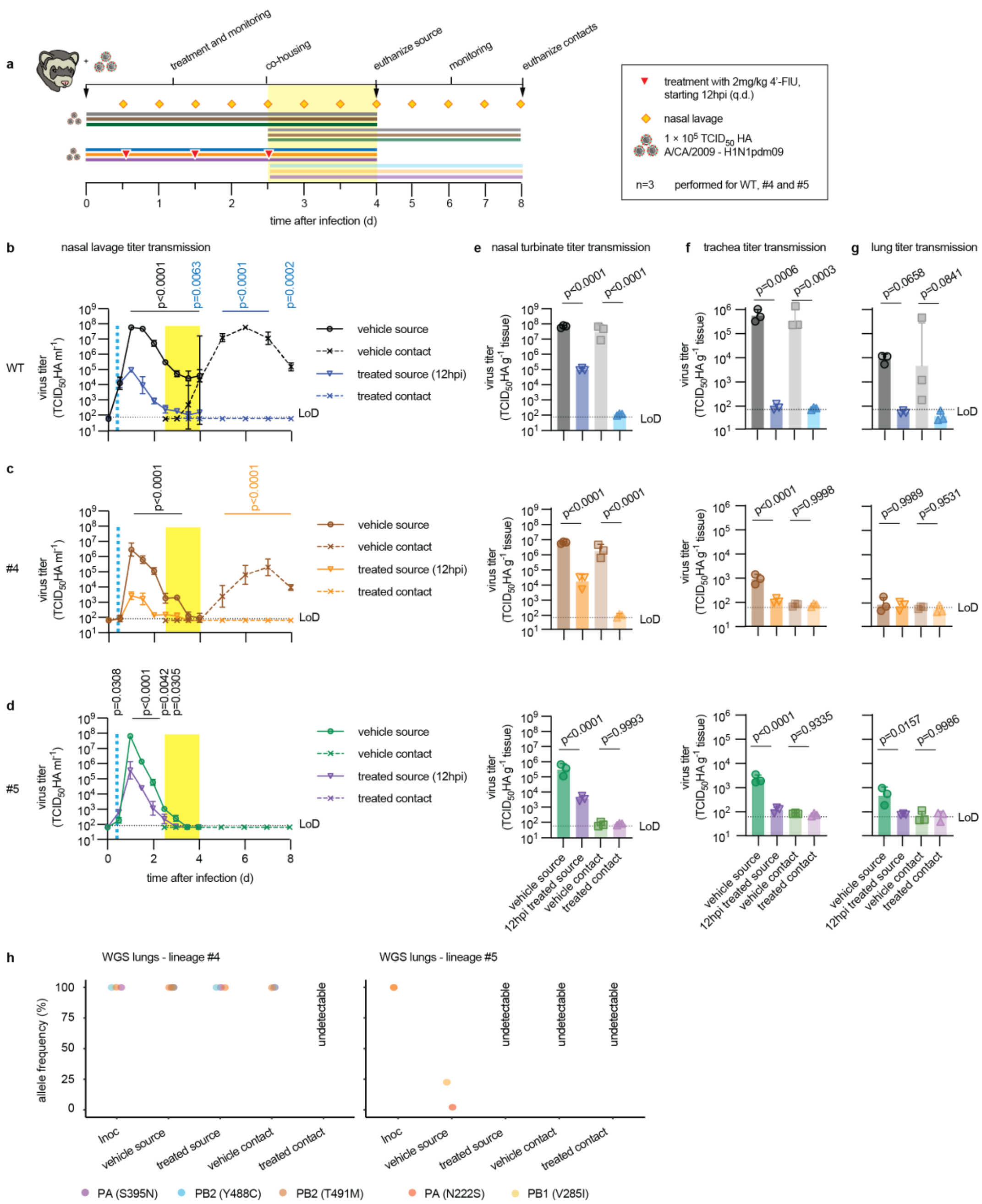

854

855 **Figure 5:** 4'-FlU-resistant CA09 are transmission-impaired in ferrets. **a)** Schematic of the direct

856 contact transmission study, assessing parent recCA09 (WT) and representatives of lineages

#1/5 and #4/6. **b-d)** Nasal lavage titers of source (solid lines) and contact (dashed lines) animals infected with parental recCA09 (b), recCA09 lineage #4 (c), or recCA09 lineage #5 (d). Vertical dashed blue line indicates start of treatment of source animals, yellow bar denotes time of co-housing. Symbols represent geometric means ± geometric SD, lines connect means. 2-way-ANOVA with Sidak's multiple comparison post-hoc test; p values are stated. **e-g)** Virus load in nasal turbinates (e), trachea (f) and lung (g) of animals from (a), determined 4 and 8 dpi for source and contact animals, respectively. Symbols represent individual animals, columns show geometric means ± geometric SD; 1-way ANOVA with Tukey's multiple comparison post-hoc test; p values are stated. **h)** Whole genome sequencing of virus inoculum (Inoc) and virus populations extracted from animals from (a) at study endpoint when possible. Relative allele frequency cut-off 3%; symbols represent individual animals.

2.3 Research Topic: Other Topic

2.3.1 Orally Efficacious Lead of the AVG Inhibitor Series Targeting a Dynamic Interface in the Respiratory Syncytial Virus Polymerase

SCIENCE ADVANCES | RESEARCH ARTICLE

MICROBIOLOGY

Orally efficacious lead of the AVG inhibitor series targeting a dynamic interface in the respiratory syncytial virus polymerase

Julien Sourimant[1], Carolin M. Lieber[1], Jeong-Joong Yoon[1], Mart Toots[1], Mugunthan Govindarajan[2], Venkata Udumula[2], Kaori Sakamoto[3], Michael G. Natchus[2], Joseph Patti[4]†, John Vernachio[4], Richard K. Plemper[1]*

Respiratory syncytial virus (RSV) is a leading cause of lower respiratory infections in infants and the immunocompromised, yet no efficient therapeutic exists. We have identified the AVG class of allosteric inhibitors of RSV RNA synthesis. Here, we demonstrate through biolayer interferometry and in vitro RNA-dependent RNA polymerase (RdRP) assays that AVG compounds bind to the viral polymerase, stalling the polymerase in initiation conformation. Resistance profiling revealed a unique escape pattern, suggesting a discrete docking pose. Affinity mapping using photoreactive AVG analogs identified the interface of polymerase core, capping, and connector domains as a molecular target site. A first-generation lead showed nanomolar potency against RSV in human airway epithelium organoids but lacked in vivo efficacy. Docking pose-informed synthetic optimization generated orally efficacious AVG-388, which showed potent efficacy in the RSV mouse model when administered therapeutically. This study maps a druggable target in the RSV RdRP and establishes clinical potential of the AVG chemotype against RSV disease.

INTRODUCTION

Respiratory syncytial virus (RSV) caused an estimated 33.1 million cases worldwide in 2015 that required 3.2 million hospitalizations and resulted in 59,800 deaths (*1*). To address this health threat, a number of vaccine and drug candidates were tested clinically. However, inducing lasting vaccine protection turned out to be challenging (*2*) and the entry inhibitor presatovir that has completed several phase 2b trials has disappointed in subsequent trials (*3*, *4*). Rapid RSV escape from all advanced entry inhibitor candidate classes through mutations mediating pan-resistance (*5*) further questions clinical potential of RSV entry inhibition. Biopharmaceuticals for immunoprophylaxis have shown promise (*6*) and the monoclonal anti-RSV antibody palivizumab is approved for human use, but the high cost of antibody therapy has prohibited broad application. Accordingly, palivizumab is predominantly reserved for high-risk patients such as the immunocompromised and infants born prematurely or with congenital heart or lung disease (*7*).

To overcome the limitations of RSV entry inhibitors (*8*), drug development efforts targeting the viral RNA-dependent RNA polymerase (RdRP) complex have intensified, motivated by the prospect of a broader window of opportunity through interference with both viral genome replication and transcription. Composed of the viral large (L) and phospho- (P) proteins, all enzymatic centers of the RdRP complex that are necessary for RNA synthesis, polyadenylation, capping, and cap-methylation of viral transcripts are located in the L protein (*9*). The template for replicase and transcriptase is a nonsegmented, single-stranded 15-kilobase RNA of negative polarity that is encapsidated by the viral nucleoprotein (N) (*10*). Accordingly, RdRP bioactivity depends on multiple intra- and intermolecular protein-protein interfaces to enable interactions between P and L (*11*), the P-L complex and the N encapsidating genomic viral RNA (*12*), P-L and the viral anti-termination cofactor M2-1 (*13*), and P-L and host cell cofactors (*14*–*16*).

In the past decade, structural insight was gained in the spatial organization of the RSV L protein (*17*, *18*), which was in all cases complexed with a fragment of P. Although some experimental RSV polymerase inhibitors are considered to interact with the N (*19*) or M2-1 proteins (*20*), most developmental candidates are thought to target the L protein directly (*21*, *22*). The two RSV L structural models offer a clear view of the core RdRP and capping domains. However, these L structures are thought to represent the conformational state of active transcription, based on the position of a "priming" loop away from the polymerase catalytic center. Conformational insight into L in initiation configuration has remained elusive, since flexibility of connector and methyltransferase (MTase) domains located downstream of the capping domain prevented structural characterization. These limitations have impaired the mechanistic understanding of allosteric polymerase inhibitors that are associated with resistance mutations located in the C-terminal regions of L (Fig. 1A), such as AstraZeneca's inhibitor AZ-27 (*23*).

We have recently identified a unique chemotype that potently blocks RSV RdRP bioactivity (*24*). A first-generation lead compound of this class, AVG-233, has nanomolar activity against a panel of clinical RSV isolates and has a promising selectivity index [SI = 50% cytotoxic concentration (CC_{50})/half-maximal effective concentration (EC_{50})] > 1660. In preparation of formal development, this study has subjected the AVG chemotype to target site identification, characterization of the molecular mechanism of action, and efficacy profiling in primary human airway epithelium (HAE) organoids and in vivo, resulting in the identification of an orally efficacious developmental lead.

[1]Center for Translational Antiviral Research, Institute for Biomedical Sciences, Georgia State University, Atlanta, GA 30303, USA. [2]Emory Institute for Drug Development, Emory University, Atlanta, GA 30322, USA. [3]Department of Pathology, College of Veterinary Medicine, University of Georgia, Athens, GA 30602, USA. [4]Aviragen Therapeutics Inc, Alpharetta, GA 30009, USA.
*Corresponding author. Email: rplemper@gsu.edu
†Present address: JP Biotech Advisors Inc, Milton, GA 30009, USA.

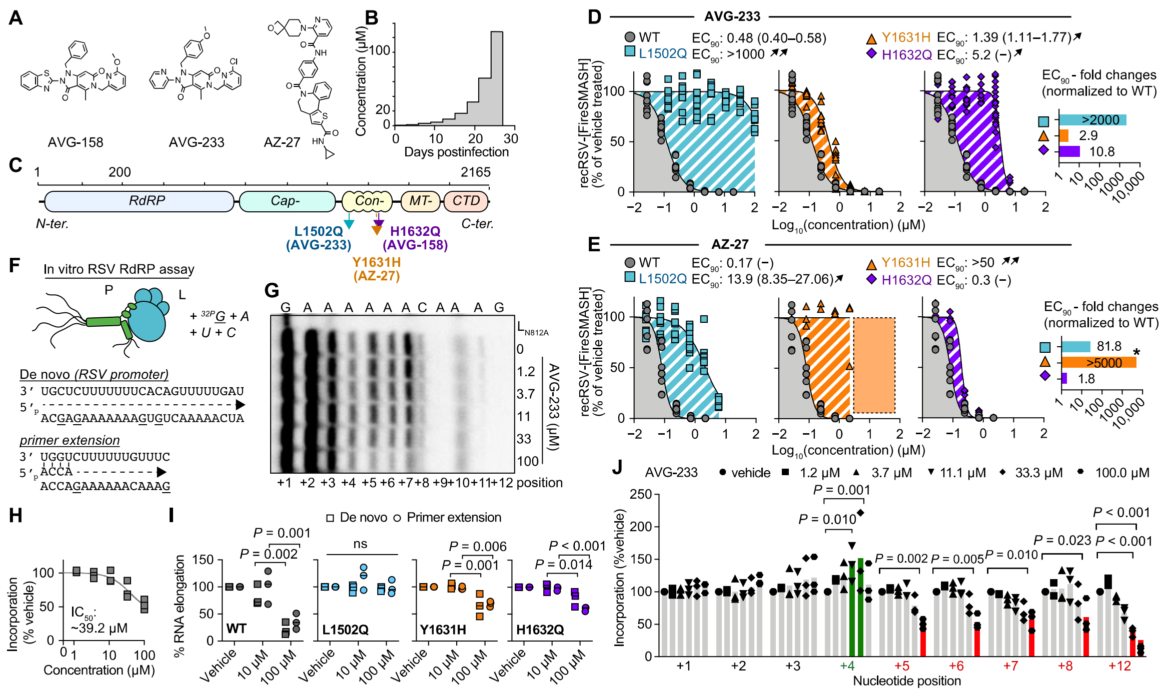

Fig. 1. Resistance and mechanistic profiling of AVG-233. (**A**) Chemical structure of AVG-158, AVG-233, and AZ-27. (**B**) Schematic of the escalating-dose viral adaptation of recRSV-mKate with AVG-158 or AVG-233. (**C**) Schematics of RSV L with candidate resistance sites for AVG-233 and AVG-158 and a reported resistance site to polymerase inhibitor AZ-27. (**D** and **E**) Dose-response inhibition of AVG-233 (D) and AZ-27 (E) against recRSV-mKate harboring L1502Q, Y1631H, or H1632Q substitution. Insets show EC_{90} fold changes relative to L wild type (WT). Highest AZ-27 concentration tested, 6 μM; dotted area and star based on reported values (*23*). (**F** to **J**) In vitro RSV RdRP assays using synthetic primer/template pairs (G to J) or promoter sequence (I). Representative autoradiogram (G) with densitometric analysis (H). (I) Relative in vitro RNA elongation in the presence of indicated doses of AVG-233 compared to vehicle treated, in the presence of L1502Q, Y1631H, or H1632Q substitution. (J) Densitometric quantitation of in vitro RNA elongation at each incorporated position in the presence of indicated concentration of AVG-233. In all panels, symbols represent independent biological repeats ($n = 3$), bars represent means, and lines represent four-parameter variable slope regression modeling. Two-way ANOVA with Dunnett's post hoc tests (I and J).

RESULTS

We have demonstrated that compounds of the AVG series potently inhibit RSV RNA synthesis (*24*). To identify the molecular target of this class, we resistance-profiled the chemotype through serial passaging of a recombinant RSV expressing a red fluorescent protein (recRSV-mKate) in three independent lines each in the presence of increasing concentrations of either AVG-233 or an earlier developmental intermediate of the series, AVG-158 (Fig. 1A). Virus populations were considered adapted when inhibitor concentrations exceeding the original EC_{50} value by 100-fold were tolerated (Fig. 1B).

Unique resistance profile of the AVG series chemotype

Sanger sequencing revealed a unique substitution in the L open reading frame for each lineage that affected either residue 1502 (L_{L1502Q}) or 1632 (L_{H1632Q}) (Fig. 1C). Resistance site L_{H1632Q} is located in immediate proximity to a known L_{Y1631H} hotspot that is reportedly involved in escape from several chemically unrelated allosteric RSV polymerase inhibitor classes such as the benzothienoazepines YM-53503 (*25*), AZ-27 (*23*), and PC786 (*26*) and the AstraZeneca inhibitor cpd1 (*27*). We therefore reengineered L_{L1502Q}, L_{H1632Q}, and L_{Y1631H} independently in RSV L expression plasmids and recRSV, and determined susceptibility to both AVG-233 and AZ-27 in minigenome and/or virus dose-response inhibition assays (fig. S1).

In the minigenome assays, the L_{L1502Q} and L_{H1632Q} mutations caused a ≥100-fold increase in EC_{50}, whereas L_{Y1631H} had only a minor (approximately fivefold increase) effect (fig. S1). Rebuilding of the mutations in recRSV did not adversely affect viral growth rates and maximal progeny titers reached in multistep growth curves (fig. S2). Consistent with the minireplicon data, L_{L1502Q} caused a >2000-fold increase in EC_{90} against AVG-233, whereas L_{Y1631H} barely conferred resistance to the compound (Fig. 1D). However, the L_{H1632Q} mutation had only a moderated effect in the context of recRSV infection, increasing in EC_{90} values only by approximately 10-fold. Resistance profiles of AZ-27 drew a mirror image of those of AVG-233; the L_{Y1631H} substitution resulted in robust resistance (>2000-fold increase in EC_{90}) consistent with previous reports (*23*), whereas L_{H1632Q} did not mediate viral escape and L_{L1502Q} had only a moderate effect (Fig. 1E).

To better understand the molecular basis for L inhibition and resistance, we purified RSV P-L polymerase complexes harboring the different substitutions (fig. S3) and subjected the preparations to in vitro RdRP assays using synthetic RNA templates and a ^{32}P-GTP (guanosine triphosphate) tracer (Fig. 1F). Consistent with previous observations (*24*), AVG-233 dose-dependently impaired RNA elongation of synthetic primer/template RNA pairs (Fig. 1G), exhibiting a ~39 μM median inhibitory concentration (IC_{50}; Fig. 1H). RNA incorporation in vitro was reduced to 36% (±14.6) in the presence of 100 μM AVG-233, but the L1502Q escape mutation restored activity to 98.7% (±12.9), indicating robust resistance (Fig. 1I and fig. S4). By comparison, Y1631H and H1632Q mediated only moderate escape from AVG-233, represented by restoring polymerase activity to 69% (±5.1) and 60% (±4.0) of untreated, respectively. Similar resistance profiles were observed when using a single-stranded RSV promoter as a template to initiate de novo RNA synthesis at the promoter. RNA incorporation after initiation was reduced to 21.7% (±11.8), 96.6% (±4.0), 66.0 (±20.8), and 79.7% (±14.5) when AVG-233 was added to complexes containing L, L_{L1502Q}, L_{Y1631H}, or L_{H1632Q}, respectively (Fig. 1I and fig. S5). The arrest of polymerization occurred predominantly after incorporation of four nucleotides and thus after an initial delay (Fig. 1J). However, we noted some variation in the extent of the delay depending on primer/template sequence (fig. S6).

To test for competition of AVG-233 with endogenous RSV polymerase substrates, we added increasing amounts of exogenous nucleosides to the culture medium of RSV-infected cells grown in the presence of a sterilizing concentration of AVG-233 (20 μM). In contrast to the known competitive inhibitor 4′-FlU (*22*), AVG-233 inhibition of RSV replication was unaffected by exogenous nucleosides, indicating that AVG class compounds block the viral RdRP by a noncompetitive mechanism (fig. S7). These results define a noncompetitive blockage of RNA synthesis after the initiation step as the primary mechanism of L inhibition by AVG-233. Whereas mechanistically similar to AZ-27, the nonoverlapping resistance profiles indicate distinct docking poses.

Positive AVG-233 target identification

A biologically active RSV polymerase can reconstitute from two independently expressed fragments that are split between the connecting and MTase domains (*28*) (Fig. 2A), indicating that each of these individual fragments retains folding competence. Using baculovirus/insect cell protein expression, we prepared full-length L and the larger N-terminal fragment of the split L (residues L_{1-1749}) that harbors all of the RdRP domain and all AVG-233 resistance sites (Fig. 2B). Direct binding of AVG-233 to these L preparations was tested through biolayer interferometry (BLI). Both standard L and the L_{1-1749} fragment bound AVG-233 with similar affinities [dissociation constants (K_D's) were 38.3 μM (16.9 to 138.8) and 53.1 μM (33.5 to 97.5), respectively] (Fig. 2, C and D), providing positive confirmation of L as the molecular target of the compound and demonstrating that the inhibitor binding site is fully present in the L_{1-1749} fragment.

Since this fragment contains the catalytic site for phosphodiester bond formation (*17*, *18*, *29*), we explored its ability to synthesize RNA in vitro, using the biochemical RdRP assay setup. Consistent with proper folding into a native conformation, the L_{1-1749} subunit was RNA synthesis competent in the biochemical assay (Fig. 2E), although with a noticeable drop in processivity after the ninth

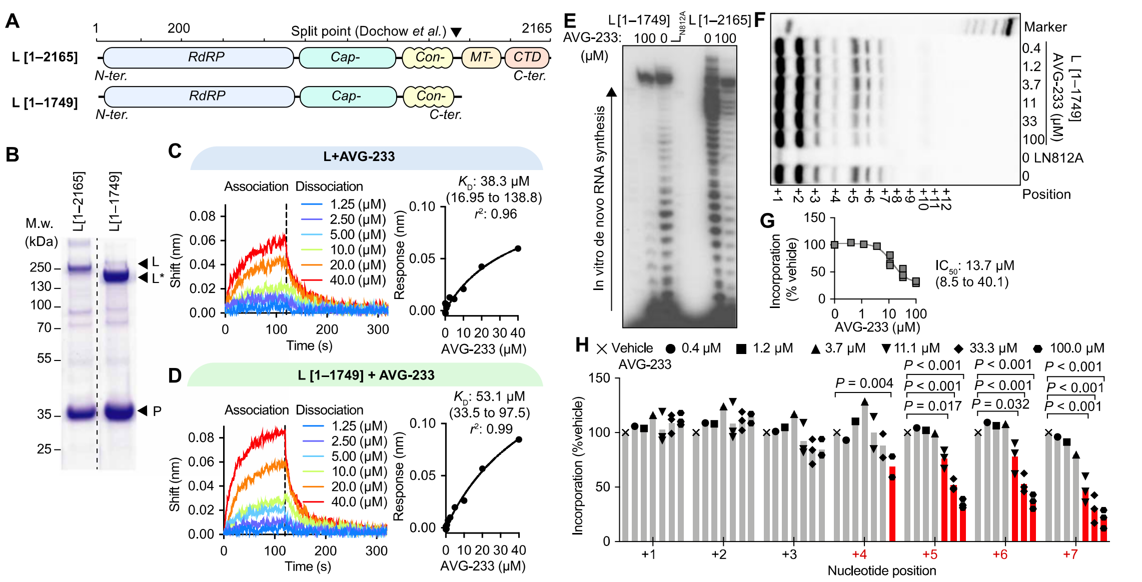

Fig. 2. Label-free positive target identification of AVG-233. (**A**) Schematic of two RSV L targets examined, representing the full-length polypeptide (top) and a folding-competent (*28*) truncated L_{1-1749} polypeptide lacking the MTase and C-terminal (CTD) domains. (**B**) Purification of polymerase complexes specified in (A) after expression in insect cells. Coomassie blue stain after SDS-PAGE fractionation. (**C** and **D**) Dose-dependent BLI-based association (120 s) and dissociation (200 s) curves (left) of AVG-233 with full-length RSV L (C) and L_{1-1749} (D), with nonlinear fit with one-site specific binding (right). (**E**) In vitro RdRP assay using a synthetic promoter RNA template for de novo RNA synthesis; representative autoradiogram. (**F** to **H**) Primer/template-based in vitro RNA elongation assay, assessing bioactivity and AVG-233 inhibition of L_{1-1749}, with representative autoradiogram (F), densitometric quantitation of elongation products (G), and relative quantitation of each RNA product (H). Symbols represent independent biological repeats ($n = 3$), and bars represent means. Two-way ANOVA with Dunnett's post hoc tests.

incorporated nucleotide compared to full-length L. This L fragment was equally susceptible to inhibition by AVG-233 in de novo RNA synthesis (Fig. 2E), confirming productive inhibitor binding.

When testing primer/template-based RNA elongation by the L_{1-1749} fragment, we observed dose-dependent inhibition by AVG-233 with an IC_{50} of 13.7 μM (Fig. 2, F and G), which did not substantially differ from the value (IC_{50} of 39.2 μM) calculated for full-length L (Fig. 1, G and H). AVG-233 suppression of RNA synthesis by the L_{1-1749} fragment was again delayed, since a significant inhibitory effect was first detectable after incorporation of four nucleotides (Fig. 2H).

Photoaffinity-based AVG-233 target site mapping

To map the molecular target site of AVG-233, we developed three chemical analogs of the compound capable of carrying diazirine or aryl azide moieties that become covalently reactive when photoactivated through exposure to high-energy ultraviolet light (Fig. 3A). The design of these analogs was guided by the three-dimensional (3D) quantitative structure-activity relationship (3D-QSAR) model that we have developed for the AVG-233 chemotype (*24*). Consistent with QSAR predictions, all three analogs retained bioactivity in cell-based assays without photoactivation with only minor (approximately 2- to 10-fold) potency penalties (Fig. 3B). Mass spectrometry (MS) analysis after photocrosslinking of these analogs to purified RSV polymerase and trypsin digestion of the covalent complexes identified for each compound a narrow set of peptides (one to four) with covalently bound ligand, consistent with high target site specificity of the cross-links (Fig. 3C). Specifically, analog A labeled a cluster of four peptides that was located in L region 1693–1749, which is thought to be part of a flexible linker between the connecting and MTase domains (Fig. 3D) (*30*). Analog B also highlighted four peptides, in this case spanning a larger area composed of the L capping (1376–1409), connecting (1554–1576 and 1675–1678), and MTase (1880–1892) domains. Analog C identified a single peptide located in the L connecting domain (1548–1576).

When projected on the structural model of the RSV L core polymerase domain (*17*, *18*), only peptide 1376–1409 could be directly observed due to poor structural resolution of the L C-terminal domain. We therefore generated a homology model of the C-terminal residues of RSV L based on the coordinates reported for the related vesicular stomatitis virus (VSV) and rabies L proteins (*31*–*33*). This model posited the AVG-233 resistance mutations and nearly all proximity residues identified through photoaffinity labeling at an interface formed by the L capping, connecting, and MTase domains (Fig. 3E). Data-guided in silico docking of AVG-233 into this site suggested that the compound may broadly restrict structural flexibility

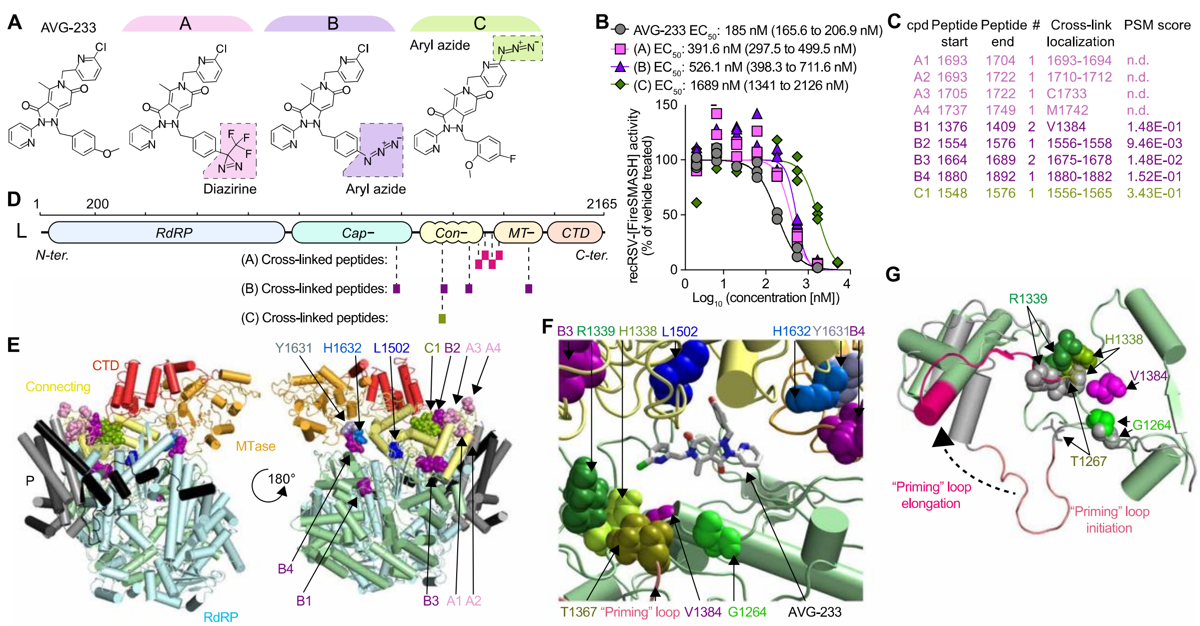

Fig. 3. AVG-233 target site mapping through photoaffinity labeling. (**A**) Chemical structures of the AVG-233 analogs synthesized. Photoactivatable groups are highlighted in colored boxes. (**B**) Dose-response curves of the AVG-233 photoreactive analogs and standard AVG-233 against recRSV-fireSMASh. Symbols represent independent repeats ($n = 3$). Four-parameter variable slope regression modeling. (**C**) RSV L-P peptides in close proximity of bound AVG-233, identified through photoaffinity labeling and LC-MS/MS analysis. Specific residue(s) engaged (cross-link localization) and confidence [peptide-spectrum matches (PSM) score] are shown. (**D**) Schematic representation of the three sets of peptides identified through each photoactivatable AVG-233 analog. (**E**) Cartoon representation of a structural model of the RSV P-L complex in the putative pre-initiation state, based on RSV P-L reconstruction (PDB 6PZK) with residues (1461–2165) modeled after VSV P-L (PDB 6U1X). Color coding as in Fig. 1. Photocrosslinking target peptides from (C) and resistance mutations from Fig. 1 are highlighted. (**F**) Molecular docking of AVG-233 into proximity of photocrosslinking targets and resistance sites L1502 and H1632. Residues involved in RNA synthesis (H1338 and R1339) and the putative priming loop are highlighted. (**G**) Predicted priming loop positions in postulated polymerase initiation and elongation conformations. Labeled are residues identified through photocrosslinking and the adjacent, predicted priming loop pivot residue G1264.

of this interface or specifically interfere with conformational rearrangement of the L priming-capping loop (Fig. 3, F and G) that facilitates polymerase switch from RNA synthesis initiation to elongation mode (*33*) through large spatial movement.

Efficacy of AVG-233 in air-liquid interface cultures of primary epithelium

Well-differentiated HAE organoids grown at air-liquid interface (Fig. 4A) represent a premier model to test potency of antivirals directed, for instance, against RSV (*34*) or influenza viruses (*35*) in disease-relevant primary human tissues. These cultures develop tight junctions and feature, among others, into mucus-producing goblet and ciliated cells (Fig. 4B and figs. S8 to 12). Following apical infection with recRSV-mKate, we noted sustained, robust virus replication resulting in peak shedding of approximately 1×10^5 infectious particles into the apical space per day over a 10-day experimental window (Fig. 4C). Consistent with previous reports (*36*), virus replicated predominantly in ciliated cells (fig. S13), forming characteristic (*37*) cytoplasmic inclusions (Fig. 4D). Our previous studies have also demonstrated that AVG-233 is well tolerated without any signs of cytotoxicity at concentrations of 100 µM. Continued multiday exposure of the airway epithelium cultures to 200 µM compound had no negative effect on tissue organization and tight junction integrity, based on confocal microscopy after ZO-I immunostaining (fig. S14) and stable trans-epithelial electrical resistance (TEER) between the basolateral and apical chambers (Fig. 4E). Basolateral AVG-233 at 5 µM strongly reduced RSV protein expression (Fig. 4F) without detectable negative effect on epithelium integrity (Fig. 4G). Dose escalation resulted in gradual inhibition of apical RSV shedding, reaching sterilizing conditions at approximately 3 µM (Fig. 4H). Regression modeling revealed an EC_{50} of 0.07 µM, which closely resembled that of N^4-hydroxycytidine (NHC) (EC_{50}, 0.05 µM), the parent molecule of the recently authorized broad-spectrum inhibitor molnupiravir (*38*, *39*). These performance parameters correspond to a robust SI > 2850 of AVG-233 in the human airway organoids.

Development of orally efficacious developmental candidates of the AVG series

When examining in vivo efficacy of AVG-233 in the mouse model of RSV infection, we noted that neither prophylactic nor therapeutic administration of the compound at a twice-daily dose of up to 200 mg/kg significantly reduced lung virus load (Fig. 5, A and B). We previously reported that AVG series compounds are rapidly metabolized in mice lung microsomes (*24*). To minimize potential metabolic liabilities, we designed a series of eight analogs with fluorine atoms introduced to block potential sites of oxidative hydroxylation on the (a) and (b) rings, and/or substitution of the chemically labile ortho-chloropyridine (c) ring (*40*–*42*) with a more inert ortho-trifluoromethyl pyridine (Fig. 5C). This series retained potent antiviral activity in cell culture (Fig. 5D and table S1) and primary HAE cells (fig. S15 and table S1). Mechanism of action was unchanged from that of AVG-233 (Fig. 5E and fig. S16), and even the substantially modified analog, AVG-388, shared resistance profile (fig. S17 and table S2) and very low cytotoxicity (fig. S18) with AVG-233.

To assess the effect of these substitutions on in vivo efficacy, we tested the six most potent analogs in the RSV mouse model. Compounds were administered orally at 50 mg/kg body weight in a twice-daily regimen, starting 12 hours after infection (Fig. 5F). Replacing the ortho-chloropyridine in ring (c) of AVG-233 with a trifluoromethyl group (AVG-436) caused a statistically significant reduction in lung viral load of 0.89 (± 0.14) $\log_{10}$ $TCID_{50}$ (median tissue culture infectious dose)/ml (Fig. 5F and table S3). A slightly

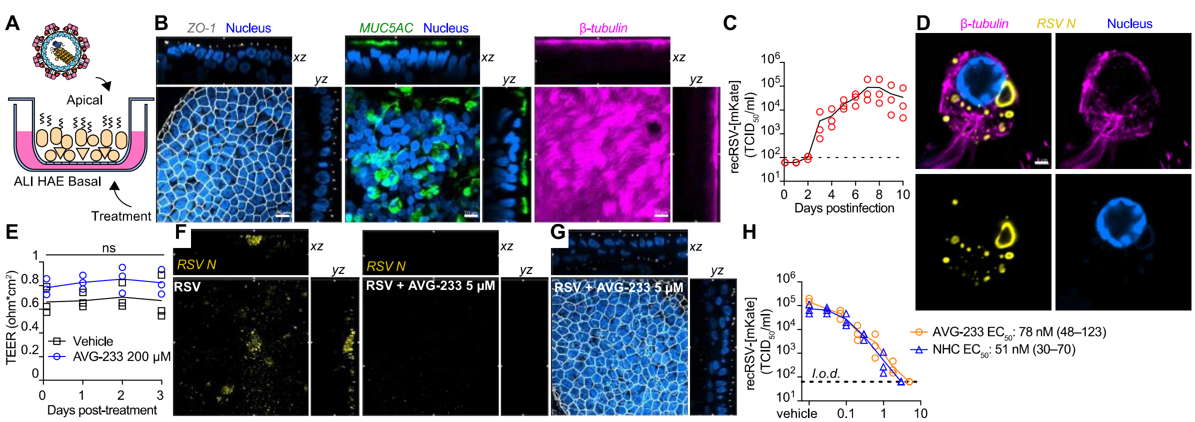

Fig. 4. Efficacy of AVG-233 in well-differentiated HAE (3D-HAE) cells grown at air-liquid interface. (**A**) Schematics of 3D-HAE. (**B**) Confocal imaging of 3D-HAE. Tight junctions immunodetected with anti–ZO-I (white). Mucus-producing goblet cells immunodetected with anti-Muc5AC (green). Ciliated cells immunodetected with anti–β-tubulin (pink). Nuclei stained with Hoechst 35443 (blue). Scale bars, 10 µm. (**C**) Multistep growth curve of recRSV-mKate in 3D-HAEs. Viral titers were assayed from the apical chambers. Symbols show biological repeats ($n = 3$); curve connects means ± SD. (**D**) Immunolabeling of recRSV-fireSMASh–induced inclusion bodies with specific anti-RSV N antibody. Scale bar, 2 µm. (**E**) Transepithelial electrical resistance of 3D-HAEs exposed basolaterally to 200 µM AVG-233 or vehicle (DMSO) for up to 3 days. Symbols represent means ± SD ($n = 3$). Two-way ANOVA with Sidak post hoc test. (**F**) Immunostaining of RSV N in RSV-infected cells with or without AVG-233 5 µM at 3 days postinfection (d.p.i.). Scale as in (B). (**G**) Immunostaining of tight junctions in RSV-infected cells with AVG-233 5 µM at 3 d.p.i. Scale as in (B). (**H**) AVG-233 and NHC virus yield reduction against recRSV-mKate in 3D-HAEs. Progeny virus titers were determined 6 days after infection; symbols show biological repeats ($n = 3$); curve connects mean values. EC_{50} calculation through four-parameter variable slope regression modeling.

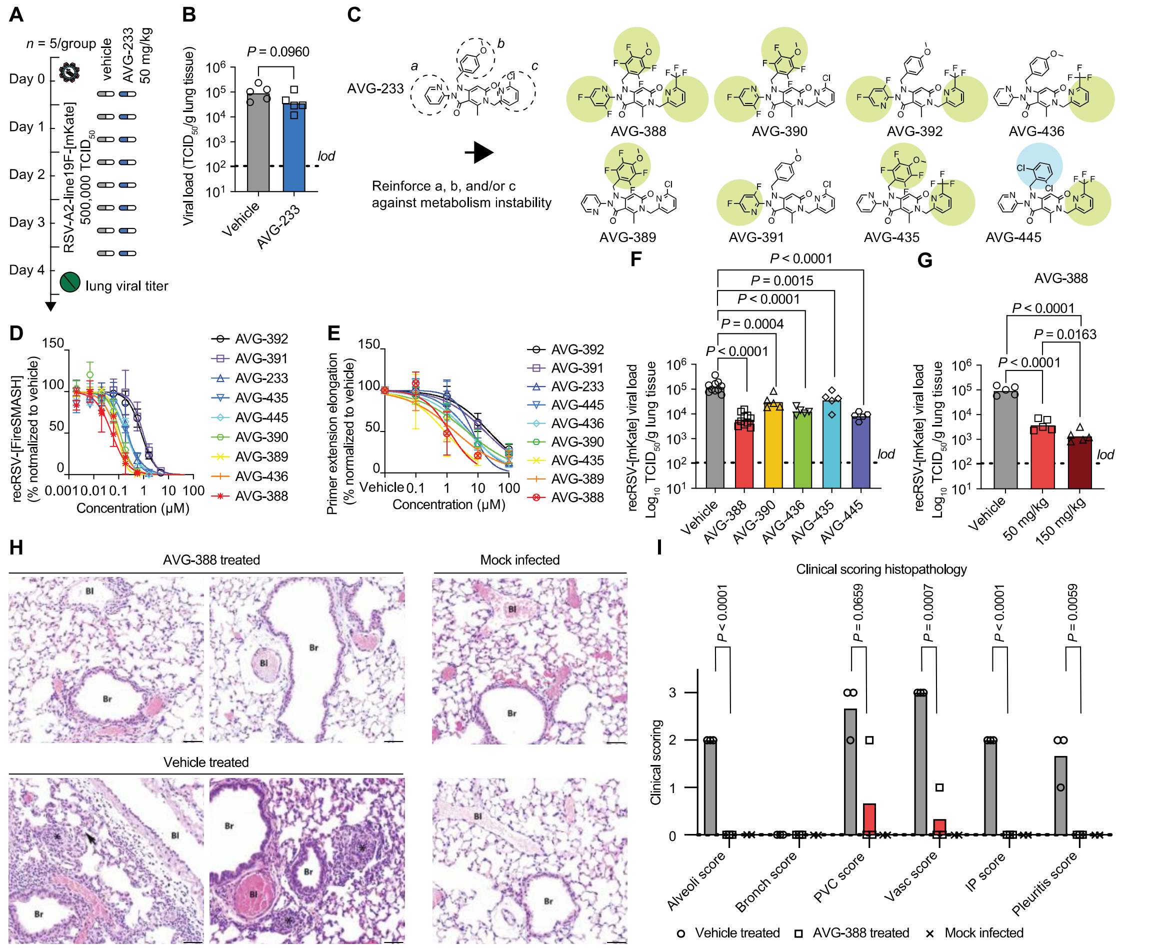

Fig. 5. Identification of orally efficacious developmental analogs of AVG-233. (**A** and **B**) Effect of AVG-233 given orally twice daily at 12 hours postinfection (A) to RSV-infected Balb/c mice on lung titers at 4.5 d.p.i. (B). (**C**) Chemical structures of AVG-233 analogs with fluoro- or ortho-chloropyridine groups. (**D** and **E**) Comparison of AVG fluorine and ortho-chloropyridine analogs on antiviral potency in cell culture against recRSV-mKate (D) and in in vitro primer extension RdRP assays (E). (**F** and **G**) Effect of AVG-233 analogs given orally twice daily at 12 hours postinfection and 50 mg/kg (F) or 50 and150 mg/kg (G; AVG-388 only) to recRSV-mKate–infected Balb/cJ mice on lung titers at 4.5 d.p.i. (**H** and **I**) Lung histopathology. Representative photomicrographs of lung sections after H&E staining of two animals per treatment group (H) and histopathology scoring (I; $n = 3$ each for AVG-388– and vehicle-treated groups, $n = 2$ for mock-infected group). Bl, blood vessel; Br, bronchiole; arrow, interstitial pneumonia; asterisks, alveolitis. Scale bars, 50 μm. The histopathology scoring scale applied is defined in Materials and Methods. Symbols in (B), (F), (G), and (I) show individual biological repeats (independent experiments or individual animals); columns represent sample means. Unpaired *t* test (B) or one-way ANOVA (F, G, and I) with Dunnett's (F and G) or Tukey's (I) multiple comparisons post hoc test; *P* values are shown.

lower antiviral effect resulted from fluorine substitutions on both the a and b moieties (AVG-390). Combining these strategies, fluorines on the (a), (b), and (c) rings (AVG-388) yielded strong antiviral efficacy with a lung virus load reduction of 1.3 (± 0.25) log_{10} $TCID_{50}$/ml compared to vehicle-treated animals. We did not observe as much benefit from combining fluorines on b and c (AVG-435), but replacing the anisole moiety of AVG-233 with a 1,3 dichlorobenzene (AVG-445) resulted in a lung titer reduction of 1.1 (± 0.16) log_{10} $TCID_{50}$/ml, nearly as potent as that seen with AVG-388.

Antiviral efficacy of AVG-388 was dose dependent, resulting in a strong reduction of 1.9 (± 0.23) log_{10} $TCID_{50}$/ml when dosed orally at 150 mg/kg twice daily (Fig. 5G and table S3) without any signs of adverse effects (fig. S19). Histopathology analysis of lung tissue extracted 4 days after infection from vehicle-treated animals revealed prominent interstitial pneumonia with multifocal pleuritis and moderate perivascular lymphohistiocytic cuffing (Fig. 5, H and I, and fig. S20). Treatment with AVG-388 at 50 mg/kg initiated 12 hours after infection prevented disease progression to viral pneumonia. Only one animal of the AVG-388 group showed mild vasculitis and perivascular cuffing. These results demonstrating oral efficacy of AVG-388 against RSV confirm successful synthetic optimization of the AVG-233 scaffold and identification of a developmental candidate for the treatment of RSV disease.

DISCUSSION

Our initial characterization of the AVG-233 class revealed that the inhibitor does not block phosphodiester bond formation per se but disturbs initiation of viral RNA synthesis at the promoter (*24*). This inhibition pattern may reflect pharmacological interference with a predicted conformational rearrangement of the polymerase complex during initiation (*43*, *44*). Three lines of experimental evidence support this view: the AVG class resistance profile, the mechanism of action (MOA) characterization in biochemical RdRP assays, and the photoaffinity labeling–based mapping of the target site.

The primary resistance hotspot of the AVG class, L residue 1502, is positioned at the interface between the large RdRP domains mediating RNA synthesis and the MTase domain required for capping of nascent viral mRNAs. A secondary escape residue, L 1632, likewise locates to this junction, as does residue 1631, which is the primary resistance site for the experimental RSV inhibitors YM-53503 (*25*), AZ-27 (*23*), PC786 (*26*), and cpd1 (*27*). Cross-resistance among chemically distinct antivirals with comparable MOA is not uncommon. However, distinct resistance profiles of mechanistically related chemotypes predicted to engage the same target domain such as AVG-233 and AZ-27 are rare but open interesting future possibilities for combination therapies. Divergent resistance profiles from mechanistically similar RSV L inhibitors indicate a unique docking pose of the AVG class.

Biochemical RdRP assays using different types of synthetic RNA templates demonstrated that compounds of the AVG class block de novo initiation of RNA synthesis and extension of a paired primer in a synthetic primer/template after the first few nucleotides. This initial delay does not represent an artifact of the RdRP assay, since we found previously that ERDRP-0519, a small-molecule inhibitor of measles virus polymerase that we have developed, completely blocks all phosphodiesterbond formation in the equivalent measles virus RdRP assay (*45*). Both AVG-233 inhibitory activities were sensitive to the L residue 1502 resistance mutation, indicating that suppressed de novo initiation and impaired RNA elongation are a consequence of a uniform AVG-233 docking pose to the L target. The apparent difference in AVG-233 EC_{50} values between cell-based and in vitro RdRP assays likely reflects a high representation of bioinactive L complexes in the P-L preparations, which is typical for purified mononegavirus polymerase complexes (*46*). However, other mechanisms are also conceivable. While absent in cellula, this unproductive material may absorb compound in the biochemical assay without appreciable inhibitory effect. Although less likely, the AVG-233 could alternatively affect transcription, since photocrosslinking proposed a docking pose in which the compound could also interfere with L activities such as cap binding and/or cap methylation. We furthermore cannot fully exclude that AVG-233 may be metabolically modified by cellular enzymes, increasing its target affinity.

Beyond resistance profiling, no physical target site has been mapped for any of the experimental RSV RdRP inhibitors. We closed this knowledge gap for the AVG class, identifying L residues in direct proximity to the docked ligand that spanned an interface between the L capping, connecting, and MTase domains. Confidence in specificity and physiological relevance of the photoaffinity labels comes from three sources: three chemically distinct analogs were generated that differentially interrogate the target site; each of these analogs maintained potent anti-RSV activity; and residues covalently identified by these analogs lined a continuous physical site in the native polymerase complex.

Structural reconstructions of RSV (*17*, *18*), closely related human metapneumovirus (*47*), and more distantly related paramyxovirus (*48*) L-P complexes have highlighted a dynamic organization of the C-terminal L domains relative to the polymerase core composed of RdRP and capping domains. On the basis of the mechanistic inhibition profile in the in vitro RdRP assays, the resistance data, and the photoaffinity maps, we considered two mechanistic alternatives as possible molecular basis for AVG-233 inhibition of L: structural lockdown of the MTase domain or positional fixation of the putative priming-capping loop.

Specifically, AVG-233 docking may trap L capping, connecting, and MTase domains in a fixed position relative to each other, resulting in a polymerase complex that is permanently locked in initiation conformation. Preventing relative repositioning of these three domains should impair proper mRNA synthesis, since the MTase must swing away from the product exit channel after cap methylation to allow nascent mRNA elongation. However, our studies revealed that AVG-233 is also active against truncated L_{1-1749} RdRP complexes lacking the MTase domain, arguing against this model of MTase blockage of the exit channel.

We therefore favor the alternative explanation that AVG-233 prevents reorganization of the L priming-capping loop (*49*) after incorporation of the first few nucleotides. In RSV L structural models, the loop is retracted downstream of a pivotal residue G1264, which clears a path for the newly synthesized RNA strand to exit the polymerase complex in post-initiation configuration (*17*, *18*). Residue G1264 is located in immediate spatial proximity to V1384, which photoaffinity mapping identified as a direct anchor point for AVG inhibitors, thus positing the docked ligand at the hinge region of the priming-capping loop. Although an actual role of the loop in priming of pneumovirus polymerases has not yet been formally proven (*47*), we note that a purified mutant RSV RdRP complex bearing a G1264A substitution was unable to elongate RNA beyond the addition of two to three nucleotides (*50*), thus mimicking the inhibition phenotype of AVG-233.

Despite predicted oral bioavailability in mice (*24*), in vivo efficacy of AVG-233 was disappointing. Our targeted synthetic program identified a trifluoromethyl substitution in the c ring as instrumental for establishing robust oral efficacy. Since antiviral activity of AVG-233 in cell-based anti-RSV and the in vitro RdRP assays closely resembled that of the efficacious analogs, we hypothesize that the chloro-substituent in ring (c) of AVG-233 presented a metabolic liability in vivo that was overcome with the trifluoromethyl replacement.

Substantiated by a robust SI profile, potent antiviral performance in human tissue organoids, and favorable pharmacokinetic properties, the orally efficacious AVG class leads have strong developmental potential. In addition to its immediate impact as a clinical candidate, the AVG chemotype has identified the interface between the RSV L capping, connecting, and MTase domains as a major druggable site that is likely mechanistically conserved in all mononegavirus polymerase proteins. Considering the available resistance information, we propose that all allosteric RSV RdRP inhibitors interfering with polymerase initiation at the promoter that have been developed to date physically engage this interface. Our results lay the foundation for formal development of the AVG class and the structure-guided identification of companion drugs with overlapping target sites but distinct resistance profiles.

MATERIALS AND METHODS

Experimental design

In this study, we explored the preclinical efficacy of a series of allosteric inhibitors of RSV RdRP using both the mice model and the disease-relevant differentiated primary cells from human bronchial/tracheal epithelium, and we determined the mechanism of action of this class in vitro. The efficacy models were chosen because they jointly provide the closest model available to RSV replication in human lungs and constitute the premier system to evaluate efficacy of drug candidates. We determined the effect of treatment on viral replication at different oral doses in a prophylactic or therapeutic setting. Efficacy was considered as a statistically significant reduction in viral titers in mice lungs and in apical shedding from differentiated human epithelium. Efficacy and cytotoxicity in cell culture were determined in a dose-dependent manner using four-parameter variable slope regression modeling and calculation of 50% maximal efficacious concentrations. The end points were predefined for each experiment. Animals were randomly assigned to each group. Numbers of independent biological repeats for all experiments are specified in the figure legends. No blinding was performed. Complete raw and analyzed numerical data are openly provided in data file S1.

Cell lines, plasmids, and viruses

HEp-2 cells [American Type Culture Collection (ATCC), CCL-23], human embryonic kidney (HEK)–293T (ATCC, CRL-3216), and baby hamster kidney cells (BHK-21; ATCC, CCL-10) stably expressing either T7 polymerase (BSR-T7/5) were grown at 37°C and 5% CO_2 in Dulbecco's modified Eagle's medium supplemented with 7.5% heat-inactivated fetal bovine serum. Insect cells from *Spodoptera frugiperda* (SF9; ATCC, CRL-1711) were propagated in suspension using Sf-900 II serum-free medium (Thermo Fisher Scientific) at 28°C without CO_2. Experiments with primary HAE cells involved tissues from the following donors: Primary human bronchial tracheal epithelial cells from a 30-year-old female ("F1" donor, LifeLine Cell Technology, catalog no. LM-0050, lot no. 3123, passage 2) and primary human normal bronchial/tracheal epithelial cells ("M4" donor, Lonza Bioscience, catalog no. CC-2540S, lot no. 0000646466, passage 2) from a 38-year-old male were cultured in BronchiaLife complete cell culture medium (LifeLine Cell Technology, catalog no. LL-0023). Differentiated HAE from F1 donor (3D-HAE) was obtained as described previously (*35*). Briefly, 33,000 low-passage (<4) cells were seeded in polyester, tissue culture–treated, 0.33-cm^2 growth area, 0.4-µm membrane pore size Transwell (Corning, catalog no. 3470). Basal medium was replaced with Pneumacult-ALI (Stemcell Technologies, catalog no. 05001) when confluency was reached, and apical medium was removed. TEER was monitored to validate differentiation with EVOM volt/ohm meter and STX2 electrode (World Precision Instruments). All cell lines used in this study were authenticated and checked for mycoplasma and microbial contamination. Note that the International Cell Line Authentication Committee lists HEp-2 cells as a commonly misidentified cell line; however, their unique ability to efficiently propagate RSV justifies their use to generate and titrate viral stocks. Recombinant RSV strain A2 with line19F and mKatushka or fireSMASh reporter gene, recRSV-mKate or recRSV-fireSMASh, respectively, was rescued and amplified as described previously (*51*, *52*). L1502Q, H1632Q, and Y1631H substitutions were introduced following a protocol described previously (*5*).

Dose-response antiviral assays

Compound stocks were prepared in dimethyl sulfoxide (DMSO) and, upon dilution in cell culture medium, reached in all wells a final DMSO concentration of 0.1%. For luciferase-based dose-response assays, HEp-2 or primary HAE cells were seeded a day before to reach 50% confluence in 96-well white plates. Threefold serial dilutions of compounds were prepared in triplicate using an automated Nimbus liquid handler (Hamilton) and transferred to the cells. Immediately after addition of compound, cells were infected with recRSV-fireSMASh. Each plate contained four wells each of positive and negative control (medium containing 100 µM cycloheximide or vehicle, respectively). Luciferase activities were determined at 48 hours after transfection using One-GLO buffer (Promega, catalog no. E6130) and a Synergy H1 (BioTek) plate reader. Normalized luciferase activities were analyzed with the following formula: % inhibition = $(\mathrm{Signal}_{\mathrm{sample}} - \mathrm{Signal}_{\mathrm{min}})/(\mathrm{Signal}_{\mathrm{max}} - \mathrm{Signal}_{\mathrm{min}}) \times 100$, and dose-response curves were further analyzed by normalized nonlinear regression with variable slope to determine EC_{50} and 95% confidence intervals (CIs) with Prism 9.0.1 for MacOS (GraphPad).

Minireplicon assays

A set of helper plasmids expressing codon-optimized RSV P, L, N, and M2-1 proteins (A2 strain) under the control of cytomegalovirus promoter and a plasmid expressing the RSV minigenome cassette containing the firefly luciferase reporter, expressed under control of RNA polymerase I promoter, were cotransfected with GeneJuice reagent (MilliporeSigma) following the manufacturer's instructions in 50% confluent HEK-293T cells or BSR-T7/5 cells as described previously (*5*). To assay RdRP complex inhibition in dose-response experiments, cells were transfected in 96-well white plates. At 4 hours after transfection, compounds were added to the cells and analyzed as described above.

Cytotoxicity assays

HEp-2 or primary HAE cells were seeded at 50% confluence in 96-well plates and incubated with threefold serial dilution of compound with positive and negative controls as described above. After 48-hour incubation at 37°C, cells were incubated with PrestoBlue (Thermo Fisher Scientific, catalog no. A-13262) for 1 hour at 37°C and fluorescence was measured with an H1 synergy plate reader (BioTek). CC_{50} and 95% CIs after normalized nonlinear regression and variable slope were determined using Prism 9.0.1 for MacOS (GraphPad).

Growth curves

HEp-2 cells seeded in 12-well plates were infected with recRSV-fireSMASh in the absence or presence of L1502Q, H1632Q, or Y1631H substitution in L, at a multiplicity of infection of 0.1 in three independent replicates. Cells were scrapped and harvested every 12 hours for 4 days following infection. After virus release through freeze-thaw and clarification, viral titers were determined through $TCID_{50}$ titration with firefly luciferase bioluminescence as the readout, using One-GLO buffer (Promega, catalog no. E6130) and a Synergy H1 (BioTek) plate reader.

Confocal microscopy

3D-HAEs were fixed for 30 min at room temperature with a solution of 4% paraformaldehyde diluted in phosphate-buffered saline

(PBS). After permeabilization and blocking with PBS + 3% bovine serum albumin (BSA) + 0.1% Triton X-100 (45 min), cells were incubated at room temperature for 1 hour with primary antibodies diluted in PBS + 0.3% BSA+ 0.05% Tween 20 (wash buffer). After three 5-min washes, cells were incubated with a secondary antibody in wash buffer for 45 min and incubated with Hoechst 34580 (BD Biosciences, catalog no. 565877) (1:1000) in wash buffer for 5 min. Membranes were mounted on glass slides with ProLong Diamond Antifade Reagent (Thermo Fisher Scientific, catalog no. P36970) and imaged with a Zeiss Axio Observer Z.1 and Zeiss LSM 800 + AiryScan module. Image analyses were performed with Zeiss Zen 3.1 Blue software (Windows 10). Representative pictures were taken with a 63× Plan Apochromat (numerical aperture, 1.40, oil) objective. Digital pictures are pseudocolored for optimal presentation. Each sample was reconstructed by stacking 0.22 μm thick optical slices for a total depth of 35 μm, unless stated otherwise in the figure legend.

Apical shed viral titer determination
3D-HAEs were washed apically with PBS without calcium and magnesium. Cells were infected apically with recRSV-mKate (500,000 $TCID_{50}$) for 2 hours at 37°C. Compound was added in the basal medium (vehicle, 0.1% final DMSO). Shed virus was harvested by incubating the apical side with 200 μl of PBS without calcium and magnesium at 37°C for 30 min. Aliquots were stored at −80°C until titration by standard $TCID_{50}$ using fluorescence to detect infected cells.

Antibodies
Antibodies used for viral titration ($TCID_{50}$) were RSV: goat anti-RSV polyclonal antibody (1:1000 dilution) (MilliporeSigma, catalog no. AB1128), followed by donkey anti-goat antibody conjugated with horseradish peroxidase (1:1000 dilution) (Jackson ImmunoResearch, catalog no. 705-035-147). Infected cells were detected using Trueblue peroxidase substrate according to the manufacturer's instructions (Fisher Scientific, catalog no. 5067428).

Primary antibodies used for confocal microscopy: Adherens junctions were visualized with E-cadherin mouse antibody (1:100 dilution) (BD Biosciences; 610181). Goblet cells were visualized with mouse anti-MUC5AC (1:200 dilution) (Thermo Fisher Scientific, catalog no. MA5-12175). Ciliated cells were visualized with rabbit anti–β IV tubulin recombinant antibody conjugated with Alexa Fluor 647 [EPR16775] (1:100 dilution) (Abcam, catalog no. ab204034). Tight junctions were visualized with mouse anti–ZO-1 (1:50 dilution) (BD Biosciences, catalog no. 610966). RSV-infected cells were visualized either as a whole with goat anti-RSV polyclonal antibody (1:1000 dilution) (MilliporeSigma, catalog no. AB1128) or with a focus on RSV-induced cytoplasmic inclusion bodies using mouse anti-RSV nucleoprotein, clone 130-12H (1:100 dilution) (MilliporeSigma, catalog no. MAB858-3). The following antibodies were used as secondary antibodies as appropriate: rabbit anti-mouse IgG (H+L) cross-adsorbed secondary antibody, Alexa Fluor 488 (1:500 dilution) (Thermo Fisher Scientific, catalog no. A-11059), or donkey anti-goat Alexa Fluor 568 (1:500 dilution) (Thermo Fisher Scientific, catalog no. A-11057).

Protein purification
RSV L + P complexes were prepared as previously described (*53*, *54*). Briefly, codon-optimized sequences of RSV L and a 6×HIS-tagged P were coexpressed in SF9 cells in serum-free medium SF900-II (Thermo Fisher Scientific) from a recombinant baculovirus vector generated with the pFastBac dual system. Cells were harvested at 78 hours after infection and lysed in 50 mM NaH_2PO_4 (pH 8.0), 150 mM NaCl, 20 mM imidazole, and 0.5% Igepal (MilliporeSigma). After purification through immobilized metal affinity chromatography with Ni-NTA Superflow resin (Qiagen), cells were dialyzed into storage buffer: 20 mM tris-HCl (pH 7.4), 150 mM NaCl, 10% glycerol, and 1 mM dithiothreitol.

In vitro polymerase assay
De novo RNA synthesis using the purified L + P complex was performed as previously described (*54*). Briefly, 100 to 200 ng of RSV L in complex with P were incubated with 2 μM RNA template corresponding to the 25 nucleotides of the RSV trailer complement sequence (3′ UGCUCUUUUUUUCACAGUUUUUGAU) (Horizon Discovery), 8 mM $MgCl_2$, 1 mM dithiothreitol, 1 mM adenosine triphosphate (ATP), 1 mM uridine triphosphate (UTP), 1 mM cytidine triphosphate (CTP), 50 μM GTP, 10 μCi of α-^{32}P–labeled GTP (Perkin-Elmer), 20 mM tris-HCl (pH 7.4), 15 mM NaCl, and 10% glycerol. Reaction was equilibrated for 10 min at 30°C before addition of L + P complexes and then incubated for 3 hours at 30°C. RNAs were precipitated for 16 hours at −20°C with 2.5 volumes of ice-cold ethanol, 0.1 volume of 3 M sodium acetate, and 625 ng of glycogen (Thermo Fisher Scientific). Pellets were washed with ice-cold 75% ethanol, dried, and resuspended in 50% deionized formamide. After a 3-min denaturation at 95°C, RNAs were separated on 7 M urea/20% polyacrylamide tris borate–EDTA gels and visualized by autoradiography using either CL-XPosure Film (Thermo Fisher Scientific) or a storage phosphor screen BAS IP MS 2040 E (GE Healthcare Life Sciences) and imaged with Typhoon FLA 7000 (GE Healthcare Life Sciences). Densitometry analysis was performed using Fiji 2.0 (*55*).

3′ Extension assays were performed on the basis of slight modifications of established assays (*46*, *56*, *57*). Briefly, 1 μM RNA template (3′ UGGUCUUUUUUGUUUC) and 200 μM 5′ phosphorylated RNA primer (5′ pACCA) (Horizon Discovery) were incubated with 8 mM $MgCl_2$, 1 mM dithiothreitol, 10 μM ATP, 10 μM UTP, 10 μM CTP, 10 μM GTP, 10 μCi of α-^{32}P–labeled GTP (Perkin-Elmer), 20 mM tris-HCl (pH 7.4), 15 mM NaCl, and 10% glycerol and, after 10 min at 30°C, with 100 ng of RSV L in complex with P in a final volume of 5 μl. After 60-min incubation at 30°C, reaction was stopped with 5 μl of deionized formamide with 25 mM EDTA. After denaturation at 95°C, RNAs were separated on 7 M urea/20% polyacrylamide tris borate–EDTA gels and visualized by autoradiography using a storage phosphor screen BAS IP MS 2040 E (GE Healthcare Life Sciences) and imaged with Typhoon FLA 7000 (GE Healthcare Life Sciences). Densitometry analysis was performed using Fiji 2.0 (*55*).

Biolayer interferometry
Purified RSV L-P complexes were buffer-exchanged for PBS (pH 7.4; room temperature) on PD-10 desalting columns (GE Healthcare), mono-biotinylated with the EZ-Link Sulfo-NHS-SS-Biotin reagent (Thermo Fisher Scientific), and loaded on Super-Streptavidin sensors (Molecular Devices) for 2 hours at 30°C to reach a shift of 1 nm. Uncoupled streptavidin was quenched for 15 min with a solution of 2 mM biocytin. In parallel, a solution of thyroglobulin (1 mg/ml; GE Healthcare) was biotinylated and loaded to 1-nm shift on control sensors. Kinetic experiments were performed at

30°C with 1000 rpm shaking in 96-well plates using the Octet Red 96 system (Fortebio). Biosensors loaded with L-P and thyroglobulin were successively equilibrated for 100 s in assay buffer (PBS, 0.01% BSA, 0.005% Tween 20, and 1% DMSO) (baseline), incubated in a dilution of compound (twofold from 40 nM to 40 μM) for 120 s (association), and then incubated in assay buffer for 200 s (dissociation). Real-time binding kinetics were analyzed and calculated using the Octet Red software package. Raw signal was processed using the double-reference method, by subtracting both the thyroglobulin signal (unspecific signal) and the signal in the absence of compound (drift), after baseline alignment and interstep correction at the dissociation. Kinetic modeling was done by analyzing association and dissociation signals using global fitting with a 1:1 model.

Photolabeling of the AVG-233 binding site

Two micrograms of RSV L-P complexes in PBS was mixed with 100 μM of compound a, b, or c for 5 min on ice and then photocrosslinked for 10 min (compound a) or 45 min (compounds b and c) at 365 nm. Samples with compounds b and c were further treated with the auto-crosslink mode of Stratalinker 1800 (Stratagene). Samples were fractionated on Bolt 4-12% Bis-Tris Plus Gels (Thermo Fisher Scientific) and MES buffer and analyzed by MS.

LC-MS/MS analyses and data processing

Liquid chromatography–MS/MS (LC-MS/MS) analysis was performed by the Proteomics and Metabolomics Facility at the Wistar Institute using a Q Exactive Plus mass spectrometer (Thermo Fisher Scientific) coupled with a Nano-ACQUITY UPLC system (Waters). Following procedures originally described in (*45*), gel bands were excised, digested in-gel with trypsin, and injected onto a UPLC Symmetry trap column (180 μm inside diameter × 2 cm packed with 5-μm C18 resin; Waters). Tryptic peptides were separated by reversed-phase high-performance LC on a BEH C18 nanocapillary analytical column (75 μm inside diameter × 25 cm, 1.7-μm particle size; Waters) using a gradient formed by solvent A (0.1% formic acid in water) and solvent B (0.1% formic acid in acetonitrile). A 30-min blank gradient was run between sample injections to minimize carryover. Eluted peptides were analyzed by the mass spectrometer set to repetitively scan mass/charge ratio (*m*/*z*) from 300 to 2000 in positive ion mode. The full-MS scan was collected at 70,000 resolution followed by data-dependent MS/MS scans at 17,500 resolution on the 20 most abundant ions exceeding a minimum threshold of 20,000. Peptide match was set as preferred, exclude isotopes option, and charge-state screening was enabled to reject unassigned charged ions. Peptide sequences were identified using pFind 3.1.5 (*58*). MS/MS spectra were searched against a custom database containing Sf9, baculovirus, and hRSV protein sequences. Search parameters include full tryptic specificity with up to three missed cleavages, peptide mass tolerance of 10 parts per million (ppm), fragment ion mass tolerance of 15 ppm, static carboxamidomethylation of Cys, and variable oxidation of Met. In addition, mass addition of 537.117924 (compound a), 470.125788 (compound b), or 484.165901 (compound c) was also considered for all amino acid residues. Consensus identification lists were generated with false discovery rates of 1% at protein and peptide levels.

Molecular modeling and docking

RSV L-P available structure encompasses residue 1–1460 of RSV, likely in a post-initiation conformation [Protein Data Bank (PDB): 6PZK] (*18*). Modeling of full-length RSV L in putative pre-initiation conformation was performed using I-Tasser server and the RSV L strain A2 (GenBank: AAC14905.1) using as a template related vesicular stomatitis virus L (PDB: 5a22), L + P (PDB: 6U1X), rabies virus L + P (PDB: 6UEB), and human metapneumovirus L C-terminal domain (PDB: 4UCY).

In vivo efficacy testing

Female Balb/cJ mice (The Jackson Laboratory, catalog no. 000651) 6 to 8 weeks of age were housed in an Animal Biosafety Level 2 (ABSL-2) facility (4- to 5-day rest). Mice were divided randomly into groups of five and infected intranasally with 500,000 $TCID_{50}$ (25 μl per nare) of recRSV-mKate in PBS. Mice were anesthetized with ketamine/xylazine. Treatments were administrated via oral gavage in a 200-μl suspension of 1% methylcellulose in water. Temperature and body weight were determined on a daily and twice-daily basis, respectively. Efficacy studies were terminated at peak viral replication at 4.5 days after infection, mice were euthanized, and lungs were harvested and weighted. Lung viral titers were determined after tissue homogenization with a bead beater with 300 μl of PBS (three bursts of 30 s at 4°C, separated by 30-s rest at 4°C). Homogenates were clarified (5 min at 4°C and 20,000*g*), aliquoted, and stored at −80°C until titration. Viral titers were determined by $TCID_{50}$ titration, adjusted to weight (grams) of lung tissue.

Histopathology analysis

For histopathology, mice were subjected to cervical dislocation 4.5 days after infection and lungs were perfused with 10% neutral buffered formalin (NBF) before extraction. Lungs were stored in 10% NBF for 24 hours, followed by incubation in 70% EtOH for 2 days and embedding into wax blocks, using a 21-hour alcohol-xylene-wax embedding sequence. Blocks were sectioned at ~4 μm thickness, and sections were mounted onto microscopy slides and stained with hematoxylin and eosin (H&E). Slides were examined by a board-certified veterinary pathologist, who was blinded to the treatment groups. Lesions were scored according to the following scale. Alveoli, bronchiolar, and pleuritis scores were as follows: 1 = focal, 2 = multifocal, and 3 = multifocal to coalescing; perivascular cuffing: 1 = one layer of leukocytes cuffing vessel, 2 = two to five layers, and 3 = six to nine layers; vasculitis score: 1 = leukocytes infiltrating vessel wall, 2 = leukocytes and smooth muscle cell separation, and 3 = fibrinoid necrosis; interstitial pneumonia: 1 = alveolar septa infiltrated by one leukocyte thickness, 2 = two leukocytes thick, and 3 = three leukocytes thick.

Chemical synthesis

All materials were obtained from commercial suppliers and used without purification, unless otherwise noted. Dry organic solvents, packaged under nitrogen in septum-sealed bottles, were purchased from EMD Millipore and Sigma-Aldrich Co. Reactions were monitored using EMD silica gel 60 F_{254} TLC plates or using an Agilent 1200 series LCMS system with a diode array detector and an Agilent 6120 quadrupole MS detector. Compound purification was accomplished by liquid chromatography on a Teledyne Isco CombiFlash RF+ flash chromatography system. Nuclear magnetic resonance (NMR) spectra were recorded on an Agilent NMR spectrometer (400 MHz) at room temperature. Chemical shifts are reported in ppm relative to residual solvent signal. The residual shifts were taken as internal references and reported in ppm.

General reaction strategy

An overview of the general synthesis strategy of the AVG chemotype is shown in fig. S21. Dimethyl-1,3-acetonedicarboxylate (6.6 ml, 45.81 mmol) was added to a suspension of 2-hydrazinopyridine (compound **1**; fig. S21) (5.0 g, 45.81 mmol) in anhydrous toluene (50 ml) to synthesize compound **2** (fig. S21). The reaction mixture was refluxed for 12 hours. After completion, the reaction mixture was concentrated under reduced pressure. The brown solid product (9.60 g, 90% yield) obtained was washed with diethyl ether and dried in vacuum oven at 50°C and used as such for further reactions.

^{1}H NMR 400 MHz, DMSO-d_6, δ 12.45 (s, 1H), 8.43 (d, J = 8 Hz, 1H), 8.02 (pseudo t, J = 8 Hz, 1H), 7.74 (d, J = 8 Hz, 1H), 7.35 (pseudo t, J = 8 Hz, 1H), 5.58 (s, 1H), 3.64 (s, 3H), 3.61 (s, 2H). ^{13}C NMR 100 MHz, DMSO-d_6, δ 170.67, 155.88, 153.23, 147.70, 146.90, 140.83, 121.25, 112.97, 88.68, 52.33, 34.99. MS [electrospray ionization and atmospheric pressure ionization (ES-API)] $[M + 1]^+$:234.0.

For synthesis of compound **3** (fig. S21), triethyl orthoacetate (11.8 ml, 64.32 mmol) and acetic acid (0.25 ml, 4.30 mmol) were added to a solution of compound **2** (5.0 g, 21.43 mmol) in anhydrous acetonitrile (50 ml). The reaction mixture was stirred at 70°C for 12 hours. After completion, the reaction mixture was concentrated under reduced pressure and washed with diethyl ether to obtain compound **3** as brownish yellow solid. ^{1}H NMR 400 MHz, DMSO-d_6, δ 14.95 (broad s, 1H), 8.43 (d, J = 8 Hz, 1H), 8.26 to 8.16 (m, 2H), 7.42 to 7.40 (m, 1H), 3.78 (s, 2H), 3.60 (s, 3H), 2.31 (s, 3H); ^{13}C NMR 100 MHz, DMSO-d_6, δ 190.38, 169.41, 163.57, 150.71, 148.11, 143.64, 141.81, 119.75, 112.63, 102.78, 51.70, 34.78, 28.11. MS (ES-API) $[M + 1]^+$: 276.0.

For synthesis of compound **4** (fig. S21), (6-chloropyridin-2-yl) methanamine dihydrochloride (0.64 g, 3 mmol) and triethylamine (1.25 ml, 9 mmol) were added to a solution of compound **3** (0.8 g, 3 mmol) in anhydrous acetonitrile (20 ml), and the reaction mixture was stirred at room temperature. After 2 hours, 1,8-diazabicyclo[5.4.0] undec-7-ene (DBU) (0.9 ml, 6 mmol) was added and stirred at room temperature for another 5 hours. After completion, the reaction mixture was concentrated under reduced pressure and the crude product was purified by flash column chromatography using dichloromethane and methanol as eluent. Product was obtained as yellow solid (0.40 g, 36% yield). ^{1}H NMR 400 MHz, DMSO-d_6, δ 11.48 (s, 1H), 8.48 to 8.46 (m, 1H), 8.37 (d, J = 8 Hz, 1H), 7.95 to 7.91 (m, 1H), 7.84 (pseudo t, J = 8 Hz, 1H), 7.42 (d, J = 8 Hz, 1H), 7.28 to 7.22 (m, 2H), 5.68 (s, 1H), 5.37 (s, 2H), 2.83 (s, 3H); ^{13}C NMR 100 MHz, DMSO-d_6, 190.38, 169.41, 163.57, 150.71, 148.11, 143.64, 141.87, 119.77, 112.62, 109.58, 102.79, 51.65, 28.11. MS (ES-API) $[M + 1]^+$: 368.0.

For synthesis of analogs **A** and **B** (fig. S21), *N*,*N*-diisopropylethylamine (0.10 ml, 0.60 mmol) and respective substituted benzyl halide (0.60 mmol) were added to a solution of compound **4** (0.18 g, 0.5 mmol) in anhydrous *N*,*N*-dimethylformamide (5 ml), and the reaction mixture was stirred at 50°C for 6 hours. After completion, the reaction mixture was concentrated under reduced pressure and the crude product was purified by flash column chromatography using dichloromethane and methanol as eluent. Desired products were obtained in 25 to 35% isolated yield.

Analog **A**: ^{1}H NMR 400 MHz, $CDCl_3$, δ 8.54 (d, J = 8 Hz, 1H) 7.85 to 7.78 (m, 2H), 7.61 (pseudo t, J = 8 Hz, 1H), 7.26 to 7.16 (m, 4H), 7.06 to 6.99 (m, 3H), 6.06 (s, 1H), 5.40 (s, 2H), 4.98 (s, 2H), 2.89 (s, 3H); ^{19}F NMR 376 MHz, $CDCl_3$, δ –65.08 (s); ^{13}C NMR 100 MHz, $CDCl_3$ (includes multiplets from ^{13}C-^{19}F couplings), δ 162.91, 162.16, 156.01, 155.20, 154.40, 151.01, 148.65, 148.31, 148.21, 139.62, 138.25, 135.33, 129.31, 129.25, 129.16, 129.09, 126.62, 126.53, 126.45, 123.53, 123.38, 123.27, 121.08, 120.93, 120.64, 120.54, 120.49, 117.17, 101.66, 90.88, 90.71, 77.09, 53.82, 48.14, 15.33. MS (ES-API) $[M + 1]^+$: 565.9.

Analog **B**: ^{1}H NMR 400 MHz, $CDCl_3$, δ 8.54 (d, J = 8 Hz, 1H), 7.85 (m, 2H), 7.61 (pseudo t, J = 8 Hz, 1H), 7.26 to 7.16 (m, 3H), 7.06 to 6.99 (m, 4H), 6.06 (s, 1H), 5.40 (s, 2H), 4.98 (s, 2H), 2.89 (s, 3H); ^{13}C NMR 100 MHz, $CDCl_3$, δ 162.95, 162.16, 156.09, 155.31, 154.22, 151.01, 148.68, 148.25, 140.28, 139.64, 138.24, 130.44, 130.31, 130.12, 123.38, 120.89, 120.64, 120.49, 119.15, 117.19, 101.90, 91.02, 53.91, 48.17, 15.31. MS (ES-API) $[M + 1]^+$: 498.9.

An overview of the preparation of analog **C** is shown in fig. S22. Sodium azide (0.32 g, 5.0 mmol) and ammonium chloride (0.26 g, 5 mmol) were added to a solution of compound **5** (0.25 g, 0.5 mmol; fig. S22, prepared as shown in fig. S21 for the synthesis of analogs **A** and **B**) in anhydrous dimethylformamide (DMF) (3 ml) and stirred at 110°C for 48 hours. After completion, the reaction mixture was concentrated under reduced pressure. The crude reaction mixture was dissolved in dichloromethane (50 ml) and extracted with water (50 ml) and brine (50 ml). The organic layer was dried over anhydrous sodium sulfate and concentrated under reduced pressure. The crude product was purified by flash column chromatography using dichloromethane and methanol as eluent. Product was isolated as pale yellow solid (0.093 g, 36% yield). ^{1}H NMR 400 MHz, $CDCl_3$, δ 8.56 (ddd, J = 5.2 Hz, 2 Hz, 0.8 Hz, 1H), 8.01 (dd, J = 8 Hz, 0.8 Hz, 1H), 7.84 to 7.80 (m, 1H), 7.72 to 7.70 (m, 1H), 7.61 (dd, J = 12 Hz, 8 Hz, 1H), 7.22 (ddd, J = 5.2 Hz, 2 Hz, 0.8 Hz, 1H), 6.88 (dd, J = 8.4 Hz, 6.4 Hz, 1H), 6.76 to 6.74 (m, 1H), 6.50 to 6.41 (m, 2H), 6.18 (s, 1H), 5.95 (s, 2H), 5.04 (s, 2H), 3.50 (s, 3H), 2.84 (s, 3H); ^{19}F NMR 376 MHz, $CDCl_3$, δ −109.51 to −109.57 (m); ^{13}C NMR 100 MHz, $CDCl_3$ (includes multiplets from ^{13}C-^{19}F couplings) δ 164.90, 162.67, 162.44, 162.10, 158.86, 155.12, 152.77, 148.94, 148.76, 148.17, 137.97, 134.09, 131.88, 120.96, 117.73, 117.40, 114.78, 113.43, 106.79, 106.58, 102.59, 99.03, 98.78, 90.84, 55.31, 48.44, 42.44, 14.86; MS (ES-API) $[M + 1]^+$: 513.0.

Statistical analysis

GraphPad Prism software (v8.3.0 Mac OSX) was used for all statistical analyses. Multiple comparisons were analyzed with one-way or two-way analysis of variance (ANOVA) with Dunnett's or Sidak's post hoc tests, as specified in figure legends. Fifty percent and 90% maximal effective concentrations were calculated using four-parameter nonlinear regression modeling. Individual biological replicates (n = 3) are represented as symbols or means with SDs. Significance threshold was set to 0.05. P values are represented as stars (*P < 0.05, **P < 0.01, ***P < 0.005, and ****P < 0.001).

Ethics statement

All animal work was performed in compliance with the *Guide for the Care and Use of Laboratory Animals* of the National Institutes of Health as well as the Animal Welfare Act Code of Federal Regulations. Experiments involving mice were approved by the Georgia State University Institutional Animal Care and Use Committee under protocols A17019 and A20012.

SUPPLEMENTARY MATERIALS

Supplementary material for this article is available at https://science.org/doi/10.1126/sciadv.abo2236

View/request a protocol for this paper from *Bio-protocol*.

REFERENCES AND NOTES

1. T. Shi, D. A. McAllister, K. L. O'Brien, E. A. F. Simoes, S. A. Madhi, B. D. Gessner, F. P. Polack, E. Balsells, S. Acacio, C. Aguayo, I. Alassani, A. Ali, M. Antonio, S. Awasthi, J. O. Awori, E. Azziz-Baumgartner, H. C. Baggett, V. L. Baillie, A. Balmaseda, A. Barahona, S. Basnet, Q. Bassat, W. Basualdo, G. Bigogo, L. Bont, R. F. Breiman, W. A. Brooks, S. Broor, N. Bruce, D. Bruden, P. Buchy, S. Campbell, P. Carosone-Link, M. Chadha, J. Chipeta, M. Chou, W. Clara, C. Cohen, E. de Cuellar, D. A. Dang, B. Dash-Yandag, M. Deloria-Knoll, M. Dherani, T. Eap, B. E. Ebruke, M. Echavarria, C. C. de Freitas Lazaro Emediato, R. A. Fasce, D. R. Feikin, L. Feng, A. Gentile, A. Gordon, D. Goswami, S. Goyet, M. Groome, N. Halasa, S. Hirve, N. Homaira, S. R. C. Howie, J. Jara, I. Jroundi, C. B. Kartasasmita, N. Khuri-Bulos, K. L. Kotloff, A. Krishnan, R. Libster, O. Lopez, M. G. Lucero, F. Lucion, S. P. Lupisan, D. N. Marcone, J. P. McCracken, M. Mejia, J. C. Moisi, J. M. Montgomery, D. P. Moore, C. Moraleda, J. Moyes, P. Munywoki, K. Mutyara, M. P. Nicol, D. J. Nokes, P. Nymadawa, M. T. da Costa Oliveira, H. Oshitani, N. Pandey, G. Paranhos-Baccala, L. N. Phillips, V. S. Picot, M. Rahman, M. Rakoto-Andrianarivelo, Z. A. Rasmussen, B. A. Rath, A. Robinson, C. Romero, G. Russomando, V. Salimi, P. Sawatwong, N. Scheltema, B. Schweiger, J. A. G. Scott, P. Seidenberg, K. Shen, R. Singleton, V. Sotomayor, T. A. Strand, A. Sutanto, M. Sylla, M. D. Tapia, S. Thamthitiwat, E. D. Thomas, R. Tokarz, C. Turner, M. Venter, S. Waicharoen, J. Wang, W. Watthanaworawit, L. M. Yoshida, H. Yu, H. J. Zar, H. Campbell, H. Nair; RSV Global Epidemiology Network, Global, regional, and national disease burden estimates of acute lower respiratory infections due to respiratory syncytial virus in young children in 2015: A systematic review and modelling study. *Lancet* **390**, 946–958 (2017).
2. N. I. Mazur, D. Higgins, M. C. Nunes, J. A. Melero, A. C. Langedijk, N. Horsley, U. J. Buchholz, P. J. Openshaw, J. S. McLellan, J. A. Englund, A. Mejias, R. A. Karron, E. A. Simoes, I. Knezevic, O. Ramilo, P. A. Piedra, H. Y. Chu, A. R. Falsey, H. Nair, L. Kragten-Tabatabaie, A. Greenough, E. Baraldi, N. G. Papadopoulos, J. Vekemans, F. P. Polack, M. Powell, A. Satav, E. E. Walsh, R. T. Stein, B. S. Graham, L. J. Bont; Respiratory Syncytial Virus Network (ReSViNET) Foundation, The respiratory syncytial virus vaccine landscape: Lessons from the graveyard and promising candidates. *Lancet Infect. Dis.* **18**, e295–e311 (2018).
3. J. Gottlieb, F. Torres, T. Haddad, G. Dhillon, D. Dilling, C. Knoop, R. Rampolla, R. Walia, V. Ahya, R. Kessler, A phase 2b randomized controlled trial of presatovir, an oral RSV fusion inhibitor, for the treatment of respiratory syncytial virus (RSV) in lung transplant (LT) recipients. *J. Heart Lung Transplant.* **37**, S155 (2018).
4. D. Hanfelt-Goade, N. Maimon, A. Nimer, F. Riviere, E. Catherinot, M. Ison, S. Jeong, E. Walsh, A. Gafter-Gvili, S. Nama, A phase 2b, randomized, double-blind, placebo-controlled trial of Presatovir (GS-5806), a novel Oral RSV fusion inhibitor, for the treatment of respiratory syncytial virus (RSV) in hospitalized adults, in *C17. New Insights in Acute Pulmonary Infections* (American Thoracic Society, 2018), p. A4457.
5. D. Yan, S. Lee, V. D. Thakkar, M. Luo, M. L. Moore, R. K. Plemper, Cross-resistance mechanism of respiratory syncytial virus against structurally diverse entry inhibitors. *Proc. Natl. Acad. Sci. U.S.A.* **111**, E3441–E3449 (2014).
6. Palivizumab, a humanized respiratory syncytial virus monoclonal antibody, reduces hospitalization from respiratory syncytial virus infection in high-risk infants. The IMpact-RSV Study Group. *Pediatrics* **102**, 531–537 (1998).
7. T. F. Feltes, A. K. Cabalka, H. C. Meissner, F. M. Piazza, D. A. Carlin, F. H. Top Jr., E. M. Connor, H. M. Sondheimer; Cardiac Synagis Study Group, Palivizumab prophylaxis reduces hospitalization due to respiratory syncytial virus in young children with hemodynamically significant congenital heart disease. *J. Pediatr.* **143**, 532–540 (2003).
8. M. Aggarwal, R. K. Plemper, Structural insight into paramyxovirus and pneumovirus entry inhibition. *Viruses* **12**, 342 (2020).
9. R. Fearns, R. K. Plemper, Polymerases of paramyxoviruses and pneumoviruses. *Virus Res.* **234**, 87–102 (2017).
10. H. Grosfeld, M. G. Hill, P. L. Collins, RNA replication by respiratory syncytial virus (RSV) is directed by the N, P, and L proteins; transcription also occurs under these conditions but requires RSV superinfection for efficient synthesis of full-length mRNA. *J. Virol.* **69**, 5677–5686 (1995).
11. J. Sourimant, M. A. Rameix-Welti, A. L. Gaillard, D. Chevret, M. Galloux, E. Gault, J. F. Eleouet, Fine mapping and characterization of the L-polymerase-binding domain of the respiratory syncytial virus phosphoprotein. *J. Virol.* **89**, 4421–4433 (2015).
12. M. Galloux, G. Gabiane, J. Sourimant, C. A. Richard, P. England, M. Moudjou, M. Aumont-Nicaise, J. Fix, M. A. Rameix-Welti, J. F. Eleouet, Identification and characterization of the binding site of the respiratory syncytial virus phosphoprotein to RNA-free nucleoprotein. *J. Virol.* **89**, 3484–3496 (2015).
13. R. Fearns, P. L. Collins, Role of the M2-1 transcription antitermination protein of respiratory syncytial virus in sequential transcription. *J. Virol.* **73**, 5852–5864 (1999).
14. E. Burke, N. M. Mahoney, S. C. Almo, S. Barik, Profilin is required for optimal actin-dependent transcription of respiratory syncytial virus genome RNA. *J. Virol.* **74**, 669–675 (2000).
15. A. P. Oliveira, F. M. Simabuco, R. E. Tamura, M. C. Guerrero, P. G. Ribeiro, T. A. Libermann, L. F. Zerbini, A. M. Ventura, Human respiratory syncytial virus N, P and M protein interactions in HEK-293T cells. *Virus Res.* **177**, 108–112 (2013).
16. C. A. Richard, V. Rincheval, S. Lassoued, J. Fix, C. Cardone, C. Esneau, S. Nekhai, M. Galloux, M. A. Rameix-Welti, C. Sizun, J. F. Eleouet, RSV hijacks cellular protein phosphatase 1 to regulate M2-1 phosphorylation and viral transcription. *PLOS Pathog.* **14**, e1006920 (2018).
17. D. Cao, Y. Gao, C. Roesler, S. Rice, P. D'Cunha, L. Zhuang, J. Slack, M. Domke, A. Antonova, S. Romanelli, S. Keating, G. Forero, P. Juneja, B. Liang, Cryo-EM structure of the respiratory syncytial virus RNA polymerase. *Nat. Commun.* **11**, 368 (2020).
18. M. S. A. Gilman, C. Liu, A. Fung, I. Behera, P. Jordan, P. Rigaux, N. Ysebaert, S. Tcherniuk, J. Sourimant, J. F. Eleouet, P. Sutto-Ortiz, E. Decroly, D. Roymans, Z. Jin, J. S. McLellan, Structure of the respiratory syncytial virus polymerase complex. *Cell* **179**, 193–204.e14 (2019).
19. J. Chapman, E. Abbott, D. G. Alber, R. C. Baxter, S. K. Bithell, E. A. Henderson, M. C. Carter, P. Chambers, A. Chubb, G. S. Cockerill, P. L. Collins, V. C. Dowdell, S. J. Keegan, R. D. Kelsey, M. J. Lockyer, C. Luongo, P. Najarro, R. J. Pickles, M. Simmonds, D. Taylor, S. Tyms, L. J. Wilson, K. L. Powell, RSV604, a novel inhibitor of respiratory syncytial virus replication. *Antimicrob. Agents Chemother.* **51**, 3346–3353 (2007).
20. B. Bailly, C. A. Richard, G. Sharma, L. Wang, L. Johansen, J. Cao, V. Pendharkar, D. C. Sharma, M. Galloux, Y. Wang, R. Cui, G. Zou, P. Guillon, M. von Itzstein, J. F. Eleouet, R. Altmeyer, Targeting human respiratory syncytial virus transcription anti-termination factor M2-1 to inhibit in vivo viral replication. *Sci. Rep.* **6**, 25806 (2016).
21. G. S. Cockerill, J. A. D. Good, N. Mathews, State of the art in respiratory syncytial virus drug discovery and development. *J. Med. Chem.* **62**, 3206–3227 (2019).
22. J. Sourimant, C. M. Lieber, M. Aggarwal, R. M. Cox, J. D. Wolf, J. J. Yoon, M. Toots, C. Ye, Z. Sticher, A. A. Kolykhalov, L. Martinez-Sobrido, G. R. Bluemling, M. G. Natchus, G. R. Painter, R. K. Plemper, 4′-Fluorouridine is an oral antiviral that blocks respiratory syncytial virus and SARS-CoV-2 replication. *Science* **375**, 161–167 (2022).
23. C. L. Tiong-Yip, L. Aschenbrenner, K. D. Johnson, R. E. McLaughlin, J. Fan, S. Challa, H. Xiong, Q. Yu, Characterization of a respiratory syncytial virus L protein inhibitor. *Antimicrob. Agents Chemother.* **58**, 3867–3873 (2014).
24. R. M. Cox, M. Toots, J. J. Yoon, J. Sourimant, B. Ludeke, R. Fearns, E. Bourque, J. Patti, E. Lee, J. Vernachio, R. K. Plemper, Development of an allosteric inhibitor class blocking RNA elongation by the respiratory syncytial virus polymerase complex. *J. Biol. Chem.* **293**, 16761–16777 (2018).
25. K. Sudo, Y. Miyazaki, N. Kojima, M. Kobayashi, H. Suzuki, M. Shintani, Y. Shimizu, YM-53403, a unique anti-respiratory syncytial virus agent with a novel mechanism of action. *Antiviral Res.* **65**, 125–131 (2005).
26. M. Coates, D. Brookes, Y. I. Kim, H. Allen, E. A. F. Fordyce, E. A. Meals, T. Colley, C. L. Ciana, G. F. Parra, V. Sherbukhin, J. A. Stockwell, J. C. Thomas, S. F. Hunt, L. Anderson-Dring, S. T. Onions, L. Cass, P. J. Murray, K. Ito, P. Strong, J. P. DeVincenzo, G. Rapeport, Preclinical characterization of PC786, an inhaled small-molecule respiratory syncytial virus L protein polymerase inhibitor. *Antimicrob. Agents Chemother.* **61**, e00737-17 (2017).
27. V. A. Laganas, E. F. Dunn, R. E. McLaughlin, C. L. Tiong-Yip, O. Yuzhakov, V. M. Isabella, P. Hill, Q. Yu, Characterization of novel respiratory syncytial virus inhibitors identified by high throughput screen. *Antiviral Res.* **115**, 71–74 (2015).
28. M. Dochow, S. A. Krumm, J. E. Crowe Jr., M. L. Moore, R. K. Plemper, Independent structural domains in paramyxovirus polymerase protein. *J. Biol. Chem.* **287**, 6878–6891 (2012).
29. O. Poch, I. Sauvaget, M. Delarue, N. Tordo, Identification of four conserved motifs among the RNA-dependent polymerase encoding elements. *EMBO J.* **8**, 3867–3874 (1989).
30. J. Fix, M. Galloux, M. L. Blondot, J. F. Eleouet, The insertion of fluorescent proteins in a variable region of respiratory syncytial virus L polymerase results in fluorescent and functional enzymes but with reduced activities. *Open Virol. J.* **5**, 103–108 (2011).
31. J. A. Horwitz, S. Jenni, S. C. Harrison, S. P. J. Whelan, Structure of a rabies virus polymerase complex from electron cryo-microscopy. *Proc. Natl. Acad. Sci. U.S.A.* **117**, 2099–2107 (2020).
32. S. Jenni, L. M. Bloyet, R. Diaz-Avalos, B. Liang, S. P. J. Whelan, N. Grigorieff, S. C. Harrison, Structure of the vesicular stomatitis virus L protein in complex with its phosphoprotein cofactor. *Cell Rep.* **30**, 53–60.e5 (2020).
33. B. Liang, Z. Li, S. Jenni, A. A. Rahmeh, B. M. Morin, T. Grant, N. Grigorieff, S. C. Harrison, S. P. J. Whelan, Structure of the L protein of vesicular stomatitis virus from electron cryomicroscopy. *Cell* **162**, 314–327 (2015).
34. R. J. Pickles, Human airway epithelial cell cultures for modeling respiratory syncytial virus infection. *Curr. Top. Microbiol. Immunol.* **372**, 371–387 (2013).
35. M. Toots, J.-J. Yoon, R. M. Cox, M. Hart, Z. M. Sticher, N. Makhsous, R. Plesker, A. H. Barrena, P. G. Reddy, D. G. Mitchell, R. C. Shean, G. R. Bluemling, A. A. Kolykhalov, A. L. Greninger, M. G. Natchus, G. R. Painter, R. K. Plemper, Characterization of orally efficacious influenza drug with high resistance barrier in ferrets and human airway epithelia. *Sci. Transl. Med.* **11**, eaax5866 (2019).
36. L. Zhang, M. E. Peeples, R. C. Boucher, P. L. Collins, R. J. Pickles, Respiratory syncytial virus infection of human airway epithelial cells is polarized, specific to ciliated cells, and without obvious cytopathology. *J. Virol.* **76**, 5654–5666 (2002).

37. V. Rincheval, M. Lelek, E. Gault, C. Bouillier, D. Sitterlin, S. Blouquit-Laye, M. Galloux, C. Zimmer, J. F. Eleouet, M. A. Rameix-Welti, Functional organization of cytoplasmic inclusion bodies in cells infected by respiratory syncytial virus. *Nat. Commun.* **8**, 563 (2017).
38. J. J. Yoon, M. Toots, S. Lee, M. E. Lee, B. Ludeke, J. M. Luczo, K. Ganti, R. M. Cox, Z. M. Sticher, V. Edpuganti, D. G. Mitchell, M. A. Lockwood, A. A. Kolykhalov, A. L. Greninger, M. L. Moore, G. R. Painter, A. C. Lowen, S. M. Tompkins, R. Fearns, M. G. Natchus, R. K. Plemper, Orally efficacious broad-spectrum ribonucleoside analog inhibitor of influenza and respiratory syncytial viruses. *Antimicrob. Agents Chemother.* **62**, e00766-18 (2018).
39. U.S. Food and Drug Administration, DA News Release Coronavirus (COVID-19) Update: FDA Authorizes Additional Oral Antiviral for Treatment of COVID-19 in Certain Adults (2021); https://www.fda.gov/news-events/press-announcements/coronavirus-covid-19-update-fda-authorizes-additional-oral-antiviral-treatment-covid-19-certain.
40. D. B. Madhura, J. Liu, B. Meibohm, R. E. Lee, Phase II metabolic pathways of spectinamide antitubercular agents: A comparative study of the reactivity of 4-substituted pyridines to glutathione conjugation. *Medchemcomm* **7**, 114–117 (2016).
41. J. Litchfield, R. Sharma, K. Atkinson, K. J. Filipski, S. W. Wright, J. A. Pfefferkorn, B. Tan, R. E. Kosa, B. Stevens, M. Tu, A. S. Kalgutkar, Intrinsic electrophilicity of the 4-methylsulfonyl-2-pyridone scaffold in glucokinase activators: Role of glutathione-S-transferases and in vivo quantitation of a glutathione conjugate in rats. *Bioorg. Med. Chem. Lett.* **20**, 6262–6267 (2010).
42. K. Inoue, T. Ohe, K. Mori, T. Sagara, Y. Ishii, M. Chiba, Aromatic substitution reaction of 2-chloropyridines catalyzed by microsomal glutathione S-transferase 1. *Drug Metab. Dispos.* **37**, 1797–1800 (2009).
43. J. R. Duvall, L. VerPlank, B. Ludeke, S. M. McLeod, M. D. Lee IV, K. Vishwanathan, C. A. Mulrooney, S. Le Quement, Q. Yu, M. A. Palmer, P. Fleming, R. Fearns, M. A. Foley, C. A. Scherer, Novel diversity-oriented synthesis-derived respiratory syncytial virus inhibitors identified via a high throughput replicon-based screen. *Antiviral Res.* **131**, 19–25 (2016).
44. S. L. Noton, K. Nagendra, E. F. Dunn, M. E. Mawhorter, Q. Yu, R. Fearns, Respiratory syncytial virus inhibitor AZ-27 differentially inhibits different polymerase activities at the promoter. *J. Virol.* **89**, 7786–7798 (2015).
45. R. M. Cox, J. Sourimant, M. Govindarajan, M. G. Natchus, R. K. Plemper, Therapeutic targeting of measles virus polymerase with ERDRP-0519 suppresses all RNA synthesis activity. *PLOS Pathog.* **17**, e1009371 (2021).
46. P. C. Jordan, C. Liu, P. Raynaud, M. K. Lo, C. F. Spiropoulou, J. A. Symons, L. Beigelman, J. Deval, Initiation, extension, and termination of RNA synthesis by a paramyxovirus polymerase. *PLOS Pathog.* **14**, e1006889 (2018).
47. J. Pan, X. Qian, S. Lattmann, A. El Sahili, T. H. Yeo, H. Jia, T. Cressey, B. Ludeke, S. Noton, M. Kalocsay, R. Fearns, J. Lescar, Structure of the human metapneumovirus polymerase phosphoprotein complex. *Nature* **577**, 275–279 (2020).
48. R. Abdella, M. Aggarwal, T. Okura, R. A. Lamb, Y. He, Structure of a paramyxovirus polymerase complex reveals a unique methyltransferase-CTD conformation. *Proc. Natl. Acad. Sci. U.S.A.* **117**, 4931–4941 (2020).
49. M. Ogino, N. Gupta, T. J. Green, T. Ogino, A dual-functional priming-capping loop of rhabdoviral RNA polymerases directs terminal de novo initiation and capping intermediate formation. *Nucleic Acids Res.* **47**, 299–309 (2019).
50. M. R. Braun, L. R. Deflube, S. L. Noton, M. E. Mawhorter, C. Z. Tremaglio, R. Fearns, RNA elongation by respiratory syncytial virus polymerase is calibrated by conserved region V. *PLOS Pathog.* **13**, e1006803 (2017).
51. A. L. Hotard, F. Y. Shaikh, S. Lee, D. Yan, M. N. Teng, R. K. Plemper, J. E. Crowe Jr., M. L. Moore, A stabilized respiratory syncytial virus reverse genetics system amenable to recombination-mediated mutagenesis. *Virology* **434**, 129–136 (2012).
52. D. Yan, M. Weisshaar, K. Lamb, H. K. Chung, M. Z. Lin, R. K. Plemper, Replication-competent influenza virus and respiratory syncytial virus luciferase reporter strains engineered for co-infections identify antiviral compounds in combination screens. *Biochemistry* **54**, 5589–5604 (2015).
53. B. Ludeke, R. Fearns, The respiratory syncytial virus polymerase can perform RNA synthesis with modified primers and nucleotide analogs. *Virology* **540**, 66–74 (2020).
54. S. L. Noton, L. R. Deflube, C. Z. Tremaglio, R. Fearns, The respiratory syncytial virus polymerase has multiple RNA synthesis activities at the promoter. *PLOS Pathog.* **8**, e1002980 (2012).
55. J. Schindelin, I. Arganda-Carreras, E. Frise, V. Kaynig, M. Longair, T. Pietzsch, S. Preibisch, C. Rueden, S. Saalfeld, B. Schmid, J. Y. Tinevez, D. J. White, V. Hartenstein, K. Eliceiri, P. Tomancak, A. Cardona, Fiji: An open-source platform for biological-image analysis. *Nat. Methods* **9**, 676–682 (2012).
56. J. Deval, J. Hong, G. Wang, J. Taylor, L. K. Smith, A. Fung, S. K. Stevens, H. Liu, Z. Jin, N. Dyatkina, M. Prhavc, A. D. Stoycheva, V. Serebryany, J. Liu, D. B. Smith, Y. Tam, Q. Zhang, M. L. Moore, R. Fearns, S. M. Chanda, L. M. Blatt, J. A. Symons, L. Beigelman, Molecular basis for the selective inhibition of respiratory syncytial virus RNA polymerase by 2'-Fluoro-4'-chloromethyl-cytidine triphosphate. *PLOS Pathog.* **11**, e1004995 (2015).
57. E. P. Tchesnokov, P. Raeisimakiani, M. Ngure, D. Marchant, M. Gotte, Recombinant RNA-dependent RNA polymerase complex of ebola virus. *Sci. Rep.* **8**, 3970 (2018).
58. H. Chi, C. Liu, H. Yang, W. F. Zeng, L. Wu, W. J. Zhou, R. M. Wang, X. N. Niu, Y. H. Ding, Y. Zhang, Z. W. Wang, Z. L. Chen, R. X. Sun, T. Liu, G. M. Tan, M. Q. Dong, P. Xu, P. H. Zhang, S. M. He, Comprehensive identification of peptides in tandem mass spectra using an efficient open search engine. *Nat. Biotechnol.* **36**, 1059–1061 (2018).
59. S. A. Jablonski, C. D. Morrow, Mutation of the aspartic acid residues of the GDD sequence motif of poliovirus RNA-dependent RNA polymerase results in enzymes with altered metal ion requirements for activity. *J. Virol.* **69**, 1532–1539 (1995).

Acknowledgments: We thank R. Fearns for the pFastbac Dual RSV L + P plasmid and an aliquot of AZ-27, B. Ludecke for advice with in vitro RdRP assays, H.-Y. Tang and the Wistar Institute Proteomics and Metabolomics Facility for assistance with proteomics analysis, and K. K. Conzelmann for the BSR-T7/5 cell line. **Funding:** This work was supported, in part, by NIH grants AI071002 (R.K.P.), AI153400 (R.K.P.), and HD079327 (R.K.P.). The funders had no role in study design, data collection and interpretation, or the decision to submit the work for publication. **Author contributions:** Conceptualization: R.K.P. Methodology: R.K.P. Investigation: J.S., C.M.L., M.T., J.-J.Y., M.G., and V.U. Analysis: J.S., C.M.L., M.T., K.S., and R.K.P. Visualization: J.S., C.M.L., and M.T. Funding acquisition: R.K.P. Project administration: R.K.P. Supervision: M.G.N., J.P., J.V., and R.K.P. Writing—original draft: J.S. and R.K.P. Writing—review and editing: R.K.P. **Competing interests:** R.K.P. and J.V. are inventors on patent 11084796 and patent application 20210403444 related to this work filed by Georgia State University Research Foundation Inc. (no. 11084796, filed on 10 May 2017, published on 10 August 2021). R.K.P. and J.V. are furthermore inventors on a patent application related to this work filed by Georgia State University Research Foundation Inc. (no. 20210403444, filed on 8 July 2021, published on 30 December 2021). The authors declare no other competing interests. **Data and materials availability:** All data needed to evaluate the conclusions in the paper are present in the paper and/or the Supplementary Materials. The AVG series compounds can be provided by Georgia State University pending scientific review and a completed material transfer agreement. Requests for the AVG series compounds should be submitted to R.K.P.

Submitted 20 January 2022
Accepted 9 May 2022
Published 24 June 2022
10.1126/sciadv.abo2236

2.4 Research Topic: Microbiome

2.4.1 Intestinal Microbiota Programming of Alveolar Macrophages Influences Severity of Respiratory Viral Infection

Intestinal microbiota programming of alveolar macrophages influences severity of respiratory viral infection

Vu L. Ngo[1#], Carolin M. Lieber[1#], Hae-ji Kang[1], Kaori Sakamoto[2], Michal Kuczma[1], Richard K. Plemper[1&*], and Andrew T. Gewirtz[1&*]

Affiliation:

1. Center for Translational Antiviral Research, Georgia State University Institute for Biomedical Sciences, Atlanta GA 30303, USA.

2. Department of Pathology, University of Georgia College of Veterinary Science, Athens GA 30602, USA

# These authors contributed equally to this work

& Denotes co-senior authors

*Corresponding authors. Email: rplemper@gsu.edu
agewirtz@gsu.edu

Abstract (132 words)

Investigating the influence of intestinal microbiota composition on respiratory viral infection (RVI) revealed that segmented filamentous bacteria (SFB), naturally acquired or exogenously administered, protected mice against influenza virus (IAV) infection, as assessed by viral titers, histopathology, and clinical disease features. Such protection, which also applied to RSV and SARS-CoV-2, was independent of interferon and adaptive immunity but required basally resident alveolar macrophages (AM), which, in SFB-negative mice, were quickly depleted as RVI progressed. Examination of AM from SFB-colonized mice revealed that they were intrinsically altered to resist IAV-induced depletion and inflammatory signaling. Yet, AM from SFB-colonized mice were not quiescent. Rather, they directly disabled IAV via enhanced complement production and phagocytosis. Transplant of SFB-transformed AM into SFB-free hosts recapitulated SFB-mediated protection against IAV mechanistically linking intestinal microbiota, AM phenotype, and RVI severity.

One sentence summary: Intestinal segmented filamentous bacteria reprogram alveolar macrophages enabling their host to withstand respiratory viruses.

INTRODUCTION

Outcomes following exposure to respiratory viruses, such influenza A viruses (IAV), respiratory syncytial virus (RSV), and SARS-CoV-2, vary widely amongst individuals, ranging from asymptomatic infection to severe lung pathology and/or death. While determinants of such heterogeneity to respiratory viral infection (RVI) are likely numerous and complex, we hypothesized that one important factor is gut microbiota composition [1], which is now appreciated to have broad influence over a range of chronic inflammatory diseases and the immune responses with which such diseases are associated [2]. For example, studies comparing mice captured in the wild to those bred for generations in well-controlled vivaria revealed vast differences in their microbiomes that resulted in wild mice having highly and broadly activated immune systems and being relatively resistant to IAV [3, 4]. Yet, differences in specific microbial species that can impact RVI outcomes, and how they might do so, have not been well defined. Hence, we studied mice raised in vivaria with discrete defined microbiome differences and, subsequently, mice differing in only the presence or absence of a single common species, namely segmented filamentous bacteria (SFB). We found that gut SFB dictated the phenotype of alveolar macrophages and, consequently, outcomes of RVI.

RESULTS

SFB protects mice from IAV infection

Appreciation of the potential of microbiota to broadly impact health led one commercial rodent supplier to offer "excluded flora (EF)" mice, which were bred in a restricted vivarium that assured absence of a discrete panel of disease-modulating commensal microbes, which might or might not otherwise be present in colonies of "specific pathogen-free (SPF)" mice commonly used in biomedical research [5]. We used such mice as a starting point to probe the influence of microbiota composition on RVI. Specifically, we compared proneness of SPF and EF mice to IAV infection 4 days following intranasal administration of 2009 pandemic A/CA/07/2009 (H1N1), herein referred to as CA09, which readily infects mice without need for species adaptation and recapitulates major clinical features of human disease in the animal model [6]. Compared to EF mice, SPF mice exhibited significantly reduced lung viral titers. Furthermore, SPF mice did not show hypothermia and weight loss observed in EF mice **(Figure 1A)**. Additionally, although not designed as a survival experiment per se, we noted that some mice of the EF mice required euthanasia. These results suggested that one or more of the microbes specifically excluded from EF mice might confer protection against IAV.

Of the panel of organisms known to be absent in EF mice, segmented filamentous bacteria (SFB) stood out as a potential modulator of IAV proneness in that SFB, despite being a strict anaerobe and, thus, restricted to the intestinal luminal surface, is known to systemically impact T-lymphocytes [7, 8]. Furthermore, SFB is a major contributor to, albeit not the sole mediator of, the spontaneous resistance to rotavirus (RV), an intestinal pathogen, that spontaneously arose in some mouse colonies [9]. SFB is very challenging to culture but can be isolated, maintained, and studied by administering it via fecal microbial transplantation (FMT). Hence, mice lacking SFB but otherwise carrying a complex SPF microbiota, herein referred to as SFB$^-$ mice, were administered a FMT from other SFB$^-$ mice, mice containing SFB as one natural component of their SPF microbiota, or germ-free mice that had been monoassociated (MA) with SFB. Such mice were inoculated with CA09 one-week post-FMT and euthanized 4d later to measure lung viral titers or monitored for 14 days to assess clinical-type disease parameters. Mice receiving FMT from mice naturally colonized with SFB exhibited IAV titer reductions of approximately one order of magnitude compared to animals that lacked SFB and, concomitantly, clinical signs of IAV infection were ameliorated **(Figure 1B).** FMT from SFB-MA mice fully recapitulated such protection while administering feces from germ-free mice was without effect (**Figure S1A).** Thus, administering SFB$^-$ mice a FMT from SFB-MA mice, hereafter referred to as administering SFB, recapitulated the differential proneness of EF and SPF mice to IAV infection, thus providing a tractable model to investigate how the presence of this specific gut microbiota constituent, within a complex microbial ecosystem, reduced IAV infection in the lung.

SFB-mediated protection against IAV infection was evident, albeit seemingly not maximal, two days post SFB administration and was undiminished three months later (longest time tested) despite gut SFB levels having declined by over 60-fold from peak to a stable plateau by this time **(Figure 1C and Figure S1B).** In accord with its relative abundance not being a critical variable, SFB colonized 24-week-old mice at 10-fold lower levels than 5-week-old mice but still protected them against IAV infection **(Figure S1C)**. Consistent with previous observations that SFB only resides in the gut lumen or attached to the apical epithelial gut surface [10], SFB was readily detected by PCR in the ileum, but was not found in the lung or spleen **(Figure 1D)**. Histopathologic examination of lung tissue did not detect any impact of SFB itself on the lung but revealed a striking suppression of IAV-induced lung pathology **(Figure 1E)**. Such protection of lung tissue was potentially attributable to the one-log reduction in observed in viral tiers conferred by SFB colonization but also hinted at the possibility that SFB had reduced IAV-induced inflammatory signaling.

SFB's protection against IAV not explained by known candidate mechanisms

SFB-mediated lasting protection against IAV contrasted with its transient protection against RV [9], suggesting that the former might be mediated by adaptive immunity. However, SFB-mediated protection against IAV was fully maintained in *Rag1*$^{-/-}$ mice, which lack most T and B lymphocytes, arguing against this notion **(Figure 2A)**. Innate antiviral immunity typically involves interferon and can involve innate lymphoid cells (ILC) and/or IL-22 and IL-17. Yet, SFB-mediated protection against IAV was maintained in *Ifnar*$^{-/-}$ mice, which lack type I interferon signaling, *Rag1*$^{-/-}$-*Il2rg*$^{-/-}$, which lack type 3 ILC, and upon antibody-mediated neutralization of IL-17 and IL-22 **(Figure 2B-D)**. SFB-mediated protection against IAV was also maintained in *Stat1*$^{-/-}$ animals, which are broadly compromised in IFN signaling **(Figure 2E)**. These results argue against a role for any of these candidate host mechanisms in mediating SFB's protection against IAV infection. We also considered a candidate microbial mechanism. Specifically, we hypothesized that the protection against IAV conferred by SFB might reflect that it induced an array of complex changes in other taxa that might then broadly impact innate immunity. However, SFB's protection was maintained in Altered Schaedler flora (ASF) mice, which harbor only a minimal 8-species microbial community [11] thus arguing against this possibility.

SFB's protection against IAV, RSV and SARS-CoV-2 associated with preservation of resident lung phagocytes

That candidate mechanisms were not experimentally substantiated led us to utilize less targeted approaches to investigate how SFB gut colonization protected mice against IAV. First, we performed transcriptomic profiling of whole lungs harvested from mice thar were untreated (naïve) or administered SFB, CA09, or a combination thereof. The results of this RNA-seq analysis were presented as a heat map, showing 4-5 individual mice per condition, of all genes whose expression was significantly altered in response to any of the three treatments **(Figure 3A)**. It illustrated that SFB, by itself, had almost no impact on lung gene expression, whereas, as expected, IAV infection, by itself, markedly remodeled the lung transcriptome. Strikingly, such IAV-induced changes in gene expression were absent in SFB-colonized mice, indicating that the presence of SFB in the gut broadly ameliorated IAV's impact on lung tissue. The majority of genes induced by CA09-induced were related to immunity and inflammation thus according with the view that much of the lung pathology in IAV infection is driven by the immune system [12] and, furthermore, the notion that SFB strongly dampened such responses.

We next used flow cytometry to examine the impact of SFB and IAV on lung populations of immune cells, focusing on innate cells given our results from KO mice had suggested lymphocytes were not required SFB-mediated protection against IAV. Consistent with other studies, intranasal administration of CA09, by itself, induced a stark depletion of basally-resident $CD103^+$ dendritic cells (cDC1) and alveolar macrophages (AM), which was followed by increased abundance of a panel of inflammatory cells including neutrophils, monocytes, and natural killer cells [13]. Analogous to the RNA-seq and histopathology results, SFB, by itself, did not significantly impact levels of lung leukocytes but wholly prevented the changes induced by CA09 **(Figure 3B and Figure S2)**. Preventing these CA09-induced changes in lung cellularity and disease was not SFB strain-specific as similar protective effects resulted from colonization of the gut by SFB strains isolated in 3 different continents **(Figure S3)**. Nor were SFB impacts specific to IAV. Rather, SFB colonization also reduced viral loads and prevented changes in lung cellularity, and reduced pro-inflammatory gene expression, following inoculation of mice with respiratory syncytial virus (RSV) and mouse-adapted SARS-CoV-2 **(Figure S4)**. which, irrespective of SFB, did not cause clinical signs of disease.

To investigate the extent to which SFB-mediated prevention of IAV-induced changes in lung cellularity simply reflected lower IAV loads, we pharmacologically restricted IAV replication via 4'-fluorouridine (4'-FIU), a broad-spectrum nucleoside analog inhibitor that we recently reported impedes IAV, RSV, and SARS-CoV-2 [14, 15]. SFB$^-$ mice received 4'-FIU via oral gavage at different dose levels in a once daily (q.d.) regimen beginning 24 hours post-inoculation. At this time, IAV levels and immune cell populations were similar in SFB$^-$ and SFB-administered mice **(Figure S2C)**, which we hereafter refer to as SFB$^+$ mice. As expected, administration of 4'-FIU to SFB$^-$ mice dose-dependently suppressed IAV replication to a similar or greater extent than SFB **(Figure 3C)**. Like SFB, 4'-FIU administration prevented the CA09-induced appearance of inflammatory cells in the lung. However, even the highest dose of 4'-FIU, which lowered IAV titers by over three orders of magnitude, did not mitigate CA09-induced ablation of cDC1 or AM suggesting that their persistence in SFB$^+$ mice may have contributed to, rather than resulted from, suppression of IAV.

Alveolar Macrophages are required for SFB-mediated protection against IAV

Potential roles for cDC1 and AM in SFB-mediated protection against IAV were tested in mice harboring deficiencies in these cells. We observed that SFB-mediated protection against IAV was maintained in *Batf3*$^{-/-}$ mice, which wholly lack cDC1 [16], but was greatly reduced in *Csf2*$^{-/-}$ mice, which have a 70% reduction in basal AM levels [17] **(Figure 4 A&B)**. The role of AM was further examined by depleting these cells with clodronate liposomes [18], an approach that we verified efficiently depleted AM but did not alter levels of other lung innate immune cells **(Figure 4Ci)**. Depletion of AM, by itself, did not significantly impact IAV titers or clinical signs of disease but eliminated the ability of SFB to lower lung IAV titers, ameliorate hypothermia and weight loss, and prevent death **(Figure 4Cii)**. These results suggested that SFB-mediated impacts on AM were germane to its protection against RVI. SFB-mediated maintenance of AM levels could conceivably have reflected increased generation of these cells, which can occur from monocyte progenitors migrating to the lung or local self-renewal [19], or that SFB colonization had resulted in AM resisting death upon RVI. SFB's prevention of AM depletion following CA09 inoculation associated with prevention of IAV-induced caspase-3 activation **(Figure 4D)**, which marks AM commitment to cell death [20], and increased expression of CD71 **(Figure 4E)**, which associates with enhanced phagocytosis and survival [21, 22]. These results suggest that SFB colonization had "emboldened" AM to resist IAV-induced depletion.

SFB's preservation of AM enables their sustained protection of EC from IAV infection

Airway epithelial cells (AEC) are primary sites replication sites of respiratory viruses, including IAV, RSV, and SARS-CoV-2. Specifically, in the case of highly pathogenic H1N1 IAV, AEC are the only site in which hemagglutinin is effectively cleaved to allow infection, replication, and generation of new infectious virions [23]. AM are known to protect lung airway epithelial cells (AEC) from IAV infection, particularly at early time points following IAV-infection, i.e. prior to their depletion [24]. Thus, we predicted that SFB's preservation of AM following CA09 inoculation might result in lower viral loads in AEC in SFB$^+$ mice. Indeed, the percentage of lung AEC, type I and II, as well as conducting AECs, displaying detectable levels of CA09, which encodes GFP, by flow cytometry, was significantly reduced in SFB$^+$ mice 4 days post-inoculation **(Figure 4E and Figure S5)**. Depletion of AM by clodronate in SFB$^+$ mice increased IAV levels to that of SFB$^-$ mice in all three lung AEC types **(Figure 4F)**. These results indicate that SFB-induced AM persistence following IAV infection enables sustained AM-mediated protection of EC, likely contributing to lower IAV burden and ameliorated pathology.

Persistence of SFB$^+$ AM upon RVI is cell-intrinsic

Persistence of AM in CA09-infected SFB$^+$ mice was potentially attributable to SFB altering the lung environment and/or reflect that AM themselves had been intrinsically transformed to better withstand IAV challenge. To differentiate between these possibilities, we adoptively transferred FACS-sorted AM from SFB$^+$ and SFB$^-$ mice to SFB$^-$ mice using donor mice with a CD45.1 subtype, thereby enabling distinction of endogenous and transplanted cells **(Figure 5)**. The degree to which AM harvested from SFB$^+$ and SFB$^-$ mice, hereafter referred to as SFB$^+$ and SFB$^-$ AM, engrafted following transplant was similar, comprising about 20% of the total AM in their new host. CA09 infection did not significantly alter proportions of endogenous vs. engrafted AM in recipients of SFB$^-$ AM but led to SFB$^+$ AM (i.e. engrafted) becoming their host's majority AM population. This shift in AM proportions reflected that endogenous AM in both recipient groups as well as engrafted SFB$^-$ AM were all depleted by CA09 infection, whereas engrafted SFB$^+$ AM fully resisted CA09-induced depletion and, concomitantly, lacked Caspse-3 activation, despite having been transplanted into an SFB-free host. Thus, colonization of the gut with SFB intrinsically altered AM to withstand IAV-induced depletion.

SFB$^+$ AM exhibited inflammatory anergy and enhanced antiviral function

Differences between SFB$^+$ and SFB$^-$ AM were characterized ex vivo as schematized **(Figure 6A).** Profiling of basal gene expression (i.e. without IAV exposure) by RNA-seq found that only 24 of the 15,510 genes expressed by AM were differentially expressed between SFB$^-$ and SFB$^+$ AM **(Figure 6B)**, 18 of which were both confirmed by PCR and biologically replicated in a distinct mouse cohort **(Figure S6A).** Six of the genes upregulated in SFB$^+$ AM are associated with an M2 macrophage phenotype. Yet, quantitation of surface expression markers previously used to distinguish M1 vs. M2 phenotypes [25] did not reveal differences between SFB$^+$ and SFB$^-$ AM **(Figure S6B)**. The genes most prominently up- and down-regulated, respectively, in SFB$^+$ AM were Tsc22d3 and Notch 4, which, respectively, function in suppressing and activating pro-inflammatory gene expression [26, 27] suggesting such signaling might be dampened in SFB$^+$ AM. Indeed, we found SFB$^+$ AM lacked the robust UV-irradiated IAV-induced activation of pro-inflammatory gene expression exhibited by SFB$^-$ AM **(Figure 6C and Figure S7A)**. Such lack of pro-inflammatory responsiveness was partially recapitulated by antibody-mediated neutralization of Notch 4 suggesting that the reduced Notch 4 expression in SFB$^+$ AM contributed to their inflammatory anergy and, consequently, the reduced inflammation observed in IAV-infected SFB$^+$ mice.

The small panel of genes upregulated in SFB$^+$ AM also included those known to function in antiviral resistance, including complement C1qa and Ifitm1 thus suggesting that SFB$^+$ AM were not anergic to IAV per se but, rather, might have better virus neutralizing capacity. We examined this possibility by incubating CA09 stocks with AM for 45 min at which time AM were removed by centrifugation and supernatant infectious titers and IAV genomes quantified. SFB^- AM lowered the infectious titers of the CA09 stocks to which they were exposed, at 37°C but not 4°C, but the extent of reduction was 150-fold greater for SFB^+ AM (**Figure 6Di**). This greater reduction in titer was accompanied by only 5-fold lower levels of PCR-quantifiable IAV genomes in supernatants of SFB^+ AM (**Figure 6Dii**). This led us to hypothesize enhanced neutralization of IAV by complement and/or other products secreted by SFB^+ AM. Indeed, we found that, even when SFB^+ AM were not exposed to virus, their supernatants from 18h cultures had greater capacity than those from SFB^- AM to lower CA09 infectious titers **(Figure 6Diii)**. Such enhanced ability of SFB^+ AM supernatants to lower IAV titers was fully reversed by antibody-mediated removal of C1qa and, moreover, was not observed in $C1qa^{-/-}$ mice **(Figure S6C)**. These results accord with recent observations that C1qa can directly bind IAV and reduce its infectivity [28]. Yet, in contrast to AM themselves, addition of AM supernatants to CA09 stocks had no impact on levels of viral genomes (**Figure S6D**) suggesting the enhanced antiviral capacity of SFB^+ AM might also involve increased viral absorption and/or uptake, potentially as a result of viral particles being more decorated with C1qa [29]. In accord with this notion, reductions in IAV genomes in supernatants of AM/CA09 mixtures were paralleled by increased IAV genomes in AM lysates **(Figure 6Div)**. The relative increase in IAV genomes in SFB^+, compared to SFB^-, AM lysates was maintained amidst chlorpromazine, but not latrunculin treatment, neither of which impacted cell viability, suggesting it might reflect enhanced phagocytosis uptake by SFB^+ AM (**Figure S6F**). In accord with this notion, SFB^+ AM exhibited modestly greater uptake of IgG-coated fluorescent beads **(Figure S6E)**. Exploring the fate of

CA09 internalized by AM during the 45 min exposure period found that, 24 h following media replacement, AM supernatants had few infectious virions while lysates contained few detectable IAV genomes **(Figure 6Div**) thus suggesting that AMs were not permissive for CA09 replication, but rather constituted a dead end for the virus. Collectively, these results indicate that elevated C1qa expression and, perhaps consequently, enhanced phagocytosis drove the increased antiviral capacity of SFB^+ AM.

SFB-induced reprogramming of AM protects mice against IAV infection

Lastly, we examined the extent to which SFB-induced reprogramming of AM contributed to SFB's protection against IAV infection. Specifically, we performed an additional series of AM transplant experiments designed to measure impacts on IAV levels and clinical-type parameters. Consistent with the notion that AM, prior to their depletion, protect against IAV infection [24], we observed that administration of SFB^- AM to a host replete with endogenous AM resulted in a modest reduction in IAV titers, gross lung damage, hypothermia, weight loss, and death following CA09 inoculation **(Figure 7A)**. Administration of SFB^+ AM provided markedly greater protection against this IAV challenge, approximating the level conferred by administration of SFB itself, as assessed by all parameters measured. Analogous patterns of results were seen following transfer of SFB^+ and SFB^- AM into mice deficient in endogenous AM, achieved via use of *Csf2*$^{-/-}$ mice or chlodronate administration **(Figure 7B and 7C)**. *Ex vivo* blockade of Notch4 on SFB^- AM prior to transplanting them also enhanced their ability to withstand IAV-induced depletion, protect EC from IAV infection, and ameliorate CA09-induced disease, but did not impact level of viral genomes in the lung **(Figure S7B)**, suggesting the ability of transplanted SFB^+ AM to do so was not mediated solely by dampened inflammatory signaling but also required such AM have enhanced antiviral function. Thus, SFB colonization of the gut stably and broadly altered the AM phenotype enabling these cells to better protect their hosts from lethal RVI.

DISCUSSION

Positioned in the lung lumen to enable their guarding the surfaces of 0_2 and CO_2 exchange, AM are amongst the first cells to encounter inhaled threats including respiratory viruses. We show herein that how AM respond to respiratory viruses is dramatically altered by the composition of the intestinal microbiota. Specifically, we report that colonization of the intestine by SFB, naturally acquired, or exogenously administered, markedly attenuates IAV-induced AM pro-inflammatory gene expression while increasing ability of AM to directly disable IAV. SFB-induced reprogramming of AM manifested in vivo by them resisting RVI-induced depletion thereby enabling their sustained protection of lung epithelial cells from infection. Collectively, these consequences of SFB-induced AM reprogramming resulted in lower viral titers, reduced inflammation and, consequently, reduced disease severity. While the general concept that microbiota composition in total can influence immune phenotype and, proneness to infection is established [30, 31], we were quite surprised that the presence of a single common commensal bacterial species, amidst the thousands of different microbial species that variably inhabit the mouse gut, had such strong impacts in RVI models and, furthermore, that such impacts were largely attributable to reprogramming of AM.

The extent to which SFB is present in humans is not well defined but it has been reported to be frequently present in children in some regions [32] and was unequivocally shown to be present in some adult individuals [33]. Yet independent of a specific role for SFB, however, our findings speak strongly to the potential of gut microbiota to influence proneness to RVI, especially via programming of AM. Both AM pro-inflammatory gene expression and AM depletion are known to correlate with RVI severity in humans but determinants of inter-individual heterogeneity in AM responses have not been defined [32]. We consider it highly unlikely that SFB is the only gut microbe capable of impacting AM phenotype and, consequently, proneness to RVI. Rather, we posit that AM are a key component of the gut-lung axis wherein an individual's microbiota in its entirety is a determinant of disease outcome following exposure to an array of respiratory viruses.

The observation that SFB^+ AM maintained an IAV-resistant phenotype following transplant to SFB^- mice is consistent with observations that AM have stable cell-type specific patterns of gene expression and methylation even when cultured extensively *ex vivo* [34]. Moreover, it accords with recently increasing appreciation that AM can be "entrained" to display long-lasting phenotypic alterations that impact their ability to manage pathogens and tumors [35]. Yet, mechanisms governing such AM entraining are not clear and, moreover, may be distinct from the AM reprogramming observed here. Specifically, previously observed AM entraining has generally involved large-scale depletion of AM, which are then replaced by cells newly recruited from bone marrow that, even after establishing residency in the lung, exhibit stark global differences in gene expression profiles. In contrast gene expression profiling of SFB^- and SFB^+ AM revealed only modest differences, likely reflecting that both AM had been generated by AM self-renewal processes that normally maintain AM homeostasis in non-traumatic states. Nonetheless, changes in basal AM gene expression we observed likely contributed to the enhanced ability of SFB^+ AM to protect their host against RVI. Indeed, the inflammatory anergy, mediated in part by reduced Notch-4 expression, and enhanced antiviral function, mediated in part by elevated C1qa expression, of SFB^+ AM plausibly directly contributed to, respectively, the reductions in lung pathology and viral loads that followed IAV inoculation. Much less clear, and thus warranting further research, is the nature of the signal that is generated by SFB colonization of the luminal surface of the intestine that drives AM reprogramming.

In addition to directly disabling IAV, AM can also protect lung EC from IAV infection via suppressing EC CysLT1 signaling, which might mediate IAV entry into these cells [24]. Thus, persistence of AM in SFB$^+$ mice, by itself, likely contributed to SFB's protection against IAV. That mechanisms driving RVI-induced AM depletion are not clear, makes determining how SFB colonization prevents such depletion challenging. Nonetheless, we speculate that reductions in inflammatory gene expression and viral loads, which SFB+ AM mediated, may have contributed to increased persistence of SFB$^+$ AM. In addition to mitigating primary RVI, AM persistence may help prevent secondary consequences of RVI. Many of the severe consequences of IAV infection in humans result from secondary bacterial infections, to which the lung is made more permissive by loss of IAV-induced AM depletion [36]. Such impaired antibacterial immunity can persist for prolonged periods perhaps reflecting that the bone-marrow derived replacement AM are not quickly optimized for mucosal host defense. Thus, microbiota mediated AM programming may not only influence severity of acute RVI but may also be a long term post-RVI health determinant.

MATERIALS AND METHODS

Mice

The following mice were purchased from The Jackson Laboratory: C57BL/6 (B6 WT), B6.129S(C)-*Batf3*^{tm1Kmm}/J, B6.129S-*Csf2*^{tm1Mlg}/J, B6.129S7-*Rag1*^{tm1Mom}/J, B6.129S2-*Ifnar1*^{tm1Agt}/Mmjax, NOD.Cg-*Rag1*^{tm1Mom} *Il2rg*^{tm1Wjl}/SzJ, B6.129S(Cg)-*Stat1*^{tm1Dlv}/J, B6(Cg)-C1qatm1d(EUCOMM)Wtsi/TennJ. The Jackson laboratory does not test mice for the presence of segmented filamentous bacteria (SFB), but all mice we tested that were purchased from this provider for this study were SFB-negative upon arrival at GSU. The following mice were purchased from Taconic Biosciences: C57BL/6 (B6 WT) Excluded Flora (EF) mice and Specific Pathogen-Free (SFP) mice, which we verified were SFB^{+} and SFB^{-}, respectively. Unless otherwise stated, mice were used at 4-5 weeks of age, and experiments were carried out using age- and gender-matched groups. The Institutional Animal Care and Use Committee of Georgia State University approved animal studies.

PCR primers, FACs antibodies, neutralization antibodies and other reagents

All reagents used in these manuscripts can be seen in Tables S1 and S2.

Cells and viruses

Madin-Darby Canine Kidney (MDCK; ATCC CCL-34), HEp-2 (ATCC CCL-23), and VeroE6 TMPRSS2 (BPS Bioscience #78081) cells were cultured in Dulbecco's Modified Eagle's Medium (DMEM) supplemented with 7.5% heat-inactivated fetal bovine serum (FBS) at 37°C and 5% CO_2. All cell lines used in this study were authenticated and checked for *Mycoplasma* and microbial contamination. Recombinant Influenza A virus was recovered based on original reports for laboratory-adapted IAV [37]. A/CA/07/2009 (H1N1) was grown on MDCK cells using serum-free DMEM supplemented with 0.5% Trypsin. Recombinant RSV strain A2 with line19F reporter gene recRSV-mKate was rescued and amplified as described previously [38], and the SARS-CoV-2 MA10 strain [39] was passaged in VeroE6 TMPRSS2 cells. All viruses used were clarified, aliquoted, and stored at -80°C. Virus stock titers were determined through $TCID_{50}$-titration.

Complex microbiota and mono-associated SFB transplantation

Fecal samples were collected from donor mice, suspended in 20% glycerol PBS solution at 40 mg/mL concentration, passed through a 40 µm filter, and stored at -80C. Frozen fecal suspensions were orally administered to recipient mice at 200 µl per mouse.

Virus infection

Unless otherwise stated, mice were 5 weeks of age at the time of infection. Mice were randomly assigned to study groups and housed under ABSL-2 or ABSL-3 conditions for infections with A/CA/07/2009 (H1N1) recombinant, recRSV-mKate, or SARS-CoV-2 MA10 strain, respectively. Seven days prior to virus infection, mice were subjected to microbiota manipulation (administration of feces from SPF or SFB-monoassociated mice). Bodyweight was determined twice daily, and body temperature determined once daily rectally. For infections, animals were anesthetized with isoflurane [rec A/CA/07/2009 (H1N1) (CA09)] or ketamine/xylazine (recRSV-mKate and MA-SARS-CoV-2), followed by intranasal inoculation with 2.5×10^{2}- 2×10^{4} $TCID_{50}$ units/animal of GFP-expressing reporter virus version of A/CA/07/2009 (H1N1) (CA09), 5.5×10^{5} of recRSV-mKate, or 4.2×10^{5} of MA-SARS-CoV-2. In all cases, virus inoculum was diluted in 50 µl and administered in amounts of 25 µl per nare, followed by treatment with 4'-FlU at specified dose levels and starting time points through oral gavage. Each individual study contained animals receiving equal volumes of vehicle through oral gavage. Animals were euthanized and organs harvested at predefined time points or when animals reached humane study endpoints. At study end point, lung tissue was harvested for virus titration or histopathology.

Histopathologic analysis

Lungs were perfused using 10% neutral-buffered formalin, dissected, and fixed. Formalin-fixed lungs were transferred to 70% EtOH, embedded in paraffin, sectioned, stained, and scored by a board-certified veterinary pathologist (KS), who was blinded to the study groups. For each parameter, the most severe lesion in the section was scored. Pleuritis, bronchiolitis, and alveolitis scoring was based on distribution: 1 = focal, 2 = multifocal, 3 = multifocal to coalescing, 4 = diffuse. For interstitial pneumonia (IP): 1 = alveolar septa expanded by 1 leukocyte thickness, 2 = 2-leukocytes thick, 3 = 3-leukocytes thick, 4 = 4-leukocytes thick. For vasculitis: 1 = vessel wall infiltrated by leukocytes, 2 = infiltration and separation of myocytes, 3 = same changes as in 2 with fibrinoid change. For perivascular cuffing (PVC): 1 = vessels surrounded by 1 leukocyte layer, 2 = 2 to 5-leukocytes thick, 3 = 6 to 10-leukocytes thick, 4 = more than 10-leukocytes thick.

Virus titration

Virus samples were serially diluted (10-fold starting at 1:10 initial dilution) in serum-free DMEM (recRSV-mKate and MA-SARS-CoV-2) and supplemented with 0.5% Trypsin (Gibco, recA/California/07/2009). Serial dilutions were added to cells seeded in 96-well plate at

1×10^4 cells per well, 24 hours before infection. Infected plates were incubated for 72 hours at 37°C with 5% CO_2, and scoring of wells based on reporter activity/syncytia.

Virus titration from tissue samples

Organs were weighed and homogenized in 300 µl PBS using a bead beatter, set to 3 cycles of 30 seconds each at 4°C, separated by 30-second rest periods. Homogenates were cleared (10 minutes at 20,000 × g and 4°C), and cleared supernatants were stored at -80°C until virus titration. Viral titers were expressed as $TCID_{50}$ units per gram input tissue.

Neutralization of IL-17 and IL-22

IL-17 (100 µg) and IL-22-Fc (150 µg) neutralizing monoclonal antibody were administered intraperitoneally shortly before microbiota transplantation and virus inoculation thereafter every other day until mice were euthanized.

Lung digestion and flow cytometry analysis/isolation of innate immune cells

Lungs were dissected from mice and finely minced with scissors before digestion (40 minutes, at 37ºC) with warm RPMI containing 10% FBS, DNase, and 1mg/mL Collagenase type IV (Sigma); lungs were further homogenized via swishing with a 3-mL syringe every 10 minutes during digestion. Following digestion, immune cells were purified with 40%/80% isotonic Percol gradient centrifugation. For flow cytometry analysis, the prepared cells were blocked with 1 µg/million cells with 2.4G2 (anti-CD16/anti-CD32) in 100 µL PBS for 15 minutes at 4ºC, followed by 2-times wash with PBS to remove residue of 2.4G2 and then incubated in conjugated mAbs CD45 BV605, MHCII BV650, CD11b APC-Cy7, CD11c BV786, Ly6C

PerCp-Cy5.5, Ly6G AF700, CD64 BV421, CD24 FITC, CD117 GV510, SiglecF PE-CF594, Fcer1 APC. Intracellular staining for cleaved caspase-3 was done using FoxP3 staining buffer purchased from eBioscience. Multi-parameter analysis was performed on a CytoFlex (Beckman Coulter) and analyzed with FlowJo software (Tree Star). Cell sorting was done using Sony SH800Z cell sorter (Sony). Gating strategy for innate immune cells was based on Yu *et al*., [40] and gating strategy for airway epithelial cells was based on Cardani *et al*., [24]. Immune cells and lung airway epithelial subtypes are defined as follow:

Cell Types	**Markers**
Alveolar macrophages	$CD45^{+}Ly6G^{-}CD11c^{+}CD11b^{+}MHCII^{+}CD64^{+}CD24^{-}Ly6C^{+}SiglecF^{+}$
Alveolar macrophages (for cell sorting)	$CD45^{+}CD11c^{+}SiglecF^{+}$
Interstitial macrophages	$CD45^{+}Ly6G^{-}CD11c^{+}CD11b^{+}MHCII^{+}CD64^{+}CD24^{-}Ly6C^{-}SiglecF^{-}$
Exudate macrophages	$CD45^{+}Ly6G^{-}CD11c^{+}CD11b^{+}MHCII^{+}CD64^{+}CD24^{-}Ly6C^{+}SiglecF^{-}$
$CD103^{+}CD11b^{-}$ DCs (cDc1)	$CD45^{+}Ly6G^{-}CD11c^{+}CD11b^{+}MHCII^{+}CD64^{-}CD24^{+}CD11b^{-}CD103^{+}$
$CD103^{-}CD11b^{+}$ DCs (cDc2)	$CD45^{+}Ly6G^{-}CD11c^{+}CD11b^{+}MHCII^{+}CD64^{-}CD24^{+}CD11b^{+}CD103^{-}$
Neutrophils	$CD45^{+}Ly6G^{+}$
Eosinophils	$CD45^{+}Ly6G^{-}CD11c^{+}CD11b^{+}MHCII^{-}SiglecF^{+}$
Basophils	$CD45^{+}Ly6G^{-}CD11c^{-}CD11b^{+}FceRI^{+}CD117^{-}$
Mast cells	$CD45^{+}Ly6G^{-}CD11c^{-}CD11b^{+}FceRI^{+}CD117^{-}$
NK cells	$CD45^{+}Ly6G^{-}CD11c^{-}CD11b^{+}FceRI^{-}$
Inflammatory monocytes	$CD45^{+}Ly6G^{-}CD11c^{+}CD11b^{+}MHCII^{-}CD64^{-}Ly6C^{+}$
Resident monocytes	$CD45^{+}Ly6G^{-}CD11c^{+}CD11b^{+}MHCII^{-}CD64^{-}Ly6C^{-}$
T cells	$CD45^{+}Ly6G^{-}CD11c^{-}CD11b^{-}MHCII^{-}CD24^{-}FceRI^{-}$

B cells	$CD45^+Ly6G^-CD11c^-CD11b^-MHCII^+CD24^+FceRI^-$
Type 1 airway epithelial cells	$CD45^-CD31^-EpCAM^+T1a^+$
Type 2 airway epithelial cells	$CD45^-CD31^-EpCAM^+T1a^-MHCII^+$
Conducting airway epithelial cells	$CD45^-CD31^-EpCAM^+T1a^-MHCII^-$

RNA-Seq

RNA was isolated from lungs or FACs-sorted alveolar macrophages using RNeasy Plus Mini Kit from Qiagen. The prepared RNA samples were then sent to the Molecular Evolution Core of Georgia Institute of Technology for library preparation and sequencing on the NextSeq instrument with a high output 2x75bp run. FASTQC was used for sequencing reads quality screening. The RNAseq data were then analyzed using the Galaxy server.

Adoptive transfer of alveolar macrophages

Lungs were harvested from CD45.1 mice and digested with Collagenase type IV as described above. Alveolar macrophages (defined at $CD45^+MHCII^+CD11c^+Siglect^+$) were stained and FACs-sorted. Small aliquot of isolated cells was used to determined purity. Unless stated otherwise, $5x10^5$ alveolar macrophages in 30 μl PBS were administered intranasally to recipient mice. One day post cells transfer, some mice were euthanized to determine transfer efficiency and survival of transferred cells; and some mice were inoculated with IAV. For survival experiments, mice were monitored twice daily for 14 days. For lung virus titers, mice were euthanized on day 4.5 post virus inoculation.

Ex vivo inhibiting Notch4 signaling in alveolar macrophages.

Alveolar macrophages were FACS-sorted as described. After sorting, cells were treated with either isotype control antibody (Cat# BE0091, BioXCell) or an anti-Notch4 monoclonal antibody (20µg/mL) (Cat# BE0129, BioXCell), known to neutralize Notch 4 [27] for 30 minutes. Cells were washed twice and resuspended in PBS and intranasally transferred to mice.

***Ex vivo* alveolar macrophages culture, virucidal assay, and anti-body mediated removal of C1qa.** Alveolar macrophages were FACS-sorted as described. After sorted cells were incubated for 18h at 37^{o}C. Cells were washed twice with serum-free media and were incubated with live CA09 (MOI = 1) in serum-free DMEM supplemented with 0.5% Trypsin (flu media) for 45min. In addition, to assess whether alveolar macrophages are the terminal destination for IAV, some cells had new flu media added and were incubated for another 24h. Viral titer and genomes were determined via $TCID_{50}$ and PCR methods. **Antibody-mediated removal of C1qa from ex vivo alveolar macrophages' supernatants.** Cell-free supernatants of 18h AM cultures were treated with C1qa polyclonal antibodies or isotype for 2 hours at 4^{o}C and protein A/G was added and centrifuged. Supernatant was harvested and incubated with CA09 stocks for 45mins, at which point IAV infection titers were assayed.

Ex Vivo alveolar AM bead uptake (i.e. Phagocytosis) assay was performed with Phagocytosis assay kit (Cat#500290, Cayman chemical). Alveolar macrophages were FACs-sorted as described. After sorting, 1x10^{5} cells were seeded in each well of a 96-well plate and incubated for 18 h at 37^{o}C. Cells were washed twice, and IgG-FITC beads were added and incubated for 2 hours at 37^{o}C. After incubation period, cells were centrifuged, and supernatants were removed and resuspended 300μl of FACs buffer. Level of cell fluorescence, an indicator of bead uptake, was measured via flow cytometry.

Quantitative real-time PCR

Total RNA from lungs or from FACs-sorted alveolar macrophages were isolated using the Qiagen RNeasy Mini Kit with on-column DNase digestion according to manufacturer's protocol. cDNA was generated using the Superscript First Strand Synthesis kit for RT-PCR and random hexamer primers (Invitrogen). Q-PCR was performed with SYBR Green using StepOnePlus PCR system (Applied Biosystem), and all genes expression was normalized to GAPDH. Primer sequences are shown in Table 1.

Quantification and statistical analysis

Results were expressed as mean ± SEM. All data was plotted in GraphPad Prism version 10. Statistical significance was assessed by One-way ANOVA, Student's t test, and Two-way ANOVA. Differences between experimental groups were considered significant if *$p<0.05$, **$p<0.01$, ***$p<0.001$, ****$p<0.0001$.

Table 1 qPCR primers

Genes	Forward 5' --> 3'	Reverse 5' --> 3'
Notch4	GAACGCGACATCAACGAGTG	GGAACCCAAGGTGTTATGGCA
Retlna	CCAATCCAGCTAACTATCCCTCC	ACCCAGTAGCAGTCATCCCA
CD209g	GGCCTCAGCGATCACAGAAG	ACAACGGCTGTCATTCCATTTA
Abca9	TCGATAGATGCAGTGAGAGTCA	CACAAGGAGCTGAATGGTCTTT
Tsc22d3	CTGTTGGCCTCGACTGCTG	GCCGAAAGTTGCTCACGAAG
Sik1	TCATGTCGGAGTTCAGTGCG	ACCTGCGTTTTGGTGACTCG
Fcrls	CTTCTGGTCTTCGCTCCTGTC	ATGGTGTAGCTTGAAGCACTG
Dmkn	AGCTGACCAGTTTTCTAAGCC	GCCAGTTGTAAGTAGGATTCACC
F13a1	GAGCAGTCCCGCCCAATAAC	CCCTCTGCGGACAATCAACTTA
Ccl24	TCTTGCTGCACGTCCTTTATT	GCATCCAGTTTTTGTATGTGCC
Ifitm1	GACAGCCACCACAATCAACAT	CCCAGGCAGCAGAAGTTCAT
Ltb4r1	ATGGCTGCAAACACTACATCTC	GACCGTGCGTTTCTGCATC
Akr1b8	GACCAAGGCAGAATCCTCACC	AGATGCCCTTCGAGTGACAGT
C1qa	AAAGGCAATCCAGGCAATATCA	TGGTTCTGGTATGGACTCTCC
Maf	AGGAGGAGGTCATCCGACTG	CTTCTCGCTCTCCAGAATGTG
Procr	AATGCCTACAACCGGACTCG	ACCAGTGATGTGTAAGAGCGA
Socs3	ATGGTCACCCACAGCAAGTTT	TCCAGTAGAATCCGCTCTCCT
Marcksl1	CAATGGAGACTTAACCCCCAAG	GGCCACTCAATTTGAAAGGCT
Kcnn4	GCTCAACCAAGTCCGCTTC	GTGATCGGAATCAGCCACAGT
Tmem119	CCTACTCTGTGTCACTCCCG	CACGTACTGCCGGAAGAAATC
Acpp	CATTGGTGTTTCGGCATGGAG	CCAAGTTCGTAGTGCTGTTCC
Gucy2c	GACTTTTCTCTCGCTTACTTGGA	TGAATGCACGAGCAAACTTGG
Il6	TGGGGCTCTTCAAAAGCTCC	AGGAACTATCACCGGATCTTCAA
Ifnb1	CAGCTCCAAGAAAGGACGAAC	GGCAGTGTAACTCTTCTGCAT
Cxcl10	CCAAGTGCTGCCGTCATTTTC	GGCTCGCAGGGATGATTTCAA
Cxcl11	GGCTTCCTTATGTTCAAACAGGG	GCCGTTACTCGGGTAAATTACA
Irf7	GAGACTGGCTATTGGGGGAG	GACCGAAATGCTTCCAGGG
Isg15	GGTGTCCGTGACTAACTCCAT	TGGAAAGGGTAAGACCGTCCT
Oas3	TCTGGGGTCGCTAAACATCAC	GATGACGAGTTCGACATCGGT
Oasl1	CAGGAGCTGTACGGCTTCC	CCTACCTTGAGTACCTTGAGCAC
Oasl2	TTGTGCGGAGGATCAGGTACT	TGATGGTGTCGCAGTCTTTGA
Ifit1	CTGAGATGTCACTTCACATGGAA	GTGCATCCCCAATGGGTTCT
Ifit2	AGTACAACGAGTAAGGAGTCACT	AGGCCAGTATGTTGCACATGG
Ifit3	CTGAAGGGGAGCGATTGATT	AACGGCACATGACCAAAGAGTAGA
Gapdh	TGGATTTGGACGCATTGGTC	TTTGCACTGGTACGTGTTGAT
Inf-NA	CAATTCAACTTGGGAATCAAAATCAGA	CTGACTGTCCAGCAGCAAAGTT
Inf-M	TGTAAAACGACGGCCAGTAGCAAAAGCAGGTAG	CAGGAAACAGCTATGACCAGTAGMAACAAGGTAG
	AGAAAAGAATGTAACAGTAACACACTCTGT	TGTTTCCACAATGTARGACCAT

Influenza A H1N1pdm09 HA genes	Probes 5'-(FAM)-CAGCCAGCAATRTTRCATTTACC-(MGB)-3'

Table S2. FACs antibodies

Specificity	Clone	Fluorochrome	Supplier	Catalog#	Dilution
CD45	30-F11	BV605	Biolegend	103155	1/800
Ly6G	1A8	AF700	BD Biosciences	561236	1/200
Ly6C	HK1.4	PercP-Cy5.5	Thermo Fisher	45-5932	1/200
CD11b	M1/70	APC-Cy7	BD Biosciences	557657	1/200
CD11c	HL3	BV786	BD Biosciences	563786	1/100
MHCII	M5/114.15.2	BV650	BD Biosciences	563415	1/1000
CD64	X54-5/7.1	BV421	Biolegend	139309	1/400
CD24	M1/69	FITC	BD Biosciences	553261	1/1000
CD117	ACK2	BV510	Biolegend	135119	1/100
SiglecF	E50-2440	PE-CF594	BD Biosciences	562757	1/1000
Fcer1	Mar-1	APC	Thermo Fisher	175898-80	1/100
Capse-3	269518	APC	R&D System	IC835R-100UG	1/50
CD86	GL-1	APC	Biolegend	105012	1/100
CD206	C068C2	APC-AF700	Biolegend	141708	1/100
CD200R	OX-90	PE	BD Biosciences	565543	1/100
CD45.1	A20	PE-Cy7	Thermo Fisher	25-0453-82	1/100
CD45.2	104	FITC	BD Biosciences	561874	1/100
T1a (Podoplanin)	8.1.1	PE	Biolegend	127408	1/100
CD31	MEC13.3	APC	Biolegend	102510	1/100
EpCam	G8.8	AF700	BioLegend	118240	1/100

Acknowledgments:

We thank Tim Denning and Ifor Williams for insightful guidance. We thank RS Baric for SARS-CoV-2 MA10 virus isolate and Georgia State University's High Containment Core and Division of Animal Resources for support. **Funding**: This work was supported, in part, by Public Health Service grants AI141222 (to RKP), AI171403 (to RKP), and AI170014 (to ATG) from the NIH/NIAID. The funders had no role in study design, data collection and interpretation, or the decision to submit the work for publication. **Author contributions:** Conceptualization: RKP, ATG. Investigation: VLN, CML, KS. Resources: RKP, ATG. Visualization: VLN, CML, KS, RKP, ATG. Validation: RKP, ATG. Funding acquisition: RKP. Project administration: RKP, ATG. Supervision: RKP, ATG, MK. Writing – original draft: ATG. Writing – review & editing: VLN, CML, KS, RKP. **Competing interests:** RKP reports contract testing from Enanta Pharmaceuticals and Atea Pharmaceuticals, and research support from Gilead Sciences, outside of the described work. All other authors declare that they have no competing interests. **Data and materials availability:** All data are available in the main text or the supplementary materials. Materials and methods are available as supplementary materials at the Science website.

References

[1] V.L. Ngo, A.T. Gewirtz, Microbiota as a potentially-modifiable factor influencing COVID-19, Curr Opin Virol, 49 (2021) 21-26.

[2] P. Brodin, Immune-microbe interactions early in life: A determinant of health and disease long term, Science, 376 (2022) 945-950.

[3] L.K. Beura, S.E. Hamilton, K. Bi, J.M. Schenkel, O.A. Odumade, K.A. Casey, E.A. Thompson, K.A. Fraser, P.C. Rosato, A. Filali-Mouhim, R.P. Sekaly, M.K. Jenkins, V. Vezys, W.N. Haining, S.C. Jameson, D. Masopust, Normalizing the environment recapitulates adult human immune traits in laboratory mice, Nature, 532 (2016) 512-516.

[4] S.P. Rosshart, B.G. Vassallo, D. Angeletti, D.S. Hutchinson, A.P. Morgan, K. Takeda, H.D. Hickman, J.A. McCulloch, J.H. Badger, N.J. Ajami, G. Trinchieri, F. Pardo-Manuel de Villena, J.W. Yewdell, B. Rehermann, Wild Mouse Gut Microbiota Promotes Host Fitness and Improves Disease Resistance, Cell, 171 (2017) 1015-1028 e1013.

[5] J. Phelan, Choosing a Health Standard for Your Model, 2016. https://www.taconic.com/taconic-insights/quality/choosing-rodent-model-health-standards.html

[6] M.J. Korth, N. Tchitchek, A.G. Benecke, M.G. Katze, Systems approaches to influenza-virus host interactions and the pathogenesis of highly virulent and pandemic viruses, Semin Immunol, 25 (2013) 228-239.

[7] Ivanov, II, D.R. Littman, Segmented filamentous bacteria take the stage, Mucosal Immunol, 3 (2010) 209-212.

[8] F. Teng, C.N. Klinger, K.M. Felix, C.P. Bradley, E. Wu, N.L. Tran, Y. Umesaki, H.J. Wu, Gut Microbiota Drive Autoimmune Arthritis by Promoting Differentiation and Migration of Peyer's Patch T Follicular Helper Cells, Immunity, 44 (2016) 875-888.

[9] Z. Shi, J. Zou, Z. Zhang, X. Zhao, J. Noriega, B. Zhang, C. Zhao, H. Ingle, K. Bittinger, L.M. Mattei, A.J. Pruijssers, R.K. Plemper, T.J. Nice, M.T. Baldridge, T.S. Dermody, B. Chassaing, A.T. Gewirtz, Segmented Filamentous Bacteria Prevent and Cure Rotavirus Infection, Cell, 179 (2019) 644-658 e613.

[10] M. Zemlin, M. Hummel, I. Anagnostopoulos, H. Stein, Improved polymerase chain reaction detection of clonally rearranged T-cell receptor beta chain genes, Diagn Mol Pathol, 7 (1998) 138-145.

[11] M. Wymore Brand, M.J. Wannemuehler, G.J. Phillips, A. Proctor, A.M. Overstreet, A.E. Jergens, R.P. Orcutt, J.G. Fox, The Altered Schaedler Flora: Continued Applications of a Defined Murine Microbial Community, ILAR J, 56 (2015) 169-178.

[12] A.H. Newton, A. Cardani, T.J. Braciale, The host immune response in respiratory virus infection: balancing virus clearance and immunopathology, Semin Immunopathol, 38 (2016) 471-482.

[13] C. Purnama, S.L. Ng, P. Tetlak, Y.A. Setiagani, M. Kandasamy, S. Baalasubramanian, K. Karjalainen, C. Ruedl, Transient ablation of alveolar macrophages leads to massive pathology of influenza infection without affecting cellular adaptive immunity, Eur J Immunol, 44 (2014) 2003-2012.

[14] C.M. Lieber, M. Aggarwal, J.J. Yoon, R.M. Cox, H.J. Kang, J. Sourimant, M. Toots, S.K. Johnson, C.A. Jones, Z.M. Sticher, A.A. Kolykhalov, M.T. Saindane, S.M. Tompkins, O. Planz, G.R. Painter, M.G. Natchus, K. Sakamoto, R.K. Plemper, 4'-Fluorouridine mitigates lethal

infection with pandemic human and highly pathogenic avian influenza viruses, PLoS Pathog, 19 (2023) e1011342.

[15] J. Sourimant, C.M. Lieber, M. Aggarwal, R.M. Cox, J.D. Wolf, J.J. Yoon, M. Toots, C. Ye, Z. Sticher, A.A. Kolykhalov, L. Martinez-Sobrido, G.R. Bluemling, M.G. Natchus, G.R. Painter, R.K. Plemper, 4'-Fluorouridine is an oral antiviral that blocks respiratory syncytial virus and SARS-CoV-2 replication, Science, 375 (2022) 161-167.

[16] C. Schneider, S.P. Nobs, A.K. Heer, M. Kurrer, G. Klinke, N. van Rooijen, J. Vogel, M. Kopf, Alveolar macrophages are essential for protection from respiratory failure and associated morbidity following influenza virus infection, PLoS Pathog, 10 (2014) e1004053.

[17] G. Dranoff, A.D. Crawford, M. Sadelain, B. Ream, A. Rashid, R.T. Bronson, G.R. Dickersin, C.J. Bachurski, E.L. Mark, J.A. Whitsett, et al., Involvement of granulocyte-macrophage colony-stimulating factor in pulmonary homeostasis, Science, 264 (1994) 713-716.

[18] T. Thepen, N. Van Rooijen, G. Kraal, Alveolar macrophage elimination in vivo is associated with an increase in pulmonary immune response in mice, J Exp Med, 170 (1989) 499-509.

[19] R. Rauschmeier, C. Gustafsson, A. Reinhardt, A.G. N, L. Tortola, D. Cansever, S. Subramanian, R. Taneja, M.J. Rossner, M.H. Sieweke, M. Greter, R. Mansson, M. Busslinger, T. Kreslavsky, Bhlhe40 and Bhlhe41 transcription factors regulate alveolar macrophage self-renewal and identity, EMBO J, 38 (2019) e101233.

[20] S.M. Behar, C.J. Martin, M.G. Booty, T. Nishimura, X. Zhao, H.X. Gan, M. Divangahi, H.G. Remold, Apoptosis is an innate defense function of macrophages against Mycobacterium tuberculosis, Mucosal Immunol, 4 (2011) 279-287.

[21] S.J. Allden, P.P. Ogger, P. Ghai, P. McErlean, R. Hewitt, R. Toshner, S.A. Walker, P. Saunders, S. Kingston, P.L. Molyneaux, T.M. Maher, C.M. Lloyd, A.J. Byrne, The Transferrin Receptor CD71 Delineates Functionally Distinct Airway Macrophage Subsets during Idiopathic Pulmonary Fibrosis, Am J Respir Crit Care Med, 200 (2019) 209-219.

[22] M.P. Kuczma, E.A. Szurek, A. Cebula, B. Chassaing, Y.J. Jung, S.M. Kang, J.G. Fox, B. Stecher, L. Ignatowicz, Commensal epitopes drive differentiation of colonic T(regs), Sci Adv, 6 (2020) eaaz3186.

[23] T. Ruan, J. Sun, W. Liu, R.A. Prinz, D. Peng, X. Liu, X. Xu, H1N1 Influenza Virus Cross-Activates Gli1 to Disrupt the Intercellular Junctions of Alveolar Epithelial Cells, Cell Rep, 31 (2020) 107801.

[24] A. Cardani, A. Boulton, T.S. Kim, T.J. Braciale, Alveolar Macrophages Prevent Lethal Influenza Pneumonia By Inhibiting Infection Of Type-1 Alveolar Epithelial Cells, PLoS Pathog, 13 (2017) e1006140.

[25] A.V. Misharin, L. Morales-Nebreda, G.M. Mutlu, G.R. Budinger, H. Perlman, Flow cytometric analysis of macrophages and dendritic cell subsets in the mouse lung, Am J Respir Cell Mol Biol, 49 (2013) 503-510.

[26] D. Berrebi, S. Bruscoli, N. Cohen, A. Foussat, G. Migliorati, L. Bouchet-Delbos, M.C. Maillot, A. Portier, J. Couderc, P. Galanaud, M. Peuchmaur, C. Riccardi, D. Emilie, Synthesis of glucocorticoid-induced leucine zipper (GILZ) by macrophages: an anti-inflammatory and immunosuppressive mechanism shared by glucocorticoids and IL-10, Blood, 101 (2003) 729-738.

[27] M. Xia, H. Harb, A. Saffari, C. Sioutas, T.A. Chatila, A Jagged 1-Notch 4 molecular switch mediates airway inflammation induced by ultrafine particles, J Allergy Clin Immunol, 142 (2018) 1243-1256 e1217.

[28] P.M. Varghese, U. Kishore, R. Rajkumari, Human C1q Regulates Influenza A Virus Infection and Inflammatory Response via Its Globular Domain, Int J Mol Sci, 23 (2022).

[29] L.B. Klickstein, S.F. Barbashov, T. Liu, R.M. Jack, A. Nicholson-Weller, Complement receptor type 1 (CR1, CD35) is a receptor for C1q, Immunity, 7 (1997) 345-355.

[30] M.C. Abt, L.C. Osborne, L.A. Monticelli, T.A. Doering, T. Alenghat, G.F. Sonnenberg, M.A. Paley, M. Antenus, K.L. Williams, J. Erikson, E.J. Wherry, D. Artis, Commensal bacteria calibrate the activation threshold of innate antiviral immunity, Immunity, 37 (2012) 158-170.

[31] T. Ichinohe, I.K. Pang, Y. Kumamoto, D.R. Peaper, J.H. Ho, T.S. Murray, A. Iwasaki, Microbiota regulates immune defense against respiratory tract influenza A virus infection, Proc Natl Acad Sci U S A, 108 (2011) 5354-5359.

[32] H. Chen, L. Wang, X. Wang, X. Wang, H. Liu, Y. Yin, Distribution and Strain Diversity of Immunoregulating Segmented Filamentous Bacteria in Human Intestinal Lavage Samples, Microb Ecol, 79 (2020) 1021-1033.

[33] H. Jonsson, L.W. Hugerth, J. Sundh, E. Lundin, A.F. Andersson, Genome sequence of segmented filamentous bacteria present in the human intestine, Commun Biol, 3 (2020) 485.

[34] S. Subramanian, C.J. Busch, K. Molawi, L. Geirsdottir, J. Maurizio, S. Vargas Aguilar, H. Belahbib, G. Gimenez, R.A.A. Yuda, M. Burkon, J. Favret, S. Gholamhosseinian Najjar, B. de Laval, P.K. Kandalla, S. Sarrazin, L. Alexopoulou, M.H. Sieweke, Long-term culture-expanded alveolar macrophages restore their full epigenetic identity after transfer in vivo, Nat Immunol, 23 (2022) 458-468.

[35] T. Wang, J. Zhang, Y. Wang, Y. Li, L. Wang, Y. Yu, Y. Yao, Influenza-trained mucosal-resident alveolar macrophages confer long-term antitumor immunity in the lungs, Nat Immunol, 24 (2023) 423-438.

[36] A.K. Verma, S. Bansal, C. Bauer, A. Muralidharan, K. Sun, Influenza Infection Induces Alveolar Macrophage Dysfunction and Thereby Enables Noninvasive Streptococcus pneumoniae to Cause Deadly Pneumonia, J Immunol, 205 (2020) 1601-1607.

[37] A. Nogales, G. Avila-Perez, J. Rangel-Moreno, K. Chiem, M.L. DeDiego, L. Martinez-Sobrido, A Novel Fluorescent and Bioluminescent Bireporter Influenza A Virus To Evaluate Viral Infections, J Virol, 93 (2019).

[38] A.L. Hotard, F.Y. Shaikh, S. Lee, D. Yan, M.N. Teng, R.K. Plemper, J.E. Crowe, Jr., M.L. Moore, A stabilized respiratory syncytial virus reverse genetics system amenable to recombination-mediated mutagenesis, Virology, 434 (2012) 129-136.

[39] K.H. Dinnon, 3rd, S.R. Leist, A. Schafer, C.E. Edwards, D.R. Martinez, S.A. Montgomery, A. West, B.L. Yount, Jr., Y.J. Hou, L.E. Adams, K.L. Gully, A.J. Brown, E. Huang, M.D. Bryant, I.C. Choong, J.S. Glenn, L.E. Gralinski, T.P. Sheahan, R.S. Baric, A mouse-adapted model of SARS-CoV-2 to test COVID-19 countermeasures, Nature, 586 (2020) 560-566.

[40] Y.R. Yu, E.G. O'Koren, D.F. Hotten, M.J. Kan, D. Kopin, E.R. Nelson, L. Que, M.D. Gunn, A Protocol for the Comprehensive Flow Cytometric Analysis of Immune Cells in Normal and Inflamed Murine Non-Lymphoid Tissues, PLoS One, 11 (2016) e0150606.

FIGURE LEGENDS

Figure 1. Colonization of the intestine with SFB protected mice from influenza virus infection.

(A) EF and SPF mice were inoculated with A/CA/07/2009 (H1N1) influenza virus (CA09) as schematized. Lung viral titers, survival, body weight, and temperature were monitored.

(B) As schematized, conventionally colonized SFB^- mice received feces that lacked SFB (SFB^-), contained SFB (SFB^+), or contained SFB but no other bacteria (SFB-MA). Seven days after post-transplant, mice were inoculated with CA09. Mice were euthanized 4.5-days later or monitored daily for survival, body weight, and temperature for 2 weeks.

(C) SFB^- mice were administered SFB 3 months or 7 days prior to CA09 inoculation. **(i)** qRT-PCR analysis of SFB colonization level over the course of 14 weeks. **(ii)** Mice were euthanized 4.5-days later or monitored daily for survival, body weight, and temperature for 2 weeks.

(D) qRT-PCR analysis of SFB level in the small intestine, lungs, and spleens after 7 days colonization.

(E) SFB^- mice were untreated (naïve) or administrated SFB. Seven days later, mice were inoculated (or not) with CA09. Mice were euthanized 4.5 days later. H&E staining lung sections scored for pleuritis, bronchiolitis, alveolitis, vasculitis, interstitial pneumonia (IP), and perivascular cuffing (PVC).

All experiments n = 5 mice per group. Data is representative of two to three independent experiments. yielding an identical pattern of results. Statistical analysis; Viral titer: One-way ANOVA or student *t* test. survival: Log-rank Mantel-Cox test. Body weights and temperature: Two-way ANOVA. *$p<0.05$, **$p<0.01$, ***$p<0.001$, ns not significant.

Figure 2. SFB mediated protection against IAV was maintained in an array of knockout mice and did not require complex gut microbiota.

Lung viral titer, survival rate, body weight change, and temperature of: SFB-negative mice were colonized with SFB for 7 days then inoculated with CA09.

(A) *rag1*$^{-/-}$ mice

(B) mice received neutralization of IL-17/IL-22 monoclonal antibodies every other day throughout the experiment

(C) *Ifnar*$^{-/-}$ mice

(D) *rag1*$^{-/-}$*yc*$^{-/-}$ mice

(E) *stat1*$^{-/-}$ mice

(F) Altered Schaedler flora (ASF) mice.

All experiments n = 5 mice per group. Statistical analysis; Viral titer: student *t* test, Survival: Log-rank Mantel-Cox test. Body weights and temperature: Two-way ANOVA. **p<0.01, ***p<0.001.

Figure 3. SFB's protection against IAV infection associated with preservation of resident lung phagocytes.

(A) SFB^- mice were untreated (naïve) or administrated SFB. Seven days later, mice were inoculated (or not) with CA09. Mice were euthanized 4.5-days later. **(i)** Whole lung gene expression assayed by RNA-seq and data are heatmap of genes that are significantly altered by 2-fold in all treatment groups relative to the naïve group. **(ii)** Quantitation of CA09 level in these extracts by qRT-PCR.

(B) SFB^- mice were untreated (naïve) or administrated SFB. Seven days later, mice were inoculated (or not) with CA09. Mice were euthanized 4.5-days later, and lung assayed by flow cytometry. **(i & ii)** Analysis of dendritic cells and alveolar macrophage; representative flow plot and frequencies and cell numbers **(i)** cDC1. **(ii)** alveolar macrophages. **(iii)** Frequencies and cell numbers of lung neutrophils, inflammatory monocytes, and NK cells.

(C) **(i)** Experimental schema: SFB^- mice colonized with SFB, inoculated with CA09, and treated with 4'-FlU at indicated doses. On day 4.5 post virus inoculation, mice were euthanized, and lungs were harvested to determine virus titers and FACs analysis. **(ii)** lung viral titer. **(iii)** FACs plot graphical representation, frequencies, and cell numbers of lung cDC1, and AMs. **(iv)** Cell numbers of lung neutrophils, inflammatory monocytes, and NK cells.

All experiment n = 4-5 per group. Data is representative of two to three independent experiments (B and C), yielding an identical pattern of results. Statistical analysis: One-way ANOVA. *$p<0.05$, **$p<0.01$, ***$p<0.001$, ****$p<0.0001$, ns not significant.

Figure 4. SFB-mediated protection against IAV infection and resulting disease required alveolar macrophages.

(A-B) (A) *batf3*$^{-/-}$ and **(B)** *csf2*$^{-/-}$ mice were administered SFB and then, 7 days later, inoculated with CA09. Lung viral titer, body weight change, temperature, and survival were monitored.

(C) (i-ii) SFB$^-$ mice were orally administered with clodronate liposomes one day before mice were euthanized. FACS analysis to determine the AMs depletion efficacy after clodronate treatment. **(i)** FACS graphical representation of lung AMs, frequency of lung AMs and others immune cells after clodronate treatment. **(ii)** SFB$^-$ mice were colonized with SFB for 7 days, and clodronate liposomes were orally administered to mice one day before CA09 inoculation. Mice were euthanized on day 4 post-virus inoculation. Lung viral titer, survival rate, body weight, temperature was measured.

(D) SFB$^-$ mice were untreated (naïve) or administrated SFB. Seven days later, mice were inoculated (or not) with CA09. Mice were euthanized 4.5-days later. Level of cleaved caspase-3 of alveolar macrophages in lung were measured with FACS

(E) SFB$^-$ mice were untreated or treated as in (D). Level of CD71 expression of alveolar macrophages in lung were measured with FACS.

(F) SFB$^-$ mice treated as described in (C) FACS plot graphical representation, and frequencies CA09 level in T1ACEs, T2AECs, and Conducting AECs were assayed by flow cytometry.

All experiment n = 5 mice per group. Data is representative of two to three independent experiments (B-F), yielding an identical pattern of results. Statistical analysis; Viral titer, relative SFB genomes, MFI, frequencies/cell numbers of immune cell data: One-way ANOVA or student *t* test. Survival data Log-rank Mantel-Cox. Body weights, temperature: Two-way ANOVA. *p<0.05, ***p<0.001, ****p<0.0001, ns not significant.

Figure 5. SFB colonization intrinsically altered AM to withstand IAV-induced depletion.

As schematized, SFB^- CD45.1 mice were administered with SFB or PBS. Seven days later, AM were isolated by FACs-sorting, and transferred to SFB- CD45.2 mice. One day post-transferred, mice were inoculated with CA09. Four days later, lungs were harvested, and AM analyzed by FACs. Representative FACs plots, cell frequencies, cell numbers, and cleaved caspase-3 level are shown.

All experiment n = 5 mice per group. Data is representative of two independent experiments (B-F), yielding an identical pattern of results. Statistical test: One-way ANOVA. $^{**}p<0.01$, $^{***}p<0.001$, $^{****}p<0.0001$, ns not significant.

Figure 6. SFB$^+$ AM exhibited inflammatory anergy and enhanced antiviral function ex vivo.

(A) Schematic design for ex vivo studies of AM.

(B) Comparison of basal SFB$^+$ and SFB$^-$ AM gene expression by RNA-seq, shown as a volcano plot.

(C) SFB$^+$ and SFB$^-$ AM were exposed to UV-CA09 with or without Notch4 neutralizing, or isotype control antibodies. RNA was harvested 24 hours later, and gene expression assayed by RT-qPCR. Results are a heat map summary with full results shown in FS7.

(D) AM and CA09 stocks were incubated at 37C, or indicated temperature, for 45 minutes and supernatant were collected. In addition, some cells had new media added and were incubated for another 24 hours. **(i)** virus infection titers in supernatant at 45 minutes and 24 hours were assayed. **(ii)** Supernatant were collected after 45 minutes incubated with CA09 and viral genomes quantitated by RT-qPCR. **(iii)** Cell-free supernatant of 15 hours AM cultures were incubated with live CA09 stocks, with or without C1qa-neutralization or isotype antibody for 45 minutes, at which point virus infection titers were assayed. **(iv)** Cell lysates were generated upon CA09 removal or 24 hours later and viral genomes quantitated by RT-qPCR.

All experiment n = 4-5 mice per group. Data is representative of two independent experiments, yielding an identical pattern of results. Statistical analysis: One-way ANOVA. *p<0.05, **p<0.01, , ****p<0.0001, ns not significant.

Figure 7. Adoptive transfer of SFB$^+$ AM enabled recipients to better manage IAV infection.

(A) As schematized, SFB$^-$ mice were administered SFB or PBS. Seven days later, AMs were isolated by FACs-sorting and transferred to SFB$^-$ mice. Mice were administered 5x10^5 cells per mouse. One day post adoptive transfer, mice were inoculated with a lethal dose of CA09. Mice were euthanized 4.5 days post-inoculation for viral titer and gross lung assessment or monitored for survival, body weight, and temperature.

(B) As schematized, AMs from SFB$^-$ *csf2*$^{+/+}$ mice were administered SFB or PBS. Seven days later, AMs were isolated by FACs-sorting and transferred to SFB$^-$ *csf2*$^{-/-}$ mice. One day post-transfer, mice were inoculated with CA09. Mice were monitored for 14 days for clinical symptoms including survival rate, body weight, and temperature.

(C) SFB$^-$ mice were administered clodronate liposomes to remove endogenous AM populations. Seven days later after initiation of depletion, mice were administered 5x10^5 AM cells harvested from the SFB$^-$ or SFB$^+$ mice. One day post transfer, mice were inoculated with CA09. Mice were euthanized on day four to assess lung viral titer and gross lung assessment or monitored for survival, body weight, and temperature.

All experiments have at least n = 5 mice per group. Data is representative of two independent experiments (A), yielding an identical pattern of results. Statistical analysis; One-way ANOVA: viral titers. Survival: Log-rank Mantel-Cox test. Body weight, temperature: Two-way ANOVA. *p<0.05, **p<0.01, ****p<0.0001, ns not significant.

Figure 1

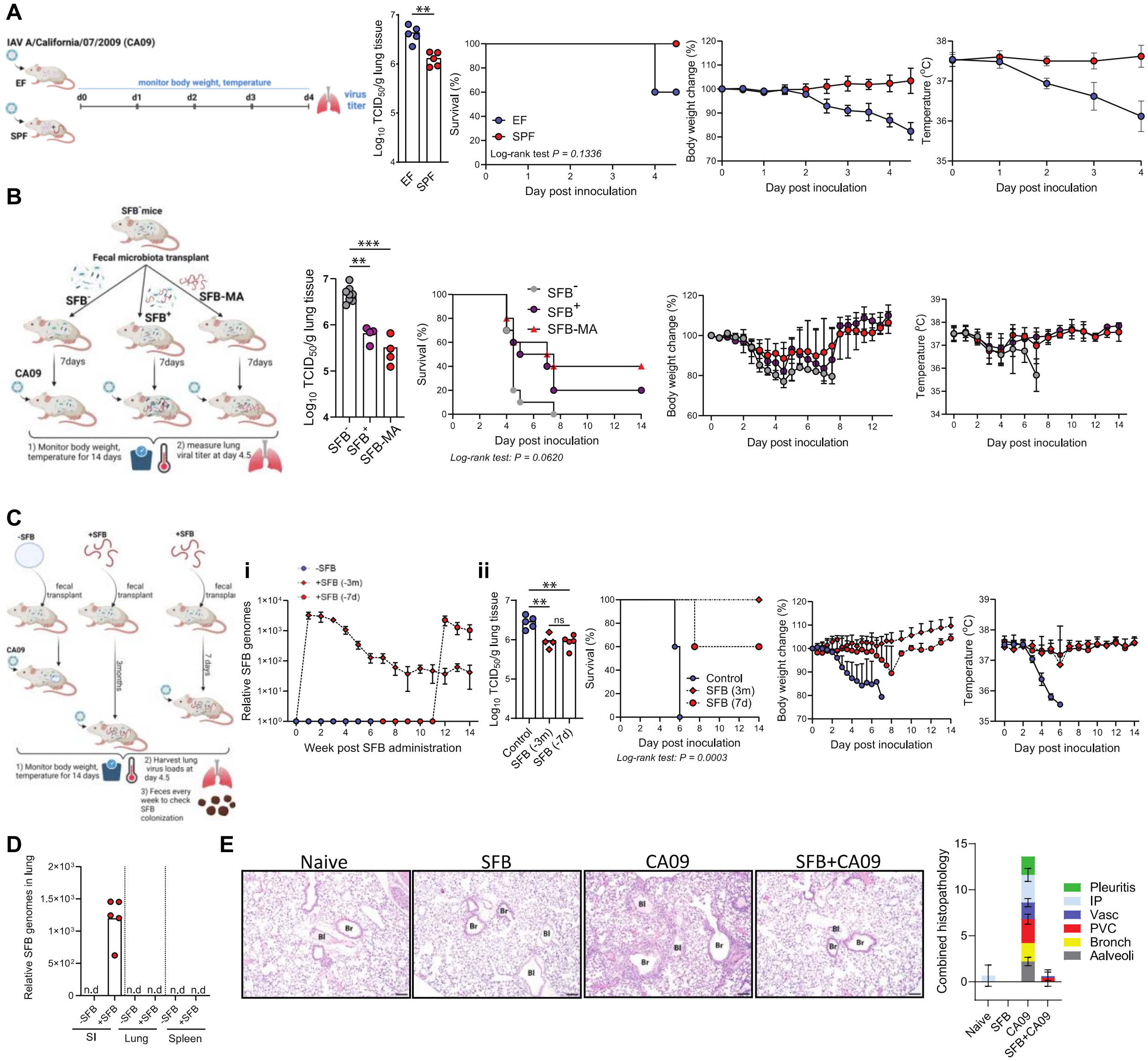
A
IAV A/California/07/2009 (CA09)
EF
SPF
monitor body weight, temperature
d0
d1
d2
d3
d4
virus titer
Log10 TCID50/g lung tissue
Survival (%)
Log-rank test P = 0.1336
Day post innoculation
Body weight change (%)
Day post inoculation
Temperature (°C)
B
SFB- mice
Fecal microbiota transplant
SFB-
SFB+
SFB-MA
7days
CA09
1) Monitor body weight, temperature for 14 days
2) measure lung viral titer at day 4.5
Log-rank test: P = 0.0620
C
-SFB
+SFB
fecal transplant
3months
7 days
1) Monitor body weight, temperature for 14 days
2) Harvest lung virus loads at day 4.5
3) Feces every week to check SFB colonization
i
-SFB
+SFB (-3m)
+SFB (-7d)
Relative SFB genomes
Week post SFB administration
ii
Control
SFB (-3m)
SFB (-7d)
ns
SFB (3m)
SFB (7d)
Log-rank test: P = 0.0003
D
Relative SFB genomes in lung
n.d
SI
Lung
Spleen
E
Naive
SFB
CA09
SFB+CA09
Combined histopathology
Pleuritis
IP
Vasc
PVC
Bronch
Aalveoli

Figure 2

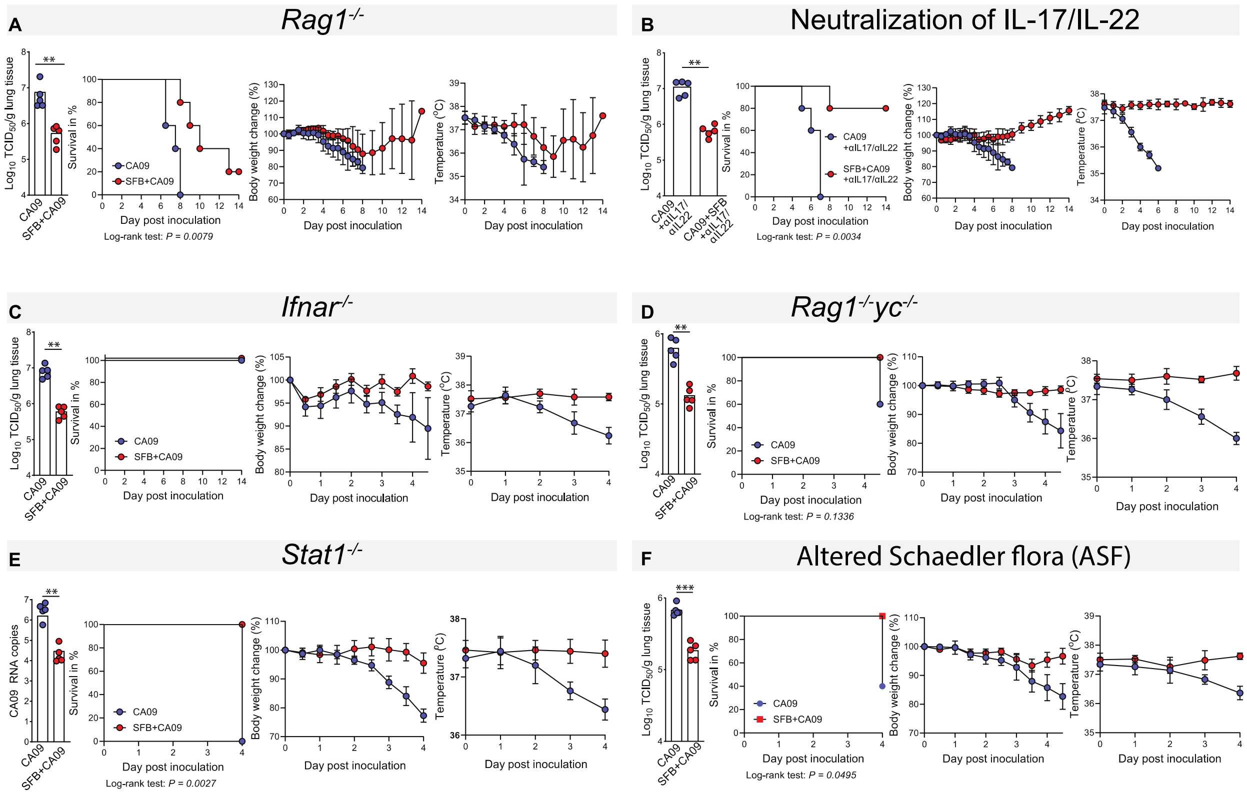
A
Rag1-/-
B
Neutralization of IL-17/IL-22
C
Ifnar-/-
D
Rag1-/-γc-/-
E
Stat1-/-
F
Altered Schaedler flora (ASF)
Log10 TCID50/g lung tissue
CA09 RNA copies
Survival in %
Body weight change (%)
Temperature (°C)
Day post inoculation
CA09
SFB+CA09
CA09 +αIL17/αIL22
SFB+CA09 +αIL17/αIL22
Log-rank test: P = 0.0079
Log-rank test: P = 0.0034
Log-rank test: P = 0.1336
Log-rank test: P = 0.0027
Log-rank test: P = 0.0495

Figure 3

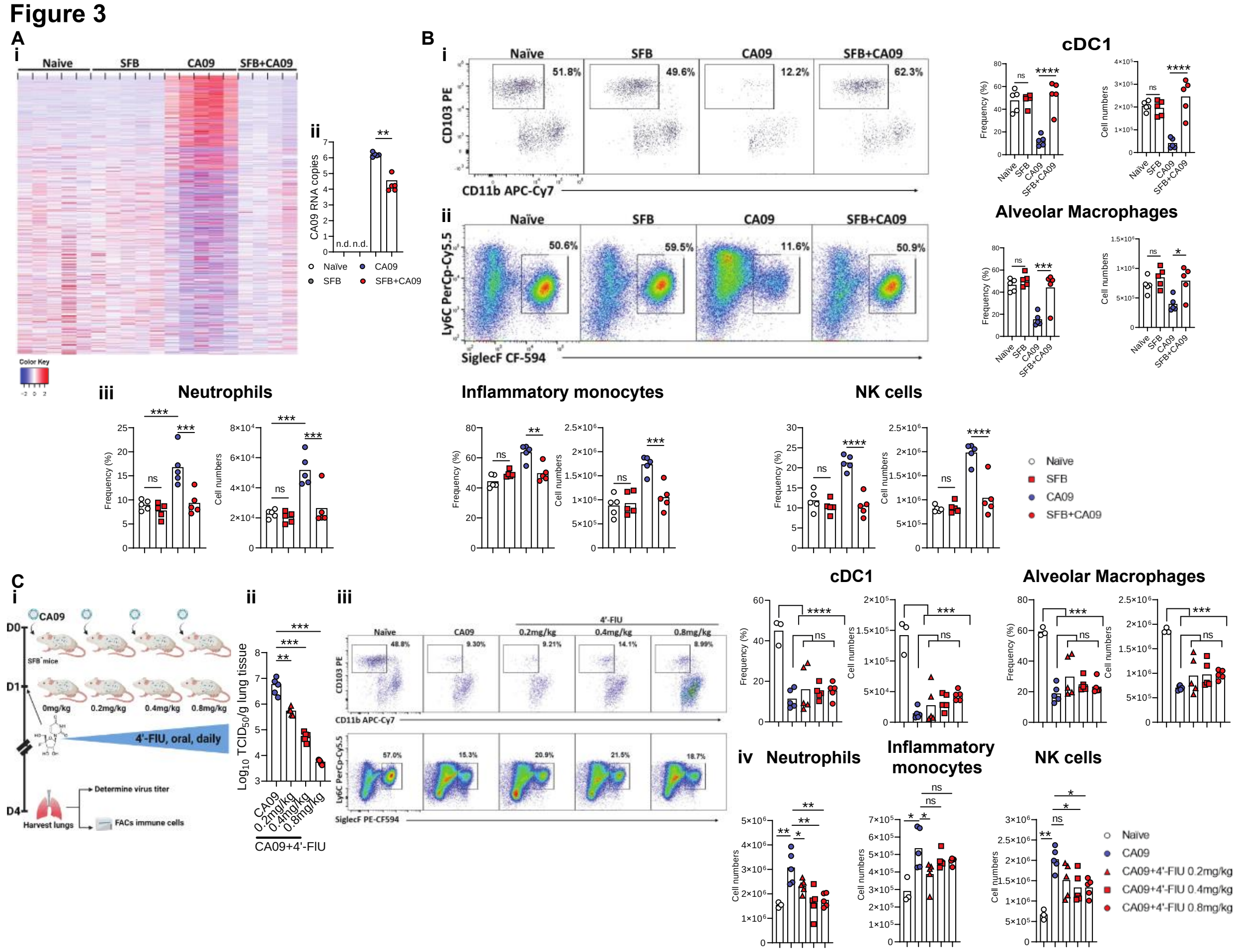
A
B
C
Naive
SFB
CA09
SFB+CA09
CA09 RNA copies
cDC1
Alveolar Macrophages
Neutrophils
Inflammatory monocytes
NK cells
CD103 PE
CD11b APC-Cy7
Ly6C PerCp-Cy5.5
SiglecF CF-594
Frequency (%)
Cell numbers
4'-FIU, oral, daily
Determine virus titer
FACs immune cells
Harvest lungs
Log10 TCID50/g lung tissue
CA09+4'-FIU
CA09+4'-FIU 0.2mg/kg
CA09+4'-FIU 0.4mg/kg
CA09+4'-FIU 0.8mg/kg

Figure 4

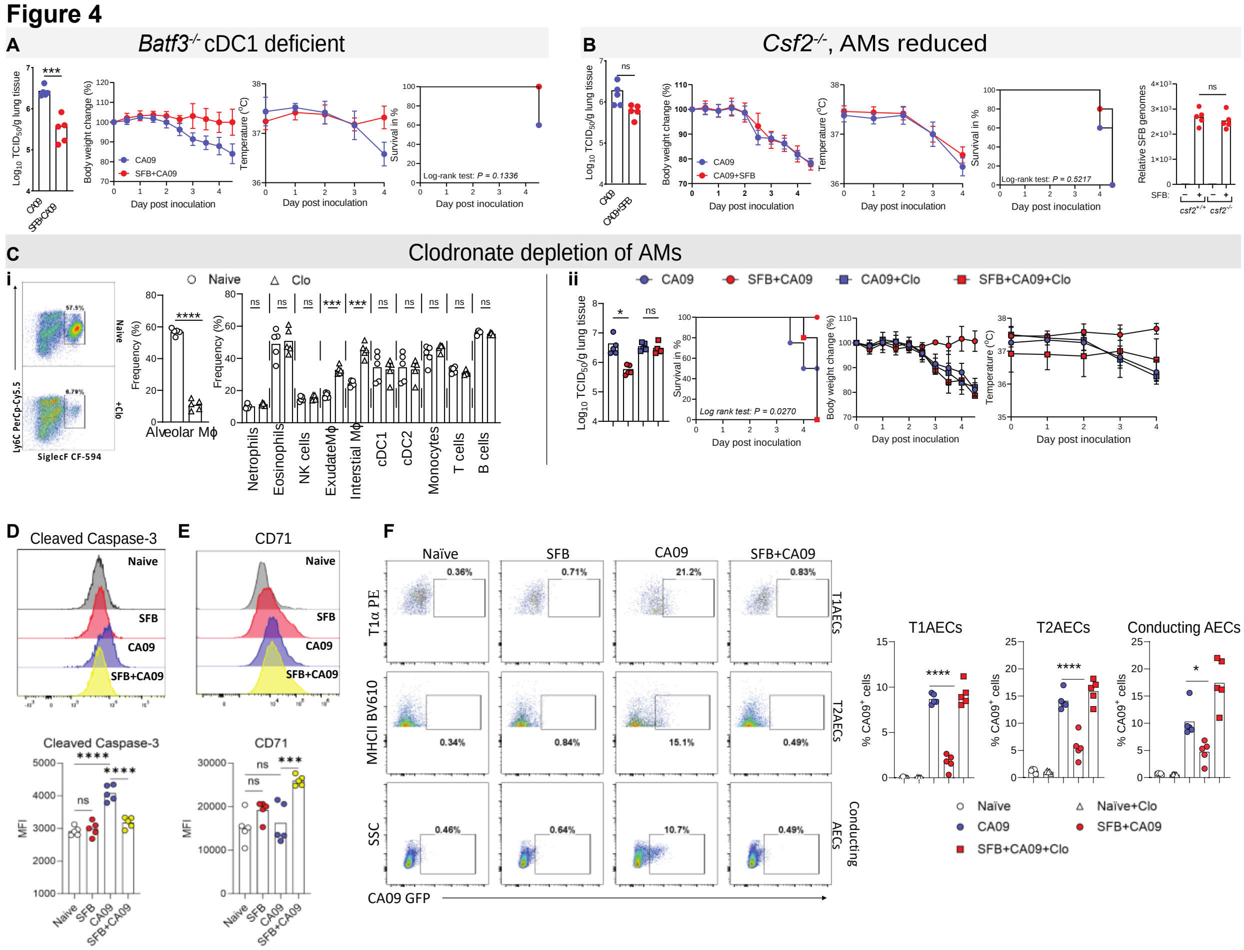
A Batf3-/- cDC1 deficient
B Csf2-/-, AMs reduced
C Clodronate depletion of AMs
D Cleaved Caspase-3
E CD71
F
Naive
SFB
CA09
SFB+CA09
T1AECs
T2AECs
Conducting AECs
CA09 GFP
Day post inoculation
Naïve+Clo
SFB+CA09+Clo

Figure 5

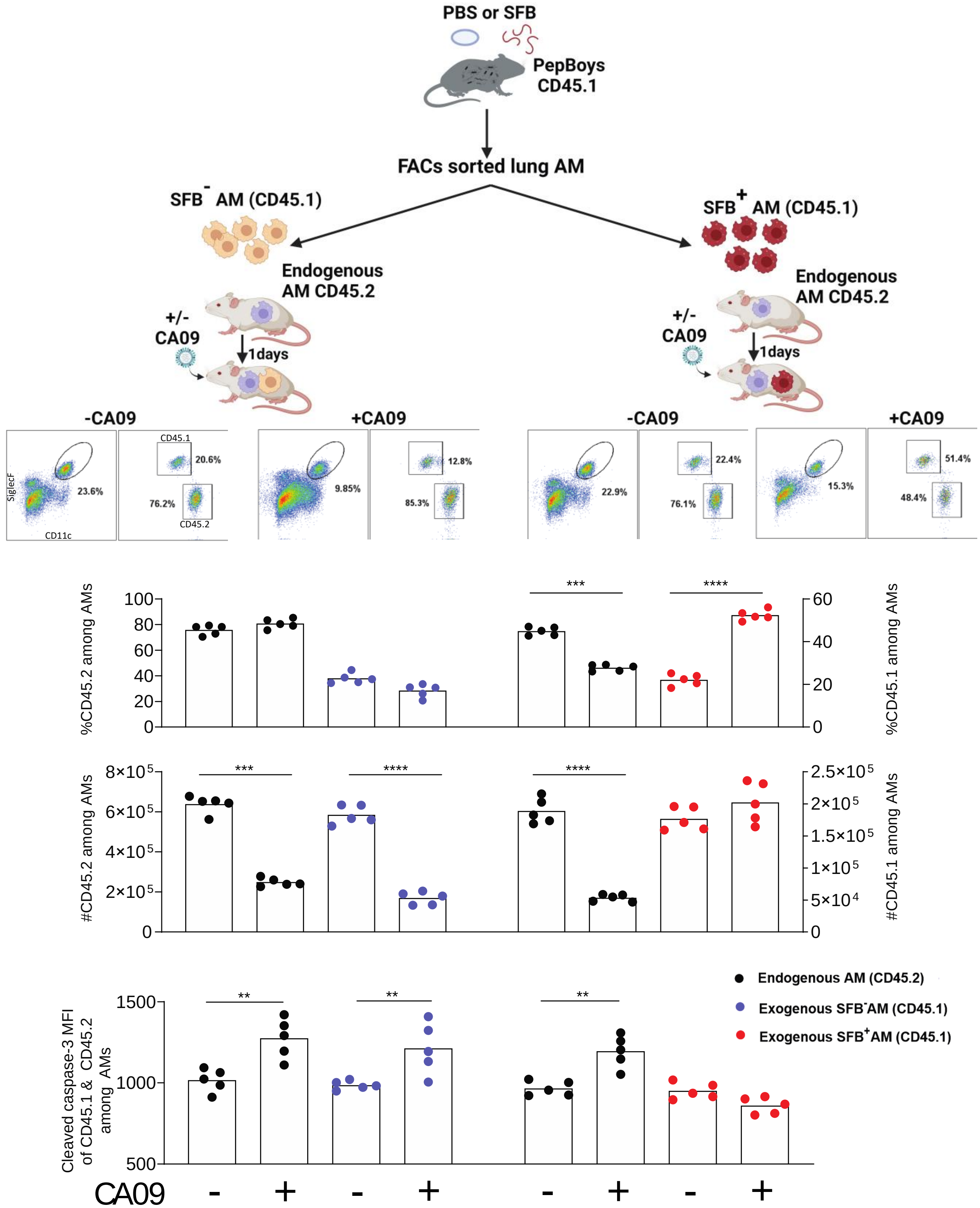
PBS or SFB
PepBoys CD45.1
FACs sorted lung AM
SFB⁻ AM (CD45.1)
SFB⁺ AM (CD45.1)
Endogenous AM CD45.2
+/- CA09
1days
-CA09
+CA09
SiglecF
CD11c
CD45.1
CD45.2
23.6%
20.6%
76.2%
9.85%
12.8%
85.3%
22.9%
22.4%
76.1%
15.3%
51.4%
48.4%
%CD45.2 among AMs
%CD45.1 among AMs
#CD45.2 among AMs
#CD45.1 among AMs
Cleaved caspase-3 MFI of CD45.1 & CD45.2 among AMs
Endogenous AM (CD45.2)
Exogenous SFB⁻AM (CD45.1)
Exogenous SFB⁺AM (CD45.1)
CA09 - + - + - + - +

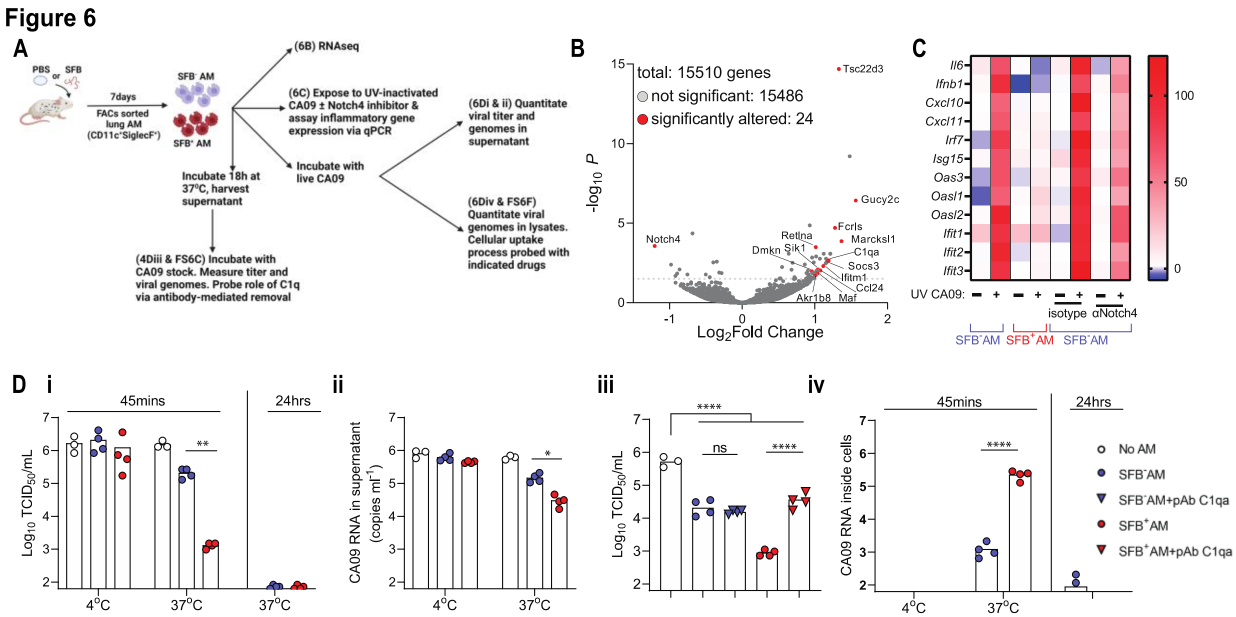
Figure 6
A
B
C
D
(6B) RNAseq
(6C) Expose to UV-inactivated CA09 ± Notch4 inhibitor & assay inflammatory gene expression via qPCR
Incubate with live CA09
(6Di & ii) Quantitate viral titer and genomes in supernatant
(6Div & FS6F) Quantitate viral genomes in lysates. Cellular uptake process probed with indicated drugs
Incubate 18h at 37°C, harvest supernatant
(4Diii & FS6C) Incubate with CA09 stock. Measure titer and viral genomes. Probe role of C1q via antibody-mediated removal
total: 15510 genes
not significant: 15486
significantly altered: 24
Log2Fold Change
UV CA09:
isotype
αNotch4
SFB⁻AM
SFB⁺AM
45mins
24hrs
Log10 TCID50/mL
CA09 RNA in supernatant (copies ml⁻¹)
CA09 RNA inside cells
No AM
SFB⁻AM
SFB⁻AM+pAb C1qa
SFB⁺AM
SFB⁺AM+pAb C1qa

Figure 7

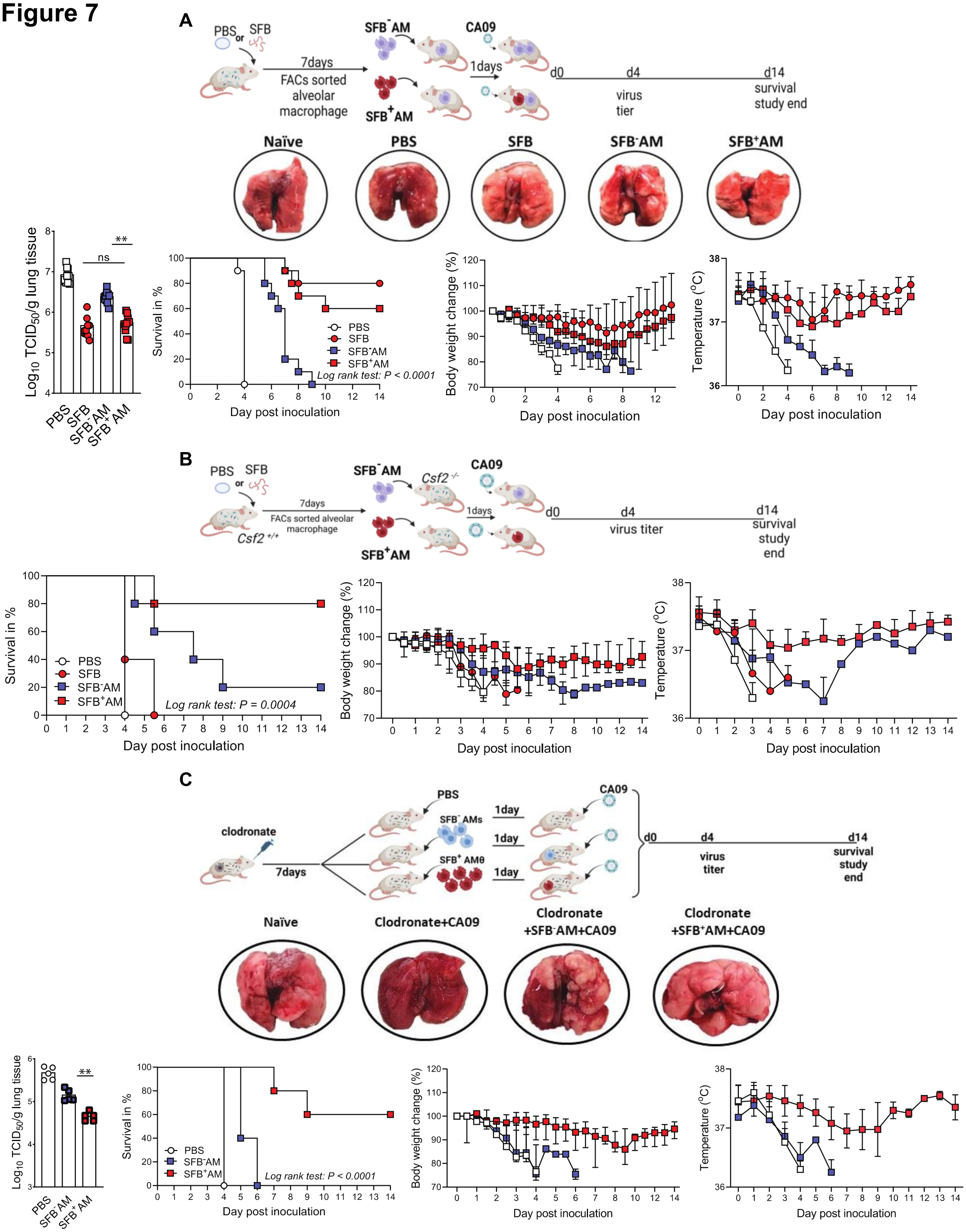
A
PBS or SFB
7days
FACs sorted alveolar macrophage
SFB⁻AM
SFB⁺AM
CA09
1days
d0
d4
virus tier
d14
survival study end
Naïve
PBS
SFB
SFB⁻AM
SFB⁺AM
Log10 TCID50/g lung tissue
ns
**
Survival in %
Day post inoculation
Log rank test: P < 0.0001
Body weight change (%)
Temperature (°C)
B
Csf2 +/+
Csf2 -/-
virus titer
Log rank test: P = 0.0004
C
clodronate
7days
PBS
SFB⁻ AMs
SFB⁺ AMθ
1day
Clodronate+CA09
Clodronate +SFB⁻AM+CA09
Clodronate +SFB⁺AM+CA09

2.4.2 Gut Microbiota-Derived Metabolites Confer Protection Against SARS-CoV-2 Infection

GUT MICROBES
2022, VOL. 14, NO. 1, e2105609 (22 pages)
https://doi.org/10.1080/19490976.2022.2105609

Taylor & Francis
Taylor & Francis Group

RESEARCH PAPER

OPEN ACCESS Check for updates

Gut microbiota-derived metabolites confer protection against SARS-CoV-2 infection

Julia A. Brown[a,b]†, Katherine Z. Sanidad[a,b]†, Serena Lucotti[a,b], Carolin M. Lieber[c], Robert M. Cox[c], Aparna Ananthanarayanan[a,b], Srijani Basu[d], Justin Chen[a], Mengrou Shan[e], Mohammed Amir[a,b], Fabian Schmidt[f], Yiska Weisblum[f], Michele Cioffi[a,b], Tingting Li[g], Florencia Madorsky Rowdo[h], M. Laura Martin[h], Chun-Jun Guo[g], Costas Lyssiotis[d], Brian T. Layden[i,j], Andrew J. Dannenberg[d]‡, Paul D. Bieniasz[f,k], Benhur Lee[l], Naohiro Inohara[e], Irina Matei[a,b], Richard K. Plemper[c], and Melody Y. Zeng[a,b]

[a]Gale and Ira Drukier Institute for Children's Health, Weill Cornell Medicine; New York, NY, USA; [b]Department of Pediatrics, Weill Cornell Medicine; New York, NY, United States of America; [c]Institute for Biomedical Sciences, Georgia State University; Atlanta, GA, United States of America; [d]Department of Medicine, Weill Cornell Medicine; New York, NY, United States of America; [e]Rogel Cancer Center, University of Michigan; Ann Arbor, MI, United States of America; [f]Laboratory of Retrovirology, The Rockefeller University; New York, NY, United States of America; [g]Jill Roberts Institute for Inflammatory Bowel Disease, Weill Cornell Medicine; New York, NY, United States of America; [h]Englander Institute for Precision Medicine, Weill Cornell Medicine; New York, NY, United States of America; [i]Department of Medicine, Division of Endocrinology, Diabetes, and Metabolism, University of Illinois at Chicago; Chicago, Illinois, United States of America; [j]Jesse Brown Veterans Affairs Medical Center; Chicago, Illinois, United States of America; [k]Howard Hughes Medical Institute, The Rockefeller University; New York, NY, United States of America; [l]Department of Microbiology, Icahn School of Medicine at Mount Sinai; New York, NY, United States of America

ABSTRACT

The gut microbiome is intricately coupled with immune regulation and metabolism, but its role in Coronavirus Disease 2019 (COVID-19) is not fully understood. Severe and fatal COVID-19 is characterized by poor anti-viral immunity and hypercoagulation, particularly in males. Here, we define multiple pathways by which the gut microbiome protects mammalian hosts from SARS-CoV-2 intranasal infection, both locally and systemically, via production of short-chain fatty acids (SCFAs). SCFAs reduced viral burdens in the airways and intestines by downregulating the SARS-CoV-2 entry receptor, angiotensin-converting enzyme 2 (ACE2), and enhancing adaptive immunity via GPR41 and 43 in male animals. We further identify a novel role for the gut microbiome in regulating systemic coagulation response by limiting megakaryocyte proliferation and platelet turnover via the Sh2b3-Mpl axis. Taken together, our findings have unraveled novel functions of SCFAs and fiber-fermenting gut bacteria to dampen viral entry and hypercoagulation and promote adaptive antiviral immunity.

Introduction

Coronavirus disease 2019 (COVID-19), caused by the newly emerged coronavirus SARS-CoV-2, has created unprecedented global health and economic crises.[1] Reduced vaccine efficacy in immunocompromised populations, such as patients with cancer or autoimmune diseases, further underscores the importance of continued research efforts to develop therapeutic modalities that complement vaccine-focused efforts to combat the COVID-19 pandemic. The human angiotensin-converting enzyme 2 (ACE2) mediates the entry of SARS-CoV-2 for infection and the manifestation of COVID-19.[2] ACE2 is expressed throughout the body, including in the intestinal epithelial cells of the gastrointestinal (GI) tract.[3] SARS-CoV-2 has frequently been detected in stool samples;[4] GI symptoms are among the early symptoms in up to 50% of COVID-19 patients.[5,6] Persistent intestinal reservoirs of SARS-CoV-2 might drive continued evolution of B cell memory responses in recovered or asymptomatic COVID-19 patients.[7] Dysfunction of the coagulation response has emerged as another hallmark that contributes to the mortality and morbidity of COVID-19.[8–11]

The gut microbiome has been found to affect the outcome of other viral respiratory infections, such as influenza, as well as the development of chronic

CONTACT Melody Y. Zeng myz4001@med.cornell.edu Department of Pediatrics, Weill Cornell Medicine; New York, NY, United States of America
†Equal contribution
‡Retired
Supplemental data for this article can be accessed online at https://doi.org/10.1080/19490976.2022.2105609

lung conditions such as asthma and COPD.[12,13] Several recent studies have found evidence of altered gut microbiome composition in COVID-19 patients.[14] However, the role of the gut microbiome in the susceptibility to SARS-CoV-2 infection and COVID-19 remains undefined.

In this study, we have demonstrated that short-chain fatty acids (SCFAs), derived from fiber-fermenting commensal bacteria, downregulate ACE2 and reduce infection by a VSV pseudovirus expressing SARS-CoV-2 spike in both mice and hamsters, promote antiviral T cell responses and the formation of spike-specific B and T cells, and dampen the coagulation response. Our findings potentially unravel gut microbiome-linked signaling pathways that can be harnessed in the development of preventive and therapeutic measures to mitigate infection by not only SARS-CoV-2 but other viral pathogens as well.

Results

Clostridia *species and SCFAs downregulate ACE2 expression in the intestine and lung*

To first address whether *Ace2* expression is affected by the gut microbiome, we compared *Ace2* expression in age- and sex-matched C57BL/6 specific pathogen-free (SPF) and germ-free (GF) mice via qPCR. *Ace2* expression was elevated at the mRNA level in the lungs, colons, small intestines, and livers in GF mice (Figure 1A), suggesting a possible role for the gut microbiome in the regulation of *Ace2*. Flow cytometry analysis of kidney cells revealed higher protein expression of ACE2 in the kidneys of GF mice (**Figure S1A**) despite no significant difference at the mRNA level, but protein expression in the other tissues was too low for accurate quantification. The expression of *Tmprss2*, a transmembrane serine protease that primes the spike protein for viral entry,[2] was not significantly altered (**Figure S1B**).

To identify gut bacteria that modify ACE2 expression, we first treated SPF mice with gentamicin or vancomycin in drinking water for 2 weeks. We observed increased *Ace2* expression in the colons of vancomycin-treated mice (Figure 1B). Both gentamicin and vancomycin treatments led to significant alterations of the gut microbiome and selective depletion of specific bacterial species (Figure 1C-D). Vancomycin is active against a diverse range of gram-positive and gram-negative bacteria, including the bacterial clusters Clostridium IV (in the family Ruminococcaceae) and Clostridium XIVa (in the family Lachnospiraceae), which are major producers of short-chain fatty acids (SCFAs).[15–17] Accordingly, 16S rRNA sequencing of fecal DNA and qPCR quantification confirmed a near-total loss of *Clostridia* in vancomycin-treated mice (Figure 1C-E). To determine whether *Clostridia* specifically regulate *Ace2* expression, we colonized GF mice with fecal bacteria from SPF mice or fecal bacteria enriched by chloroform-resistant *Clostridia* as previously described[18] (**Figure S1C**). While *Tmprss2* was not affected, *Ace2* expression was significantly reduced in the colons of GF mice colonized with fecal bacteria (CONV, conventionalized); importantly, colonization with *Clostridia*-enriched bacteria reduced *Ace2* expression to the levels seen in SPF mice (Figure 1F**, Figure S1D**).

Clostridia are major producers of SCFAs, such as acetate, butyrate, and propionate.[17] Accordingly, fecal butyrate and propionate concentrations were drastically decreased in vancomycin-treated mice (**Figure S1E**). Likewise, colonization with SPF fecal bacteria or *Clostridia*-enriched bacteria in GF mice significantly increased fecal propionate and butyrate (Figure 1G). To determine if SCFAs alone could reduce *Ace2* expression, we administered a combination of three SCFAs (40mM acetate, 25.9mM propionate, and 67.5mM butyrate[19]) in drinking water to GF mice for 2 weeks, which reduced *Ace2* expression in the colons and kidneys, and reduced *Tmprss2* expression in the lung and liver (Figure 1H**, Figure S1F**). Similarly, western blot analysis (Figure 1I) and immunofluorescence imaging (Figure 1J) of kidneys from GF mice treated with the SCFA cocktail or butyrate alone showed reduced expression of ACE2 at the protein level. Interestingly, this phenotype was observed only in male but not female SCFA-treated mice (**Figure S1G**), suggesting a sex-biased mechanism behind SCFA regulation of ACE2 expression.

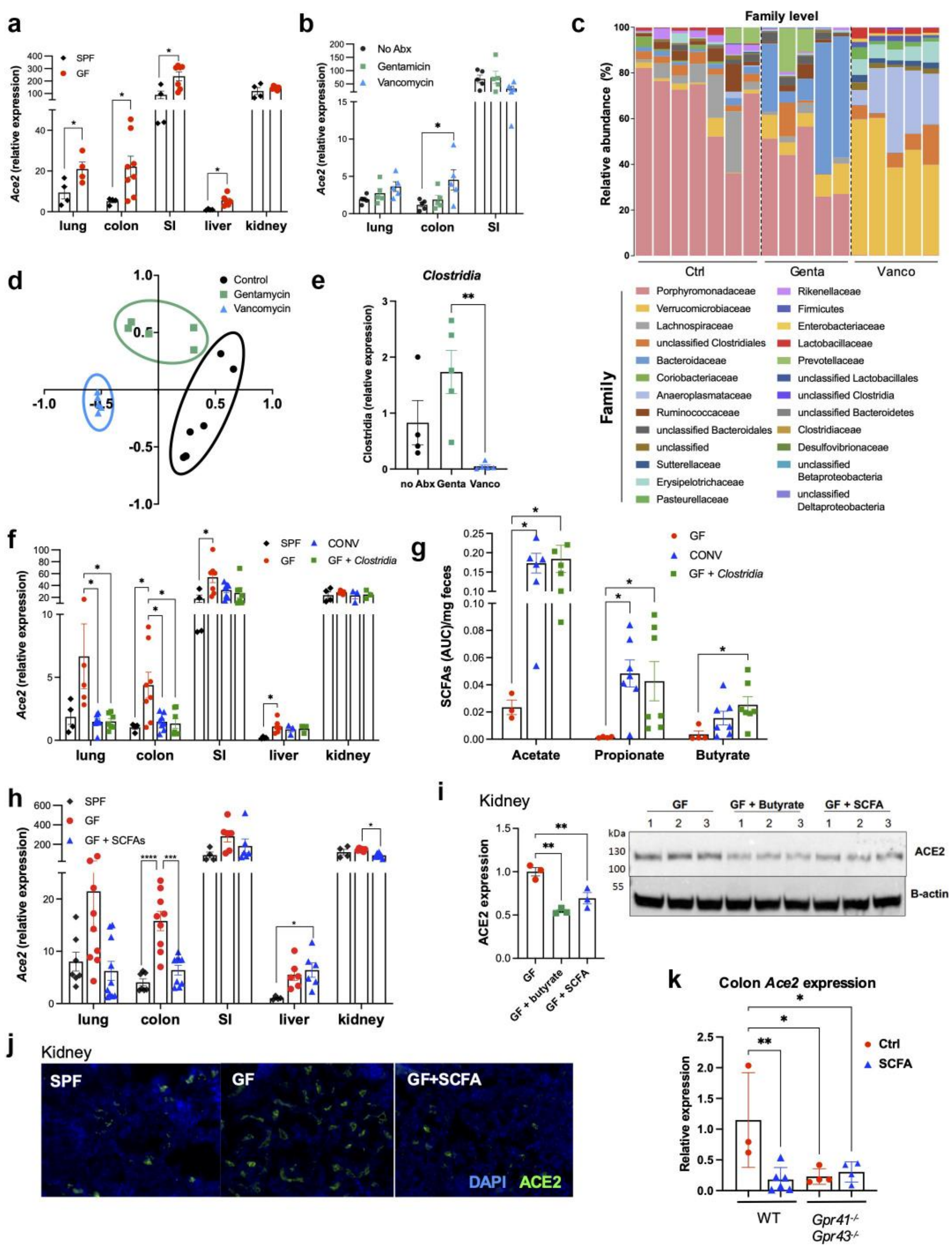

Fig 1. Commensal Clostridia species reduce Ace2 expression via SCFA production. (A) *Ace2* mRNA expression in male SPF and GF mice. (B) *Ace2* mRNA expression in SPF and GF mice treated with antibiotics for two weeks. (C–D) 16S rRNA sequencing was performed. (C) Relative abundance is shown at the family level; (D) non-metric multidimensional scaling analysis is shown. (E) The relative abundance of *Clostridia* species in fecal pellets of antibiotic-treated mice was measured by qPCR. (F–G) *Ace2* mRNA expression (F) and fecal SCFA concentrations (G) in SPF, GF, and GF mice colonized with either bulk fecal bacteria from SPF mice (CONV, conventionalized) or fecal bacteria enriched for *Clostridia*. (H) *Ace2* mRNA expression in SPF, GF, or SCFA-treated GF mice. (I–J) ACE2 protein expression was measured via Western blot (i; densitometry relative to the Ctrl condition) and immunofluorescence (j; images are representative of 2 independent experiments) in kidneys from GF mice given control or SCFA water (butyrate alone or a cocktail of acetate, butyrate, and propionate). (K) *Ace2* mRNA expression in the colons of control- or SCFA-treated wild type or *Gpr41*$^{-/-}$*Gpr43*$^{-/-}$ mice. Error bars indicate mean±SEM. Significance was determined using one-way ANOVA with Tukey's test for multiple comparisons. (A–H) represent 2-3 independent experiments; images in (I–K) are representative of 2 independent experiments. SI = small intestine; FB = fecal bacteria. *p<0.05; **p<0.01. See also **Figures S1 and S2A.**

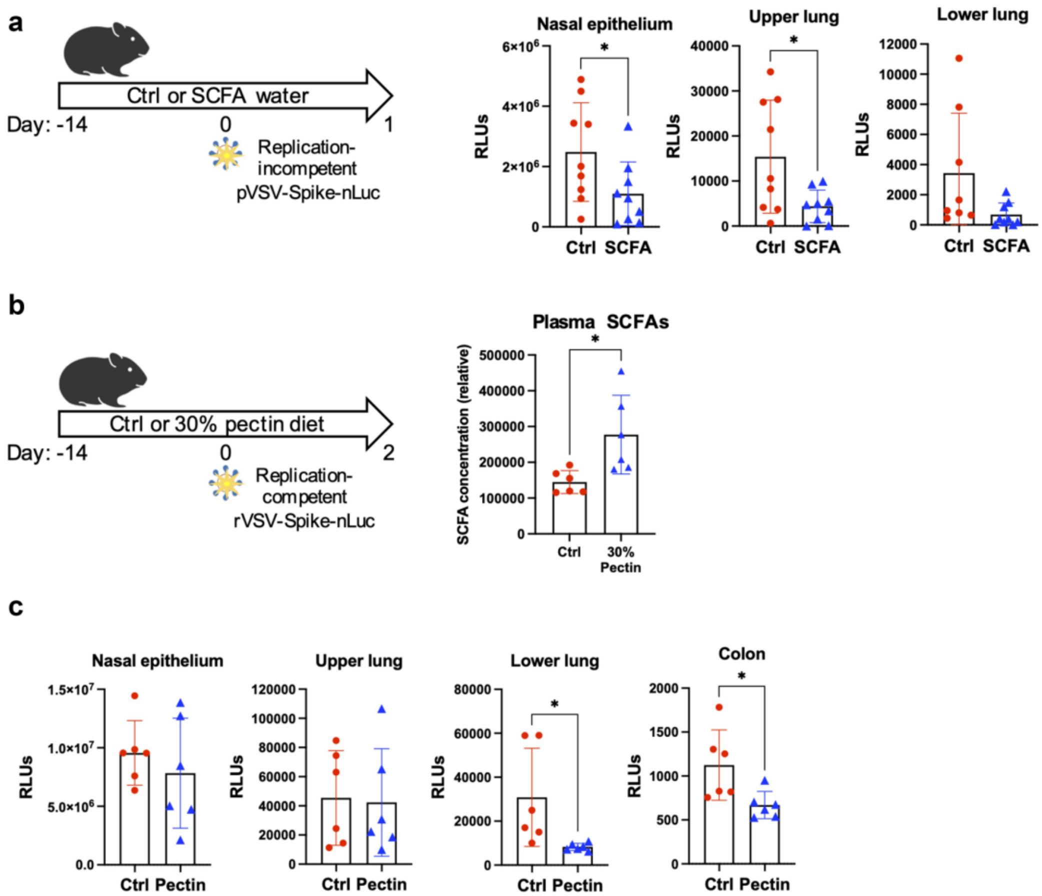

Fig 2. Treatment with SCFAs or SCFA-promoting pectin reduces viral entry in animals. (A) Luciferase activity in tissue homogenates from control or SCFA-treated Syrian hamsters 24 hours post infection with pVSV/Spike-nLuc pseudovirus. (B) Plasma SCFA concentrations from hamsters given a control diet or 30% pectin diet for two weeks were measured via LCMS; measurements for individual SCFAs are shown in **Figure S2C**. (C) Luciferase activity in tissue homogenates from control or pectin-treated Syrian hamsters 48 hours post infection with replication-competent rVSV/Spike-nLuc. Error bars indicate mean±SEM. Significance was determined using unpaired t-test. All data represent 2-3 independent experiments. RLU = relative light unit; SI = small intestine. *$p<0.05$. See also **Figure S2.**

SCFAs directly interact with the G protein coupled receptors GPR41 (FFAR3) and GPR43 (FFAR2), which are expressed on diverse tissues including intestinal epithelia and immune cells.[20] SCFA treatment did not affect *Ace2* expression in the lungs or colons of *Gpr41*$^{-/-}$*Gpr43*$^{-/-}$, *Gpr41*$^{-/-}$, or *Gpr43*$^{-/-}$ mice (Figure 1K, **Figure S1H**), indicating that both receptors are likely involved in mediating SCFA regulation of *Ace2* expression. Additionally, the treatment of human liver organoids with SCFAs for 24 hours resulted in a reduction of *Ace2* expression (**Figure S2A**), suggesting that SCFAs may directly affect *Ace2* expression.

SCFAs confer protection against intranasal infection in animals

Since ACE2 is the major entry receptor for SARS-CoV-2, we hypothesized that SCFA downregulation of ACE2 might reduce viral entry. Accordingly, we treated 9-week-old male Syrian hamsters with SCFA water for 2 weeks before intranasal infection with 5x10^5 infectious units (IU) of a replication-incompetent vesicular stomatitis virus (VSV) pseudovirus expressing SARS-CoV-2 spike protein and nanoluciferase (designated **pVSV/Spike-nLuc**). After 24 hours, we analyzed viral burdens by measuring luciferase activity in homogenized tissues. Luciferase activity in the lung and nasal epithelium of SCFA-treated hamsters was reduced compared to that of control hamsters, indicating reduced infection (Figure 2A).

Dietary fibers, such as pectin, can be fermented by gut bacteria into SCFAs.[21] We analyzed the expression of *Ace2* and *Tmprss2* in mice whose diets were supplemented with 5% or 30% pectin, and found both to be reduced in both the lungs and colons of mice receiving pectin supplementation (**Figure S2B**). We gave hamsters a 30% pectin diet for 2 weeks and found increased total SCFA levels in the plasma (Figure 2B, **Figure S2C**) and reduced luciferase activity in the lung and colon following infection with a replication competent chimeric VSV virus expressing SARS-CoV-2 spike and nanoluciferase (designated **rVSV/Spike-nLuc**; Figure 2C). Similar increases in plasma SCFA levels were observed in mice given 30% pectin for 2 weeks or hamsters given SCFA water for 2 weeks (**Figure S2D-E**). Of note, measurement of fecal SCFA levels proved unfeasible due to the high level of fat trapping in the stool of pectin-treated hamsters, which prevented efficient extraction of fecal metabolites for quantification. We additionally infected SCFA-treated GF mice with a replication-competent chimeric VSV virus expressing GFP and the SARS-CoV-2 beta variant spike protein (designated **rVSV/Spikeβ-GFP**), which can use murine ACE2 to infect cells.[22] Consistent with our results in hamsters, 2 d post infection, we found reduced infection in the lungs of SCFA-treated GF mice, as determined by measuring GFP+ cells by flow cytometry (**Figure S2F**).

In order to confirm whether SCFA treatment is protective in the context of SARS-CoV-2 infection, we treated wild-type male SPF mice with SCFA water for 2 weeks before infection with 4x10^{5} PFU of SARS-CoV-2 gamma variant, and harvested lung tissue 2.5 d post infection, when lung viral titer peak. SCFA-treated mice exhibited a trend towards reduced weight loss (Figure 3A), as well as reduced viral titers (Figure 3B) and viral RNA (Figure 3C) in the lung. Together, these data indicate that SCFAs reduce viral burden following infection with SARS-CoV-2 or VSV-SARS-CoV-2 chimeras.

SCFAs enhance adaptive immunity against VSV/SARS-CoV-2 chimeric viruses via GPR41/GPR43 in a sex-dependent manner

SCFAs can prime the immune system to respond to infection.[13] To examine the impact of SCFA treatment on the immune response to SARS-CoV-2 infection independently of its effect on ACE2

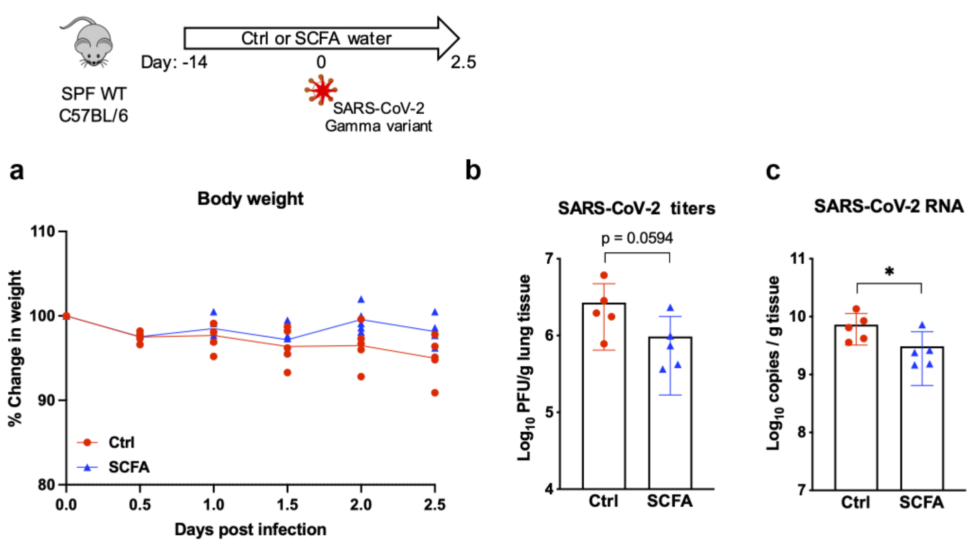

Fig 3. SCFA treatment reduces SARS-CoV-2 viral burdens in mice. Male SPF mice were treated with control or SCFA water for two weeks before infection with 4x10^{5} PFU of SARS-CoV-2 (gamma variant). (A) Weight change is shown as percentage of starting body weight. 2.5 d post infection, lung tissue was harvested and infectious viral titers (B) and viral RNA (C) were measured. Error bars indicate mean ±SEM. For (A), significance was determined using two-way ANOVA with Šídák's multiple comparisons test; for (B) and (C), significance was determined using unpaired t-test. *p<0.05

expression, we used mice expressing both mouse and human ACE2,[23] designated **hACE2 mice**, in which human ACE2 is constitutively expressed in epithelial cells under the K18 promoter and is thus unaffected by SCFA treatment (**Figure S3A**). We treated hACE2 mice with SCFA water for 2 weeks before intranasal infection with rVSV/Spike-nLuc, which can interact with human ACE2 but not mouse ACE2. After 48 hours, we observed reduced luciferase activity in the nasal epithelium, lungs, and small intestines of SCFA-treated mice compared to control mice, indicating reduced infection (Figure 4A**, Figure S3B**). Flow cytometry analysis of lung immune cells revealed increased IFNγ expression in CD4+ and CD8+ T cells, increased Treg development, and heightened granzyme B production in CD8+ T cells (Figure 4C**, Figure S3C**). SCFA-treated mice also had more dendritic cells in the lung, although lung macrophages and polymorphonuclear cells (PMN) were not affected (**Figure S3D**). Together, these results suggest that SCFAs promote antiviral immune responses in the lung during acute infection.

To determine whether SCFAs affect the memory response, we treated hACE2 mice with control or SCFA water for 2 weeks before intranasal administration of $6x10^4$ PFU of rVSV/Spikeβ-GFP, followed by a secondary dose of $3x10^5$ PFU administered 4 weeks later (Figure 4C). Two weeks following the primary infection, flow cytometry analysis of blood immune cells showed that spike-specific B cells and CD4+ T cells were significantly elevated in the blood of SCFA-treated mice (Figure 4D). IgG from male SCFA-treated mice also more effectively neutralized rVSV/Spikeβ-GFP infection in Vero cells (Figure 4E); interestingly, this difference was not found in IgG from female mice (**Figure S4A**). Spike-specific B cells remained elevated for 4 weeks following the primary infection (**Figure S4B**). Following the secondary infection, GFP+ cells were significantly reduced in the lungs of SCFA-treated mice, indicating reduced viral burdens (Figure 4F). Importantly, SCFA treatment did not promote the generation of spike-specific B and T cells, antibody neutralization, or viral clearance in *Gpr41*$^{-/-}$*Gpr43*$^{-/-}$ mice (Figure 4G-K), indicating a role for one or both of these receptors.

In hACE2 mice, human ACE2 expression is not affected by SCFA treatment (**Figure S3A**), which suggested that the effect of SCFA treatment on the immune response is independent of its effect on SARS-CoV-2 viral entry. To confirm this, we inoculated wild-type control or SCFA-treated mice with heat-inactivated rVSV/Spikeβ-GFP (two doses of 10^6 PFU each, spaced 1 week apart; **Figure S4C**). Seven days following the second dose, SCFA-treated mice exhibited higher levels of spike-specific B cells and CD8+ T cells as well as increased IFNγ production in CD4+ T cells (**Figure S4D**). Plasma from SCFA-treated mice likewise neutralized rVSV/Spikeβ-GFP infection in Vero cells; consistent with our results in hACE2 mice, this phenotype was observed primarily in male mice (**Figure S4E**). Together, our data suggest that SCFAs enhance antiviral adaptive responses via the GPR41/GPR43 axis in a sex-biased manner.

SCFAs regulate the coagulation response via the Sh2b3-Mpl axis to modulate platelet turnover

In order to identify other mechanisms by which SCFAs influence the outcome of SARS-CoV-2 infection, we performed RNA-seq on lungs from male GF mice given control or SCFA water for 2 weeks. Differentially regulated genes with $p < 0.001$ are shown in **Table S1**, and a volcano plot showing significantly altered genes is shown in Figure 5A. Of particular interest is the gene *Sh2b3*, also known as lymphocyte adaptor protein (LNK), which was upregulated in SCFA-treated mice (Figure 5A). *Sh2b3* is an adaptor protein that regulates a diverse array of signal transduction pathways, including the thrombopoietin (TPO) pathway; importantly, it is a major negative regulator of megakaryopoiesis and thrombopoiesis, thus playing an important role in regulating the coagulation response.[24] Hypercoagulation and increased megakaryopoiesis are features of severe COVID-19.[9,11] Using publicly available RNA-seq data,[25–27] we found reduced expression of *Sh2b3* in a lung biopsy from a deceased COVID-19 patient compared to lung biopsies from two healthy controls (Figure 5B), as well as significantly reduced expression of *Sh2b3* in peripheral blood mononuclear

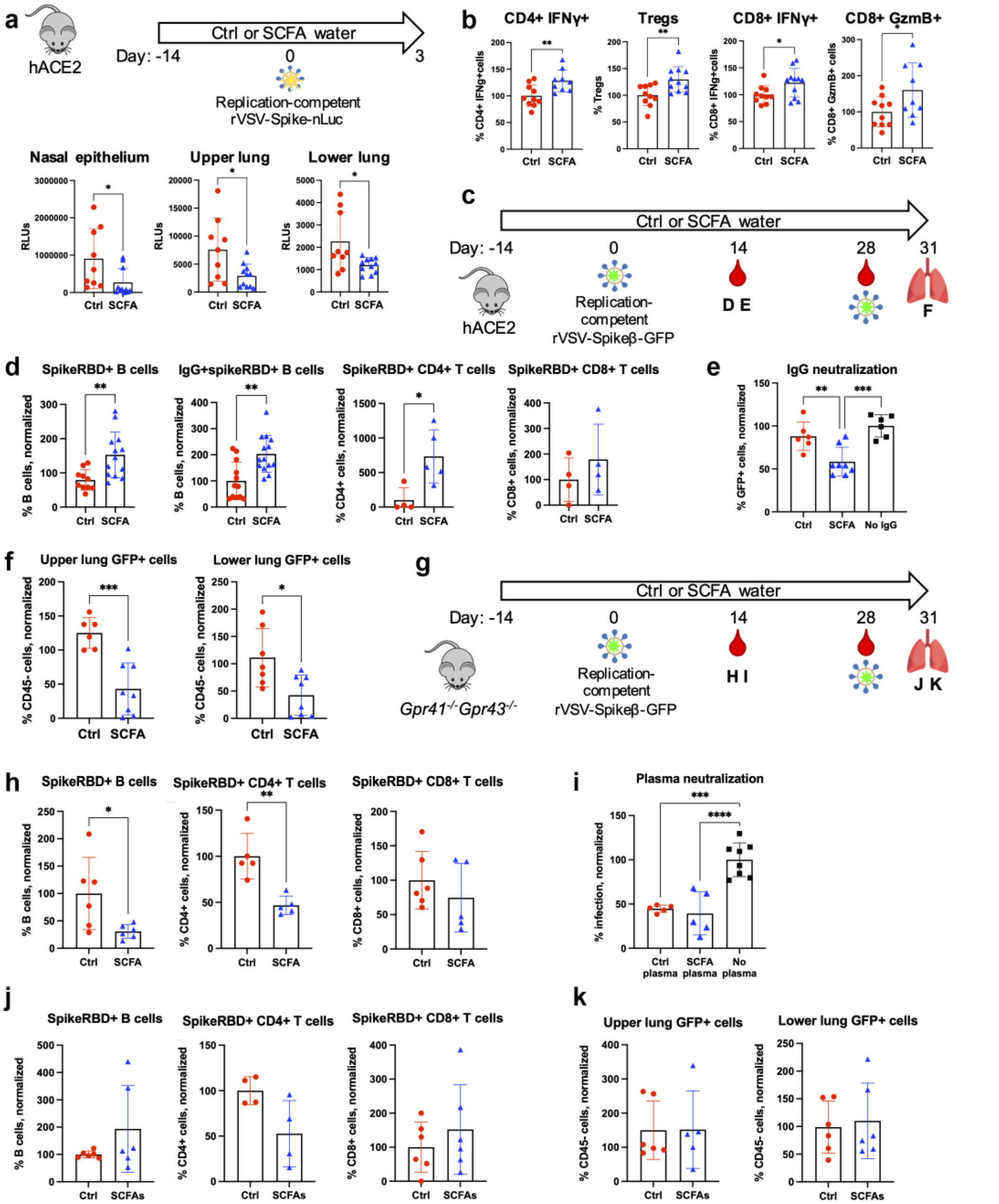

Fig 4. SCFAs enhance adaptive immunity against rVSV/Spikeβ-GFP via GPR41/GPR43 in a sex-dependent manner. (A–B) hACE2 mice were given control or SCFA water for two weeks before intranasal inoculation with replication-competent rVSV/Spike-nLuc. 48h later, (A) viral burdens were determined by measuring luciferase activity; and (B) lung T cells were stimulated with PMA/ionomycin for two hours before flow cytometry analysis. (C–K) The impact of SCFA treatment on adaptive immunity to rVSV/Spikeβ-GFP. (C,G) Overview of experiment. hACE2 (C) or *Gpr41*$^{-/-}$*Gpr43*$^{-/-}$ (G) mice were given control or SCFA water for two weeks before intranasal infection with 6x10^4 IU of replication-competent rVSV/Spikeβ-GFP. Blood was collected two and four weeks post infection for analysis of immune cells. Four weeks post infection, mice were reinfected with 5x10^5 IU of rVSV/Spikeβ-GFP and sacrificed after 3 d. (D–E, H–I) Two weeks following the primary infection, (D, H) blood immune cells were analyzed via flow cytometry, and purified IgG (E) or plasma (i) preincubated with rVSV/Spikeβ-GFP before infecting Vero-TMPRSS2 cells. 24 hours later, GFP+ cells were measured via flow cytometry. Results from only the male mice are shown. Data are shown as percentage of the no IgG/plasma condition. (F, J-K) Lung B and T cells (**J**) and GFP+ cells (F, K) in the lung 72 hours after the secondary infection. Error bars indicate mean±SEM. For (E) and (I), significance was determined using one-way ANOVA with Tukey's test for multiple comparisons; for all other panels, significance was determined using unpaired t-test. All data represent 2 independent experiments. *p<0.05; **p<0.01; ***p<0.001; ****p<0.0001. See also **Figures S3-S4**.

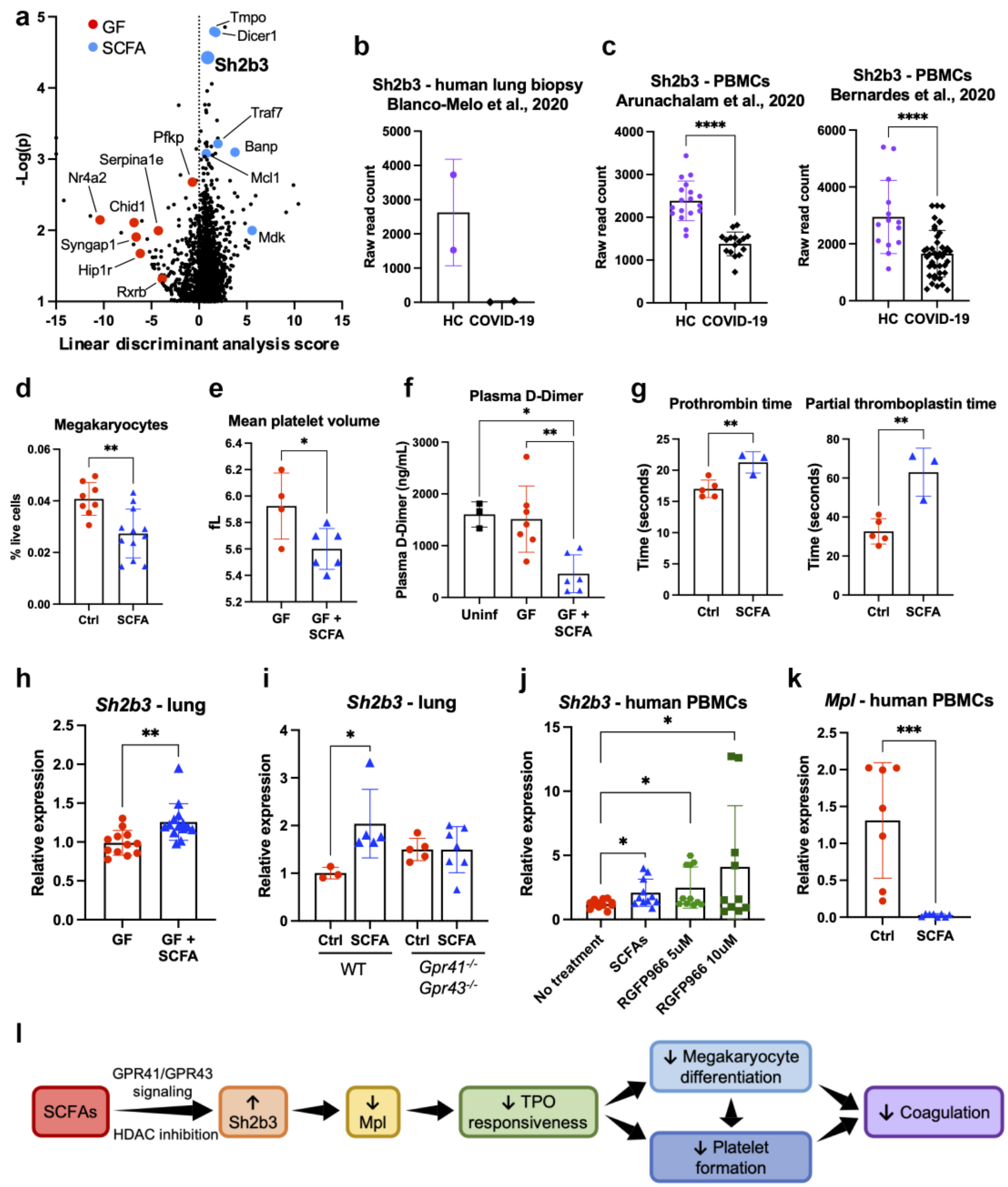

Fig 5. SCFAs regulate the coagulation response via the Sh2b3-Mpl axis to modulate platelet turnover. (A) RNA-seq analysis of lung tissue from control- or SCFA-treated GF mice. The volcano plot showing significantly differentially regulated genes is shown. Negative linear discriminant analysis (LDA) scores indicate genes that are upregulated in GF mice and positive LDA scores indicate genes that are upregulated in SCFA-treated mice. (B-C) Using publiclyavailable RNAseq datasets (GEO accession numbers: GSE147507, GSE152418, GSE161777), *Sh2b3* expression in human lung biopsy tissue (B) and human PBMCs (C) was compared between COVID-19 patients and healthy controls (HC). (D) Bone marrow megakaryocytes were measured in control- or SCFA-treated SPF mice via flow cytometry. (E) Mean platelet volume in control- or SCFA-treated GF mice. (F) Plasma D-dimer levels in control- or SCFA-treated GF mice 72 hours post infection with rVSV/Spikeb-GFP. (G) Prothrombin time and partial thromboplastin time assay on blood from male SPF mice given control water or SCFA water for two weeks. (H) Sh2b3 mRNA expression in control- or SCFA-treated GF mice. (I) Sh2b3 mRNA expression in control- or SCFA-treated SPF WT or *Gpr41-/-Gpr43-/-*mice. (J) *Sh2b3* mRNA expression in PBMCs from healthy human donors treated with SCFAs or the HDAC3 inhibitor RGFP966. (K) *Mpl* mRNA expression in PBMCs from healthy human donors treated with SCFAs. (L) Possible mechanism behind SCFA regulation of coagulation. Error bars indicate mean±SEM. For (F) and (I), significance was determined using one-way ANOVA with Tukey's test for multiple comparisons; for all other panels, significance was determined using unpaired t-test. *p<0.05; **p<0.01; ***p<0.001; ****p<0.0001. See also Figure S5 and Table S1.

cells (PBMCs) from hospitalized COVID-19 patients collected 5-20 d post-symptom onset (Figure 5C). We thus speculated that SCFA-mediated upregulation of *Sh2b3* might limit the coagulation response, potentially ameliorating COVID-19-associated coagulopathy.

Consistent with the established role of *Sh2b3* as a negative regulator of megakaryopoiesis, we found reduced megakaryocytes in the bone marrow of WT SPF SCFA-treated mice (Figure 5D). We performed a complete blood count on GF mice treated with control or SCFA water, and found that while SCFAs did not affect platelet count or platelet size distribution (**Figure S5A**), the mean platelet volume (MPV) was significantly reduced in SCFA-treated mice (Figure 5E). A higher MPV is indicative of a younger platelet population, composed of larger platelet cells that are more metabolically and thrombocytically active.[28] The reduced MPV in SCFA-treated mice may therefore suggest reduced platelet turnover. Finally, we treated GF mice with SCFA water for 2 weeks before infecting with $6x10^4$ IU of rVSV/Spikeβ-GFP. Three days post infection, blood from SCFA-treated mice had significantly lower levels of D-dimer (Figure 5F) and elevated prothrombin time and partial thromboplastin time (Figure 5G), indicating a reduced coagulation response.

We confirmed our RNA-seq results by measuring *Sh2b3* expression via qPCR in lung tissue from SPF or GF mice given control or SCFA water for 2 weeks. Consistent with the RNA-seq results, we found that SCFA treatment significantly increased *Sh2b3* expression in the lungs (Figure 5H). However, *Sh2b3* expression was not affected by SCFA treatment in *Gpr41*$^{-/-}$*Gpr43*$^{-/-}$, *Gpr41*$^{-/-}$, or *Gpr43*$^{-/-}$, mice (Figure 5I**, Figure S5B**); likewise, SCFA treatment did not affect MPV, plasma D-dimer levels, or bone marrow megakaryocytes (**Figure S5C**) in *Gpr41*$^{-/-}$*Gpr43*$^{-/-}$ mice. Since SCFAs are well-established inhibitors of histone deacetylases (HDACs),[20]and there is evidence that *Sh2b3* expression is sensitive to acetylation,[29,30] we treated human PBMCs from healthy donors with SCFAs or the HDAC3 inhibitor RGFP966 and found that both were capable of promoting *Sh2b3* expression (Figure 5J), suggesting that SCFA regulation of Sh2b3 may have an epigenetic component in addition to the GPR41/GPR43 axis. Interestingly, unlike the ACE2 and antibody neutralization phenotypes we observed, SCFA enhancement of Sh2b3 did not exhibit a sex bias in either human PBMCs or mouse lungs (**Figure S5D-E**).

TPO signaling via its receptor, *Mpl* (myeloproliferative leukemia protein), which is primarily expressed in hematopoietic cells, drives megakaryopoiesis and is negatively regulated by *Sh2b3*.[24,31] Since the liver is the primary producer of TPO, we investigated the expression of *Sh2b3* and TPO in the livers of control- or SCFA-treated GF mice, and found that while *Sh2b3* was upregulated following SCFA treatment, TPO expression was unaffected (**Figure S5F)**. However, we found that in human PBMCs, SCFA treatment significantly reduced *Mpl* expression (Figure 5K). Our data suggest that SCFA-mediated upregulation of *Sh2b3* leads to inhibition of *Mpl* signaling in megakaryocytes, reducing both megakaryocyte proliferation and platelet production, leading to reduced platelet turnover, and limiting coagulation (Figure 5L).

Discussion

Altogether, we have elucidated a novel role for the gut microbiome, via SCFA production, in the host response to SARS-CoV-2 infection. SCFA treatment reduced the expression of *Ace2,* lowered viral burdens, and promoted adaptive immunity against VSV/SARS-CoV-2 chimeras. We have also uncovered a novel function of SCFAs in limiting the coagulation response via the *Sh2b3-Mpl* axis to modulate megakaryopoiesis and platelet turnover.

Our work suggests a gut-lung axis during SARS-CoV-2 infection that may dictate disease severity by regulating viral entry, adaptive immunity, and coagulation response. In the context of COVID-19, several studies have found altered microbiomes following SARS-CoV-2 infection.[32–36] However, due to the high variability of the human microbiomes, which may have been influenced by the infection and medications in COVID-19 patients, controlled animal studies might help define the role of the gut microbiome in host response to SARS-CoV-2 infection. Interferon signaling is efficiently suppressed by at least 13 components of the SARS-CoV-2 genome, including spike protein, the nucleocapsid proteins nsp1 and nsp6, and accessory proteins ORF3b and

ORF6.[37] Poor T cell responses, characterized by low numbers of IFNγ+ CD4+ T cells and cytotoxic SARS-CoV-2-specific CD8+ T cells, are associated with severe or fatal COVID-19 outcomes.[38] Enhanced megakaryopoiesis and excessive influx of neutrophils into the lung are further hallmarks of severe COVID-19.[8,26] SCFAs modulate the immune response in many ways, including promoting regulatory and effector T cell development, T cell memory, and plasma cell differentiation.[13,39–41] Here, we found that SCFAs enhance antiviral T cell responses, spike-specific B and T cells, and antibody neutralization following intranasal infection with a VSV pseudovirus expressing the spike protein. Importantly, we observed these phenotypes in hACE2 mice, in which human *Ace2* expression is not affected by SCFA treatment, and in wild-type mice inoculated with heat-inactivated virus, suggesting that the enhancement of immune responses that we observed is independent of the effect of SCFAs on ACE2-mediated viral entry, and may thus have an effect on other disease states as well.

We found that SCFAs affected *Ace2* expression and antibody neutralization only in male mice, but found no sex differences in the effect of SCFAs on the coagulation response. Our observations of a sex-biased effect of SCFA on antibody neutralization are intriguing. Females tend to have increased antibody responses to infection or vaccination,[42] which has been reported in COVID-19 as well.[43–45] In mice, the microbiome has sex-specific effects on antibody production and autoimmunity,[42] and X inactivation escape of TLR7 has been linked to increased B cell responsiveness and class switching to IgG.[46] Likewise, the mechanisms behind sex-specific regulation of *Ace2* are not fully explored, but *Ace2* expression is influenced by both Sry and 17β-estradiol, and *Ace2* has been found to escape X chromosome inactivation.[47–49] The contributions of sex hormones and chromosomal sex on the interactions between the immune system and the microbiome have yet to be fully explored but may contribute to the sex bias seen in COVID-19 severity. Future work is required to delineate the mechanism underlying SCFA-mediated sex bias in adaptive immunity and to address whether this phenomenon is restricted to SARS-CoV-2 infection.

Our findings have uncovered a novel function of the gut microbiome in the regulation of coagulation. Suppression of the coagulation response via regulation of the Sh2b3-Mpl axis presents a third potential axis by which SCFAs might promote better SARS-CoV-2 infection outcomes. Dysfunction of the coagulation response has emerged as a hallmark of severe COVID-19,[9,11] driven in part by hyperinflammation;[9] this is also found in other severe viral pneumonias, including SARS, MERS, and H1N1 influenza,[50,51] and accounts for a significant percentage of mortality and morbidity in cancer patients.[52] Abnormalities associated with COVID-19 include capillary microthrombi, elevated D-dimer, venous thromboembolism, elevated risk of stroke, enhanced megakaryocyte activation, and thrombocytopenia often followed by rebound thrombocytosis.[9,11,26,50] The latter, together with observations of elevated mean platelet volume and increased platelet activity in COVID-19 patients,[11] suggest that COVID-19-associated hypercoagulation is partly due to increased platelet production in response to increased platelet consumption, resulting in a population of newer, more active platelets. It remains unclear why certain patients are more susceptible to hypercoagulation. Our findings suggest that the abundance of fiber-fermenting gut bacteria or SCFAs may influence the propensity for overexuberant coagulation in response to infection, by limiting platelet turnover through regulation of megakaryocyte responsiveness to TPO. The SCFA-Sh2b3-Mpl axis might be a potential therapeutic target to dampen hypercoagulation triggered by severe viral infections or other conditions.

Because SARS-CoV-2 requires BSL-3 conditions, the majority of experiments in our study were done using recombinant VSV-based pseudoviruses and chimeric viruses, which presents a major limitation. While these constructs enabled us to specifically examine the effect of SCFAs on viral entry and on immune responses to the SARS-CoV-2 spike protein, they may not fully recapitulate the complex interactions between SARS-CoV-2, the immune system, and the coagulation response. Our observations that SCFA treatment can reduce viral RNA levels following SARS-CoV-2 infection are encouraging, but more work is required to further examine the effect of SCFAs on the immune and coagulation responses in the context of a genuine SARS-CoV-2 infection.

Additional future work is also required to further elucidate the mechanisms underlying SCFA modulation of *Ace2* and *Sh2b3* expression. Our observations indicate that GPR41 and GPR43 are necessary for SCFA-mediated suppression of *Ace2* and enhancement of immune responses and *Sh2b3* expression; however, an epigenetic component also seems likely, as SCFAs are known histone deacetylase (HDAC) inhibitors.[20] *Ace2* is upregulated by the class III HDAC SIRT1,[53] and the HDAC inhibitor valproic acid (an SCFA derivative) reduces *Ace2* expression *in vitro*.[54] The epigenetic regulation of *Sh2b3* is less well established, but there is evidence that *Sh2b3* expression is sensitive to acetylation,[29,30] further supported by our study. However, more work is required to determine whether HDAC inhibition affects *Ace2* or *Sh2b3* expression *in vivo* and to define the relative contributions of the GPR41/GPR43 axis and the epigenetic axis. Further exploration of the mechanism by which SCFAs mediate *Ace2* and *Sh2b3* expression may lead to novel avenues for treatment not only of SARS-CoV-2 but a variety of disease states ranging from viral pneumonias to hypertension to stroke.

Materials and Methods

Animals

Wild-type or K18-hACE2 mice on C57BL/6 background, raised in germ-free or specific pathogen-free conditions, were originally purchased from the Jackson Laboratory and maintained and expanded in-house by the Zeng laboratory. *Ffar2*$^{-/-}$ and *Ffar3*$^{-/-}$ mice on C57BL/6J background were generously provided by Dr Brian Layden (University of Illinois) and maintained and expanded in-house. *Ffar2*$^{-/-}$*Ffar3*$^{-/-}$ mice were generated by crossing *Ffar2*$^{-/-}$ and *Ffar3*$^{-/-}$ mice, and genotypes were confirmed by PCR. Syrian hamsters were purchased from Charles River Laboratories. All mice were 8 weeks of age, and all hamsters were 9 weeks of age at the time treatment commenced. Male mice were used except where otherwise specified. Littermate controls were used, and animals were cohoused after weaning. SPF animals were housed in microisolator cages in the barrier facility of Weill Cornell Medicine. Infected animals were housed in the BSL2+ biocontainment facility of Weill Cornell Medicine or the BSL3 biocontainment facility at Georgia State University. Germ-free mice were bred and maintained in semi-rigid gnotobiotic isolators and transferred into individually ventilated isocages for experimentation. All animal experiments were approved by the Institutional Animal Care and Use Committee (IACUC) at Weill Cornell Medicine (IACUC protocol 2019-0004) or Georgia State University (IACUC protocols A20043 and A20044).

Cell lines

Vero-TMPRSS2 cells were generously provided by Dr Benhur Lee (Icahn School of Medicine at Mount Sinai) and are previously described.[55] Vero-TMPRSS2 cells were maintained in DMEM (Gibco 11965-092) supplemented with 10% fetal bovine serum (FBS; Gibco 10437-028) and penicillin–streptomycin (1:50; Sigma P4458) at 37°C in a 5% CO_2 atmosphere. I1 hybridoma cells (ATCC CRL-2700) were obtained from the ATCC and maintained at 37°C in 100% room air, in minimal essential media with Hank's balanced salts (Gibco 11575032) supplemented with 2mM L-glutamine (Sigma G7513) and 20% FBS.

Generation of rVSVΔG/NG/NanoLuc-SARS-CoV-2 pseudovirus (pVSV/Spike-nLuc)

The rVSVΔG/NG/NanoLuc-SARS-CoV-2 pseudovirus was generated as previously described.[56] Briefly, an mNeonGreen/FMDV2A/NanoLuc luciferase cDNA cassette was inserted into the rVSVΔG plasmid (Kerafast EH1007)[57] between the M and L genes (maintaining the VSV intergenic sequences). The resulting plasmid was then transfected into 293T cells infected with recombinant T7-expressing vaccinia virus (vTF7-3), together with the rVSV pseudovirus rescue plasmids (pBS-N, pBS-P, pBS-L, and pBS-G; Kerafast EH1008), in order to rescue VSV-G-expressing pseudovirus particles carrying the NeonGreen/NanoLuc reporter cassette. Twenty-four hours post transfection, the supernatant was collected, filtered using a 0.1 μm filter to remove the residual vaccinia virus, and used to infect 293T cells transfected with SARS-CoV-2 spike protein lacking the C-terminal 19 codons. After 16 hours, the supernatant was collected, centrifuged briefly to remove cell debris, and concentrated via PEG precipitation. The concentrated pseudovirus was aliquoted and stored at -80°C. Prior to infection, pseudovirus stocks were incubated for 1 hour at 37°C with 20% I1 hybridoma (ATCC CRL-2700) supernatant, which contains anti-VSV-G antibodies, to neutralize residual VSV-G pseudovirus particles.

Generation of replication-competent VSV/SARS-CoV-2 chimera (rVSV/Spike-nLuc)

The replication-competent VSV/SARS-CoV-2 chimera was generated as previously described.[56] Briefly, a codon-optimized sequence encoding the SARS-CoV-2 spike protein (SinoBiological VG40592-UT) lacking the C-terminal 18 codons was inserted into a plasmid encoding the VSV antigenome containing Nano luciferase, immediately upstream of the L protein, following a strategy previously described for the generation of a VSV/HIV-1 chimera.[58] The resulting plasmid was then transfected into vTF7-3-infected 293T cells, together with the rVSV rescue plasmids, in the same manner as described for the generation of VSVΔG pseudovirus. The supernatant was filtered to remove residual vaccinia virus, passaged once in 293T cells transfected with VSV-G protein to amplify, and then subsequently passaged several times in ACE2-expressing 293T cells.

Generation of replication-competent rVSV/Spikeβ-GFP chimera

The replication competent chimeric rVSV-Spikeβ-GFP virus was generated as previously described.[59] Briefly, the pEMC-VSV-eGFP-CoV2-S plasmid (GenBank Accession: MW816496) was generated by cloning the VSV-eGFP sequence[60] into pEMC vector (pEMC-VSV-eGFP) and then replacing the VSV-G open reading frame with a codon-optimized SARS-CoV-2 Spike (BEI NR-52310) carrying the beta variant mutations D80A, D215G, del242-244, K417N, E484K, N501Y, D614G, and A701V (from EPI_ISL_745109; GenBank Accession: MW816499), and truncated to lack the final 21 amino acids.[61] Sequences encoding the VSV N, P, M, G, and L proteins were also cloned into pCI vector to make expression plasmids for virus rescue, resulting in plasmids: pCI-VSV-N, pCI-VSV-P, pCI-VSV-M, pCI-VSV-G, and pCI-VSV-L. To rescue the virus, 293T cells expressing ACE2 and TMPRSS2 were transfected with 2000 ng of pEMC-VSV-EGFP-CoV2 spike, 2500 ng of pCAGGS-T7opt66, 850 ng of pCI-VSV-N, 400 ng of pCI-VSV-P, 100 ng of pCI-VSV-M, 100 ng of pCI- VSV-G, 100 ng of pCI-VSV-L using Lipofectamine LTX (Invitrogen). Cells were maintained for 4–5 d until GFP-positive syncytia appeared. Rescued viruses were then amplified in Vero-CCL81-TMPRSS2 cells[55] and concentrated via PEG precipitation.

Human PBMCs

Blood samples were obtained from healthy adult volunteers (seven females and three males) and PBMCs were extracted for *in vitro* SCFA or HDAC inhibitor treatment. Informed consent was obtained from all subjects. This study was approved by the Weill Cornell Medicine Institutional Review Board (protocol # 0604008488).

Oral administration of antibiotics, SCFAs, or pectin

Antibiotic drinking water was prepared using 1 g gentamicin sulfate (Millipore 345814) or 0.5 g vancomycin hydrochloride (Sigma V2002) in 1 L tap water and filtered through a 0.22 µm sterile filter. Mice were given antibiotic drinking water ad libitum for 3 weeks before tissues or fecal pellets were collected for further analyses. SCFA drinking water was prepared following a previously described protocol,[19] using 67.5 mM sodium butyrate (Sigma 303410), 40 mM sodium acetate (Sigma S2889), and 25.9 mM sodium propionate (Sigma P1880) in 1 L tap water and filtered through a 0.22 µm sterile filter. Mice and hamsters were given SCFAs in drinking water ad libitum for a minimum of 2 weeks before further experimentation. For pectin diet experiments, mice or hamsters were given control diet, 5% pectin diet, or 30% pectin diet ad libitum for a minimum of 2 weeks before further experimentation. The 5% and 30% pectin diets were custom designed by Research Diets based on the standard AIN93G formula (Research Diets D10012G). The formulation for each diet is listed in **Table S2**.

qPCR

Total RNA was extracted from tissue samples using Trizol (Invitrogen 15596026) following the manufacturer's instructions. 2000ng RNA per sample was used to generate cDNA using Applied Biosystems High-Capacity cDNA Reverse Transcription Kit (Applied Biosystems 4368814) following the manufacturer's instructions. cDNA was diluted to 1:5 in water before performing qPCR using Intact Genomics ig SYBR Green 2x Master Mix (Intact Genomics 3354). qPCR was carried out with the CFX384 Real-Time System C1000 Touch Thermal Cycler (Bio-Rad Laboratories). Cycling conditions were as follows: Initial denaturation 95°C for 2 minutes, 40 cycles of denaturation at 95°C for 5 seconds followed by annealing/extension at 60°C for 30 seconds. Primers used are listed in **Table S3**. Relative expression was calculated using the ΔΔCt method, using β-actin as the reference gene.

16S rRNA sequencing analysis

Fecal samples were freshly collected, and DNA was extracted using the E.Z.N.A. stool DNA kit (Omega Bio-tek D4015-02). The V4 region of the 16S rRNA gene was amplified using universal primers (listed in **Table S3**) and sequenced using an Illumina MiSeq apparatus as previously described.[62] Paired-end reads were analyzed and classified into operational taxonomic units (OTUs) at >97% identity level using Mothur v.1.40.5.[62,63] Taxonomic assignments were determined using the SILVA 16S rRNA reference file release 132[64] and the Ribosomal Database Project (RDP) training set version 16.[65]

Preparation of Clostridia*-enriched fecal bacteria*

Clostridia-enriched fecal bacteria were prepared as previously described.[18] Briefly, a donor SPF WT mouse was euthanized, and the entire gut from rectum to duodenum was removed intact into a petri dish in the laminar flow hood. This was immediately introduced into an anaerobic chamber. One fecal pellet from the upper colon and a similar amount of cecal contents were removed and homogenized into 18 mL anaerobic PBS. 15 mL was transferred to a Hungate tube, sealed, and removed from the chamber. 470 μL chloroform was injected through the rubber stopper, and the contents were shaken vigorously by hand for 5 minutes and then in a rotary shaker for 1 hour at 37°C. To remove the chloroform, a 25G exhaust needle was inserted through the rubber stopper, and then a 5" × 25G pencil point needle (Reli) was carefully inserted until reaching the bottom of the tube. This was connected to a CO2 tank via a regulator and 0.2 μm filter. CO_2 was bubbled through the solution for 10 minutes, and the solution was taken immediately for gavage into GF mice (0.2 mL per mouse).

Quantification of SCFAs in mouse fecal samples

After 2 weeks of antibiotic treatment or colonization with fecal bacteria, fecal pellets were collected, and approximately 10 mg of each sample was directly resuspended in 100 μL SCFA derivatization solution (prepared as previously described[66]). Glass beads were added, and samples were vortexed for 10 minutes to disperse the feces. Samples were then incubated at 60°C for 1 hour and chilled on ice and then centrifuged at 21000 × g for 20 minutes. The supernatant was then mixed with the D3-leucine internal standard (Sigma 486825) at a ratio of 5 parts supernatant to 1 part internal standard solution (0.0125 mg/mL D3-leucine). Samples were analyzed by LC-MS using the following solvent system for SCFA detection: A: H_2O with 0.1% formic acid (Sigma F0507); B: Methanol (Sigma 322415) with 0.1% formic acid. 1 μL of each sample was injected, and the flow rate was 0.35 mL/min with a column temperature of 40 C. The gradient for HPLC-MS analysis was as follows: 0-6.0 min 99.5% A – 70.0% A, 6.0-9.0 min 70.0% A-2.0%A, 9.0-9.4 min 2.0% A-2.0%A, 9.4–9.6 min 2.0%A 99.5% A. Peaks were assigned by comparison with authentic standards, and relative analyte concentrations were quantified by comparing their peak areas with those of the internal standard (D3-Leucine).

Western blotting of ACE2

Tissues were homogenized in RIPA buffer with protease and phosphatase inhibitors (Roche 11873580001), and tissue lysates were collected. Protein concentrations in the lysates were measured using a Pierce™ BCA Protein Assay Kit (Thermo Scientific 23225). Lysates were normalized and then resolved using NuPAGE 4–12% Bis-Tris gels (Invitrogen NP0321) and transferred onto a PVDF membrane (Bio-Rad Laboratories). The membrane was blocked using 3% non-fat milk for 1 h at room temperature and then probed with a rat anti-mouse ACE2 antibody (1:500; R&D Systems MAB3437) at 4°C overnight. The membrane was probed with goat anti-rat HRP antibody (1:5000; Invitrogen 31470) for 1 h at room temperature. SuperSignal™ West Pico PLUS Chemiluminescent Substrate (Thermo Scientific 34579) was added to the membrane, and the blot was imaged using a ChemiDoc™ XRS+ Molecular Imager (Bio-Rad Laboratories). β-actin antibody (GenScript A00730) was used as a loading control. Densitometry analyses of protein bands were performed using ImageJ software.

Immunofluorescence staining of ACE2 in mouse tissues

Mouse tissues were fixed using 4% paraformaldehyde (PFA; Thermo Scientific J19943-K2) overnight. Tissues were washed with PBS and then placed into 30% sucrose overnight. Tissues were then placed into Tissue-Tek O.C.T. gel (Sakura 4583), and 5 μM sections were placed onto microscope slides. Tissue sections were permeabilized with 0.5% TritonX100 for 15 min at room temperature. Antigen retrieval was conducted on tissues using Citrate Buffer Antigen Retriever (Sigma C9999) for 30 min at 85°C. After a wash step, sections were blocked with 5% horse serum in PBS for 60 min at room temperature, then incubated with goat anti-mouse ACE2 (1:200; R&D Systems AF3437) at 4°C overnight. After a wash step, sections were incubated with donkey anti-goat IgG H&L Alexa Fluor 488 antibody (1:200; Abcam ab150129) and counterstained with DAPI (1:5000) for 5 min. After staining, coverslips were mounted onto tissue sections using ProLong™ Gold Antifade Mountant (Invitrogen P36930). The images were captured using a Zeiss AxioObserver inverted fluorescence microscope.

Human liver organoid experiments

Human liver organoids were generated as previously described.[67] Briefly, human hepatocytes and human nonparenchymal fractions were obtained from the Liver Tissue Cell Distribution System (Pittsburgh, Pennsylvania). Human liver tissue was digested to obtain cellular fractions. 2,500 cells were mixed 1:1 with Matrigel (Corning 354234) and placed at the bottom of a 6-well plate at a density of 5 drops per well. Plates were incubated for 5 min at 37°C before culture media was added. Organoid culture media consisted of DMEM/F12 media (Thermo Fisher 10565018) supplemented with B27 supplement without vitamin A (1:50; Life Technologies 12587-010), N2 supplement (1:100; Life Technologies 17502-048), 1 mM N-acetylcysteine (Sigma A0737), 10% (vol/vol) Rspo1-conditioned medium (produced as previously described[68]), 10 mM nicotinamide (Sigma N0636), 10 nM recombinant human [Leu[15]]-gastrin I (Sigma G9145), 50 ng/mL recombinant human EGF (Peprotech AF-100-15), 100 ng/mL recombinant human FGF-10 (Peprotech 100-26), 25 ng/mL recombinant human HGF (Peprotech 100-39), 10 μM Forskolin (Tocris Bioscience 1099), and 5 μM A83-01 (Tocris Bioscience 2939). Organoids were maintained at 37°C in a 5% CO_2 atmosphere, and the medium was changed every 3–4 d; cultures were initially split after 14 d and subsequently split every 5–7 d. SCFA treatment was initiated when the organoids were approximately 30% confluent (~2 d after splitting) by adding a cocktail of acetate, butyrate, and propionate to the organoid medium (low dose: 100μM acetate, 50μM butyrate, 200μM propionate; high dose: 1mM acetate, 0.5mM butyrate, 2mM propionate). After 48 hours, the growth medium was removed, and the organoids and Matrigel were homogenized in Trizol by pipetting up and down, after which RNA was extracted and qPCR performed as described above.

Infection of mice and hamsters with pseudoviruses and chimeric viruses

Eight-week-old mice were treated with SCFAs for 2 weeks before intranasal infection with $6x10^4$ IU (20 µL per mouse, 10 µL per nare) of either the pVSV/Spike-nLuc pseudovirus, the replication-competent rVSV/Spike-nLuc chimera, or the replication-competent rVSV-Spikeβ-GFP chimera. Mice were euthanized via CO_2 inhalation for 2 d (for pVSV/Spike-nLuc infection) or 3 d (for rVSV/Spike-nLuc or rVSV/Spikeβ-GFP infection) post infection. Nine-week-old male Syrian hamsters were given either SCFA drinking water or a high-fiber diet (AIN93G supplemented with 30% pectin) for 2 weeks before intranasal inoculation with $5x10^5$ IU (100 µL per hamster, 50 µL per nare) of either the pVSV-Spike-nLuc pseudovirus or the rVSV-Spike-nLuc chimeric virus. Hamsters were euthanized by CO_2 inhalation 24 hours (for pseudovirus-infected hamsters) or 48 hours (for chimera virus-infected hamsters) post infection. For inoculation with heat-inactivated virus, rVSV/Spikeβ-GFP was incubated for 30 minutes at 56°C prior to inoculation.

Measurement of viral loads

For animals infected with luciferase reporter viruses, infection was measured via luciferase production in infected tissues using the Promega Nano-Glo Luciferase Assay System (Promega N1120). Tissue samples were weighed, and 10 µL lysis buffer (PBS + 1% Tween-20) was added per 1 mg of tissue. Samples were minced with sterile scissors and sonicated briefly, then incubated at room temperature for a minimum of 10 minutes to allow lysis to proceed. 50 µL of tissue lysate was mixed with 100 µL Nano-Glo Luciferase Assay Reagent, and the total endpoint luminescence was read immediately. For animals infected with GFP reporter viruses, infection was measured by quantifying GFP+ cells via flow cytometry. Lung tissue was pushed through a 100 µm filter to create a single-cell suspension in PBS with 1% bovine serum albumin (BSA; Sigma A2153) and 0.1 mg/mL DNase I (Sigma DN25), then incubated with Fixable Viability Dye eFluor™ 780 (1:3000; eBioscience 65-0865-14) and Alexa Fluor 700 conjugated anti-CD45 antibody (1:200, BioLegend 103128) at 4°C for 30 minutes, washed and resuspended in PBS with BSA and DNAse I, and analyzed on a Cytek Aurora flow cytometer (BD).

SARS-CoV-2 infections

Five-week-old male C57BL/6 mice were randomly divided into two study groups (n = 5 each) that received filtered tap or SCFA water (3.3 g sodium acetate; 7.5 g sodium butyrate and 2.5 g sodium propionate per 1 L water), respectively, during a 14-d pre-infection period. Animals were monitored daily. For infection, mice were transferred into ABSL-3 containment and inoculated intranasally with $4x10^5$ PFU (25 µl per nare) of SARS-CoV-2 gamma variant (lineage P.1., isolate hCoV-19/Japan/TY7-503/2021; BEI Resources NR54982). Infected animals were continued on filtered tap or SCFA water as before. Body temperature was monitored daily and body weight measured twice daily. All animals were euthanized 2.5 d after infection and lungs, colons and kidneys harvested. Lungs were weighed and homogenized with a bead beater in 300 µl PBS in 3 bursts of 30 seconds each at 4°C. Samples were clarified for 10 minutes at 4°C and 14,000 g, supernatants aliquoted and stored at -80°C prior to titration by plaque assays on Vero-TMPRSS2 cells. Virus titers were normalized to the weight of the input lung tissue and buffer volume. For qPCR-based detection of viral RNA, lung, colon, and kidney samples were stored in RNAlater at -80°C. Tissues were weighted and homogenized as above, followed by total RNA extraction using a RNeasy mini kit (Qiagen). All experimentation with SARS-CoV-2 was performed under ABSL3 biocontainment conditions and was approved by the Institutional Biosafety Committee (IBC) of Georgia State University (IBC protocol B20006).

Plaque assay

Samples were serially diluted (tenfold dilutions starting at a 1:10 initial dilution) in DMEM medium supplemented with 2% FBS containing Antibiotic-Antimycotic (Gibco). The serial dilutions were added to Vero-TMPRSS2 cells seeded in 12-well plates at 3×10^5 cells per well 24 hours previously. The virus was allowed to adsorb for 1 hour at 37 C. Subsequently, the inoculum was removed, and the cells were overlaid with 1.2% Avicel (FMC BioPolymer) in DMEM and incubated for 3 d at 37°C with 5% CO2. After 3 d, the Avicel was removed, cells were washed once with PBS, fixed with 10% neutral buffered formalin, and plaques were visualized using 1% crystal violet.

Quantitation of SARS-CoV-2 viral RNA

SARS-CoV-2 RNA was detected using the nCoV_IP2 primer-probe set (National Reference Center for Respiratory Viruses, Institute Pasteur;[69] see **Table S3**) which targets the SARS-CoV-2 RdRP gene. RT-qPCR reactions were performed using an Applied Biosystems 7500 real-time PCR system using the StepOnePlus real-time PCR package. For amplification, a TaqMan fast virus 1-step master mix (Thermo Fisher Scientific) was used. To determine RNA copies, raw data were processed using a standard curve that was created generated from viral cDNA using the nCoV_IP2 forward primer and the nCoV_IP4 reverse primer. Results were normalized to the wet biomass of the input tissue.

Lung immune cell profiling

Lung tissue was minced using sterile scissors, incubated at 37°C for 30 minutes in RPMI-1640 (Sigma R0883) containing 10% fetal bovine serum (FBS; Gibco 10437-028), 0.1mg/mL DNase I (Sigma DN25), 0.8mg/mL dispase (Gibco 17105-041), and 1 mg/mL collagenase type 3 (Worthington Biochemical LS004183), and pushed through a 100μm filter to create a single-cell suspension. Cells were then washed twice in PBS, resuspended in 4 mL of RPMI-1640 with 10% FBS and 40% Percoll (Cytiva 17089101), and centrifuged at 2000 rpm for 30 minutes with no braking in order to pellet the immune cells. Cells were then resuspended in RPMI-1640 (Sigma R0883) with 10% FBS and GolgiPlug Protein Transport Inhibitor (1:1000, BD Biosciences 51-2301KZ) and stimulated for 2 hours with phorbol 12-myristate 13-acetate (PMA, 50ng/mL; Sigma P8139) and ionomycin (1μg/mL; Sigma I0634) at 37°C. After two hours, cells were washed twice in FACS buffer (PBS with 1% BSA), blocked for 15 minutes in PBS with 3% BSA, and incubated with Fixable Viability Dye eFluor™ 780 (1:3000; eBioscience 65-0865-14) and surface antibodies (see **Table S4**; anti-mouse IgG was used at 1:500, and all other antibodies were used at 1:200) at 4°C for 30 minutes in the dark. Cells were then washed twice in FACS buffer and incubated in Fix/Perm solution (eBioscience 00-5523-00) for 30 minutes at 4°C in the dark. Cells were then washed twice in permeabilization buffer (eBioscience 00-5523-00) and incubated with intracellular antibodies (see **Table S4**; all antibodies were used at 1:200) for 30 minutes at 4°C in the dark. Cells were then washed twice in permeabilization buffer, resuspended in FACS buffer, and analyzed on a Cytek Aurora flow cytometer.

Detection of Spike-specific B and T cells

Spike-specific B and T cells were detected using biotinylated recombinant SARS-CoV-2 Spike receptor-binding domain (RBD; BioLegend 793904) labeled with streptavidin-Pacific Orange conjugate (SA-PO; Invitrogen S32365) prepared as previously described.[70] Briefly, spike RBD was mixed with SA-PO at a 2:1 mass ratio/4:1 molar ratio (e.g. 25 ng RBD with 12.5 SA-PO) and incubated on ice for 1 hour in the dark. Excess biotin and SA-PO were removed using 7K MWCO Zeba Spin Desalting Columns (Thermo Fisher 89882). Cells were prepared and blocked as described above, then incubated for 30 minutes at 4°C in the dark with an antibody cocktail containing Fixable Viability Dye eFluor™ 780 (1:3000; eBioscience 65-0865-14); anti-CD45, CD3, CD4, CD8, B220, MHCII, and IgG antibodies (anti-IgG was used at 1:500 and all other antibodies at 1:200; see **Table S4**); and 25 ng SAPO-labeled Spike RBD per 50uL of antibody mix. Cells were then washed twice in FACS buffer and analyzed on a Cytek Aurora flow cytometer.

IgG neutralization assay

Blood was collected from mice two-week post primary infection and purified using a Melon Gel IgG Spin Purification Kit (Thermo 45206) following manufacturer's instructions. Purified IgG was diluted 1:20 and incubated with $1x10^5$ IU of rVSV-Spikeβ-GFP for 1 hour at 37°C before being added to Vero-TMPRSS2 cells at an MOI of 1. Cells were incubated at 37°C for 18 hours, washed once in PBS, and detached from the plate using TrypLE Express enzyme (Gibco 12604013). Cells were washed twice in PBS, incubated with in FACS buffer with Fixable Viability Dye eFluor™ 780 (1:3000; eBioscience 65-0865-14) for 30 minutes at 4°C in the dark, washed twice in FACS buffer, and analyzed using a Cytek Aurora flow cytometer.

RNA-seq analysis of mouse lung tissue

Eight-week-old male GF mice were given control water or SCFA water for 2 weeks before lung tissue was harvested. Total RNA from whole lung tissue was isolated using the Qiagen RNeasy® Mini Kit (Qiagen 74104) according to the manufacturer's instructions. Illumina stranded mRNA library prep, paired-end sequencing using the Illumina NovaSeq 6000 system, quality check, and sorting of reads with barcodes were performed by the Weill Cornell Medicine Genomics Resources Core Facility. Annotation, mapping, and counting of the resulted reads were analyzed by SALMON[71] with default parameters and mouse cDNA sequences of GRCm38, which was obtained from Ensembl of European Molecular Biology Laboratory's European Bioinformatics Institute, Cambridge, UK. To discover transcripts that exhibit differential abundance, we used LEfSe followed by multiple hypotheses correction using signal-to-noise ratio and false discovery rate analyses as described.[72] Differences at LEfSe $p < 0.05$ and FDR <0.05 were considered significant, with negative linear discriminant analysis (LDA) scores indicating genes that were upregulated in GF mice and positive LDA scores indicating genes that were upregulated in SCFA-treated mice.

Ex vivo human PBMC experiments

PBMCs were purified from blood using Ficoll-Paque (Cytiva 17144002) following manufacturer's instructions. The purified cells were washed twice in PBS, then resuspended in RPMI-1640 with 10% FBS and penicillin–streptomycin (1:50; Sigma P4458). For SCFA treatments, a cocktail of sodium acetate, sodium butyrate, and sodium propionate was added to the culture media to a final concentration of 100µM sodium acetate, 50µM sodium butyrate, and 200µM sodium propionate. For HDAC inhibition, RGFP966 (Selleck Chemicals S7229) was added to the culture media to a final concentration of 5µM or 10µM. 5×10^5 cells were used for each experimental condition. Cells were incubated at 37°C for 24 hours, after which they were washed twice in PBS and RNA was extracted and qPCR performed as described above.

Megakaryocyte flow analysis

Bone marrow from control or SCFA-treated mice was flushed from femurs and tibias with sterile PBS, washed with FACS buffer, and pushed through a 100 µm filter to create a single-cell suspension. Cells were blocked in BD mouse Fc Block (1:100; BD Biosciences 553141) for 30 minutes at 4°C in the dark, washed in FACS buffer and incubated with anti-mouse c-Kit, CD41, and GPIbβ antibodies (all at 1:100; see **Table S4**) for 30 minutes at 4°C in the dark. Cells were then washed in FACS buffer, incubated with Fixable Viability Dye eFluor™ 780 (1:3000; eBioscience 65-0865-14), fixed with 1% paraformaldehyde (Thermo Scientific J19943-K2) and analyzed on a BD FACSymphony™ A5 flow cytometer.

Blood counts and D-Dimer analysis

At 3 d after infection, animals were euthanized via CO_2 asphyxiation, and blood was immediately collected via cardiac puncture into syringes containing sodium citrate (Sigma 1613859) at a final concentration of 0.32% (w/v). Whole citrated blood was analyzed for complete blood count with automated differentials using a Beckman DxH 900 hematology analyzer (Beckman Coulter). Plasma was obtained by centrifuging citrated blood at 1000xg for 15 minutes at 4°C followed by 10,000xg centrifugation for 10 minutes at 4°C to remove all cells and debris. Plasma D-Dimer concentration was measured by a commercially available ELISA (LSBio LS-F6179) following the manufacturer's instructions.

Statistical analyses

All the statistical analyses were performed using Prism 9 (GraphPad Software, San Diego, CA).

Normality was determined using the Shapiro–Wilk normality test. Differences between two groups were evaluated using the unpaired *t*-test (for parametric data) or Mann–Whitney test (for nonparametric data), and comparisons of more than 3 groups were evaluated using ordinary one-way ANOVA followed by Tukey's correction for multiple comparisons (for parametric data) or Kruskal–Wallis test followed by Dunn's correction for multiple comparisons (for nonparametric data). Differences of $p<0.05$ were considered significant in all statistical analyses. Statistically significant differences are shown with asterisks as follows: $^{*}p<0.05$, $^{**}p<0.01$, $^{***}p<0.001$ and $^{****}p<0.0001$; comparisons which were nonsignificant are unmarked. Each figure shows data for individual animals or biological replicates.

Acknowledgements

The authors thank G.F. Sonnenberg for a critical review of the manuscript, R. Pinefor for from the Weill Cornell Gnotobiotic Animal Facility for assistance with gnotobiotic animal studies, and T. Miller for assistance with flow cytometry.

Disclosure statement

A provisional patent application for SCFAs and Sh2b3 in the treatment of coagulation by MYZ is pending.

Funding

This work was supported by the National Institute of Diabetes and Digestive and Kidney Diseases [K01 DK114376] and funds from the Gale and Ira Drukier Institute for Children's Health and Children's Health Council at Weill Cornell Medicine, seed grants from the Center for Immunology and Office of Academic Integration of Cornell University and Center for IBD Research at Weill Cornell Medicine, and the Hartwell Foundation (all to MYZ), a CTSC TL1 Scholar Award at Weill Cornell Medicine (award number TL1TR002386) and the Biocodex MicrobiotaFoundation Grant (to JAB), and a postdoctoral fellowship from the HartwellFoundation (to KZS). BTL is supported by NIH (R01DK104927, R01HL148271, U01DK127378, P30DK020595, and the Department of Veterans Affairs (I01BX003382). CJG is supported by the AGA Research Foundation, WCM-RAPPInitiative, the. W. M. Keck Foundation, and the National Institutes of Health (DP2HD101401-01).

Author contributions

MYZ: Conceptualization and supervision of the project and writing of the manuscript. JAB and KZS: Majority of the experiments and writing of the manuscript. SL, CML, RMC, AA, SB, JC, MS, FS, YW, TL, MA, CJG, CL, and DCL: Assistance with experiments. FMR, LM, MC, BTL, AJD, PDB, BL, IM, and RKP: Contribution of key reagents. NI: Analysis of RNA-seq and 16S rRNA sequencing data. All authors reviewed and edited the manuscript.

Data availability

Gene Expression Omnibus accession numbers for the publicly available RNA-seq datasets used in this study are as follows: Blanco-Melo et al. study[27], GSE147507; Arunachalam et al. study[25], GSE152418; Bernardes et al. study[26], GSE161777. The GEO accession number for the 16S rRNA and RNA-seq data generated for this study is GSE189794.

References

1. World Health Organization. WHO Coronavirus (COVID-19) Dashboard [Internet]. [accessed 2021 Aug 5]. https://covid19.who.int/
2. Hoffmann M, Kleine-Weber H, Schroeder S, Krüger N, Herrler T, Erichsen S, Schiergens TS, Herrler G, Wu NH, Nitsche A, et al. SARS-CoV-2 cell entry depends on ACE2 and TMPRSS2 and is blocked by a clinically proven protease inhibitor. Cell. 2020;181 (2):271–280.e8. Internet]. [accessed doi:10.1016/j.cell. 2020.02.052.
3. Hamming I, Timens W, Bulthuis MLC, Lely AT, Navis GJ, van Goor H. Tissue distribution of ACE2 protein, the functional receptor for SARS coronavirus. A first step in understanding SARS pathogenesis. J Pathol. Internet]. [accessed. 2004;203(2):631–637. doi:10.1002/PATH.1570.
4. Zheng S, Fan J, Yu F, Feng B, Lou B, Zou Q, Xie G, Lin S, Wang R, Yang X, et al. Viral load dynamics and disease severity in patients infected with SARS-CoV-2 in Zhejiang province, China, January-March 2020: retrospective cohort study. BMJ. Internet]. [accessed 2020;369. doi:10.1136/BMJ.M1443
5. D'Amico F, Baumgart DC, Danese S, Peyrin-Biroulet L. Diarrhea during COVID-19 infection: pathogenesis, epidemiology, prevention, and management. Clin Gastroenterol Hepatol. Internet]. [accessed. 2020;18 (8):1663–1672. doi:10.1016/J.CGH.2020.04.001.
6. Devaux CA, Lagier JC, Raoult D. New insights into the physiopathology of COVID-19: SARS-CoV-2-associated gastrointestinal illness. Front Med. 2021;8. [accessed 2021 May 10 10.3389/fmed.2021. 640073Internet

7. Gaebler C, Wang Z, Lorenzi JCC, Muecksch F, Finkin S, Tokuyama M, Cho A, Jankovic M, Schaefer-Babajew D, Oliveira TY, et at. Evolution of antibody immunity to SARS-CoV-2. Nature. 2021;591(7851):639–644. Internet]. [accessed doi:10.1038/s41586-021-03207-w.
8. Bonaventura A, Vecchié A, Dagna L, Martinod K, Dixon DL, Van Tassell BW, Dentali F, Montecucco F, Massberg S, Levi M, et al. Endothelial dysfunction and immunothrombosis as key pathogenic mechanisms in COVID-19. Nat Rev Immunol. Internet]. [accessed. 2021;21(5):319–329. doi:10.1038/s41577-021-00536-9.
9. Connors JM, Levy JH. COVID-19 and its implications for thrombosis and anticoagulation. Blood. Internet]. [accessed. 2020;135(23):2033. doi:10.1182/BLOOD.2020006000.
10. Nicolai L, Leunig A, Brambs S, Kaiser R, Joppich M, Hoffknecht ML, Gold C, Engel A, Polewka V, Muenchhoff M, et al. Vascular neutrophilic inflammation and immunothrombosis distinguish severe COVID-19 from influenza pneumonia. J Thromb Haemost. 2021;19(2):574–581. Internet]. [accessed doi:10.1111/jth.15179.
11. Wool GD, Miller JL. The impact of COVID-19 disease on platelets and coagulation. Pathobiology. Internet]. [accessed. 2021;88(1):15–27. doi:10.1159/000512007.
12. Budden KF, Gellatly SL, Wood DLA, Cooper MA, Morrison M, Hugenholtz P, Hansbro PM. Emerging pathogenic links between microbiota and the gut-lung axis. Nat Rev Microbiol. Internet]. [accessed. 2017;15(1):55–63. doi:10.1038/nrmicro.2016.142.
13. Dang AT, Marsland BJ. Microbes, metabolites, and the gut-lung axis. Mucosal Immunol. Internet]. [accessed. 2019;12(4):843–850. doi:10.1038/s41385-019-0160-6.
14. Chen J, Hall S, Vitetta L. Altered gut microbial metabolites could mediate the effects of risk factors in Covid-19. Rev Med Virol. Internet]. [accessed. 2021;31(5):1–13. doi:10.1002/RMV.2211.
15. Ubeda C, Taur Y, Jenq RR, Equinda MJ, Son T, Samstein M, Viale A, Socci ND, Van Den Brink MRM, Kamboj M, et al. Vancomycin-resistant Enterococcus domination of intestinal microbiota is enabled by antibiotic treatment in mice and precedes bloodstream invasion in humans. J Clin Invest. Internet]. [accessed. 2010;120(12):4332–4341. doi:10.1172/JCI43918.
16. Ubeda C, Pamer EG. Antibiotics, microbiota, and immune defense. Trends Immunol. 2012;33(9):459–466. doi:10.1016/j.it.2012.05.003.
17. Luu M, Visekruna A. Short-chain fatty acids: bacterial messengers modulating the immunometabolism of T cells. Eur J Immunol. Internet]. [accessed. 2019;49(6):842–848. doi:10.1002/EJI.201848009.
18. Kim Y-G, Sakamoto K, Seo S-U, Pickard JM, GillillandIII MG, Pudlo NA, Hoostal M, Li X, Wang TD, Feehley T, et al. Neonatal acquisition of Clostridia species protects against colonization by bacterial pathogens. Science. 2017;356(6335):315. (80-) Internet]. [accessed doi:10.1126/SCIENCE.AAG2029.
19. Smith PM, Howitt MR, Panikov N, Michaud M, Gallini CA, Bohlooly-Y M, Glickman JN, Garrett WS. The microbial metabolites, short-chain fatty acids, regulate colonic Treg cell homeostasis. Science. (80-) Internet]. [accessed. 2013;341(6145):569–573. doi:10.1126/science.1241165.
20. Tan J, McKenzie C, Potamitis M, Thorburn AN, Mackay CR, Macia L. 2014. The role of short-chain fatty acids in health and disease. In: AltF.W., editor. Adv Immunol. Vol. 121 . Cambridge, MA, USA: Academic Press Inc; p. 91–119. doi:10.1016/B978-0-12-800100-4.00003-9.
21. Lewis G, Wang B, Jahani PS, Hurrell BP, Banie H, Muench GRA, Maazi H, Helou DG, Howard E, Galle-Treger L, et al. Dietary fiber-induced microbial short chain fatty acids suppress ILC2-dependent airway inflammation. Front Immunol. Internet]. [accessed 2019;10. doi:10.3389/FIMMU.2019.02051
22. Wang R, Zhang Q, Ge J, Ren W, Zhang R, Lan J, Ju B, Su B, Yu F, Chen P, et al. Analysis of SARS-CoV-2 variant mutations reveals neutralization escape mechanisms and the ability to use ACE2 receptors from additional species. Immunity. 2021;54(7):1611. Internet]. [accessed doi:10.1016/J.IMMUNI.2021.06.003.
23. McCray Jr PB, Pewe L, Wohlford-Lenane C, Hickey M, Manzel L, Shi L, Netland J, Jia HP, Halabi C, Sigmund CD, et al. Lethal infection of K18-hACE2 mice infected with severe acute respiratory syndrome coronavirus. J Virol. 2007;81(2):813. Internet]. [accessed doi:10.1128/JVI.02012-06.
24. Takizawa H, Eto K, Yoshikawa A, Nakauchi H, Takatsu K, Takaki S. Growth and maturation of megakaryocytes is regulated by Lnk/Sh2b3 adaptor protein through crosstalk between cytokine- and integrin-mediated signals. Exp Hematol. Internet]. [accessed. 2008;36(7):897–906. doi:10.1016/j.exphem.2008.02.004.
25. Arunachalam PS, Wimmers F, Mok CKP, Perera RAPM, Scott M, Hagan T, Sigal N, Feng Y, Bristow L, Tsang OT-Y, et al. Systems biological assessment of immunity to mild versus severe COVID-19 infection in humans. Science. 2020;369(6508):1210. (80-) Internet]. [accessed doi:10.1126/SCIENCE.ABC6261.
26. Bernardes JP, Mishra N, Tran F, Bahmer T, Best L, Blase JI, Bordoni D, Franzenburg J, Geisen U, Josephs-Spaulding J, et al. Longitudinal multi-omics analyses identify responses of megakaryocytes, erythroid cells, and plasmablasts as hallmarks of severe COVID-19. Immunity. 2020;53(6):1296. Internet]. [accessed doi:10.1016/J.IMMUNI.2020.11.017.
27. Blanco-Melo D, Nilsson-Payant BE, Liu WC, Uhl S, Hoagland D, Møller R, Jordan TX, Oishi K, Panis M, Sachs D, et al. Imbalanced host response to SARS-CoV-2 drives development of COVID-19. Cell. 2020;181(5):1036–1045. doi:10.1016/j.cell.2020.04.026.
28. Martin JF, Trowbridge EA, Salmon G, Plumb J. The biological significance of platelet volume: its relationship to bleeding time, platelet thromboxane B2 production and

megakaryocyte nuclear DNA concentration. Thromb Res. Internet]. [accessed. 1983;32(5):443–460. doi:10.1016/0049-3848(83)90255-4.

29. Cielo D, Galatola M, Fernandez-Jimenez N, Leo L, De Garcia-Etxebarria K, Loganes C, Tommasini A, Not T, Auricchio R, Greco L, et al. Combined analysis of methylation and gene expression profiles in separate compartments of small bowel mucosa identified celiac disease patients. Signatures Sci Rep. Internet]. [accessed 2019;9(1)doi:10.1038/S41598-019-46468-2
30. Harb H, Alhamwe BA, Acevedo N, Frumento P, Johansson C, Eick L, Papadogiannakis N, Alm J, Renz H, Potaczek DP, et al. Epigenetic modifications in placenta are associated with the child's sensitization to allergens. Biomed Res Int. 2019; 2019:1–11. [accessed 2021 Aug 21]. Internet. doi:10.1155/2019/1315257.
31. Tong W, Lodish HF. Lnk inhibits Tpo–mpl signaling and Tpo-mediated megakaryocytopoiesis. J Exp Med. Internet]. [accessed. 2004;200(5):569. doi:10.1084/JEM.20040762.
32. Dhar D, Mohanty A. Gut microbiota and Covid-19-possible link and implications. Virus Res. 2020;285:198018. [accessed 2021 Aug 2. Internet: doi:10.1016/J.VIRUSRES.2020.198018.
33. Gu S, Chen Y, Wu Z, Chen Y, Gao H, Lv L, Guo F, Zhang X, Luo R, Huang C, et al. Alterations of the gut microbiota in patients with coronavirus disease 2019 or H1N1 influenza. Clin Infect Dis. 2020;71(10):2669–2678. doi:10.1093/cid/ciaa709.
34. Gu J, Han B, Wang J. COVID-19: Gastrointestinal manifestations and potential fecal–oral transmission. Gastroenterology. Internet]. [accessed. 2020;158(6):1518. doi:10.1053/J.GASTRO.2020.02.054.
35. Tao W, Zhang G, Wang X, Guo M, Zeng W, Xu Z, Cao D, Pan A, Wang Y, Zhang K, et al. Analysis of the intestinal microbiota in COVID-19 patients and its correlation with the inflammatory factor IL-18. Med Microecol. 2020;5:100023. doi:10.1016/J.MEDMIC.2020.100023.
36. Zuo T, Zhang F, Lui GCY, Yeoh YK, Li AYL, Zhan H, Wan Y, Chung ACK, Cheung CP, Chen N, et al. Alterations in gut microbiota of patients with COVID-19 during time of hospitalization. Gastroenterology. 2020;159(3):944–955.e8. Internet]. [accessed doi:10.1053/j.gastro.2020.05.048.
37. Lowery SA, Sariol A, Perlman S. Innate immune and inflammatory responses to SARS-CoV-2: implications for COVID-19. Cell Host Microbe. Internet]. [accessed. 2021;29(7):1052. doi:10.1016/J.CHOM.2021.05.004.
38. Sette A, Crotty S. Adaptive immunity to SARS-CoV-2 and COVID-19. Cell. [Internet]. [accessed. 2021;184(4):861–880. doi:10.1016/j.cell.2021.01.007.
39. Bachem A, Makhlouf C, Binger KJ, De Souza DP, Tull D, Hochheiser K, Whitney PG, Fernandez-Ruiz D, Dähling S, Kastenmüller W, et al. Microbiota-derived short-chain fatty acids promote the memory potential of antigen-activated CD8+ T cells. Immunity. 2019;51(2):285–297.e5. Internet]. [accessed doi:10.1016/J.IMMUNI.2019.06.002.
40. Kim M, Qie Y, Park J, Kim CH. Gut microbial metabolites fuel host antibody responses. Cell Host Microbe. Internet]. [accessed. 2016;20(2):202–214. doi:10.1016/j.chom.2016.07.001.
41. Lynn DJ, Benson SC, Lynn MA, Pulendran B. Modulation of immune responses to vaccination by the microbiota: implications and potential mechanisms. Nat Rev Immunol. Internet]. [accessed. 2021;22(1):33–46. doi:10.1038/s41577-021-00554-7.
42. Klein SL, Flanagan KL. Sex differences in immune responses. Nat Rev Immunol. Internet]. [accessed. 2016;16(10):626–638. doi:10.1038/nri.2016.90.
43. Di Resta C, Ferrari D, Viganò M, Moro M, Sabetta E, Minerva M, Ambrosio A, Locatelli M, Tomaiuolo R. The gender impact assessment among healthcare workers in the SARS-CoV-2 vaccination—an analysis of serological response and side effects. Vaccines. Internet]. [accessed. 2021;9(5):522. doi:10.3390/VACCINES9050522.
44. Salvagno GL, Henry BM, Piazza G, Di Pighi L, De Nitto S, Bragantini D, Gianfilippi GL, Lippi G. Anti-SARS-CoV-2 receptor-binding domain total antibodies response in seropositive and seronegative healthcare workers undergoing COVID-19 mRNA BNT162b2 vaccination. Diagnostics. Internet]. [accessed. 2021;11(5):832. doi:10.3390/DIAGNOSTICS11050832.
45. Lo Sasso B, Giglio RV, Vidali M, Scazzone C, Bivona G, Gambino CM, Ciaccio AM, Agnello L, Ciaccio M. Evaluation of anti-SARS-Cov-2 S-RBD IgG antibodies after COVID-19 mRNA BNT162b2 vaccine. Diagnostics. Internet]. [accessed. 2021;11(7):1135. doi:10.3390/DIAGNOSTICS11071135.
46. Souyris M, Cenac C, Azar P, Daviaud D, Canivet A, Grunenwald S, Pienkowski C, Chaumeil J, Mejía JE, Guéry J-C. TLR7 escapes X chromosome inactivation in immune cells. Sci Immunol. Internet]. [accessed 2018;3(19): . doi:10.1126/SCIIMMUNOL.AAP8855
47. Liu J, Ji H, Zheng W, Wu X, Zhu JJ, Arnold AP, Sandberg K. Sex differences in renal angiotensin converting enzyme 2 (ACE2) activity are 17β-oestradiol-dependent and sex chromosome-independent. Biol Sex Differ. Internet]. [accessed 2010;1(1): . doi:10.1186/2042-6410-1-6
48. Milsted A, Underwood AC, Dunmire J, Delpuerto HL, Martins AS, Ely DL, Turner ME. Regulation of multiple renin-angiotensin system genes by Sry. J Hypertens. Internet]. [accessed. 2010;28(1):59–64. doi:10.1097/HJH.0b013e328332b88d.
49. Tukiainen T, Villani AC, Yen A, Rivas MA, Marshall JL, Satija R, Aguirre M, Gauthier L, Fleharty M, Kirby A, et al. Landscape of X chromosome inactivation across human tissues. Nature. 2017;550(7675):244–248. Internet]. [accessed doi:10.1038/nature24265.

50. Giannis D, Ziogas IA, Gianni P. Coagulation disorders in coronavirus infected patients: COVID-19, SARS-CoV-1, MERS-CoV and lessons from the past. J Clin Virol. 2020;127:104362. [accessed 2021 Aug 2. Internet: doi:10.1016/J.JCV.2020.104362.
51. Obi AT, Tignanelli CJ, Jacobs BN, Arya S, Park PK, Wakefield TW, Henke PK, Napolitano LM. Empirical systemic anticoagulation is associated with decreased venous thromboembolism in critically ill influenza A H1N1 acute respiratory distress syndrome patients. J Vasc Surg Venous Lymphat Disord. 2019;7 (3):317–324. doi:10.1016/J.JVSV.2018.08.010.
52. Caine GJ, Stonelake PS, Lip GY, Kehoe ST. The hypercoagulable state of malignancy: pathogenesis and current debate. Neoplasia. Internet]. [accessed. 2002;4 (6):465. doi:10.1038/SJ.NEO.7900263.
53. Clarke NE, Belyaev ND, Lambert DW, Turner AJ. Epigenetic regulation of angiotensin-converting enzyme 2 (ACE2) by SIRT1 under conditions of cell energy stress. Clin Sci. Internet]. [accessed. 2014;126 (7):507–516. doi:10.1042/CS20130291.
54. Singh S, Singh KK. Valproic acid in prevention and treatment of COVID-19. Int J Respir Pulm Med. 2020;7(3). doi:10.23937/2378-3516/1410138.
55. Oguntuyo KY, Stevens CS, Hung CT, Ikegame S, Acklin JA, Kowdle SS, Carmichael JC, Chiu HP, Azarm KD, Haas GD, et al. Quantifying absolute neutralization titers against SARS-CoV-2 by a standardized virus neutralization assay allows for cross-cohort comparisons of COVID-19 sera. MBio. 2021;12(1):1–23. Internet]. [accessed doi:10.1128/MBIO.02492-20.
56. Schmidt F, Weisblum Y, Muecksch F, Hoffmann -H-H, Michailidis E, Lorenzi JCC, Mendoza P, Rutkowska M, Bednarski E, Gaebler C, et al. Measuring SARS-CoV-2 neutralizing antibody activity using pseudotyped and chimeric viruses. J Exp Med. 2020;217(11):e20201181. Internet]. [accessed doi:10.1084/jem.20201181.
57. Whitt MA. Generation of VSV pseudotypes using recombinant ΔG-VSV for studies on virus entry, identification of entry inhibitors, and immune responses to vaccines. J Virol Methods. Internet]. [accessed. 2010;169 (2):365–374. doi:10.1016/j.jviromet.2010.08.006.
58. Liberatore RA, Mastrocola EJ, Cassella E, Schmidt F, Willen JR, Voronin D, Zang T, Hatziioannou T, Bieniasz PD. Rhabdo-immunodeficiency virus, a murine model of acute HIV-1 infection. Elife. 2019;8. [accessed 2021 Jan 7 Internet doi:10.7554/eLife.49875.
59. Ikegame S, Siddiquey MNA, Hung C-T, Haas G, Brambilla L, Oguntuyo KY, Kowdle S, Chiu H-P, Stevens CS, Vilardo AE, et al. Neutralizing activity of Sputnik V vaccine sera against SARS-CoV-2 variants. Nat Commun. 2021;12(1):1–11. Internet]. [accessed doi:10.1038/s41467-021-24909-9.
60. Ramsburg E, Publicover J, Buonocore L, Poholek A, Robek M, Palin A, Rose JK. A vesicular stomatitis virus recombinant expressing granulocyte-macrophage colony-stimulating factor induces enhanced t-cell responses and is highly attenuated for replication in animals. J Virol. Internet]. [accessed. 2005;79 (24):15043. doi:10.1128/JVI.79.24.15043-15053.2005.
61. Case JB, Rothlauf PW, Chen RE, Liu Z, Zhao H, Kim AS, Bloyet L-M, Zeng Q, Tahan S, Droit L, et al. Neutralizing antibody and soluble ACE2 inhibition of a replication-competent VSV-SARS-CoV-2 and a clinical isolate of SARS-CoV-2. Cell Host Microbe. 2020;28 (3):475. Internet]. [accessed doi:10.1016/J.CHOM.2020.06.021.
62. Kozich JJ, Westcott SL, Baxter NT, Highlander SK, Schloss PD. Development of a dual-index sequencing strategy and curation pipeline for analyzing amplicon sequence data on the MiSeq Illumina sequencing platform. Appl Environ Microbiol. Internet]. [accessed. 2013;79(17):5112. doi:10.1128/AEM.01043-13.
63. Schloss PD, Westcott SL, Ryabin T, Hall JR, Hartmann M, Hollister EB, Lesniewski RA, Oakley BB, Parks DH, Robinson CJ, et al. Introducing mothur: open-source, platform-independent, community-supported software for describing and comparing microbial communities. Appl Environ Microbiol. 2009;75(23):7537–7541. Internet]. [accessed doi:10.1128/AEM.01541-09.
64. Quast C, Pruesse E, Yilmaz P, Gerken J, Schweer T, Yarza P, Peplies J, Glöckner FO. The SILVA ribosomal RNA gene database project: improved data processing and web-based tools. Nucleic Acids Res. Internet]. [accessed. 2013;41(D1):D590–D596. doi:10.1093/NAR/GKS1219.
65. Wang Q, Garrity GM, Tiedje JM, Cole JR. Naïve Bayesian classifier for rapid assignment of rRNA sequences into the new bacterial taxonomy. Appl Environ Microbiol. Internet]. [accessed. 2007;73 (16):5261–5267. doi:10.1128/AEM.00062-07.
66. Lu Y, Yao D, Chen C. 2-Hydrazinoquinoline as a derivatization agent for LC-MS-based metabolomic investigation of diabetic ketoacidosis. Metabolites. Internet]. [accessed. 2013;3(4):993. doi:10.3390/METABO3040993.
67. Yang L, Han Y, Nilsson-Payant BE, Gupta V, Wang P, Duan X, Tang X, Zhu J, Zhao Z, Jaffré F, et al. A Human pluripotent stem cell-based platform to study SARS-CoV-2 tropism and model virus infection in human cells and organoids. Cell Stem Cell. 2020;27(1):125–136.e7. doi:10.1016/J.STEM.2020.06.015.
68. Broutier L, Andersson-Rolf A, Hindley CJ, Boj SF, Clevers H, Koo B-K, Huch M. Culture and establishment of self-renewing human and mouse adult liver and pancreas 3D organoids and their genetic manipulation. Nat Protoc. Internet]. [accessed. 2016;11(9):1724–1743. doi:10.1038/nprot.2016.097.
69. Etievant S, Bal A, Escuret V, Brengel-Pesce K, Bouscambert M, Cheynet V, Generenaz L, Oriol G, Destras G, Billaud G, et al. Performance assessment of

SARS-CoV-2 PCR assays developed by WHO referral laboratories. J Clin Med. 2020;9(6):1–10. Internet]. [accessed doi:10.3390/JCM9061871.

70. Goel RR, Apostolidis SA, Painter MM, Mathew D, Pattekar A, Kuthuru O, Gouma S, Hicks P, Meng W, Rosenfeld AM, et al. Distinct antibody and memory B cell responses in SARS-CoV-2 naïve and recovered individuals following mRNA vaccination. Sci Immunol. 2021;6(58):1–19. Internet]. [accessed doi:10.1126/sciimmunol.abi6950.

71. Patro R, Duggal G, Love MI, Irizarry RA, Kingsford C. Salmon: fast and bias-aware quantification of transcript expression using dual-phase inference. Nat Methods. Internet]. [accessed. 2017;14(4):417. doi:10.1038/NMETH.4197.

72. Caruso R, Ono M, Bunker ME, Núñez G, Inohara N. Dynamic and asymmetric changes of the microbial communities after cohousing in laboratory mice. Cell Rep. Internet]. [accessed. 2019;27(11):3401. doi:10.1016/J.CELREP.2019.05.042.

3. CONCLUSIONS

Since this dissertation is divided into four result sections based on thematic areas, also the conclusion is divided into four sections. Each subchapter of the four result sections includes a research specific discussion in the article which brings the topic into a broader field. The overall conclusion here focusses on one specific aspect for each section:

i) Sex as a biological variable in the COVID-19-like disease in the dwarf hamster model in comparison to human COVID-19

ii) Comparative analysis of pre-clinical candidate 4'-Fluorouridine and currently approved influenza antivirals

iii) Reasons for why the allosteric AVG inhibitor series against respiratory syncytial virus should be continued to formal development

iv) Possible mechanisms of how SFB colonization in the gut may alter the AM phenotype, enabling better protection against respiratory viral infections

3.1 Sex as a Biological Variable in the COVID-19-like Disease in the Dwarf Hamster Model in Comparison to Human COVID-19

This dissertation used three antivirals which received emergency proof authorization during the recent SARS-CoV-2 pandemic (Cox et al., 2023; Cox, Wolf, Lieber, et al., 2021; Lieber et al., 2022). Paxlovid-like nirmatrelvir/ritonavir and molnupiravir were utilized in the ferret model and the Roborovski dwarf hamster model. The dwarf hamster model is characterized by acute COVID-19-like lower respiratory tract disease and recapitulated the pathogenicity of the variants of concerns (VOC) associated with highest lethality in humans: VOC delta, followed by VOC gamma and VOC omicron (Lieber et al., 2022). Paxlovid-like nirmatrelvir/ritonavir and molnupiravir mediated full survival whereas 60-90% of the vehicle-treated animals succumbed disease (Lieber et al., 2022). Furthermore, significant titer reductions in the lower respiratory tract were noted upon treatment. Titer reductions of VOC omicron were surprisingly diverse, resulting in the definition of 3 distinct outcome groups: low responders with 1 order of magnitude reduction, standard responders with a decrease in viral titer by up to 3 orders of magnitude, and super responders in which the drug was sterilizing (Cox et al., 2023; Lieber et al., 2022). The role of biological sex on antiviral efficacy was determined by graphically blotting lung viral titers according to the biological sex (powered for numbers for molnupiravir-treated hamsters (Lieber et al., 2022) and trend seeing for paxlovid-like nirmatrelvir/ritonavir-treated animals (Cox et al., 2023)). Lung titer reductions in treated males were highly significant compared to male vehicle-treated animals whereas female molnupiravir-treated hamsters did not show a significant change to female-vehicle/all vehicle-treated animals (Lieber et al., 2022).

What is the general morbidity and mortality rate of COVID-19 in humans and is there a correlation to biological sex? Are there similar reports in the human host and explanations which influence treatment success?

A large body of evidence supports that men account for up to 75% of COVID-19 deaths and have a three-times greater risk of requiring intensive care (Chaturvedi, Lui, Aaronson, White, & Samuels, 2022; Ramírez-Soto, Ortega-Cáceres, & Arroyo-Hernández, 2021). Furthermore, men have higher rates of organ dysfunction, such as fatal gastrointestinal disease, acute kidney injury, and respiratory failure when infected with SARS-CoV-2 (Greco et al., 2021; Toth-Manikowski et al., 2021). These are extremely concerning facts and it is important to look at baseline comorbidity differences, which may include obesity, hypertension and cardiovascular diseases (E. Liu, Lee, Lui, White, & Samuels, 2022; Womersley, Ripullone, Peters, & Woodward, 2020). Controlling comorbidities is difficult but even if questionnaires are used and the comorbidities are measured, it is not possible to assess lifestyle, as well as behavioral and social differences. Interestingly, males also had higher rates of morbidity and mortality in the 2012 MERS endemic and in the 2002 SARS-CoV infection outbreak (Alwani et al., 2021; Lakbar, Luque-Paz, Mege, Einav, & Leone, 2020). Further epidemiological differences were reported with regards to sepsis (Nasir et al., 2015).

As discussed above, many non-genetic factors play an important role too. A higher proportion of men have been shown to engage in ‘deleterious behaviors’ like excessive alcohol consumption and smoking (Chaturvedi et al., 2022; "Smoking prevalence and attributable disease burden in 195 countries and territories, 1990-2015: a systematic analysis from the Global Burden of Disease Study 2015," 2017). Smoking is associated with an increased expression of Angiotensin Converting Enzyme 2 (ACE2) receptors which thereby impact SARS-CoV-2 entry into cells (Cai, 2020) and big surveys have shown that males, in general, exhibit a decreased compliance with precautionary measures to limit the spread of COVID-19, like masking and social distancing (Howard, 2021; Solomou & Constantinidou, 2020).

The Roborovski dwarf hamsters, used in this thesis, are outbred animals which were not raised under controlled conditions. These variables include individual differences in age, bodyweight, microbiome, drug metabolism and prior disease history which are equally present in human patients (Cox et al., 2023; Lieber et al., 2022; Trimpert, Vladimirova, Dietert, Abdelgawad, Kunec, Dokel, et al., 2020). The male and female, omicron-infected, and vehicle-treated dwarf hamsters did not show differences in viral titers in the lower respiratory tract.

Hormone variability may also play a role in differing morbidity and mortality for COVID-19 between sexes (Chaturvedi et al., 2022), which was not analyzed in the dwarf hamster model.

Are the available vaccines and approved antivirals differently efficacious in men and women what was seen in the dwarf hamster model for VOC omicron? In general, less than 5% of all recent studies include sex as an analytical variable (Brady, Nielsen, Andersen, & Oertelt-Prigione, 2021) and intersex and transgender individuals are not formally represented (Castañeda, 2022; Waddick, 2023). But several phase 3 randomized, multicenter studies have shown that the vaccines were similarly efficacious in men versus women with no statistical difference in vaccine efficacy for the Janssen, Moderna and Pfizer-BioNTech vaccines (Jensen et al., 2022). The paxlovid clinical trial included 332 males in the paxlovid group and 366 men in the placebo group. 384 women received paxlovid in the trial and 351 females were included in the placebo group. 4 males and equal females died (paxlovid group) and 41 males and 25 females succumbed disease in the placebo group (Hammond et al., 2022). Unfortunately, the adverse event summary does not include a differentiation of males/females. The molnupiravir clinical trial had 566/582 (molnupiravir/placebo) males and 554/544 (molnupiravir/placebo) females included (Jayk Bernal et al., 2022). 32 males and 16 females died under molnupiravir treatment in this trial and 41 males, and 27 females died which received a placebo. Also in this trial, the adverse event summary table does not include a differentiation of males to females (Jayk Bernal et al., 2022).

Overall, all approved vaccines and antiviral medications do not show a major efficacy advantage for one particular sex and also the dwarf hamsters of this dissertation all survived under treatment (Cox et al., 2023; Lieber et al., 2022). No direct comparison can be made between humans and dwarf hamsters since no lung titer data exists for humans.

But why are women still underrepresented in most clinical trials, and gender-specific analysis is uncommon? Sex differences in metabolism are believed to be the major cause of differential pharmacokinetics between men and women (B. N. Wu & O'Sullivan, 2011). Many CYP450 enzymes show a sex-dependent difference in activity. Most of the enzymes have a higher activity in men than in women (T. Chu, 2014). Sex differences are also found in other pharmacokinetic parameters for example drug absorption, distribution, and excretion. This dissertation explored the pharmacokinetic properties of molnupiravir in dwarf hamsters to see whether plasma profiles and tissue distribution were unexpectedly affected by biological sex (Lieber et al., 2022). No major differences were observed between male and female dwarf hamsters.

What are further reasons for sex difference? Women are more frequently overdosed, simply due to the reason that there is an anatomical difference between men and women (Bredella, 2017). The average man weighs 78kg and has a body surface of 18,000cm^2 with total body water of 42 liters (Soldin & Mattison, 2009). In comparison, women weigh 68kg in average, have a body surface which is 2,000cm^2 smaller of that of men and only 29 liters of total body water. The volume of distribution is smaller in women as well, also the free fraction of drug is larger and the clearance from the body is slower (Soldin & Mattison, 2009). The same general pattern is seen in adult male dwarf hamsters, which are also in average 5 grams heavier than same-aged female hamsters. In general, only limited tools are commercially available to determine different factors such as cytokine levels in the novel model.

Furthermore, women are more sensitive due to alterations in receptor number, receptor binding, and in signal transduction pathway following receptor binding. Generally, women take greater amounts of medications (Orlando et al., 2020) which leads to drug interactions with alterations in pharmacokinetics and pharmacodynamics. The drug absorption is route-specific since chemicals or drugs cross body surfaces for example the skin, the gastrointestinal tract or the respiratory tract to enter the systemic circulation (Soldin & Mattison, 2009) and it is known that the absorption rate is drug-specific. Further major factors are gut motility, the gut flora, ingestion, and food interactions. The FDA made regulations on inclusion of women in clinical trials because the differences in drug pharmacokinetics and pharmacodynamics must be assessed (Soldin & Mattison, 2009). But until today, only modest knowledge on appropriate dose, dosing schedule and treatment intervals is available, and most data is obtained by posthoc analysis.

In conclusion, the biggest disadvantage in the dwarf hamster model is also biggest advantage in this model to see the complex and multifactorial diversity similar to humans.

3.2 Comparative Analysis of Pre-Clinical Candidate 4'-Fluorouridine and Currently Approved Influenza Antivirals

The therapeutic time window of pre-clinical candidate 4'-Fluorouridine (4'-FlU) was analyzed in detail in this dissertation. Broad-spectrum 4'-FlU showed potent titer reductions in *in vitro* and *ex vivo* assays against several different RNA viruses, both negative and positive sense, including respiratory syncytial virus (RSV), influenza virus, and SARS-CoV-2 (Lieber et al., 2023; Sourimant, Lieber, Aggarwal, et al., 2022). Greatest susceptibility was observed against influenza viruses, which was confirmed by *in vitro* RdRP assays. The compound mediated full survival in the influenza mouse model when treatment was initiated up to 60 hours post infection at 2 mg/kg bodyweight once daily, given in three consecutive doses (Lieber et al., 2023). Further, 4’-FlU mediated significant lung titer reductions in immunocompromised mice and mice infected with highly pathogenic avian influenza viruses.

Placing 4’-FlU performance in context of six prescription influenza antivirals that are FDA approved in the United States as of September 2023: Two of them, amantadine and rimantadine, are no longer recommended for antiviral treatment or prophylaxis due to widespread high levels of resistance (Hersh, Maselli, & Cabana, 2009). The four remaining influenza antiviral medications were recommended for the influenza season 2022-2023 (Terrie, 2022). Orally available oseltamivir phosphate (Tamiflu), inhaled zanamivir (Relenza) and intravenous peramivir (Rapivab) are neuraminidase inhibitors. In contrast, baloxavir marboxil (Xofluza) is an orally available cap-dependent endonuclease inhibitor (CDC, 2022b). Leading in clinical use are oseltamivir phosphate and baloxavir marboxil.

Oseltamivir phosphate was approved for the prevention of influenza in adults and children aged one year and older (Cooper et al., 2003). Treatment should be initiated within 48 hours after symptom onset and must be taken twice daily for five days (Fiore et al., 2011). The most common side effects are nausea and vomiting, but overall oseltamivir phosphate is well tolerated (Hayden et al., 1999). Contraindications include hypersensitivities, and it should not be used if viral resistance is confirmed. Since no human clinical data is available yet for 4’-FlU, the rodent model will be used to compare 4’-FlU performance with approved drugs. In the reference study, mice were infected intranasally with $10^{4.5}$ pfu/ml of a mildly virulent H3N1 strain which is a genetic reassortant of an H3N2 and H1N1 (Wong, Jones, Anderson, & Gualano, 2011). Oseltamivir phosphate was administered twice daily via oral gavage at 10 mg/kg/day starting 24 or 48 hours post infection. In this dissertation, mice were infected with a lethal dose of a pathogenic pandemic09 (H1N1 strain) and 4'-FlU was dosed once daily at 2 mg/kg bodyweight (Lieber et al., 2023). Oseltamivir phosphate did not show significant titer reductions when dosed therapeutically starting at 24 and 48 hours after infection (titers measured on day 5 post infection) (Wong et al., 2011) whereas 4'-FlU reduced the viral titer by approximately 3 and 1.5 orders of magnitude (treatment initiated 24 and 48 hour after infection, titers of day 4.5 post infection), respectively (Lieber et al., 2023). Beside the titer reduction, 4'-FlU was clearly superior in mice since the therapeutic window is wider and a once daily treatment regimen is sufficient, which consistently ensures better patient compliances than a twice daily regimen (Kardas, 2007).

Baloxavir marboxil was approved in October 2018 by the FDA for post-exposure prophylaxis of influenza in people aged 5 years and older excluding pregnant, breastfeeding and immunosuppressed people due to a lack of information (CDC, 2022a). The drug is administered as an oral suspension or tablet (single dose) based on the individual's weight (Tejus, Mathur, Pradhan, Malik, & Salmani, 2022). 40 mg is given for people weighing between 40 and 80 kg and 80 mg for individuals heavier than 80 kg. Treatment-emergent adverse events were observed during the phase 2 and 3 trials and included diarrhea and bronchitis as well as emergence of resistance was seen which reduced the susceptibility (Hayden et al., 2018). Similar to oseltamivir phosphate, baloxavir marboxil should be administered within 48 hours of treatment onset. Viral shedding typically decreases within 48 hours after dosing compared to 96 hours after placebo or oseltamivir phosphate (Ng, 2019). In this dissertation, 4'-FlU was tested in the highly transmissible ferret model (Lieber et al., 2023) and blocked transmission to untreated and uninfected ferrets when administered 12 hours post infection in a direct contact transmission study. Furthermore, 2 doses 4'-FlU of 2 mg/kg bodyweight resulted in sterilizing titer results in infected ferrets.

Several studies were performed in mice using oral baloxavir marboxil. Overall, a dose-dependent virus titer reduction in the lungs was observed (Ando et al., 2021) which was comparable to the effect of 4'-FlU described in this thesis. Experiments in immunologically deficient mice, for example nude mice with a genetic mutation that causes the thymus to be deteriorated or absent, were furthermore utilized for efficacy testing of baloxavir marboxil (Kiso, Yamayoshi, Murakami, & Kawaoka, 2020). Daily treatment increased overall survival in the infected mice but did not clear the virus from their respiratory organs which resulted in loss in bodyweight after the treatment was terminated. In comparison, 4'-FlU efficacy was tested in RAG1-/- and IFNAR-/- mice infected with a lethal dose of influenza virus (Lieber et al., 2023). Therapeutic treatment mediated full survival. Both studies, the nude mice and the efficacy study with 4'-FlU in immunocompromised hosts, were performed with an H1N1 virus (A/California/04/2009 vs A/California/07/2009, respectively) and treated once daily but treatment duration differed massively. The nude mice were treated for 28 days (Kiso et al., 2020) whereas 4'-FlU was given only for 5 consecutive days (Lieber et al., 2023). Future studies could include an experimental approach to show whether 4'-FlU clears the virus in nude mice. Both immunocompromised mouse models used in this dissertation show that the antiviral activity of 4'-FlU is not strictly dependent on a fully immunocompetent host to clear the infection (Lieber et al., 2023).

Overall, 4'-FlU showed an exceptionally wide therapeutic time window for treatment onset in mice infected with influenza virus and RSV and potent titer reductions in the different animal species. Broad-spectrum efficacy, also against highly pathogenic avian influenza virus, oral bioavailability, the suitability of a once daily treatment regimen and a high barrier to resistance (Sourimant, Lieber, Aggarwal, et al., 2022) make 4'-FlU an ideal candidate for formal development and superior compared to the currently approved antivirals.

3.3 Reasons for Why the Allosteric AVG Inhibitor Series Against Respiratory Syncytial Virus Should be Continued to Formal Development

This dissertation mapped and characterized a non-nucleoside orally efficacious small-molecule inhibitor of the RSV polymerase (Sourimant, Lieber, Yoon, et al., 2022). But recently, the FDA approved Beyfortus, a new monoclonal antibody (mAb) (FDA, 2023b) and two vaccines, recommended for adults over 60 years of age (FDA, 2023a). So, is there still a need for additional antivirals for the same target virus and are there any disadvantages of the newly approved mAb?

The FDA approved Beyfortus (nirsevimab-alip) for the prevention of RSV lower respiratory tract disease on July 17, 2023 (FDA, 2023b). The mAb received approval in neonates and infants which were born during or entering their first RSV season, and in children up to 2 years of age, who remain vulnerable to severe RSV through their second RSV season. The approval of Beyfortus addresses a great need for products to help reduce the impact of RSV disease since the population at risk includes infants, especially if prematurely born and infants with congenital heart disease or chronic lung disease, which might advance to lower respiratory tract disease and viral pneumonia (FDA, 2023b). Beyfortus is an engineered protein that mimics the immune system's ability to fight RSV and is administered intramuscularly as a single dose (FDA, 2023b). All three clinical trials, which determined the safety and efficacy of this product in preterm infants, concluded that Beyfortus reduced the risk of RSV lower respiratory tract infection by approximately 70-75% relative to the placebo group (AstraZeneca, 2023a, 2023b; LLC, 2019). Side effects included rash and injection site reactions, and the mAb should not be given to infants or children with hypersensitivity to other IgG mAbs or bleeding disorders (FDA, 2023b).

Generally, monoclonal antibodies are less versatile due to their high single-epitope selectivity (Schofield, 2022). Furthermore, mAbs are expensive, ranging from $5,000 (without sponsor) to $100,000 (mAbs in oncology) (Hernandez et al., 2018; Laufer et al., 2021) and need long production timelines (Kelley, 2020). An enormous inequality has been observed with clinical use of mAb biologics. Antibody therapies have been increasingly and consistently approved in high-income countries, whereas low- and middle-income countries have licensed far fewer mAbs (Gieber, Muturi-Kioi, Malhotra, & Sitlani, 2023). In general, it is highly criticized that not the full global scale, including different socioeconomic levels, geographic regions, and demographic groups, was considered during clinical evaluations (Atal, Trinquart, Ravaud, & Porcher, 2018). Furthermore, cultural traditions, regional infrastructures and comorbidities vary widely and should be considered as factors that impact the execution of clinical studies (Gieber et al., 2023). Only a third of all interventional clinical trials occur outside of the US or the European Union (EU), and even less mAb trials specifically are performed outside of the US/EU (only 12%) (Gieber et al., 2023).

This dissertation mapped and characterized the AVG class of allosteric inhibitors of RSV RNA synthesis which stalls the polymerase initiation conformation (Sourimant, Lieber, Yoon, et al., 2022). Docking pose-informed synthetic optimization generated orally efficacious inhibitors like AVG-388, which showed potent efficacy in the RSV mouse model. All compounds were well tolerated with no adverse effects observed. Scale-up chemistry was established, supporting cost-effective production that is a prerequisite for deployment also in low- and middle-income countries, in which the clinical need is greatest.

3.4 Possible Mechanisms of How SFB Colonization in the Gut May Alter the AM Phenotype, Enabling Better Protection Against Respiratory Viral Infections

This dissertation showed that colonization with segmented filamentous bacteria (SFB) in the gut alters the phenotype of alveolar macrophages (AMs), enabling these cells to better protect their hosts from lethal respiratory viral infections (V. Ngo et al., 2023). These findings contribute insight to cross-organ communication, identifying AMs as central effectors. Furthermore, the stability of the reprogramming process is demonstrated in various studies. But how do these findings contribute towards the understanding of the gut-lung axis? And are there more disease models where SFB play a role?

The gut-lung axis is an emerging concept that links the state of the gut microbiota to respiratory health outcomes (Price & O'Toole, 2021). The gut microbiota has been suggested to influence lung health outcomes in multiple diseases like cystic fibrosis, chronic obstructive pulmonary disease, and asthma. Moreover, rheumatoid arthritis is a long-lasting, chronic autoimmune disease which mostly affects joints (NIH, 2022b). However, 19-58% of the patients develop lung complications (Olson et al., 2011) and this condition is ranked as the second most common cause of death of arthritis patients. It was demonstrated that SFB acts as an environmental cue to enhance autoimmune arthritis by inducing T follicular helper cells and T helper 17 cells (Teng et al., 2016; H. J. Wu et al., 2010). SFB remotely provoked inducible Bronchus-Associated Lymphoid Tissue (iBALT)-like structure formation in the lung by upregulating mucosal Th17 cells (Bradley et al., 2017). Thus, SBF induced a strong lung Th17 cell response, which is essential for rheumatoid arthritis-related lung pathology prior to arthritis development, and Th17 cells mediated the crosstalk between gut microbiota and the lung (Bradley et al., 2017).

In contrast to these findings, SFB mediated protection was fully maintained upon antibody-mediated neutralization of IL-17 and IL-22 in SFB-colonized and influenza virus-infected mice (V. Ngo et al., 2023) and a significant titer difference between SFB-colonized and non-colonized mice was observed. This implicates a novel immunomodulatory mechanism that is independent of the well-characterized Th17 response for SFB. Furthermore, no involvement of the adaptive immune system, type I and III interferon, and type 3 innate lymphoid cells was seen (V. Ngo et al., 2023). Whereas these observations strongly support the existence of a distinct, presently underappreciated gut-lung axis pathway, currently unaddressed mechanistic questions abound concerning the crosstalk between SFB and AMs that must be pursued in future work. It should be noted that SFB were found in the human microbiome (Chen et al., 2020; Jonsson, Hugerth, Sundh, Lundin, & Andersson, 2020). However, it is currently not known whether people colonized with SFB show different susceptibility to respiratory pathogens or infectious diseases in general. The animal work carried out in this dissertation should therefore be viewed primarily as fundamental proof-of-concept for a novel AM-driven crosstalk between the gut microbiome and respiratory immune responses to invading RNA viruses. A comparable specific role of individual human microbiome components in modulating severity of respiratory viral infections must be determined separately.

REFERENCES

Abdelrahman, Z., Li, M., & Wang, X. (2020). Comparative Review of SARS-CoV-2, SARS-CoV, MERS-CoV, and Influenza A Respiratory Viruses. *Front Immunol, 11*, 552909. doi:10.3389/fimmu.2020.552909

Adamoski, D., Baura, V. A., Rodrigues, A. C., Royer, C. A., Aoki, M. N., Tschá, M. K., . . . Carvalho de Oliveira, J. (2022). SARS-CoV-2 Delta and Omicron Variants Surge in Curitiba, Southern Brazil, and Its Impact on Overall COVID-19 Lethality. *Viruses, 14*(4). doi:10.3390/v14040809

Akin, L., & Gözel, M. G. (2020). Understanding dynamics of pandemics. *Turk J Med Sci, 50*(Si-1), 515-519. doi:10.3906/sag-2004-133

Aleem, A., Akbar Samad, A. B., & Vaqar, S. (2023). Emerging Variants of SARS-CoV-2 and Novel Therapeutics Against Coronavirus (COVID-19). In *StatPearls*. Treasure Island (FL) ineligible companies. Disclosure: Abdul Bari Akbar Samad declares no relevant financial relationships with ineligible companies. Disclosure: Sarosh Vaqar declares no relevant financial relationships with ineligible companies.: StatPearls Publishing

Copyright © 2023, StatPearls Publishing LLC.

Alwani, M., Yassin, A., Al-Zoubi, R. M., Aboumarzouk, O. M., Nettleship, J., Kelly, D., . . . Shabsigh, R. (2021). Sex-based differences in severity and mortality in COVID-19. *Rev Med Virol, 31*(6), e2223. doi:10.1002/rmv.2223

Ando, Y., Noshi, T., Sato, K., Ishibashi, T., Yoshida, Y., Hasegawa, T., . . . Naito, A. (2021). Pharmacokinetic and pharmacodynamic analysis of baloxavir marboxil, a novel cap-dependent endonuclease inhibitor, in a murine model of influenza virus infection. *J Antimicrob Chemother, 76*(1), 189-198. doi:10.1093/jac/dkaa393

AstraZeneca. (2023a). A Study to Evaluate the Safety and Efficacy of MEDI8897 for the Prevention of Medically Attended Lower Respiratory Tract Infection Due to Respiratory Syncytial Virus in Healthy Late Preterm and Term Infants (MELODY) [Press release]. Retrieved from https://classic.clinicaltrials.gov/ct2/show/NCT03979313

AstraZeneca. (2023b). A Study to Evaluate the Safety of MEDI8897 for the Prevention of Medically Attended Respiratory Syncytial Virus(RSV) Lower Respiratory Track Infection (LRTI) in High-risk Children [Press release]. Retrieved from https://classic.clinicaltrials.gov/ct2/show/NCT03959488

Atal, I., Trinquart, L., Ravaud, P., & Porcher, R. (2018). A mapping of 115,000 randomized trials revealed a mismatch between research effort and health needs in non-high-income regions. *J Clin Epidemiol, 98*, 123-132. doi:10.1016/j.jclinepi.2018.01.006

Azzeri, A., Ramlee, M. N. A., Noor, M. I. M., Jaafar, M. H., Rocmah, T. N., & Dahlui, M. (2022). Economic Burden of SARS-CoV-2 Patients with Multi-Morbidity: A Systematic Review Protocol. *Int J Environ Res Public Health, 19*(20). doi:10.3390/ijerph192013157

Bartley, J. M., Cadar, A. N., & Martin, D. E. (2021). Better, Faster, Stronger: mRNA Vaccines Show Promise for Influenza Vaccination in Older Adults. *Immunol Invest, 50*(7), 810-820. doi:10.1080/08820139.2021.1909617

Bartley, J. M., Zhou, X., Kuchel, G. A., Weinstock, G. M., & Haynes, L. (2017). Impact of Age, Caloric Restriction, and Influenza Infection on Mouse Gut Microbiome: An Exploratory

Study of the Role of Age-Related Microbiome Changes on Influenza Responses. *Front Immunol, 8*, 1164. doi:10.3389/fimmu.2017.01164

Belshe, R. B., Richardson, L. S., London, W. T., Sly, D. L., Lorfeld, J. H., Camargo, E., . . . Chanock, R. M. (1977). Experimental respiratory syncytial virus infection of four species of primates. *J Med Virol, 1*(3), 157-162. doi:10.1002/jmv.1890010302

Blaurock, C., Breithaupt, A., Weber, S., Wylezich, C., Keller, M., Mohl, B. P., . . . Balkema-Buschmann, A. (2022). Compellingly high SARS-CoV-2 susceptibility of Golden Syrian hamsters suggests multiple zoonotic infections of pet hamsters during the COVID-19 pandemic. *Sci Rep, 12*(1), 15069. doi:10.1038/s41598-022-19222-4

Blount, R. E., Jr., Morris, J. A., & Savage, R. E. (1956). Recovery of cytopathogenic agent from chimpanzees with coryza. *Proc Soc Exp Biol Med, 92*(3), 544-549. doi:10.3181/00379727-92-22538

Boukhvalova, M. S., & Blanco, J. C. (2013). The cotton rat Sigmodon hispidus model of respiratory syncytial virus infection. *Curr Top Microbiol Immunol, 372*, 347-358. doi:10.1007/978-3-642-38919-1_17

Bradley, C. P., Teng, F., Felix, K. M., Sano, T., Naskar, D., Block, K. E., . . . Wu, H. J. (2017). Segmented Filamentous Bacteria Provoke Lung Autoimmunity by Inducing Gut-Lung Axis Th17 Cells Expressing Dual TCRs. *Cell Host Microbe, 22*(5), 697-704.e694. doi:10.1016/j.chom.2017.10.007

Brady, E., Nielsen, M. W., Andersen, J. P., & Oertelt-Prigione, S. (2021). Lack of consideration of sex and gender in COVID-19 clinical studies. *Nat Commun, 12*(1), 4015. doi:10.1038/s41467-021-24265-8

Bredella, M. A. (2017). Sex Differences in Body Composition. *Adv Exp Med Biol, 1043*, 9-27. doi:10.1007/978-3-319-70178-3_2

Brown, J. A., Sanidad, K. Z., Lucotti, S., Lieber, C. M., Cox, R. M., Ananthanarayanan, A., . . . Zeng, M. Y. (2022). Gut microbiota-derived metabolites confer protection against SARS-CoV-2 infection. *Gut Microbes, 14*(1), 2105609. doi:10.1080/19490976.2022.2105609

Byrd, L. G., & Prince, G. A. (1997). Animal models of respiratory syncytial virus infection. *Clin Infect Dis, 25*(6), 1363-1368. doi:10.1086/516152

Cai, H. (2020). Sex difference and smoking predisposition in patients with COVID-19. *Lancet Respir Med, 8*(4), e20. doi:10.1016/s2213-2600(20)30117-x

Cao, Z., Gao, W., Bao, H., Feng, H., Mei, S., Chen, P., . . . Zhao, R. (2023). VV116 versus Nirmatrelvir-Ritonavir for Oral Treatment of Covid-19. *N Engl J Med, 388*(5), 406-417. doi:10.1056/NEJMoa2208822

Castañeda, R. (2022). Overcoming obstacles in trans and nonbinary participation in clinical trials. *Clinical Trials Arena*. Retrieved from https://www.clinicaltrialsarena.com/news/transgender-clinical-trials/?cf-view

CDC. (2022a). Influenza Antiviral Drug Baloxavir Marboxil. Retrieved from https://www.cdc.gov/flu/treatment/baloxavir-marboxil.htm

CDC. (2022b). Influenza Antiviral Medications: Summary for Clinicians. Retrieved from https://www.cdc.gov/flu/professionals/antivirals/summary-clinicians.htm

CDC. (2023a, August 30, 2023). Healthcare Providers: RSV Vaccination for Adults 60 Years of Age and Over. Retrieved from https://www.cdc.gov/vaccines/vpd/rsv/hcp/older-adults.html

CDC. (2023b, April 26, 2023). RSV Transmission. Retrieved from https://www.cdc.gov/rsv/about/transmission.html

CDC. (2023c, November 3, 2022). U.S. Approaches Record Number of Avian Influenza Outbreaks in Wild Birds and Poultry. Retrieved from https://www.cdc.gov/flu/avianflu/spotlights/2022-2023/nearing-record-number-avian-influenza.htm

Chaturvedi, R., Lui, B., Aaronson, J. A., White, R. S., & Samuels, J. D. (2022). COVID-19 complications in males and females: recent developments. *J Comp Eff Res, 11*(9), 689-698. doi:10.2217/cer-2022-0027

Chauhan, R. P., & Gordon, M. L. (2022). An overview of influenza A virus genes, protein functions, and replication cycle highlighting important updates. *Virus Genes, 58*(4), 255-269. doi:10.1007/s11262-022-01904-w

Chen, H., Wang, L., Wang, X., Wang, X., Liu, H., & Yin, Y. (2020). Distribution and Strain Diversity of Immunoregulating Segmented Filamentous Bacteria in Human Intestinal Lavage Samples. *Microb Ecol, 79*(4), 1021-1033. doi:10.1007/s00248-019-01441-4

Chenchula, S., Karunakaran, P., Sharma, S., & Chavan, M. (2022). Current evidence on efficacy of COVID-19 booster dose vaccination against the Omicron variant: A systematic review. *J Med Virol, 94*(7), 2969-2976. doi:10.1002/jmv.27697

Choi, J. Y., & Smith, D. M. (2021). SARS-CoV-2 Variants of Concern. *Yonsei Med J, 62*(11), 961-968. doi:10.3349/ymj.2021.62.11.961

Chu, H., Chan, J. F., & Yuen, K. Y. (2022). Animal models in SARS-CoV-2 research. *Nat Methods, 19*(4), 392-394. doi:10.1038/s41592-022-01447-w

Chu, T. (2014). Gender Differences in Pharmacokinetics. *U.S.Pharmacist*. Retrieved from https://www.uspharmacist.com/article/gender-differences-in-pharmacokinetics#:~:text=Sex%20differences%20in%20metabolism%20(phase,in%20men%20than%20in%20women

CNN. (2023, August 4, 2023). CDC recommends new preventive RSV shot for all infants. Retrieved from https://www.cnn.com/2023/08/03/health/rsv-infant-nirsevimab-beyfortus-acip/index.html

Cooper, N. J., Sutton, A. J., Abrams, K. R., Wailoo, A., Turner, D., & Nicholson, K. G. (2003). Effectiveness of neuraminidase inhibitors in treatment and prevention of influenza A and B: systematic review and meta-analyses of randomised controlled trials. *Bmj, 326*(7401), 1235. doi:10.1136/bmj.326.7401.1235

Cox, R. M., Lieber, C. M., Wolf, J. D., Karimi, A., Lieberman, N. A. P., Sticher, Z. M., . . . Plemper, R. K. (2022). Paxlovid-like nirmatrelvir/ritonavir fails to block SARS-CoV-2 transmission in ferrets. *bioRxiv*. doi:10.1101/2022.11.20.517271

Cox, R. M., Lieber, C. M., Wolf, J. D., Karimi, A., Lieberman, N. A. P., Sticher, Z. M., . . . Plemper, R. K. (2023). Comparing molnupiravir and nirmatrelvir/ritonavir efficacy and the effects on SARS-CoV-2 transmission in animal models. *Nat Commun, 14*(1), 4731. doi:10.1038/s41467-023-40556-8

Cox, R. M., Toots, M., Yoon, J. J., Sourimant, J., Ludeke, B., Fearns, R., . . . Plemper, R. K. (2018). Development of an allosteric inhibitor class blocking RNA elongation by the respiratory syncytial virus polymerase complex. *J Biol Chem, 293*(43), 16761-16777. doi:10.1074/jbc.RA118.004862

Cox, R. M., Wolf, J. D., Lieber, C. M., Sourimant, J., Lin, M. J., Babusis, D., . . . Plemper, R. K. (2021). Oral prodrug of remdesivir parent GS-441524 is efficacious against SARS-CoV-2 in ferrets. *Nat Commun, 12*(1), 6415. doi:10.1038/s41467-021-26760-4

Cox, R. M., Wolf, J. D., & Plemper, R. K. (2021). Therapeutically administered ribonucleoside analogue MK-4482/EIDD-2801 blocks SARS-CoV-2 transmission in ferrets. *Nat Microbiol, 6*(1), 11-18. doi:10.1038/s41564-020-00835-2

Crook, H., Raza, S., Nowell, J., Young, M., & Edison, P. (2021). Long covid-mechanisms, risk factors, and management. *Bmj, 374*, n1648. doi:10.1136/bmj.n1648

Crowe, J. E., Jr., Bui, P. T., Davis, A. R., Chanock, R. M., & Murphy, B. R. (1994). A further attenuated derivative of a cold-passaged temperature-sensitive mutant of human respiratory syncytial virus retains immunogenicity and protective efficacy against wild-type challenge in seronegative chimpanzees. *Vaccine, 12*(9), 783-790. doi:10.1016/0264-410x(94)90286-0

Crowe, J. E., Jr., Collins, P. L., London, W. T., Chanock, R. M., & Murphy, B. R. (1993). A comparison in chimpanzees of the immunogenicity and efficacy of live attenuated respiratory syncytial virus (RSV) temperature-sensitive mutant vaccines and vaccinia virus recombinants that express the surface glycoproteins of RSV. *Vaccine, 11*(14), 1395-1404. doi:10.1016/0264-410x(93)90168-w

Dubey, S., Biswas, P., Ghosh, R., Chatterjee, S., Dubey, M. J., Chatterjee, S., . . . Lavie, C. J. (2020). Psychosocial impact of COVID-19. *Diabetes Metab Syndr, 14*(5), 779-788. doi:10.1016/j.dsx.2020.05.035

Eisfeld, A. J., Gasper, D. J., Suresh, M., & Kawaoka, Y. (2018). C57BL/6J and C57BL/6NJ Mice Are Differentially Susceptible to Inflammation-Associated Disease Caused by Influenza A Virus. *Front Microbiol, 9*, 3307. doi:10.3389/fmicb.2018.03307

El-Sayed, A., Aleya, L., & Kamel, M. (2021). Microbiota's role in health and diseases. *Environ Sci Pollut Res Int, 28*(28), 36967-36983. doi:10.1007/s11356-021-14593-z

Elderfield, R., & Barclay, W. (2011). Influenza pandemics. *Adv Exp Med Biol, 719*, 81-103. doi:10.1007/978-1-4614-0204-6_8

Falsey, A. R., Hennessey, P. A., Formica, M. A., Cox, C., & Walsh, E. E. (2005). Respiratory syncytial virus infection in elderly and high-risk adults. *N Engl J Med, 352*(17), 1749-1759. doi:10.1056/NEJMoa043951

FDA. (2023a, May 03, 2023). FDA Approves First Respiratory Syncytial Virus (RSV) Vaccine. *Arexvy Approved for Individuals 60 Years of Age and Older.* Retrieved from https://www.fda.gov/news-events/press-announcements/fda-approves-first-respiratory-syncytial-virus-rsv-vaccine

FDA. (2023b). FDA Approves New Drug to Prevent RSV in Babies and Toddlers. Retrieved from https://www.fda.gov/news-events/press-announcements/fda-approves-new-drug-prevent-rsv-babies-and-toddlers

Fineberg, H. V. (2014). Pandemic preparedness and response--lessons from the H1N1 influenza of 2009. *N Engl J Med, 370*(14), 1335-1342. doi:10.1056/NEJMra1208802

Fiore, A. E., Fry, A., Shay, D., Gubareva, L., Bresee, J. S., & Uyeki, T. M. (2011). Antiviral agents for the treatment and chemoprophylaxis of influenza --- recommendations of the Advisory Committee on Immunization Practices (ACIP). *MMWR Recomm Rep, 60*(1), 1-24.

Florescu, D. F., & Kalil, A. C. (2014). The complex link between influenza and severe sepsis. *Virulence, 5*(1), 137-142. doi:10.4161/viru.27103

Fredell, E. (2023). Gut Microbiome Communication: The Gut-Organ Axis. *American Society for Microbiology*. Retrieved from https://asm.org/Articles/2023/January/Gut-Microbiome-Communication-The-Gut-Organ-Axis#:~:text=The%20gut%2Dorgan%20axis%20is,gut%20microbiome%20affects%20human%20health.

Gaebler, C., Wang, Z., Lorenzi, J. C. C., Muecksch, F., Finkin, S., Tokuyama, M., . . . Nussenzweig, M. C. (2021). Evolution of antibody immunity to SARS-CoV-2. *Nature, 591*(7851), 639-644. doi:10.1038/s41586-021-03207-w

Gaitonde, D. Y., Moore, F. C., & Morgan, M. K. (2019). Influenza: Diagnosis and Treatment. *Am Fam Physician, 100*(12), 751-758. Retrieved from https://www.aafp.org/dam/brand/aafp/pubs/afp/issues/2019/1215/p751.pdf

Gieber, L., Muturi-Kioi, V., Malhotra, S., & Sitlani, A. (2023). Clinical and Regulatory Challenges and Opportunities for Monoclonal Antibodies in Low- and Middle-Income Countries: Lessons from COVID-19 and Beyond. *Pharmaceut Med, 37*(3), 203-214. doi:10.1007/s40290-023-00473-z

Godshall, C. E., & Banach, D. B. (2021). Pandemic Preparedness. *Infect Dis Clin North Am, 35*(4), 1077-1089. doi:10.1016/j.idc.2021.07.008

Golden, J. W., Li, R., Cline, C. R., Zeng, X., Mucker, E. M., Fuentes-Lao, A. J., . . . Hooper, J. W. (2022). Hamsters Expressing Human Angiotensin-Converting Enzyme 2 Develop Severe Disease following Exposure to SARS-CoV-2. *mBio, 13*(1), e0290621. doi:10.1128/mbio.02906-21

Gopalakrishnan, V., Helmink, B. A., Spencer, C. N., Reuben, A., & Wargo, J. A. (2018). The Influence of the Gut Microbiome on Cancer, Immunity, and Cancer Immunotherapy. *Cancer Cell, 33*(4), 570-580. doi:10.1016/j.ccell.2018.03.015

Gottlieb, R. L., Vaca, C. E., Paredes, R., Mera, J., Webb, B. J., Perez, G., . . . Hill, J. A. (2022). Early Remdesivir to Prevent Progression to Severe Covid-19 in Outpatients. *N Engl J Med, 386*(4), 305-315. doi:10.1056/NEJMoa2116846

Greco, S., Fabbri, N., Bella, A., Bonsi, B., Parini, S., Rocchi, C., . . . Feo, C. V. (2021). COVID-19 inpatients with gastrointestinal onset: sex and care needs' differences in the district of Ferrara, Italy. *BMC Infect Dis, 21*(1), 739. doi:10.1186/s12879-021-06476-y

Griffiths, C., Drews, S. J., & Marchant, D. J. (2017). Respiratory Syncytial Virus: Infection, Detection, and New Options for Prevention and Treatment. *Clin Microbiol Rev, 30*(1), 277-319. doi:10.1128/cmr.00010-16

Hammond, J., Leister-Tebbe, H., Gardner, A., Abreu, P., Bao, W., Wisemandle, W., . . . Rusnak, J. M. (2022). Oral Nirmatrelvir for High-Risk, Nonhospitalized Adults with Covid-19. *N Engl J Med, 386*(15), 1397-1408. doi:10.1056/NEJMoa2118542

Hayden, F. G., Atmar, R. L., Schilling, M., Johnson, C., Poretz, D., Paar, D., . . . Mills, R. G. (1999). Use of the selective oral neuraminidase inhibitor oseltamivir to prevent influenza. *N Engl J Med, 341*(18), 1336-1343. doi:10.1056/nejm199910283411802

Hayden, F. G., Sugaya, N., Hirotsu, N., Lee, N., de Jong, M. D., Hurt, A. C., . . . Watanabe, A. (2018). Baloxavir Marboxil for Uncomplicated Influenza in Adults and Adolescents. *N Engl J Med, 379*(10), 913-923. doi:10.1056/NEJMoa1716197

Hegele, R. G., Robinson, P. J., Gonzalez, S., & Hogg, J. C. (1993). Production of acute bronchiolitis in guinea-pigs by human respiratory syncytial virus. *Eur Respir J, 6*(9), 1324-1331.

Heintz-Buschart, A., & Wilmes, P. (2018). Human Gut Microbiome: Function Matters. *Trends Microbiol, 26*(7), 563-574. doi:10.1016/j.tim.2017.11.002

Hernandez, I., Bott, S. W., Patel, A. S., Wolf, C. G., Hospodar, A. R., Sampathkumar, S., & Shrank, W. H. (2018). Pricing of monoclonal antibody therapies: higher if used for cancer? *Am J Manag Care, 24*(2), 109-112.

Hersh, A. L., Maselli, J. H., & Cabana, M. D. (2009). Changes in prescribing of antiviral medications for influenza associated with new treatment guidelines. *Am J Public Health, 99 Suppl 2*(Suppl 2), S362-364. doi:10.2105/ajph.2009.171462

Hoffmann, M., Kleine-Weber, H., Schroeder, S., Krüger, N., Herrler, T., Erichsen, S., . . . Pöhlmann, S. (2020). SARS-CoV-2 Cell Entry Depends on ACE2 and TMPRSS2 and Is Blocked by a Clinically Proven Protease Inhibitor. *Cell, 181*(2), 271-280.e278. doi:10.1016/j.cell.2020.02.052

Howard, M. C. (2021). Gender, face mask perceptions, and face mask wearing: Are men being dangerous during the COVID-19 pandemic? *Pers Individ Dif, 170*, 110417. doi:10.1016/j.paid.2020.110417

Hsieh, Y. C., Wu, T. Z., Liu, D. P., Shao, P. L., Chang, L. Y., Lu, C. Y., . . . Huang, L. M. (2006). Influenza pandemics: past, present and future. *J Formos Med Assoc, 105*(1), 1-6. doi:10.1016/s0929-6646(09)60102-9

Hu, K., Lin, L., Liang, Y., Shao, X., Hu, Z., Luo, H., & Lei, M. (2021). COVID-19: risk factors for severe cases of the Delta variant. *Aging (Albany NY), 13*(20), 23459-23470. doi:10.18632/aging.203655

Hui, D. S. C., & Zumla, A. (2019). Severe Acute Respiratory Syndrome: Historical, Epidemiologic, and Clinical Features. *Infect Dis Clin North Am, 33*(4), 869-889. doi:10.1016/j.idc.2019.07.001

Jayk Bernal, A., Gomes da Silva, M. M., Musungaie, D. B., Kovalchuk, E., Gonzalez, A., Delos Reyes, V., . . . De Anda, C. (2022). Molnupiravir for Oral Treatment of Covid-19 in Nonhospitalized Patients. *N Engl J Med, 386*(6), 509-520. doi:10.1056/NEJMoa2116044

Jensen, A., Stromme, M., Moyassari, S., Chadha, A. S., Tartaglia, M. C., Szoeke, C., & Ferretti, M. T. (2022). COVID-19 vaccines: Considering sex differences in efficacy and safety. *Contemp Clin Trials, 115*, 106700. doi:10.1016/j.cct.2022.106700

Jonsson, H., Hugerth, L. W., Sundh, J., Lundin, E., & Andersson, A. F. (2020). Genome sequence of segmented filamentous bacteria present in the human intestine. *Commun Biol, 3*(1), 485. doi:10.1038/s42003-020-01214-7

Juozapaitis, M., & Antoniukas, L. (2007). [Influenza virus]. *Medicina (Kaunas), 43*(12), 919-929.

Kabinger, F., Stiller, C., Schmitzová, J., Dienemann, C., Kokic, G., Hillen, H. S., . . . Cramer, P. (2021). Mechanism of molnupiravir-induced SARS-CoV-2 mutagenesis. *Nat Struct Mol Biol, 28*(9), 740-746. doi:10.1038/s41594-021-00651-0

Kardas, P. (2007). Comparison of patient compliance with once-daily and twice-daily antibiotic regimens in respiratory tract infections: results of a randomized trial. *J Antimicrob Chemother, 59*(3), 531-536. doi:10.1093/jac/dkl528

Keilman, L. J. (2019). Seasonal Influenza (Flu). *Nurs Clin North Am, 54*(2), 227-243. doi:10.1016/j.cnur.2019.02.009

Kelley, B. (2020). Developing therapeutic monoclonal antibodies at pandemic pace. *Nat Biotechnol, 38*(5), 540-545. doi:10.1038/s41587-020-0512-5

Kido, H., Chida, J., Yao, M., & Wang, S. (2010). [Mechanisms of multi-organ failure in severe influenza]. *Nihon Rinsho, 68*(8), 1565-1573.

Kiso, M., Yamayoshi, S., Murakami, J., & Kawaoka, Y. (2020). Baloxavir Marboxil Treatment of Nude Mice Infected With Influenza A Virus. *J Infect Dis, 221*(10), 1699-1702. doi:10.1093/infdis/jiz665

Kokic, G., Hillen, H. S., Tegunov, D., Dienemann, C., Seitz, F., Schmitzova, J., . . . Cramer, P. (2021). Mechanism of SARS-CoV-2 polymerase stalling by remdesivir. *Nat Commun, 12*(1), 279. doi:10.1038/s41467-020-20542-0

Krammer, F., Smith, G. J. D., Fouchier, R. A. M., Peiris, M., Kedzierska, K., Doherty, P. C., . . . García-Sastre, A. (2018). Influenza. *Nat Rev Dis Primers, 4*(1), 3. doi:10.1038/s41572-018-0002-y

Lakbar, I., Luque-Paz, D., Mege, J. L., Einav, S., & Leone, M. (2020). COVID-19 gender susceptibility and outcomes: A systematic review. *PLoS One, 15*(11), e0241827. doi:10.1371/journal.pone.0241827

Laufer, R. S., Driscoll, A. J., Baral, R., Buchwald, A. G., Campbell, J. D., Coulibaly, F., . . . Fitzpatrick, M. C. (2021). Cost-effectiveness of infant respiratory syncytial virus preventive interventions in Mali: A modeling study to inform policy and investment decisions. *Vaccine, 39*(35), 5037-5045. doi:10.1016/j.vaccine.2021.06.086

Lauring, A. S., Tenforde, M. W., Chappell, J. D., Gaglani, M., Ginde, A. A., McNeal, T., . . . Self, W. H. (2022). Clinical severity of, and effectiveness of mRNA vaccines against, covid-19 from omicron, delta, and alpha SARS-CoV-2 variants in the United States: prospective observational study. *Bmj, 376*, e069761. doi:10.1136/bmj-2021-069761

Leroux-Roels, I., Davis, M. G., Steenackers, K., Essink, B., Vandermeulen, C., Fogarty, C., . . . Hulstrøm, V. (2023). Safety and Immunogenicity of a Respiratory Syncytial Virus Prefusion F (RSVPreF3) Candidate Vaccine in Older Adults: Phase 1/2 Randomized Clinical Trial. *J Infect Dis, 227*(6), 761-772. doi:10.1093/infdis/jiac327

Lieber, C. M., Aggarwal, M., Yoon, J. J., Cox, R. M., Kang, H. J., Sourimant, J., . . . Plemper, R. K. (2023). 4'-Fluorouridine mitigates lethal infection with pandemic human and highly pathogenic avian influenza viruses. *PLoS Pathog, 19*(4), e1011342. doi:10.1371/journal.ppat.1011342

Lieber, C. M., Cox, R. M., Sourimant, J., Wolf, J. D., Juergens, K., Phung, Q., . . . Plemper, R. K. (2022). SARS-CoV-2 VOC type and biological sex affect molnupiravir efficacy in severe COVID-19 dwarf hamster model. *Nat Commun, 13*(1), 4416. doi:10.1038/s41467-022-32045-1

Lieber, C. M., & Plemper, R. K. (2022). 4'-Fluorouridine Is a Broad-Spectrum Orally Available First-Line Antiviral That May Improve Pandemic Preparedness. *DNA Cell Biol, 41*(8), 699-704. doi:10.1089/dna.2022.0312

Liu, E., Lee, H., Lui, B., White, R. S., & Samuels, J. D. (2022). Respiratory and nonrespiratory COVID-19 complications in patients with obesity: recent developments. *J Comp Eff Res, 11*(5), 371-381. doi:10.2217/cer-2021-0237

Liu, J., Pan, X., Zhang, S., Li, M., Ma, K., Fan, C., . . . Chen, D. (2023). Efficacy and safety of Paxlovid in severe adult patients with SARS-Cov-2 infection: a multicenter randomized controlled study. *Lancet Reg Health West Pac, 33*, 100694. doi:10.1016/j.lanwpc.2023.100694

LLC, M. (2019). *A Study to Evaluate the Safety and Efficacy of MEDI8897 for the Prevention of Medically Attended RSV LRTI in Healthy Preterm Infants. (MEDI8897 Ph2b)*. Retrieved from https://classic.clinicaltrials.gov/ct2/show/NCT02878330

Lu, S., Zhao, Y., Yu, W., Yang, Y., Gao, J., Wang, J., . . . Peng, X. (2020). Comparison of nonhuman primates identified the suitable model for COVID-19. *Signal Transduct Target Ther, 5*(1), 157. doi:10.1038/s41392-020-00269-6

Machitani, M., Yasukawa, M., Nakashima, J., Furuichi, Y., & Masutomi, K. (2020). RNA-dependent RNA polymerase, RdRP, a promising therapeutic target for cancer and potentially COVID-19. *Cancer Sci, 111*(11), 3976-3984. doi:10.1111/cas.14618

Marriott, A. C., Gooch, K. E., Brown, P. J., Ryan, K. A., Jones, N. J., Merredew, N., . . . Carroll, M. W. (2021). Severity of heterosubtypic influenza virus infection in ferrets is reduced by live attenuated influenza vaccine. *NPJ Vaccines, 6*(1), 43. doi:10.1038/s41541-021-00306-7

Meletis, G., Tychala, A., Gkeka, I., Gkotzia, A., Triantafyllou, A., Pappa, S., . . . Skoura, L. (2022). Clinical Performance Evaluation of the NeuMoDx Flu A-B/RSV/SARS-CoV-2 Vantage Assay. *Diagnostics (Basel), 12*(12). doi:10.3390/diagnostics12123201

Mostafa, H. H., Carroll, K. C., Hicken, R., Berry, G. J., Manji, R., Smith, E., . . . Loeffelholz, M. J. (2021). Multicenter Evaluation of the Cepheid Xpert Xpress SARS-CoV-2/Flu/RSV Test. *J Clin Microbiol, 59*(3). doi:10.1128/jcm.02955-20

Nasir, N., Jamil, B., Siddiqui, S., Talat, N., Khan, F. A., & Hussain, R. (2015). Mortality in Sepsis and its relationship with Gender. *Pak J Med Sci, 31*(5), 1201-1206. doi:10.12669/pjms.315.6925

Ng, K. E. (2019). Xofluza (Baloxavir Marboxil) for the Treatment Of Acute Uncomplicated Influenza. *P t, 44*(1), 9-11.

Ngo, V., Lieber, C., Kang, H.-j., Sakomoto, K., Kuczma, M. P., Plemper, R. K., & Gewirtz, A. T. (2023). Intestinal microbiota programming of alveolar macrophages influences severity of respiratory viral infection. *bioRxiv*, 2023.2009.2021.558814. doi:10.1101/2023.09.21.558814

Ngo, V. L., Shi, Z., Jiang, B., & Gewirtz, A. T. (2023). Segmented filamentous bacteria impede rotavirus infection via retinoic acid receptor-mediated signaling. *Gut Microbes, 15*(1), 2174407. doi:10.1080/19490976.2023.2174407

NIH. (2022a). Respiratory Syncytial Virus - Diseases and Conditions. Retrieved from https://www.niaid.nih.gov/diseases-conditions/respiratory-syncytial-virus-rsv

NIH. (2022b). Rheumatoid Arthritis. Retrieved from https://www.niams.nih.gov/health-topics/rheumatoid-arthritis#:~:text=Rheumatoid%20arthritis%20(RA)%20is%20a,loss%20of%20function%20in%20joints.

Nogales, A., Baker, S. F., & Martínez-Sobrido, L. (2015). Replication-competent influenza A viruses expressing a red fluorescent protein. *Virology, 476*, 206-216. doi:10.1016/j.virol.2014.12.006

Nypaver, C., Dehlinger, C., & Carter, C. (2021). Influenza and Influenza Vaccine: A Review. *J Midwifery Womens Health, 66*(1), 45-53. doi:10.1111/jmwh.13203

Oladunni, F. S., Park, J. G., Pino, P. A., Gonzalez, O., Akhter, A., Allué-Guardia, A., . . . Torrelles, J. B. (2020). Lethality of SARS-CoV-2 infection in K18 human angiotensin-converting enzyme 2 transgenic mice. *Nat Commun, 11*(1), 6122. doi:10.1038/s41467-020-19891-7

Olivier, A., Gallup, J., de Macedo, M. M., Varga, S. M., & Ackermann, M. (2009). Human respiratory syncytial virus A2 strain replicates and induces innate immune responses by respiratory epithelia of neonatal lambs. *Int J Exp Pathol, 90*(4), 431-438. doi:10.1111/j.1365-2613.2009.00643.x

Olson, A. L., Swigris, J. J., Sprunger, D. B., Fischer, A., Fernandez-Perez, E. R., Solomon, J., . . . Brown, K. K. (2011). Rheumatoid arthritis-interstitial lung disease-associated mortality. *Am J Respir Crit Care Med, 183*(3), 372-378. doi:10.1164/rccm.201004-0622OC

Oncodesign-services. (2023). Using Microbiome insights in discovery and preclinical services. *Non-exhaustive list of pathologies related to microbiome disorders.* Retrieved from https://www.oncodesign-services.com/microbiome/

Openshaw, P. J. (2013). The mouse model of respiratory syncytial virus disease. *Curr Top Microbiol Immunol, 372*, 359-369. doi:10.1007/978-3-642-38919-1_18

Orlando, V., Mucherino, S., Guarino, I., Guerriero, F., Trama, U., & Menditto, E. (2020). Gender Differences in Medication Use: A Drug Utilization Study Based on Real World Data. *Int J Environ Res Public Health, 17*(11). doi:10.3390/ijerph17113926

Owen, D. R., Allerton, C. M. N., Anderson, A. S., Aschenbrenner, L., Avery, M., Berritt, S., . . . Zhu, Y. (2021). An oral SARS-CoV-2 M(pro) inhibitor clinical candidate for the treatment of COVID-19. *Science, 374*(6575), 1586-1593. doi:10.1126/science.abl4784

Pfizer. (2023, May 31, 2023). U.S. FDA Approves ABRYSVO™, Pfizer's Vaccine for the Prevention of Respiratory Syncytial Virus (RSV) in Older Adults. Retrieved from https://www.pfizer.com/news/press-release/press-release-detail/us-fda-approves-abrysvotm-pfizers-vaccine-prevention

Pica, N., Chou, Y. Y., Bouvier, N. M., & Palese, P. (2012). Transmission of influenza B viruses in the guinea pig. *J Virol, 86*(8), 4279-4287. doi:10.1128/jvi.06645-11

Pleschka, S. (2013). Overview of influenza viruses. *Curr Top Microbiol Immunol, 370*, 1-20. doi:10.1007/82_2012_272

Price, C. E., & O'Toole, G. A. (2021). The Gut-Lung Axis in Cystic Fibrosis. *J Bacteriol, 203*(20), e0031121. doi:10.1128/jb.00311-21

Prince, G. A., Horswood, R. L., Berndt, J., Suffin, S. C., & Chanock, R. M. (1979). Respiratory syncytial virus infection in inbred mice. *Infect Immun, 26*(2), 764-766. doi:10.1128/iai.26.2.764-766.1979

Prince, G. A., & Porter, D. D. (1976). The pathogenesis of respiratory syncytial virus infection in infant ferrets. *Am J Pathol, 82*(2), 339-352. Retrieved from https://www.ncbi.nlm.nih.gov/pmc/articles/PMC2032397/pdf/amjpathol00453-0105.pdf

Pruijssers, A. J., George, A. S., Schäfer, A., Leist, S. R., Gralinksi, L. E., Dinnon, K. H., 3rd, . . . Sheahan, T. P. (2020). Remdesivir Inhibits SARS-CoV-2 in Human Lung Cells and Chimeric SARS-CoV Expressing the SARS-CoV-2 RNA Polymerase in Mice. *Cell Rep, 32*(3), 107940. doi:10.1016/j.celrep.2020.107940

Radovanovic, M., Petrovic, M., Barsoum, M. K., Nordstrom, C. W., Calvin, A. D., Dumic, I., . . . Hanna, R. D. (2022). Influenza Myopericarditis and Pericarditis: A Literature Review. *J Clin Med, 11*(14). doi:10.3390/jcm11144123

Raman, R., Patel, K. J., & Ranjan, K. (2021). COVID-19: Unmasking Emerging SARS-CoV-2 Variants, Vaccines and Therapeutic Strategies. *Biomolecules, 11*(7). doi:10.3390/biom11070993

Ramírez-Soto, M. C., Ortega-Cáceres, G., & Arroyo-Hernández, H. (2021). Sex differences in COVID-19 fatality rate and risk of death: An analysis in 73 countries, 2020-2021. *Infez Med, 29*(3), 402-407. doi:10.53854/liim-2903-11

Rodriguez, L., Nogales, A., & Martínez-Sobrido, L. (2017). Influenza A Virus Studies in a Mouse Model of Infection. *J Vis Exp*(127). doi:10.3791/55898

Schofield, D. (2022). What are disadvantages of monoclonal antibodies? *evitria*. Retrieved from https://www.evitria.com/journal/monoclonal-antibodies/disadvantages-monoclonal-antibodies/

Shanks, G. D., & Brundage, J. F. (2012). Pathogenic responses among young adults during the 1918 influenza pandemic. *Emerg Infect Dis, 18*(2), 201-207. doi:10.3201/eid1802.102042

Sharma, A., Ahmad Farouk, I., & Lal, S. K. (2021). COVID-19: A Review on the Novel Coronavirus Disease Evolution, Transmission, Detection, Control and Prevention. *Viruses, 13*(2). doi:10.3390/v13020202

Sharma, A., Wu, W., Sung, B., Huang, J., Tsao, T., Li, X., . . . Worgall, S. (2016). Respiratory Syncytial Virus (RSV) Pulmonary Infection in Humanized Mice Induces Human Anti-RSV Immune Responses and Pathology. *J Virol, 90*(10), 5068-5074. doi:10.1128/jvi.00259-16

Sia, S. F., Yan, L. M., Chin, A. W. H., Fung, K., Choy, K. T., Wong, A. Y. L., . . . Yen, H. L. (2020). Pathogenesis and transmission of SARS-CoV-2 in golden hamsters. *Nature, 583*(7818), 834-838. doi:10.1038/s41586-020-2342-5

Smith, D. K., Seales, S., & Budzik, C. (2017). Respiratory Syncytial Virus Bronchiolitis in Children. *Am Fam Physician, 95*(2), 94-99. Retrieved from https://www.aafp.org/dam/brand/aafp/pubs/afp/issues/2017/0115/p94.pdf

Smoking prevalence and attributable disease burden in 195 countries and territories, 1990-2015: a systematic analysis from the Global Burden of Disease Study 2015. (2017). *Lancet, 389*(10082), 1885-1906. doi:10.1016/s0140-6736(17)30819-x

Soldin, O. P., & Mattison, D. R. (2009). Sex differences in pharmacokinetics and pharmacodynamics. *Clin Pharmacokinet, 48*(3), 143-157. doi:10.2165/00003088-200948030-00001

Solomou, I., & Constantinidou, F. (2020). Prevalence and Predictors of Anxiety and Depression Symptoms during the COVID-19 Pandemic and Compliance with Precautionary Measures: Age and Sex Matter. *Int J Environ Res Public Health, 17*(14). doi:10.3390/ijerph17144924

Sourimant, J., Lieber, C. M., Aggarwal, M., Cox, R. M., Wolf, J. D., Yoon, J. J., . . . Plemper, R. K. (2022). 4'-Fluorouridine is an oral antiviral that blocks respiratory syncytial virus and SARS-CoV-2 replication. *Science, 375*(6577), 161-167. doi:10.1126/science.abj5508

Sourimant, J., Lieber, C. M., Yoon, J. J., Toots, M., Govindarajan, M., Udumula, V., . . . Plemper, R. K. (2022). Orally efficacious lead of the AVG inhibitor series targeting a dynamic interface in the respiratory syncytial virus polymerase. *Sci Adv, 8*(25), eabo2236. doi:10.1126/sciadv.abo2236

Steinbrück, L., Klingen, T. R., & McHardy, A. C. (2014). Computational prediction of vaccine strains for human influenza A (H3N2) viruses. *J Virol, 88*(20), 12123-12132. doi:10.1128/jvi.01861-14

Sutton, T. C. (2018). The Pandemic Threat of Emerging H5 and H7 Avian Influenza Viruses. *Viruses, 10*(9). doi:10.3390/v10090461

Tarsitani, L., Vassalini, P., Koukopoulos, A., Borrazzo, C., Alessi, F., Di Nicolantonio, C., . . . d'Ettorre, G. (2021). Post-traumatic Stress Disorder Among COVID-19 Survivors at 3-Month Follow-up After Hospital Discharge. *J Gen Intern Med, 36*(6), 1702-1707. doi:10.1007/s11606-021-06731-7

Taubenberger, J. K., & Kash, J. C. (2010). Influenza virus evolution, host adaptation, and pandemic formation. *Cell Host Microbe, 7*(6), 440-451. doi:10.1016/j.chom.2010.05.009

Taubenberger, J. K., & Morens, D. M. (2006). 1918 Influenza: the mother of all pandemics. *Emerg Infect Dis, 12*(1), 15-22. doi:10.3201/eid1201.050979

Taylor, G. (2017). Animal models of respiratory syncytial virus infection. *Vaccine, 35*(3), 469-480. doi:10.1016/j.vaccine.2016.11.054

Tejus, A., Mathur, A. G., Pradhan, S., Malik, S., & Salmani, M. F. (2022). Drug update - Baloxavir marboxil: Latest entrant into the arena of pharmacotherapy of influenza. *Med J Armed Forces India, 78*(2), 125-130. doi:10.1016/j.mjafi.2021.09.005

Teng, F., Klinger, C. N., Felix, K. M., Bradley, C. P., Wu, E., Tran, N. L., . . . Wu, H. J. (2016). Gut Microbiota Drive Autoimmune Arthritis by Promoting Differentiation and Migration of Peyer's Patch T Follicular Helper Cells. *Immunity, 44*(4), 875-888. doi:10.1016/j.immuni.2016.03.013

Terrie, Y. C. (2022). Antiviral Recommendations for the 2022–2023 Influenza Season. *U.S.Pharmacist*. Retrieved from https://www.uspharmacist.com/article/antiviral-recommendations-for-the-2022-2023-influenza-season#:~:text=For%20the%202022–2023%20influenza%20season%2C%20the%20CDC%20recommends%20the,%2C%20peramivir%2C%20and%20baloxavir%20marboxil.

Thangavel, R. R., & Bouvier, N. M. (2014). Animal models for influenza virus pathogenesis, transmission, and immunology. *J Immunol Methods, 410*, 60-79. doi:10.1016/j.jim.2014.03.023

Tian, L., Qiang, T., Liang, C., Ren, X., Jia, M., Zhang, J., . . . Liu, H. (2021). RNA-dependent RNA polymerase (RdRp) inhibitors: The current landscape and repurposing for the COVID-19 pandemic. *Eur J Med Chem, 213*, 113201. doi:10.1016/j.ejmech.2021.113201

Toots, M., Yoon, J. J., Hart, M., Natchus, M. G., Painter, G. R., & Plemper, R. K. (2020). Quantitative efficacy paradigms of the influenza clinical drug candidate EIDD-2801 in the ferret model. *Transl Res, 218*, 16-28. doi:10.1016/j.trsl.2019.12.002

Toth-Manikowski, S. M., Caldwell, J., Joo, M., Chen, J., Meza, N., Bruinius, J., . . . Ricardo, A. C. (2021). Sex-related differences in mortality, acute kidney injury, and respiratory failure among critically ill patients with COVID-19. *Medicine (Baltimore), 100*(50), e28302. doi:10.1097/md.0000000000028302

Trimpert, J., Vladimirova, D., Dietert, K., Abdelgawad, A., Kunec, D., Dokel, S., . . . Osterrieder, N. (2020). The Roborovski Dwarf Hamster Is A Highly Susceptible Model for a Rapid and

Fatal Course of SARS-CoV-2 Infection. *Cell Rep, 33*(10), 108488. doi:10.1016/j.celrep.2020.108488

Trimpert, J., Vladimirova, D., Dietert, K., Abdelgawad, A., Kunec, D., Dökel, S., . . . Osterrieder, N. (2020). The Roborovski Dwarf Hamster Is A Highly Susceptible Model for a Rapid and Fatal Course of SARS-CoV-2 Infection. *Cell Rep, 33*(10), 108488. doi:10.1016/j.celrep.2020.108488

Ulbegi Polat, H., Abaci, I., Tas Ekiz, A., Aksoy, O., Oktelik, F. B., Yilmaz, V., . . . Deniz, G. (2023). Therapeutic Effect of C-Vx Substance in K18-hACE2 Transgenic Mice Infected with SARS-CoV-2. *Int J Mol Sci, 24*(15). doi:10.3390/ijms241511957

Uraki, R., Kiso, M., Iida, S., Imai, M., Takashita, E., Kuroda, M., . . . Kawaoka, Y. (2022). Characterization and antiviral susceptibility of SARS-CoV-2 Omicron BA.2. *Nature, 607*(7917), 119-127. doi:10.1038/s41586-022-04856-1

Uyeki, T. M. (2017). Influenza. *Ann Intern Med, 167*(5), Itc33-itc48. doi:10.7326/aitc201709050

V'Kovski, P., Kratzel, A., Steiner, S., Stalder, H., & Thiel, V. (2021). Coronavirus biology and replication: implications for SARS-CoV-2. *Nat Rev Microbiol, 19*(3), 155-170. doi:10.1038/s41579-020-00468-6

Vandamme, T. F. (2014). Use of rodents as models of human diseases. *J Pharm Bioallied Sci, 6*(1), 2-9. doi:10.4103/0975-7406.124301

Vicenti, I., Zazzi, M., & Saladini, F. (2021). SARS-CoV-2 RNA-dependent RNA polymerase as a therapeutic target for COVID-19. *Expert Opin Ther Pat, 31*(4), 325-337. doi:10.1080/13543776.2021.1880568

Waddick, K. (2023). Transgender patients are rarely included in clinical trials. Can pharma fix it? *PharmaVoice*. Retrieved from https://www.pharmavoice.com/news/transgender-nonbinary-clinical-trial-diversity/654213/

Wang, C. C., Prather, K. A., Sznitman, J., Jimenez, J. L., Lakdawala, S. S., Tufekci, Z., & Marr, L. C. (2021). Airborne transmission of respiratory viruses. *Science, 373*(6558). doi:10.1126/science.abd9149

Wang, D., Zhu, W., Yang, L., & Shu, Y. (2021). The Epidemiology, Virology, and Pathogenicity of Human Infections with Avian Influenza Viruses. *Cold Spring Harb Perspect Med, 11*(4). doi:10.1101/cshperspect.a038620

Webster, R. G., & Govorkova, E. A. (2014). Continuing challenges in influenza. *Ann N Y Acad Sci, 1323*(1), 115-139. doi:10.1111/nyas.12462

WHO. (2022). The number of Flu cases Worldwide: A global perspective. Retrieved from https://www.familiesfightingflu.org/number-of-flu-cases-worldwide/#:~:text=Here%20are%20some%20statistics%20on,case%20of%20flu%20each%20year

WHO. (2023). WHO Coronavirus (COVID-19) Dashboard. Retrieved from https://covid19.who.int

Williams, T. C., Sinha, I., Barr, I. G., & Zambon, M. (2021). Transmission of paediatric respiratory syncytial virus and influenza in the wake of the COVID-19 pandemic. *Euro Surveill, 26*(29). doi:10.2807/1560-7917.Es.2021.26.29.2100186

Womersley, K., Ripullone, K., Peters, S. A., & Woodward, M. (2020). Covid-19: Male disadvantage highlights the importance of sex disaggregated data. *Bmj, 370*, m2870. doi:10.1136/bmj.m2870

Wong, Z. X., Jones, J. E., Anderson, G. P., & Gualano, R. C. (2011). Oseltamivir treatment of mice before or after mild influenza infection reduced cellular and cytokine inflammation in the lung. *Influenza Other Respir Viruses, 5*(5), 343-350. doi:10.1111/j.1750-2659.2011.00235.x

Wright, P. F., Woodend, W. G., & Chanock, R. M. (1970). Temperature-sensitive mutants of respiratory syncytial virus: in-vivo studies in hamsters. *J Infect Dis, 122*(6), 501-512. doi:10.1093/infdis/122.6.501

Wu, B. N., & O'Sullivan, A. J. (2011). Sex differences in energy metabolism need to be considered with lifestyle modifications in humans. *J Nutr Metab, 2011*, 391809. doi:10.1155/2011/391809

Wu, H. J., Ivanov, II, Darce, J., Hattori, K., Shima, T., Umesaki, Y., . . . Mathis, D. (2010). Gut-residing segmented filamentous bacteria drive autoimmune arthritis via T helper 17 cells. *Immunity, 32*(6), 815-827. doi:10.1016/j.immuni.2010.06.001

Xu, C. J., Scheltema, N. M., Qi, C., Vedder, R., Klein, L. B. C., Nibbelke, E. E., . . . Koppelman, G. H. (2021). Infant RSV immunoprophylaxis changes nasal epithelial DNA methylation at 6 years of age. *Pediatr Pulmonol, 56*(12), 3822-3831. doi:10.1002/ppul.25643

Yoon, J. J., Toots, M., Lee, S., Lee, M. E., Ludeke, B., Luczo, J. M., . . . Plemper, R. K. (2018). Orally Efficacious Broad-Spectrum Ribonucleoside Analog Inhibitor of Influenza and Respiratory Syncytial Viruses. *Antimicrob Agents Chemother, 62*(8). doi:10.1128/aac.00766-18

Young, M., & Smitherman, L. (2021). Socioeconomic Impact of RSV Hospitalization. *Infect Dis Ther, 10*(Suppl 1), 35-45. doi:10.1007/s40121-020-00390-7

Yu, J., Liu, C., Xiao, Y., Xiang, Z., Zhou, H., Chen, L., . . . Wang, J. (2019). Respiratory Syncytial Virus Seasonality, Beijing, China, 2007-2015. *Emerg Infect Dis, 25*(6), 1127-1135. doi:10.3201/eid2506.180532

Zhang, H., Hale, B. G., Xu, K., & Sun, B. (2013). Viral and host factors required for avian H5N1 influenza A virus replication in mammalian cells. *Viruses, 5*(6), 1431-1446. doi:10.3390/v5061431

Zheng, J., Wong, L. R., Li, K., Verma, A. K., Ortiz, M. E., Wohlford-Lenane, C., . . . Perlman, S. (2021). COVID-19 treatments and pathogenesis including anosmia in K18-hACE2 mice. *Nature, 589*(7843), 603-607. doi:10.1038/s41586-020-2943-z

VITAE

Education

- Doctor of Philosophy (December 2023): Translational Biomedical Sciences; Georgia State University; Atlanta, USA
- Master of Science (2019): Molecular Medicine; University of Tuebingen; Tuebingen, Germany
- Bachelor of Science (2018): Molecular Medicine; University of Tuebingen; Tuebingen, Germany

Research Experience

- Graduate Research Assistant: Institute for Biomedical Sciences; Aug. 2019 – present; Georgia State University
- Graduate Research Assistant: Atriva Therapeutics; Apr. 2019 – Aug. 2019; University of Tuebingen
- Graduate Theme-Based Molecular Immunology Lab; Mar. 2019 – Sept. 2019; University of Tuebingen
- Graduate Research Assistant: Institute for Clinical Epidemiology and Applied Biometry; University of Tuebingen; Jan. 2018 – Mar. 2019
- Graduate Theme-Based Molecular Oncology Lab; Dec. 2018 – Jan. 2019; University of Tuebingen
- Graduate Theme-Based Molecular Immunology Lab; Oct. 2018 – Nov. 2018; University of Tuebingen
- Corporate-oriented internship at Atriva Therapeutics; Jun. 2018 – Aug. 2018; Atriva Therapeutics
- Internship at Criminal Investigation Department; Jul. 2018; Department of Criminal Investigation
- Undergraduate Theme-Based Molecular Bioscience Lab; Sept. 2016 – Jun. 2017; Newcastle University
- Undergraduate Theme-Based Molecular Bioscience Lab; Oct. 2014 – Jun. 2018; University of Tuebingen

Presentations/Conventions/Conferences

- Antiviral Countermeasures Development Center Retreat; Oct. 2023; Emory University – Atlanta
- American Society for Virology Conference; Jul. 2023; University of Georgia – Athens
- American Society for Virology Conference; Jul. 2022; University of Wisconsin – Madison
- Measles Virus Mini Symposium; Jul. 2022; Mayo Clinic
- Biotechnology Innovation Organization Convention; Jun. 2020; BIO Digital Week
- American Society for Virology Conference; Jun. 2020; Colorado State University (meeting canceled due to COVID-19 pandemic)

Professional Organizations

- American Society for Virology (ASV)
- Biotechnology Innovation Organization (BIO)
- German Chemistry Community
- German Agriculture Community

Awards

- Rosalind Franklin Society Award (2023)
- American Society for Virology Student Travel Award (2023)
- Georgia State University Dissertation Grant Proposal Award (2022)
- American Society for Virology Student Travel Award (2022)
- American Society for Virology Student Travel Award (2021) – meeting cancelled due to Covid-19 pandemic
- Erasmus award, promotion for the research year at Newcastle University (2016)
- Chemistry Award of German Chemistry Community (2014)
- Agriculture Award of German Agriculture Community (2014)
- Price of School – Award received for one of the three highest academic standings (2014)